RICE UNIVERSITY

Analysis of Passive Radiation Shielding from Galactic Cosmic Rays in Cis-Lunar Space

by

David Warden

A Thesis Submitted
in Partial Fulfillment of the
Requirements for the Degree

Doctor of Philosophy

Approved, Thesis Committee:

Yildiz Bayazitoglu, Chair
H. S. Cameron Chair Professor in
Mechanical Engineering and Professor of
Materials Science and NanoEngineering

David Alexander OBE
Professor of Physics and Astronomy
Director, Rice Space Institute

Laura Schaefer
Burton J. and Ann M. McMurtry Chair
and Professor, and Department Chair,
Mechanical Engineering Department

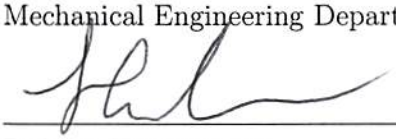

Pedram Hassanzadeh
Assistant Professor of Mechanical
Engineering

Houston, Texas
April, 2019

Life is not about finding yourself;

it's about creating yourself.

—Bob Dylan, Nobel Laureate in Literature, 2016

Ite, inflammate omnia!

—Ignacio López de Loyola, Soldier & Saint, 1541

Acknowledgments

I wish to thank my wife Lucia, four children, four grandchildren, and friends for their support and extreme patience during this educational process. Utmost thanks goes to my advisor, Dr. Yildez Bayazitoglu, for being brave enough to take me on as a student in the first instance, and for her support and attention throughout. My committee members deserve a special thanks: Dr. David Alexander for his many creative insights from the perspective of physics; Dr. Laura Schaefer for her many perceptive suggestions for the thesis text; and Dr. Pedram Hassanzadeh for his clear and calm advice on many topics. I also want to thank Dr. Pol Spanos for his mentoring over the years.

—David Warden

ABSTRACT

Analysis of Passive Radiation Shielding
from Galactic Cosmic Rays in Cis-Lunar Space

by

David Warden

Adequate long-term radiation protection protocols do not yet exist for the contemplated spaceflights beyond the Earth's magnetosphere or for colonization of places like the Moon and Mars. These destinations subject humans and equipment to long-term radiation exposure hazards, primarily by Galactic Cosmic Rays (GCR).

Using currently available radiation shielding regimes, scientists have made educated guesses that astronauts could survive a spaceflight to Mars or an asteroid, but the cost to human health may well be a markedly increased risk of a variety of health hazards, many of which can be fatal. Long-term colonization of places like the Moon or Mars require better radiation shielding protocols, and medical countermeasures.

This thesis first examines the relevant radiation environments for the contemplated human spaceflights, then presents a discussion of the physics and governing equations for radiation transport through materials, and thereafter examines the current state-of–the-art for passive and active radiation protection materials and designs for spacecraft.

Our research has developed a new radiation shielding evaluation method that calibrates the evaluation model with actual radiation exposure data from the International Space Station (ISS), to provide more accurate assessment of radiation

shielding requirements for operations in cis-lunar space, and to establish an empirical link to the medical histories of the ISS astronauts to better assess long-term radiation exposure hazards. The new method is used to evaluate the effectiveness of various materials and shielding designs for passive radiation shielding from GCRs for spacecraft and space habitats, and it is shown to significantly reduce the uncertainty in determining the mass of shielding material required to obtain acceptable exposure levels. The results indicate that newly-developed hydrogen-rich nanomaterials provide increased radiation protection effectiveness, and that further improvements to shielding effectiveness can be achieved by utilizing materials in multilayer configurations. Finally, we introduce a new mechanism for radiation shielding for future study that uses the wave-like behavior of the most harmful GCR-induced radiation species to passively effect diffraction and/or reflection, and thereby potentially reduced radiation exposure.

Contents

Abstract iii

List of Figures viii

List of Tables xix

Nomenclature xxiii

1 Framing the Problem 1

1.1 The Unsolved Problem of Radiation Protection 2

1.2 Motivation for this Research 4

1.3 Overview of Current Solutions 5

1.4 Summary of Research Results for GCR Shielding 7

2 The Radiation Environment in Cis-Lunar Space 16

2.1 The Sources of Radiation 18

2.2 The Focus on Galactic Cosmic Rays 25

2.3 Evaluating Human Hazards from GCR Radiation 32

2.4 Evaluating Equipment Hazards from GCR Radiation 42

3 Overview of the Physics of Radiation Shielding 44

3.1 GCR Radiation Interaction with Materials 46

3.2 Stopping Power and Linear Energy Transfer 51

3.3 GCR Ion Range in Shielding Materials 61

3.4 Secondary Particle Generation 69

3.5 Design Process for Evaluating Shielding Effectiveness 77

4 Governing Equations and Methods to Analyze Radiation Transport in Shielding Materials 81

4.1 The Deterministic Approach 82

4.2 The Monte Carlo Simulation Approach 91

4.3 Boundary Conditions and Verification 96

4.3.1 The Galactic Cosmic Ray Models 96

4.3.2 Verification of HZETRN and MULASSIS 100

4.3.3 Radiation Shielding Evaluation Framework 104

5 State-of-the-Art for Radiation Shielding in the Cis-Lunar Space Environment 112

5.1 Passive versus Active Shielding Approaches 113

5.2 State-of-the-Art in Evaluating Shielding Materials 118

5.3 Review and Limitations of Experimental Analyses 128

6 Evaluation of GCR Radiation Shielding Effectiveness – New Methods and Materials 132

6.1 A Proposed New Metric for Evaluating GCR Shielding 133

6.2 Calibration Calculations on Standard Materials 156

6.3 Analysis of Multilayered Shielding Designs 173

6.4 Analysis of a New Material for GCR Shielding: PBN+H 177

6.5 Dimensionless Evaluation Parameters for GCR Shielding 182

6.6 Potential Practical GCR Radiation Shielding Designs 188

7 Sensitivity and Uncertainty Analysis 200

7.1 The Galactic Cosmic Ray Models 201

7.2 The Radiation Transport Models 215

7.2.1 The HZETRN Radiation Transport Code 216

7.2.2 The MULASSIS Monte Carlo Code 238
7.3 The Biological Assessment Models 252
7.4 Summary of the Total Uncertainty Analysis 259

8 Future Study: Ion Particle Wave Diffraction 262
8.1 Wave Behavior of Particle Radiation 263
8.2 Matter-Wave Diffraction of GCR Ions 272
8.3 Matter-Wave Considerations for GCR Shielding 281

9 Conclusion 286

Appendices 294

A Key Equations 295
A.1 Lorentz Factor Derivation 295
A.2 Elastic Collision Energy Loss Derivation 300
A.3 Ion Stopping Power Derivation 304
A.4 Boltzmann Equation Application to GCR Ion Transport 311
A.5 NASA HZETRN Ion Transport Numerical Algorithm 321

B Simulation and Calculation Data 339
B.1 OLTARIS Data for GCR Radiation in Cis-Lunar Space 339
B.2 OLTARIS Data for Radiation at ISS Orbit 342
B.3 OLTARIS Data: Dose and Dose Equivalent Calculations 345
B.4 OLTARIS Dose Equivalent Calibration Calculations 348
B.5 MULASSIS Representative Data 350

Bibliography 354

Figures

2.1 Comparative Radiation Environments: LEO and Cis-lunar. From J. Norbury, NASA Langley, adapted from Wikipedia 2014. 17

2.2 Sources of Space Radiation. From Benton, 2001. 18

2.3 Solar Particle Events Correlated with Sunspot Cycle. 20

2.4 Galactic Cosmic Ray pathway from source to Earth. Simpson,(1983). 23

2.5 Relative Composition and Flux of Galactic Cosmic Rays. From T. Slaba, Radiation Transport Methods, NASA, 2015. 26

2.6 Comparative Shielding Thickness from Space Radiation Risks in Terms of "Areal Density." Adapted from J. Norbury, Space Radiation, NASA Langley, 2015; Koontz, Spaceflight Ionization Radiation Environments, NASA, 2017. 28

2.7 Full GCR Spectrum and Effect of Earth's Magnetosphere. 29

2.8 GCR Induced Secondary Radiation in the Atmosphere. 30

2.9 GCR Impact is a Function of Ion Species and Energy. 34

2.10 Comparison of GCR Biological Harm Models using Radiation (w_R) and Tissue (w_T) Weighting Factors, and Quality Factors (Q), for two Different Harm Assessment Models, ICRP-60 and ICRP-103. From Durante, 2011. 36

2.11 Dose Equivalent behind different shielding materials of varying areal density from a One-Year exposure to the Cis-lunar GCR radiation during the 1977 solar minimum, comparing ICRP-103 and ICRP-60 biological assessment factors. 37

2.12 GCR Radiation Risk to Humans: Flux, Absorbed Dose, and Dose Equivalent Exposures. From J. Chancellor, Texas A&M (2016), adapted from Durante, 2011 (Figure 5). 39
2.13 Comparative Human Radiation Dose Equivalent Exposure Levels. From Norbury, 2015. 40
2.14 Equipment Hazards from Space Radiation. From Mazur, 2007. 43

3.1 Primary GCR Interaction with Target Material. Adapted from Wikipedia images and Slaba, 2015. 47
3.2 Comparison of Particle Ionization Tracks in Nuclear Emulsions and Human Cells, showing the Physical Damage. From Cucinotta, 2013. . 48
3.3 GCR Nuclear Destruction Scenarios. From Slaba, 2015 and Durante, 2011, respectively. 49
3.4 Comparision of Electronic and Nuclear Contributions to Mass Stopping Power. Calculated using the NIST PSTAR program. *See* Berger, 2002. 59
3.5 Total Mass Stopping Power of an Incident Proton in Various Materials. Calculated using the NIST PSTAR program. *See* Berger, 2002. 60
3.6 Proton Range in Aluminum (red line), showing energy required to penetrate 5 gm/cm^2 (blue line) and 20 gm/cm^2 (yellow line). From Durante, 2014. 62
3.7 Range of Ions in Water. From Brookhaven National Laboratory Technical Data Files: https://www.bnl.gov. 63
3.8 Linear Energy Transfer (LET) of Proton and Iron ions as a Function of Depth in High Density Polyethylene (HDPE). From Brookhaven National Laboratory Technical Data Files: https://www.bnl.gov. . . . 65

3.9 Range of a 1 GeV Proton in Polyethelene (HDPE) and Aluminum. Calculated using NIST PSTAR program. *See* Berger, 2002. 67
3.10 Bragg Peaks of Energy Loss from Ionizing Radiation as a Function of Depth in Human Tissue (a), and in Various Other Materials (b). From J. Chancellor, 2015, Texas A&M Lecture Notes and Durante, 2014, respectively. 68
3.11 Transport of Primary GCR and Secondary Emissions in Spacecraft. From Benton, 2011. 71

4.1 Radiation Transport Model. From Slaba, 2015. 85
4.2 One Dimensional Linear Steady-State Boltzmann Equation for GCR Transport in a Target Medium. Adapted from Slaba, 2015. 88
4.3 HZETRN Raditaion Transport Code Implemented in OLTARIS. . . . 89
4.4 Overview of Monte Carlo Radiation Transport Simulations. Adapted from Slaba, 2015. 93
4.5 GCR Flux at the Heliosphere Boundary (solid lines), and at 1 AU during Solar Minimum (a) and Maximum (b) Conditions (dashed lines). From Slaba, 2015. 98
4.6 Comparison of Various GCR Models. From Mrigakshi, 2013. 99
4.7 Framework for Radiation Shielding Evaluation. From Slaba, 2015. . . 104
4.8 GCR Flux at 1 AU at Solar Minimum used as Input Boundary Conditions for (a) Badhwar-O'Neill 2010 Model and (b) MULASSIS. From Mrigakshi, 2012 and CREME96 Input File, adapted from Bernabeu, 2007. 105
4.9 Geometry Model for Shielding Evaluation. 107
4.10 Convergence Analysis with MULASSIS for Aluminum Shielding with Incident GCR Radiation. 111

5.1 Long-held Views on Possible Active Radiation Protection Schemes. From von Braun, 1969; Choutko & Ting, 2008 (photo at Rice's Baker Institute, 2013). 114
5.2 Heavy Lift Launches Required for Protection with Passive Shielding. From Westover, 2012. 115
5.3 Lunar Habitat Concepts: Lunar Regolith, Burial, and Lava Tubes. Adapted from De Angelis, 2002 and Schneider, 2010 117
5.4 Passive Shielding Material Evaluations using HZETRN from 2001-2014. Figure (a) from Wilson, 2001, Figure (b) from Durant, 2014. 118
5.5 GCR Stopping Range in Various Materials. From Wilson, 1997. . . . 120
5.6 Passive Shielding Evaluation of Some New and Proposed Materials. From Thibeault, 2015. 122
5.7 Mult-layer so-called "Graded-Z" Concept Models. Figure (a) from Truscott, 2010, and Figure (b) from Emmanuel, 2015. 124
5.8 Passive Shielding Evaluation for Three Different GCR Environments: Free Space at 1 *AU*, Lunar Surface, and Mars Surface. From Durante, 2014 (solid lines for 1977 solar minimum; dashed lines for 1990 solar maximum). 126
5.9 Shielding Evaluation Models for Lunar Surface Habitats. From Kuznetsov, 2012, and Jia, 2010. 127

6.1 Differential GCR Flux at 1 *AU* in Free Space – No Shielding. 134
6.2 GCR Flux of All Ions of Selected Energy Levels at 1 *AU* in Free Space. 136
6.3 Shielding Effect of Magnetosphere on Free-Space GCR Ion Penetration. Figure (a) is from Matthiä, 2009, and Figure (b) is from Aguilar, 2002. 140

6.4 Average Annualized Radiation Environment in the ISS Orbit at an Altitude of 400 kms (orbit tracking between 51.6^0 North and South Latitudes). 145
6.5 Differential GCR Flux Comparison for Hydrogen Ions at 1 AU and at ISS in Free Space – No Shielding. 146
6.6 Calculations of Dose (top graph) and Dose Equivalent (bottom graph) in Aluminum Shielding in the Cis-Lunar and ISS Orbit Radiation Environments. 151
6.7 Comparison of Particle Contribution to Dose Equivalent from Primary GCR at 1 AU and ISS as a function of depth in Aluminum Shielding. 153
6.8 Total Particle Contribution to Dose Equivalent from Primary GCR and Trapped Protons and Albedo Neutrons at the ISS Orbit as a function of depth in Aluminum Shielding. 154
6.9 Calculations of Dose Equivalent behind Aluminum Shielding and Liquid Hydrogen Shielding in Cis-Lunar Space as Compared to the Baseline of Aluminum Shielding in the ISS Orbit Radiation Environment. 158
6.10 Comparison Calculations of Dose Equivalent behind Various Shielding Materials in Cis-Lunar Space (HZETRN, BON2010 at 2010 Solar Min & ICRP-60). 159
6.11 Dose Equivalent Behind Shielding Materials in 1 AU Radiation Environment at Various Physical Thicknesses (expanding the shallow depth in (a)). 162
6.12 Dose Equivalent Behind Shielding Materials in 1 AU Radiation Environment: (a) our research, (b) Bernabeu, 2007 (MULASSIS with ICRP-60). 164
6.13 Secondary Neutrons from Primary GCR Protons 168

6.14 Secondary Neutrons from Primary GCR Helium Ions 169
6.15 Secondary Neutrons from Primary GCR Iron Ions 170
6.16 Fluence of Neutrons Produced by GCR Hydrogen Ions behind Various Shielding Materials of Various Thicknesses (MULASSIS Run Data). . 171
6.17 Fluence of Neutrons Produced by Full GCR Spectrum behind Various Shielding Materials of Various Thicknesses (HZETRN Run Data). . . 172
6.18 Annual Dose Equivalent for Different Materials of Varying Areal Densities with CREME96 GCR, 1977 Solar Minimum GCR, ICRP-103 Weighting Factors, and using the MULASSIS Monte Carlo Approach. 174
6.19 Dose Equivalent Evaluations for Multi-layered Shielding with Polyethylene, Aluminum and Boron Nitride plus Hydrogen 5% by Weight Combinations (MULASSIS with ICRP-103). 175
6.20 Comparative Dose Equivalent Results for a Multilayer Al-HDPE Shielding the 2010 BON GCR Model, 2010 Solar Minimum, ICRP-60 Weighting Factors, and using the OLTARIS (HZETRN) Approach. . 177
6.21 Rice University's New Proposed Nano-Structures for Hydrogen Storage. 178
6.22 Radiation Shielding Effectiveness of PBN Structures. 180
6.23 NISS Number as a Function of Areal Density. 186
6.24 NISS Number as a Function of Physical Thickness. 187
6.25 Basic Configurations for Alternative Spacecraft Shielding Designs. . . 189
6.26 Comparative Analysis of Five Spacecraft Shielding Designs. 190
6.27 Comparative Analysis of Two Spacecraft Shielding Designs Operating in 1 AU Radiation Environment, and Standard Aluminum Operating in 1 AU and ISS Orbit Radiation Environments. 191
6.28 Comparative NISS Number Analysis of Two Spacecraft Shielding Designs and Standard Aluminum. 193

6.29 Comparative GCR Induced Radiation Exposure Levels Behind Various Shielding Materials in the 1 AU, Lunar and Martian Radiation Environments. From Durante, 2014. 197

7.1 GCR Flux for Hydrogen, Helium, and Iron Ions generated by the 2010 Badhwar-O'Neill model for input to HZETRN (Solid lines for 2010 Solar Minimum; Dashed lines for 2001 Solar Maximum.) 203

7.2 Dose Equivalent Comparison behind Aluminum and Polyethylene Shielding Material, as between 2010 Solar Minimum (solid lines) and 2001 Solar Maximum (dashed lines) – BON2010 GCR Model, with ICRP-60 Biological Weighting Factors. 204

7.3 GCR Flux for Hydrogen and Helium ions generated by Three Models: 2010 Badhwar-O'Neill, 2013 Matthia, and 2016 SINP (all at 2010 Solar Minimum). 206

7.4 (a) GCR Flux for Iron ion generated by Three Different Models: 2010 Badhwar-O'Neill, 2013 Matthia, and 2016 SINP (all at 2010 Solar Minimum); and (b) Comparison between Badhwar-O'Neill (BON) 2014 and Badhwar-O'Neill (BON) 2010 GCR Models (both at 2010 Solar Minimum), for H, He, and Fe Ions. 207

7.5 Dose Equivalent Comparison behind Aluminum Shielding Material, as between 2010 Badhwar-O'Neill, 2013 Matthia, 2016 SINP GCR, and 2014 Badhwar-O'Neill Models (all at 2010 Solar Minimum), with ICRP-60 Weighting Factors. 208

7.6 Absolute relative flux as a percentage between AMS data and various GCR models, including Badhwar-O'Neill (BON) 2014, Matthia 2013 (denoted as "DLR"), and SINP 2016. From Norbury (2018). 212

7.7 GCR Flux Comparison between 2010 Badhwar-O'Neill and CREME96 Models, at 2010 and 1997 solar minimum, respectively. . . 213

7.8 Comparison of Dose Equivalent Results at interior points as Target Material Depth (Thickness) is varied, using HZETRN, Badhwar-O'Neill (BON) 2010 GCR Model (at 2010 Solar Minimum), and ICRP-60. 230
7.9 Calculated Dose Equivalent exposure rate changes at interior points as a function of total shielding thickness (using HZETRN with aluminum slab geometry and 2010 Badhwar-O'Neill GCR Model at 2010 Solar Minimum). 232
7.10 Neutron flux at particular interior points as a function of total shielding thickness (using HZETRN with aluminum slab geometry and 2010 Badhwar-O'Neill GCR Model at 2010 Solar Minimum in 1 *AU* environment). 235
7.11 Calculated Dose Equivalent exposure rate changes at particular interior points as a function of total shielding thickness (using HZETRN with aluminum slab geometry and 2010 Badhwar-O'Neill GCR Model at 2010 Solar Minimum in 1 *AU* environment). 236
7.12 Comparison of Dose Equivalent Results as between MULASSIS with the CREME96 GCR model (at 1977 solar minimum) and HZETRN with the Badhwar-O'Neill 2010 GCR Model (at 2010 Solar Minimum), and both using ICRP-60. 243
7.13 Calculated Dose Equivalent exposure rates comparing MULASSIS with HZETRN using the same aluminum slab geometry and same GCR Model: 2010 Badhwar-O'Neill (at 2010 Solar Minimum). 244
7.14 (a) GCR Ion Contribution to Total Dose Equivalent exposure rates comparing MULASSIS with HZETRN with an aluminum slab geometry (2010 Badhwar-O'Neill (at 2010 Solar Minimum), and ICRP-60); (b) Range of Ions in Aluminum as a Function of Kinetic Energy, from Wilson, et al. (2005). 247

7.15 Dose Equivalent Comparison behind Aluminum Shielding Material for 1 *AU* and ISS Orbit Radiation Environments, using 2010 Badhwar-O'Neill GCR Model (at both "solar min and max") with ICRP-60 Biological Weighting Factors. 255

7.16 Calculated Dose Equivalent Variation as a Function of Radiation Environment Total Spectrum Energy, for 1 *AU* and ISS Orbit, using 2010 Badhwar-O'Neill GCR Model with ICRP-60 Biological Weighting Factors. 257

8.1 Fondation et Institut Louis de Broglie, and Participants at Fifth Solvay Conference on Physics in 1927, at Brussels, Belgium. 267

8.2 Calculated de Broglie Wavelengths of Various GCR Particles at 1 *AU* Environment, and for Trapped Protons and Albedo Neutrons in ISS Orbit (2010 Badhwar-O'Neill Model at 2010 Solar Minimum). 275

8.3 Particle Flux of Neutrons and Iron resulting from GCR Radiation at the Orbit of the International Space Station, assuming 20 gm/cm^2 Equivalent of Aluminum Shielding (2010 Badhwar-O'Neill GCR Model, at 2010 Solar Minimum). 277

8.4 Calculated de Broglie Wavelengths of Neutrons and Protons at ISS Orbit, overlaid on the Calculated de Broglie Wavelength of GCR Protons at 1 *AU* (2010 Badhwar-O'Neill GCR Model, at 2010 Solar Minimum). 278

9.1 Results Summary for Improved Radiation Shielding Evaluation. . . . 292

A.1 Light clock at rest (a) and moving (b). From J.-M. Lévy; American Journal of Physics 2007, 75, 615-618. 296

A.2 Rest inertial frame S and moving inertial frame S′ with a relative velocity v, with the respective coordinates of a single Event being (t, x, y, z) and (t', x', y', z'). Adapted from W. Rindler, Introduction to Special Relativity, 2d Ed. 1991. 297

A.3 Two-Dimensional Elastic Collision Scenario. Adapted from Class Notes, MECH 592 & PHYS 541, Rice University. 301

A.4 Stopping Power of Ion-Electron Interaction in Target Medium. From Lecture Notes, MECH 592 & PHYS 541, Rice University. 304

A.5 Transport of Particles through a Spherical Region. From Wilson, 1991. 311

A.6 Comparison of Scaled Proton Range, r/ν_j, and actual ^{4}He range, r_j as a function of ion energy (MeV/n), as provided by Dr. Tony Slaba of NASA's Langley Research Center (TP-216213). 326

A.7 HZETRN Light Particle Transport Procedure implemented in OLTARIS, as provided by Dr. Tony Slaba of NASA's Langley Research Center (TP-216213). 333

B.1 Isotopes Available in OLTARIS. *See* Singleterry, 2011. 340

B.2 Sample GCR Flux Data at 1 AU for Hydrogen and Iron Ions. 341

B.3 Sample GCR Flux Data at ISS Orbit for Hydrogen and Iron Ions. . . 343

B.4 Sample Flux Data at ISS Orbit for Van Allen Belt Trapped Protons and Secondary Albedo Neutrons. 344

B.5 Sample Dose and Dose Equivalent Calculations in Aluminum Slab at ISS Orbit and Cis-lunar Space. 346

B.6 Sample Dose and Dose Equivalent Calculations at Various Thickness Points in Aluminum Slab, at ISS Orbit and Cis-lunar Space, done Particle-by-Particle. 347

B.7 Sample Dose Equivalent Calculations for Various Materials at Physical Thickness Points for 1 *AU* GCR Cis-lunar Space Radiation Environment. 349
B.8 Sample Dose Equivalent Calculations using MULASSIS Monte Carlo Simulation for Various Materials for 1 *AU* GCR Cis-lunar Space Radiation Environment. 351
B.9 Fluence Data for Neutrons behind Aluminum – $10 gm/cm^2$. 352
B.10 Fluence Data for Neutrons behind Aluminum – $20 gm/cm^2$. 353

Tables

6.1 No Shielding Calculated Absorbed Dose and Dose Equivalent comparison for 1 AU and ISS Orbit – BON2010 GCR Model at 2010 Solar Min & ICRP-60. 147

6.2 Aluminum Shielding ($20 gm/cm^2$) Calculated Dose and Dose Equivalent for 1 AU and ISS Orbit – BON2010 GCR Model at 2010 Solar Min & ICRP-60. 148

6.3 Dose Equivalent behind Various Shielding Materials of 7.4 cm Thickness in 1 AU Radiation Environment in Cis-lunar Space. 163

6.4 Comparative Evaluation of Dose Equivalent Radiation Exposure in a 1 AU GCR Environment behind Various Shielding Materials, and as Compared to the Verified ISS Baseline Radiation Exposure. 181

6.5 Mass Stopping Power Number for Various GCR Shielding Materials. . 184

6.6 Shielding Design Materials and Areal Density Thickness (gm/cm^2). . 190

7.1 Total Calculated GCR Kinetic Energy and Resulting Calculated Dose Equivalent using HZETRN for BON2010, BON2014, Matthia 2013, and SINP 2016 GCR Models; and using MULASSIS for the CREME96 Model (at solar mins). 210

7.2 Comparison of percentage contribution to calculated dose equivalent as between three primary GCR ions for MULASSIS and HZETRN, at 20 gm/cm^2 depth in an aluminum target (using Badhwar-O'Neill BON2010 GCR Models at 2010 Solar Minimum and ICRP-60). 245

7.3 Total Calculated Kinetic Energy and Resulting Calculated Dose Equivalent for Various Radiation Environments at 1 AU and ISS Orbit, behind Aluminum shielding of 5 gm/cm^2 and 20 gm/cm^2 areal densities (Al-5 and Al-20), using HZETRN with Badhwar-O'Neill BON 2010, and ICRP-60. 256

8.1 Typical de Broglie Wavelengths for Various Primary and Secondary GCR Particles at Representative Kinetic Energy Levels. 279

Nomenclature

β	ratio of particle velocity to speed of light, $\frac{v}{c}$
γ	Lorentz factor $=\frac{1}{\sqrt{1-\beta^2}}$
$\phi_j(\mathbf{x}, \mathbf{\Omega}, E)$	steady-state ion flux density ($\left[\frac{particles}{cm^2-sr-s-Mev/n}\right]$)
ρ	shielding target density (g/cm^3)
σ	fragmentation cross section
A_P	atomic mass of projectile (g/mol)
A_T	atomic mass of target (g/mol)
AU	Astronomical Unit (1 $AU \approx 93$ million miles)
c	speed of light in vacuum ($\approx 2.9979 \times 10^8 m/s$)
$C(\beta)$	shell correction in Bethe-Bloch equation
c_1, c_2	semi-empirical terms employed in the Bradt-Peters equation
D	absorbed dose ($Grays$)
E	incident particle energy (MeV)
e	electron charge ($\approx 1.602 \times 10^{-19} Coulombs$)
eV	electron volt ($1eV = 1.6021766208 \times 10^{-19} Joules$ or $[\frac{kg-m^2}{s^2}]$)
H	dose equivalent ($Sieverts$)

h Planck's constant ($6.62607 \times 10^{-34} Joule - sec$)

I mean excitation energy (eV)

$L_1(\beta)$ Barkas correction to Bethe-Bloch equation

$L_2(\beta)$ Bloch term to Bethe-Bloch equation

$L_3(\beta)$ Mott and density corrections to Bethe-Bloch equation

m_0, m_n, m_e rest mass; e.g., of a nucleon or electron (g)

N_A Avogadro number ($\approx 6.022 \times 10^{23}/mol$)

r_0 nucleon radius used in Bradt-Peters equation

S stopping power (approximately equal to linear energy transfer, LET) (MeV/cm)

w_R radiation weighting factor

Z_p atomic number of projectile

Z_T atomic number of target

BON NASA's Badhwar-O'Niell GCR Model

CERN Conseil Européen pour la Recherche Nucléaire

CREME96 The Cosmic Ray Effects on Micro-Electronics (1996 Revision)

ESA The European Space Agency

GCR Galactic Cosmic Rays

GEANT4 The GEometry ANd Tracking toolkit

HZE High charge and high energy particles

HZETRN NASA's High Charge and Energy Transport Code

ICRP The International Commission on Radiological Protection

ISS International Space Station

LEO Low Earth Orbit

MULASSIS the Multi-Layered Shielding Simulation Software Code

NASA National Aeronautics and Space Administration

NCRP National Council on Radiation Protection and Measurements

OLTARIS NASA's On-Line Tool for the Assessment of Radiation in Space

SEU single event upset

SPE Solar Particle Events

@starttoclot

Chapter 1

Framing the Problem

"When the sun dies, the Earth will die and then everything we have done up to that moment will be lost: Homer will die, Michelangelo will die ... Galileo, Leonardo, Shakespeare, Einstein will all die from human memory. So let us save them, let us save ourselves ... and escape to continue life on other planets."
—Oriana Fallaci, Italian journalist, from her book *If the Sun Dies*, Atheneum, 1967 (1929-2006)

"It is in our nature to explore, to reach out into the unknown. The only true failure would be not to explore at all. By endurance we conquer."
—Sir Ernest Henry Shackleton CVO OBE FRGS, Anglo-Irish Antarctic polar explorer (1874-1922)

Though governments, politicians, and even some scientists, speak cavalierly these days of increasingly long and ambitious human spaceflight voyages into our solar system, many omit to mention the as yet unsolved problem of assuring adequate protection against the long-term radiation hazards, posed primarily by Galactic Cosmic Rays. Historically, most human spaceflight activities have taken place in Low Earth Orbit (LEO), where the radiation hazard is attenuated by the protection afforded by the Earth's magnetic field, which form the Van Allen belts of trapped radiation particles. Indeed, only 24 men have travelled outside that relatively protected zone – those that went to the Moon – and even then for only a very short period of time of less than a few weeks in duration. By contrast, in the space environment beyond LEO and the relative protection of the Earth's magnetosphere, both humans and equipment will be exposed to markedly increased radiation intensity, and making matters worse, the contemplated voyages will require exposure times of some three years – over 50-times as long as any previous human spaceflight outside LEO.

1.1 The Unsolved Problem of Radiation Protection

The hazardous radiation environment is one of the most critical issues required to be fully addressed for space missions. It is an inherently interdisciplinary endeavor, requiring, at a minimum, contributions from the fields of physics, engineering, materials science, mathematics, numerical analysis, biology and medicine.

The radiation encountered in the cis-lunar region of space beyond LEO results primarily from Solar Particle Events (SPE) and Galactic Cosmic Rays (GCR). The energy and species spectra of both radiation sources are well understood in the cis-lunar region — that region beyond the Earth's magnetosphere and in the vicinity of the Moon — and thus it serves as a good proxy for the radiation regimes to be encountered in the contemplated human space voyages. The sporadic, short duration of SPEs, and the improving predictability and generally lower energy [1], have allowed the development of adequate radiation shielding protocols. But, GCR radiation is a different matter: it is constant, isotropic, and contains high-energy species that cannot be adequately shielded by currently employed shielding regimes.

The problem posed by the prospect of deep-space exploration is simply stated: can humans and equipment be adequately protected from the radiation hazards in the cis-lunar region and beyond? The technical risk to making these ambitious spaceflights is not related to the hardware. The rockets and spacecraft exist, or are well within the contemplation of the current state-of-the-art. But the problem of protection from the unavoidable long-term radiation exposures has not been resolved.

Using currently available radiation shielding regimes, scientists have made educated guesses that astronauts could survive a spaceflight to Mars or an asteroid, but the cost to human health may well be a markedly increased risk of health hazards, including various forms of cancer, DNA damage, eyesight impairment, and cellular

destruction that could lead to a variety of other problems, including central nervous system and cognitive impairment. [2, 3] The biological assessment for space travel in the cis-lunar region is nascent, primarily because of the paucity of data on human subjects. [4] Only very recently, a study of the Apollo astronauts who went to the Moon concluded that even their short duration space travel outside the Earth's magnetosphere markedly increased the incidence of cardiovascular disease, as compared with astronauts who flew only in LEO. [5]

What is known with certainty is that the current radiation protection regimes do not completely shield the radiation spectrum encountered in GCR, and in some cases actually can be counter-productive and increase the hazard. Thus, while a contemplated space voyage of three-years in duration may be survivable, it is clear that long-term health degradation is likely to occur. As was reported by NASA scientists in 2005 in the AIAA: "Exposure from the hazards of severe space radiation in deep space long duration missions is 'the show stopper.'" [6] But since that proclamation the current standard spacecraft shielding – aluminum – has not changed, nor has there been any human medical data obtained as to long-term exposure hazards to GCR at 1 *AU*. More recently in 2018, scientists writing in *Nature* concluded: "Despite years of research, understanding of the space radiation environment and the risk it poses to long-duration astronauts remains limited. There is a disparity between research results and observed empirical effects seen in human astronaut crews, likely due to the numerous factors that limit terrestrial simulation of the complex space environment and extrapolation of human clinical consequences from varied animal models." [7] Obviously, multiple space voyages to, or colonization of, places like the Moon or Mars are simply pure fantasy without better radiation shielding protocols.

The research described in this thesis has developed new radiation shielding eval-

uation protocols, including tying the expected calculated biological harm to verified radiation exposure data from the International Space Station (ISS). The new metrics are used to evaluate the effectiveness of various materials and shielding designs for passive radiation shielding from GCRs for spacecraft and space habitats, using both deterministic and Monte Carlo techniques. The results indicate that newly-developed hydrogen-rich nanomaterials and hybrid nanostructures provide increased radiation protection, and that further improvements to shielding effectiveness can be achieved by utilizing these, along with other materials, in multilayer configurations. In addition, this research proposes a potential new area for future study regarding shielding design that takes advantage of the wave-like behavior of the most harmful GCR-induced radiation species, in order to passively effect diffraction and/or reflection of the incident radiation and thereby potentially create reduced radiation exposure.

1.2 Motivation for this Research

All research is personal at some level, and the work underlying this thesis is no exception. The problem arose during discussion of the possibility of storing live frozen cell lines of endangered and important species of life on the Moon; specifically, how to protect them from the harsh radiation environment long enough until they could be physically buried deep in the lunar regolith? Burial would afford a protection level equivalent to that on Earth, but the natural sequence of hardware capability called for a robotic landing of the payload on the surface of the Moon, and a number of years before the burial operation could be completed. Thus the need for an interim radiation protection scheme.

The idea is not a fantasy, but rather an extension of current activities on Earth whereby the frozen cell lines of thousands of important species are being collected

and stored in at least a dozen facilities around the world. But the cost of doing so is prohibitive for the long-term storage envisioned – 100s of years – as the cell lines must be stored at or below a temperature of 77 Kelvin, which, of course, does not occur naturally anywhere on Earth. But on the Moon there are places in permanently dark craters where the ambient temperature is sufficiently low that the cell lines could be stored passively, and doing so would be economically superior to Earth-based storage facilities for the time periods contemplated and more secure. However, the interim radiation protection issue must be addressed, but conveniently only with respect to the GCR, as an acceptable crater location – e.g., Shackleton Crater at the lunar south pole – never sees the Sun, and thus is not subjected to SPEs.

1.3 Overview of Current Solutions

Radiation is one of the most critical hazards that humans and equipment encounter in spaceflight missions. This is particularly so as spacefaring nations push their exploration interests to longer and deeper space voyages. Beyond LEO, without the protection afforded by the Earth's magnetic field, these contemplated ambitious space voyages will incur increased risks from radiation exposure, resulting in both increased health hazards and equipment degradation. Hence more efficient shielding materials and methods are necessary to help mitigate this radiation issue.

Shielding protocols from these radiation hazards have been an important design topic for decades. Passive shielding – i.e., a material barrier which is often also a structural component – has been employed thus far in spacecraft designs, and only modest improvements for better effectiveness have been made over the years. Active shielding of various kinds, generally using some kind of electrical or magnetic field, show some promise as an improved method, but are still fundamentally at only a

conceptual stage, and operationally and economically impractical. There are also active investigations of medical countermeasures that human space travelers could possibly employ, but these are still at the theoretical investigative stage and untested. The only other ways to avoid increased radiation exposure in long duration space flights are to increase one's distance from the radiation source (not possible for the isotropic GCR), or to decrease the time of exposure by travelling at much higher velocities (not possible at this time with currently available propulsion systems). [8]

Thus, passive shielding is currently the only viable operational solution path. Currently, aluminum is the most widely used passive shielding material for spacecrafts. Though structurally stable, aluminum is not theoretically as good a shielding material as materials with higher hydrogen content. It has been shown in recent research that elements with the largest charge-to-mass ratio appear to be the best shielding material against the "high atomic number and energy" (HZE) ions found in the GCR. [9] And in this regard, recent advancements in material science and nanoengineering, producing new materials for a variety of other purposes, have also inadvertently possibly provided some new potential radiation shielding materials. Indeed, several materials have been proposed which provide good hydrogen storage, and thus may be good candidates for shielding against GCR.

Multilayered shielding is another possible solution to the radiation issue, with each layer addressing a unique characteristic of the incoming space radiation. For example, a combination of aluminum and polyethylene is used by NASA in some test areas of the ISS [9], and adding water-filled bladders has also been considered. [10] Such dual-layered structures can have a better shielding effectiveness than a single aluminum layer of the same areal densities (gm/cm^2). [11] [12]

More effective shielding materials and shielding designs may be the most practi-

cal near-term solution to the deep space GCR radiation issue. New state-of-the-art materials and multilayered configurations have been studied with the up-to-date radiation transport codes in the research presented in this thesis in order to determine better fundamental shielding design criteria and to find possible candidates for more effective GCR shielding in spacecraft and space habitats.

1.4 Summary of Research Results for GCR Shielding

At a high level, the approach used in this research to analyze shielding for spacecraft operating in the 1 *AU* GCR radiation environment involved the following steps: modeling the appropriate GCR-induced radiation environment, simulating the radiation transport process in the shielding material, and measuring and evaluating the final impact of the radiation on the target. Each chapter of this thesis is summarized below, followed by a summary of the specific results from the research effort.

Summary of Chapters

In Chapter 1 the research problem is framed involving the need to find solutions for protecting astronauts from radiation exposure hazards outside LEO for the contemplated long-term missions to the Moon, Mars and the asteroids. A summary of the specific research results is also provided.

In Chapter 2 the radiation environment in cis-lunar space is identified, including an explanation of the sources of radiation and why the focus of this thesis is on Galactic Cosmic Rays. Also discussed is an introduction to the metrics used in measuring the human and equipment impact to the GCR radiation hazards, and our evaluation of the large error introduced into analyses by use of various radiation exposure metrics and biological assessment models, using the MULASSIS Monte Carlo code; which

results were recently published. [13]

Chapter 3 provides an overview of the physics involved in radiation shielding analyses. The energy loss mechanisms of particle radiation impacting materials are reviewed, with particular emphasis on the concepts of the stopping power of materials, the linear energy transfer in materials from the incident radiation, and the range of penetration of particle radiation into materials. In the process, secondary particle radiation generation by the incident radiation is introduced, along with a newly developed comprehensive ten-step design process to be used to evaluate GCR shielding effectiveness.

Chapter 4 introduces the governing equations for evaluating radiation transport in shielding materials, and shows how those general equations are simplified – as they must be – to provide both Monte Carlo simulation and analytically deterministic approaches. The Monte Carlo transport code used here is MULASSIS, which is based on the GEANT4 codes developed by CERN, while the deterministic code is OLTARIS, which is a derivative of the HZETRN code developed at NASA. In connection with the Monte Carlo simulation, a convergence study was first performed to verify that the most appropriate number of primary particles has been used in MULASSIS. The input boundary conditions to these models are also discussed, as well as verification efforts. For ease in making comparisons among the various materials and shielding designs examined, a uniform simulation geometry was used, composed of semi-infinite slabs made of different shielding materials, and a water phantom is employed to model the target — the human body tissue — and to capture and identify the radiation species exiting the shielding.

Chapter 5 presents a review of the state-of-the-art for radiation shielding in the cis-lunar space environment, including both passive and active shielding approaches and

particular problems regarding shielding for spacecraft and space habitats. In addition, recent analyses of standard shielding materials are reviewed, and the limitations of those analyses discussed, along with the constraints of actual experimental analyses.

Chapter 6 presents the major results of our research effort in regard to evaluating GCR shielding effectiveness. First, a new evaluation metric is introduced in order to correlate the calculated evaluation metrics at 1 *AU* and in the ISS orbit on a consistent basis, and then this "ISS Baseline" radiation exposure metric is verified with actual data. This new approach greatly reduces the uncertainty endemic to current methods of calculating radiation dose equivalent exposure rates behind shielding, and empirically ties the evaluation of shielding in the 1 *AU* GCR environment to the ISS astronaut medical data regarding long-term health risks.

Next, a series of calibration calculations are done to attempt to tie the modeled examination of various shielding materials used in this research to results of published studies, which effort (1) confirms the inconsistent application of the various radiation assessment models, and (2) illustrates that liquid hydrogen may be able to provide sufficient shielding in the 1 *AU* radiation environment to replicate the ISS Baseline radiation exposure level. As part of the calibration effort, it is suggested that a fluence analysis of the GCR ion spectrum behind shielding can be used to improve radiation shielding evaluation, a method of improved shielding evaluation we published a year ago. [14]

Next, new design protocols are introduced that include using various new and standard shielding materials in multilayer configurations in order to determine the best order to use materials to filter or block parts of the GCR particle radiation spectrum in such a way as to make succeeding layers more effective in blocking or attenuating the incident radiation that passes through the first layers. These analyses

are performed with both deterministic and Monte Carlo approaches.

Next, a new material developed by Rice University for the purpose of providing hydrogen storage for automobiles is examined as a potential superior GCR shielding material. It is a pillared boron nitride hybrid nanostructure that appears to have superior structural and shielding characteristics over standard spacecraft materials currently in use.

In addition, two dimensionless evaluation parameters are introduced to allow a relatively quick way to evaluate shielding materials and design effectiveness with respect to replicating the ISS radiation environment on spacecraft operating in the 1 *AU* cis-lunar space region. The Normalized International Space Station (NISS) number for evaluating shielding effectiveness was recently introduced in our recent publication. [13]

Finally, several practical shielding design protocols for spacecraft operating in the 1 *AU* cis-lunar radiation environment are investigated using the new shielding metrics. In addition, two *in situ* space habitat materials are proposed for use on the Moon and Mars, lunar regolith and Martian soil, respectively, and are evaluated at a high level, with reference to prior studies.

Chapter 7 presents an uncertainty analysis to better quantify the errors and uncertainties involved in the spacecraft shielding evaluation models, including the GCR models, the radiation transport codes, and the biological assessment models, and to demonstrate the utility of adding the proposed new ISS Baseline metric as a shielding evaluation tool.

Chapter 8 introduces an entirely new hypothetical approach to space radiation shielding design based on the wave-like characteristics of high velocity ion species found in the GCR, which cannot be stopped by conventional practical spacecraft

shielding protocols. An overview of the basic physics is presented and a hypotheses presented as to how certain materials may be utilized to take advantage of the ability to diffract and/or reflect certain radiation particles to potentially provide a radiation shielding advantage.

Finally, in Chapter 9 our research results are summarized and further research endeavors proposed.

Summary of Research Results

This research effort has produced the following specific results:

1. Though not a result per se, a distillation of the literature regarding analysis of radiation shielding for spacecraft by numerical, Monte Carlo simulation, and experimental means, and a summary of the current state-of-the-art for both spacecraft radiation shielding analysis and current practices and proposed approaches to solving the cis-lunar radiation exposure problem is presented. *See* Chapters 4 and 5.

2. A comprehensive step-by-step design protocol for evaluating spacecraft radiation shielding materials and designs was compiled, including a new ten-step design process for evaluating shielding effectiveness. *See* Chapter 3.

3. A critique of the current modeling efforts for evaluating GCR shielding effectiveness was done, and found that the current work produces absolute value exposure metrics that are not verified against actual human medical data, and that the models themselves are employed in inconsistent ways regarding GCR input boundary conditions, calculation techniques, and assessments of human impact, all of which induces multiple channels for error such that the results reported in the literature are inconsistent and difficult to assess on a comparable basis.

Specifically, an analysis of two commonly used radiation weighting factor models, ICRP-60 and ICRP-103, was done using the MULASSIS Monte Carlo simulation

code, and it was determined that the dose equivalent calculations varied by some 45% – a clearly unacceptably large variance. This work was reported in our AIAA Journal of Spacecraft and Rockets paper. [13] *See* Chapter 2.

Additionally, an analysis was conducted attempting to duplicate NASA published dose equivalent radiation exposure rates behind various thicknesses of aluminum, polyethylene, and a variety of other materials, and comparable "absolute value" results could not be obtained using the OLTARIS (HZETRN) deterministic code employed by NASA, though the calibration effort did produce the same trends in terms of the relative effectiveness of each material tested. This work was reported in our AIAA Journal of Spacecraft and Rockets paper. [13] *See* Section 6.2.

An analysis was also done to compare dose equivalent radiation exposure rates produced by the OLTARIS (HZETRN) deterministic code as compared to that for the MULASSIS Monte Carlo simulation code, for the same materials, and the Monte Carlo results were found to be almost half the numerical values for that particular metric. This work was reported in our AIAA Journal of Spacecraft and Rockets paper. [13] *See* Section 6.3.

4. A new GCR shielding evaluation metric is introduced in an attempt to minimize the errors induced by the various radiation impact models currently used to calculate dose equivalent and effective dose metrics, and which also empirically ties calculated evaluations of shielding in the 1 AU cis-lunar radiation environment to the voluminous astronaut medical data from those who have spent time on the International Space Station, in order to improve assessment of actual health risks due to long-term GCR radiation exposure provided by particular shielding protocols. The calculation of this new evaluation metric for the 1 AU environment is tied in a consistent way to a calculated model of the ISS Baseline radiation exposure inside the ISS, and that

model, in turn, is verified against actual radiation flux and exposure measurements taken on the ISS. This work was reported in our AIAA Journal of Spacecraft and Rockets paper. [13] *See* Section 6.1.

5. A series of comparative calibration calculations were performed on various standard shielding materials; and using the new evaluation metric it was determined that the use of liquid hydrogen as a shielding medium could potentially provide an interior radiation environment *less* hazardous than the ISS Baseline exposure rate for spacecraft operating in the cis-lunar space region. This work was reported in our AIAA Journal of Spacecraft and Rockets paper. [13] *See* Section 6.2.

6. A fluence analysis procedure is proposed as one way of by-passing the various errors introduced in calculating other shielding effectiveness metrics, such as dose equivalent, and for use as a tool to optimize multilayer shielding designs by introducing layers of specific materials to "tune" the flux of GCR particles and secondary emissions behind shielding. The early part of this research has been published in the AIAA Journal of Thermophysics and Heat Transfer [14], and the work presented here has been extended since that time. *See* Section 6.2.

7. A multilayer shielding design evaluation methodology is introduced as a way to optimize shielding performance, and was tested numerically on various combinations of aluminum and polyethylene in which it was determined that the order of layering makes a difference in overall shielding effectiveness. The early part of this research has been published in the AIAA Journal of Thermophysics and Heat Transfer [14], and the work presented here has been extended since that time. *See* Section 6.3.

8. Two dimensionless parameters are introduced for (1) quickly evaluating GCR radiation shielding effectiveness (the MSP number), and (2) allowing quick comparison of a particular shielding protocol with the ISS Baseline radiation exposure metric

(the NISS number). The NISS number was introduced in our AIAA Journal of Spacecraft and Rockets paper. [13] *See* Section 6.5.

9. A newly developed nanoscale material developed by others at Rice University to fabricate a hydrogen fuel storage device for automobiles, called pillared boron nitride with infused hydrogen, was evaluated as a potential GCR radiation shielding material. We determined that such a material may potentially have sufficient structural rigidity to be used in fabricating spacecraft components, and has improved radiation effectiveness as good or better than polyethylene, thus potentially providing an improved GCR shielding material than is currently available. *See* Section 6.4.

10. Several practical radiation design problems are considered which show: (1) that it may be possible to get very close to replicating the ISS Baseline exposure level on spacecraft operating in cis-lunar space using multiple layers of standard materials (which evaluations are published in our AIAA Journal of Spacecraft and Rockets paper [13]); (2) that using lunar regolith of moderate thicknesses in the range of 15 *cms* will shield a habitat on the surface of the Moon to the ISS Baseline standard; and (3) that the Mars surface radiation environment is approximately the same as the ISS Baseline exposure level, and that shielding habitats with Martian soil brick will improve the radiation situation. In both the case of the Moon or Mars, greater thicknesses of regolith/soil shielding could theoretically reduce the radiation exposure levels closer to those experienced on Earth. *See* Section 6.6.

11. An uncertainty analysis was undertaken to better quantify the errors and uncertainties involved in the spacecraft shielding evaluation models, including the GCR models, the radiation transport codes, and the biological assessment models. As part of this effort, the major reasons for the large discrepancies between HZETRN and MULASSIS GCR evaluation results were determined, and the effect of the en-

hancement to HZETRN to account for back-scatter neutrons on interior shielding radiation intensity was evaluated. In addition, the new "ISS Baseline" evaluation metric developed in this research was found to reduce uncertainties in the dose equivalent radiation exposure estimates to the range of 5%, if the objective of the shielding design is to replicate the ISS radiation environment for spacecraft operating in cis-lunar space at 1 AU, which allows a more accurate determination of required shielding mass for spacecraft intended to operate in the cis-lunar region. *See* Chapter 7.

12. The de Broglie matter-wave wavelengths are calculated for various GCR radiation primary ions and secondary emissions at representative average kinetic energy levels in several space radiation environments of interest: 1 AU, low Earth orbit in the specific orbit of the International Space Station, and inside the ISS itself. The possibility of developing new materials for shielding protocols that might take advantage of the diffraction and/or reflection of certain GCR radiation species is introduced as a possible future research endeavor for an appropriate team. *See* Chapter 8.

Chapter 2

The Radiation Environment in Cis-Lunar Space

"We choose to go to the moon in this decade and do the other things, not because they are easy, but because they are hard."
—John Fitzgerald Kennedy, 35th President of the United States, *Address at Rice University, September 12, 1962* (1917-1963)

"Nothing will stop us. The road to the stars is steep and dangerous. But we're not afraid . . . space flights can't be stopped. This isn't the work of one man or even a group of men. It is a historical process which mankind is carrying out in accordance with the natural laws of human development."
—Yuri A. Gagarin, first Soviet (Russian) cosmonaut and first person to orbit the Earth (1934-1968)

"If somebody'd said before the flight, 'Are you going to get carried away looking at the Earth from the Moon?' I would have said, 'No, no way.' But yet when I first looked back at the Earth, standing on the Moon, I cried."
—Alan B. Shepard Jr., first American astronaut (1923-1998)

The radiation environment in the vicinity of the Moon – in the so-called "cis-lunar space environment" – is well understood as a result of several probes in recent years specifically intent on actual measurements to test the modeling that had previously been relied upon. The Advanced Composition Explorer (ACE) was launched in 1997 to the Earth-Sun L_1 Lagrange point some 1.5 million kilometers from Earth, where it continues to measure energetic particles in the solar wind, SPEs and GCRs. [15] [16] [17] The Lunar Reconnaissance Orbiter (LRO) was launched in 2009, and continues to this day to measure the GCR in the cis-lunar region through its on board Cosmic Ray Telescope for the Effects of Radiation (CRaTER). [18] The Mars Science Laboratory (MSL) with the Curiosity Rover was launched in 2011 and landed on Mars in 2012, but during its 253 days of cruise it made important measurements of the GCR spectrum

between the Earth and Mars. [19]

As shown in Figure 2.1a, the Earth's magnetic field creates the Van Allen belts by trapping various energetic particles, which help shield the Earth and LEO from radiation, with the inner belt at approximately 18,000 km comprised primarily of protons and the outer belt at approximately 36,000 km comprised primarily of electrons. [20] In contrast, the region of space around the Moon noted in Figure 2.1b – some 400,000 km from the Earth – is beyond any natural protective mechanisms, and is subjected to the full unabated space radiation environment.

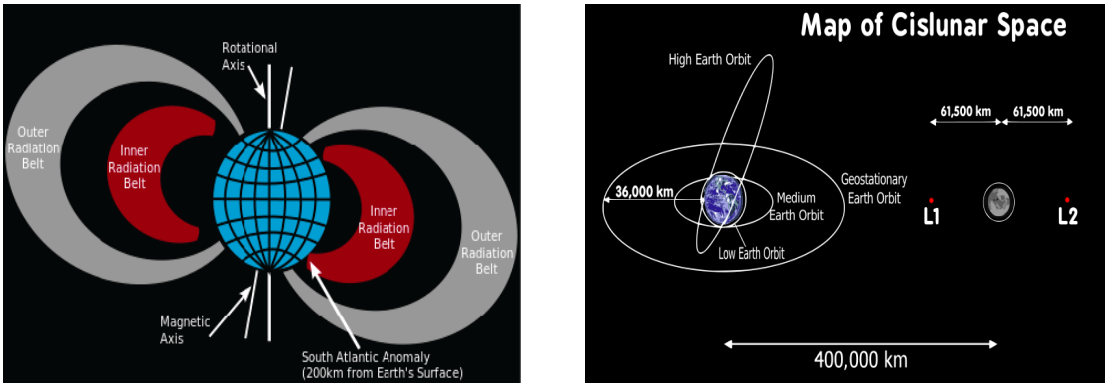

(a) Near-earth Radiation Environment (b) Cis-lunar Space Environment

Figure 2.1 : Comparative Radiation Environments: LEO and Cis-lunar. From J. Norbury, NASA Langley, adapted from Wikipedia 2014.

The GCR models have been appropriately updated and calibrated to the available actual data [21] [22], so that today there is little doubt about the general radiation environment in the cis-lunar region, and this serves as a good proxy for the radiation environment found in the regions where humans may travel in the near future – the Moon, Mars, and the asteroids. [1]

[1]Indeed, the actual GCR measurements have caused some scientists to begin to have doubts that the long duration spaceflights can be safely undertaken when the GCR is at its highest intensity. [23]

2.1 The Sources of Radiation

In the cis-lunar environment the sources of radiation are the Sun and the Galactic Cosmic Ray (GCR) radiation that comes from outside the solar system. As depicted in Figure 2.2, the Sun is a source for both electromagnetic radiation and energetic particle radiation. [8] [24]

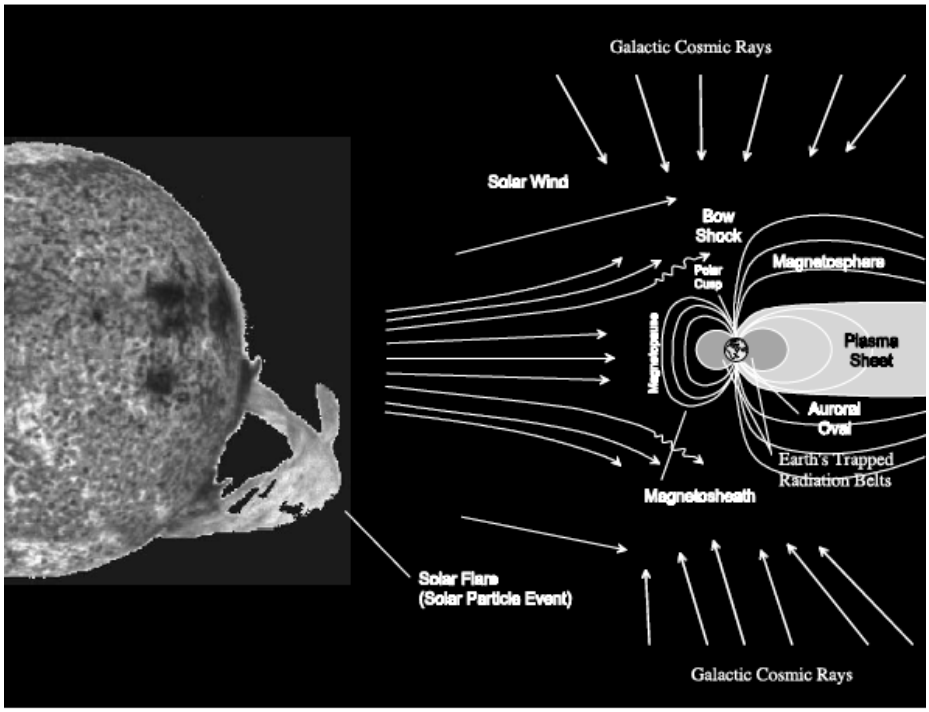

Figure 2.2 : Sources of Space Radiation. From Benton, 2001.

The Sun's electromagnetic radiation is carried by "massless" photons travelling at the speed of light, and radiates at all wavelengths as a black body at a temperature of 5780 K, with a radiant energy per unit surface area given by the Stefan-Boltzmann law, $E = \epsilon\sigma T^4$. The Stefan–Boltzmann constant derives from other known constants of nature, and has a value of $\sigma = \frac{2\pi^5 k^4}{15c^2h^3} = 5.670373 \times 10^{-8}\,\mathrm{W\,m^{-2}K^{-4}}$, where k is the Boltzmann constant, h is Planck's constant, and c is the speed of light in a

vacuum. The energy carried by the photons is solely a function of their wavelength, λ, and is calculated as follows: $E = \frac{hc}{\lambda}$. In accordance with Planck's law, which describes the spectral density of electromagnetic radiation emitted by a black body in thermal equilibrium at a given temperature (from which Wein's displacement law can be derived to determine λ_{max}), it is apparent that most of the Sun's electromagnetic radiation is easily shielded, as its electromagnetic energy is distributed at wavelengths approximately 43% in the visible light range, 37% in the infrared range, and 7% in the ultraviolet range. [25]

But the Sun is also the source of some relatively high energy particle radiation that needs to be considered in spaceflight operations, specifically the solar wind and Solar Particle Events (SPE). The solar wind is a relatively constant flow of charged particles from the Sun travelling at approximately 200-800 km/sec, consisting primarily of protons and electrons with energies in the range of 1.5-10 KeV/n (thousand electron volts per nucleon). While the solar wind is easily shielded and of little danger, not so SPEs which are charged particle eruptions from the Sun due to solar flares and coronal mass ejections. SPEs are primarily comprised of ions of hydrogen (protons) and helium, with some heavier ions, with energies in the range of 10-100 MeV/n (million electron volts per nucleon). Fortunately, our ability to predict SPEs is improving because the solar flare or coronal mass ejection can be observed [1], and are of relatively short duration as the flux of particles passes the cis-lunar area, usually on the order of several hours to less than week. [26] Nevertheless, SPEs can be exceedingly dangerous to humans and equipment because the number of particles can be very high – often four to eight orders of magnitude higher per event than the GCR flux on an annual basis; but, of course, the bulk of these particles carry lower kinetic energies. [27] However, workable shielding protocols exist for SPEs, where ade-

quate protection can be obtained behind slightly thicker standard shielding materials – so-called "storm shelter" safe places designed into a spacecraft or habitat. [28] [29]

Importantly, both the solar wind and SPEs are modulated in intensity and frequency, respectively, by the 22-year solar magnetic cycle and the 11-year sunspot cycle; i.e., the frequency with which there are increased numbers of sunspots on the Sun. [30] Sunspots are temporary cooler regions on the Sun, often visible as dark spots, induced by changes in the local magnetic field that inhibit convection and result in phenomenon that cause increased particle emissions. The increased solar activity associated with a higher number of sunspots causes a change in the interplanetary magnetic field carried by the solar wind and also correlates well with increased numbers of SPEs, as shown in Figure 2.3. Interestingly, while there are clearly more SPEs during peak sunspot periods, the intensity of individual SPEs does not necessarily diminish in the lower sunspot activity period, as can be seen in Figure 2.3b.

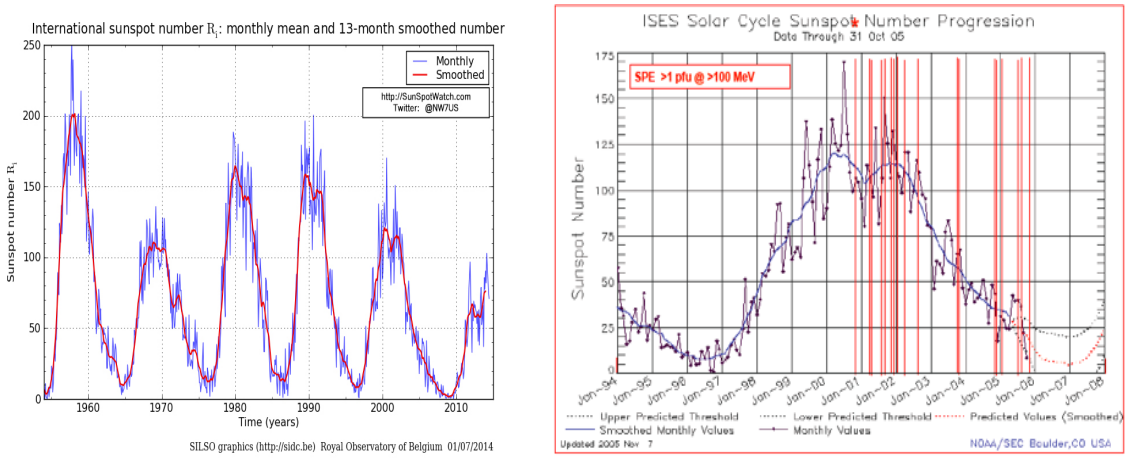

(a) Historical Eleven-Year Sunspot Cycle. (b) Correlation of SPEs with Sunspot Cycle.

Figure 2.3 : Solar Particle Events Correlated with Sunspot Cycle.

It is also instructive to note that, while not a "source" of radiation, the Van Allen belts themselves create a radiation hazard, even as they also create a shield

to radiation for the Earth and many LEO trajectories below them. The trapped protons in the lower belt shown in Figure 2.1a, are generally high enough that most LEO trajectories avoid it, except that a portion of the belt extends down to 200 km in the South Atlantic, where, for example, the International Space Station orbit occasionally traverses – and when it does, extra caution is taken by retreating to the better shielded areas. The higher belt containing trapped electrons greatly impacts satellites placed in geosynchronous orbit (GEO) – that orbit at 35,786 km where the orbit period matches the rotation of the Earth so that satellites stay over the same spot on the Earth – and thus they must be adequately shielded against the electron hazard, which is fairly easily done. The trapped radiation in the Van Allen belts may be characterized as "high flux, low energy particles" for which adequate shielding protocols exist, and which do not present a serious hazard to humans or equipment leaving the region below the Earth's magnetosphere if they are traversed quickly with standard shielding. [31] [32] [33] [34]

The final source of radiation in cis-lunar space are the Galactic Cosmic Rays (GCR). Compared to SPEs, the GCR have generally a smaller flux, but are of much higher energy. The GCR particles travel at near relativistic speeds, come from outside the solar system, and in general have the highest flux density in the kinetic energies range of 10^8 to 10^{10} eV/n (electron volts per nucleon), with some particles reaching energies around 10^{20} eV/n – thus several to many orders of magnitude higher energies than SPEs and the solar wind. [35] The GCR is composed primarily of fully ionized protons and heavier nuclei, fully stripped of their orbital electrons – approximately 98% nuclei and 2% electrons and positrons – with the nuclear component comprising approximately 87% hydrogen (protons), 12% helium (α particles), and 1% heavier nuclei (the so-called "HZE ions" – "high charge and energy ions"). [36]

As a matter of historical interest, cosmic rays were first formally discovered in 1912 by Victor Hess, for which he later received the Nobel Prize in physics in 1936, after a series of balloon-based experiments measured increasing rates of ionized particles with increasing altitude. Hess concluded that the increasing ionization rate with height meant that the ionizing radiation must come from space, and eliminated the Sun as a source by noting the absence of day-night variations. Because the radiation penetrated the atmosphere, it was initially believed that it was γ-rays, but later measurements in 1927 showed a variation with latitude that brought the focus to our present understanding that the GCR (and many of the secondaries) are, in fact, charged particles rather than photons. [29] [37]

Unlike most SPE particles which can be stopped by adequate shielding, GCR particles penetrate the spacecraft and other surfaces, and produce secondary particles, including neutrons, lighter nuclei, gamma rays and electrons. These secondaries carry the transferred high energy from the initial incident particle deeper into or entirely through shielding materials, and can be more hazardous to humans than the initial incident GCR particle that caused the cascade of secondary emissions. Indeed, these fission products, even though carrying less energy than the initial incident particle, have the ability to damage critical cellular components when passing through the tissues of the human body. [8]

But exactly where the GCR originate is still not fully understood. Galactic Cosmic Rays are generally thought to result from supernovae (star explosions), neutron stars, pulsars or other sources inside our own galaxy (a common spiral galaxy called the Milky Way, which some estimate may be only one of 2 trillion galaxies in the observable universe, based on Hubble telescope data). [38] And with estimates that our galaxy contains some 10 billion stars, there are sufficient candidates for GCR particle

creation. [29] However, the higher kinetic energy particles ($> 10^{17}\ eV$) have a radius of gyration (the so-called Larmor radius) in the interstellar magnetic field larger than can be contained in the disk of our galaxy, and thus these ultra-high-energy nuclei are likely of extra-galactic origin.[2] [36]

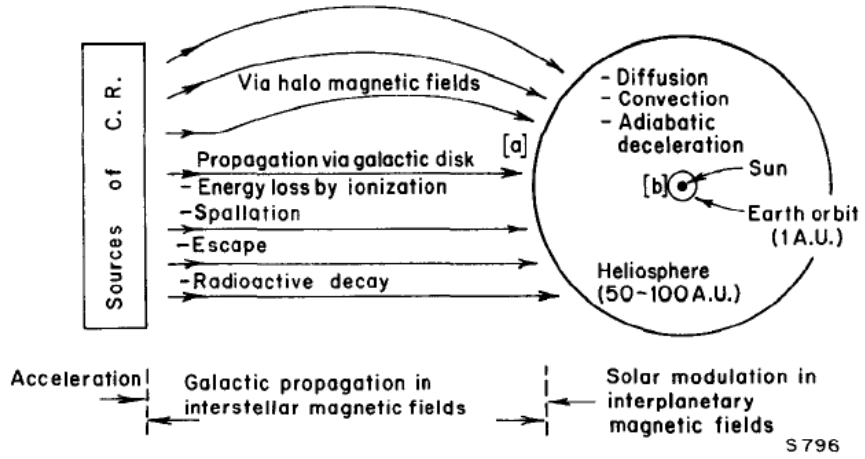

Figure 7 A schematic representation of the life history of a cosmic ray from acceleration in the source region to observation at Earth [b].

Figure 2.4 : Galactic Cosmic Ray pathway from source to Earth. Simpson,(1983).

From their source or insertion point in our galaxy, the GCR then travel to Earth along magnetic field lines, as shown in Figure 2.4. As a result of these interstellar magnetic fields being very irregular in orientation and the Larmor radii being a significant fraction of the thickness of our galactic disk, the paths followed by GCR particles within our galaxy are irregular, particularly for the majority of the flux

[2]It is estimated that our galaxy has a spheroidal center with a thin disk-like structure extending to a radius of about 15,000 parsec, with the disk itself being very thin at some 200 - 300 parsec (where 1 parsec (pc) corresponds to 3.26 light-years, or 1 $pc = 3.086 \times 10^{18}\ cm$). The Sun is about 8,500 pc from the center of our galaxy, thus clearly within the thin disk region. Thus, calculating the Larmor radius of a GCR particle as a function of its kinetic energy, $r_L \approx \frac{E}{ZeB}$, where the average intensity of the galactic magnetic field is $B \approx 4\mu G$. Then for a GCR particle with $E = 10^{15} eV$, $r_L = 10^{18} cm = 0.3 pc$, but for a GCR particle with $E = 10^{18} eV$, $r_L = 10^{21} cm = 300 pc$. Thus, GCR particles with $E > 10^{17} eV$ clearly could not be contained within the galactic disk of 200 - 300 pc, and likely originate outside our galaxy. [29]

which have kinetic energies below 10^{17} eV. Thus, an observer within the heliosphere of the Sun (the termination shock point where the solar wind transitions to subsonic speed relative to the Sun at ≈ 100 AU) would see the GCR as isotropic; i.e., of equal flux and particle distribution from every direction. [36] [39]

Of particular importance, as shown later in more detail, is that once a cosmic ray enters the heliosphere of the solar system, the GCR flux intensity begins to be modulated by the heliospheric field, which is modulated by the 11-year sunspot cycle. This modulation has its greatest impact for GCR particles with energies less than 1 GeV/n (giga electron volts per nucleon, or 10^9 eV/n), as a result of the outward flowing solar wind carrying varying magnetic fields to the heliosphere boundary as it is modulated by solar activity. [38] While the impact will vary depending on the GCR particle energy at the heliosphere, it is estimated, for example, that a GCR particle with a kinetic energy of 500 MeV per nucleon at the heliosphere boundary, may lose as much as one-third of its kinetic energy by the time it reaches 1 AU, the cis-lunar vicinity. [36] Taking the entire GCR energy spectrum into account, it has been estimated that the cosmic ray flux is decreased by a factor of 3 to 4 during the high sunspot periods as compared to phases during minimum solar activity [38], and, in addition, there may be other mechanisms in play that have caused *extended* solar minimum periods, and thus longer periods of *increased* GCR flux. [40]

Thus, it is readily apparent that the GCR radiation impact could at least be minimized by timing missions during the period of peak sunspot activity in the 11-year cycle, but of course one must then pay extra attention to SPE prediction and shielding because those events will also be at a peak during that same time period. Accordingly, some scientists have recently opined that with current shielding protocols it may be too dangerous for humans to undertake the contemplated long-term missions

in the cis-lunar region, unless restricted to the peak sunspot activity interval in order to take advantage of the decreased GCR intensity caused by the solar wind during that time period. [23]

For completeness, there have also been observed additional ionized particles, called anomalous cosmic rays (ACR), that originate from neutral interstellar particles that get pushed into the heliosphere, and then are ionized by interaction with the solar wind or directly by solar ultraviolet light. These particles are then swept into the outer heliosphere and accelerated to a kinetic energy in the range of 100 MeV/n or less, and while at this relatively low energy they do not seriously impact shielding design for humans (not to mention that they are far beyond 1 AU), they can cause equipment damage to probes travelling at the outer edge of the solar system. [41]

Whatever the true sources of the GCR, it is clear that since the origin is at such a great distance and in every direction, that the GCR in the cis-lunar vicinity may be considered isotropic. [42] Moreover, the actual measurements made by various spacecraft probes in the general cis-lunar region, as noted above, during the last twenty years in various energy ranges has allowed the GCR models to be better correlated, and thus provide a high degree of confidence in both the GCR energy spectrum and species delineation. Indeed, some scientists have concluded that the current GCR models are accurate to within 10% for most ions at energies $< 5\ GeV/n$, which is also the region in which solar modulation is most pronounced. [38]

2.2 The Focus on Galactic Cosmic Rays

The decision to focus on GCR radiation in this thesis is two-fold: (1) shielding materials and protocols for the solar wind and SPE radiation are well understood and adequate, but not so for GCR radiation; and (2) the motivation for this research –

examining storage of live frozen cell lines on the Moon – conveniently finds the best storage places in craters on the Moon that are permanently shaded from the Sun, in order to have the very low ambient temperature required, and thus are not exposed to SPEs, but they still have exposure to the isotropic GCR flux that must be addressed.

GCRs are more difficult to shield due to the unceasing, isotropic, and high energy nature of the GCR spectrum. Although the flux of Galactic Cosmic Rays is relatively smaller than some SPEs, the GCR contain heavier and higher energy ions, and thus their contribution to ionizing radiation and biological impact can ultimately be much higher than SPEs. The high energy GCR particles can penetrate the standard spacecraft hulls, and also produce dangerous secondary radiation particles in this process. The GCR ions and the secondaries interact with molecules in human cells, can alter DNA, and can cause severe damage to the human body. [9] [43]

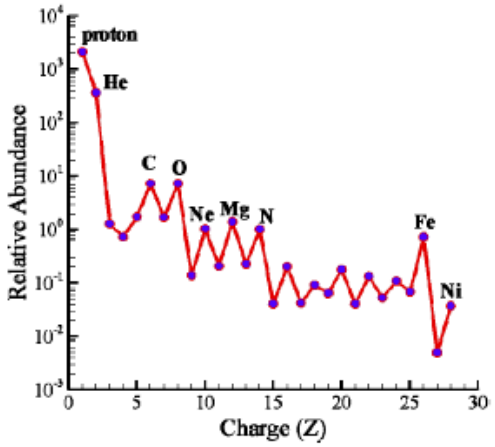

Relative abundance of elements in the 1977 solar minimum GCR environment, normalized to neon

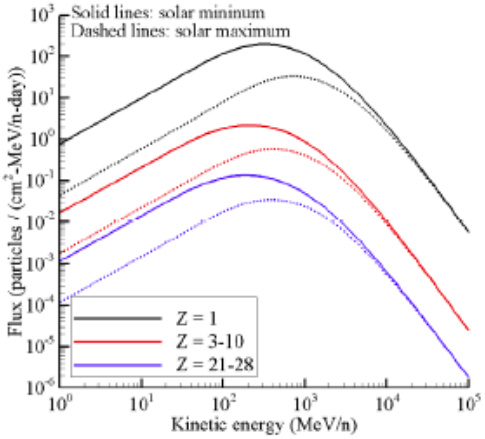

GCR flux at solar minimum and solar maximum

Figure 2.5 : Relative Composition and Flux of Galactic Cosmic Rays. From T. Slaba, Radiation Transport Methods, NASA, 2015.

Regardless of the target – whether human tissue or equipment components – the

damage caused by the GCR is a direct function of the flux density and energy of the incident particles. Thus any analysis of shielding effectiveness in cis-lunar space must start with the GCR composition and energy spectrum, as is shown in Figure 2.5.

While the GCR HZE component is a very small fraction of all the ions, and contains some of all the elements, the majority have an atomic number (charge, Z) below Z = 28 (nickel). [27] Due to the small peak in comparative abundance in the GCR for iron ($^{56}_{26}$Fe) at the heavy end of the spectrum, iron particles often are used as a surrogate for all HZE in assessing shielding effectiveness. As can be seen in Figure 2.5, the ratio of the number of iron ions to hydrogen ions in the entire GCR energy spectrum is approximately 2000:1, but at their peak fluence level (about 1 GeV/n), the iron ion will have a kinetic energy of 56 GeV, while the proton carries only 1 GeV. Thus, the relative damage potential of the iron ion is much higher and more difficult to shield, not only due to a higher kinetic energy, but it also produces more secondary ions and other radiation emissions. Note also that all of the GCR ion species find their peak fluence at around 1 GeV/n, and below that energy level they are highly moderated by the Sun's increased sunspot activity through modulation of the interplanetary magnetic field. To put the relative GCR particle flux into perspective, it is estimated that outside LEO in the region of cis-lunar space, every cell in an astronaut's body (containing $\approx 37 \times 10^{12}$ cells) is traversed by a hydrogen ion every few days, and by heavier ions only every few months. [8]

Finally, it also lends perspective to understand what can stop the high energy GCR particles. To do this, the metric used in the literature for comparative shielding thickness analysis is introduced – the so-called "areal density" – which is measured in units of grams per square centimeter (gm/cm^2). This metric puts all shielding materials on a normalized basis in terms of the amount of material traversed by the

radiation; i.e., the number of atoms and electrons encountered, because these are the internal structural elements in the shielding materials that are the major contributors that attenuate or shield the GCR particle radiation.

Earth:	1,033 gm/cm^2	[atmosphere, lower incident flux due to geomagnetic field]
Mars:	16 gm/cm^2	[very thin atmosphere, no magnetic field]
ISS:	15-20 gm/cm^2	[aluminum hull plus equipment racks, up to 50 gm/cm^2 in areas with food and water storage]
Apollo:	5 gm/cm^2	[aluminum hull]
Moon:	0	[no atmosphere, no magnetic field]

Figure 2.6 : Comparative Shielding Thickness from Space Radiation Risks in Terms of "Areal Density." Adapted from J. Norbury, Space Radiation, NASA Langley, 2015; Koontz, Spaceflight Ionization Radiation Environments, NASA, 2017.

Figure 2.6, shows the comparative shielding thickness for various commonly encountered scenarios where GCR radiation is a factor. The use of areal density to compare shielding materials better illustrates the amount of material traversed by the incident radiation, which is a function of the density of the material under consideration, rather than physical thickness. For example, an areal density of $5gm/cm^2$ of aluminum (with a density of $\rho = 2.7gm/cm^3$) equates to a thickness of 1.85 cm (0.73 inches), while the same areal density for water ($\rho = 1gm/cm^3$) would equate to thickness of 5 cm (1.97 inches). Of course, the Earth's atmospheric density varies with altitude, but is generally thought to have a thickness of about 11 miles (17.7 km) through the troposphere (where 80% of the material constituents reside), and extending up to 50 miles (80.5 km) if one includes the stratosphere. In terms of areal density, the Earth's atmosphere provides almost two orders of magnitude more

material for shielding GCRs than some of the other scenarios in Figure 2.6.

In terms of shielding effectiveness, the Earth's atmosphere and the Van Allen belts are believed to shield virtually all primary incident GCR particles [38], but of course many of their secondary particles and other resulting radiation emissions reach the Earth's surface. [44] [26] As can be seen in Figure 2.7, the magnetosphere itself mitigates many GCR and SPE particles at the lower latitudes, but at the poles the top of the atmosphere is subjected to almost the full cis-lunar flux. Indeed, the GCR flux is estimated to increase by three times beyond LEO outside the Earth's magnetoshpere. [45]

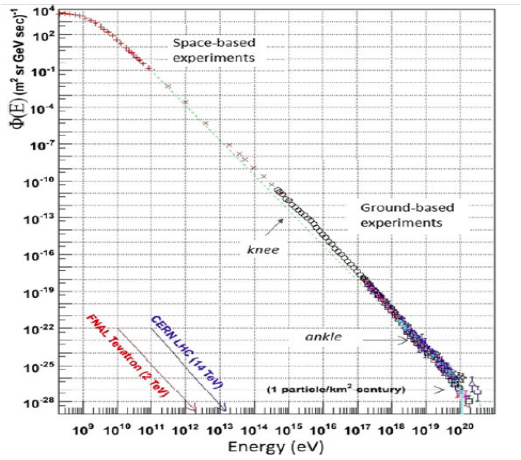

(a) Full GCR Energy Spectrum Flux in Cis-lunar Space. From Spurio, Cosmic Rays and Our Galaxy, 2015.

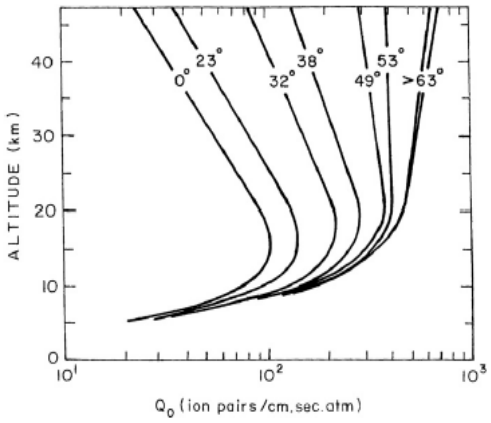

(b) GCR Incident in the Atmosphere as a Function of Latitude due to Magnetosphere. From Singh, Impact of GCRs on Earth, 2011.

Figure 2.7 : Full GCR Spectrum and Effect of Earth's Magnetosphere.

In fact, air crews on polar routes are exposed to a similar hourly radiation dose as are crews on the International Space Station (ISS) orbiting in LEO at a lower latitude under the Van Allen belts. [26] The full GCR energy spectrum in cis-lunar space is shown in Figure 2.7a, including the very infrequent ultra-high energy particles. The dependence on latitude of the shielding effect from the Earth's magnetic field, as

shown in Figure 2.7b, is expected given its dipole orientation that creates the shape of the Van Allen belts (*see* Figure 2.1a). It is estimated that at lower latitudes the Van Allen belts block all particles from the solar wind and most GCR and SPE particles with kinetic energies below 1 GeV. [26] [39] Importantly, the flux of the higher energy GCR particles decreases rapidly with increasing energy, as shown in Figure 2.7a. For example, the flux for the highest energy GCR particle ever detected – $\approx 10^{20} eV$ – is only one particle per square kilometer per century (*see* Figure 2.7a). [26]

Further, even though in theory a GCR particle with a kinetic energy of 15 GeV could reach the surface of the Earth at the equator, nearly all of these high energy GCR particles will be annihilated as they impact other particles in the atmosphere, and create a cascade of secondary radiation particles and emissions, as shown in Figure 2.8a. [44] [37] Of particular interest in Figure 2.8b is the change in ion species from the very high altitudes of the exosphere where the incident primary GCR particles first begin to impact the atmosphere, and the many secondary species found lower in the stratosphere and troposphere. [44]

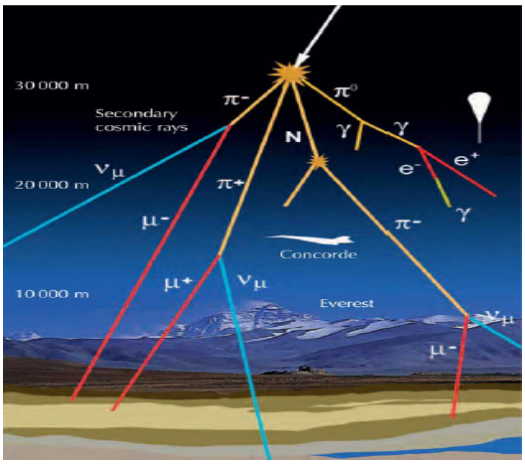

(a) GCR Secondary Cascade Radiation in the Atmosphere. From Norbury, 2015.

(b) GCR Ionization Density Height Profile in the Atmosphere. From Singh, 2011.

Figure 2.8 : GCR Induced Secondary Radiation in the Atmosphere.

After passing through the atmosphere, these secondary GCR emissions are estimated to contribute only about 16% of the normal background radiation dose exposure to humans on Earth. *See* 2008 UNSCEAR Report, Table 12 at page 339. [46] Thus, the combination of the Van Allen belts and the Earth's atmosphere is a very effective GCR radiation shield. And even though the most energetic GCR particle observed can have a kinetic energy of about $10^{20}eV$ in the cis-lunar region, by the time it travels through the Van Allen belts and cascades into thousands of secondaries in the atmosphere, it is relatively harmless.[3]

However, the combination of a magnetic field and a thick atmosphere is not available to a traveler in cis-lunar space, where the structural integrity of the shielding material and physical limitations on weight and thickness are necessary design considerations for spacecraft and habitats. In point of fact, to have the same areal density provided by the Earth's atmosphere in an aluminum shield would require a thickness of 3.8 meters – clearly impractical for spacecraft design. Even with the slightly enhanced shielding on the International Space Station using standard materials, and the decreased GCR intensity due to the Van Allen belts, it is estimated that the GCR make up more than 80% of the effective radiation doses to crews on the ISS. [38] Thus, it is obvious that GCR radiation poses a potentially serious limitation for both humans and equipment that are expected to spend considerable time in the cis-lunar radiation environment. Indeed, recent studies regarding the Apollo astronauts indi-

[3]One author has noted that such a GCR particle with a kinetic energy of $10^{20}eV$, or about 16 Joules, would be "an energy equivalent to that of a well served tennis ball!" *See* Morison, 2008 at page 198. [47] But a quick calculation reveals that would equate to a tennis serve of only some 60 mph, which is considerably less than an average Rafael Nadal serve of some 125 mph (more on such calculations in Chapter 3). Nevertheless, it is a substantial "whallop" for a particle literally the size of the nucleus of an atom! And, the author does point out that such a GCR particle would have considerably higher energy than the highest energy protons produced by the Large Hadron Collider at CERN – the world's largest and most powerful particle accelerator – of about $7 \times 10^{12}eV$.

cate that this time limitation may be much shorter than the several-year long missions currently contemplated, without improved GCR shielding protocols. [5] [23]

2.3 Evaluating Human Hazards from GCR Radiation

All assessments of GCR particle radiation exposure damage must start with a clear understanding of the particle species spectrum, and their fluence and flux. With that knowledge, the energy spectrum can be determined and this data becomes the input to radiation transport schemes to evaluate various shielding materials, or is used in various ways to estimate the damage that may be inflicted on various targets (e.g., humans and their internal organs), either directly without shielding or behind various shielding designs. [37]

The fluence of radiation particles is a measure of the number of particles (dN) incident per unit area cross section (dA), and the particle radiation flux (ϕ) is merely the fluence measured during a specified time interval (dt). Since the incident GCR radiation in free space is isotropic, the number of incident particles is measured per unit solid angle in steradians ($d\Omega$). Thus, the GCR differential flux per unit energy, expressed in commonly used units, is the number of particles incident per unit solid angle, with a given kinetic energy, crossing a given area, per unit time:

$$d\phi = \frac{dN}{dA\ d\Omega\ dt\ dE} \qquad \left[\frac{\text{particles}}{(cm^2 - sr - s - MeV/n)}\right] \tag{2.1}$$

To examine the differential flux in free space, one would integrate over the full 4π solid angle, and by lengthening the time interval to days, one gets the differential flux in units like that shown in Figure 2.5: $\left[\ \frac{\text{particles}}{(cm^2 - MeV/n - day)}\right]$. From this general expression for the flux of the incident radiation, and calculations for the energy imparted by each

particle (which are introduced in Chapter 3), the total energy imparted by the GCR particle radiation can be determined, and that is used in various ways to determine the physical or biological response to the incident radiation. [38] [37]

To evaluate the damage caused by GCR radiation to humans, one must take the flux calculation through additional steps in order to attempt to correlate the energy deposited to biological impact and damage. This involves making a number of assumptions, sometimes with little or no actual experimental data to support them, and thus results in "best estimates" or guesses about the ultimate biological impact. Nevertheless, it is the best there is at this time.

The first step is to determine the "absorbed dose" per unit mass (dD), defined as the energy (dE) imparted into the target per unit mass (dm) by the ionizing radiation, applicable to both direct and indirect ionizing radiation. A first order estimation of the energy deposited by a GCR particle can be determined by calculating that particle's "Linear Energy Transfer" ($LET = -dE/dx$ per particle), which is approximately equal to the so-called "Stopping Power" (S) of the target material impacted by the GCR particle, all of which is explained more fully in Chapter 3. Thus, the total absorbed dose in a given target mass during a given time interval is:

$$D = \int_0^\infty \frac{dE}{m} = \int_0^\infty \frac{LET}{\rho_{target}}\ \phi\ dE \approx \int_0^\infty \frac{S}{\rho_{target}}\ \phi\ dE \tag{2.2}$$

The unit for absorbed dose is the Gray (Gy), where 1 Gray equals 1 joule per kilogram, ($1Gy = 1J/kg$).[4] [37] [48]

[4]Another commonly used unit of measure for the absorbed dose is the rad, where $1rad = 100ergs/g = 0.01Gy$. The physical units for absorbed dose are energy per mass, which is calculated from the LET (energy deposited per distance per particle in the target), times the total flux of particles, ϕ, during the prescribed time interval (particles per cross section of area in the target), divided by the density of the target, ρ_{target}, (mass per volume of target material). Thus, for example, if the flux, ϕ, for all GCR particles for the entire energy spectrum has units of $particles/cm^2$,

Once the absorbed dose is determined, various models about the target material are used to determine the impact of the radiation; e.g., if the human body is to be evaluated for the biological impact of the GCR radiation, then some means of correlating the absorbed dose to the harm caused must be employed. This analysis is complicated by the paucity of actual human data, and by the fact that the various species and energies of the the incident radiation impact tissues in the human body in different ways, as illustrated in Figure 2.9. [49]

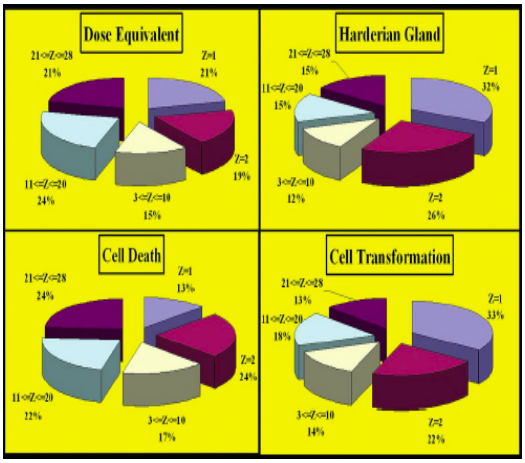

(a) GCR Impact Varies by Ion Species. From Durant, 2011.

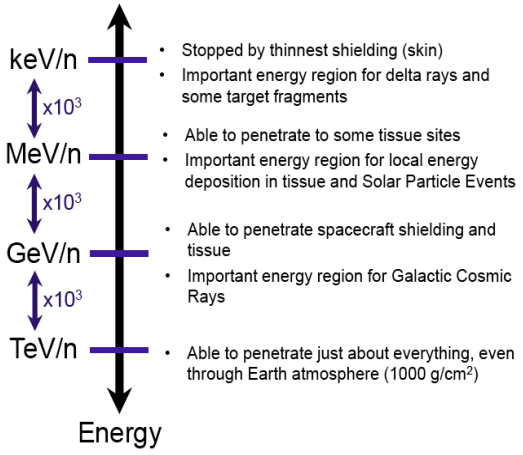

(b) GCR Impact as a Function of Energy. From Slaba, 2015.

Figure 2.9 : GCR Impact is a Function of Ion Species and Energy.

Nevertheless, drawing on radiation impact data in the medical research field, primarily on animals (because so little actual data exists on humans), certain metrics have been developed to measure the GCR exposure's impact on the human body. One widely used metric is the "dose equivalent" (H), which has two commonly used, but different, incarnations in the literature – defined as the absorbed dose modified

and the LET for each particle has units of $KeV/\mu m$, and the density, ρ_{target}, is in units of gm/cm^3, then the result would be multiplied by a conversion factor of 1.602×10^{-9} to express in units of J/kg or Grays. [48]

by a either a quality factor (Q), which is solely a function of the incident radiation energy, or by a weighting factor (w_R), which varies with the type (R) of the incident and/or secondary radiation species impacting the target:

$$H = \int_0^\infty Q(E)\ D(E)\ dE \tag{2.3}$$

$$H = \sum_R \sum_E w_R\ D_R(E) \tag{2.4}$$

where Q is the dimensionless quality factor, and w_R is the dimensionless radiation weighting factor, and the dose equivalent is measured in units of Sieverts (Sv), where 1 Sv is equal to 1 J/kg (joule/kilogram).[5] In other words, Sieverts have exactly the same physical units as Grays, but use of the units of Sieverts for the dose equivalent metric denotes that the absorbed dose has been adjusted to correlated to the expected biological damage in a human target, thus attempting to take into account the fundamental fact that the biological response will vary with radiation type and/or energy. However, in the absence of of actual scientific and medical data, these are obviously only approximate, and somewhat arbitrary and inconsistent, schemes to evaluate a human target's biological response. [38]

To further illustrate the point, it is instructive to understand how the scientific and medical community has adjusted these factors over the last twenty years. The radiation weighting factors, w_R, were recommended in 2007 by the International Commission on Radiological Protection (ICRP) in report ICRP-103 [50], where generally the larger the radiation weighting factor, the more damaging the biological impact.

[5] Another commonly used unit of measure for the dose eqivalent is the rem (Radiation Equivalent Man), where $1rem = 0.01Sv$.

Before 2007, most research reported in the literature used the quality factor analysis for biological impact put forth in 1990 in report ICRP-60. [51]

Figure 2.10 shows the differences in weighting factors versus the previously recommended quality factors for assessing biological impact from GRC radiation, including the highly dangerous neutron secondary emissions that result from the fission reactions of the incident radiation with atoms in the shielding or target materials.

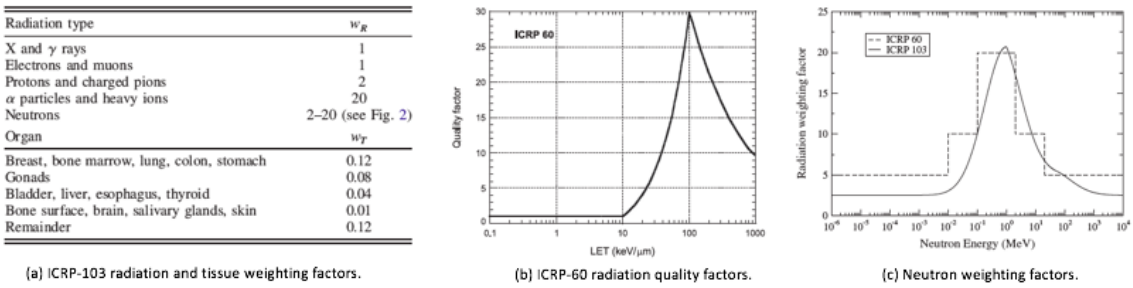

Radiation type	w_R
X and γ rays	1
Electrons and muons	1
Protons and charged pions	2
α particles and heavy ions	20
Neutrons	2–20 (see Fig. 2)
Organ	w_T
Breast, bone marrow, lung, colon, stomach	0.12
Gonads	0.08
Bladder, liver, esophagus, thyroid	0.04
Bone surface, brain, salivary glands, skin	0.01
Remainder	0.12

(a) ICRP-103 radiation and tissue weighting factors. (b) ICRP-60 radiation quality factors. (c) Neutron weighting factors.

Figure 2.10 : Comparison of GCR Biological Harm Models using Radiation (w_R) and Tissue (w_T) Weighting Factors, and Quality Factors (Q), for two Different Harm Assessment Models, ICRP-60 and ICRP-103. From Durante, 2011.

These differences need to be taken into account when comparing research results; many recent studies use the ICRP-103 model, available after 2007, but NASA still uses the ICRP-60 model. For example, the use of a weighting factor, w_R, of 20 in ICRP-103 for heavy charged particles may be overly conservative, but, as shown in Figure 2.10c, the ICRP-103 also reduces the impact of the more prevalent proton ions, and gives a more granular weighting to secondary neutron emissions, especially in the energy range between $10^{-2}MeV$ to $10^{3}MeV$, where they are relatively more harmful than the rest of the neutron energy spectrum. [52]

In fact, the differences turn out to be non-trivial indeed. To illustrate the point, we conducted an analysis using the MULASSIS radiation transport code (more on that in Chapter 4) to determine the dose equivalent impact in a human target for

a moderate exposure time of one-year from GCR radiation, as shown in our Figure 2.11. [53]

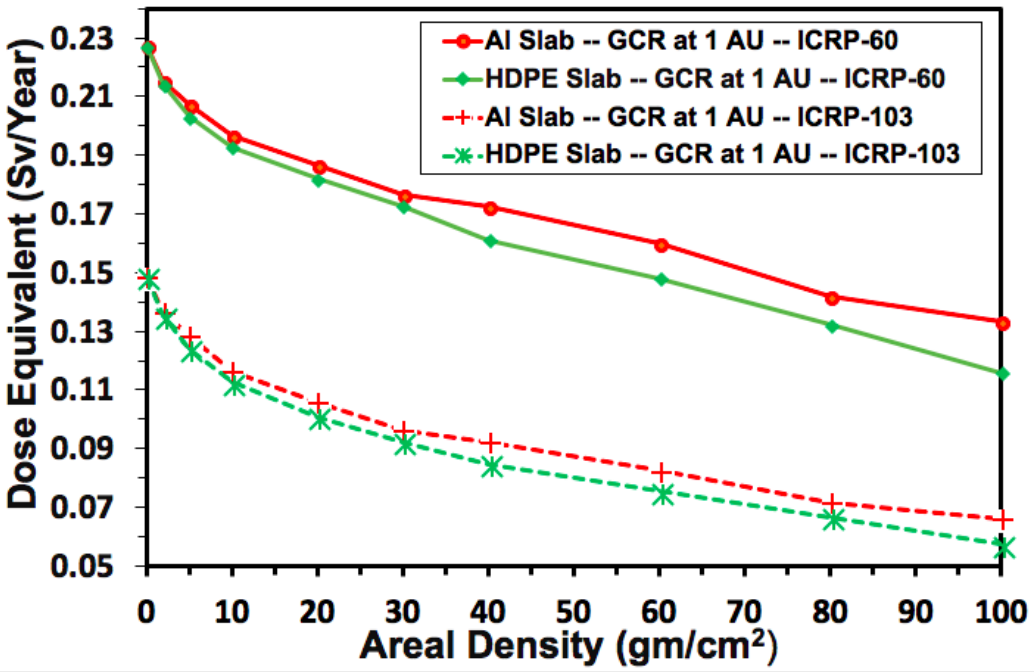

Figure 2.11 : Dose Equivalent behind different shielding materials of varying areal density from a One-Year exposure to the Cis-lunar GCR radiation during the 1977 solar minimum, comparing ICRP-103 and ICRP-60 biological assessment factors.

The two upper curves in Figure 2.11 show the dose equivalent behind aluminum and polyethylene using the ICRP-60 quality factor, while the lower curves are the same calculations using the ICRP-103 weighting factors. Using the the more recent ICRP-103 recommendations actually reduces the calculated dose equivalent by some 45%, as compared to that with ICRP-60. Furthermore, the total ionizing dose tends to drop a bit faster for increasing areal density (i.e., thickness) of the shielding material with ICRP-103. This is probably because the primary and secondary protons in the GCR have a much larger flux than the HZE ions, and the new weighting factors for protons in ICRP-103 is on average lower than one would calculate under the quality

factor method, thus reducing the total dose equivalent accordingly. Therefore, it is evident that great care must be taken in comparing research results in the literature regarding dose equivalent estimates.

Finally, to evaluate the probability of harm from radiation exposure on different organs or tissues that may result in different health impacts (e.g., leukemia, cardiovascular disease, etc.), the metric of "effective dose" (E) is employed. The effective dose is the dose equivalent – assuming a uniform whole-body GCR exposure – modified by a tissue weighting factor (w_T) prescribed by ICRP-103, shown in Figure 2.10a:

$$E = \sum_T w_T \; H \tag{2.5}$$

The units for the effective dose are Sieverts (Sv), and the dimensionless tissue weighting factor, w_T, ranges from 0.01 for skin tissue to 0.12 for bone marrow [53], and by design the sum of all w_T for all different tissues is 1.0 for the whole human body. Again, an imprecise way of evaluating the expected harm from GRC radiation exposure, but the best available given the lack of scientific data. [38]

To summarize, when considering the impact of GCR on humans it is obviously necessary to consider both the energy spectrum and the type of radiation involved. As shown in Figure 2.12, it is not enough to simply know the flux of particles in the incident GCR, because the ultimate purveyor of harm is the "dose equivalent" (H) calculation – which derives from the "absorbed dose" (D), which in turn is a function of the flux and energy of the GCR radiation particles.

Thus, when the entire GCR spectrum in cis-lunar space is examined in terms of the impact on humans, the highest flux particles (protons) impart an order of magnitude *less* potential harm than the heavier ions. For example, iron ions have a flux several

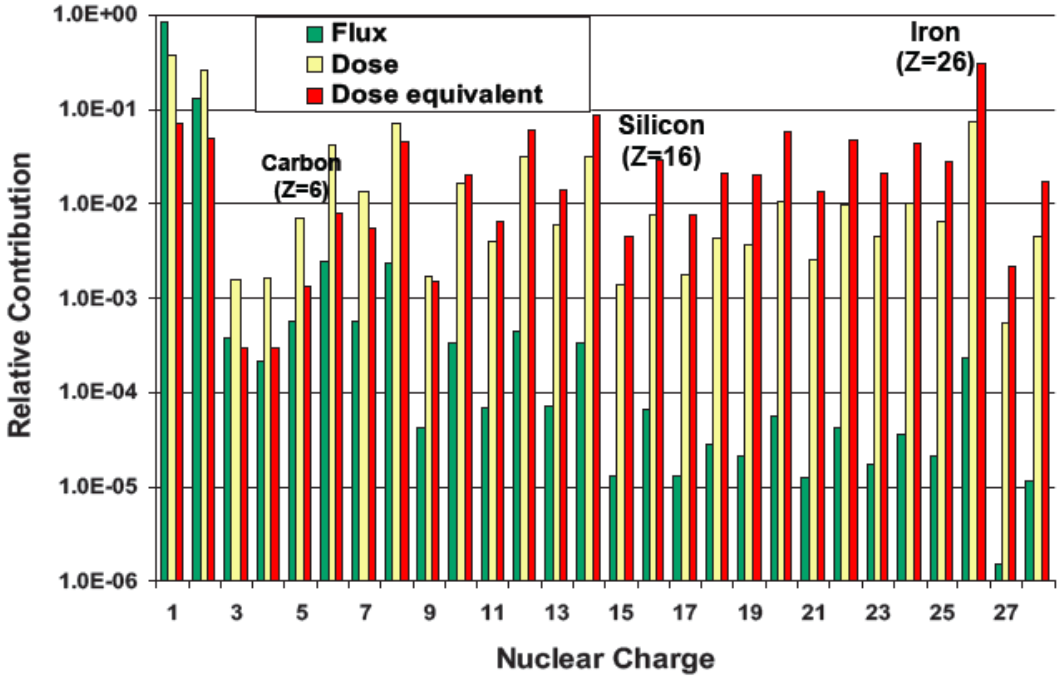

Figure 2.12 : GCR Radiation Risk to Humans: Flux, Absorbed Dose, and Dose Equivalent Exposures. From J. Chancellor, Texas A&M (2016), adapted from Durante, 2011 (Figure 5).

orders of magnitude less than protons, yet impart a much higher dose equivalent impact in humans. Such features of the potential GCR impact on humans become an important consideration in optimizing shielding designs. Indeed, it was part of the impetus (in addition to the inevitable errors introduced in using the calculated dose equivalent metric) for focusing on the fluence of particular particle species in the GCR in the early work of this research for evaluating various shielding materials and designs; an approach that was published in regard to our preliminary research. [14]

The final step in evaluating the harm to humans of long-term exposure to GCRs is to have some understanding of the ultimate medical impact for known radiation exposures. Figure 2.13 provides a variety of data on human radiation exposures.

	Dose Equivalent (mSv)
Chest x-ray	0.1
USA annual background	4
Public annual limit (above background)	1
International Airline crews	4
Radiation worker annual limit	20
No observed effects (Abomb)(instant)	200
Blood count changes	>200
Acute Radiation Syndrome (ASR)	1,000
Death (instantaneous dose)	3,000
Mir, ISS (with shield) annual	150
Large solar flare (free space)	10,000

ICRP cancer risk estimate: 5% per Gy ~ 5% per Sv (for Q=1)

1 in 20,000 risk of fatal cancer per 1mSv dose (lifetime)

(a) Radiation Exposures in Various Scenarios.

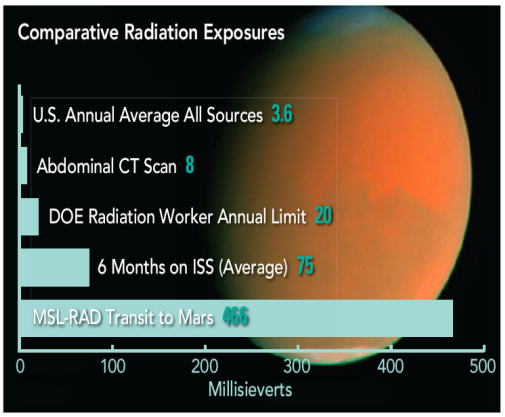

[Kerr, Science 340, 1031, 2013]

(b) Radiation Exposures in Space.

Figure 2.13 : Comparative Human Radiation Dose Equivalent Exposure Levels. From Norbury, 2015.

Note that the human exposure levels are reported in units of "millisieverts" ($1Sv = 10^3\ mSv = 10^6\ \mu Sv$). Figure 2.13a provides some commonly experienced radiation exposures, while Figure 2.13b extends this information to expected exposures on the ISS and in transit to Mars. The annual average dose equivalent rate on Earth is about 4 mSv per year; whereas the annual dose equivalent rate on Mars is about 150 mSv per year, and roughly the same exposure rate is experienced on the ISS, while on the Moon the dose equivalent exposure rate is about 350 mSv per year. [38] Recall that the GCR radiation is isotropic, so that these surface exposures on planetary bodies are naturally shielded from half of the incident GCR radiation extant in the free-space environment.

NASA has adopted limits on astronaut whole-body effective dose radiation exposures of 0.5 $Sv/year$, and 0.4 - 3.0 $Sv/career$ (depending on age and gender – older is more tolerant, as are males), based on a postulated 3% greater fatal risk of cancer (National Council on Radiation Protection - NCRP Report No. 132). [54] [38] [55]

To avoid radiation induced nervous system maladies, the annual exposure limit may be as low as 0.1 $Sv/year$. [56] Thus, a Mars mission lasting 3-years that could impose an exposure of some 1.5 Sv from the GCR alone behind standard spacecraft shielding (and maybe more if SPEs were to occur), could violate the current annual exposure limitation standard for all, and the career limitation standard for most, astronaut candidates (note that the 3.0 $Sv/career$ level is only for males older than 55 years). Indeed, one study indicated that with current standard shielding protocol employed on the ISS (e.g., 20 gm/cm^2 of aluminum), a Mars voyage would incur a 10% (male) to 13% (female) *increase* of risk of fatal cancer – far above the current NASA standard. [45] But even these estimates are made with the qualification that "large uncertainties exist in estimating the health risks of space radiation, chiefly the understanding of the radiobiology of heavy ions and dose rate and dose protraction effects, and the limitations in human epidemiology data." [57] And importantly, recent *actual* data may indicate that these calculated exposure limits are set too high – the Apollo astronauts who travelled to the Moon had only a total mission effective dose exposure of about 50 mSv over a short nominal three-week period,[6] yet recent studies have shown an increased occurrence of cardiovascular disease, as compared to all other astronauts. [2] [5] [23] However, NASA's Report on Human Health Risks has noted that differences of opinion have been reported with respect to "space-relevant ionizing radiation-induced cardiovascular disease," which highlights the continuing need for research to better define human health risks for even low doses of radiation, particularly in a microgravity environment [2] [59] [60].

The import of all of this analysis is that the actual numerical results of the calcula-

[6]Starting with the Apollo 14 measured mission radiation exposure of 1.4 $rads = 0.014\ Gy$, times an average quality factor of 4 equates to 56 mSv. [58]

tions for exposure impact on humans should be used with some care and skepticism. Because of the variability in the biological models used, and the lack of any real long-term human exposure data, the results are hard to compare; and indeed, often confusing. We will really only know the actual impact of long-term exposure from GCRs on humans when we start to get real data in the full cis-lunar radiation environment. Nevertheless, the analysis is useful in providing a rough idea of the radiation exposure levels to be expected on longer spaceflights, and highlights the need for better shielding protocols.

2.4 Evaluating Equipment Hazards from GCR Radiation

The hazards to equipment are modelled very differently from human exposure, in that equipment suffers degradation of materials and damage to sensitive components, such as the silicon used in computer chips, primarily as a function of the impact of total ionizing dose (TID) and non-ionizing dose, called displacement damage dose (DDD), both of which accumulate over time, or by single event effects (SEE), which are the ionizing and non-ionizing dose associated with single particle strikes to critical areas. [31] Figure 2.14 illustrates the problems.

Radiation damage to equipment occurs in all spaceflight orbital environments, as shown in Figure 2.14a, and has been studied primarily with respect to Earth orbiting satellites and probes that have been launched into various positions in the solar system. [61] Of particular interest, are SEE (which sometimes result in a single event upset – SEU), shown in Figure 2.14b. An SEE can occur to many electronic devices that have component dimensions so small that the currents induced from the passage of a single energetic particle in the GCR (or SPEs or Van Allen belts) may be sufficient to alter the operating characteristics of the device. Indeed, the physical

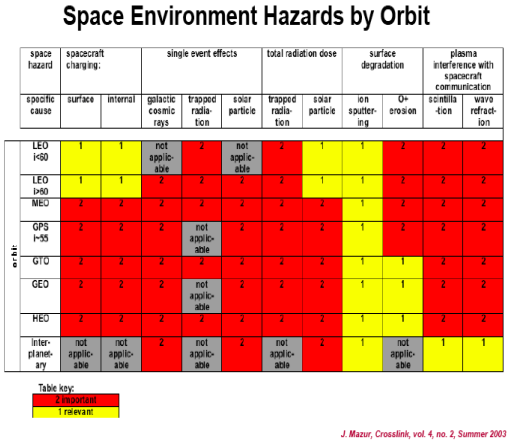

(a) Equipment Hazards in Space.

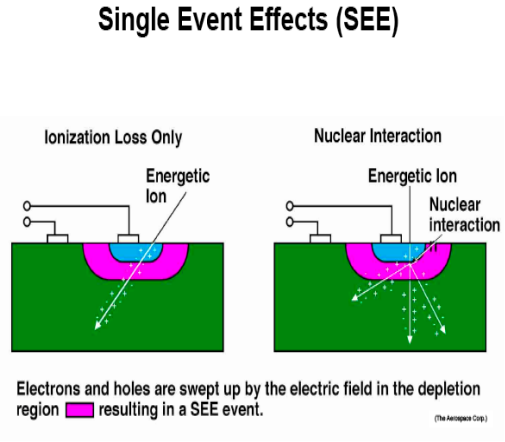

(b) Equipment Hazards - Single Event Effects.

Figure 2.14 : Equipment Hazards from Space Radiation. From Mazur, 2007.

damage caused by a highly energetic GCR particle in the silicon of an important chip in a device could cause complete malfunction – a classic SEU. [62]

So-called "radiation hardening" of devices to prevent SEE includes using shielding and employing less sensitive components; i.e., chips with a lesser density of electronic components etched on their surface. In addition, some work has been done on satellite shielding for the low-energy electrons and protons in the Van Allen belts to optimize the shielding effects by using a variety of very thin materials in particular layered orders. [34] Though the cis-lunar GCR radiation environment is much different (and therefore the related physical principles are also different), part of the research in this thesis employs the concept of using multiple layers of various different shielding materials in order to attempt to optimize attenuation of GCR primary ions and their secondary emissions.

Chapter 3

Overview of the Physics of Radiation Shielding

"For those who want some proof that physicists are human, the proof is in the idiocy of all the different units which they use for measuring energy."
—Richard P. Feynman, American theoretical physicist, Nobel Laureate (1918-1988)

It is the transfer of energy from the high energy ion particles that comprise the GCR to the human tissue or equipment components that causes the harm from such radiation. Thus, it is fundamental in evaluating GCR radiation shielding to have a convenient and uniform way to measure that energy. The standard unit of energy employed in the literature for GCR radiation species is the electron Volt (eV): defined as the kinetic energy gained (or lost) by an electron passing through a potential difference of one volt. [63] It is a derived term (and a non-SI unit, though accepted for use expressed in SI units) – determined experimentally – whereby one electron volt is equal to one Volt (which is 1 $Joule/Coulomb = 1J/C$) times the elemental charge of an electron ($e = 1.6021766208 \times 10^{-19} Coulombs$): thus yielding, 1 $eV = 1.6021766208 \times 10^{-19} Joules$ (in base SI units, $\frac{kg-m^2}{s^2}$). [63]

The relatively tiny amount of energy of an electron Volt can, of course, be expressed in terms of other common units of energy: 1 erg (the amount of work done by a force of one dyne exerted for a distance of one centimeter) $= 6.24150647996 \times 10^{11} eV$; 1 *calorie* (the amount of energy required to raise one gram of water one degree Centigrade at one atmosphere of pressure) $= 2.616875 \times 10^{19} eV$; 1 BTU (the amount of energy required to raise the temperature of one pound of water by one degree Fahren-

heit) $= 6.585 \times 10^{21} eV$; 1 $kiloWatt-hour$ $(kW-h)$ (the amount of energy converted if work is done at an average rate of one thousand watts for one hour, where 1 watt $= 1\ J/s$) $= 2.25 \times 10^{25} eV$; and then finally to return to the empirical starting point, 1 $Joule$ (the work required to move an electric charge of one Coulomb through an electrical potential difference of one Volt) $= 6.24 \times 10^{18} eV$. [25, 63]

By way of reference to commonly experienced energy levels: visible light has a photon energy of 1.6 eV to 3.4 eV; the amount of energy required to ionize atomic hydrogen is 13.6 eV; the average energy released in the nuclear fission of one U-235 atom is 200 MeV (million electron volts); the kinetic energy of a flying mosquito is about 1.56 TeV (trillion or teraelectron volts); the energy consumed by a single 100-watt light bulb in one second is about $6.24 \times 10^{20} eV$; and the total energy released from a 15 kt TNT equivalent yield nuclear fission device (the yield of the Hiroshima atomic bomb) is about $3.9176 \times 10^{32} eV$.[1]

The electron volt has been used for years in the fields of physics and astronomy, and thereby has evolved to common usage for the purposes of describing the GCR spectrum and evaluating various radiation shielding protocols. By way of example, a typical mid-range GCR particle has an energy level of 1 GeV/n (billion or gigaelectron volts per nucleon); thus, if the particle is an iron ion ($^{56}_{26}$Fe) the total kinetic energy carried by that single ion would be about 56 GeV, and at a typical daily fluence in the GCR of some 3.26×10^5 particles per square meter, the total energy deposited by

[1]Some of these energy levels are easily found in textbooks and others are readily calculable:

For example, the kinetic energy of a flying mosquito with a mass of 2 mg moving at a velocity of 0.5 m/s is solved with standard classical mechanics: $ke = \frac{1}{2}mv^2 = \frac{1}{2}(2mg)(\frac{gm}{10^3 mg})(\frac{kg}{10^3 gm})(0.5\frac{m}{s})^2 = 0.25 \times 10^{-6}\ \frac{kg-m^2}{s^2} = (0.25 \times 10^{-6} J)(\frac{1eV}{1.602 \times 10^{-19} J}) = 1.56 \times 10^{12} eV = 1.56 TeV$.

In similar fashion, the energy released by the 15 kiloton TNT equivalent Hiroshima atomic bomb (noting that 1 ton TNT (energy equivalent) equals $4.184 \times 10^9 J$, [63]) would be calculated as follows: $E_{A-bomb} = (15 \times 10^3 tonTNT)(\frac{4.184 \times 10^9 J}{1 tonTNT})(\frac{1eV}{1.602 \times 10^{-19} J}) = 3.9176 \times 10^{32} eV$.

only the iron ions in the 1 GeV/n energy range (a relatively low flux ion in the GCR spectrum) would be about 18.3 TeV per day,[2] and while this is more energy than a flying mosquito, but much less than an atomic bomb, it is nevertheless dangerous to humans and equipment under long-term exposure situations. Considering that all iron ions in the full GCR energy spectrum comprise well less than one-percent of the total GCR flux, then when one totals the energy carried by the entire GCR spectrum – all ions over all energy levels – the potential harm is more readily apparent.

3.1 GCR Radiation Interaction with Materials

As GCR radiation particles – comprised of fully ionized ions (98%) and free electrons (2%) – penetrate a bulk target material of shielding and/or tissue, physical interactions slow and modify the original incident particles, and may also produce secondary particles, including other ions, neutrons and fragments. [27] The incoming GCR particles cause ionization of the atoms and molecules in the target material, both *directly* by electromagnetic interaction stripping away of electrons due to their high incident kinetic energy, and *indirectly* by nuclear collisions. This ionization and excitation of target atoms in the shielding material or tissue results in energy loss from the incident GCR particles. [64]

As shown in Figure 3.1a, direct ionizing radiation involves the positively charged particles, such as protons, α particles, and HZE ions interacting with the orbital electrons of the target material, and eventually losing their kinetic energy, causing them to decelerate and stop. The ejected electrons (and the small number of incident

[2]This calculation is based on the output of the CREME96 GCR model, indicating a differential flux of 1 GeV/n iron ions of 3.26×10^5 particles per square meter per day, thus the kinetic energy is: $KE_{1GeV-Fe} = (\frac{3.26 \times 10^5 particles}{m^2 - day})(56GeV) = 18.256\ TeV/m^2 - day$.

electrons in the GCR) become so-called δ-rays, which may have sufficient energy to ionize other atoms in the target material, and which then lose their energy by emission of bremsstralung radiation (photon emissions).

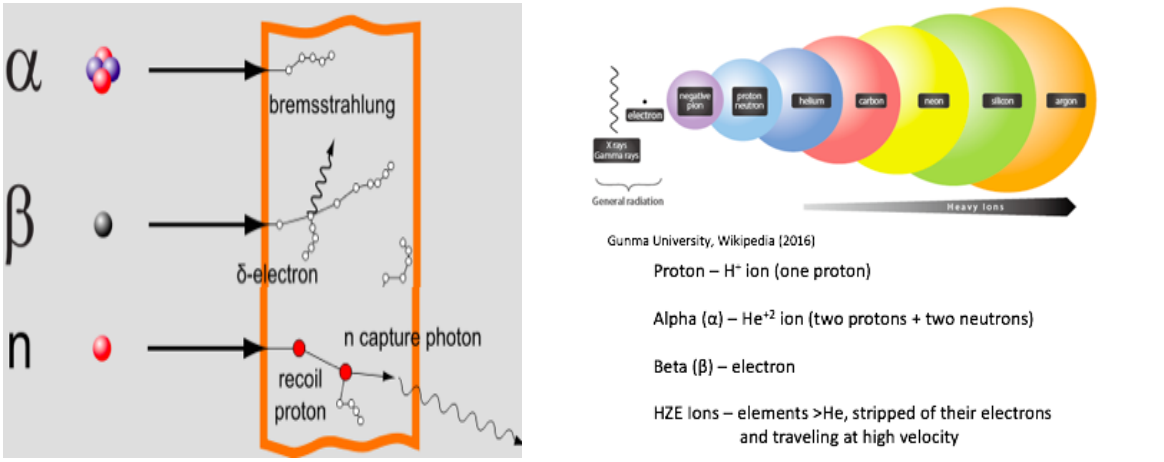

(a) GCR Interaction with Materials. (b) GCR Ions (98%) and Free Electrons (2%).

Figure 3.1 : Primary GCR Interaction with Target Material. Adapted from Wikipedia images and Slaba, 2015.

Indirect ionizing radiation occurs as a result of the process by which particles with no charge lose their kinetic energy during nuclear interactions. Primary Galactic Cosmic Rays don't have uncharged particles, but during the interactions with shielding materials, uncharged particles like neutrons and gamma rays are produced. The energy loss mechanism for these uncharged secondary components of incident GCR particles is different than for the positively charged ions, and thus leads to considerations of different shielding materials than might be optimal for the incident GCR spectrum. As will be demonstrated, in optimizing multilayer shielding protocols, it becomes necessary to weigh the characteristics of materials most effective in stopping high energy positively charged ions, with the propensity of such shielding materials to create secondary emissions, and then to determine subsequent materials

in the layered configuration that can effectively stop such secondary radiation.

The atomic ionization of the target material by GCR particles themselves, and the further ionization by the liberated electrons (δ-rays) and other secondary emissions, creates physical damage in shielding materials and tissue by leaving an ionization track. [64] In space, each cell within an astronaut's body is exposed every few days to a nuclear particle that comprises the GCR. [8] [65] This ionization process is illustrated in Figure 3.2.

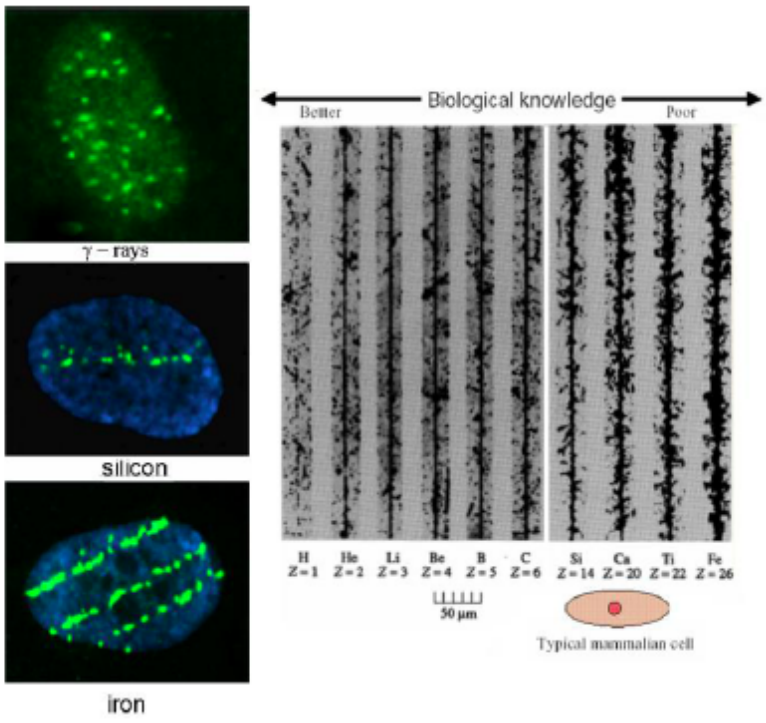

Figure 3.2 : Comparison of Particle Ionization Tracks in Nuclear Emulsions and Human Cells, showing the Physical Damage. From Cucinotta, 2013.

The left panel in Figure 3.2 are human cells exposed to γ-rays, Si-ions, and Fe-ions, where each green area corresponds to DNA double-strand breaks. The high energy γ-rays are photons created as a result nuclear collisions, and can be a sufficiently energetic form of electromagnetic radiation to ionize other atoms in the target material,

causing damage along the way. Note that the damage caused by the electromagnetic γ-ray ionization is uniformly distributed in the target, whereas that caused by the incident GCR ion particles present damage along distinctive tracks. As shown in the right panel, the ionization damage increases with the atomic charge (and mass) of the incident GCR ion; in fact the number of δ-rays is proportional to $\frac{Z^2}{\beta^2}$. [64]

As was made clear in the earlier discussion of radiation weighting factors used to estimate the dose equivalent metric (*see* Figure 2.10), neutron radiation is one of the most dangerous indirect ionizing radiation species. While high and medium energy neutrons are rather easy to stop, low energy neutrons experience complex hadronic interactions in shielding materials and are very hard to stop. [66] Neutrons can cause severe biological damage for this reason, and although secondary radiation is of overall lower energy and lower flux, nevertheless, it can significantly increase the biological damage.

Figure 3.3 illustrates the primary mechanisms of secondary emissions due to nuclear collisions in the target material by primary GCR particles.

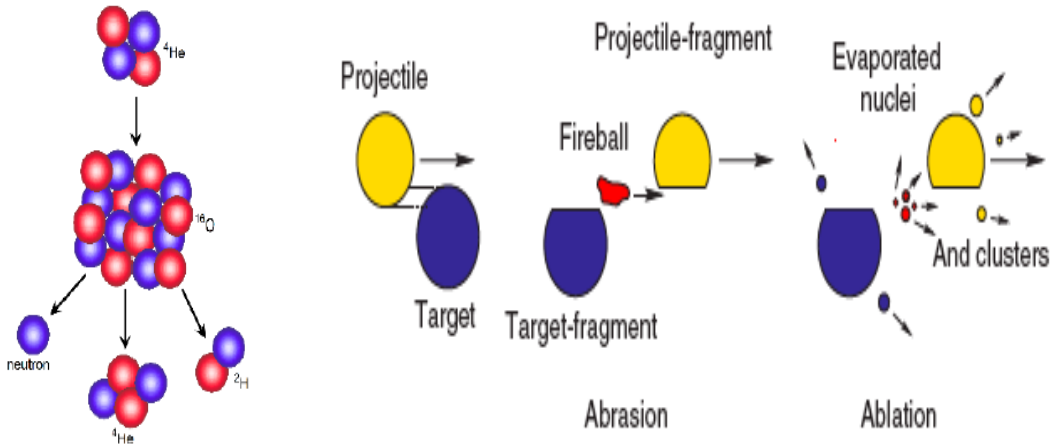

(a) GCR Collision Senarios. (b) GCR Fragmentation Scenarios.

Figure 3.3 : GCR Nuclear Destruction Scenarios. From Slaba, 2015 and Durante, 2011, respectively.

These nuclear interactions can occur as elastic, inelastic, or nuclear reaction encounters. In an elastic collision the final products are identical to the initial particles and kinetic energy and momentum are conserved (a classic "pool-ball" collision). In an inelastic collision, the final products are identical to the initial particles, but kinetic energy is *not* conserved, because some of the initial energy is converted to atomic excitation or ionization energy, or gamma-ray emissions by bremsstrahlung radiation. Finally, in a nuclear reaction the collision causes the atoms and molecules to break into different ones, or to fragment the target constituents in various ways, creating spallation products different from the initial particle. [27] These considerations will become important when considering the transport of the GCR particles and their secondaries through various shielding materials, discussed in Chapter 4, and, as mentioned previously, in the selection of shielding materials, where possible, to reduce the propensity to create secondary emissions.

The ultimate biological effect of different types of particles are usually assessed using the ratio of equivalent dose to that of γ-rays that cause the identical effect – called the "relative biological effectiveness" (RBE). [38] But, of course, this analysis is severely limited by the lack of human data in the energy range of GCR particles – the studies are limited primarily to medical patients exposed therapeutically to radiation and radiation workers – all relatively short-exposures to low-level radiation. No data exists for long-term exposure to the higher-energy GCR radiation. As a result, the deeper studies involve animals and cell cultures only, and ultimately we are left with the recommendations of advisory panels that make a best-guess subjective judgment of available RBE data to evaluate human risk. [64] *See, e.g.,* the discussion on Quality Factors and Weighting Factors in Chapter 2.

Moreover, as mentioned previously, the results of studies reported in the literature

are sometimes inconsistent (though confusingly reported in the same units of Sieverts), and are often calculated by different methods which purport to quantify the biological risk. [54] Thus, while obviously useful, the differing assessments of biological risk associated with different parts of the GCR radiation spectrum subjected to various shielding schemes, require careful attention to the calculation methods utilized, as previously noted, in order to assess true comparability. [42]

For this reason, in terms of evaluating the relative effectiveness of various shielding materials and designs, it has been suggested, in our preliminary reported research results, that consideration and analysis of the actual fluence of the radiation spectrum behind shielding be considered for optimization purposes [14], as all radiation damage is directly related to the flux of the various radiation species and their energy spectrum. Use of such a fundamental metric is particularly helpful when examining multilayer shielding designs, because the physical mechanism and ability to stop the primary and secondary particles varies with their kinetic energy, atomic charge, and whether they carry a relative negative, positive, or neutral charge.

3.2 Stopping Power and Linear Energy Transfer

In the previous discussion it was noted that particles traversing a material may interact through elastic and/or inelastic collisions with the target material's electrons, atoms and molecules; however, it is important to note that these interactions occur with very different frequency. For example, the cross section for a heavy charged particle interacting with atomic electrons in a material – i.e., the probability for that interaction to occur – is several orders of magnitude higher than that for elastic nuclear scattering or nuclear reactions. [38] As a result, many elastic atomic collisions with electrons occur in a centimeter track of ordinary matter ($\approx 10^6$), whereas by contrast,

many orders of magnitude fewer nuclear collisions occur, either elastic or inelastic. [67] Consequently, a heavy charged particle traversing matter loses the greater fraction of its energy to electronic excitation of the material – ionization and excitation of atoms by interacting with, and sometimes dislodging, the orbital electrons. [68] In addition, a heavy ion can transfer only a small fraction of its energy in a single electronic collision, thus the deflection of the incident ion is negligible and it will travel in almost a straight path, continuously losing small amounts of energy as a result of many collisions with atomic electrons. [38]

Before focusing on the Stopping Power formulation, it is of preliminary interest to note that the maximum energy transfer from the heavy charged ion to an electron in the target material is given by:

$$Q_{max} = \frac{4mM(Mv^2/2)}{(M+m)^2} \quad \Rightarrow M >> m \Rightarrow \quad \approx \frac{4mE}{M} \tag{3.1}$$

where m is the mass of the smaller body (e.g., electron in the target material), M is the mass of the larger body (e.g., incident heavy ion), and E is the kinetic energy of the larger body. *See* Appendix A for more details on this derivation. Thus, for a proton with a kinetic energy of 50 MeV colliding directly with an electron, $Q_{max} = 0.11MeV$, or only about 0.2% of the incident particle energy is transferred.[3]

Of course, the energy transfer will be much larger if the incident ion collides with a larger particle, such as a proton or neutron, in the target material atomic structure, but such nuclear interactions are much less frequent, as compared to the atomic interactions with orbital electrons in the target material. While those interactions

[3] The mass of a proton is $M_p = 1.67\times10^{-27}kg$, and the mass of an electron is $m_e = 9.11\times10^{-31}kg$; thus, the maximum energy transfer in a head-on collision from the incident proton to the electron is $Q_{max} = \frac{(4)(9.11\times10^{-31})(50MeV)}{1.67\times10^{-27}} = 0.11MeV$

with the larger particles may not be the predominate contributor to the LET and Stopping Power of the incident heavy ion, they are very important from the standpoint of the secondary particles such interactions generate, and the subsequent LET of those emissions. And, of course, such nuclear interactions *are* the predominate contributor to stopping uncharged particles, such as secondary neutrons.

The forces at play between the incident ion and other charged particles in the target material – predominately electrons – can be calculated in accordance with Coulomb's inverse square law relating the force to the magnitude of the two charged particles and the distance between them: $F = k_0 \frac{q_1 q_2}{r^2}$, where Coulomb's constant, $k_0 = 8.99 \times 10^9 Nm^2 C^{-2}$. From this, the energy deposited in the target material can be determined, and ultimately, then, an estimate of the so-called "Stopping Power" S of the material with respect to incident particle radiation from the GCR may be determined, and thereby facilitate evaluation of different shielding materials.

The first step is to calculate the so-called Linear Energy Transfer (LET) – the energy locally deposited in the target material over a distance dx by the incident ion: LET = $-\frac{dE}{dx}$ (MeV/cm) – conventionally shown as a negative quantity to indicate energy loss. Then, due to the fact that most of the energy is transferred in electronic collisions, the Stopping Power of the target material is very nearly equal to the LET in magnitude, differing only by a small amount of energy lost by nuclear collisions, bremsstrahlung radiation emitted as electrons are dislodged, and Cherenkov radiation emitted as some relativistic incident charged particles pass through the target material at greater than the phase velocity of light in that medium. [69] [70] Thus, for all practical purposes in evaluating the GCR spectrum incident on shielding materials the Stopping Power is approximately the same as the LET, i.e., the linear rate of energy loss to atomic electrons along the path of a heavy charged particle in a medium,

and is the basic physical quantity that determines the absorbed dose to the target material (as discussed in Chapter 2):

$$S \approx LET = -\frac{dE}{dx} \quad (MeV/cm) \tag{3.2}$$

The classical derivation of the Stopping Power was done by Niels Bohr in 1915 [71], and proceeds by calculating the transfer of momentum from the incident heavy ion to the electrons in the target medium as a result of Coulombic interactions for a differential volume. [71] The energy transfer to the electron is then calculated directly by the relationship between momentum, p, and energy, $Q = \frac{1}{2}m_e v^2 = \frac{p^2}{2m_e}$. Then, the differential rate of energy loss due to these interactions is calculated by integrating over all individual energy transfers for all electrons encountered by the heavy ion in the differential volume of the target material along the path of the incident ion, over the range Q_{min} (the distance at which the energy transfer is less than the minimum ionization energy of the target material) to Q_{max} (a head-on collision between the ion and an electron). Thus, in terms of classical mechanics, the Stopping Power of a material can be calculated as follows:

$$S = -\frac{dE}{dx} = \frac{4\pi n k_0^2 Z_p^2 e^4}{m_e v^2}\frac{1}{2}\ln\frac{2m_e v^2}{h\omega} = \frac{4\pi n k_0^2 Z_p^2 e^4}{m_e v^2}\frac{1}{2}\ln\frac{2m_e v^2}{I} \tag{3.3}$$

where S has units of MeV/cm, k_0 is Coulomb's constant, n is the number of electrons per unit volume in the target medium, Z_p is the atomic number of the incident heavy ion particle, e is the charge of an electron, m_e is the rest mass of an electron, v is the velocity of the incident heavy ion, h is Plank's constant, $\frac{1}{\omega}$ is the period of the electron in its orbit around an atom in the target medium, and I is the ionization potential of the target medium. *See* Appendix A for more details on this derivation.

Of immediate interest, it is evident from this formulation that the Stopping Power is inversely proportional to the square of the velocity of the incident ion particle, and proportional to the square of its charge; and the primary characteristic of the target material itself that matters is the number of electrons per unit volume – i.e., not necessarily the density of the target material.

By 1932 the Stopping Power formulation had been revised by Hans Bethe to include relativistic effects of the high energy ions:

$$S = -\frac{dE}{dx} = \frac{4\pi n k_0^2 Z_p^2 e^4}{m_e c^2 \beta^2} \Big[ln \frac{2 m_e c^2 \beta^2}{I(1-\beta^2)} - \beta^2 \Big] \tag{3.4}$$

where c is the speed of light in a vacuum, $\beta = v/c$ is the ratio of the incident heavy ion velocity to that of the speed of light, and I is the mean excitation energy of the target medium.[4] [74] Of course, if $v << c$, this formulation reduces to the classical formulation originally derived by Bohr.

And even the Bethe formulation was found lacking in replicating experimental observations at the low and very high energy extremes of the incident particles, and more recently other corrections have been included to account for such things as electron spin, magnetic moments, and accounting for differences in electrons located in the inner shells of the target medium atoms. For example, in 1992 Bichsel introduced the following formulation of Stopping Power that is now generally agreed to adequately correlate with actual data, and has been dubbed the Bethe-Bloch equation (including the several correction factors):

[4] The mean excitation energy is often best determined experimentally, but sometimes estimated as $I = \omega h$, or as $I = h\omega/Z_T$, or with empirical expressions like $I = 11.2 + 11.7 eV Z_T$, for $2 \leq Z_T \leq 13$, and etc. [72] [73].

$$S = \frac{4\pi Z_p^2 \rho Z_T N_A e^4}{A_T m_e \beta^2 c^2}\left[ln\Big(\frac{2m_e c^2\beta^2\gamma^2}{I}\Big) - \beta^2 - \frac{C\big(\beta\big)}{Z_T} + Z_p L_1\big(\beta\big) + Z_p^2 L_2\big(\beta\big) + L_3\big(\beta\big)\right] \quad (3.5)$$

[72] [68] [75] Here the density of the target medium is (ρ), its charge (Z_T), its atomic weight (A_T), and the Avogadro number is (N_A).[5] In addition, the various relativistic and quantum mechanics "correction factors" have been added over the years to improve accuracy in the low and high ion energy ranges, including the argument of the logarithm, the shell correction term ($C\beta$), the Barkas correction ($L_1(\beta)$), the Bloch term ($L_2(\beta)$), and the Mott and density corrections ($L_3(\beta)$). [72] [75] [9]

Examination of these equations reveals that the Stopping Power (or LET of the incident ion) increases as the ratio of the shielding material atomic charge to atomic weight, $\frac{Z_T}{A_T}$. Thus, when considering the predominate Stopping Power electron interaction mechanism, shielding materials composed of elements with the largest charge-to-mass ratio will be the most effective in slowing down and stopping the positively charged high atomic number and energy particles (HZE) found in GCR. [41] As hydrogen has the highest charge-to-mass ratio of any element, this naturally points to shielding materials with high hydrogen content (e.g., $\frac{Z_T}{A_T}$ is 1 for hydrogen, but only 0.48 for aluminum). This consideration, taken alone, leads to the conclusion that heavier shielding materials will be less effective in stopping the GCR ions, i.e., the energy deposited by a positively charged ion will actually *decrease* for heavier shielding materials. [9]

[5] As can be seen, the front part of this formulation is essentially the same as the Bethe relativistic formulation, when one considers that the Coulomb constant in SI units is $k_0 = \frac{1}{4\pi\epsilon_0} = c^2 \times 10^{-7} H/m$ (where ϵ_0 is the magnetic field free space permittivity in a vacuum, and H (henry), is in units of $kg - m^2 - C^{-2}) = 8.987 \times 10^9 N - m^2 - C^{-2}$, and that target material electron density is $n = N_A Z_T \rho / A_T$.

The nuclear interaction of a particle traversing a material includes both elastic and inelastic collisions, as discussed above, and contributes to slowing and/or stopping the incident GCR ion particle. The ultimate nature of these interactions depends in large part on both the atomic structures of the incident ion and target material, as well as the kinetic energy of the incident ion. Light and/or lower-energy projectiles can be scattered or absorbed, where the transferred energy may leave the target in an excited state and cause γ-ray emissions, whereas heavier and/or high-energy incident ions may break the target nucleus producing secondary emissions, including lighter atomic weight atoms, fragments, and neutrons. The probability for each of these possible reactions is measure by its so-called cross section (σ), which is at its most fundamental a geometric calculation based on the physical sizes of the incident ion and the target atoms. [76] Cross section values must be calculated for each possible type of interaction, and are usually measured in units of barns ($1b = 10^{-24} cm^2$). [38]

In 1950 Bradt and Peters first published their research indicating that the incident GCR at the Earth had undergone nuclear reactions while traveling from their source to the solar system, giving rise to the creation of a wide variety of elements and the concept that primary GCR ions collided with interstellar material on their journey. [77] Later, this work gave rise to geometric calculations of cross sections for particular ion/atomic interactions in target materials based on classical mechanics, which was found experimentally valid over a wide range of energies. [78] Over the succeeding years, further analysis has resulted in the nuclear reaction cross section being approximated by the the so-called Bradt-Peters equation:

$$\sigma = \pi r_0^2 c_1\big(E\big)\Big(A_p^{\frac{1}{3}} + A_T^{\frac{1}{3}} - c_2\big(E\big)\Big)^2 \tag{3.6}$$

[79] [9] [38] Here the total fragmentation cross-section (also referred to as the absorption cross-section), σ, is proportional to $A_T^{\frac{2}{3}}$, the atomic mass of the shielding material. This relationship also suggests lighter materials, having smaller nuclei and thus more of them per unit mass, will have more nuclear interactions, and thus be more effective in stopping incident GCR ions. [9]

Thus, the total Stopping Power is comprised of the atomic reactions ($\sigma^{at} \approx 10^{-16} cm^2$), the elastic collisions ($\sigma^{el} \approx 10^{-19} cm^2$), and nuclear/fragmentation reactions ($\sigma^{r} \approx 10^{-24} cm^2$), where the energy transferred is calculated using formulations for S, Q, and nuclear fragmentation models. [38] For general order of magnitude purposes, the average energy transfer involved in each type of reaction is: atomic reactions $\approx 10^2 eV$; elastic collision $\approx 10^6 eV$; and nuclear reaction $\approx 10^8 eV$. [67]

Even though a nuclear reaction transfers much more energy than an atomic reaction with the outer-shell electrons, the nuclear stopping component is actually quite small, especially for ions with kinetic energy above 200 KeV/n, where it is typically less than 1% of the electronic stopping component. [80] The relative magnitude of the contribution of electronic and nuclear reactions to the total Stopping Power is aptly illustrated by calculating the so-called "total mass stopping power" using the Bethe-Bloch equation and the Everhardt formulation (*see* Everhart, 1955 [78]) for nuclear collisions, by utilizing the National Institute of Standards and Technology (NIST) PSTAR program (https://physics.nist.gov). [81].

As shown in Figure 3.4, the mass stopping power is simply the Stopping Power divided by the target material mass (S/ρ in units of $MeV - cm^2/gm$), and illustrates the energy deposition from the incident ion per unit of areal density (i.e., the energy lost by radiation traversing a unit distance ($-dE/dx$) per unit density).

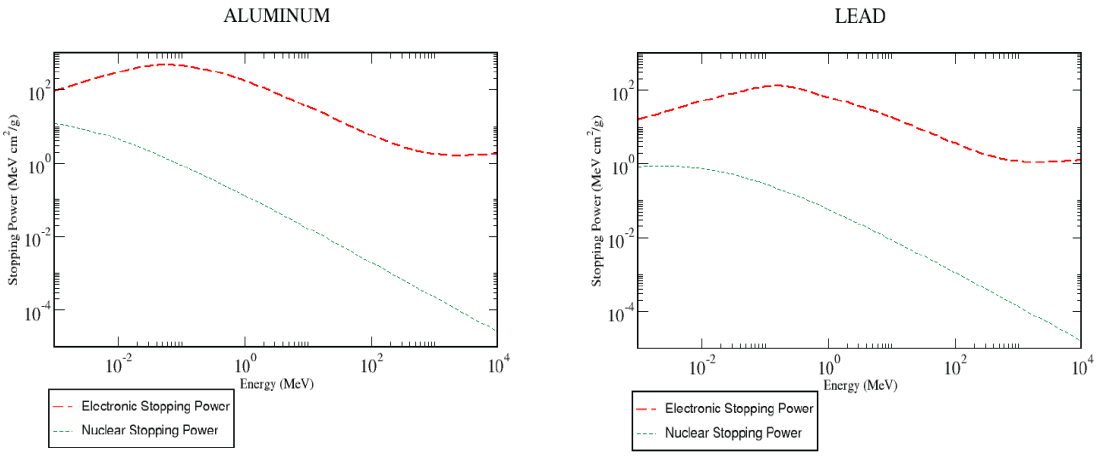

(a) Mass Stopping Power - Aluminum. (b) Mass Stopping Power - Lead.

Figure 3.4 : Comparision of Electronic and Nuclear Contributions to Mass Stopping Power. Calculated using the NIST PSTAR program. *See* Berger, 2002.

These calculations dramatically illustrates the predominance of the electronic mechanism for slowing and stopping positively charged incident ions as they traverse shielding materials. For example, consider an incident GRC proton with a kinetic energy of $10^3 MeV$, or $1 GeV$, (the peak fluence for GCR protons, as shown in Figure 2.5). The total mass stopping power in aluminum is 1.75 $MeV cm^2/gm$, of which 99.99% is due to electronic reactions; and the same is true of lead, with some 99.98% due to electronic reactions. This data demonstrates that while heavier materials will cause the nuclear reaction component contribution to the total mass stopping power to increase, it still remains a minor part of the total. Of course, the nuclear collision/fragmentation aspect will predominate when one considers the stopping of uncharged particles, like secondary neutrons.

A further relevant conclusion may be inferred from the calculation of the mass stopping power of an incident proton in various types of target materials, as shown in Figure 3.5. For example, consider again an incident GRC proton with a kinetic

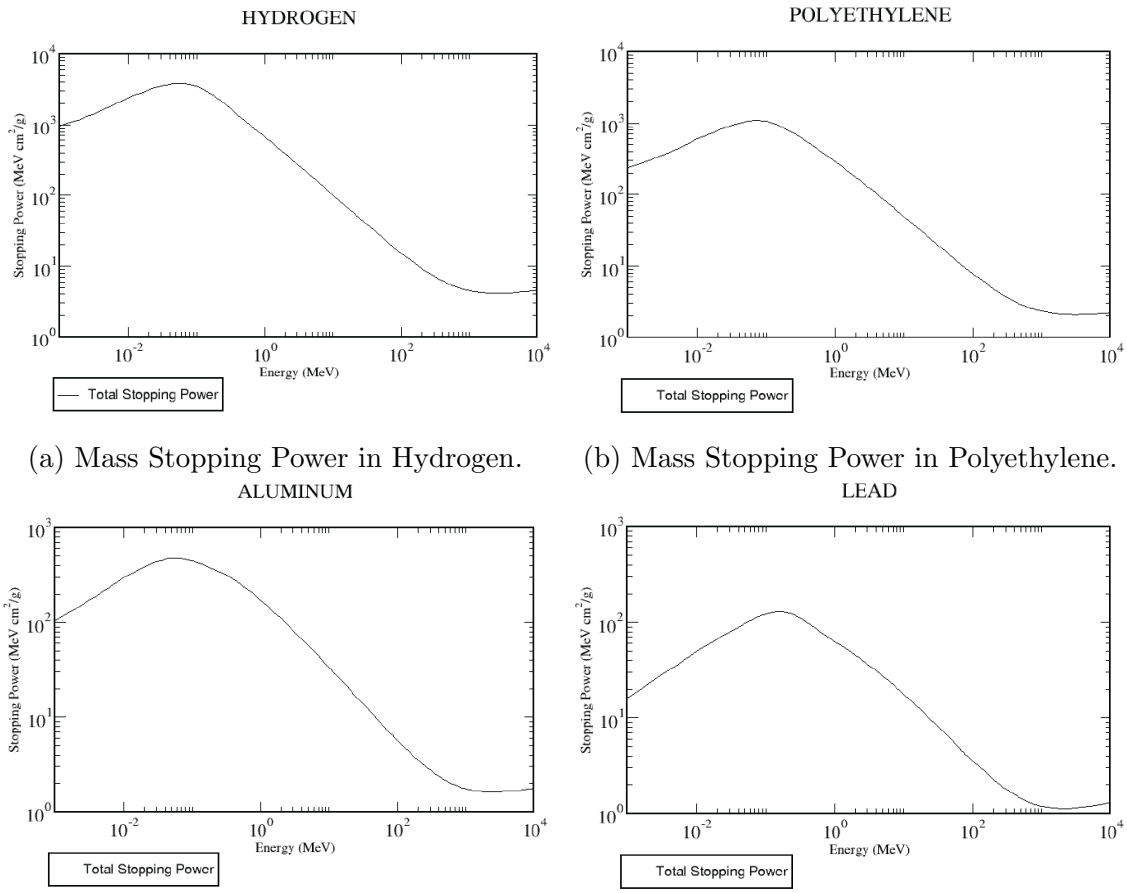

(a) Mass Stopping Power in Hydrogen.

(b) Mass Stopping Power in Polyethylene.

(c) Mass Stopping Power in Aluminum.

(d) Mass Stopping Power in Lead.

Figure 3.5 : Total Mass Stopping Power of an Incident Proton in Various Materials. Calculated using the NIST PSTAR program. *See* Berger, 2002.

energy of $10^3 MeV$, or $1 GeV$. The total mass stopping power for such a proton in hydrogen is 4.497 $MeV cm^2/gm$, whereas in polyethylene it is 2.320 $MeV cm^2/gm$, in aluminum it is 1.750 $MeV cm^2/gm$, and in lead it is 1.186 $MeV cm^2/gm$. Thus, though perhaps not intuitive, it is clear that the denser a shielding material, the *less* effective that material is in stopping high energy ions in the GCR.

An understanding of the energy deposited in a target medium (LET) is needed to evaluate the ability of a material to slow down or stop an incident GCR particle

(Stopping Power) and to calculate the absorbed dose and other metrics that attempt to evaluate health impacts, and thus adds information helpful to selecting optimal shielding materials. Conveniently, for GCR radiation $S \approx LET$, but how both mechanisms change with different shielding materials and designs is only part of the story.

3.3 GCR Ion Range in Shielding Materials

The range of an incident particle as it travels through a target material is defined as the average distance traveled before the particle loses all of its kinetic energy and stops. Intuitively, the range increases with increasing kinetic energy of the incident particle, and is typically a few gm/cm^2 at 50 MeV/n, to more than 100 gm/cm^2 at 1000 MeV/n. [64]

As shown previously (*see* Figure 2.6), the shielding provided by a spacecraft wall is around 5 gm/cm^2 of aluminum, and the effective shielding on the ISS is close to 20 gm/cm^2 of aluminum in several locations, because of the presence of payloads and equipment racks. While calculation of the Stopping Power of incident GCR particles will demonstrate a material's relative effectiveness in slowing down the particle, the next question becomes whether the material is thick enough to actually stop the incident particle. That requires calculation of the range of the particle (R) in the particular material:

$$R = \int_0^\infty dx = \int_E^0 \left[\frac{dE}{dx}\right]^{-1} = \int_0^E \frac{dE}{S(E)} \tag{3.7}$$

where the Stopping Power as function of energy ($S(E)$) is again approximated by the linear energy transfer ($LET = -\frac{dE}{dx}$) by the incident particle into the shielding medium. [38] [82]

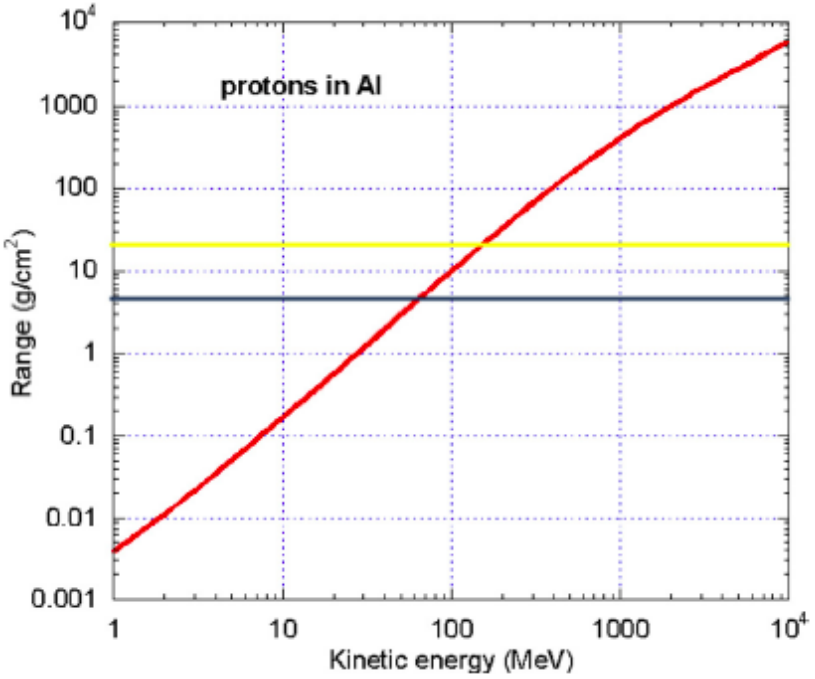

Figure 3.6 : Proton Range in Aluminum (red line), showing energy required to penetrate 5 gm/cm^2 (blue line) and 20 gm/cm^2 (yellow line). From Durante, 2014.

A calculation of the range of a proton in aluminum is shown in Figure 3.6 – the range is expressed areal density, which converts to physical thickness by dividing by the material density ($\rho_{Al} = 2.7gm/cm^3$). Thus, for the shielding provided by a typical spacecraft hull of $5gm/cm^2$ (the blue line) or by the ISS of $20gm/cm^2$ in some areas (the yellow line), such shielding will only stop all protons with kinetic energies less than some 100-200 MeV. While that shielding is adequate for the protons found in most SPEs, it will clearly not stop much of the GCR proton spectrum. [38] In fact, at the energy level of maximum fluence for protons in the GCR ($\approx 10^3 MeV$), it is apparent that most protons will pass through the shielding with sufficient energy to deposit damaging levels of energy in a human or equipment target; i.e., protons with residual energies above a few MeV can penetrate the skin and deposit their energy in

inner body organs. [9] For example, a 1 GeV proton can travel through 412 gm/cm^2 of aluminum, which is a physical thickness of 152.6 cm, or about 5.0 ft (calculated using PSTAR program) – clearly an impractical thickness for spacecraft design.

It is also instructive to note that the heavier ions in the GCR will have a shorter range in any particular shielding material, due primarily to having a much higher LET, as shown in Figure 3.7.

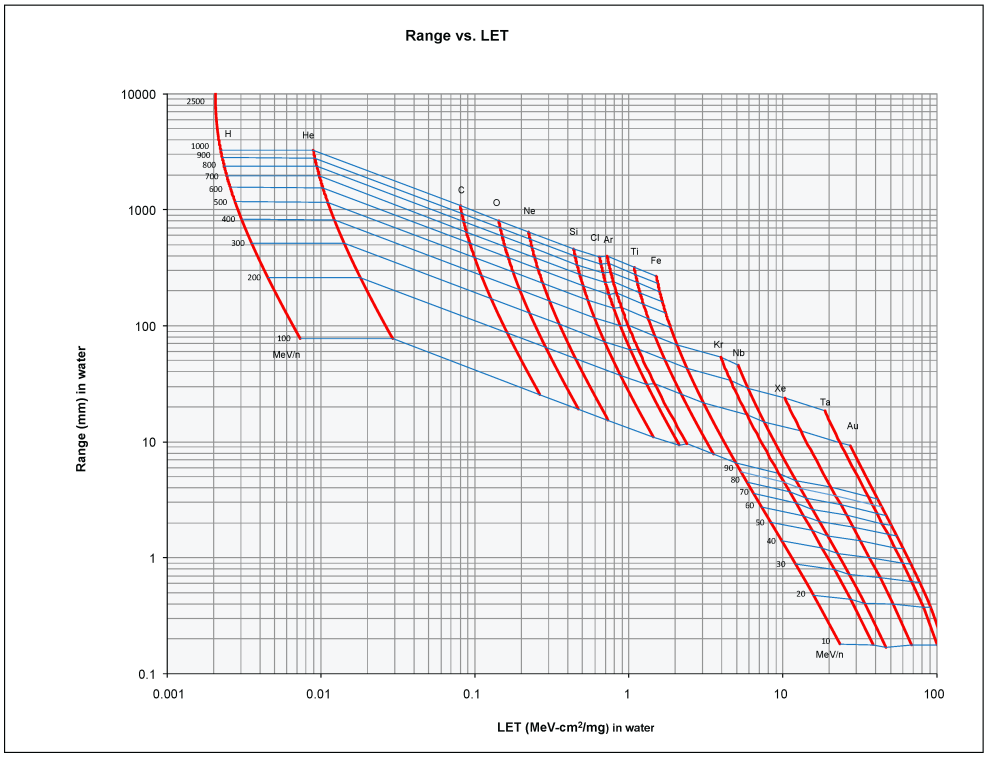

Figure 3.7 : Range of Ions in Water. From Brookhaven National Laboratory Technical Data Files: https://www.bnl.gov.

Thus, reading from Figure 3.7, a 1 GeV/n proton has a range of some 320 cm in water, while a 1 GeV/n iron ion has a range of only some 28 cm (and this even as the iron ion has a larger total kinetic energy of 56 GeV). The same holds true in other materials. For example, a 1 GeV/n proton has a range in HDPE of some 318 cm (*see*

Figure 3.9a), whereas the range of a 1 GeV/n iron ion has a measured range in HDPE of only some 25 cm (*see* Figure 3.10b). And the same is true for aluminum, where the 1 GeV/n proton has a range of some 152 cm, and the iron ion only 11 cm (areal densities of some 412 gm/cm^2 and 30 gm/cm^2, respectively). Recalling again that the peak fluence for *all* ions in the GCR is around 1 GeV/n, it is readily apparent that even the heavier ions will not be stopped by current standard spacecraft shielding protocols – again, the physical thickness required is impractical from a design standpoint – *see* Figure 2.6 and accompanying discussion. Thus, it is clear that both the mass and physical thickness of shielding materials are important design constraints, and along with those considerations, whether the shielding material is useful in other ways; e.g., as structural elements or necessary payloads, such as water or fuel.

Of particular importance to consider when designing shielding for positively charged ions, is that the energy release in the target medium is not linear, but in fact the LET is at a maximum some distant into the interior of the target as the ion particle gradually loses velocity – this peak energy deposition is known as the Bragg peak. [9] Examination of the equations for calculating $LET = -\frac{dE}{dx}$ show that the incremental energy deposited per incremental depth into the target medium is inversely proportional to the square of the velocity of the ion particle; thus, as the ion particle is slowed in the shielding medium, the ΔE will tend to increase, and peak as $v \to 0$.

But this is not the entire story, as demonstrated in Figure 3.8. These are graphs of experimental data done with single-ion radiation beams at Brookhaven National Laboratory in order to measure the actual energy deposited as a function of depth in a target shielding medium of High Density Polyethylene (HDPE – $\rho = 0.97 gm/cm^3$) – a material that has been used in some areas on the ISS.

The atomic Coulomb interactions of the incoming ion with the target shielding

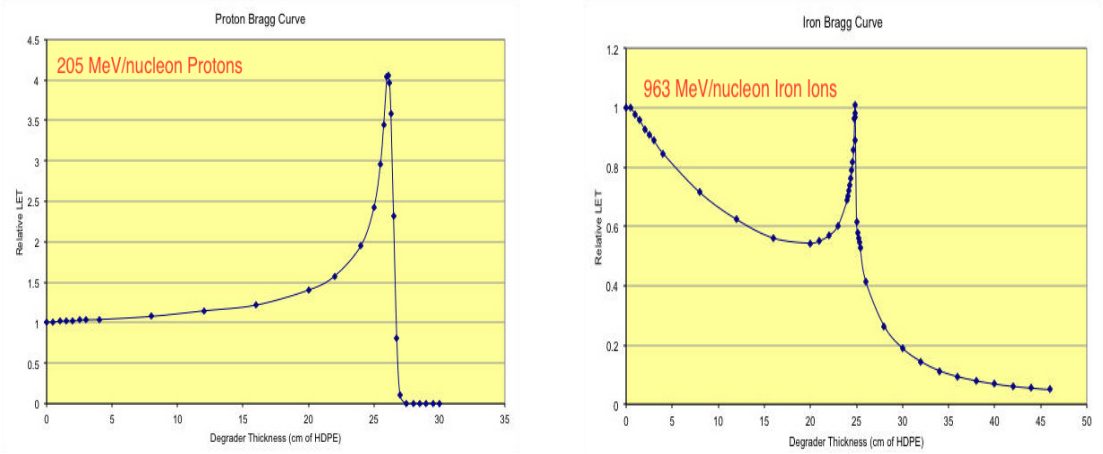

(a) LET of 205 MeV/n Proton in HDPE. (b) LET of 963 MeV/n Iron ion in HDPE.

Figure 3.8 : Linear Energy Transfer (LET) of Proton and Iron ions as a Function of Depth in High Density Polyethylene (HDPE). From Brookhaven National Laboratory Technical Data Files: https://www.bnl.gov.

material will begin to slow it down (per the Bethe-Bloch equation), but heavier ions will also undergo nuclear reactions with the shielding material, and a contribution to the LET will occur as a result of elastic collisions with nuclei and fragmentation of the primary incident ion. [73] Thus, as shown in Figure 3.8a, the proton, which is not susceptible to fragmentation, shows an initial slow, but steady, deposition of energy, until its velocity slows sufficiently that the LET peaks and the ion is stopped, at about 26 cm (about 10 $inches$) for this relatively low energy proton. However, the data for the iron ion indicates a more complex set of interactions, as shown in Figure 3.8b. First, when some of the incident iron ions fragment upon colliding with the target material atoms into lower-Z ions, the LET of the sum of these secondary ions is less than had the primary ion stayed in tact – mainly due to the fact that the secondary ion emissions are not fully ionized (i.e., stripped of all electrons, like the primary incident particle), and that the fragmented ions tend to pick up free electrons in the target material (thus further reducing their net charge), both factors leading

to a reduced LET. [83] Thus, the total LET measured may initially drop until a peak energy deposition is achieved as the primary iron ions are stopped, with a noticeable tail of penetrating fragments beyond the Bragg peak. This aptly illustrates the point with respect to the HZE ions in the GCR that while a particular shielding material may stop the primary ion at a certain range (here the 963 MeV iron ions are stopped in HDPE at some 25 cm), many of the secondary fragments are not stopped until 40-45 cm of HPDE shielding is traversed; thus a necessary increase in HDPE shielding material is required from some 9.8 *inches* at the Bragg peak range, to almost 18 *inches* to stop the secondary fragments – obviously severely restricting the useful interior volume of a spacecraft or habitat.

Further, calculations using the PSTAR program indicate that a 1 GeV/n proton has a range in HDPE of some 308 gm/cm^2 in areal density (actual thickness = 318 cm), and in aluminum of some 412 gm/cm^2 in areal density (actual thickness = 153 cm), as shown in Figure 3.9. Similarly, measurements of a 1 GeV/n iron ion indicate a Bragg peak range in HDPE of about 24 gm/cm^2 in areal density (actual thickness = 24.7 cm), and in aluminum of about 30 gm/cm^2 in areal density (actual thickness = 11.1 cm), both considerably shorter than the proton range in the same materials. But considerable care must be taken to fully understand the implications of these metrics – areal density versus actual physical thickness – in optimizing shielding selection.[6]

For example, this analysis indicates that for all ions in the GCR that lighter materials result in a shorter range for the ion if viewed from the standpoint of areal density – the normalized basis to compare shielding materials in terms of the amount

[6] *See,e.g.*, Figure 3.9 and Figure 3.10b, noting that the range in both is measured in areal density and therefore must be divided by the density of the target material in order to evaluate actual physical thickness; e.g., 0.97 gm/cm^3 for HDPE and 2.7 gm/cm^3 for aluminum. Note that the same results obtain with calculated values of the range using the SRIM (Stopping and Range of Ions in Matter) program (http://www.srim.org/). [73]

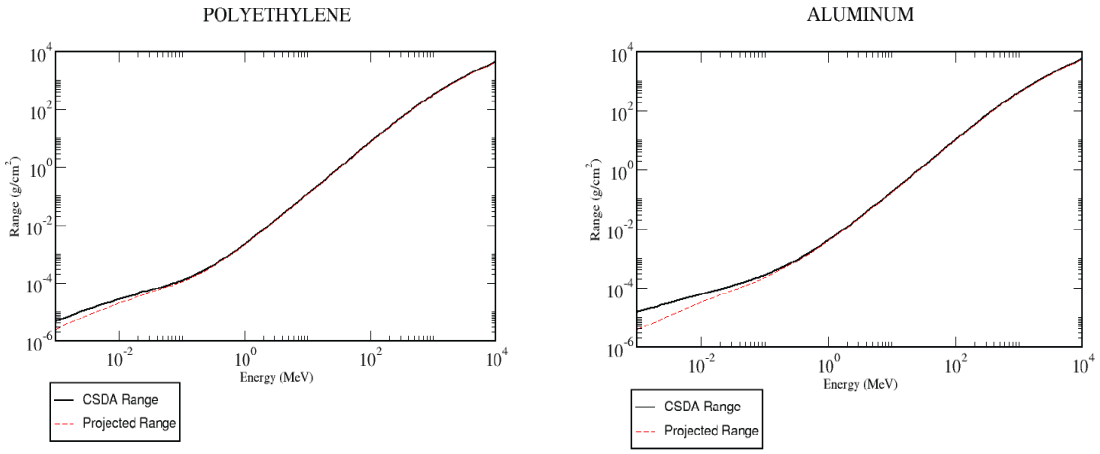

(a) Range of 1 GeV/n Proton in HDPE. (b) Range of 1 GeV.Proton in Aluminum.

Figure 3.9 : Range of a 1 GeV Proton in Polyethelene (HDPE) and Aluminum. Calculated using NIST PSTAR program. *See* Berger, 2002.

of matter traversed by the radiation – and thus would seem to dictate selection of lighter materials for shielding in order to optimize effectiveness. But this ignores the practical consideration of physical thickness, where, as in this example, the lighter HDPE material must be over twice as thick as aluminum to accomplish the same shielding effectiveness – possibly a serious design constraint. And a further complicating factor is the propensity for the HZE ions ($Z > 2$) in the GCR to fragment, creating secondary emissions with significantly longer range than the primary ion, and with sufficient energy to cause damage to human tissue and equipment.

These characteristics of positively charged ions traversing materials, like those in the primary GCR spectrum, as opposed to other kinds of radiation, can have beneficial utility for medical treatments, as shown in Figure 3.10, but also create serious problems from the standpoint of shielding the GCR ions.

As shown in Figure 3.10a, a radiation treatment by a positively charged proton or carbon ion can be directed to a tumor in the interior of the human body, and by ad-

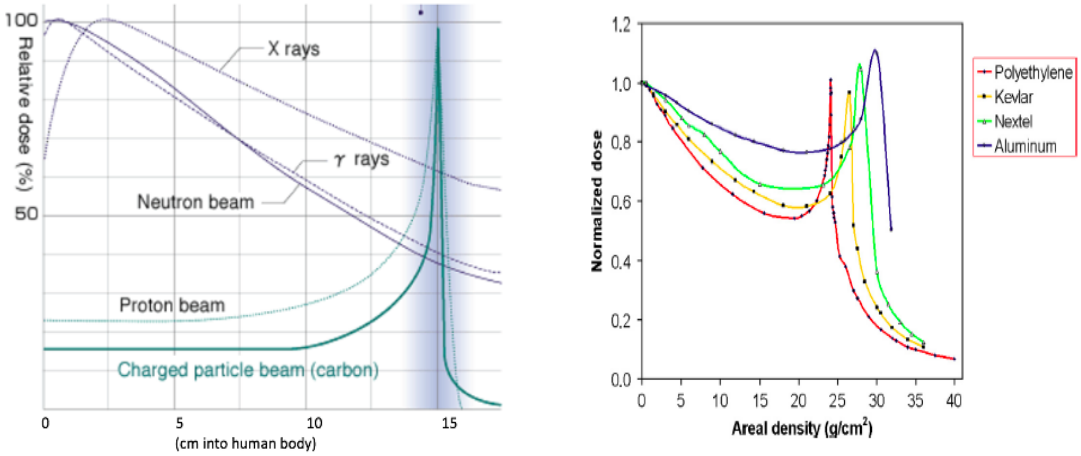

(a) Radiation Energy Loss in Tissue. (b) Bragg Peaks for 1 GeV/n Fe Ion.

Figure 3.10 : Bragg Peaks of Energy Loss from Ionizing Radiation as a Function of Depth in Human Tissue (a), and in Various Other Materials (b). From J. Chancellor, 2015, Texas A&M Lecture Notes and Durante, 2014, respectively.

justing its kinetic energy, the ion can be made to release most of its energy at a depth of some 15 cm, without doing much damage to the overlying or underlying tissues. This provides significant medical advantages in attempting radiation treatments over other types of radiation, which transfer most of their energy near the surface of the skin. But this energy release characteristic of ions is problematic in GCR radiation shielding protocols, especially when the thickness of the shielding cannot fully stop the ion particle in question, as is true of standard spacecraft shielding over most relevant energies in the GCR (*see* Figure 3.6). This point is aptly demonstrated by noting in Figure 3.10b that a 1 GeV/n iron ion (near the peak fluence in the GCR energy spectrum) traversing aluminum will release most of its energy into the shielding material at an areal density of about 30 gm/cm^2, or about 11 cm (4.3 $inches$) in actual thickness. This is some six times thicker than standard spacecraft hulls of 5 gm/cm^2 (*see* Figure 2.6), and thus such an iron ion will likely pass through the aluminum hull without losing much of its energy, and be capable of causing damage

to human tissue and to equipment on the interior of the vehicle. [84] Indeed, ions with sufficient range to fully traverse the shielding will emerge with a higher LET and may be more biologically damaging to human tissue behind the shielding than had there been no shielding at all. [85]

Note also that the curves in Figure 3.10b are from actual measurements in the laboratory using a 1 GeV/n iron ion beam, which has been used in the literature as a very rough proxy for the heavy ion component of the GCR. But of course such analyses ignore the much higher fluence of protons and alpha particles in the GCR, and, as noted above, the fluence of all GCR ions peak at around a kinetic energy of 1 GeV/n (see Figure 2.5), and thus most will pass through current standard shielding protocols. [85] Nevertheless, such experimental measurements are useful in teasing out potential metrics for optimizing shielding material selection, as discussed above, and by examination of Figure 3.10b one can readily see that the polyethylene curve has a steeper initial slope and shorter range on an areal density basis. *See also*, Zeitlin, 2006. [85] In addition, there has been much recent work at Brookhaven National Laboratory to utilize a basket of ion beams in seriatum fashion to attempt to better replicate the impact of the GCR spectrum on shielding and the targets behind shielding. [86] [87]

3.4 Secondary Particle Generation

Although most of the energy loss of primary particles as they pass through shielding materials is by ionization through Coulomb collisions with orbital electrons and nuclei, the energy of these incident particles is sufficiently high that a fraction of the particles will undergo nuclear reactions, which is a matter of importance in shielding design because of the generation of new harmful energetic particles – the so-called secondary emissions. [68] [24] Nuclear reactions, which occur through interactions of

Galactic Cosmic Ray ions with the nuclei of atoms in shielding materials or tissue, lead to the production of secondary radiation, including neutrons and other charged particles from the atoms of the shielding material or tissue. The outcome of such nuclear reactions depends strongly on the nature and energies of both the projectile and the target. Light projectiles with low energies can be scattered, leaving the nucleus in an excited state that eventually will release a gamma ray, or it can be absorbed. Projectiles with high energies will break the target nucleus producing a number of recoil fragments and, typically, several high energy neutrons. The probability that a certain reaction channel takes place is represented by its cross-section, σ, discussed above. The cross-section concept can be viewed as the effective area of a target as seen by a projectile. Hence, the higher the cross-section, the bigger the target area, and thus, the higher the probability that a particular type of reaction occurs.

The mean free path for a nuclear reaction *decreases* with increasing mass of the incident GCR particle: on the order of about 10 gm/cm^2 for heavy nuclei such as iron ($^{56}_{26}$Fe – A=56; Z=26), to more than 20 gm/cm^2 for protons ($^{1}_{1}$H – A=1; Z=1). [64] As a result, for the GCR spectrum impacting conventional spacecraft shielding, considering both species and energy levels, it is clear that nuclear reactions will occur in both the shielding and the human tissue or equipment behind the shielding. Thus, there will be both primary radiation particles and secondary emissions to consider in shielding designs, as shown in Figure 3.11.

The two types of nuclear interactions between primary GCR ions and target nuclei include both target and projectile fragmentation scenarios. Target fragmentation occurs when a high energy charged primary ion collides with a nucleus in the shielding material or in human tissue. The collision results in the transfer of kinetic energy into new secondary radiations through several processes, including direct knockout of

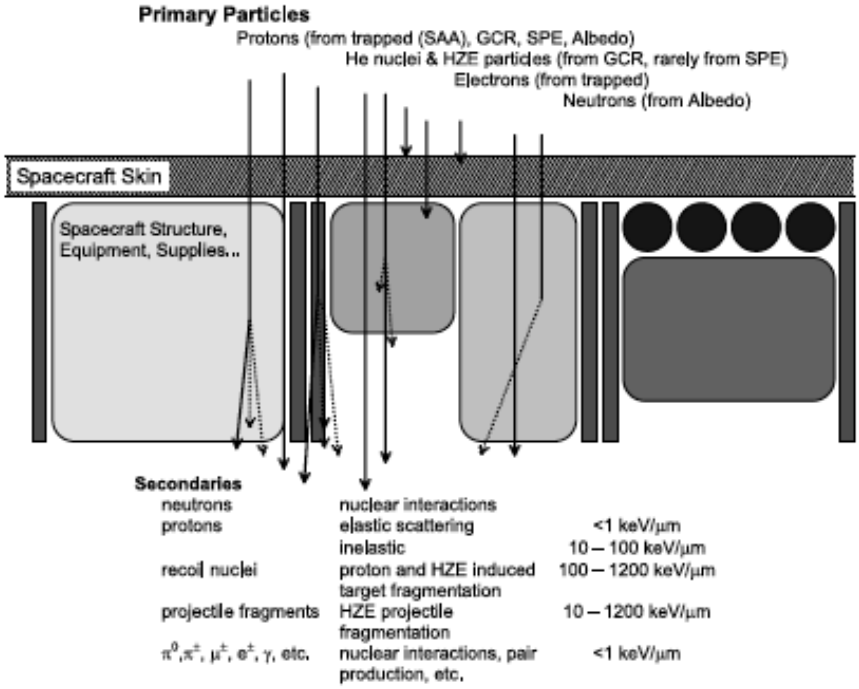

Figure 3.11 : Transport of Primary GCR and Secondary Emissions in Spacecraft. From Benton, 2011.

nuclear constituents, resonant excitation followed by particle emission, and pair production (e.g., the creation of an electron and a positron by a sufficiently high energy photon interacting with a target nucleus). [24] Projectile fragmentation occurs when the collision results in the incident ion breaking up into lighter ions, free protons and neutrons, and other fragments. The secondaries produced continue to traverse the medium, and may themselves undergo further nuclear reactions. Through these processes, a single GCR particle incident on a shielding material may attenuate through energy transfer to electrons of the media, or if a nuclear reaction occurs, generate a multitude of secondary emissions which can cause an increase in exposure behind the shielding, and thus an increase of radiation constituent fluence and absorbed dose to

the humans or equipment.[7] [68]

As noted above, high-energy radiation can penetrate to a depth in standard shielding materials to the point that the thickness required is not practical for spacecraft. And while a moderately thick shielding can reduce the absorbed dose in the target behind the shield, as the thickness increases, the shield effectiveness drops due to the production of a large number of secondary particles, including neutrons, caused by nuclear interactions of the GCR with the shield. [41] These particles will generally have a lower energy, but can have higher quality factors than incident cosmic primary particles, as noted above. [9] For example, the production of secondary neutron emissions in spacecraft shielding can significantly increase the harm to human occupants, due to the higher contribution that neutrons have to the dose equivalent calculations. In fact, neutrons contribute in the range of 30-60% of the entire dose equivalent exposure in the LEO orbit of the ISS due to having a quality factor some 4-5 times that of charged particles. [24] And, as it turns out, denser shielding materials may produce more unwanted secondary particles than lighter materials, mainly due to the higher ratio of neutrons to protons as one advances to nuclei with atomic charge $Z > 20$; e.g., even a 1 GeV proton impacting a lead target will on average generate 25 neutrons. [70] In addition, for habitats on the surface of the Moon or Mars, one must also consider the secondary emission flux from GCR ions impacting the surface itself. These include the so-called "albedo neutrons" and other secondary emissions that back scatter upward upon undergoing a nuclear interaction with an incident GCR ion. [89] [90] Thus, optimizing shielding protocols must include consideration of both

[7] Indeed, scientists at Texas A&M have used the fact that a heavy ion will fragment into lighter ions in order to construct a target that will deconstruct the 1 GeV iron ion beam available at Brookhaven National Laboratory into a fluence of ions that more closely replicates the actual GCR spectrum, and thus allow on-Earth testing in a more realistic GCR-like radiation environment. [88]

a shielding material's propensity to create secondary neutrons and any other back scatter secondaries, and then, once created, how to stop those neutrons.

Importantly, slowing and stopping neutrons as they traverse matter is accomplished differently from ions, due to their lack of charge, thus eliminating the primary stopping force subjected to ions, the Coulomb collisions with electrons and nuclei. Neutrons are usually classified according to their energies, mainly because their interaction cross-sections are highly energy dependent, thus resulting in very different behaviour when traversing matter. [70] Neutrons with energies above 1 GeV are dubbed "high energy" and tend to behave like protons with similar energies and mean free paths, until some of the energy is dissipated. So-called "fast neutrons" have energies from 100 KeV up to about 20 MeV, and in this range the most probable energy loss interaction in a target medium is by elastic scattering. However, "fast neutrons" may also lose energy by other interactions, including: (1) inelastic scattering (mainly for neutrons with an energy greater than 1 MeV), where the target nucleus is left in an excited state and later decays by gamma ray emissions; (2) radiative neutron capture, where the target nucleus absorbs the neutron and enters an excited state that is dissipated by gamma ray emissions; and (3) neutron capture followed by the emission of a charged particle or by fission. [70] Generally, "fast neutrons" will undergo these energy loss interactions until their kinetic energy is equal to the medium's thermal temperature, where neutron capture will occur. Finally, "slow neutrons" have energies less than 0.5 eV, and the most probable interactions are elastic scattering until the energy is reduced to the local thermal temperature, followed by neutron capture. At these low energies, neutrons are considered to be near thermal equilibrium with their surroundings, and their energy is distributed according to the Maxwell-Boltzmann distribution – an energy of some 0.025 eV, corresponding to the spectrum peak at

room temperature (20 °C). [70]

Secondary neutrons produced in nuclear reactions by heavy charged particles in matter will usually undergo elastic scattering, losing their energy until they reach the thermal range, when they can be captured by atomic nuclei. Thus, neutron elastic scattering is the most important process in slowing down and stopping neutrons as they traverse shielding materials. As observed previously, the maximum neutron energy loss in a single scattering occurs in a head-on collision, and in accordance with energy conservation principles, is given by:

$$Q_{max} = \frac{4mM(Mv^2/2)}{(M+m)^2} = \frac{4mME_n}{(M+m)^2} \tag{3.8}$$

where M is the mass of the projectile, m is the mass of the target atom, and E_n is the initial neutron energy. It can be deduced, therefore, that the maximum energy loss in neutron elastic scattering occurs when hydrogen is the target material, where the neutron is totally stopped as $Q_{max} \approx E_n$, generating a recoil proton. From this consideration alone, hydrogen, with a single proton as its nucleus with a mass approximately equal to a neutron, would be a good neutron moderator, reducing the energy of passing neutrons to lower energies, and then stopped through neutron capture.

But, of course, the actual cross section for the neutron-nuclei elastic scattering interaction is also an important factor, and this will change with the energy of the incident neutron, as well as the chemical composition of the target material. In simplistic terms, the interaction cross section can be viewed in geometric terms based on the relative size of the projectile and target nucleus, noting that protons and neutrons have roughly the same mean radius of $\approx 10^{-13} cm$. Thus, the effective area

of a proton or neutron would be $\pi r^2 \approx 4 \times 10^{-26} cm^2$. It therefore follows from the assumption that atomic nuclei comprised of protons and neutrons would generally take a spherical shape, that the nucleus of an atom with atomic number A, will have a diameter of $A^{\frac{1}{3}}$ times that of neutron, and a geometric cross section that is $A^{\frac{2}{3}}$ times that of a neutron. Accordingly, from a purely geometric perspective, the cross section of a neutron interacting with a target atom of atomic weight A would be: $\sigma \approx 4 \times 10^{-26} A^{\frac{2}{3}} cm^2$. Similarly, the mean free path of a neutron or proton (the so-called "hadronic interaction length" – the distance between two collision interactions) can be calculated from the geometry as the inverse of the product of the number of atoms per unit volume times the cross section. Thus, the mean free path of a neutron or proton in a material of atomic number A, based purely on the geometry, would be: $\lambda_{mfp} = \frac{1}{N\sigma} \approx (\frac{A}{N_A \rho})(\frac{1}{4 \times 10^{-26} A^{\frac{2}{3}}}) \approx (\frac{A^{\frac{1}{3}}}{\rho})(35 gm/cm^2)$, where $35 gm/cm^2$ is the conventional value of the hadronic interaction length. [79]

But the story is not complete without an infusion of quantum mechanics at this atomic level of interaction; specifically, the impact of the de Broglie wave associated with each particle, where the wavelength is a function of the the kinetic energy (i.e., velocity) of the particle:

$$\lambda = \frac{h}{p} = \frac{h}{\gamma m_0 v} = \frac{h}{m_0 v} \sqrt{1 - \frac{v^2}{c^2}} \tag{3.9}$$

where h is Planck's constant, p is the particle's momentum, γ the Lorentz factor, m_0 the particle's rest mass, v the particle's velocity, and c the speed of light in a vacuum. If this wavelength is small with respect to the size of the nucleus, then the geometric approximation for the cross section is reasonably accurate; but not so if the wavelength is comparable in size to the target nucleus, giving rise to the wide

variation of the cross section as a function of particle energy. [70] Thus, for example, a 10 MeV neutron will have a de Broglie wavelength on the order of $\approx 10^{-12}cm$, comparable to or larger than many target nuclei, and thus the cross section will not be well approximated geometrically. Conversely, at kinetic energies above 1 GeV the de Broglie wavelength is very short, and the geometric cross sections are fairly accurate. [70] This seems to be consistent with other research that discovered early-on that high energy neutrons traverse further through materials like lead, than slower (lower energy) neutrons. [91] [92]

Thus, while hydrogen may be a good neutron moderator at some energy levels, one must also consider that capture by a hydrogen atom causes the release of a fairly high energy gamma ray, which is difficult to shield. Boron could also be incorporated into a shielding material to take advantage of its high cross-section for neutron absorption (and with a much lower energy gamma ray emission than occurs with hydrogen). Thus, one could envision an optimal shielding for neutrons to incorporate a dense first layer (iron or lead) to slow the neutron particle, followed by a hydrogenous material infused with boron. But for the primary GCR species this may not be optimal because the dense layer will create more secondary emissions, including neutrons. [93] [94] [95]

In summary, one may conclude that shielding considerations for neutrons should attempt to accomplish three objectives: (1) slow the neutron emission; (2) capture the neutron to stop it; and (3) shield the resulting gamma ray emission. This analysis further demonstrates the importance in taking into consideration the change in fluence species that will result with secondary emissions from incident GCR ions in the design of shielding, and that the secondary particles – particularly neutrons – will have a different physical stopping mechanism to consider than the incident GCR ions, and thus may dictate different materials be considered, perhaps in a layered configuration

to accommodate optimizing the ability to slow and stop both, while at the same time minimizing the production of secondary particle emissions.

3.5 Design Process for Evaluating Shielding Effectiveness

From a basic understanding of the radiation environment in cis-lunar space, the physics of radiation transport through shielding materials and human tissue, and the potential biological impact of the radiation – the focus of Chapters 2 and 3, we have deduced the following general conclusions with respect to optimizing shielding materials and passive design protocols for protection from long-term exposure to Galactic Cosmic Rays expected on contemplated missions to the Moon and Mars:

1. Ultimately, it is the fluence of incident GCR particles and their energy spectrum that causes harm to humans and equipment, and thus careful analysis of the flux of the incident GCR particles and the secondary emissions they produce *behind* shielding is a fundamental metric to examine in terms of optimizing shielding protocols.

2. The metrics that attempt to measure actual human biological response and radiation exposure limits to GCR, such as relative biological effectiveness (RBE), equivalent dose, or effective dose, while useful, must be used with care and skepticism because they are not correlated with actual realistic human response data, and much of the proffered comparative data is presented in the literature with inconsistent underlying assumptions.

3. Standard spacecraft shielding comprised of some 2 *cm* of aluminum (and sometimes augmented by a backing of high density polyethylene and/or payloads and consumables) is ineffective in completely stopping much of the GCR flux, thus any improvements that can decrease the radiation exposure behind shielding will also decrease the health and equipment damage risks associated with the contemplated

long-term spaceflight missions the the Moon and Mars.

4. The primary physical stopping mechanism for the positively charged incident GCR ions is the Coulombic interaction of the ion with the shielding electrons. Thus, materials with a higher charge-to-mass ratio (Z/A) will be more effective in slowing and stopping the primary ions. This metric, taken alone, would indicate that lighter hydrogenous materials would make preferred shielding materials; and indeed, liquid hydrogen might be the best.

5. Given the mass and space limitations inherent in spacecraft design, shielding must often perform multiple functions; e.g., serve as a structural component or be another useful mission ingredient, such as water, fuel, or necessary payload. Consequently, what seems the optimal shielding for the GCR – liquid hydrogen – is likely impractical (not to mention the difficulties in handling), and using standard shielding materials in sufficient thickness to effectively stop the GCR will certainly be too heavy and bulky. In addition, shielding must maintain its integrity in the harsh space environment throughout the mission.

6. Secondary radiation emissions must also be considered in shielding design. In addition to interacting with the target electron field, the incident GCR particles also interact directly with atoms within the shielding material by direct nuclear collisions, causing fragmentation of the primary ion and of the target molecules and atoms, thereby creating a cascade of secondary emissions, yielding electrons, lighter ions, gamma rays, and neutrons, some of which can be more dangerous to human health than the incident GCR particle by itself. These so-called "secondary particles" become part of the radiation spectrum that the shielding material must try to stop. Importantly, in the case of neutrons, which carry no charge, the primary stopping mechanism is by nuclear interactions, as they are not affected by the negatively

charged electron field, which is fundamentally different from that for the primary and secondary ions. Thus, an important metric in shielding optimization becomes minimizing the creation of secondary emissions, as well as being able to efficiently stop them once they are created.

7. Neutrons are the most hazardous secondary emission product to human health, and while hydrogenous materials make a good neutron absorption medium, use of them comes at a high cost by way of emission of of high energy gamma rays. In addition, the neutron absorption cross-section changes with the kinetic energy of the neutron for any material; thus materials effective for high energy neutrons may become less effective as a neutron's energy is depleted during the collision process. Indeed, the theoretical optimal shielding design for neutrons would probably start with a dense material to provide initial energy attenuation, followed by a lighter material designed to have a high absorption cross-section, while minimizing the energy level of tertiary gamma ray emissions (such as boron).

8. The range of ions in a given material as a function of both kinetic energy and charge is an important shielding design consideration, as lighter ions penetrate deeper, and the fragmented secondaries of HZE primary ions often penetrate well beyond the Bragg peak of the primary incident ion. Indeed, since LET increases as the velocity of an ion is decreased, too thin a shielding material may produce a scenario where most of the ion's energy is deposited in human tissue or equipment after exiting the shielding, rather than being absorbed by the shielding material itself.

9. Further improvements in passive radiation shielding must look beyond the material itself, because the theoretical optimal shielding material for HZE ions in the GCR is provided by pure liquid hydrogen, and even that is not attainable as a practical matter. In terms of being both effective shielding and structurally functional,

combinations of materials may offer good solutions, because each layer of a multilayered passive shield can address a particular radiation issue. Thus, consideration of multilayer configurations for shielding protocols is of interest in terms of optimizing the material specification for various layers of a shield to minimize biological harm and/or equipment damage. Optimizing a so-called "Graded-Z" shield of multiple layers of different materials necessarily ties back to an analysis of the flux of particles of various types that are incident and produced as secondaries, and then penetrate the shielding regime.

10. The ultimate objective of GCR radiation shielding is to maximize the stopping power of the shield for the positively charged incident ions in the GCR spectrum, while at the same time minimizing the creation of harmful secondary radiation species, and simultaneously maximizing the absorption of those that are created, including dangerous neutrons. Since there are competing physical processes at work, optimization will require a carefully examined balance of the structural and weight requirements of spacecraft design against the physics of shielding and harm to humans and equipment.

Chapter 4

Governing Equations and Methods to Analyze Radiation Transport in Shielding Materials

"An engineering science aims to organize the design principles used in engineering practice into a discipline and thus to exhibit the similarities between different areas of engineering practice and to emphasize the power of fundamental concepts. In short, an engineering science is predominated by theoretical analysis and very often uses the tool of advanced mathematics."
—Qian Xuesen, Co-founder of Caltech's Jet Propulsion Lab, Father of Chinese rocketry (1911-2009)

"Eppur si muove!"
—Galileo Galilei, Italian physicist and astronomer, purportedly muttered upon being sentenced to prison on June 22, 1633 by the Roman Inquisition after confessing to heresy for publishing the conclusions of his scientific observations that the Earth orbited the Sun, in conflict with the Ptolemaic geocentric model then approved by the Catholic Church ("Nevertheless, it moves!"). (1564-1642)

Armed with the boundary condition describing the GCR flux and energy spectrum at 1 *AU* discussed in Chapter 2 and the governing equations of the physics of radiation transport described in Chapter 3, one can begin to evaluate various GCR shielding protocols for extended space travel in the cis-lunar region. Of course, experiments could be – and have been – done in the laboratory to evaluate shielding materials, but these suffer from an inability to create an accurate representation of the incident GCR environment due to restrictions on using only one radiation beam species at a time and very short radiation exposure times. [88] As a result, radiation shielding for spacecraft or space habitats is generally evaluated by computational methods, rather than by ground-based experiments or actual *in situ* measurements; the former suffers from the inability to replicate the GCR spectrum in the laboratory, and the latter has been impractical because of the minimal human space travel beyond LEO, not

to mention the high cost associated with conducting such experiments during actual flight for initial design purposes.

The objective of radiation transport analysis to evaluate shielding protocols, regardless of the method employed, centers on accounting for all incident radiation particles as they traverse the shielding medium through conservation principles – conservation of mass, momentum, and energy. By knowing the species and energy spectrum of the radiation exiting the shielding material and available to impact the human or equipment targets, one can evaluate the effectiveness of various shielding materials and designs. Generally, two computational methods have been employed: (1) deterministic analytical or numerical approaches that frame the problem of transport of radiation through a medium in terms of the Boltzmann transport equation, and (2) Monte Carlo simulations that apply the fundamental physics for various interaction scenarios as a particle is traced through the medium, based on probability assessments for each possible interaction at each step of the process. The deterministic approach is quicker computationally, but of course requires that the general transport equation be greatly simplified by various, hopefully reasonable, assumptions. Monte Carlo simulations in theory may offer better accuracy, but require greatly increased computational time, and still suffer from inherent flaws associated with estimating probabilities of the chain of possible interactions an ion may encounter as it traverses the shielding medium. Both methods are represented in the literature, and thus both are employed in this research.

4.1 The Deterministic Approach

The description of the passage of high-energy particles through matter for the purpose of evaluating spacecraft shielding materials was initiated by NASA as early

as the 1970s, where a deterministic approach was employed by framing the problem in terms of solving the general Boltzmann transport equation. [96] [97] As a general proposition, the Boltzmann transport equation is used to study the non-equilibrium behavior of a collection of particles, and states that the rate of change of a function which specifies the probability of finding a particle in a unit volume of so-called "phase space" – a six dimensional designation of the position and velocity of the particles as a function of time (in the x-y-z coordinate space) – is equal to the sum of terms arising from external forces, diffusion of particles, and collisions of the particles. [98] It is a powerful tool initially devised by Ludwig Boltzmann in 1872 to examine the macroscopic properties of a gaseous fluid, such as density or temperature gradients, based upon the statistical behavior of the constituent molecules, and opened the door to the new field of statistical mechanics. [99] For a homogeneous gas (i.e., the mass of all molecules is the same), determination of the probability density function, f, as the probability of N molecules having a position and velocity within a phase-space volume of a differential cubic length and cubic velocity at a particular time t involves solving the equation $dN = f(\mathbf{r}, \mathbf{v}, t)d^3\mathbf{r}d^3\mathbf{v}$. The solution involves a six-fold integral over position and velocity, and from that result an expression can be written describing the change in probability density function with respect to time, which is the general form of the Boltzmann transport equation:

$$\frac{\partial f}{\partial t} = \left(\frac{\partial f}{\partial t}\right)_{force} + \left(\frac{\partial f}{\partial t}\right)_{diff} + \left(\frac{\partial f}{\partial t}\right)_{coll} \tag{4.1}$$

Then after substituting in independently derived expressions for the external force, diffusion, and collision terms, one is left with a so-called nonlinear "integro-differential equation" (i.e., one that involves both integrals and derivatives of a function), where

the unknown is the probability density function in six-dimensional phase space of a particle's position and velocity. From this result, one may derive the fluid dynamic conservation laws of mass, momentum and energy by calculating moments of the Boltzmann equation for quantities that are conserved. [100] However, given the complexity and lack of unique solutions, in actual practice numerical methods (along with simplifying assumptions) are most often used to obtain approximate solutions to the Boltzmann equation.[1] [99] Note that if the collision term is ignored in a particular application, it is referred to as a "Vlasov equation." [100]

In similar fashion, though fortunately somewhat less complex due to some simplifying characteristics of the problem, the GCR radiation impinging on a medium, such as shielding materials and human tissue, can be described in terms of the Boltzmann equation. Importantly, since the the atomic and nuclear processes involved as the incident particles traverse the target medium happen very quickly – in microseconds – as compared to the time over which any variations in the space radiation environment take place, one may ultimately employ a time-independent, steady-state Boltzmann description, balancing the gains and losses of the particle fields interacting with the shielding material and human tissue. [96] Thus, conceptually, applying the Boltzmann framework to the radiation transport problem is a relatively simple exercise of applying conservation principles to account for each particle at each energy, as they traverse the target, recognizing of course that some will be absorbed, some will change direction as a result of a nuclear collision, some will pass completely through, and some will collide with target nuclei and cause a cascade of secondary particles,

[1]Indeed, it took over fifty years for others to first be able to obtain an approximate solution to the original derivation by Boltzmann. [101] It is perhaps no wonder then that in 1906, at age 62, Ludwig Boltzmann committed suicide by hanging himself, as was perhaps foreshadowed by a poem he wrote about his hero called "Beethoven in Heaven." [102]

all of which need to be tracked. [27]

The GCR particle transport equations are derived by balancing the change in particle flux as it crosses a small volume of material, with the gains and losses caused by nuclear collisions. A simplified version of the problem is depicted in Figure 4.1.

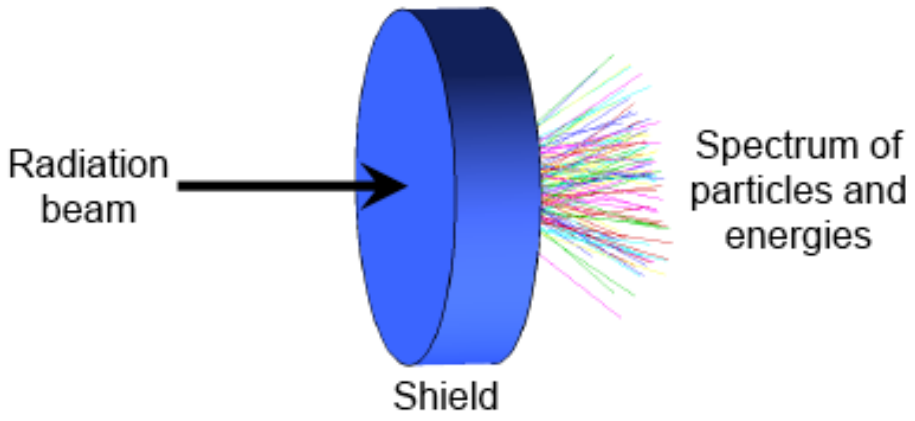

Figure 4.1 : Radiation Transport Model. From Slaba, 2015.

Recalling that it is the flux density of the radiation ($\phi_j(\mathbf{x}, \mathbf{\Omega}, E)$) that is the main physical quantity that determines the physical or biological response to the GCR radiation, the resulting general equation for the differential flux during a specified time period in a closed, convex, homogeneous differential volume of target material (e.g., envision a sphere in three dimensions) is given by:

$$\mathbf{\Omega} \cdot \nabla \phi_j(\mathbf{x}, \mathbf{\Omega}, E) = \sum_k \int_{E=0}^{\infty} \int_{4\pi} \sigma_{jk}(E, E', \mathbf{\Omega}, \mathbf{\Omega}') \phi_k(\mathbf{x}, \mathbf{\Omega}', E') d\mathbf{\Omega}' dE' - \sigma_j(E) \phi_j(\mathbf{x}, \mathbf{\Omega}, E) \quad (4.2)$$

where $\mathbf{x}$ is the position vector to the center of the spherical domain, $\mathbf{\Omega}$ is the direction vector, E is the energy of a particle, and $\sigma_j(E)$ and $\sigma_{jk}(E, E', \mathbf{\Omega}, \mathbf{\Omega}')$ are the macroscopic cross sections of the target medium. The cross sections repre-

sent the probabilities of certain specific interactions, where $\sigma_{jk}(E, E', \mathbf{\Omega}, \mathbf{\Omega}')$ represents all processes whereby type k particles moving in direction $\mathbf{\Omega}'$ with energy E' produce a type j particle moving in direction $\mathbf{\Omega}$ with energy E, and $\sigma_j(E)$ is the total cross section with the target medium for each particle type of energy E for atomic electron collisions, elastic nuclear scattering, and nuclear reactions, where $\sigma_j(E) = \sigma_j^{at}(E) + \sigma_j^{el}(E) + \sigma_j^{nr}(E)$. [96] [103] The steady-state flux density, $\phi_j(\mathbf{x}, \mathbf{\Omega}, E)$, when accumulated over a specific time interval (e.g., seconds), has units of $\left[\frac{particles}{cm^2-sr-s-Mev/n}\right]$, consistent with the formulation in Eq. 2.1. [104] *See* Appendix A for a more detailed description of the physical model and derivation.

Thus, Eq. 4.2 simply states that the change in flux density of type j particles, at location $\mathbf{x}$ in the target, travelling in direction $\mathbf{\Omega}$, with energy E is equal to the number of type j particles produced by all other particles and by all processes (spallation, fragmentation, or nuclear fission), minus the number of type j particles absorbed in the medium by all processes (electron and nuclei collisions). [96] [105] [97] [103] [104] However, by the time one considers *all* particle types incident in the GCR, and *all* particle types created as secondary emissions, travelling in *all* directions, and at *all* energies, the solution to Eq. 4.2 "involves hundreds of multidimensional integro-differential equations which are coupled together by thousands of cross terms and must be solved self-consistently subject to boundary conditions ultimately related to the external environment and the geometry of the astronaut's body and/or a complex vehicle." [38] Obviously, some simplifying assumptions are in order.

NASA and academic collaborators have been working for the past 40 years to simplify this formulation of the GCR radiation transport problem sufficiently to make a useful tool for evaluating shielding. The result was the development of the HZETRN (High-Charge-Energy Transport) code [68] [97] [106] [103], with modifications and

improvements that continue to be added to this day. In addition, HZETRN has recently been made more widely available to researchers through an internet-accessed version called OLTARIS (On-Line Tool for the Assessment of Radiation In Space). [107]

There were principally two key simplification measures required to put Eq. 4.2 into a more usable form for practical applications.

First, handling the millions of atomic collisions per centimeter of ordinary matter that an impinging ion has with the target medium electrons has been transformed from a discrete examination of each interaction into the so-called continuous slowing down approximation (CSDA), on the assumptions that the exchange of energy happens so quickly and with so many interactions, that it can be viewed as a continuous process. This has been done by evaluating the atomic microscopic cross section contributions in terms of Stopping Power, which is determined by calculating the linear energy transfer (LET) by Eq. 3.5.

Second, the Boltzmann formulation is reduced to a one dimensional analysis. This enables a measure of computational simplicity by numerical means, and such a simplifying assumption is justified by the fact that the GCR ions impacting a target medium are slowed down in large part by the Coulombic collisions with target electrons and nuclei, interactions which in most respects do not involve a physical collision, but rather a passing within the zone of the impact parameter b (*see* Eq. A.11). Thus, the path of the principle incident ion is not altered to any great degree, as demonstrated by the representative GCR ion tracks in a silicon target, as previously shown in Figure 3.2.

As a result, Eq. 4.2 can be rewritten to determine the steady-state flux density in one dimension at a particular linear depth into the target medium, as follows:

$$\Big[\frac{\partial}{\partial x} - \frac{\partial}{\partial E}S_j(E) + \sigma_j(E)\Big]\phi_j(x,E) \quad = \quad \sum_k \int \sigma_{k\to j}(E,E')\phi_k(x,E')dE' \qquad (4.3)$$

This is the general form of the transport equation for GCR traversing a target medium incorporated in the NASA HZETRN code, though as explained in Appendix A.5, it has been simplified further into two cases, for light and heavy particles. [96] [105] [68] [97] [108] [104] [103] By expanding the terms, the contributions to the gains and losses of the GCR particles can be better visualized, as shown in Figure 4.2.

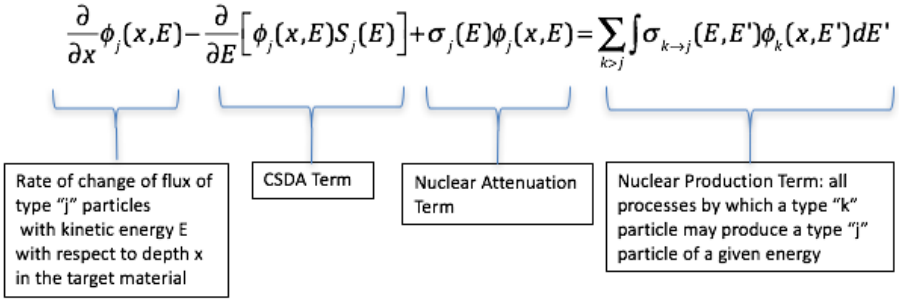

Figure 4.2 : One Dimensional Linear Steady-State Boltzmann Equation for GCR Transport in a Target Medium. Adapted from Slaba, 2015.

On the left hand side of the equation are the terms associated with atomic and nuclear reactions that slow down and absorb the incident ion particle, and on the right hand side of the equation are the terms that account for the creation of secondary emissions from the radiation particles. Thus, this formulation, with several additional simplifying assumptions, allows determination of the ion flux density, $\phi_j(x,E)$, of an ion particle type j with an energy E (MeV/n) (*see* Eq. 3.5), at a depth of x (g/cm^2) in a shielding medium.

The HZETRN code incorporates all of the physics modules and data to allow

calculation of the steady-state flux density for a range of 59 ion species from protons to nickel and selected secondary-produced ion particles and neutrons [109], including a main program and some 63 subroutines and 37 function models, together comprising state-of-the-art methodologies and databases to evaluate shielding protocols in a variety of space radiation environments. [107] The high-level functional aspects of HZETRN as implemented in OLTARIS are shown in Figure 4.3.

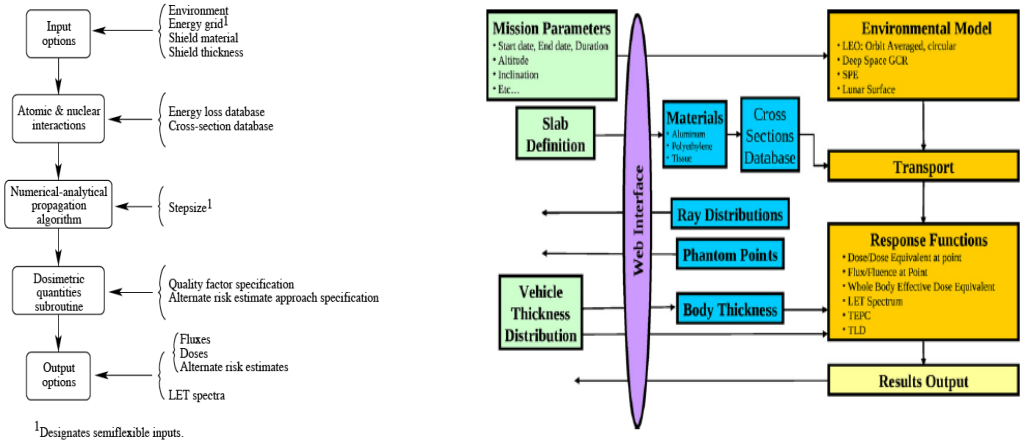

(a) Computational Structure of HZETRN. From Wilson, 1995.

(b) OLTARIS Program Flow. From Singleterry, 2011.

Figure 4.3 : HZETRN Raditaion Transport Code Implemented in OLTARIS.

The code is broken down into five basic elements, as shown in Figure 4.3a: (1) Input options, including radiation environment boundary conditions, shielding/target material properties, geometry specification; (2) Physics descriptions and data bases; (3) Radiation transport functions; (4) Risk parameters to allow calculations of biological impacts; and (5) Response output functions, including flux/fluence, calculated dose, and related metrics. [68] [107] In the OLTARIS implementation, the green boxes in Figure 4.3b indicate required user data inputs, the blue boxes indicate data the user may select and download, and the gold boxes represent the computational modules

(radiation environment model, particle transport algorithms, and output response calculations). OLTARIS allows specifying a spacecraft or habitat structure or a slab geometry, the latter of which is employed in this research in order to allow easy comparison of various shielding materials and protocols. OLTARIS also has a variety of material specifications for commonly used materials in the space sector (e.g., aluminum, polyethylene, etc.), but importantly it also allows user modifications to input new materials to test by specifying the material's elemental mass percentage, its molecular mass percentage, or its chemical formula. [107]

The process begins by creating the desired radiation environment as the boundary condition for the incident radiation – for this research only the GCR spectrum will be used, and OLTARIS has implemented the so-called Badhwar–O'Neill galactic cosmic ray model (more on that later). While OLTARIS allows a range of SPE, GCR and other radiation environment boundary conditions, this research will focus on the GCR environment in the cis-lunar region, as discussed in Chapter 2, and for calibration purposes the GCR-induced environment in LEO. Once the radiation input species and energy spectrum is determined, the relevant cross sections are calculated separately for the heavier ions ($Z > 2$, $A > 4$) using a code that essentially implements Eq. 3.6, while the total and differential energy cross sections for neutrons and light ion projectiles are calculated with separate HZETRN subroutines, which are largely based on empirical data. The radiation transport algorithms then solve the Boltzmann equation using the CDSA and straight-ahead linear simplifying assumptions implemented in Eq. 4.3, with Stopping Power and Range calculations employing Eq. 3.5 and Eq. 3.7, respectively. There are other slight nuances and simplifying assumptions that reduce the calculation burden for heavy ion projectiles and fragments, but they introduce only slight accuracy uncertainties. Finally, the flux density result from

solving the Boltzmann equation is used to calculate dose, dose equivalent, and other metrics, consistent with the equations discussed in Chapter 2. [68] [107]

Since the original implementation, some enhancements have been included, particularly in better describing the interaction cross sections, and consideration has recently been given to adding limited three dimensional aspects. [103] [110] [111] [107]

4.2 The Monte Carlo Simulation Approach

Los Alamos, New Mexico will forever conjure up images of the war-time Manhattan project and the unique group of scientists assembled, who together created the first atomic bomb and the first computer (ENIAC), but in the process also created a very powerful problem solving technique that came to be called the Monte Carlo method. [112] The Monte Carlo method is, essentially, a statistical approach to the study of differential equations, or more generally, of integro-differential equations that occur in various branches of the natural sciences, such as the Boltzmann equation. [113] It came into vogue in the mid-1940s as a re-birth of traditional statistical sampling methods with the advent of computers that could handle many calculations relatively quickly. [114] Los Alamos scientist Stanislaw Ulam is credited with the intuition: while playing the card game of solitaire, he wondered how one might calculate the chances that a particular laying out of the hand of 52 cards would result in a successful completion of the game, and being unable to solve the problem analytically, had the idea that a series of randomly sampled shuffled decks and keeping track of the successful outcomes, could solve the problem statistically. Ulam shared the idea with his colleague John von Neumann, and an early problem to which it was applied was solving the Boltzmann equation for the transport of neutrons in shielding. [115] [112] Work on that problem was an initially secret project at Los Alamos Laboratories in

1946, and was reportedly given the code name "Monte Carlo" by colleague Nicholas Metropolis (after the country with the famous casino) [112], because the solution method involved the application of probability and statistics to the natural sciences. For the problem then at hand, distributions of random numbers were used to reflect a particular process in a sequence of processes, such as the diffusion of neutrons in various materials, to calculate samples that would approximate the real diffusion history. [114] Thus, the statistical sampling was controlled by a series of random numbers that dictated which physical probability functions (i.e., the energy dependent cross sections) would be employed to calculate the series of individual interactions that the neutron might encounter as it traversed the shielding material; e.g., elastic scattering, absorption with related photon emissions, generation of secondary particles, or exiting the medium. [112] The method was made public in 1949, which is generally accepted as the birth date of the Monte Carlo method. [116] [117]

There are several Monte Carlo radiation transport programs that have found application in solving space radiation transport problems, including Geant4, FLUKA, PHITS, and MCMP-X. [38] [118] The codes differ by the nuclear interaction models employed and the geometric methods for describing the target medium, some of which can be quite complex three-dimensional structures. But these codes function in similar ways: (1) an input source of particles must be specified in terms of starting position, particle type, and initial direction and energy (or momentum) within a three-dimensional geometry; (2) the particular geometry of the target must be described; (3) the target material must be described; and finally (4) a random number generator then controls the transport by a weighted selection from among possible physics processes that the particle can encounter. After the result of each interaction is calculated, consistent with the principles covered in Chapter 3 [119], the new di-

rection and energy for the particle is used, along with the target medium description, to determine the distance the particle will travel before another interaction, and then the type and impact of that next interaction will be calculated and used to provide the starting metrics (direction and energy) for the next step. This general Monte Carlo process for the transport of GCR ions in a medium is depicted in Figure 4.4.

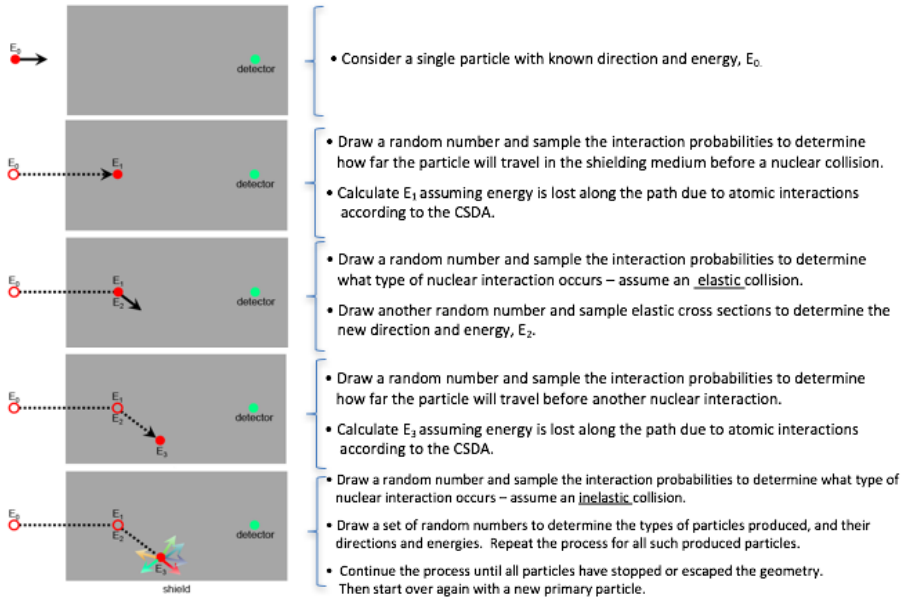

Figure 4.4 : Overview of Monte Carlo Radiation Transport Simulations. Adapted from Slaba, 2015.

If the geometry is a complex three-dimensional spacecraft or space habitat, all the codes share the problem of very long computation times to transport the GCR radiation spectrum.[2] [118]

[2] Consider, for example, that the GCR spectrum may have an integral fluence of particles at all relevant energies of over $3,000\ particles/m^2 - sr - s$, then a spherical spacecraft of radius $5m$ would be impacted by almost 2 million GCR particles every second. Thus, to simulate the transport of these GCR particles over even a short time of 10-minutes, would require the computer code to fully transport over a billion particles. [118]

Geant4 ("GEometry ANd Tracking") is a platform for "the simulation of the passage of particles through matter" using Monte Carlo methods, presented as a "toolkit" of a wide variety of options that need to be tied together by the user's tailored coding, and thus is not in a "ready-to-run" format. It is the result of a worldwide collaboration of physicists and software engineers, under the auspices of CERN (Conseil Européen pour la Recherche Nucléaire) in Geneva, to simulate high energy particle interactions. It has been used widely in space science, medical applications, accelerator and nuclear physics. The code is implemented using the C++ language, and offers a comprehensive range of physics processes, including electromagnetic, hadronic and optical processes, and has available a large set of long-lived particles, materials and elements, over a wide energy range starting from thermal energies (for neutrons) and extending in to the TeV energy range. [120] [121] While developed in the context of high energy physics experiments, it is also currently used in nuclear physics, space applications, medical physics and astrophysics. Geant4 is at present the standard Monte Carlo code used by European Space Agency for detailed radiation transport analyses. [66] Importantly, the Geant4 worldwide community continues to improve and update the code.[3] [126] [127]

For this research, a derivative of the Geant4 Monte Carlo code is employed, be-

[3] Other commonly used Monte Carlo simulation codes have various distinguishing features. FLUKA (FLUctuating KAskade) is a FORTRAN based code that is presented to the user community in an almost "ready-to-use" format that was developed under the auspices of Italy's INFA (Istituto Nazionale di Fisica Nucleare) and CERN, but often runs into "compiler issues" as the code is updated and new and faster processors become available. Aside from that, FLUKA has advantages in the way it handles heavy ions and their secondaries, particularly low energy fragments that can cause harm to humans. [122] [118] PHITS (Particle and Heavy-Ion Transport code System) is a general purpose FORTRAN based Monte Carlo heavy ion radiation transport program developed through the collaboration of several institutes in Europe and the Japan Atomic Energy Agency, and can deal with the transport of neutrons, protons, heavy ions, photons, and electrons, over wide energy ranges using various nuclear reaction models and data libraries. [123] [124] MCMP-X (Monte Carlo Multi-Purpose) is an early Monte Carlo transport code developed by Los Alamos National Laboratory, and is not widely used in the worldwide research community because its distribution is restricted under ITAR regulations. [118] [125]

cause its simple one-dimensional geometry specifications make comparison of the relative effectiveness of various shielding materials more meaningful, and also reduces the computation time required to achieve statistically acceptable results. In addition, this code has the ability to employ a layered geometry of different materials, which is a key factor of a hypothesis tested in this research for improving shielding effectiveness (i.e., that multiple layers might be better). Thus, for this research the Monte Carlo code used is MULASSIS (the Multi-Layered Shielding Simulation Software tool), developed by QinetiQ, the European Space Agency (ESA), The Belgian Institute for Space Aeronomy (BIRA), and the European Organization for Nuclear Research, based on the widely utilized Geant4 "toolkit" components. [128]

MULASSIS can simulate the particle interactions with almost any shielding material, for both primary and secondary particles. It allows slab or spherical geometry of up to 26 distinct layers. In the slab geometry mode, the incident beam is generated along the thickness, but only one ion species can be considered at a time. This is different from HZETRN and makes analysis of the entire GCR spectrum and its secondaries more cumbersome; but does allow evaluation of the separate contributions to fluence and dose by different types of input particles. The energy spectrum and related flux of each particle type is defined by the user, including the angular distribution of the incident ions. In this research, the energy spectrum data are inputted in tabulated mode based on the CREME96 GCR model output, and the angular distribution of incident beam is omnidirectional, consistent with the actual GCR isotropic fluence. [129] The MULASSIS simulation output metrics include fluence, total ionizing dose and/or total non-ionizing dose collected in each layer. This information provides both dose equivalent and fluence on the back side of the shielding in order to evaluate and compare various shielding materials.

4.3 Boundary Conditions and Verification

As discussed previously, all efforts to evaluate radiation shielding in Earth-based analyses are fraught with error – deterministic, Monte Carlo, and experimental. Nevertheless, these tools are the best available to formulate adequate radiation protection protocols for the long-term spaceflights currently contemplated, and, despite their short-comings, can lead to important insights until sufficient actual data is collected in future years on the spaceflights themselves. Accordingly, it is of some import to review the inputs to the models, the verification efforts, and the simulation and modeling parameters that might best be employed to advance the state-of-the-art.

4.3.1 The Galactic Cosmic Ray Models

In order to assess astronaut exposure and electronic equipment impacts associated with GCR exposure, models are used to describe the key input boundary condition to the radiation transport calculations of the GCR spectrum, both species and energy, at the location of the spacecraft or habitat. An early effort to describe the GCR radiation environment was done by the Naval Research Laboratory in the 1980s, in connection with evaluating the single event upset (SEU) rates for equipment launched into space (*see* Chapter 2), resulting in the development of the early versions of the Cosmic Ray Effects on Micro-electronics programs, called CREME. [130] It was a semi-empirical model that summarized the then existing GCR data in terms of empirical fits for the differential flux of each ion from hydrogen to nickel as a function of energy per nucleon, along with a solar modulation parameter that replicated the 11-year sunspot cycle, the latter of which turned out to be a major weakness of the model. [131] [132]

By the early 1990s increased accuracy for a GCR model was desired by the research community, and NASA offered a model for the differential energy spectra of

galactic cosmic radiation, as a function of solar activity, based on standard diffusion-convection theory, which came to be called the Badhwar-O'Neill model (BON). [133] The Badhwar-O'Neill model numerically solves the Fokker-Planck equation – a partial differential equation formulation that describes the time evolution of the probability density function of the velocity of a particle under the influence of various random forces – to account for particle transport in the heliosphere due to diffusion, convection, and adiabatic deceleration, starting from a boundary condition outside the heliosphere defined by the the Local Interstellar (LIS) parameters of the GCR, and all assuming quasi-steady state and a symmetric spherical interplanetary heliosphere medium. [21] *See* Chapter 2 for a discussion of the source of GCR radiation. Thus, under these assumptions the equation takes the following form:

$$\frac{1}{r^2}\frac{\partial}{\partial r}(r^2 V_s U) - \frac{1}{3}\Big[\frac{1}{r^2}\frac{\partial}{\partial r}(r^2 V_s)\Big]\Big[\frac{\partial}{\partial T}(\alpha T U)\Big] = \frac{1}{r^2}\frac{\partial}{\partial r}(r^2 \kappa \frac{\partial U}{\partial r})$$

where r is the radial distance in astronomical units (AU), T is the kinetic energy (MeV/n), $U(r,T)$ is the GCR flux ($\#/m^2 - sr - s - MeV/n$), $V_s(r)$ is the solar wind ($\approx 400 km/s$), κ is the particle diffusion coefficient, and $\alpha = (T + 2T_0)/(T + T_0)$, where T_0 is the rest energy of the GCR particle. Additionally, at the boundary of the heliosphere, $R_b \approx 100 AU$, the solar wind and heliospheric magnetic field modulation is assumed negligible, and thus $U_0 = U(R_b, T)$ is a known quantity described by the Local Interstellar parameters determined by tying back, ion-by-ion, to measured GCR data at 1 AU. [21]

Not to be outdone, the Naval Research Laboratory updated its GCR model in 1996, now called CREME96 [134], which was adopted as a standard by the International Standards Organization (ISO), and was based on the improved semi-empirical

Nymmik model with respect to the solar modulation impact, using a vast amount of newly available GCR measurement data. [135] CREME96 continues to be refined as more observational data on the GCR becomes available from spaceflights and probes. [22] NASA has also been busy making improvements to its numerically-based Badhwar-O'Neill GCR model. [136] [21] [137]

Regardless the GCR model used, the change in flux at 1 AU due to solar modulation is dramatic, particularly for ions with energies below 1 GeV; *see* Figure 4.5.

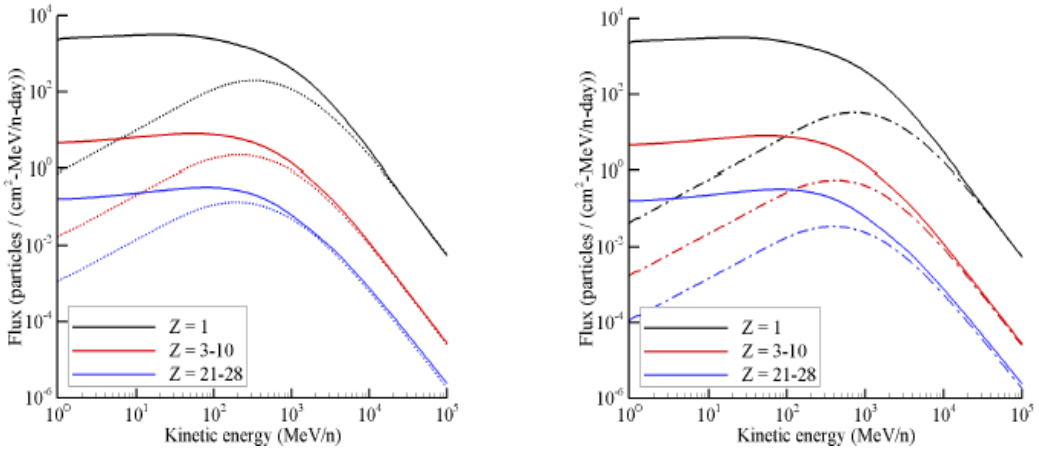

(a) GCR Flux at Solar Minimum. (b) GCR Flux at Solar Maximum.

Figure 4.5 : GCR Flux at the Heliosphere Boundary (solid lines), and at 1 AU during Solar Minimum (a) and Maximum (b) Conditions (dashed lines). From Slaba, 2015.

The solid lines represent GCR flux at the boundary of the heliosphere, and the effect of solar modulation, which is correlated with sunspot activity, is readily apparent: at minimum solar activity, the solar wind and magnetic fields provide less resistance to incoming GCR radiation particles, and vice-versa during maximum solar activity. Thus, it is the time periods during minimum solar activity that create the higher GCR flux at 1 AU, the region of cis-lunar space.

As this research employs both deterministic and Monte Carlo methods to eval-

uate GCR shielding effectiveness, it should be noted that the HZETRN code and OLTARIS use the Badhwar-O'Neill GCR model, while the MULASSIS Monte Carlo code uses CREME96 to input the GCR boundary conditions. These different GCR models inject differences by way of initial boundary conditions that must be taken into account in any comparative analysis, and while there is general agreement that the current GCR models have an accuracy of about ±10% [38], larger errors are induced by the radiation transport models for which the GCR spectrum is the input boundary condition.

Specifically, one study was undertaken to calculate the absorbed dose and dose equivalent in an unshielded water sphere exposed to GCR intensities predicted by CREME96, CREME2009 and Badhwar–O'Neill2010 models for a location outside the Earth's magnetosphere and for the ISS orbit. [138] This work revealed differences in the calculated absorbed dose and dose equivalent, as shown in Figure 4.6.

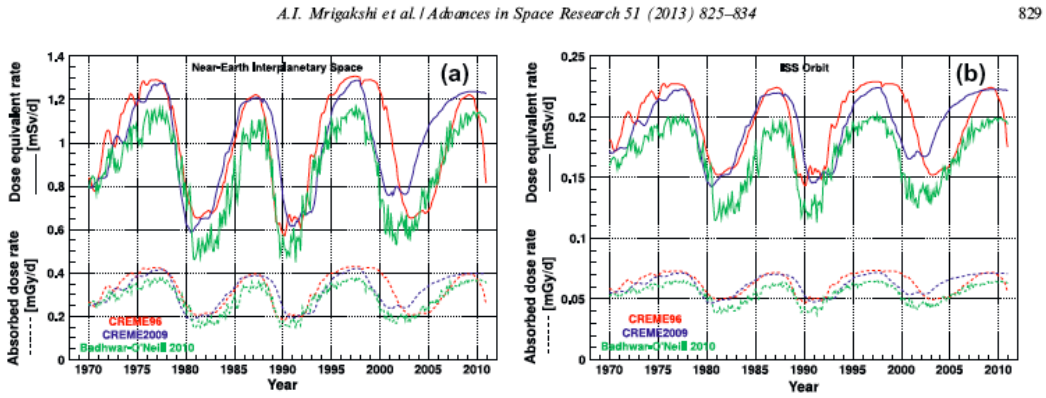

Fig. 2. Absorbed dose (dashed lines) and dose equivalent rates (solid lines) in the water sphere calculated from the spectra described by CREME96 (red), CREME2009 (blue) and BON2010 (green) for near-Earth interplanetary space (Fig. 2a) and for ISS orbit (Fig. 2b). (For interpretation of the references to color in this figure legend, the reader is referred to the web version of this article.)

Figure 4.6 : Comparison of Various GCR Models. From Mrigakshi, 2013.

In particular, the author noted that total absorbed doses over a long period of time could be significantly different, depending upon the choice of GCR model used as

an input boundary condition. However, more recent studies have concluded that the GCR models themselves are getting to better agreement, as more actual measured GCR data from spacecraft and probes is used to calibrate them. [139] But even so, propagated uncertainties between GCR models in calculating final metrics, such as dose equivalent, generally can result in induced errors in the range of ±20%. [140] One study, using a different GCR model claiming to be better calibrated to solar modulation effects, found differences in dose equivalent, for example, at the 2010 solar minimum of some 25% from the Badhwar-O'Neill 2010 model, and at the 2004 solar maximum period of some 55% from the CREME2009 model. [141] Obviously, when comparing results one must be careful to ensure that the same GCR model and boundary conditions have been used.

4.3.2 Verification of HZETRN and MULASSIS

Not only do different GCR models inject differences in initial boundary conditions, but the two radiation transport schemes used in this research have their own differences, as described above, making it imperative that any comparative results be done under the same conditions: the same radiation environment input, the same transport code, the same geometry, and the same materials.

Shortly after creating the HZETRN code, NASA began the process of verifying it and concluded that without much real spaceflight data, the best way was to compare results from HZETRN with the results of Monte Carlo simulations. Early comparisons showed generally good correlation for primary particles in simple shielding protocols of aluminum and iron, followed by a water target, but less so when one followed secondary ion emissions and neutrons. [68]

In 2012, Lin, et al. published a study that compared results of GCR radiation

impacting a slab geometry of aluminum as between the deterministic HZETRN code and the Geant4 Monte Carlo simulation (the basis for the MULASSIS Monte Carlo code), and found: "the dose values and the particle spectra from the HZETRN deterministic code are, in general, rather consistent with the Geant4 Monte Carlo results, except for neutrons (especially low energy neutrons)" and "the dose equivalent results from HZETRN and Geant4 are not far from each other, but the HZETRN dose equivalent values behind shielding are often lower than those from Geant4." [142]

Another recent study published in 2015 by Aghara, et al. compared the results from OLTARIS (deterministic method using the HZETRN code) and the PHITS Monte Carlo code for a Solar Particle Event (SPE) radiation environment input impacting an aluminum shielding material, and found that the particle fluence behind the shielding showed good agreement, except that the neutron particle fluence from OLTARIS was significantly lower at low energies. [143] This would be consistent with the Lin study previously discussed, in that neutrons tend to have a high quality factor, so that lower neutron fluence would result in lower calculated dose equivalent values.

An extensive NASA study first published in 2009 by Heinbockel, et al. compared the HZETRN code and the FLUKA Monte Carlo code for a GCR radiation environment input and a 20 gm/cm^2 slab of aluminum (2.9 $inches$), behind which a 30 gm/cm^2 water target is placed to replicate a human body. [144] This research was part of a systematic effort by NASA of verification and validation to quantify the accuracy of HZETRN and determine areas where it could be improved, and specifically determined comparisons of dose and dose equivalent values at various depths in the water slab, as well as the proton and neutron flux in the water target. [145] The results gave generally good agreement in trend, but significantly different results

in various energy ranges, which the authors opined was likely due to differences in the way cross sections were calculated, differences in quality factors used to calculate the dose equivalent quantity, and the differences in the way the HZETRN code treats light ions versus the heavier ions. [145] Of course, such differences could have been easily predicted to cause different results, but the study has utility in providing a rough quantification of the variations. A more recent NASA study published in 2016 by Slaba, et al. compared analyses of GCR radiation impacting aluminum shielding, using both the deterministic HZETRN code and the Geant4 Monte Carlo code, and found good agreement except in the nucleon and light ion treatment, essentially confirming, without saying as much, the results of Heinbockel, et al. in 2009 and Lin, et al. in 2002. [146]

Two other GCR shielding evaluation studies of aluminum for particular mission types tangentially discovered that the results obtained for dose equivalent calculations using the MULASSIS Monte Carlo code were some 50-60% lower than those calculated with HZETRN code, without giving any definitive analysis or explanation as to why. *See*, the 2007 Bernabeu, et al. study of a mission in the solar system [42], and the 2009 Borggräfe, et al. study of a mission to Mars [147]. In similar fashion, a 2010 Jia, et al. study of lunar regolith habitat shielding effectiveness using the Geant4 and FLUKA Monte Carlo codes produced a four-fold difference in the calculation of effective dose from that determined with previous deterministic methods, which was attributed to differences in radiation environment inputs and other calculation differences, including radiation weighting factors. [89]

Finally, there have been limited attempts to verify the various codes by experiments, which are hampered by the inability to recreate the GCR spectrum in the laboratory, as discussed previously. A 2002 Stephens, et al. experiment was done

whereby a NASA food pantry locker from the MIR space station was subjected to 1 GeV iron ion beam, and also simulated with a proprietary Monte Carlo code, to measure and calculate, respectively, the fluence of primary and secondary particles inside the food locker, with the following conclusion: "The agreement between the model and experiment are within the errors attributable to the uncertainties in the presumed fragmentation cross sections" [148] – a vague assessment at best. The 2016 Emmanuel, et al. experimental work concerned studying shielding for satellite components for high elliptical orbits, where they would be subjected to high intensity proton and electron radiation environments within the Van Allen belts. Here they subjected thin layers of aluminum, polyethylene, and carbon fiber individually to a 70 MeV proton beam and then to a 10 MeV beam of electrons, and also simulated the experimental setup using the MULASSIS Monte Carlo code, and found the prediction of range and deposited dose for the protons to be within 7% (experiment versus simulation), but the results for electrons varied between 2-75%. [149]

The import of all of this is that the various transport codes have been validated for fluence analysis in the GCR spectrum with respect to very limited experimental data, but have general agreement with respect to each other in regard to the heavier ion induced metrics. [38] This becomes problematic in terms of trying to predict real-life biological harm when one considers that the lighter ions make up most of the GCR fluence and that neutron secondaries can be very harmful (*see* Chapter 2). Thus, to make dependable comparative analyses of shielding materials, one must take great care to use the same radiation transport models with the same inputs and the same calculation procedures for the output metrics. In addition, it is of some utility to use both deterministic and Monte Carlo methods to ensure that radiation shielding materials have been examined with the best state-of-the-art analytical tools, a far less

expensive undertaking than trying to initially evaluate the myriad shielding protocols and materials experimentally.

4.3.3 Radiation Shielding Evaluation Framework

The components necessary to evaluate spacecraft radiation shielding materials and protocols generally involve the five shown in Figure 4.7.

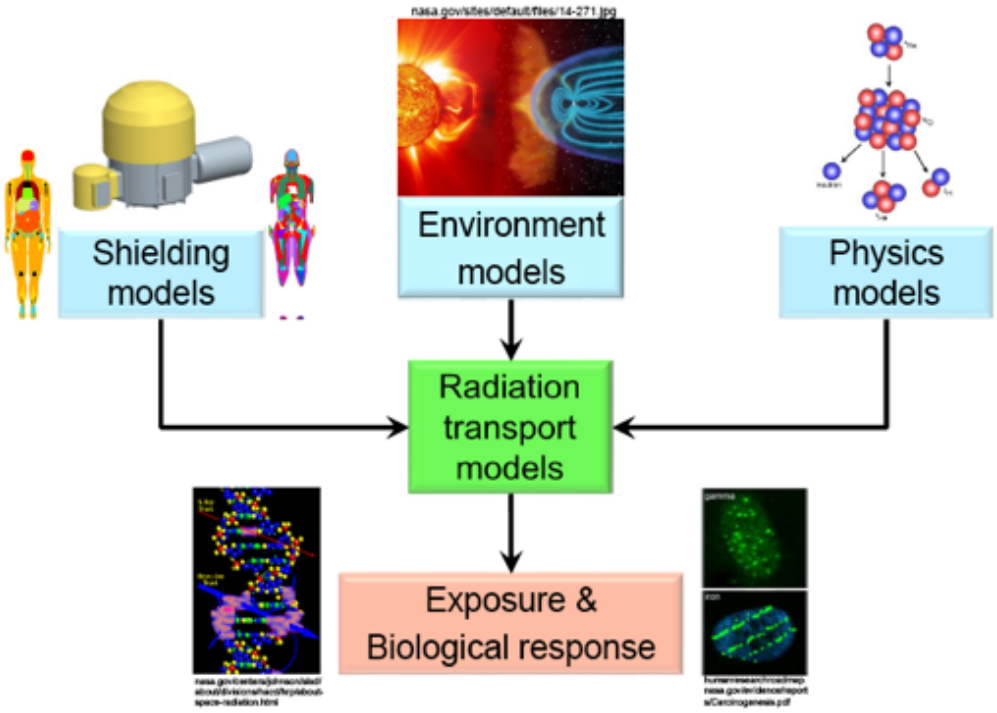

Figure 4.7 : Framework for Radiation Shielding Evaluation. From Slaba, 2015.

In this research, the choice of the radiation transport code will dictate the environmental and physics models employed; thus, for HZETRN the GCR boundary conditions will be provided by the Badhwar-O'Neill 2010 model, and for MULASSIS the GCR input will be provided by the CREME96 model, and in both cases the appro-

priate physics models will be employed to describe transport of GCR ions and their generated secondaries in the target medium. [150] To make meaningful comparisons between the various materials and designs evaluated, a simple slab geometry is used, with a focus on examination of the particle fluence behind the shielding, and new normalized comparative analysis metrics using the dose equivalent calculations.

The GCR Input Boundary Conditions

The GCR spectrum applied as an input is the GCR radiation environment at 1 *AU* in the cis-lunar region during the worst-case scenario of a solar minimum period, which puts the GCR intensity at its highest, as shown in Figure 4.8.

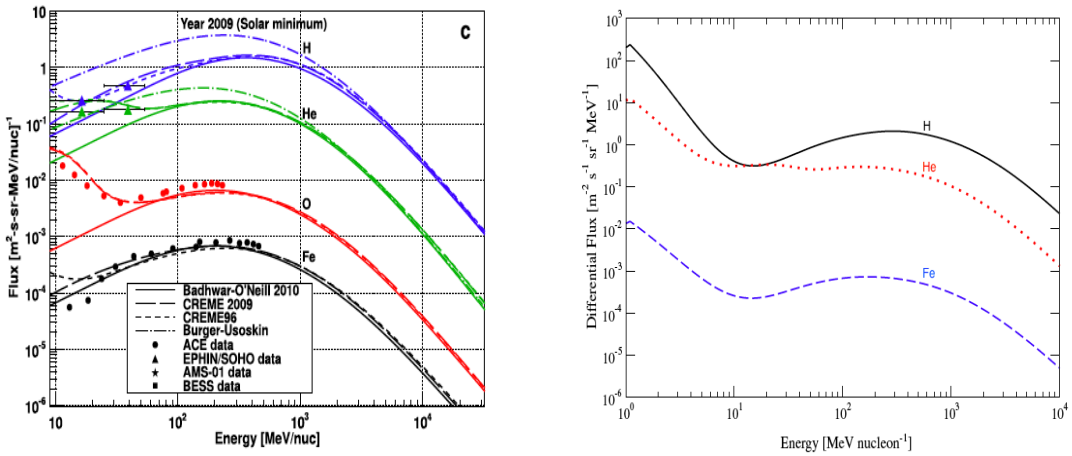

(a) GCR Flux at 2009 Solar Minimum. (b) GCR Flux at 1977 Solar Minimum.

Figure 4.8 : GCR Flux at 1 *AU* at Solar Minimum used as Input Boundary Conditions for (a) Badhwar-O'Neill 2010 Model and (b) MULASSIS.
From Mrigakshi, 2012 and CREME96 Input File, adapted from Bernabeu, 2007.

While the mathematical model embedded in HZETRN includes consideration of 59 ions in the GCR spectrum conveniently at once [151], the Monte Carlo codes require making a full simulation run, ion-by-ion, at every point in the shielding/target medium where the flux is to be recorded – thus requiring hundreds of runs or more

for each shielding setup. To alleviate this burden, many researchers run the proton and helium ions for the lighter end of the spectrum, since those comprise about 98% of the GCR particles, and then run the iron ion as a proxy for all of the heavy ions, since it has the largest fluence of that group. [84] This method may cause an underestimation in the dose equivalent calculation, but the savings in computer time may justify doing so, as long as comparative results are run on the same basis. Therefore, for the MULASSIS Monte Carlo simulation runs, the GCR input boundary conditions are as shown in Figure 4.8b. Finally, the GCR boundary conditions assume fully ionized particles (impacts Stopping Power and Range calculations), and because the GCR is isotropic, it is assumed to impact a slab in an omnidirectional fashion for the purposes of the MULASSIS Monte Carlo runs.

The Shield Evaluation Geometry

In this research, the different shielding materials examined are modelled as slabs, with the areal density of the total shielding ranging from 2 g/cm^2 to as much as 100 g/cm^2. This allows comparison of various shielding materials on a normalized basis of actual material traversed by the incident radiation, but presenting the results in that fashion does tend to somewhat mask the practical parameter of the physical thickness of the shielding materials; e.g., 100 g/cm^2 of aluminum will be about 37 cm thick, while an equal areal density of polyethylene is about 107 cm thick. This has obvious practical implications in shielding design, and as a result an effort will be made to also present the results in actual thickness metrics where deemed relevant.

To evaluate the biological impact on the human body of the GCR spectrum and secondaries on the back side of the shielding, a water phantom of 30 g/cm^2 is used to collect the radiation flux data, which is a commonly used proxy for the human body, as over 70% of human organs by weight are composed of water. [144] [42]

Examination of shielding materials with HZETRN, in its OLTARIS format, and with the MULASSIS Monte Carlo code allows simulations with multiple layers of different shielding materials. The general geometric setup for evaluating the comparative effectiveness of various shielding materials and designs in this research is shown in Figure 4.9.

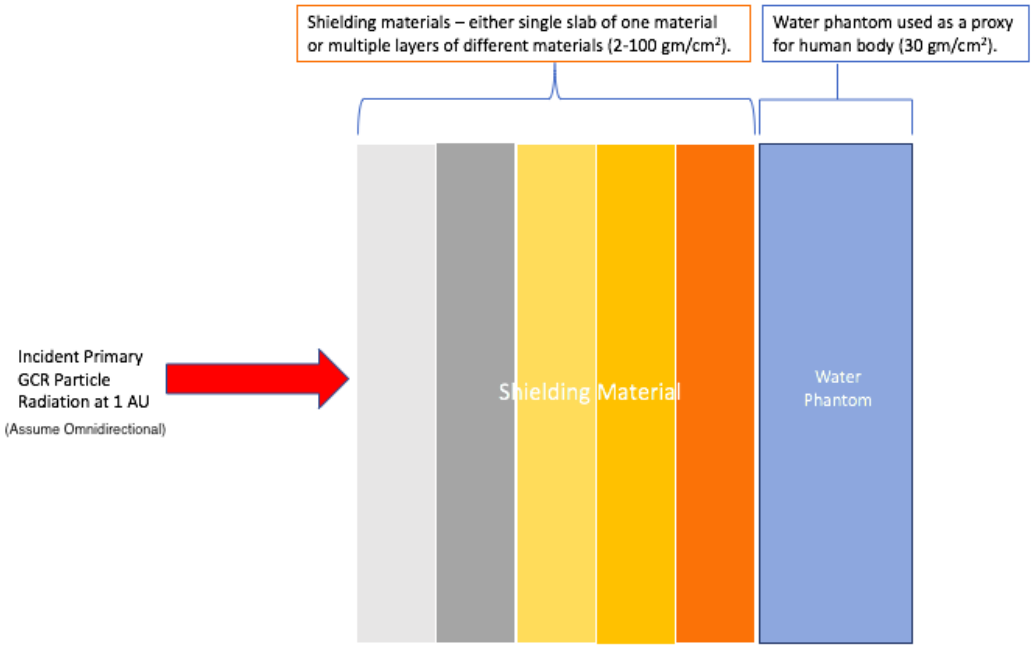

Figure 4.9 : Geometry Model for Shielding Evaluation.

This research examines single layer shielding analyses for comparison to the results obtained for various multilayer configurations, because combinations of materials can potentially provide better solutions, as each layer can address a particular radiation issue. Investigation of multilayered, so-called "Graded-Z" shielding, has already been studied using MULASSIS (but not HZETRN) in connection with protection for electronics in the trapped electron Van Allen belt, where many satellites operate [129] [34] [150], and preliminary analyses have been done in respect to polyethy-

lene behind aluminum, but these efforts are less about any synergies involved in a multilayered configuration and more about relative structural and Stopping Power considerations. [42] NASA has expressed the view that the future of more efficient and effective radiation shielding for spacecraft will take the form of multilayered materials, much like the Micrometeoroids and Orbital Debris (MMOD) shielding, but little investigative work has been done to date. [152] Since no reported comparisons of multilayered shielding configurations exist, this research will include such analyses. In addition, in future research a spherical geometric model simulation could also be utilized to test the metrics of absorbed dose and dose equivalent with those obtained in the slab configurations; but again, the most important criterion in comparative analyses is to keep model parameters consistent throughout.

The Shielding Evaluation Output Metrics

The most-used options for output metrics provided by HZETRN and MULASSIS include the total ionizing absorbed dose in Grays (Gy) as a function of depth into a shielding medium, as well as behind shielding, which is post-processed into dose equivalent in Sieverts (Sv) by multiplying by the radiation weighting factors. These dosimetric units are correlated with an assessment of biological harm from the radiation, though little verification has been done, all as discussed in Section 2.3. Nevertheless, the standard biological impact parameter used in most research is the dose equivalent (H), which is the product of the absorbed dose received in a water/tissue phantom for each particle type and its weighting factor (w_R), which, in turn, is a function of the type of radiation and in some cases the energies for specific particles (*see* Section 2.3). Results obtained in this research from the MULASSIS Monte Carlo method generally used the radiation weighting factors from the ICRP

103 publication. [52] Note that the HZETRN response functions utilize the earlier ICRP 60 weighting factors, and in connection with earlier research conducted by Li, Warden and Bayazitoglu, a comparison was run using the MULASSIS radiation transport code which showed large differences, on the order of a 45% decrease in dose equivalent, by using the newer quality factor estimates (*see* Chapter 2 and Figure 2.11). [14] While using the newer ICRP 103 weighting factors may make comparison with other studies on an absolute basis somewhat problematic, as discussed previously, nevertheless the comparison of the *relative* effectiveness of shielding materials is not disturbed, and doing so gives a more accurate picture of the relative danger of particular secondary products, such as neutrons. The dose-depth curves are plotted to show the shielding effect by different materials of varying areal density.

Fluence analysis has been only rarely performed in prior work. Both methods can produce a fluence analysis, but in different ways. With HZETRN, a flux/fluence array can be obtained versus depth in the shielding material, energy, and isotope (though no such analyses have been published). MULASSIS allows fluence analysis for electron, pion, muon, neutron, and proton emissions, but requires the various different particles to be collected and assessed in individual simulation runs (one particle at a time), making the analysis effort somewhat tedious and time consuming. However, fluence analysis behind shielding is helpful in showing the detailed attenuation effect of, and fragmentation products caused by, different shielding materials and designs. In addition, a fluence analysis ties directly into the fundamental data that is collected in laboratory experiments, and thus could be ultimately used to correlate and verify the analytical results for shielding materials and designs that show promise, and therefore may warrant further actual experimental investigation. Fluence analysis may also be particularly useful in understanding the propensity for

various shielding protocols to produce secondary neutrons. As GCR ions travel into the shielding materials, inevitably neutrons are produced, and these can be the most harmful secondary radiation to the human body, especially for neutrons with energy levels between $10^{-1}MeV$ to $10MeV$, which have weighting factors up to 22. [52] Thus, though secondary radiation is obviously of lower energy, it nevertheless can significantly increase the biological damage, and therefore it is useful to understand which shielding materials or configurations best attenuate particular secondary emissions.

The Convergence Study

In connection with related research conducted by Li, Warden and Bayazitoglu [14], test simulation runs were made with the MULASSIS Monte Carlo code to determine the optimal number of GCR input particles required for each simulation run in order to have convergence of the Monte Carlo results, given the input spectrum and geometry employed, as described in Figure 4.9. It was determined that using 100,000 input particles per simulation run at a particular location within the model geometry took only a modest amount of computer time per evaluation run, and produced acceptable results (relative error of 0.1%) as running 10 times that number of input particles with much longer computer time required. *See* Chapter 7 for full discussion.

As a general matter, the more primary particles used per evaluation run – i.e., the more individual particle histories obtained – in a Monte Carlo code simulation, the more statistically accurate the results. However, a huge number of primary particle runs can make the simulations very time consuming. Thus, a convergence study has been performed in order to find an appropriate number that is both accurate and time-efficient.

MULASSIS offers primary particle numbers in powers of ten, from 10 to $10,000,000$.

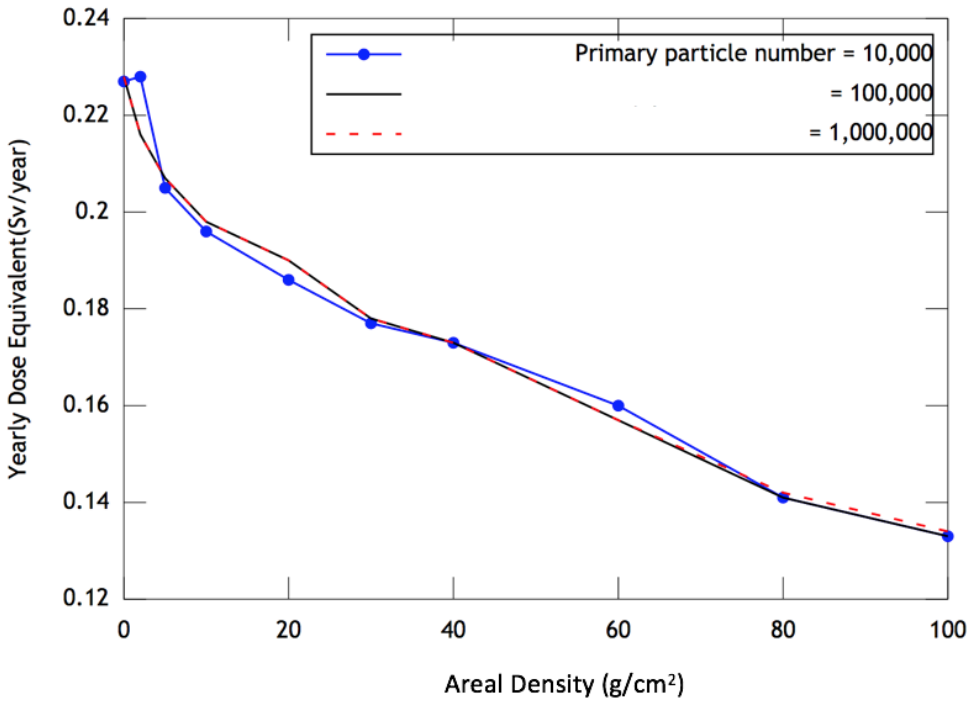

Figure 4.10 : Convergence Analysis with MULASSIS for Aluminum Shielding with Incident GCR Radiation.

Figure 4.10 shows the convergence study with three successively larger primary particle numbers used: $10,000$; $100,000$; and $1,000,000$. Results obtained from using $100,000$ and $1,000,000$ initial particle histories agree well, which means that the calculation converges at around $100,000$ particles, as shown. In contrast, using just $10,000$ input particles gave relatively less accurate results (standard deviation of $1.8 \times 10^{-3} Sv/yr$, and an absolute relative difference percentage of 1.3%), even though the simulation time was much shorter. Accordingly, $100,000$ input primary particles was chosen as an appropriate number to use in later simulations with MULASSIS with the slab geometry described in Figure 4.9 (standard deviation of $1.1 \times 10^{-4} Sv/yr$, and an absolute relative difference percentage of 0.1%).

Chapter 5

State-of-the-Art for Radiation Shielding in the Cis-Lunar Space Environment

"Vous avez confirmé dans les lieux pleins d'ennui ce que Newton connût sans sortir de chez lui."
——Voltaire (François-Marie Arouet), French writer, to the French mathematician P. L. M. Maupertuis, who organized an arduous expedition to Lapland to measure the length of one degree of meridian in the northern latitudes ("You have confirmed in the lands full of boredom what Newton knew without leaving home.") (1694-1778)

"If I have seen further than others, it is by standing upon the shoulders of giants."
——Sir Isaac Newton, English mathematician, astronomer, and physicist (1643-1727)

Solving the radiation exposure problem that comes with space travel has not been easy; in fact, the "solutions" implemented to date consist primarily of accepting a slightly higher risk of health hazards (though the precise amount is hard to quantify), and creating so-called "storm shelters" on the ISS for added protection during Solar Particle Events. But the advent of planned long-term voyages to the Moon and Mars – outside LEO and the protective zones created by the Earth's magnetosphere – dictates that additional steps now need to be taken to better protect humans and equipment from the radiation hazards in cis-lunar space, as well as to better assess the health risks. In this Chapter the history and state-of-the-art of spacecraft radiation shielding is discussed, including a review of passive and active shielding protocols and the related problems with shielding spacecraft and habitats, the current evaluations of standard materials for shielding purposes, and a review, and identification of limitations, of experimental analyses of proposed shielding materials.

5.1 Passive versus Active Shielding Approaches

Shielding from space radiation hazards has been a significant topic for decades. Space radiation shielding protocols are generally classified as either "active" or "passive" shielding schemes. In general terms, active shielding schemes include some means of creating a local electromagnetic field to deflect space radiation, much in the same way the magnetosphere does with respect to radiation impinging on the Earth. [9] In contrast, passive shielding schemes seek to put materials between the incident radiation and the human or equipment to be protected that take advantage of the interactions between the radiation and the atoms in the shielding material to attenuate and absorb the incident radiation, as previously discussed in Chapter 3. A good passive shielding design should not only provide effective protection, but also be multifunctional (structural, equipment racks, fuel or water tanks, etc.), cost-effective, nontoxic, durable and have a propensity to generate fewer secondary radiation emissions. [95] In the 60-years since the first spacecraft was launched (Sputnik – October 4, 1957), only passive radiation shielding schemes have been employed, and those generally limited to aluminum structural hulls, and in a few instances strategically placed polyethylene blocks.

Active radiation protection schemes have been considered since early in the space age, and include generating electromagnetic fields in numerous ways: electrostatic shields, plasma shields, and confined or unconfined magnetic fields. [153] [38] [154] Early on in the space age, even luminaries like Dr. Wernher von Braun envisioned that active shielding protocols would be needed for space travel in the solar system, as shown in Figure 5.1a, taken from an article he published in a 1969 edition of Popular Science magazine. [155] And over 40-years later, many still hope that some kind of active radiation protection protocol can be developed, including Physics Nobel

Laureate Dr. Samuel Chao Chung Ting of the Massachusetts Institute of Technology, as shown in Figure 5.1b.

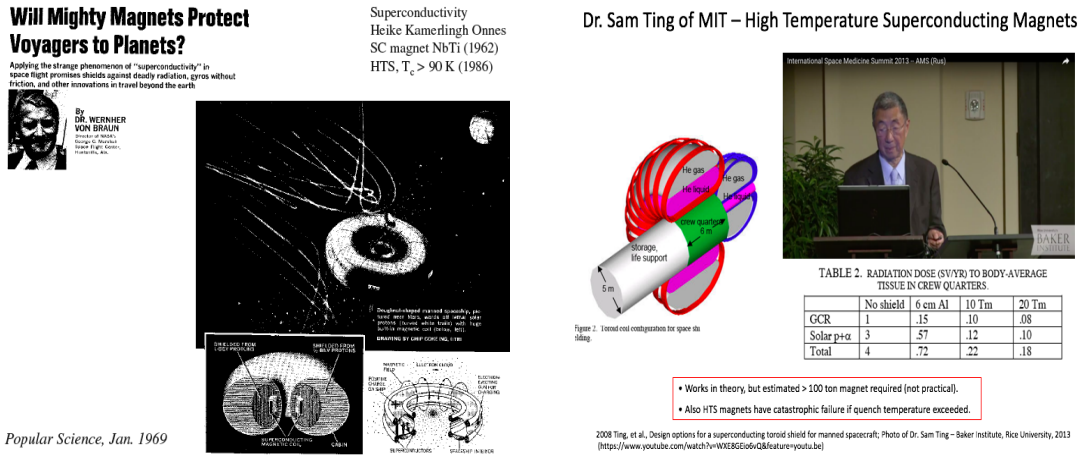

(a) Dr. Wernher von Braun. (b) Dr. Sam Ting.

Figure 5.1 : Long-held Views on Possible Active Radiation Protection Schemes. From von Braun, 1969; Choutko & Ting, 2008 (photo at Rice's Baker Institute, 2013).

These active radiation schemes are based on the principle of deflection of the high energy GCR particles, rather than stopping and absorbing them in a material. [156] [154] The idea is appealing because of the inability of currently known shielding materials to stop all GCR radiation particles; indeed, as shown in Figure 3.6 and the related text in Chapter 3, even protons with energies higher than 100 MeV easily penetrate standard spacecraft hull shielding.

For this very reason, NASA has recently been studying various active radiation protection proposals, with a particular focus on using magnetic coils affixed around the outside of a spacecraft to generate an adequate magnetic field to deflect the GCR ions. [157] [158] The earlier 2008 study by Ting, et al. had demonstrated the theoretical capability of using superconducting magnets, whose coils are built with so-called "high temperature superconducting materials" to make them energy efficient

– and by high temperature they mean maintaining the magnet's coils at around 77 K, rather than the much lower temperature required by early superconducting materials. [156] NASA became interested in the potential for such active shielding schemes because to build a spacecraft with adequate passive shielding to actually stop all radiation would require very thick (and too heavy) spacecraft hulls, as shown in Figure 5.2. *See also* recent work by Barthel based upon the NASA data. [159]

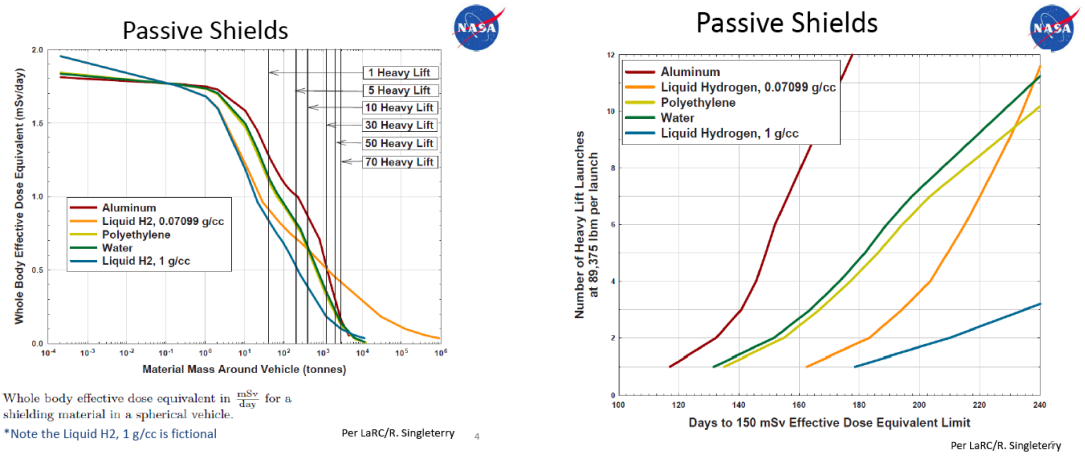

(a) Passive Shielding Material Mass. (b) Number of Heavy Lifts Required.

Figure 5.2 : Heavy Lift Launches Required for Protection with Passive Shielding. From Westover, 2012.

In this work, NASA estimated that at a specified effective dose limit, voyages of only 180 days could be done, even if the mission was supported by twelve heavy-lift launches to bring the materials to LEO for spacecraft construction, as shown in Figure 5.2b, and many more required to reduce the exposure significantly to allow longer voyages at the same risk tolerance, as shown in Figure 5.2a.

But the possibility of a complete solution to the radiation protection problem using active radiation shielding schemes is still very much undecided, as all current active shielding proposals have the same problem that passive shielding has: too much

mass. It has been estimated that even modest sized spacecraft would require a system of superconducting magnetic coils, and associated infrastructure, energy supply and cryogenic thermal control systems, that would weigh in the range of 100-300 tons, and possibly more. [156] [157] [160] Moreover, analyses with modified versions of both HZETRN and Geant4 transport codes indicated that even at those sizes, the amount of radiation deflection provides only modest health exposure improvements. [161] [160] In addition, there are also serious operational issues to consider, not the least of which is to avoid exceeding the quench temperature on the superconducting magnets – that temperature above which the coil material ceases to be superconducting. There has been some evidence that doing so could cause a catastrophic failure of the magnet (i.e., explosion), which would obviously be undesirable on a space voyage (and could have been one reason that the initially proposed superconducting magnet for Dr. Ting's Alpha Magnetic Spectrometer was changed to a conventional magnet before being installed on the ISS). And additional operational problems would arise from the magnetic field interfering with the operation of the spacecraft, particularly guidance and communication systems. [158]

Finally, in the electromagnetic field arena there has been some limited work on electrostatic shields set up by large electrically charged spheres placed in a wide array. However, this is likely too cumbersome for a spacecraft; but could possibly be viable for a Moon base, for example, with the caveat that initial examination indicates that the power requirements may be very large for even modest protection capabilities. [162] [153]

As a result of these considerations, for the foreseeable future passive radiation shielding will probably be the only economic and practical design alternative. For spacecraft, that will mean some kind of structural material, such as aluminum, and

perhaps other infrastructure components, as discussed previously. For surface space habitats, consideration has been given to buried facilities into the lunar surface, for example, or natural caves or lava tubes, all of which use a meter or more of regolith or rock to provide adequate radiation protection, as shown in Figure 5.3. [163] [164]

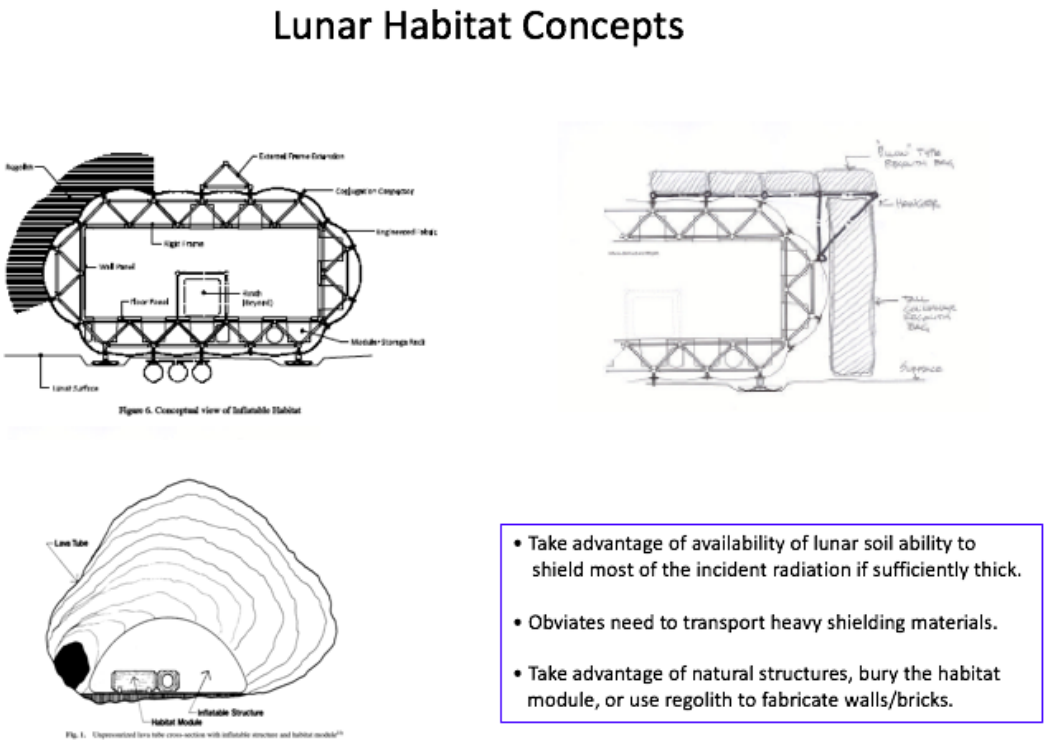

Figure 5.3 : Lunar Habitat Concepts: Lunar Regolith, Burial, and Lava Tubes. Adapted from De Angelis, 2002 and Schneider, 2010

Finally, there are some novel theoretical radiation protection ideas that don't fit neatly into the active/passive classification, including (1) medical countermeasures for human space travelers (i.e., medicines), and (2) hibernation for long space voyages, which induces a state of reduced metabolic activity, for which there is some animal data that suggests that adverse radiation effects are reduced. [165] [166] However, both concepts are only at the theoretical stage, and untested.

5.2 State-of-the-Art in Evaluating Shielding Materials

The current state-of-the-art involves only "passive" space radiation protection schemes. Thus the core evaluation principle is one of examining various shielding materials and designs for their ability to attenuate or stop the incident radiation, minimize generation of secondary radiation emissions, and at the same time satisfy a structural or other infrastructure purpose; and do it all at minimal mass.

Specific Stand-Alone Shielding Material Evaluations

The standard material used for passive shielding on spacecraft has been an aluminum hull of some 5 gm/cm^2, chosen over other readily available materials for its relatively low atomic number, light weight and structural stability. It was probably initially the right choice, as the comparison reveals, and adequate for space flights in LEO within the protective zone of the Earth's magnetosphere. *See* Figure 5.4.

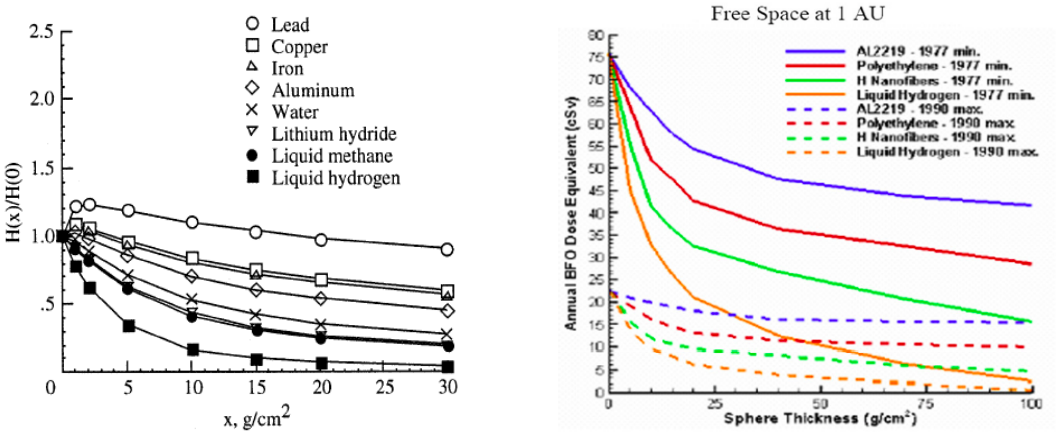

(a) Readily Available Materials. (b) Standard Shielding Materials.

Figure 5.4 : Passive Shielding Material Evaluations using HZETRN from 2001-2014. Figure (a) from Wilson, 2001, Figure (b) from Durant, 2014.

As can be seen in Figure 5.4a, based on the HZETRN generated metric of dose equiv-

alent, aluminum is really the best choice of those materials with structural integrity, a characteristic the lighter materials lack. This is expected if one recalls the discussion in Chapter 3, regarding the fact that the Coulomb force is the dominate force in the interactions between the GCR ions and a shielding material. Thus, materials with a larger charge-to-mass ratio should, in theory, be more effective in Stopping Power; i.e., those materials with the most electrons per unit mass and the least mean excitation energy. [41] And this is borne out in the illustrated results – hydrogen is a favored material and lead is less efficient as an energy absorber.

In Figure 5.4b, the HZETRN analysis confirms the theory that increasing the relative amount of hydrogen in a material, which has the largest charge-to-mass ratio, will increase the shielding effectiveness (i.e., reduce the dose equivalent). Thus, polyethylene is better than aluminum, and liquid hydrogen is the best. Of course, for the same protection level the polyethylene would have to be physically much thicker, and by itself it has no structural integrity. The other material shown in Figure 5.4a (the green curve) is described as a theoretical storage container fabricated with an unspecified graphite nanofiber material, in which hydrogen would be stored, and it shows better performance than aluminum or polyethylene. [9] In addition, the data would suggest that the mysterious graphite nanofiber container significantly decreases the radiation shielding effectiveness over the liquid hydrogen itself, as one would expect from the physics. But the most troubling part of the green curve in Figure 5.4b labeled "H Nanofibers" is that the referenced work cited from which this figure was taken – "Modified from Wilson et al. (1997), courtesy of NASA" – has no mention of nanofibers anywhere in its 493 pages. [41] Indeed, the green curve in Figure 5.4b may refer to lithium hydride (which is mentioned in the text), but like liquid hydrogen itself, would be operationally difficult and unstable to handle – matters the authors

neglect to address. [9] Thus, the evidence suggests that nanofibers were *not* actually investigated in connection with the 2014 Durant, et al. study.

Figure 5.5 illustrates an additional point about heavy shielding materials.

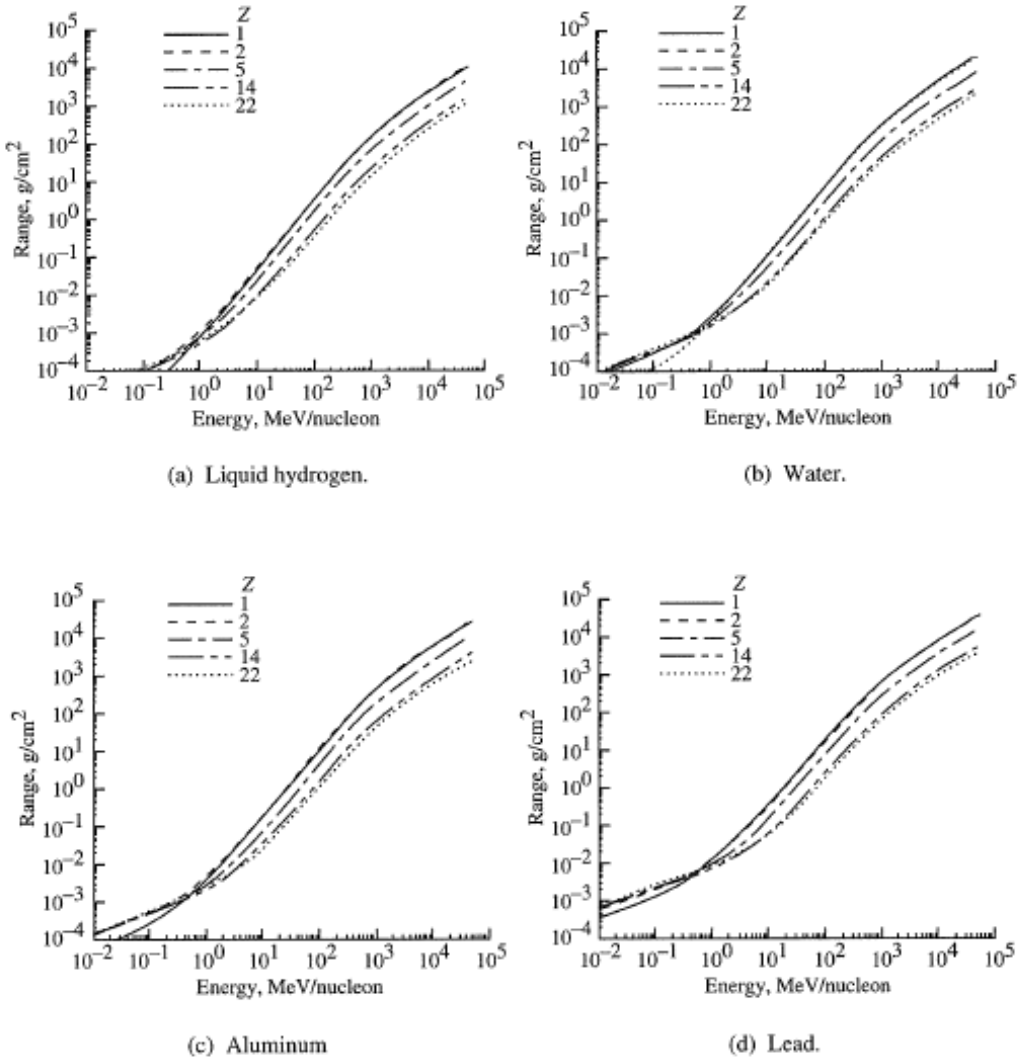

Figure 5.5 : GCR Stopping Range in Various Materials. From Wilson, 1997.

From these curves, it is clear that while the Range of *all GCR ions* is less in the lighter atomic weight shielding materials (consistent with the results in Figure 5.4);

nevertheless *in all materials*, the lighter GCR ions have a longer Range than the heavier ones. Thus, in every material, the iron ions are stopped in a shorter distance in the target material than the protons of the same energy. (*See, e.g.,* Section 3.3.) Because the heavier GCR ions tend to fragment when they collide with the target material nuclei, lighter secondary ion emissions will occur and have the effect of extending the Range of the original incident particle. Thus, heavy GCR ions can be converted into lighter ions and neutrons, with the result that this cascade of dangerous secondary emissions may not be stopped, particularly when the shielding is relatively thin, and then exit the backside where harm to humans and equipment will be caused. This effect can be observed easily in Figure 5.4a for lead, copper, and iron, where the dose equivalent value initially rises with increasing shielding thickness – contrary to what might be initially expected. As shown below, the same phenomenon occurs with other materials with relatively high atomic weights, including aluminum and lunar regolith (*see, e.g.,* Figures 5.6 and 5.9).

Recently, NASA reported its examination of one new material as a potential radiation shield, using the OLTARIS (i.e., HZETRN) radiation transport code for the analysis. [95] The NASA team first determined that the state-of-the-art for considering the use of polymer matrix composites filled with micro-scale materials and nano-materials for use as radiation shields in the aerospace, medicine, and nuclear sectors was presented in a review article by Nambiar, et al., 2012. [167] [95] That article considered shielding for all types of high energy and ionizing radiation, and concluded, from a theoretical standpoint, "that polymers reinforced with micro-scale or nano-scale structures have great potential to be used as radiation shielding materials in all the three industries discussed," but with respect to GCR-type ion particle radiation, reported only one inconclusive experiment (more on that later). [167] Presumably based

on this survey, NASA undertook to examine the boron nitride nanotube (BNNT) as a potential radiation shield material; a material that had previously been studied at NASA for structural purposes, and which could theoretically be processed into structural BNNT and used for load bearing structures. [168] The NASA team theorized that the ability to bind hydrogen to the BNNT structure would possibly result in an improved shielding for GCR ions (based on the physics already discussed in Chapter 3), and in addition it was thought the high cross section presented by boron to neutrons would help in mitigating the dangerous impact of secondary neutron emissions. The results are presented in Figure 5.6.

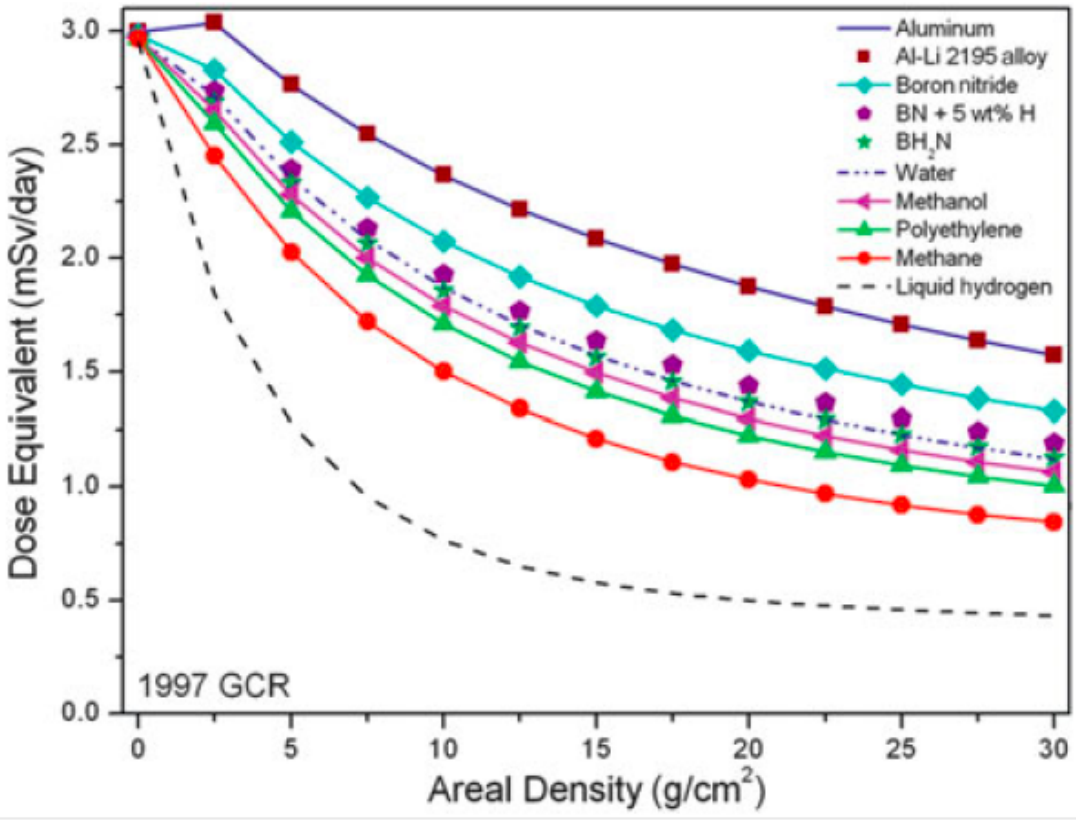

Figure 5.6 : Passive Shielding Evaluation of Some New and Proposed Materials. From Thibeault, 2015.

The first thing to note are the "calibration" runs with aluminum, polyethylene, and liquid hydrogen, in order to establish a relative performance bandwidth from the standard spacecraft shielding material to the theoretical best shielding material for GCR ions (liquid hydrogen). The relative effectiveness results of the various materials are reported in terms of dose equivalent, and are as expected, and consistent with earlier reported work. Also note that for the heavier, less hydrogen-rich material – here, aluminum – that the phenomenon discussed above is clearly visible: as the shielding thickness is increased to a point, the harm actually increases initially.

The NASA study concluded that the BNNTs alone (without added hydrogen) "do not outperform current state-of-the-art radiation shielding materials," but by the addition of 5% by weight of hydrogen, the theoretical performance approaches that of water or polyethylene (neither of which is a candidate as a structural material). They also report, however, that other research has indicated a maximum insertion of hydrogen into BNNTs of only 4.2% by weight. [95] The NASA team has also filed a patent application on the use of BNNTs for radiation shielding purposes, but as of this date it is still pending and no patent has issued. [169]

Another study investigated the Stopping Power of asteroid and meteor typical compositions and concluded that it was comparable to that of aluminum; the idea being that in space those materials would be freely available without the high cost of lifting them into orbit. [170] However, the study neglected any consideration of secondary particle production and glossed over the economics (and feasibility) of collecting and processing the material in space to make a viable shielding material.

The challenge in material selection is to produce shields which are structurely sound, thermally stable, resistant to degradation over the mission lifetime, and which optimize shield performance. As a NASA study aptly concluded: "Clearly, a materials

development program to develop shielding technology is highly desirable." [41]

Multilayer Shielding Design Analyses

The idea of using a multilayered shield to protect against radiation hazards is not new, but the concept has not been analyzed with respect to shielding against the GCR in cis-lunar space. The parameters for this research as it pertains to investigating multilayered shielding configurations were introduced in Subsection 4.3.3, and in the text associated with Figure 4.9.

Most of the reported research considering the use of multiple layers of different materials to better attenuate radiation hazards has been done in connection with protecting satellite components, especially those in Earth orbits that would intersect one of the Van Allen belts, where high levels of electrons and protons are trapped. [129] [34] [150] [171] These multilayer shielding concept models are aptly illustrated in Figure 5.7.

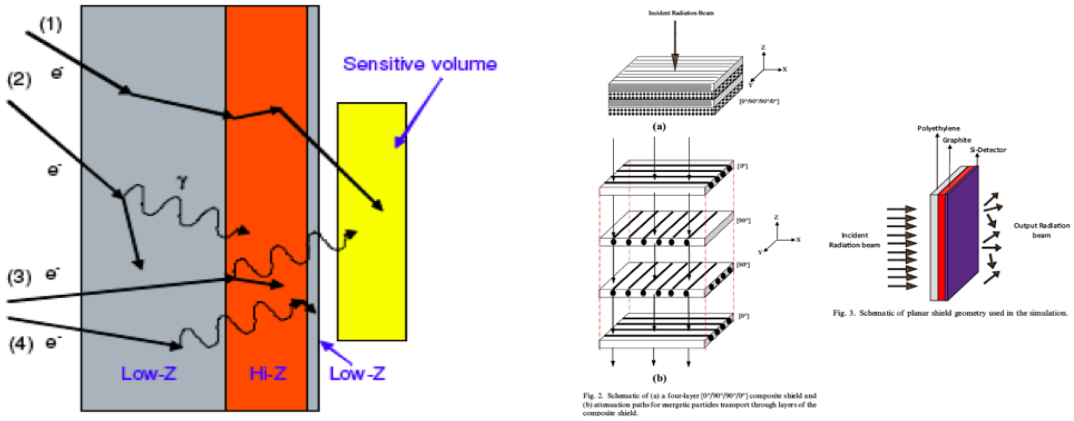

(a) Aluminum/Tungsten. (b) Polyethylene/Graphite.

Figure 5.7 : Mult-layer so-called "Graded-Z" Concept Models.
Figure (a) from Truscott, 2010, and Figure (b) from Emmanuel, 2015.

One recent study (illustrated in Figure 5.7b) involved examining the impact of radiation protection for a satellite in a so-called Molniya orbit (high elliptical orbit with an inclination of 63.4°, a period of one-half day, and an apogee around 40,000 km) where the spacecraft spends most of its time in both of the electron and proton rich Van Allen belts, along with increased GCR exposure as compared to a lower standard LEO orbit, where the issue was trying to add some measure of structural rigidity to polyethylene shielding material, while maximizing the radiation protection. However, the layered materials did not provide appreciable better radiation protection results. [172]

In the GCR protection context, one study conducted at Aachen University, Germany, examined the standard stand-alone materials of aluminum, water, polyethylene, lithium hydride and graphite, and also looked at one multiple layer configuration using the MULASSIS Monte Carlo radiation transport code, to compare the effective dose between aluminum by itself, and aluminum with polyethylene blocks behind it. [147] Not surprisingly, the research reported an improved shield effectiveness with the dual-layered design, a result that was predictable from the physics and had been already discovered in actual experimental measurements done in limited areas on the ISS in its LEO orbit.[1]

A rather unique shielding proposal designed to take advantage of the high effectiveness of hydrogen in attenuating ions, is a modified layered implementation involving a multitude of hydrogen-filled glass beads sandwiched within an appropriate binder, which, as would be expected, reported some theoretical improvements over bare aluminum on proton attenuation and neutron secondary generation (but nothing about

[1] Private conversation with NASA astronaut and Commander of the ISS on Expedition X, Dr. Leroy Chiao.

the GCR generally), and was granted U.S. Patent No. 7,964,859 B2 in 2011. [173]

Finally, as mentioned in Subsection 4.3.3, NASA has expressed the view, without supporting explanation, that the future of more efficient and effective radiation shielding for spacecraft will take the form of multilayered materials, much like the Micrometeroids and Orbital Debris (MMOD) shielding. [152]

Radiation Protection on the Moon or Mars

When evaluating radiation protection schemes on the surface of a large body in space – like the Moon or Mars – several additional considerations must be taken into account. First, when considering a habitat located on the surface, the large mass of the celestial body itself will block half of the incident isotropic GCR radiation, as shown by the resulting equivalent dose levels in Figure 5.8.

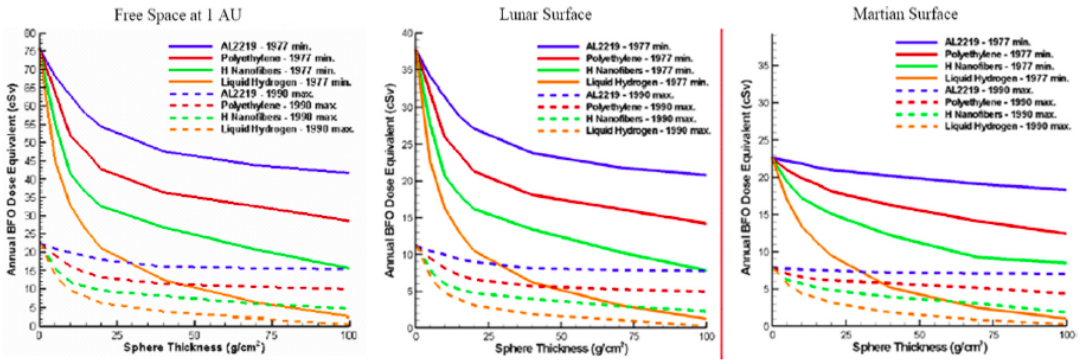

Figure 5.8 : Passive Shielding Evaluation for Three Different GCR Environments: Free Space at 1 *AU*, Lunar Surface, and Mars Surface. From Durante, 2014 (solid lines for 1977 solar minimum; dashed lines for 1990 solar maximum).

As can be easily seen, the effective dose for each type of shielding is a direct function of the GCR input environment; thus, the lunar surface is simply one-half that of free space at 1 *AU*, and the Martian surface is one-half, minus the additional small attenuation provided by the thin Martian atmosphere. [9]

In addition, the surface complicates the radiation transport modeling. The major complication is that the surface generates an array of secondary emissions, some of which recoil and are then present in the habitat to inflict further damage, as was reported in a study done at the Skobeltsyn Institute of Nuclear Physics, Moscow State University. [174] In fact, both the shielding and the lunar soil will produce secondary emissions, including dangerous neutrons, and, importantly, the secondary neutron generation from the lunar surface can actually be higher than those generated from the shielding material, particularly at the thinner shielding thicknesses. [174] In another study in 2010 by Jia, et al. of the shielding effectiveness of lunar regolith, it was determined that the so-called albedo radiation (the recoil and upward moving secondary emissions) generated by the lunar surface would be different with and without the habitat. [89] These considerations are illustrated in Figure 5.9.

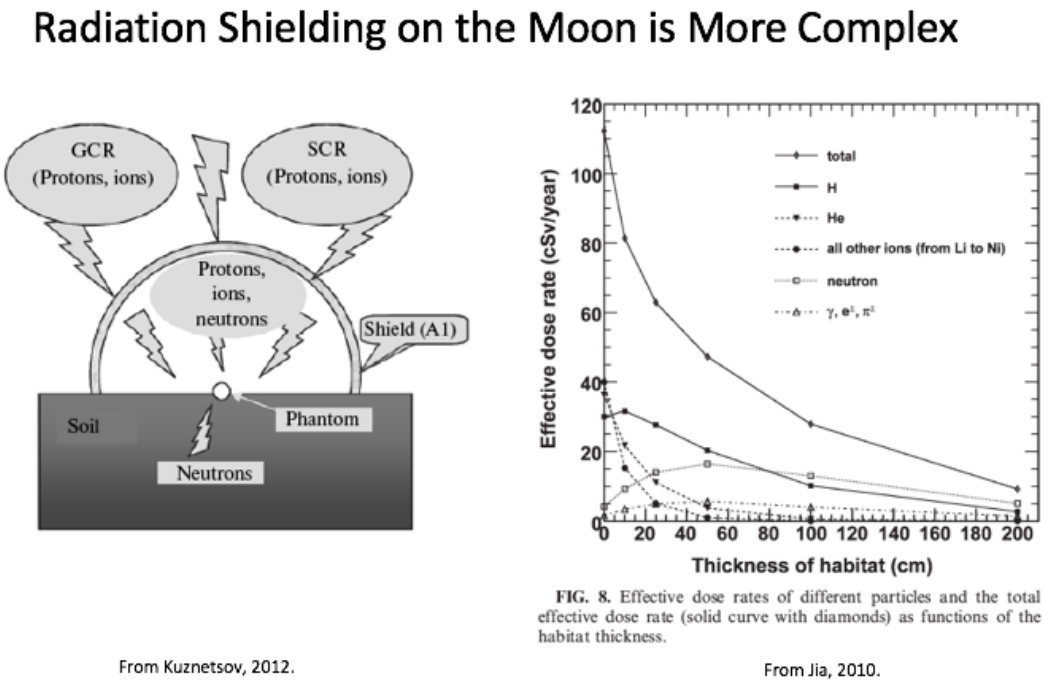

Figure 5.9 : Shielding Evaluation Models for Lunar Surface Habitats.
From Kuznetsov, 2012, and Jia, 2010.

Note also the phenomenon previously discussed that the contribution to the effective dose from some particles – here protons and neutrons – actually increases initially with increasing thickness of the lunar regolith shielding material until a point when the shielding begins to attenuate some of the secondary emissions, just as occurs with other materials, such as aluminum. [89]

Finally, there are on-going studies to better refine the radiation environment at the lunar surface and Martian surface (for both GCR and SPEs), as more data is collected from the various probes, satellites and robotic surface vehicles. [175] [176]

5.3 Review and Limitations of Experimental Analyses

Relatively little experimental analysis of shielding materials has been done to gauge their effectiveness for protecting against GCR radiation, because it is expensive, difficult to make comparative assessments between various shielding materials and designs, and it is not possible to recreate the entire GCR spectrum (both species and energy levels) in the laboratory. But there have been some.

For example, one experiment conducted at the NASA Space Radiation Laboratory at Brookhaven National Laboratory (BNL) sought to measure the nuclear fragments resulting from a 1 GeV/n iron ion beam impacting different standard shielding materials (aluminum, polyethylene, and lead), and confirmed that the highest fragmentation occurred in the polyethylene target and the lowest in lead. [177] This experiment, and others in a similar vein, gathered important data regarding various interaction cross sections that helped to better calibrate radiation transport models, and one on thin polyethylene materials confirmed against Monte Carlo simulations that using a single iron ion beam was a good proxy for all heavy ions in the GCR, in terms of dose measurements. [84] In addition, such results tend to indicate the importance of nuclear

fragmentation in a shielding material's ability to reduce the physical absorbed dose and biological harm behind shielding caused by heavy ions in the GCR.

In another similar experiment, using the Heavy Ion Medical Accelerator in Chiba (HIMAC), located at the National Institute of Radiological Science in Japan, a wide variety of targets, both elemental and composite, were placed in the ion particle beam, and the spectra of particles emerging from the targets were measured using a stack of silicon detectors. The results, presented in terms of dose reduction per gm/cm^2 of target material (i.e., areal density), support the conclusions of earlier calculations indicating that performance improves as the shield's mass number decreases, with hydrogen being by far the most effective shielding material, and that, as depth increases, the incremental benefit of adding shielding decreases. [85]

Other experiments have been performed in order to verify the radiation transport calculations and simulation codes, as discussed in Section 4.3; for example, (1) irradiating a MIR space station food locker, and then favorably comparing the results to a proprietary Monte Carlo simulation [148], and (2) irradiating layered polyethylene and carbon fiber materials for electron and proton radiation protection for satellites orbiting within the Van Allen belts, and then comparing to a MULASSIS simulation model, demonstrating that the addition of material to provide structural rigidity does not appreciable degrade the radiation shielding capabilities in such an environment. [149]

One experiment was conducted at BNL to determine whether adding graphite nanofibers to ultrahigh molecular weight polyethylene (UHMWPE) to improve its structural integrity would degrade the radiation shielding performance, with the results showing that the high radiation shielding performance associated with the UHMWPE was not significantly degraded, but with otherwise mixed results. [178]

In addition, NASA's team that recently reported study results using the OLTARIS deterministic code to examine the potential use of boron nitride nanotubes (BNNT) impregnated with hydrogen [95], initially indicated that a second phase of their work would be to conduct experiments using the 1 GeV iron ion beam at BNL on the BNNT target material, but nothing has been reported as of this date. [168]

Thus, for over a decade, researchers have been making use of the BNL and other laboratories to conduct studies of the effects of space radiation on materials and biological samples. Most accelerator-based space radiation experiments have been performed with single ion beams at fixed energies. However, the actual GCR space radiation environment consists of a wide variety of ion species with a continuous range of energies, and thus the experimental results are somewhat impaired – more so for biological assessments than for evaluations of various potential shielding materials.

Due to recent developments in beam switching technology implemented at BNL, it is now possible to rapidly switch ion species and energies, allowing for the possibility to more realistically simulate the actual radiation environment found in space. However, only a handful of ion species are available and there are many issues to resolve in developing a true GCR simulator. [179] [87]

A major problem with studies on the effects of galactic cosmic ray radiation that utilize mono-energetic single-ion particle beams is that the projected doses for long-term exploration missions are given using short duration highly-acute exposures. This methodology does not replicate the multi-ion species and energies found in the space radiation environment, nor does it reflect the low dose rate found in interplanetary space. Recently, a device has been proposed that can accurately generate the linear energy transfer spectrum of the GCR radiation environment experimentally by perturbing the intrinsic properties of hydrogen-rich crystalline materials in order to

instigate specific nuclear spallation and fragmentation processes when placed in an accelerated mono-energetic heavy ion beam. [88] This has the potential to allow utilizing the BNL's 1 GeV/n iron ion beam to accurately generate the entire GCR spectrum, and thus provide for more realistic Earth-based experiments, which may have its best application with radio-biological studies.

As the research presented in this thesis is focused on determining the metrics for better evaluating various potential shielding materials and designs, and identifying promising candidates, on a *relative* basis compared to standard shielding materials, the expense and time involved in carrying out a related experiment is not justified at this juncture. However, the results of this research may allow framing a proposal for complimentary experimental work in the future.

Chapter 6

Evaluation of GCR Radiation Shielding Effectiveness – New Methods and Materials

"The scientist describes what is; the engineer creates what never was."
—Theodore von Kármán, Hungarian-American mathematician, aerospace engineer, and physicist, Co-founder of Caltech's Jet Propulsion Lab (1881-1963)

"Why should a financial engineer be paid four times to a hundred times more than a real engineer? A real engineer builds bridges, a financial engineer builds dreams. And when those dreams turn out to be nightmares, other people pay for it."
—Andrew Sheng, Chief Adviser, China Banking Regulatory Commission, in *Inside Job*, 2010 (1946)

A good shielding material and shield design should optimize several objectives: (1) effectively attenuate the incident GCR radiation, (2) produce minimal secondary radiation particles, (3) effectively attenuate any secondaries produced, (4) have adequate mission-length durability in the radiation environment, and (5) provide ancillary functions, such as being structural components.

Passive radiation shielding designs are currently the most practical solution to the long-term, deep space GCR radiation exposure issue. State-of-the-art materials and several multilayered configurations have been studied with both the HZETRN and MULASSIS radiation transport codes, with a focus on a new evaluation metric that utilizes relative dose equivalent calculations, and analysis of various secondary particle fluences behind shielding, in order to demonstrate techniques to better identify material candidates and design configurations for more effective GCR shielding. We obtained these results by conducting over one-hundred radiation transport simulation runs and related calculations; with representative samples shown in Appendix B.

6.1 A Proposed New Metric for Evaluating GCR Shielding

Given the paucity of biological and medical data that can tie the calculated exposure metrics of absorbed dose and dose equivalent to actual biological harm for long-term GCR exposure in the region of cis-lunar space (1 AU), we propose a new shielding evaluation metric that calibrates the shielding evaluation model with radiation exposure data from the International Space Station in order to more accurately evaluate shielding for spacecraft operating in the cis-lunar region, and in the process ties the evaluation results to the available medical data from ISS astronauts in a consistent way. This new evaluation metric relies on a comparison of the relative shielding effectiveness at 1 AU in the cis-lunar space radiation environment, to that in the radiation environment in the ISS, where hundreds of astronauts have flown and spent considerable time, and for which there is voluminous medical data. Thus, it is a measure of how well a proposed shielding protocol replicates the ISS radiation exposure levels, where the biological impact of long-term radiation exposure is being well documented and better understood. By evaluating shielding protocols for spacecraft operating in the cis-lunar region as a function of the ISS radiation environment, the new metric and evaluation procedure mitigates the inherent source of error in model calculations that rely on the different versions of radiation quality factors, radiation weighting factors, and tissue weighting factors discussed in Chapter 2.

For the purposes of this research, the comparison to be used is between the radiation environment in cis-lunar space at 1 AU (without consideration of SPEs), with the radiation environment in the ISS orbit at an altitude of 400 kms with a circular orbit at a 51.64° inclination. Thus, in the cis-lunar region the radiation is the GCR (as modulated by solar activity), and at the ISS orbit the radiation environment is the same GCR boundary condition, but as partially blocked by the Earth and attenuated

by the magnetosphere, plus two additional sources; (1) the albedo neutron secondary emissions caused by the GCR interacting with constituents in the Earth's atmosphere, and (2) a small component of trapped protons (where the ISS intersects an unusually low segment of the inner Van Allen belt, called the South Atlantic Anomaly).

The GCR Radiation Environment at 1 *AU* – No Shielding

In order to develop this new proposed GCR comparative metric the boundary input radiation flux in both areas of interest must be clearly understood – in cis-lunar space at 1 *AU* and at the 400 *km* altitude of the ISS orbit.

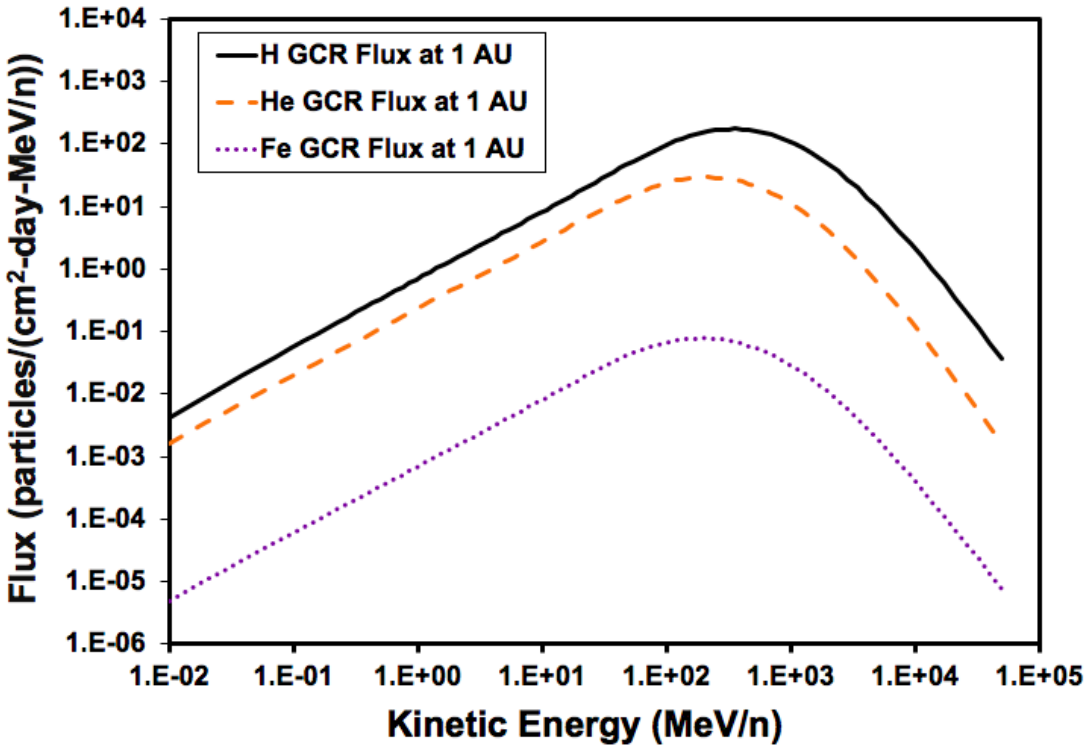

Figure 6.1 : Differential GCR Flux at 1 *AU* in Free Space – No Shielding.

Our Figure 6.1 shows the calculated values for the GCR flux at 1 *AU* for hydrogen, helium and iron ions, using the Badhwar-O'Neill 2010 GCR model at the 2010 solar

minimum – which we used to generate the primary comparative boundary conditions in this research, because it represents a maximum GCR flux condition, our design criterion. The differential flux versus energy for all 59 ions in the GCR up to nickel could be plotted, but it is common (and less cluttered) to show the two highest flux ions (hydrogen and helium), and then let the iron ion stand as a proxy for the rest.[1]

Comparison of these calculations with other similar published results shows general agreement in the GCR flux, as shown in Figure 2.5. In addition, Figure 2.5 shows the relative abundance of all the ions, and aptly demonstrates that hydrogen and helium are expected to be several orders of magnitude more abundant than any other ions. And the calculated model data is in agreement. For example, our data from which Figure 6.1 is plotted indicates that the differential flux at 1 GeV/n for hydrogen is about 102 $particles/(cm^2 - day)$, for helium that flux is about 10 $particles/(cm^2 - day)$, and for iron ions that flux is about 0.023 $particles/(cm^2 - day)$. Thus, assuming that the 56 heavier ions (up to nickel) have on average about the same fluence as the calculated iron ion, the total differential GCR flux at 1 GeV/n would be $102 + 10 + (0.023)(56) = 113.3$ $particles/(cm^2 - day)$. These calculations indicate that at the 2010 solar minimum, the 1 GeV/n segment of the GCR ion flux is about 90% hydrogen (protons), 9% helium, and 1% for all ions with atomic charge $Z \geq 3$.

Our results comport reasonably well with other accepted estimates of the entire nuclei GCR flux integrated over the entire energy spectrum of about 87% protons, 12% helium and 1% heavier ions, given that the relative ratios obviously differ as a

[1] While the HZETRN transport code return results for the flux contribution of all GCR ions up to nickel (noting that there are two helium ions: ^{3}He and ^{4}He) the MULASSIS Monte Carlo simulations must be run ion-by-ion, and thus it is much more efficient to use the iron ion as a proxy for all ions $Z \geq 3$, which turns out to be a fairly accurate assumption in terms of both fluence and energy distribution. [42] In any event, it makes little difference in comparative analyses as long as the same input parameters are used in each model calculation.

function of both ion kinetic energy and the time period of the measurement in the solar cycle. *See* discussion in Section 2.1 and Simpson, 1983. [36]

We further verified our results by calculating the flux for all ions over a range of points in the GCR ion kinetic energy spectrum, above and below which the fluence of particles is relatively *de minimis* during the flux time period of a day, e.g., at 1 MeV/n, 1 GeV/n, and 10 GeV/n, as shown in our Figure 6.2.

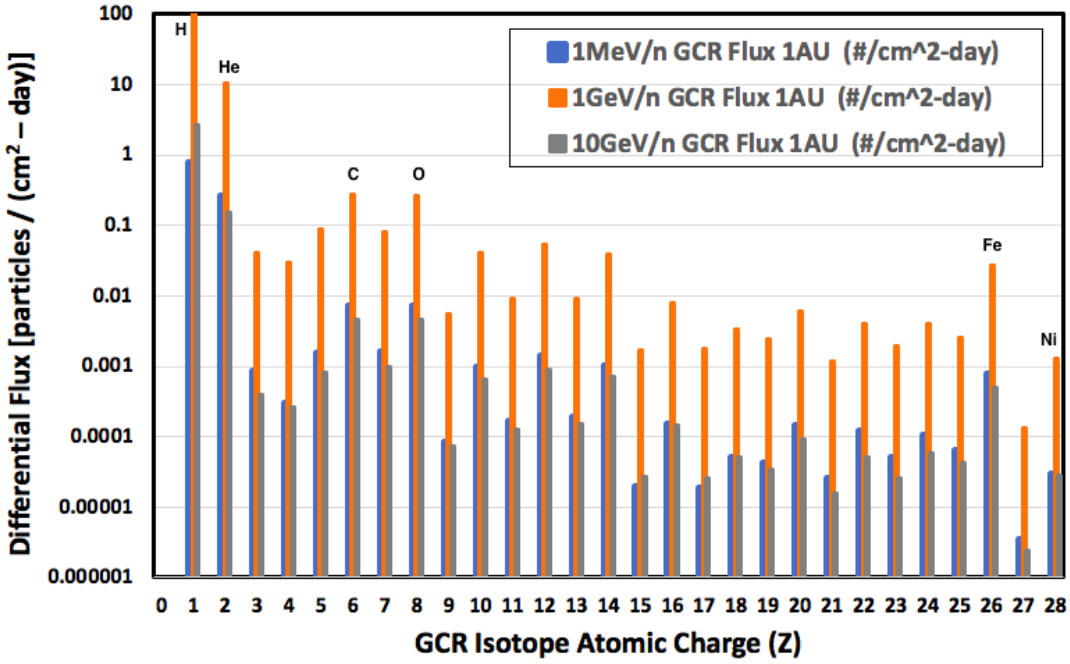

Figure 6.2 : GCR Flux of All Ions of Selected Energy Levels at 1 AU in Free Space.

For example, our data for this set of calculations indicates that the total differential GCR flux for all ions at 1 GeV/n is 113.8 $particles/(cm^2 - day)$, which compares closely to the value obtained by using the flux of iron ions at that energy level as a proxy of 113.3 $particles/(cm^2 - day)$. Further, the calculated ratio of hydrogen to helium to iron ions at this energy level (1 GeV ratio of H:He:Fe) is 90%:9.1%:0.9% – very close to the "iron ion proxy" method.

It is further evident from our Figure 6.2 that the relative distribution of ions in the GCR is similar at each energy level; for example, protons always have the highest differential flux, followed by helium, and the rest are orders of magnitude less. The calculated ratio of H:He:Fe at 1 MeV/n is 73%:25%:2%, and 10 GeV/n is 94.1%:5.3%:0.6%. These data indicate a general trend within this energy range of a slightly decreasing percentage of ions with $Z \geq 3$ in the GCR with increasing kinetic energy, and the ratios compare favorably with other published data, particularly in the range of maximum fluence of 100 MeV/n to 1 GeV/n (as shown in Figure 6.1), such that confidence can appropriately be place on these calculated results as representative of the GCR boundary conditions at 1 AU in cis-lunar space.

The GCR Radiation Environment at the ISS Orbit – No Shielding

The next task is to calculate the input boundary conditions for the radiation environment for the ISS orbit using the same GCR model: Badhwar-O'Neill 2010 at the 2010 solar minimum (and again, to be consistent, ignoring any SPEs). The radiation environment for the ISS orbit consists of three parts: (1) the GCR flux as diminished by the Earth and the surrounding magnetosphere, (2) the local radiation environment of back-scattered neutrons from the GCR ions interacting with the Earth's atmospheric constituents (the albedo neutrons); and (3) the trapped proton radiation in a small part of the lower Van Allen belt called the South Atlantic Anomaly that extends down to 200 kms, within the ISS orbit altitude. The ISS orbits at an inclination of 51.64° with respect to the Earth's equatorial plane, at an average altitude of 400 kms in a nearly circular orbit (perigee of about 398 kms and apogee of about 406 kms), at a velocity of some 7.67 kms/s ($\approx$ 17,200 mph), with an orbital decay of some 2 $kms/month$, and an orbital period of about 92.7 $mins$ (about 15.5

orbits per day). These orbital parameters establish the spatial and temporal location of the ISS in low Earth orbit, and thereby dictate its incident radiation environment.

The GCR flux is attenuated in low Earth orbit by two mechanisms: first, by the fact that the Earth itself acts as a shield against the full isotropic flux of the GCR, and second by the magnetic field surrounding the Earth (the magnetosphere) stopping or slowing down the GCR ions. The former effect is primarily geometric – a measure of the solid angle obstructed by the Earth at varying altitudes – at the surface the Earth obstructs approximately one-half of the total isotropic flux experienced in free space, and somewhat less at an altitude of 400 kms, on the order of 0.39 would be obstructed.[2] Thus, while the GCR flux in free space is isotropic over a solid angle of 4π steradians, at an altitude of 400 kms the incident radiation flux is diminished to $0.61 \times 4\pi$ steradians of the full isotropic flux.

The shielding effect of the magnetosphere is a bit more complex to determine, and derives from the fairly simple principle that the magnetic field will exert a force on a charged particle moving through it in accordance with the Lorenz force law, and deflect or trap particles below a certain kinetic energy; but its ability to do so varies with location and angle of entry of the GCR particle into the magnetosphere. [180] As depicted in Figure 2.2, the magnetosphere is shaped by the solar wind and by the dipole nature of the Earth's magnetic field, both of which are constantly changing, and is also modulated by the solar wind and heliosphere magnetic field, just as is the flux of the GCR in the solar system, as previously discussed in Chapter 2. As a result, the magnetic field is very weak at the magnetic poles (off-set from the geographic poles

[2] To calculate the fraction of the full 4π steradian GCR flux for an altitude h above the Earth, with radius $r = 6,378kms$, one can calculate the solid angle occulted by the Earth – i.e., blocked from view – and then subtract that from the full isotropic flux, as follows: GCR Flux in LEO at altitude h equals $1.0 - (1/\pi \times \arcsin \frac{r}{r+h}) \times$ Free Space GCR flux, for $0 \leq h \geq \infty$. A purely geometric assessment, that of course does not take into account the effect of the magnetosphere.

by some 11°), and the magnetosphere is relatively thin on the side of the Earth facing toward the Sun (extending to some 65,000 kms), where it is compressed by the solar wind, but stretched out on the back side to some 600,000 kms.

All of these physical characteristics of the magnetosphere effect the ability of GCR ions to penetrate the Earth's magnetic field, along with the GCR ion's so-called magnetic rigidity, which is defined as the particle's momentum per unit charge – a metric describing the particle's resistance to deflection by a magnetic field.[3] [181] Thus, the higher the rigidity for a GCR ion, the more easily it will be able to penetrate the magnetosphere, all other variables being equal. The models attempting to simulate the shielding effect of the magnetosphere employ the concept of a GCR particle's cut-off rigidity, R_C, whereby particles with potential energies less than the cut-off rigidity are deflected by the Earth's magnetic field, or are trapped in the periodic orbits of the

---

[3] The formulation for magnetic rigidity derives from the principles of electromagnetism. A charged particle passing through a magnetic field experiences a force dictated by the Lorentz force law:

$$\mathbf{F} = m\mathbf{a} = q(\mathbf{E} + \mathbf{v} \times \mathbf{B})$$

In the absence of an electric field, and assuming for the moment that the particles in question enter the magnetosphere perpendicular to the magnetic field lines, this formulation can be re-written as follows:

$$ma = m\frac{dv}{dt} = \frac{dp}{dt} = qvB$$

The gyro-radius of a charged particle – i.e., the radius of the orbit of a charged particle moving in a uniform, perpendicular magnetic field – along with that particle's mass and velocity, determines the centripetal force acting on the particle as $\frac{mv^2}{r_g}$. Therefore, in a steady-state situation, equating the Lorentz force with the centripetal force results in the following:

$$qvB = \frac{mv^2}{r_g} = \frac{mv^2}{1}\frac{qB}{mv} \Longrightarrow r_g = \frac{mv}{qB} = \frac{p}{qB}[SI] = \frac{pc}{qB}[csg]$$

The magnetic rigidity R is a measure of the particle's resistance to deflection by a magnetic field, defined as the gyro-radius times the strength of the magnetic field, and is usually given in units of volts (potential energy – "energy per unit charge"):

$$R \equiv r_g B = \frac{p}{q} \Rightarrow v \to c \Rightarrow R = \frac{\gamma p}{Ze} \Rightarrow \frac{A}{Z}\sqrt{E^2 + 2EE_0}$$

where E is the particle's kinetic energy per nucleon (in electron volts), E_0 is the particle's rest energy, and R is in units of volts. Thus, a 10 GeV/n proton has a rigidity of 10.9 GV (giga-volts).

Van Allen belts; and conversely, particles with potential energies above the R_C level penetrate the magnetic field and contribute to the radiation environment in low Earth orbit directly and through generation of secondary particles as they interact with the atmosphere. [30] [182] Indeed, actual measurements have been taken in the ISS orbit, and other low Earth orbits with lower inclinations, to validate the cut-off rigidity method of mapping the radiation environment below the magnetosphere. [183] [184] These concepts are aptly illustrated in Figure 6.3.

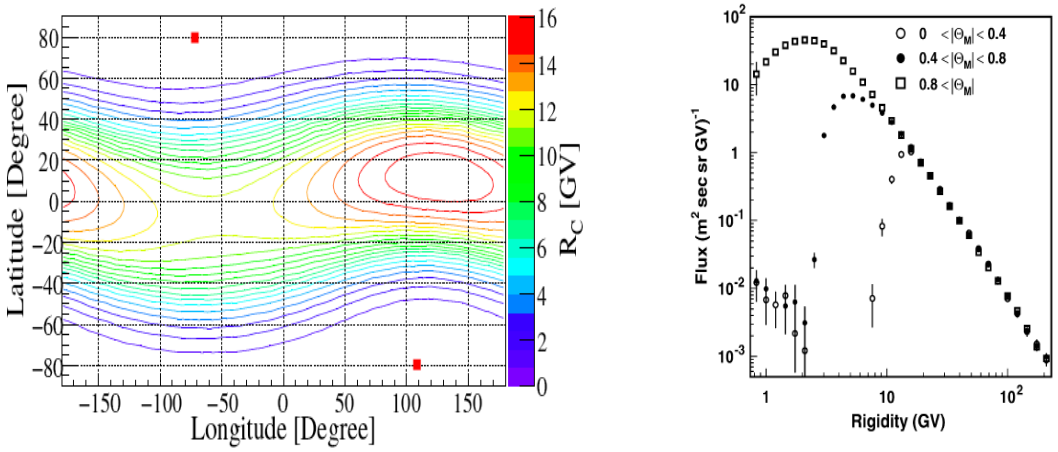

(a) Global 2005 R_C by Longitude and Latitude. (b) Helium Flux.

Figure 6.3 : Shielding Effect of Magnetosphere on Free-Space GCR Ion Penetration. Figure (a) is from Matthiä, 2009, and Figure (b) is from Aguilar, 2002.

From Figure 6.3a, a mapping of the global cut-off rigidity, R_C, in 2005, it is evident that the ability of GCR ions to penetrate the magnetosphere varies with both latitude and longitude. The red dots on the figure represent the location of the magnetic poles, and it is clear that the cut-off rigidity decreases markedly in the higher latitudes, thus allowing a greater portion of the free-space GCR flux to penetrate to the Earth. Figure 6.3b is a plot of data obtained from the ISS orbit of the helium ion flux as a function of latitude (measured in radians), clearly showing

a sharp drop off of the helium flux with decreasing latitude; e.g., the top curve (squares) is the helium flux at the ISS orbit above 45° latitude (0.8 radians), and the flux dramatically decreases in the lower particle energy spectrum in the 22° to 45° latitude range (solid dots), and decreases even more in the 0° to 22° latitude range (open dots). Because the ISS orbits the Earth at an inclination of about 51.6°, its orbit will track geographically between 51.6° N. latitude and 51.6° S. latitude, and thus its GCR radiation exposure below the magnetosphere in low Earth orbit will constantly change. However, since the exposure time period of interest for evaluating shielding is fairly long ($\geq$ 1 year) relative to the ISS orbital period ($\approx 90 mins$), it is reasonable to use averaged GCR flux values for a particular orbit (inclination and altitude) to evaluate shielding materials.

In addition, the magnetosphere also causes belts of trapped electrons and protons to form (the Van Allen belts), as shown in Figure 2.1a, where the lower proton-rich Van Allen belt in the southern Atlantic area – called the South Atlantic Anomaly (SAA), caused by a distortion in the Earth's magnetic field – is low enough that the ISS can traverse a portion of it during a few minutes of each orbit that tracks that geographic area (about once every three months). [185] [186] This provides an addition to the radiation environment of a high flux of moderate energy protons that must be added to the radiation exposure. Measurements on some Shuttle flights (not the ISS) have indicated that about 35% of the dose equivalent exposure to humans in some LEO positions could come from the trapped proton flux in the SAA. [187]

NASA and others have been studying the impact of the magnetosphere in shielding the GCR for many years, and there are several approaches employed to determine its effect on the GCR flux, all of which fundamentally reduce to determining a geomagnetic transmission scaling factor that changes by latitude and longitude, as well

as timing within the solar sunspot cycles, to determine the GCR energy spectrum and species that can penetrate the magnetosphere in each location, and thereby add to the local radiation environment. [30] [188] [189] Both MULASSIS and OLTARIS have been recently modified by ESA and NASA, respectively, to provide the ability to calculate each of the effects of the magnetosphere on the low Earth orbit radiation environment, and these model input boundary conditions have been reasonably verified with actual measurements from both the International Space Station and the Russian MIR Space Station. [187] [134] [107]

The final major contribution to the radiation environment in low Earth orbit comes from albedo neutron radiation resulting from interactions with the GCR ions and the Earth's atmosphere. The GCR does not contain any significant amount of free neutrons, but the GCR ions produce free neutrons as secondary emissions as they collide with atmospheric molecules, either as fragments of the projectile ion or remnants of the target nuclei, and by neutrons being ejected from target atoms that are excited by scattering events with the incident GCR ions, as discussed previously in Chapters 2 & 3. The atmosphere itself can be modelled as an air column with an areal density of about 1,033 gm/cm^2 (approximate composition: 78.2% nitrogen, 20.4% oxygen, 0.9% argon, 0.4% water vapor, and 0.04% carbon dioxide; with trace amounts of neon, helium, and methane), with 99.99997% of its mass below an altitude of 100 kms (62 miles) – the Von Kármán line – above which is considered "space" by international convention. [190][4] *See* discussion in Chapter 2 and Figure 2.6.

[4] The Earth's atmosphere has been modeled in much more detail by dividing it into 180 concentric spherical shells to better simulate the actual density and temperature profile from sea level to an air-space boundary set at 65 kms altitude in accordance with the U.S. Standard Atmosphere, established 1976. In this set-up, above 2 kms, the atmospheric composition has been kept constant at 23.3% oxygen, 75.4% nitrogen and 1.3% argon by mass, while below this level hydrogen gas has been included from 0.06% at sea-level to 0.01% by mass at 2 kms to account for water vapor abundance. [191]

For example, the Earth's atmosphere and the Van Allen belts together are believed to shield most of the primary incident GCR particles [38], but the interaction of those particles with the atmospheric molecules generates many secondary emissions that reach the Earth's surface [44] [26], and ultimately accounts for about 16% of the normal background radiation dose exposure at the surface. [46] But some primary incident GCR particles can reach the surface; for example, protons (which have the longest range of the positively charged ions) with a kinetic energy of 5 GeV have a range in air of about 2,600 gm/cm^2 – more than sufficient to penetrate entirely through the 1,033 gm/cm^2 areal density of the atmosphere, assuming they are slowed only by the Coulomb force and have no actual physical collisions with target nuclei. *See* Section 3.3. On the contrary, primary GCR protons with an energy of 1 GeV can penetrate only 320 gm/cm^2 in air, and thus will not reach the Earth's surface; however, since the the density of the atmosphere is not uniform (i.e., much less dense at the top), such a proton could have a range down to an altitude of about 8 kms (about 25,000 feet), and thus could contribute to the radiation environment experienced by many passenger airplanes. To complete the picture, the threshold energy required by a primary GCR proton to reach the Earth's surface is about 2.75 GeV, which is well above the peak flux level, as shown in Figure 6.1. Furthermore, that energy level corresponds to a rigidity of 3.6 GV, which means that primary GCR protons at that energy level can penetrate the magnetosphere only at very high latitudes ($\geq 60°$) (*see* Figure 6.3a). *See also*, calculation techniques employed in Suparta, 2014. [192]

Neutrons are a different matter, as they are produced primarily as secondary emissions in the atmosphere (below the magnetosphere), and due to their zero charge they are not slowed by the Coulomb force, and thus can have a much longer range than the GCR primary ions. That some of these secondary neutrons impact the

Earth's surface is proved not only by the physics, but by the neutron monitoring stations located at various places around the globe; and not surprisingly, the count rate is higher in the higher latitudes where the cut-off rigidity, (R_C), to the primary GCR particles that produce the secondary neutron emissions is lower.[5] [193] [182] [30] Neutron emissions are of particular concern because the relatively low energy neutrons – in the range between $10^{-2}MeV$ to $10^{3}MeV$ – are relatively more harmful to humans than the rest of the neutron spectrum. *See* Figure 2.10 and accompanying text regarding radiation weighting factors in Chapter 2. NASA has modeled the albedo neutron environment, and incorporated a version of that into OLTARIS, where results for the ISS orbit indicate that the albedo neutron contributes approximately 12% to the total human exposure in terms of the dose equivalent metric. [107] [187] The MULASSIS Monte Carlo transport code does not currently have the capability to add the albedo neutron flux.

With all of these factors in mind, we determined the differential flux of the free-space GCR induced radiation environment at the ISS orbit at an altitude of 400 kms using the HZETRN radiation transport code, as implemented in OLTARIS, to take into account the blocking effect of the Earth on the otherwise isotropic GCR spectrum, the attenuation of the GCR ions by the magnetosphere as a function of ion kinetic energy, and the deflection of GCR ions with energies below the rigidity cut-off level by the magnetosphere. In addition, we determined the differential flux of both the trapped protons (due to the ISS traversing the South Atlantic Anomaly of

[5] For example, the neutron count rates at McMurdo Station in Antarctica ($77.9°SLat., 166.6°ELong.$), with $R_C = 0.3GV$, and Oulu Station in Finland ($65°NLat., 25°ELong.$), with $R_C = 0.8GV$, both have higher neutron count rates than at Kiel Station in Germany ($54°NLat., 10°ELong.$), with $R_C = 2.36GV$. *See* NMDB data base founded under the European Union's FP7 program (http://www.nmdb.eu/?q=node/8); and the Oulu Station Sodankyla Geophysical Observatory neutron monitor database (http://cosmicrays.oulu.fi).

the lower Van Allen belt) and the albedo neutron flux. These results were obtained by using the Badhwar-O'Neill 2010 GCR model as the input boundary condition, during the 2010 solar activity minimum, and all the data are averaged over a nominal one-year mission. The results are shown in our Figure 6.4.

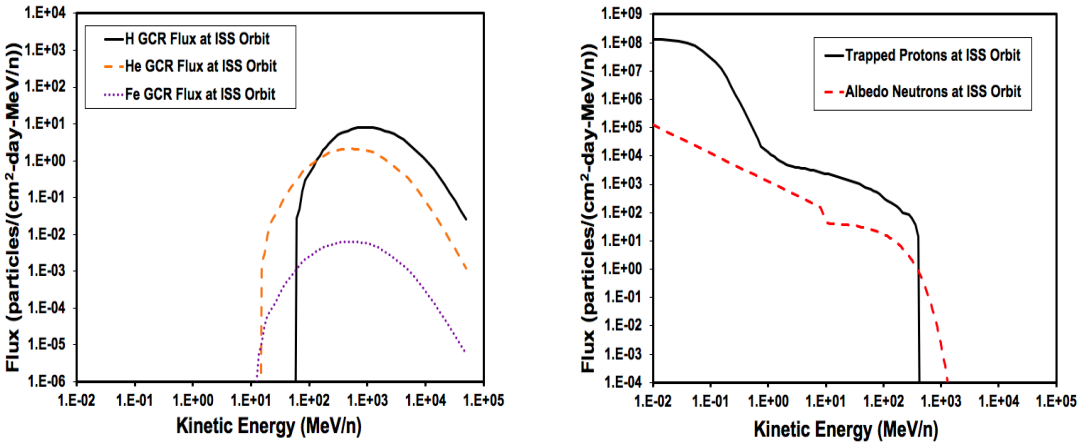

(a) Direct GCR Flux at ISS. (b) Trapped Proton & Albedo Neutron Flux.

Figure 6.4 : Average Annualized Radiation Environment in the ISS Orbit at an Altitude of 400 kms (orbit tracking between 51.6^0 North and South Latitudes).

Both graphs in Figure 6.4 are shown with the same range on the Energy axis to better visualize the total radiation flux spectrum for the ISS orbit at an altitude of 400 kms; which is the same range for the Energy axis used in Figure 6.1, to better visualize comparison of the 1 AU free-space boundary condition for the GCR flux with that at the ISS orbit. Figure 6.4a clearly shows the effect of the the rigidity cut-off energy imposed by the magnetosphere in limiting the flux of GCR ions below the energy range of 15-60 MeV/n. In addition, Figure 6.4b shows that the trapped protons in the Van Allen belt have a maximum energy of about 400 MeV/n; and that there is a significant neutron flux with energies in the range of between $10^{-2}MeV$ to 10^3MeV, which have the highest radiation weighting factors in relation to causing

biological harm to humans (*see* Figure 2.10).

The dramatic attenuation of the primary GCR fluence by the magnetosphere can perhaps best be appreciated by over-laying the data for the flux at 1 AU and that in the ISS orbit, as shown in our Figure 6.5.

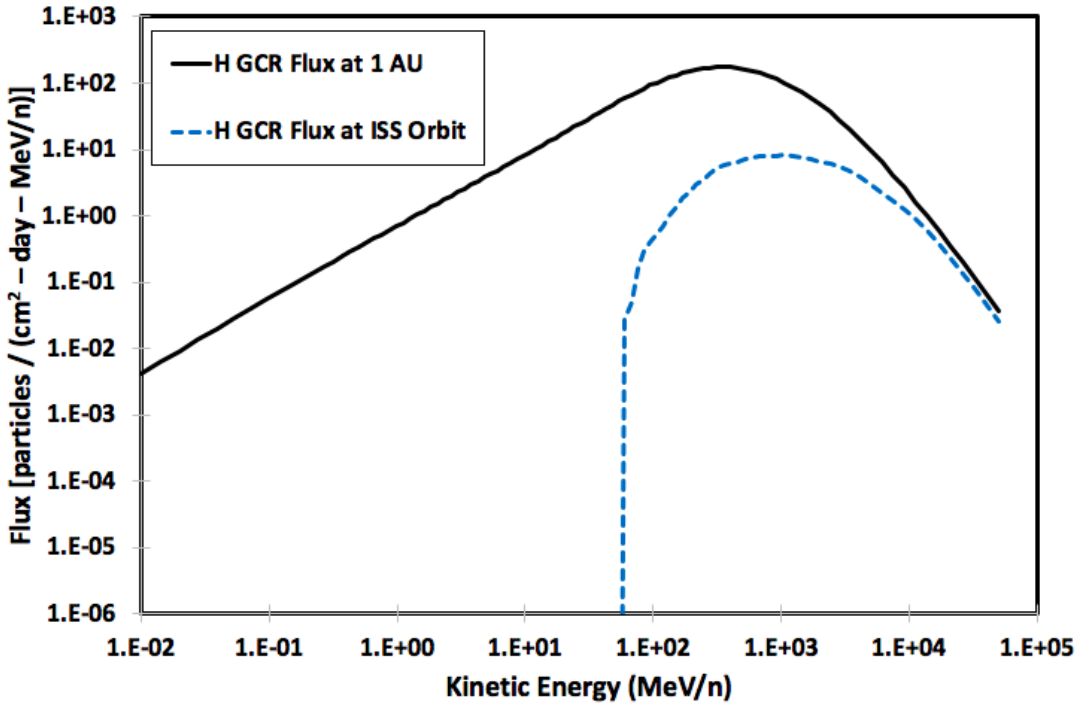

Figure 6.5 : Differential GCR Flux Comparison for Hydrogen Ions at 1 AU and at ISS in Free Space – No Shielding.

When one compares the ion flux for the free-space GCR at 1 AU (previously shown in in Figure 6.1 for several GCR ions) to that at the ISS orbit, the attenuation impact of the magnetosphere is aptly demonstrated; e.g., at 1 GeV/n the hydrogen flux is cut from 102 $particles/(cm^2 - day - MeV/n)$ down to about 8 $particles/(cm^2 - day - MeV/n)$ – over an order magnitude decrease in particle flux at that energy level. Above a kinetic energy of 10 GeV/n, the GCR hydrogen flux is about the same at 1 AU and at the ISS orbit, minus that blocked by the Earth. But as the energy per

nucleon decreases, the magnetosphere has an increasingly large impact in reducing the primary GCR flux. Note that this Figure 6.5 does not include the additional trapped proton flux or the albedo neutron flux, both of which must be taken into account when calculating absorbed dose and dose equivalent metrics at the ISS orbit.

Calculating Our New GCR Shielding Evaluation Metric

In addition to flux ion species and energy analysis discussed above, our calculations comparing the metrics of absorbed dose and dose equivalent between the radiation environments at 1 *AU* and the ISS orbit, with identical methods and input parameters, allows tying the relative GCR shielding effectiveness of various materials and designs to NASA's wealth of actual long-term medical monitoring data for astronauts who have flown on the ISS. We submit that a reasonable goal of a GCR shielding design for long-term spaceflights in the cis-lunar region should be to get as close as possible to the differential flux and relative radiation exposure levels experienced on the ISS, because of the ISS medical data that tends to validate the NASA radiation risk tolerance levels (*see* Figure 2.13a, and accompanying text in Chapter 2).

Our radiation exposure calculations with no shielding are shown in Table 6.1.

	Unshielded Exposure Metrics	
Radiation Environment	Absorbed Dose (mGy/day)	Dose Equivalent (mSv/day)
GCR at 1 *AU*	0.35	2.258
GCR at ISS	0.049	0.3395
Protons & Neutrons at ISS	4.53	21.5
Total Radiation at ISS Orbit	4.58	21.78

Table 6.1 : No Shielding Calculated Absorbed Dose and Dose Equivalent comparison for 1 *AU* and ISS Orbit – BON2010 GCR Model at 2010 Solar Min & ICRP-60.

Thus, our calculations show the primary GCR itself will cause an absorbed dose rate of about 0.35 mGy/day at 1 AU, whereas at the ISS orbit the primary GCR imposes an absorbed dose rate of only 0.049 mGy/day – a seven-fold decrease; and the comparison is almost the same for the dose equivalent metric. In the ISS orbit there is also a very high flux of trapped protons and albedo neutrons, which contribute a great deal to the unshielded exposure scenario – at levels potentially fatal to humans (*see* Figure 2.13). However, this exposure from the lower Van Allen belt is short in duration and the radiation is of relatively low energy, and thus easily shielded.

As a result, the more relevant metric to use as part of our new comparative shielding evaluation metric is to establish the "baseline radiation exposure" behind approximately 20 gm/cm^2 of aluminum, as that is the rough estimate for the effective shielding on the International Space Station, counting the hull and equipment racks; though in some places on the ISS with food and water storage, the shielding effect is as high as 50 gm/cm^2 of aluminum equivalent. Our exposure rate calculations behind 20 gm/cm^2 of aluminum shielding are shown in Table 6.2.

	Shielded Exposure Metrics (Aluminum - $20gm/cm^2$)	
Radiation Environment	Absorbed Dose (mGy/day)	Dose Equivalent (mSv/day)
GCR at 1 AU	0.37	1.34
GCR at ISS	0.056	0.233
Protons & Neutrons at ISS	0.11	0.174
Total Radiation at ISS Orbit	0.17	0.41

Table 6.2 : Aluminum Shielding ($20gm/cm^2$) Calculated Dose and Dose Equivalent for 1 AU and ISS Orbit – BON2010 GCR Model at 2010 Solar Min & ICRP-60.

Thus, assuming use of precisely the same radiation transport model and input bound-

ary conditions, if one found a shielding material or design that achieved, for example, a dose equivalent calculated value of 0.41 mSv/day when exposed to the GCR environment at 1 AU, then that shielding protocol would provide an exposure level equivalent to the exposure level on the ISS, for which there is actual medical data available to evaluate the long-term health risks to humans. We call this calculated dose equivalent exposure rate the "ISS Baseline" model.[6]

As to the important question of verification, the ISS Baseline model compares favorably to other such calculation attempts reported in the literature.[7] Thus, by carefully employing identical modeling parameters for the assessment of shielding in the 1 AU radiation environment as in modeling the ISS orbit environment, our new procedure evaluates shielding materials and designs on a strict comparable basis. This methodology provides assessment of a proposed shielding protocol in terms of how well it recreates the same radiation environment that would be encountered on the inside of the ISS. But it does so only on a calculated basis; e.g., the calculated dose equivalent metric at 1 AU as compared to the same calculated metric inside the ISS. This is certainly useful, and eliminates the errors in assessment introduced by the different radiation quality factors and weighting factors. But it is only half the battle to getting the most information out of our new shielding evaluation metric.

---

[6] For shielding at 1 AU to reproduce this level would require reducing the dose equivalent exposure rate to about 31% of that obtained using the same ISS shielding in cis-lunar space. To do so would obviously require materials other than aluminum, and perhaps additional design innovations. Whether that objective is achievable or not, our new evaluation metric measures how close a particular shielding design comes to that goal – a useful piece of information.

[7] The calculated values in Table 6.2 are fairly close to the only other mention in the literature of similar calculations for the total radiation exposure inside various Shuttle craft flights of about 450 $\mu Sv/day$, versus ours at 410 $\mu Sv/day$ for the ISS, a mere 10% difference that is easily explained by different GCR model inputs and different LEO orbits. [187] Another study calculated GCR-induced absorbed dose rates at extreme points in an ISS orbit of 0.031 to 0.077 mGy/day, which compares favorably to our average of 0.056 mGy/day, but completely ignored the trapped protons and neutrons, which comprise 40% of the exposure. [30]

To be able to confidently use our new evaluation metric to tie to actual medical data of the astronauts on the ISS, and thus allow using the modeling effort of the 1 AU design protocol to be assessed in terms of actual health risks in a meaningful way, the ISS-based calculated assessment must also be correlated with and verified by actual measured exposure data on the ISS. Fortunately, this can be done.

Thus, further verification confidence is obtained for using the inside-ISS radiation environment as a comparative metric for shielding effectiveness by the favorable comparison of the calculated dose equivalent values shown in Table 6.2 with actual on-orbit measurements. For example, one NASA study took radiation exposure data from "crew passive dosimeters" for ISS crews at altitudes varying from 190 to 250 nautical miles (352 to 463 kms), and after making some reasonable assumptions, found measured dose inside the ISS to be a maximum of 0.436 mSv/day at the highest altitude of 463 kms at solar minimum conditions. When the full range of data is considered, these "measurement" values compare reasonably well with the calculated dose equivalent at 400 kms ISS altitude of 0.41 mSv/day for a nominal aluminum shielding of 20 gm/cm^2.[8]

Thus, for the radiation measurements used to calibrate the ISS Baseline model, the effective aluminum thickness of 20 gm/cm^2 provides good correlation. But if actual

[8]As one might expect, at lower ISS altitudes, the radiation exposure rate inside the ISS was somewhat less: e.g., at 388 kms altitude, the exposure rate was 0.213 mSv/day, and at 352 kms altitude the exposure rate was 0.146 mSv/day. [194] NASA estimates that astronaut exposures in LEO range from 12 to 28 $mrad/day$, with the higher exposures for those who do multiple space walks. Thus, for model calibration purposes, we have selected 17 $mrads/day$, which equates to some 0.41 mSv/day, using the ratio to convert from Grays to Sieverts in Table 6.2. However, the ISS Baseline shielding evaluation point can be set at any point within this range, depending upon how much "safety factor" one wanted to build into the model. For example, if the ISS Baseline is set to 0.41 mSv/day, that equates to a dose equivalent exposure rate of 0.15 $Sv/year$, well within the NASA risk limitation level of 0.5 $Sv/year$ (*see* Figure 2.13a, noting 150 $mSv/year$). But in evaluating shielding for cis-lunar operations, one might decide that the NASA annual limit would be a more reasonable (and attainable) design objective, and thus calibrate the ISS Baseline model to that number.

inside-ISS radiation measurements were different, or done with a different method, the ISS Baseline model can be re-calibrated to the new data by adjusting the equivalent aluminum shielding level for the ISS. The two shielding assessment models – at 1 *AU* and the ISS Baseline – are correlated by having the same calculation inputs and methods; and the ISS Baseline model is calibrated to actual ISS data, thus empirically tying the 1 *AU* shielding evaluation model to the medical data from the ISS.

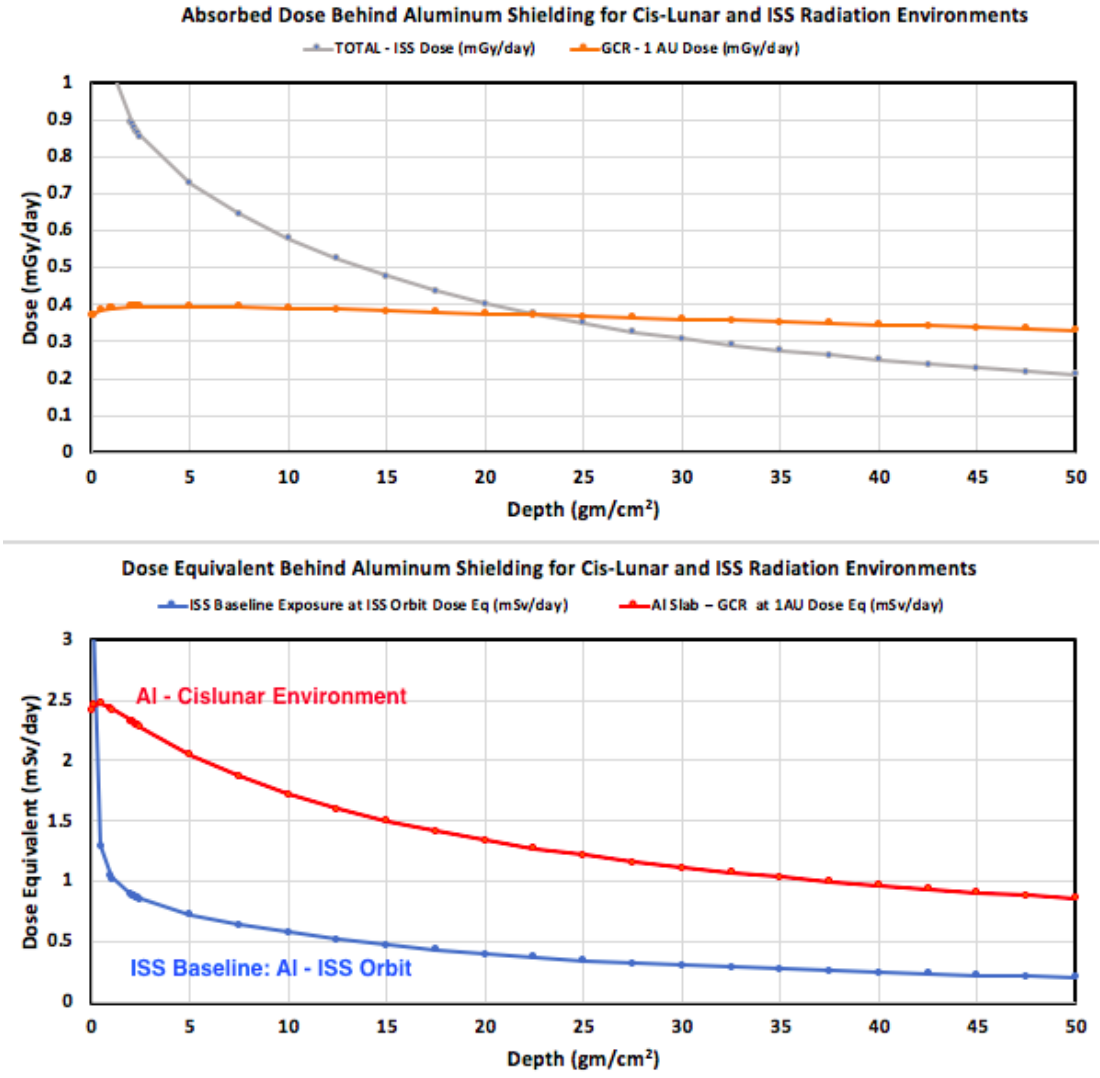

Figure 6.6 : Calculations of Dose (top graph) and Dose Equivalent (bottom graph) in Aluminum Shielding in the Cis-Lunar and ISS Orbit Radiation Environments.

Further useful information may be obtained from our new comparative metric by examining how the absorbed dose and dose equivalent vary as function of depth (areal density) in the shielding material – here aluminum – as shown in our Figure 6.6. The gap that must be bridged by better shielding in the cis-lunar radiation environment in order to meet the exposure rate levels in the ISS orbit behind aluminum shielding of various thicknesses is immediately apparent in the lower graph of Figure 6.6; e.g., the data used in Table 6.2 for the 20 gm/cm^2 areal density thickness can be easily picked off the chart. It is also apparent that for thicknesses greater than 20 gm/cm^2 that the gap narrows very slowly, and that for aluminum shielding the practical thickness level will be reached long before that material can afford the same shielding effectiveness at 1 AU as is experienced inside the ISS (e.g., even at 50 gm/cm^2 aluminum is already an impractical 18.5 cms thick, and the gap is still fairly large). Also of interest is that as aluminum shielding gets even thicker its effectiveness actually *decreases*, due to secondary neutron production. [195] [196] However, the fundamental point to observe in using our new metric to evaluate shielding materials is the baseline dose equivalent inside the ISS – which is the ISS Baseline against which other shielding materials and designs can be evaluated. The closer a shielding protocol gets to this baseline measurement, the more relevant and accurate the medical data from the ISS astronauts is in assessing long-term radiation exposure risks.

Of interest on the lower graph of Figure 6.6 is that the dose equivalent initially increases somewhat with increased aluminum shielding thickness (as does the absorbed dose in the upper chart). This is due to the production of secondary emissions by the shielding material itself, and is even more pronounced for heavier materials. Note in the upper graph that the absorbed dose rate at the ISS orbit is higher than that from the GCR at 1 AU, until an effective shielding thickness of over 7.5 cm (20 gm/cm^2) is

reached, but the lower graph reveals that the dose equivalent rate at the ISS orbit is always lower than that at 1 AU, after a very small shielding thickness of only 0.2 cm. This is due to the higher flux of protons and neutrons in the ISS orbit environment having relatively low kinetic energies, and thus a lower dose and dose equivalent rate; and they are also more easily stopped in the shielding material.

Finally, we calculated the contribution to the total dose equivalent by each radiation particle, a factor that could be important to consider in designing multilayered radiation shielding protocols. This is shown in our Figures 6.7 and 6.8 (where each color denotes a specific depth into the shield, and adds to 100%).

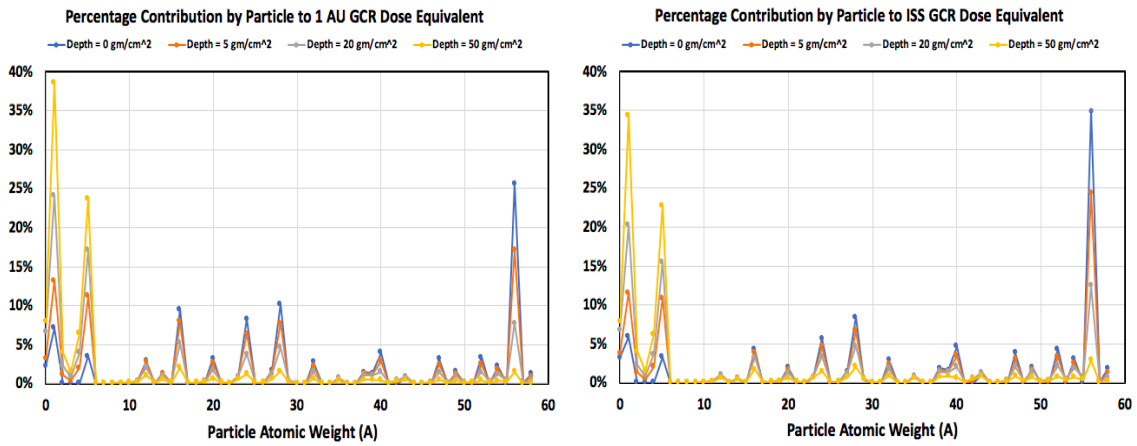

(a) Particle Contribution from GCR at 1 AU. (b) Particle Contribution from GCR at ISS.

Figure 6.7 : Comparison of Particle Contribution to Dose Equivalent from Primary GCR at 1 AU and ISS as a function of depth in Aluminum Shielding.

In Figure 6.7 shows that the spectrum of particle contribution to the dose equivalent from the primary GCR at 1 AU and at the ISS orbit is similar, but with some subtle differences. For example, iron particles in the GCR dominate in percentage contribution at the surface of the shielding, while protons gain dominance in thicker shielding. Though the flux of protons in the GCR at 1 AU is much greater than that

of iron ions (which carry more energy for a given kinetic energy per nucleon), as the shielding gets thicker, the iron ions are stopped before the hydrogen ions, due to their greater range in aluminum for a given kinetic energy. Also, in Figure 6.7b, it is clear that the proton contribution at the ISS orbit has been diminished from the primary GCR, due to the lower energy proton flux being stopped by the magnetosphere.

Our Figure 6.8 helps illustrate the complete story about the radiation environment at the ISS orbit – the baseline shielding metric objective.

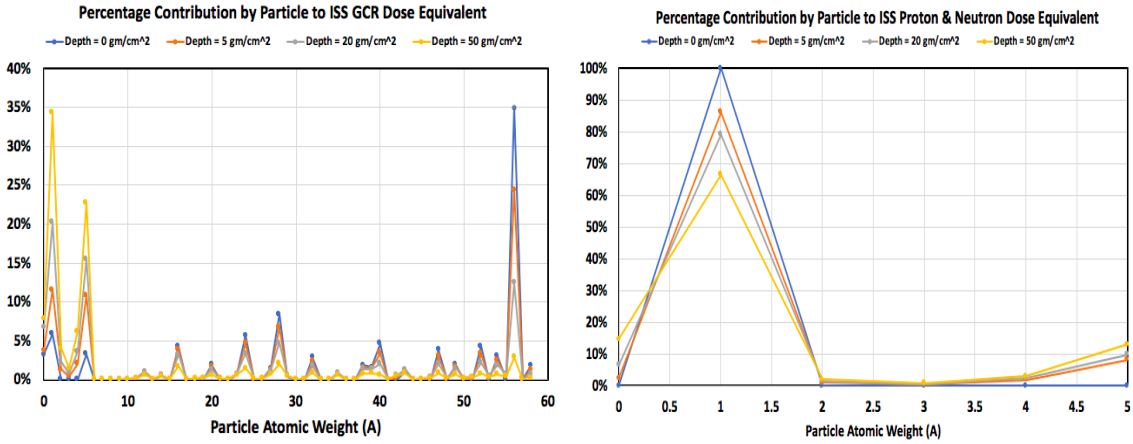

(a) Particle Contribution from GCR at ISS. (b) Contribution of Protons & Neutrons.

Figure 6.8 : Total Particle Contribution to Dose Equivalent from Primary GCR and Trapped Protons and Albedo Neutrons at the ISS Orbit as a function of depth in Aluminum Shielding.

Figure 6.8a is the same as Figure 6.7b, and illustrates the percentage contribution to the dose equivalent exposure rate from the primary GCR ions that are present at the ISS orbit; but behind aluminum shielding with an areal density thickness of 20 gm/cm^2 the GCR contribution is only 57% of the total dose equivalent exposure rate of 410 $\mu Sv/day$, as was shown in Table 6.2. Thus, at that shielding thickness, protons from the GCR contribute about 20% of the GCR total – some 47 $\mu Sv/day$; while trapped protons in the ISS orbit, from Figure 6.8b, contribute about 80% of the other

174 $\mu Sv/day$ total exposure rate – or some 139 $\mu Sv/day$. Thus, at the ISS orbit, protons are responsible for a whopping 186 $\mu Sv/day$, or about 45%. This is valuable shielding design information when considering multilayer designs, because knowing the radiation particle species will aid in selecting the most effective materials.

The same set of calculations could be run for the other ions that show up in a 20 gm/cm^2 aluminum shielding material as primary and secondary emissions (mainly protons and neutrons), but since protons clearly dominate, doing so is unnecessary to point out that the comparative metric proposed here is not entirely the result of identical particle fluence spectra in the cis-lunar and ISS orbit regions. Thus, while evaluating shielding in terms of attempting to get as close as possible to the baseline dose equivalent exposure level at the ISS orbit, one is cautioned to remember that the particle spectra are slightly different. Thus, "scaling up" the evaluation models from the ISS orbit to the 1 AU radiation environment injects some small error (about 5%, which is discussed in detail in Chapter 7), and while "dose may be dose," it is not necessarily true that an identical dose equivalent rate will impact human health in the same ways if the radiation particle spectrum is different. This latter issue may deserve further consideration by medical experts.

Regardless of this one concern in not being able to "scale up" to an identical radiation spectrum, the objective of using the ISS Baseline objective as a standard against which to gauge new shielding materials and designs is a worthwhile endeavor. There is no long-term medical data to assess the health effects to the GCR radiation environment in cis-lunar space; thus replicating the internal radiation environment of the ISS on spacecraft travelling in cis-lunar space by shielding protocols is the only way to take advantage of the wealth of medical data gathered in LEO to assess future radiation exposure risks. Moreover, the radiation transport models cannot be relied

on for absolute answers, because they are not corroborated by any long-term GCR exposure human medical data, as discussed previously in Chapter 1. The value of the radiation exposure metrics "spit out" by the myriad of different calculations and models can only be relied upon if used in a comparative way; and only then when precisely the same calculation methods and input boundary conditions are used to evaluate different protocols. Until long-term human exposure medical histories are obtained in cis-lunar spaceflights, the only way to accurately discern actual health risk is to begin to tie the modeling efforts to actual medical data on the ISS; and for long-term GCR radiation exposure, other than our new proposed evaluation metric, that has not yet been done.[9]

6.2 Calibration Calculations on Standard Materials

Calibration of the models used in this research is done in an effort to replicate the results published in the literature on standard shielding materials – at least on a comparative trend basis – to obtain a reliable standard against which to measure the effectiveness of the new materials and layered configurations examined in subsequent sections. It has been proposed in many studies that liquid hydrogen makes the best GCR shielding material. [9] [95] But of course, liquid hydrogen has no structural integrity, thus requiring some kind of container that would undoubtedly produce secondary particle emissions, and while it could provide an ancillary service as a fuel,

[9] It would be folly to rely on the models of the GCR and radiation transport to provide meaningful absolute radiation exposure rates to evaluate particular human health risks with any certainty. In a private conversation with Chris Sandridge of NASA's Langley Research center about this issue, he said:"In general, it's very difficult to reproduce numbers from [published] papers ... there are just too many unknowns as to how the authors computed their results, like which version of transport was used. A recent update to OLTARIS can have 50% or more difference in dose equivalent for deep transport." [197]

it is also dangerous and difficult to handle, including requiring a means to keep it at a temperature below 20 K, its boiling point at atmospheric pressure.

Nevertheless, we made calibration runs for liquid hydrogen and other materials already presented in the literature, including aluminum, polyethylene, and a NASA proposed new material, boron nitride nanotubes infused with hydrogen. [95] The focus on hydrogen derives from the physics discussed in Chapter 3, which tends to ascribe more efficient positive ion stopping capability to materials with a higher hydrogen content, and of course these principles form the basis of both the OLTARIS (HZETRN) and MULASSIS radiation transport codes.

The ISS Baseline Metric Compared with the Theoretical Best

In order to evaluate passive shielding materials, we first compared our ISS Baseline metric of radiation exposure in the ISS to that which would result from the theoretical best GCR shielding material, liquid hydrogen, in the 1 AU cis-lunar radiation environment. *See* our Figure 6.9.

The data illustrated here includes that from the lower graph of Figure 6.6, which shows the dose equivalent calculations for various thicknesses of aluminum shielding in the radiation environments at 1 AU and at the ISS orbit, and then adds the data for shielding at 1 AU for a hypothetical theoretically-best liquid hydrogen shield. This clearly demonstrates that in theory it is possible with a liquid hydrogen shield to create a radiation environment for a spacecraft in cis-lunar space less harmful than the radiation environment on the International Space Station. The numbers tell the story: the dose equivalent exposure level on the ISS is approximately 0.4 mSv/day at the 20 gm/cm^2 equivalent aluminum shielding thickness level; whereas, the same "behind-shielding" exposure level can be achieved at 1 AU with a 12.5 gm/cm^2 areal

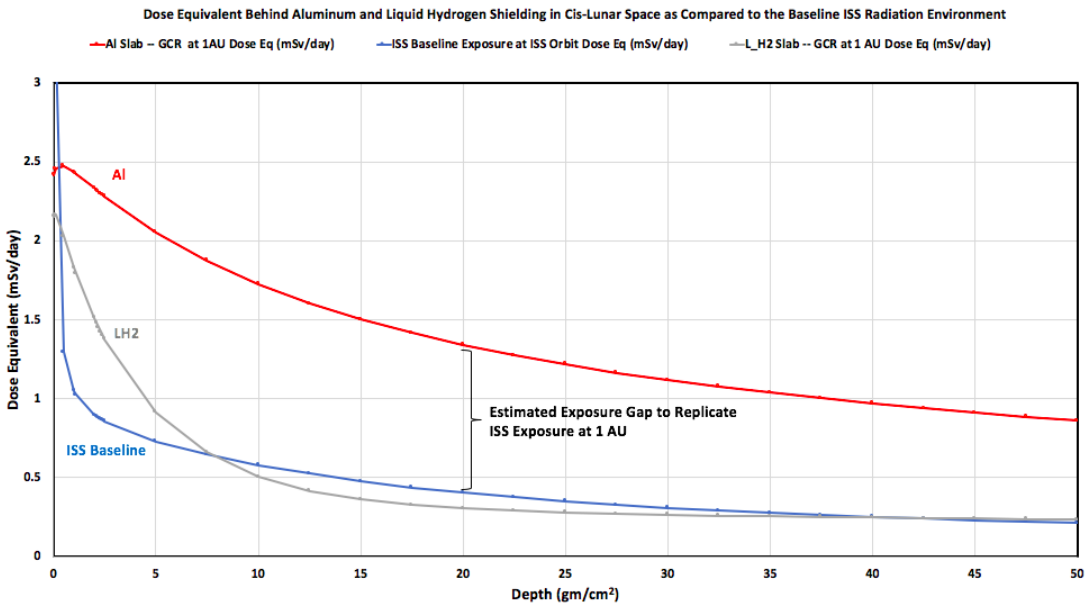

Figure 6.9 : Calculations of Dose Equivalent behind Aluminum Shielding and Liquid Hydrogen Shielding in Cis-Lunar Space as Compared to the Baseline of Aluminum Shielding in the ISS Orbit Radiation Environment.

density thickness of liquid hydrogen. However, given the density of liquid hydrogen of 0.0708 gm/cm^3, the physical thickness required would be 176 cms – about 5.8 feet. Obviously, this would require quite a large structure, but for a long space voyage lasting several years it is not hard to imagine the necessity for additional fuel – maybe liquid hydrogen – and tanks or fuel bladders to contain it on the outside of the spacecraft that could be nominally of this size.

The data shown in Figure 6.9 illustrates the "exposure gap" between standard aluminum shielding at 1 AU as compared to the ISS orbit; and at the very least demonstrates the theoretical possibility of replicating the ISS exposure levels in 1 AU operations, thus allowing the voluminous medical database for ISS astronauts to be of considerable use in assessing radiation risks for long term space voyages.

Calibration with Standard Materials in the Literature

Our initial calibration results for a variety of materials are shown in Figure 6.10.

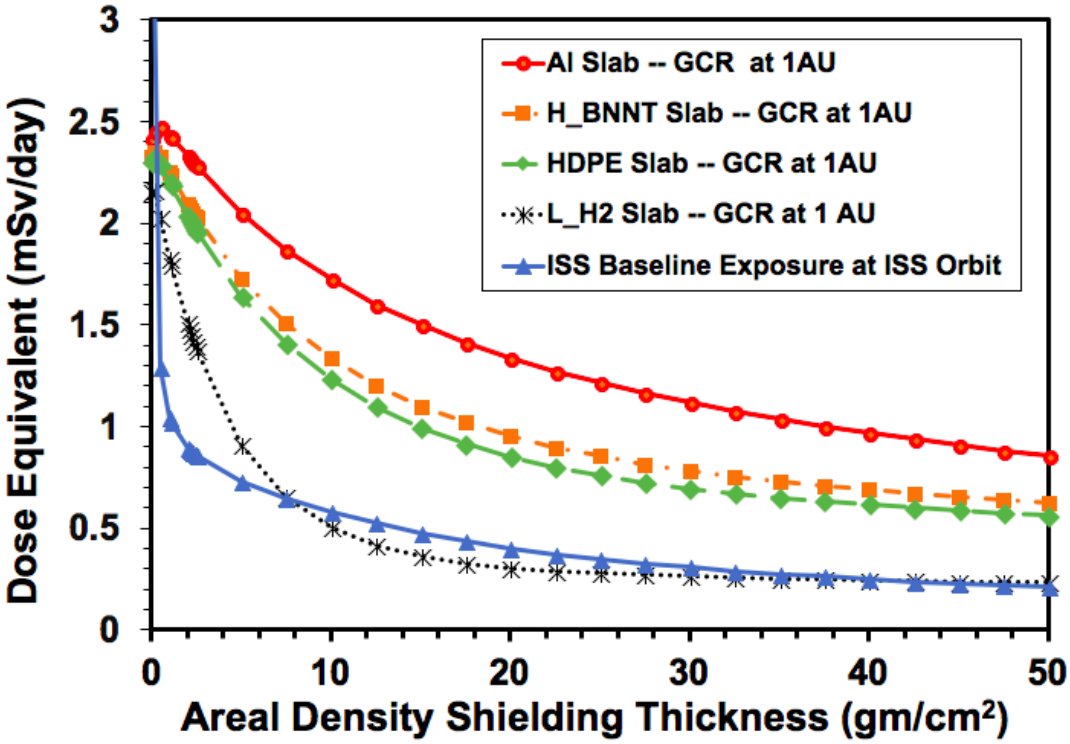

Figure 6.10 : Comparison Calculations of Dose Equivalent behind Various Shielding Materials in Cis-Lunar Space (HZETRN, BON2010 at 2010 Solar Min & ICRP-60).

An adequate calibration of the models used in this research against shielding evaluation results reported in the literature is obtained by considering materials that span the range of shielding material effectiveness – the standard aluminum shield to the theoretical best of liquid hydrogen – and then considering some materials within the range; namely, high density polyethylene (HDPE – CH_2) and hydrogenated boron nitride nanotubes (H-BNNT – $H-BN$). Aluminum has been, and continues to be, the spacecraft hull material of choice, and thus will be a primary radiation shield and structural element in spacecraft for the foreseeable future. As discussed in the previous section, liquid hydrogen may be the theoretical best GCR shielding material.

While perhaps a half-dozen other materials have been considered in the literature, including water (H_2O) and methane (CH_4), which give intermediate results but have no structural integrity, a good representative material for an intermediate GCR radiation shielding capability is polyethylene. In addition, it is also instructive to review NASA's look at a new material, boron nitride nanotubes with hydrogen infused into the structure in the amount of 5% by weight. [95] Both of these materials have at least some structural integrity.

While the absolute value of the dose equivalent exposure level in the calculations shown in our Figure 6.10 is different from that reported by NASA in the literature (*see* Figure 5.6); nevertheless, the relative shielding effectiveness is the same – with aluminum being the worst, liquid hydrogen the best, and HDPE and H-BNNT being comparable. [95] For example, the NASA published results show a maximum dose equivalent exposure level behind aluminum of about 3 mSv/day, while the calculations here produce a maximum of about 2.5 mSv/day. But the NASA work used a different GCR input boundary condition (the 1997 solar minimum as opposed to the 2010 solar minimum), and may have had other differences not specified in its publications; e.g., an unknown base GCR model and an unknown exposure radiation Quality Factor model (*see* previous footnote relating conversation with NASA).

Indeed, several additional calculations were made with HZETRN by changing the Quality Factor model from ICRP-60 to a NASA proprietary model embedded in OLTARIS, which then almost replicated the maximum reported exposure level, but not the identical curve as a function of areal density. As mentioned previously, private discussions with NASA Langley Research personnel revealed that it is a common occurrence that independent researchers cannot match exactly the published NASA results, because the publications do not reveal all of the model parameters used. [197]

This fact is not surprising and merely highlights the need to use identical versions of the radiation transport models and identical input boundary conditions in order to properly evaluate the relative effectiveness of shielding materials and protocols, as well as to compare the results to the ISS Baseline radiation environment.

NASA's Langley Research Center began examining boron nitride nanotubes in 2012 because of its ability to store hydrogen, its relatively large cross section to neutron radiation particles, and its potential as a structural material (much better than polyethylene). [168] It is instructive to note that NASA found that boron nitride nanotubes alone were only marginally better than aluminum as a radiation shield, and that it improved to almost the level of polyethylene when modeled with 5% hydrogen infusion by weight. *See* Figure 5.6. However, NASA was never able to achieve 5% by weight hydrogen infusion in actual practice, but only achieved 4.2% by weight, which would obviously provide a less effective GCR shielding material. [95] In addition, in 2012 NASA indicated that their investigation of boron nitride nanotubes as a shielding material was at a low technical readiness level: "This early study is focused on a visionary aerospace concept ... TRL = 1-2 in maturity, aiming 10 or more years in the future." [168] Yet, three years later NASA published the exact same preliminary results they had in 2012, and have not published sufficient modeling information to precisely replicate their work.[10] [95]

The relative effectiveness in shielding GCR radiation on an areal density basis provides a good assessment of how effective a material is in stopping the positive ions

[10] In the calibration calculations here, the H-BNNT material with 5% hydrogen by weight is input into the calculations with a density of 1.4 gm/cm^3, as per the early NASA technical information bulletin. [168] However, boron nitride itself has a density of 2.1 gm/cm^3, and other studies indicate that formulating boron nitride nanotubes for use as a radiation shielding material would yield a density of some 2.62 gm/cm^3. [198] Using either of these densities and infusing the nanotubes with 5% hydrogen by weight, will still result in a density much greater than that used by NASA in its modeling, thus the NASA results should perhaps be viewed with some skepticism at this stage.

in the GCR, but the practical aspect of the actual physical thickness of each material must also be considered to evaluate practical applications, because the densities vary widely. This aspect of shielding design is aptly illustrated in Figure 6.11.

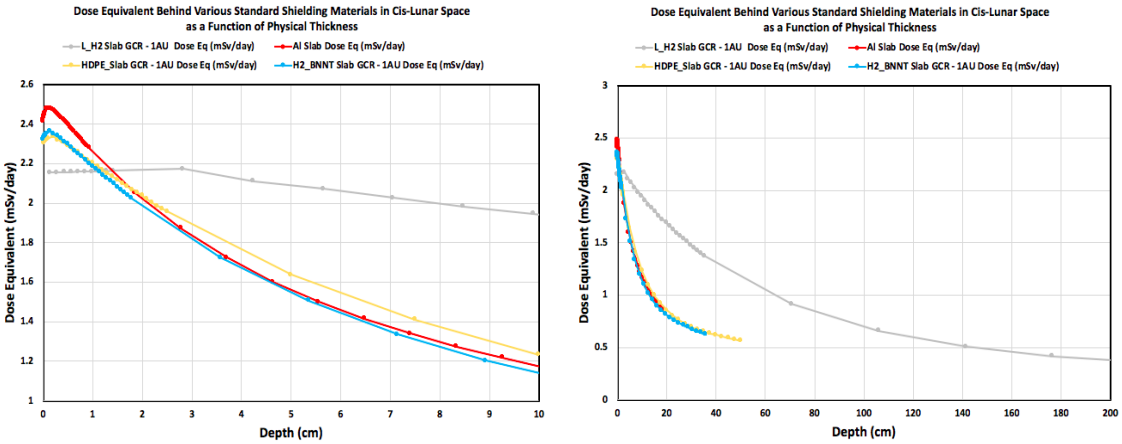

(a) Dose Equivalent vs. Shallow Depth. (b) Dose Equivalent vs. Deep Depth.

Figure 6.11 : Dose Equivalent Behind Shielding Materials in 1 *AU* Radiation Environment at Various Physical Thicknesses (expanding the shallow depth in (a)).

As can be seen, for very thin shielding materials of less than 1 *cm* in thickness, liquid hydrogen provides superior results, as it does for thicknesses greater than some 140 *cms*, over the other three materials considered. However, in the more practical thickness regimes for a spacecraft structure, aluminum provides comparable shielding effectiveness to both HDPE and H-BNNT, as shown in Figure 6.11a. Thus, even though liquid hydrogen may be the theoretical best GCR shielding material, from a design perspective one must also consider the physical size of shielding material required, as well as other possible ancillary functions that the material could provide.

Another interesting fact revealed by the data in Figure 6.11a is that on a comparable thickness basis, aluminum, polyethylene and hydrogenated BNNT all give about the same shielding effectiveness. As a result, actual radiation shielding design

considerations may dictate use of the material that is best suited for other required purposes, such as structural elements, etc.

The interplay between the most effective GCR radiation shielding material and the practical size considerations is clearly demonstrated by examining the 1 *AU* cis-lunar GCR radiation shielding effectiveness of these materials for a standard thickness of some 20 gm/cm^2 of aluminum, or about 7.4 cm (2.9 inches), as shown in Table 6.3.

Shielding Material of 7.4 cm Thickness	Dose Equivalent (mSv/day)
Liquid Hydrogen	2.01
Aluminum	1.34
Polyethylene	1.41
BNNT + 5% Hydrogen	1.27

Table 6.3 : Dose Equivalent behind Various Shielding Materials of 7.4 cm Thickness in 1 *AU* Radiation Environment in Cis-lunar Space.

As can be seen, when put on an equal thickness basis at what might be considered the outer limit for the use of aluminum as a structural element in a spacecraft – some 3-inches – then aluminum is almost the best GCR radiation shield. However, examination of Figure 6.10 reveals that liquid hydrogen at greater thicknesses becomes the better shield; and indeed is the only material that can replicate at the 1 *AU* cis-lunar radiation environment the same low dose equivalent exposure experienced in LEO on the inside of the ISS, albeit at a large physical thickness of some 5.8 feet.

The final calibration calculation effort useful in making comparisons to some of the reported literature is to examine these same materials using the MULASSIS Monte Carlo radiation transport simulation code. The same materials are evaluated – aluminum, liquid hydrogen, HDPE, and H-BNNT. However, there are some unavoidable obvious differences: the MULASSIS model uses a different GCR input boundary con-

dition known as the CREME96 GCR model, and of course, each ion must be run separately through the Monte Carlo simulation, thus only protons, helium ions, and iron ions (as the proxy for all others) are included, which is the standard methodology, as previously discussed. The results, along with published results for comparison (Figure 6.12b), are shown together in Figure 6.12.

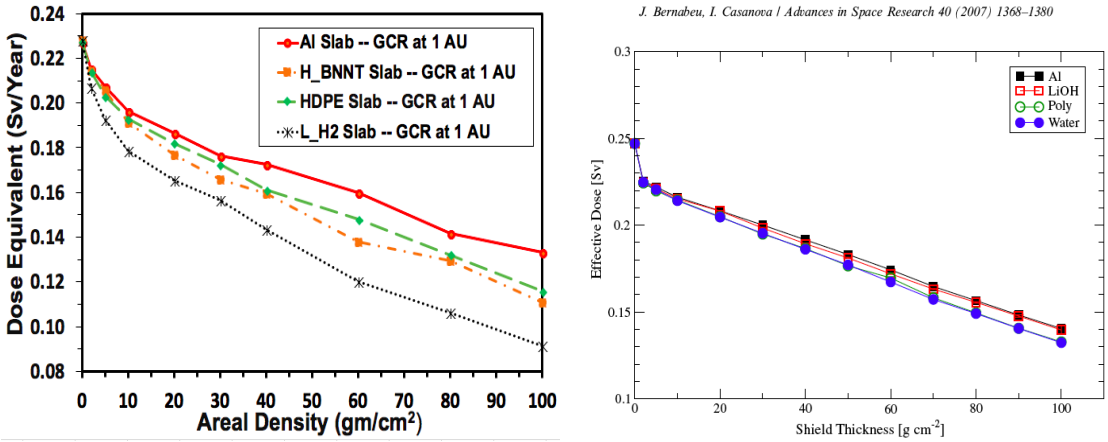

(a) DE – MULASSIS Monte Carlo. (b) DE – Published MULASSIS Results.

Figure 6.12 : Dose Equivalent Behind Shielding Materials in 1 *AU* Radiation Environment: (a) our research, (b) Bernabeu, 2007 (MULASSIS with ICRP-60).

The most important point to note is that the MULASSIS simulation runs done comport well with the published data in the 2007 study by Bernabeu, et al. [42] For example, the dose equivalent found in this research behind 20 gm/cm^2 of aluminum shielding is 0.1865 $Sv/year$, or 0.51 mSv/day. This compares reasonably well with the published results shown in Figure 6.12b of about 0.210 $Sv/year$.[11] In addition,

[11] Note that the graphical results shown in Figure 6.12b are likely labeled incorrectly as "Effective Dose." It should be labeled "Dose Equivalent" as the paper indicates that all simulation results were obtained in that metric, and because the "Effective Dose" is really a metric that is limited to specific organs in the human body, and summing them all together, as this paper says was done, would simply give one the whole body radiation dose. [42] *See* discussion of Dose Equivalent and Effective Dose in Chapter 2.

the MULASSIS results give the same trend results in terms of material effectiveness in shielding GCR radiation as those obtained using NASA's HZETRN calculation method; e.g., both polyethylene and hydrogenated boron nitride nanotubes are better shielding materials than aluminum, and liquid hydrogen appears to be the best.

However, the absolute value of the dose equivalent exposure rate calculated with MULASSIS is much lower than that calculated with OLTARIS (HZETRN). For example, the dose equivalent behind 20 gm/cm^2 of aluminum for the deterministic calculations above indicate an exposure rate of 1.34 mSv/day (*see* Figure 6.10), as opposed to the rate obtained by the Monte Carlo method of 0.51 mSv/day (*see* Figure 6.12a). Such large discrepancies between HZETRN and MULASSIS results were noted in the Bernabeu, et al. study: "In the GCR case (Fig. 13) MULASSIS always yields lower values (dose equivalent is about half of that calculated by HZETRN)." [42] The larger discrepancy here is likely due in part to the fact that different GCR input boundary conditions are employed (*see, e.g.,* Figure 4.8), coupled with all the other reasons Bernabeu, et al. gave as speculation for the large differences, including the fact that MULASSIS does not transport all the GCR ions, leaving out the heavier ions (except iron) which may contribute to higher doses due to their relatively higher LET values. This discrepancy is discussed in more detail in Chapter 7, but highlights the importance of evaluating shielding materials on a strict comparative basis – a point emphasized in our research, but largely ignored in the literature – and in *not* relying on the absolute value of calculated or simulated exposure levels as having a strong connection to reality. Thus, the import of our new evaluation technique developed in Section 6.1 is obvious; i.e., relating comparative shielding effectiveness to its ability to recreate the equivalent interior ISS radiation environment for spacecraft operating in the cis-lunar region with a 1 AU GCR exposure.

While NASA's newly proposed nano-material (H-BNNT) may someday become a suitable structural component, aluminum has generally been the preferred shielding because it is a good structural material, even though it clearly has inferior radiation shielding characteristics. Polyethylene, water, and liquid hydrogen are better radiation shielding materials, but lack the structural integrity, plus their low densities dictate a physically larger thickness that may be impractical in spacecraft design.

Fluence Analysis as a Shielding Evaluation Tool

The objective of fluence analysis is to determine how many particles of a certain type pass through the shielding regime, and thus contribute to the total absorbed dose and dose equivalent behind the shielding in the interior spaces occupied by humans and equipment. By knowing the fluence of various radiation particles and their energy spectrum, it may be possible to better tune a multilayered shielding regime to improve overall effectiveness. As with any radiation transport analysis, it is critical to assess results only on a comparative basis, with the same GCR input boundary conditions and radiation transport calculations; but unlike with the dose equivalent analysis, there are no weighting factors or quality factors to consider.

Preliminary fluence analyses using the MULASSIS Monte Carlo method were completed early in this research effort by Li, Warden and Bayazitoglu, and have been published [14], and are summarized here. We used the CREME96 GCR model, and focused on the generation of secondary neutrons in various shielding materials and comparative attenuation effectiveness. Because each GCR ion must be simulated separately with the Monte Carlo code, the work focused only on hydrogen, helium and iron ions in the GCR (the standard proxy in using MULASSIS).

These particular fluence analyses were chosen because all shielding materials will

produce secondary emissions, including both ions and neutrons (for which the stopping mechanisms are different), and in terms of potential biological harm, the secondary neutrons in the energy range of $10^{-2}MeV$ to $10^{3}MeV$ are the most dangerous. *See* Figure 2.10 and accompanying text. Our Figures 6.13, 6.14, and 6.15 show the results of neutron fluence behind various shielding materials.

The graphs in these figures show the neutron fluence behind shielding ($\frac{particles}{cm^2-bin}$) for average energy bin levels (over the range $0 - 10^{6}KeV$) produced as secondaries by incident GCR hydrogen, helium and iron ions on various shielding materials over a range of thicknesses expressed in areal density (gm/cm^2). It is clear that for each primary ion examined that aluminum shielding produces the most secondary neutrons, whereas polyethylene and liquid hydrogen produce far fewer neutrons in total. Of interest with respect to the recent NASA work, is that the base material boron nitride produces a relatively high level of neutrons behind shielding (despite its high neutron cross section), and its performance improves only when it is produced in nano-tube form and infused with hydrogen.

Clearly, materials with higher hydrogen content produce fewer secondary neutrons in total behind shielding, and in particular such materials produce fewer neutrons in the most risky low energy part of the spectrum. In addition, the neutron fluence produced by GCR iron ions increases dramatically after entering the shielding material, which is different from that of GCR proton and helium ions. This is probably due to the heavier atomic weight of iron. High hydrogen content materials aid in better fragmentation of the iron ions, but the secondary neutrons produced behind the shielding are mostly in the higher energy regime, which are not as biologically dangerous as neutrons with energies of around $10^{3}KeV$.

It is perhaps somewhat easier to evaluate the data when it is viewed piecemeal

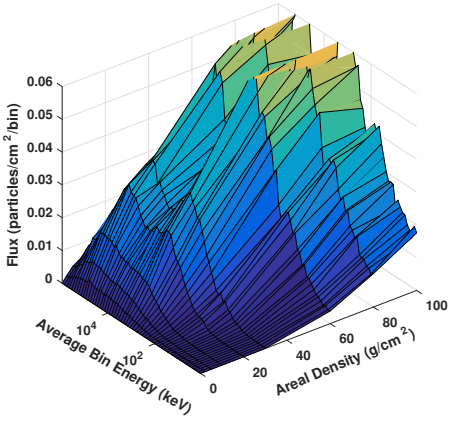

(a) Aluminum

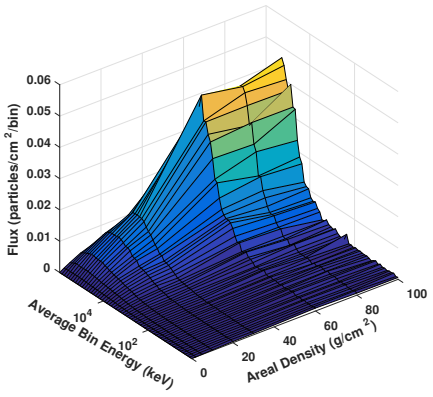

(b) Polyethylene

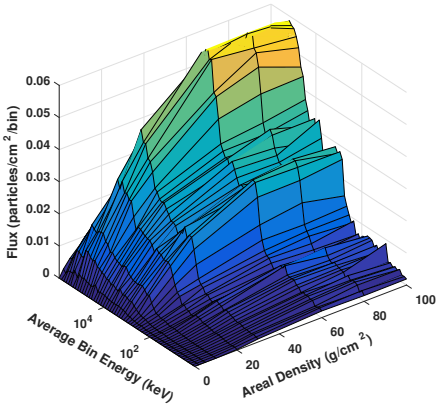

(c) Boron nitride

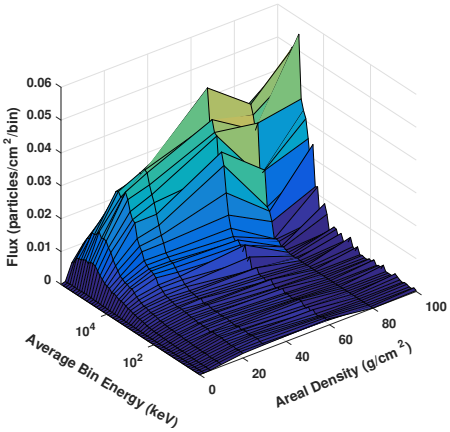

(d) Boron nitride + H5%w

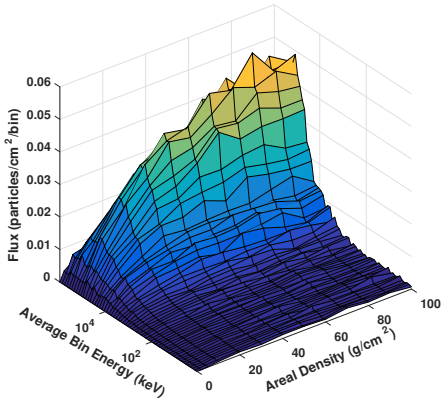

(e) Water

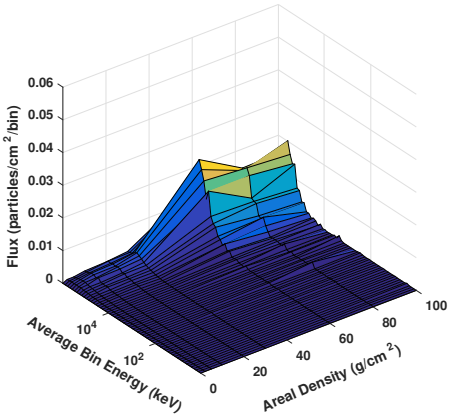

(f) Liquid hydrogen

Figure 6.13 : Secondary Neutrons from Primary GCR Protons

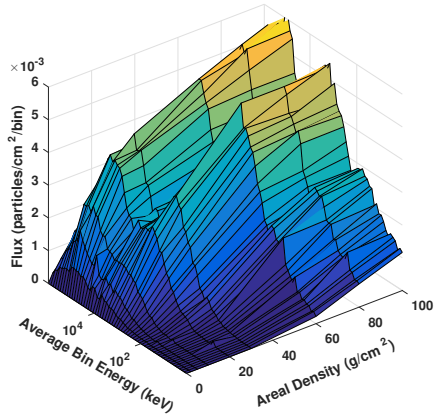

(a) Aluminum

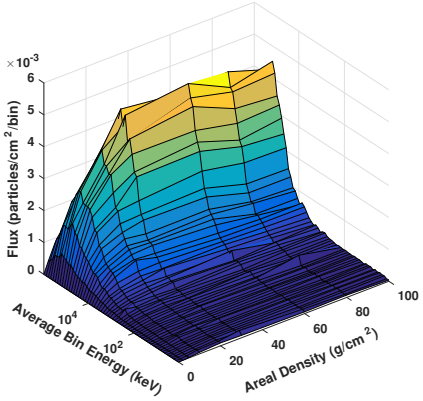

(b) Polyethylene

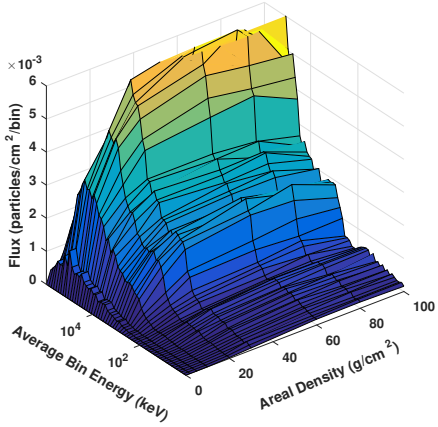

(c) Boron nitride

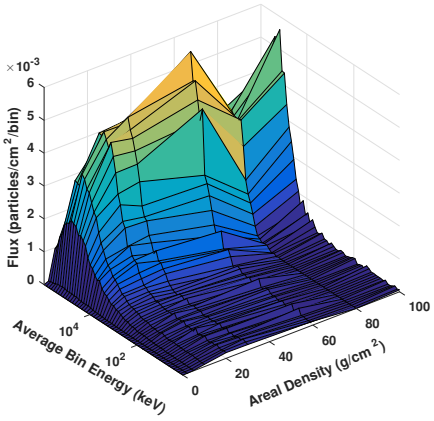

(d) Boron nitride + H5%w

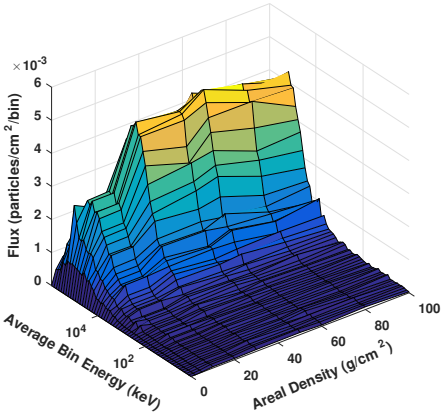

(e) Water

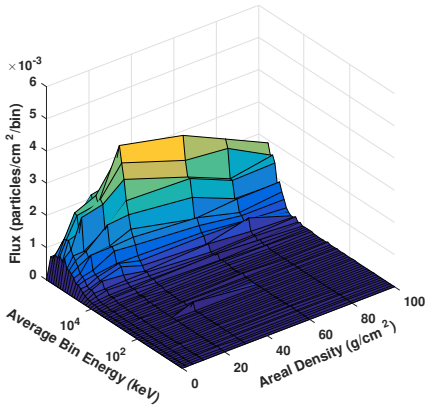

(f) Liquid hydrogen

Figure 6.14 : Secondary Neutrons from Primary GCR Helium Ions

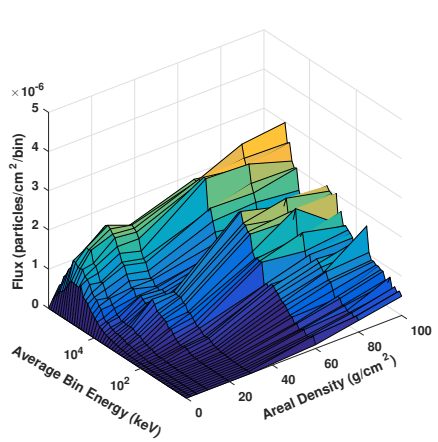

(a) Aluminum

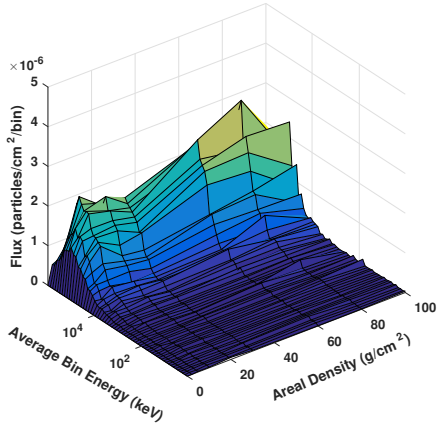

(b) Polyethylene

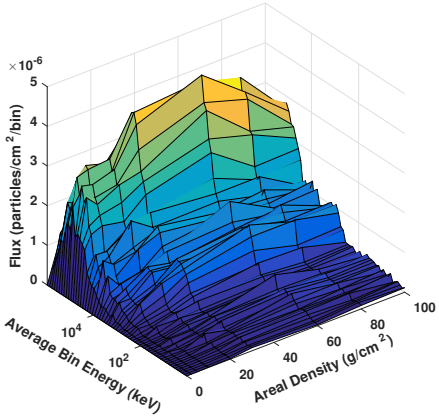

(c) Boron nitride

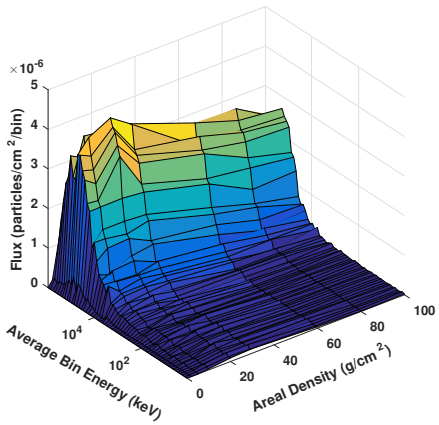

(d) Boron nitride + H5%w

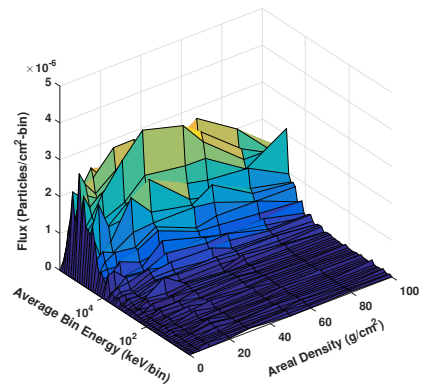

(e) Water

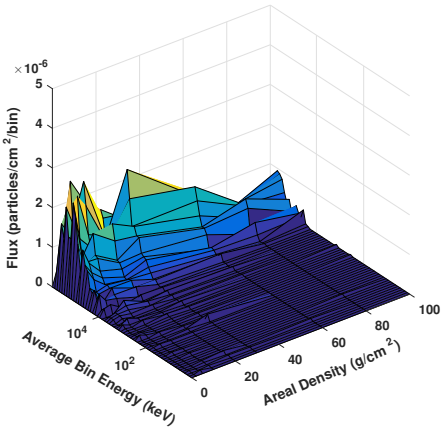

(f) Liquid hydrogen

Figure 6.15 : Secondary Neutrons from Primary GCR Iron Ions

in a two-dimensional graph, holding one of the axes constant, such as thickness in terms of areal density, and displaying the data for a single primary GCR ion, such as hydrogen, all as is shown in our Figure 6.16.

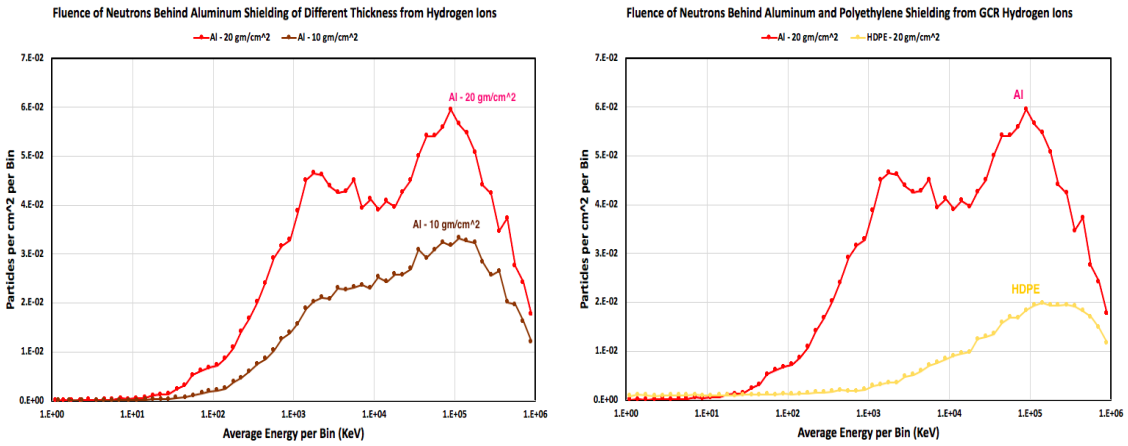

(a) Neutron Fluence behind Al. (b) Neutron Fluence behind Al and HDPE.

Figure 6.16 : Fluence of Neutrons Produced by GCR Hydrogen Ions behind Various Shielding Materials of Various Thicknesses (MULASSIS Run Data).

For example, Figure 6.16a shows the neutron fluence data behind aluminum shielding as the thickness of the shielding is increased from 10 gm/cm^2 to 20 gm/cm^2. Due to the fact that aluminum is a fairly high producer of neutron secondary emissions, and relatively poor at attenuating them, the neutron fluence behind aluminum shielding actual increases in this range for increasing thickness – perhaps a counter-intuitive result. However, reference to Figure 6.16b shows that for equal areal densities, the neutron fluence behind polyethylene is much lower than that of aluminum, particularly in the important energy range around $10^3 KeV$ – a more intuitive result, given the physics discussed in Chapter 3.

Many additional "slices" of the fluence data can be examined in detail – e.g., particle type vs. energy vs. shielding material vs. shielding depth – depending

upon the result one is trying to achieve behind the shielding design. The point to be made here is that because different materials have different propensities for attenuating certain types of particles, as well as for creating secondary emissions, a fluence analysis can be a worthwhile exercise in "tuning" the shielding design for optimal results, particularly one comprised of multiple layers of different materials.

We also used the NASA HZETRN radiation transport code to perform a fluence analysis by particle type, as we previously did in examining each GCR particle contribution to the dose equivalent in Figures 6.7 and 6.8. We calculated the number of particles of a particular type behind various shielding materials using data from multiple HZETRN runs, which has the advantage that virtually the entire primary GCR spectrum is included, in contrast to more Monte Carlo simulations required by MULASSIS. Our Figure 6.17 illustrates an example with respect to neutron fluence.

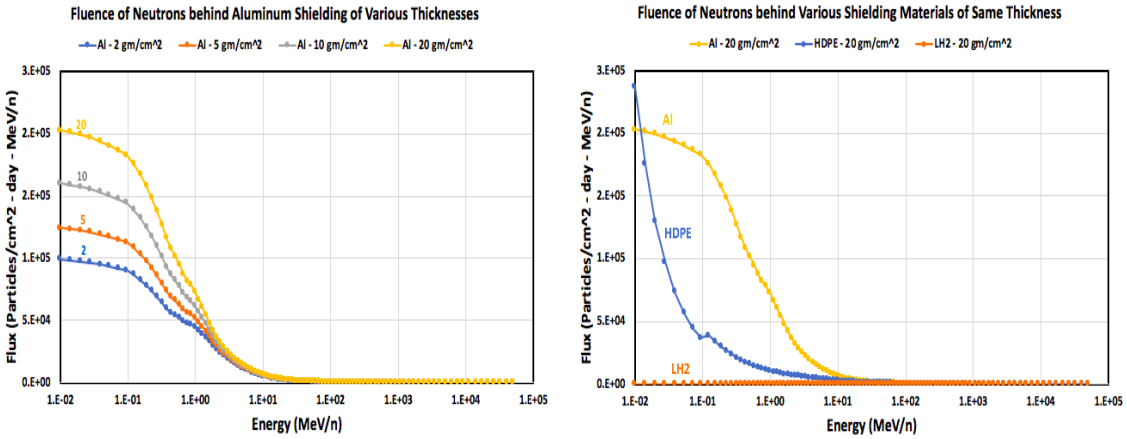

(a) Neutron Flux behind Al. (b) Neutron Flux behind Al, HDPE, & LH2.

Figure 6.17 : Fluence of Neutrons Produced by Full GCR Spectrum behind Various Shielding Materials of Various Thicknesses (HZETRN Run Data).

As can be seen in Figure 6.17a, for neutrons in the most biologically dangerous energy range, the flux behind aluminum shielding in the cis-lunar region exposed to 1

AU GCR actually *increases* with increasing thicknesses. This is due to the fact that aluminum – a standard spacecraft construction and shielding material – will create many secondary neutron emissions upon bombardment by GCR particles, and it is relatively poor in stopping them, thus they have a long range.

Figure 6.17b illustrates another phenomenon that is revealed by fluence analysis – for a given areal density (here 20 gm/cm^2), the lighter and higher hydrogen content materials produce fewer secondary neutrons behind the shielding. Liquid hydrogen neutron production is extremely low, but not zero, illustrating both its low propensity to produce secondary neutrons and its low ability to attenuate them.

Fluence analyses can be performed for the entire GCR primary spectrum in order to "tune" the shield design to minimize particular particles, and thereby reduce the danger to humans or equipment, and has recently been employed to study the incremental benefit from using the trash from space voyages as radiation shielding. [199]

6.3 Analysis of Multilayered Shielding Designs

As discussed previously in Chapter 5, multilayered radiation shielding designs have been employed in satellites to improve shielding of sensitive equipment from the high-flux electron fields in the upper Van Allen belts, e.g., Truscott, 2010 [34], but little analysis has been given to such protocols for GCR shielding. Given the different ranges, cross sections, and propensity to cause biological harm of the different primary and secondary radiation emissions in the GCR environment, it is only logical that multilayered analysis be part of the shielding design procedure. Thus, the considerations of radiation shielding effectiveness, as well as structural integrity, lead directly to the question of whether certain layered shields could be constructed that would provide better overall radiation shielding metrics. Our research presents

the technique as an additional tool for "tuning" shielding performance, along with some results to illustrate the utility of such analysis.

In early work in this research by Li, Warden and Bayazitoglu using the MULASSIS Monte Carlo approach, some simple layered configurations were examined. This work involved an analysis of the shielding materials reported in the NASA Langley Research Center work of Thibeault, et al., 2015 [95], discussed earlier, and then extended that work to consider various multilayered combinations. Our results are summarized in Figure 6.18, and have been published. [14]

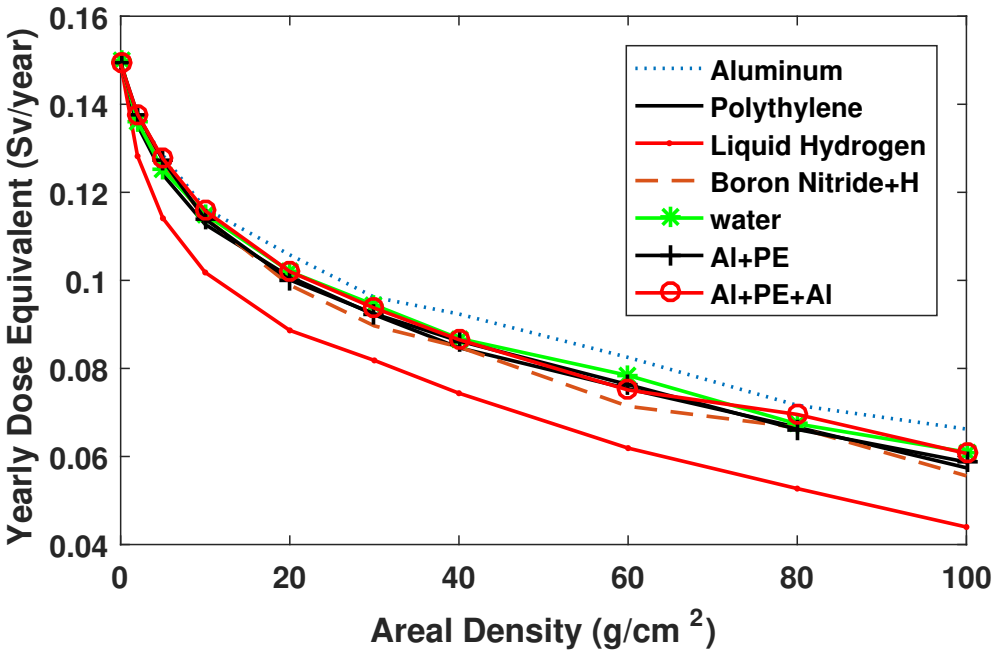

Figure 6.18 : Annual Dose Equivalent for Different Materials of Varying Areal Densities with CREME96 GCR, 1977 Solar Minimum GCR, ICRP-103 Weighting Factors, and using the MULASSIS Monte Carlo Approach.

The results for the standard suite of materials were as expected – aluminum was inferior to all other materials examined, and liquid hydrogen was the best. In addition, the shielding effectiveness of two combinations of aluminum and polyethylene were

also considered. The first combination is aluminum of 2 g/cm^2 thickness, followed by polyethylene (PE) of varying areal densities from $0 - 98 g/cm^2$. The second combination is a "sandwich" Al-PE-Al structure proposed in Borggrafe, et al. [12], where the areal density percentage of polyethylene was studied from 0 to 96%. These two kinds of Al-PE multilayers were examined using the MULASSIS radiation transport code and compared to shielding with aluminum alone, as well as the other materials previously examined by NASA. One can readily see that by adding the polyethylene layer behind the aluminum that the shielding effectiveness is improved by some 6%. But layering in a different way in the "sandwich" Al-PE-Al configuration does not improve shielding effectiveness over the single-layer materials.

In addition to the aluminum and polyethylene layers, polyethylene and boron nitride plus hydrogen of 5% by weight were selected for comparative analysis, partly because of boron nitride's propensity to attenuate secondary neutron emissions. Our results are shown in Figure 6.19.

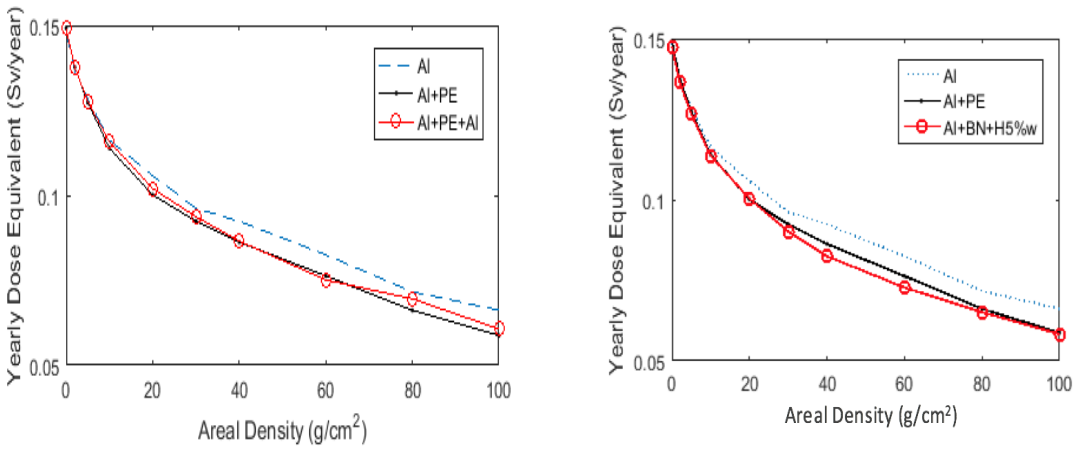

(a) Al-PE Combinations.

(b) PE-Boron Nitride with 5% H.

Figure 6.19 : Dose Equivalent Evaluations for Multi-layered Shielding with Polyethylene, Aluminum and Boron Nitride plus Hydrogen 5% by Weight Combinations (MULASSIS with ICRP-103).

The results shown in Figure 6.19a show the two aluminum with polyethylene combinations in a less cluttered format. Then Figure 6.19b shows the results of layering polyethylene with the NASA contrived material of boron nitride nanotubes with hydrogen infused in the amount of 5% by weight, with the common comparative elements being aluminum by itself and the Al-PE combination described above. As anticipated, the shielding effectiveness of Al-BN+H5% structure is similar to, and perhaps slightly better than that of Al-PE combination at the same areal densities. This is most likely because of the effectiveness of the increased hydrogen content in attenuating primary GCR ions and the high neutron cross section of boron.

It is also possible to do multilayer shielding analyses using the HZETRN radiation transport computation method, and actually somewhat less time consuming, though one is cautioned to use only comparative results when evaluating shielding, as previously discussed. Figure 6.20 shows our comparative results for a multilayer design of 2 gm/cm^2 aluminum shielding on top of polyethylene (HDPE).

As can be seen, the multilayer approach can be used to give some structural rigidity to the design with an outer layer of aluminum, and with the HDPE inner layer the entire shield achieves results comparable to HDPE by itself, reducing the dose equivalent exposure by some 34% over that of aluminum alone, and cutting the "exposure gap" between aluminum and that of the ISS Baseline exposure in half.

Many different combinations of shielding materials could be tested in this way for particular applications that may impose physical constraints, e.g., thickness of the shield or structural requirements, in order to find an optimal radiation shielding design from the GCR at 1 AU – preferably an exposure level as close to the baseline exposure inside the International Space Station.

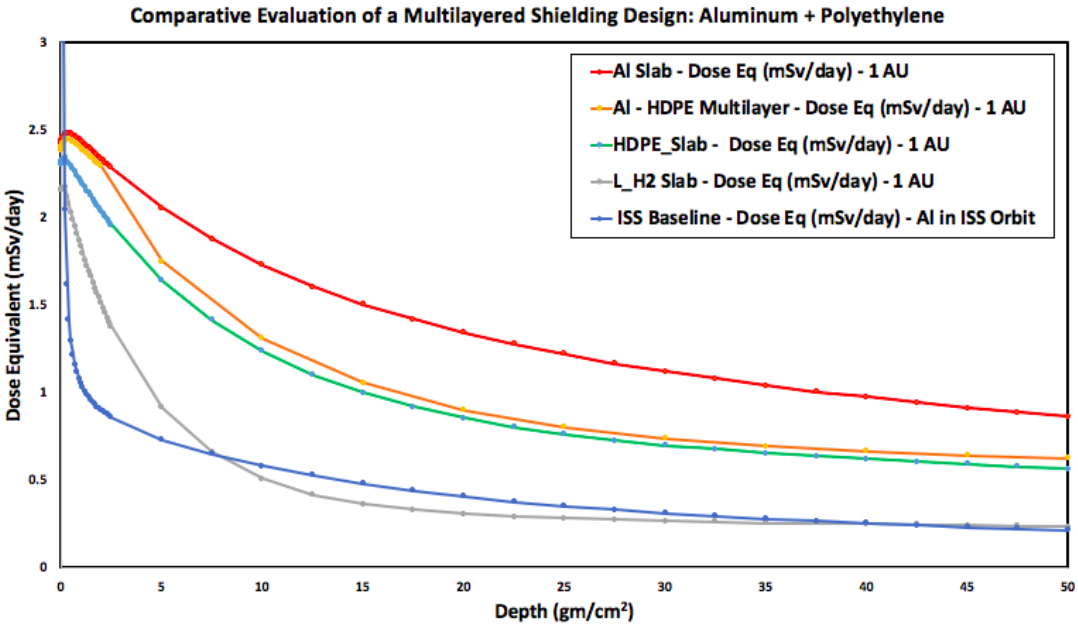

Figure 6.20 : Comparative Dose Equivalent Results for a Multilayer Al-HDPE Shielding the 2010 BON GCR Model, 2010 Solar Minimum, ICRP-60 Weighting Factors, and using the OLTARIS (HZETRN) Approach.

6.4 Analysis of a New Material for GCR Shielding: PBN+H

NASA concluded some years ago that the best path to better passive GCR radiation shielding protocols would be to develop new materials with a greater hydrogen content than polyethylene, and which also had sufficient structural integrity to serve multi-purpose functions on a spacecraft and which could withstand the radiation environment without degradation. However, to date NASA has only seriously considered a boron nitride nanotube material with a maximum 4.2% hydrogen infusion. [95] As we showed above, this material has some promise but is no better than high density polyethylene in terms of radiation shielding effectiveness.

New materials proposed by Rice University researchers for the purpose of hydrogen storage facilities (e.g., for automobiles) may also find utility as an improved

radiation protection material, though it was not initially proposed in that role. They call the new materials "three-dimensional pillared boron nitride (PBN) and pillared graphene boron nitride (PGBN)." [200] The research suggests that these new hybrid nano-structures can be infused with higher volumes of hydrogen than was previously thought possible in nano-materials, as shown in Figure 6.21.

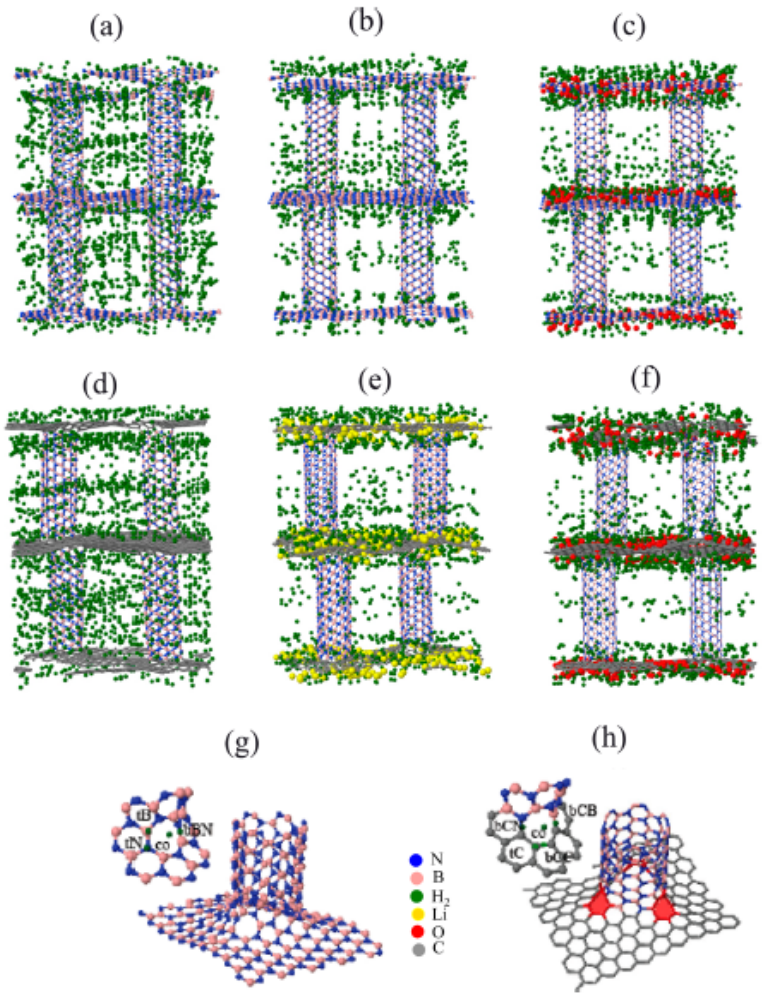

Figure 1. Hydrogen molecule distribution for (a) PBN and molecular dynamic-optimized hydrogen adsorption (b) in pure PBN and (c) O-doped PBN, (d) the same as the (a) plot for PGBN, (e) Li-doped PGBN, and (f) O-doped PGBN. Schematic of different H_2 molecule adsorption sites for (g) pure PBN and (h) PGBN. Blue indicates nitrogen; pink, boron; gray, carbon; green, hydrogen; yellow, Li; and red, oxygen.

Figure 6.21 : Rice University's New Proposed Nano-Structures for Hydrogen Storage.

As shown, several different hybrid structures are proposed, utilizing pillared boron

nitride nanotubes, with other combinations, including a bonded graphene sheet and alternately doping the structure with lithium (Li) or oxygen (O) atoms to increase hydrogen bonding. Importantly, the increased hydrogen content is achieved without doping the structure with heavy metals, which would be counter-productive to radiation shielding properties, as pointed out in the recent NASA work. [95] Preliminary calculations by the Rice University research team indicate that the pristine PBN structures can absorb up to 4.8% hydrogen by weight at room temperature, increasing to some 9.6% hydrogen when the structure is doped with oxygen atoms, and increasing further to some 13.6% hydrogen if the temperature is decreased to 77K; the PGBN structure can achieve almost 15% hydrogen absorption by weight. [200]

The question then becomes: Does it make any difference? The comparative shielding effectiveness results to the 1 *AU* GCR environment are shown in Figure 6.22.

As is shown, for a given areal density the higher the hydrogen content the lower the dose equivalent radiation exposure rate – as expected. But is there a significant improvement over the earlier reported NASA BNNT material (which for modeling purposes is assumed approximately equivalent to the pristine PBN with 5% hydrogen by weight)? For an equivalent areal density of 20 gm/cm^2, the results tend to show a decrease in dose equivalent exposure rate from 1.0453 mSv/day down to 0.867 mSv/day with PBN plus 15% – or an incremental decrease of 0.1783 mSv/day, approximately a 17% decrease. For a three-year mission this would equate to a decreased exposure about of 0.2 Sv, which could be significant for some astronauts, given the range of the current NASA career limitations of 0.4 - 3.0 $Sv/career$ discussed in Chapter 2; e.g., *see* Figure 2.13, and accompanying text.

The comparative data is further illustrated in Table 6.4.

Thus, additional research progress in developing new hybrid nano-structure ma-

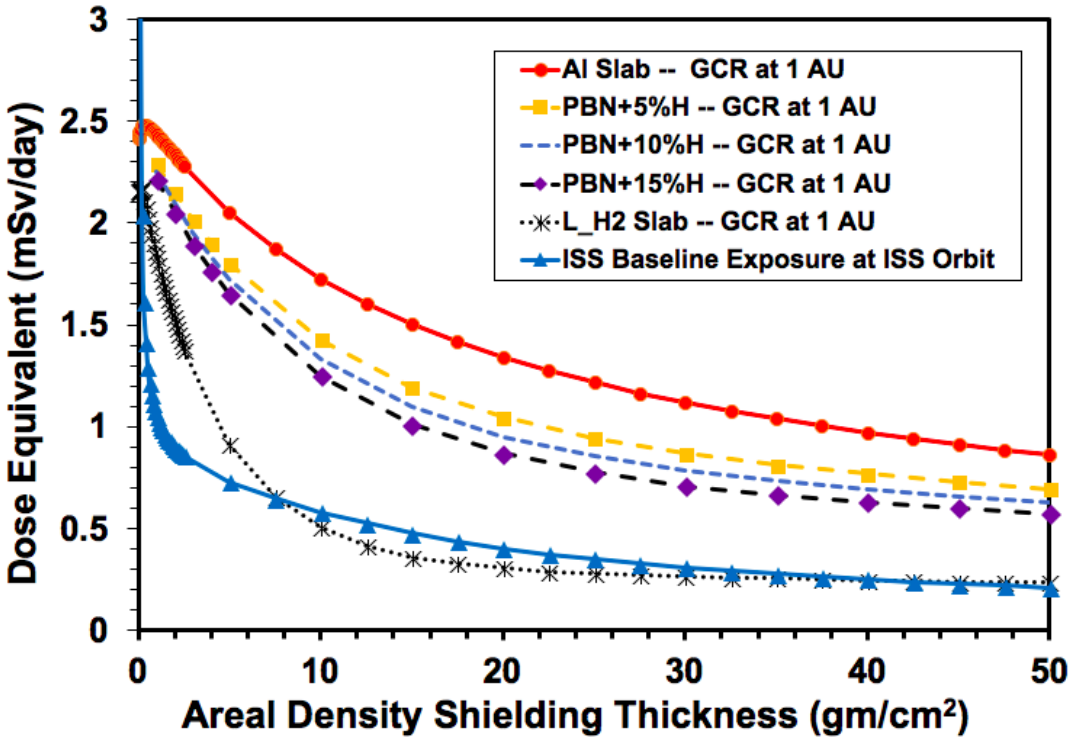

Figure 6.22 : Radiation Shielding Effectiveness of PBN Structures.

terials that have the required physical integrity to become structural elements on a spacecraft, and which can absorb only a little more hydrogen, would provide a structural material that was also superior to HDPE in radiation protection effectiveness. Note that we found the PGBN material to be inferior to the PBN material because of its graphene component. Note also that on an equivalent thickness basis that the PBN material quickly becomes superior to HDPE as a radiation shield, as hydrogen content exceeds more than 10% by weight.[12]

[12] The areal density of 20 gm/cm^2 to illustrate the dose equivalent exposure rate behind various shielding materials in Table 6.4 was chosen because the ISS shielding has been equated to about that areal density of aluminum. Thus, the other materials are put on the same basis, though for most of them it would result in an impractical physical thickness for spacecraft hull construction (i.e., aluminum would be 7.4 cm thick). Also, recall that ISS Baseline exposure rate results primarily from the fact that the radiation environment at the ISS orbit is much lower than at 1 AU in cis-lunar space. Finally, the physical thickness comparison at 30 cm was calculated from the areal density dose

GCR Radiation Shielding Evaluation
1 *AU* GCR for Various Materials

Material	Dose Eq (mSv/day) (20 gm/cm^2 Areal Density)	Dose Eq (mSv/day) (30 cm Thick)
Aluminum	1.340	0.92
PBN+H5%	1.045	0.77
PBN+H10%	0.949	0.70
PBN+H15%	0.867	0.64
HPDE	0.854	0.70
LH2	0.305	1.48
ISS Baseline	0.410	N/A

Table 6.4 : Comparative Evaluation of Dose Equivalent Radiation Exposure in a 1 *AU* GCR Environment behind Various Shielding Materials, and as Compared to the Verified ISS Baseline Radiation Exposure.

Our data also confirms the distinct advantage of high density polyethylene over aluminum for shielding GCR radiation, as has been shown previously. Indeed, if spacecraft could be constructed of HDPE alone, the dose equivalent radiation exposure rate could be cut by about 36% over that of aluminum, and get over halfway to the ISS Baseline exposure from that behind aluminum. On a three-year mission this would equate to a decreased exposure of about 0.53 Sv – more than a career limit for some astronauts. One can also see from the data that the new PBN material increases in radiation shielding effectiveness as the percentage of hydrogen is increased, and that at 15% hydrogen it is already very close to that of HDPE.

Of course, these new materials have yet to be manufactured, and before use in a spacecraft, must be tested for radiation degradation, although other physical pa-

equivalent data, and the density of the pristine boron nitride structure was assume to 1.4 gm/cm^3 – as per NASA's reported estimate, as previously discussed – and then the density of each PBN material was diminished by the amount of hydrogen absorbed on a weighted percentage basis.

rameters have already been examined. [201] [202] [203] [204] Recent NASA work also cites to several materials studies completed with favorable results on boron nitride nanotubes, which may be directly applicable to the PBN structure. [95] Also, before using a new material in spacecraft manufacturing that was also intended as a radiation shield, it would be useful to do experiments with the Brookhaven National Laboratory 1 GeV iron ion radiation beam on samples of the material, on a comparative basis with other materials, even though such experiments have serious deficiencies, as previously discussed in Chapter 5.

6.5 Dimensionless Evaluation Parameters for GCR Shielding

It is sometimes convenient to attempt to distill from cumbersome calculations simple parameters that can approximate the results that would be obtained with more detailed and expensive analyses – at least within a prescribed range. That is especially true in situations, as here, where the detailed analyses must be done on a precisely comparative basis, or risk anomalous conclusions. In terms of evaluating the effectiveness of shielding GCR in the cis-lunar radiation environment, two such parameters are proposed; one devolves directly from the radiation transport physics, and the second is a convenient dimensionless metric that measures the effectiveness of a GCR shielding material in terms of the verified radiation exposure on the interior of the International Space Station, and thus empirically ties the calculated shielding evaluation results at 1 AU to the bulk of the medical data available, to allow better evaluation of human health risks.

The Mass Stopping Power Number

The first evaluation parameter devolves directly from the Bethe-Bloch equation

that is employed to calculate the electronic attenuation component of the electrons in a shielding material as the forces act on the positively charged GCR ions in accordance with Coulomb's inverse square law. *See* Equation 3.5. Importantly, the electronic attenuation component is by far the largest acting on the GCR ions – well over 95% – as discussed in Chapter 3. [80] [81] Of course, the Coulomb forces have little impact on some secondary emissions, such as neutrons, that carry no charge, and for those the nuclear reactions are the predominate attenuation mechanism.

The starting point is the Bethe-Bloch equation, discussed in both Chapter 3 and Appendix A, which is repeated here for convenience:

$$S = \frac{4\pi Z_p^2 \rho Z_T N_A e^4}{A_T m_e \beta^2 c^2} \left[ln\Big(\frac{2m_e c^2 \beta^2 \gamma^2}{I}\Big) - \beta^2 - \frac{C\big(\beta\big)}{Z_T} + Z_p L_1\big(\beta\big) + Z_p^2 L_2\big(\beta\big) + L_3\big(\beta\big) \right] \tag{6.1}$$

As explained in Appendix A, the last four terms within the large brackets are minor correction factors that impact the calculation only when considering very low energy ions traversing a target material, which is minor in the case of GCR radiation. Thus, the formula quickly reduces to Hans Bethe's early formulation, as follows:

$$S = \frac{4\pi Z_p^2 \rho Z_T N_A e^4}{A_T m_e \beta^2 c^2} \left[ln\Big(\frac{2m_e c^2 \beta^2 \gamma^2}{I}\Big) - \beta^2 \right] \tag{6.2}$$

Viewed in this light, it is obvious that the only variables that have anything to do with the shielding material are ρ (its density), Z_T (its atomic charge), and A_T (its atomic weight). Thus, the Stopping Power of a material per unit mass, sometimes referred to as the "mass stopping power" [9], is proportional to the ratio of the atomic charge to the atomic weight of the shielding material, as follows:

$$\frac{S}{\rho} \propto \frac{Z_T}{A_T} \tag{6.3}$$

This simple expression for what might be called a "mass stopping power number" – MSP number – can, we submit, provide a quick rough comparative measure of GCR shielding effectiveness, where $S \approx LET$, in units of MeV/cm, and the material density, ρ, is in units of gm/cm^3; nevertheless, the MSP number is deemed dimensionless in the common parlance of the so-called "natural unit" system,[13] and provides a "dimensionless" measure of the electronic Stopping Power of a shielding material, normalized to that of hydrogen, as shown in Table 6.5.[14]

Mass Stopping Power Number		
Material	Atomic Charge/Atomic Weight (Z_T/A_T)	Normalized MSP No.
Aluminum (Al)	13/26.98	0.486
HPDE (CH_2)	6+2/12.01+2.016	0.575
LH2 (H_2)	1/1.008	1.0
PBN (BN)	(85%) 12/24.82	
+H15%	(15%) 1/1.008	0.565

Table 6.5 : Mass Stopping Power Number for Various GCR Shielding Materials.

As can be seen, the shielding material effectiveness is best for liquid hydrogen with $MSP \approx 1$, and decreases as the elemental composition becomes heavier; thus the

[13] The MSP number is dimensionless in the sense that no units are generally expressed for Z or A in the "natural unit" system. Strictly speaking, however, Z has units of the elemental charge $e = 1.602 \times 10^{-19} C$, and A has units of $1amu = 1gm/mol$.

[14] Recall that the Stopping Power is the predominate attenuation term for the GCR ions, and is accounted for as the so-called CSDA term in the simplified one-dimensional linear steady-state Boltzmann equation for GCR transport in a target medium. *See* Equation 4.3 and Figure 4.2.

comparative effectiveness predicted by the MSP number is consistent with the more detailed calculations previously discussed in this Chapter 6.

Note, however, that the MSP number does not derive from the total mass stopping power, as illustrated in Figures 3.4 and 3.5, and as discussed in the accompanying text. But it *does* derive from the predominate forces that attenuate positive GCR ions in shielding materials, from an "absorbed dose" perspective. *See, e.g.,* Equation 2.2, which calculates absorbed dose as a function of mass stopping power (S/ρ_{target}) and the flux of GCR particles. Thus, the MSP number does not rate shielding effectiveness in relation to human health risks in a direct way; e.g., by delineating the relative harm done by the different GCR ions, but rather only in relation to the physical ability of the shielding material to attenuate and absorb the incident GCR ions.

The Dimensionless Normalized International Space Station Number

We now propose a simple dimensionless parameter that does derive from metrics that tie directly to predicted human harm due to exposure to GCR radiation as the "Normalized International Space Station Number" – the NISS number. While calculating the NISS number does require conducting the previously discussed detailed calculations concerning the ISS Baseline, it allows a quick visualization of how close the subject shielding material and design comes to creating in a spacecraft operating in cis-lunar space at 1 AU the same radiation environment encountered in the interior of the International Space Station (ISS); i.e., one for which there is sufficient medical data to truly evaluate human long-term radiation exposure health risks.

Calculating the NISS number first involves calculating the dose equivalent exposure rate behind the shielding material or design being evaluated, and then comparing it to the dose equivalent exposure rate inside the ISS. As mentioned previously, care

must be taken to do the calculations on precisely the same basis: same radiation transport scheme; same geometry; same GCR radiation input boundary conditions; and same radiation weighting factor models. The NISS number is simply the ratio of the dose equivalent exposure rate behind the shielding being evaluated in the 1 AU GCR radiation environment, as compared to that metric inside the ISS; i.e., behind shielding which is the equivalent of 20 gm/cm^2 of aluminum in the radiation environment at the ISS orbit. In order to evaluate a particular shielding material one might consider the NISS number as a function of areal density, as shown in Figure 6.23.

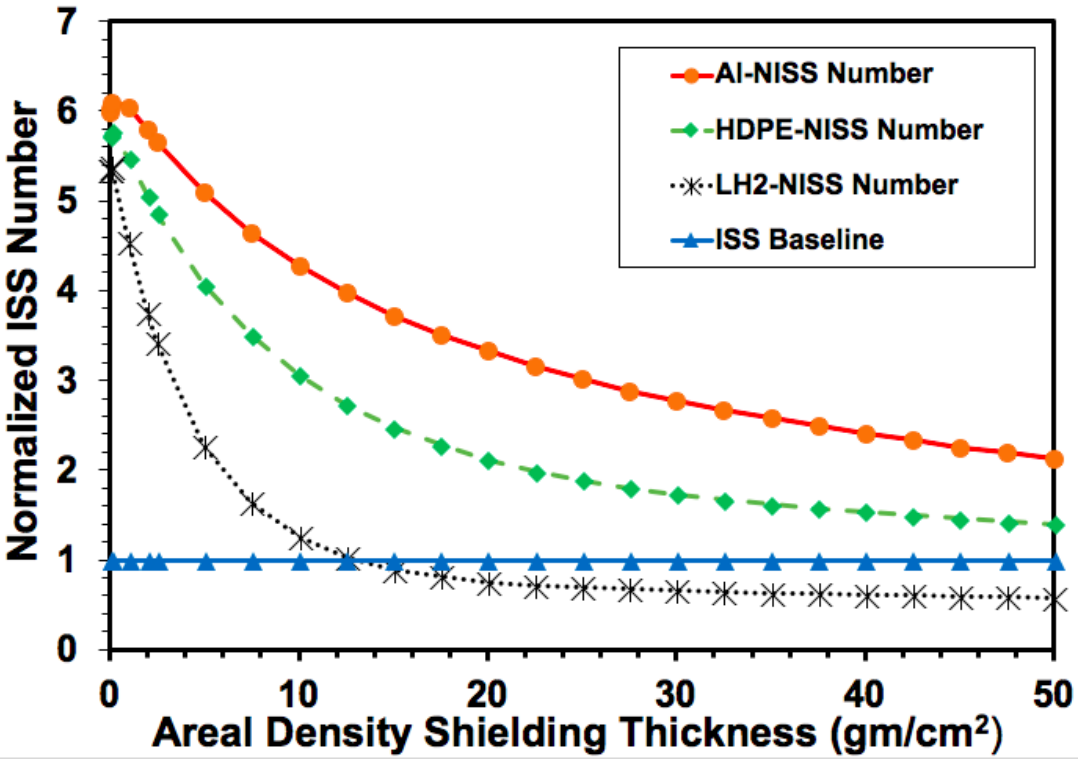

Figure 6.23 : NISS Number as a Function of Areal Density.

This method of visualizing comparative shielding material effectiveness clearly demonstrates how far off of the objective dose equivalent exposure rate of the ISS baseline is achieved for each material considered, at various areal densities. For example, for

a standard Apollo spacecraft with an aluminum hull of 5 gm/cm^2 (*see, e.g.,* Figure 2.6) operating in cis-lunar space, the NISS number is about 5.1; i.e., the dose equivalent exposure rate is just over five-times that encountered inside the ISS – probably too large a deviation to make the medical data for ISS astronauts relevant to the evaluation of radiation hazards in cis-lunar space. However, if somehow the ISS was operating in cis-lunar space, with its 20 gm/cm^2 equivalent aluminum shielding, the NISS number would be reduced to 3.3; and if that same areal density of shielding could somehow be made of polyethylene, the NISS would be reduced further to 2.1 – only two-times the dose equivalent exposure rate encountered inside the ISS.

But in spacecraft shielding design, it is not only the material that must be considered, but also the physical size, a problem illustrated in Figure 6.24 by examining the NISS number as function of actual thickness.

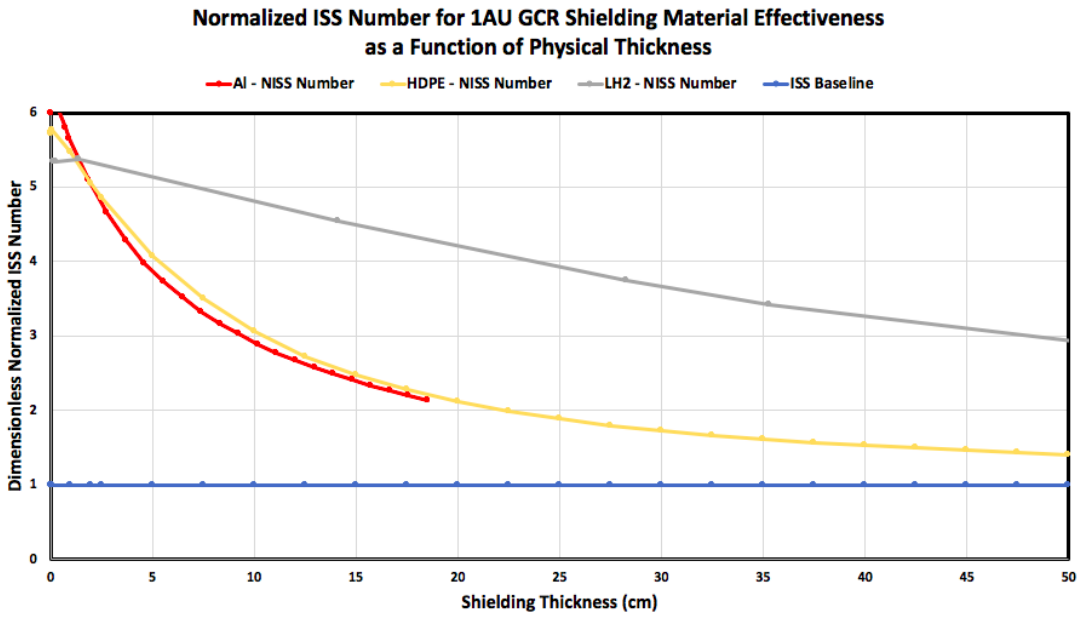

Figure 6.24 : NISS Number as a Function of Physical Thickness.

Here the density of the shielding material dictates the actual size required to achieve a

specific result. For example, it would require 18.5 *cm* of aluminum to achieve a NISS number of 2.1 – about twice the dose equivalent exposure rate of the ISS – definitely an impractical thickness for an aluminum spacecraft hull. Interestingly, the NISS number calculated as a function of physical thickness reveals the counter-intuitive result that if "actual thickness" is a critical design limitation, then aluminum and polyethylene are equally good (or poor) shielding materials. For example, if design limitations impose a maximum shielding thickness of 10 *cm*, then both aluminum and HDPE achieve a NISS number of about three.

The NISS number provides a convenient way to examine shielding materials and size limitations to optimize effectiveness, and importantly, also allows comparison of the net shielding effectiveness to the ISS Baseline dose equivalent exposure rate, for which much medical data exists to allow assessment of human radiation health risks.

6.6 Potential Practical GCR Radiation Shielding Designs

The essence of engineering is not necessarily to find the precise theoretical answer to a problem, but rather to apply theory to achieve a workable solution in a potentially practical application. Thus, our research effort would be remiss without at least a nod to a practical problem.

An Inelegant, but Workable, Spacecraft Radiation Shield Design

NASA and others have proposed nominal three-year missions to Mars or the asteroids. The question becomes: Is there a possible shielding design that would attenuate the GCR radiation for operations in the 1 *AU* cis-lunar space radiation environment such that the dose equivalent exposure rate would approximate that encountered on the interior of the International Space Station? If so, then the plethora of medi-

cal data from long-term ISS astronauts will be useful in assessing the true radiation exposure health risks encountered on the proposed three-year missions.

As an exercise in shielding material and design evaluation, five shielding designs for a spacecraft operating in the 1 AU cis-lunar space radiation environment were considered, as shown in Figure 6.25, primarily of two basic designs: (1) an exterior insulated fuel tank that would completely wrap around the spacecraft; and (2) an exterior non-structural insulation/shielding comprised of polyethylene.

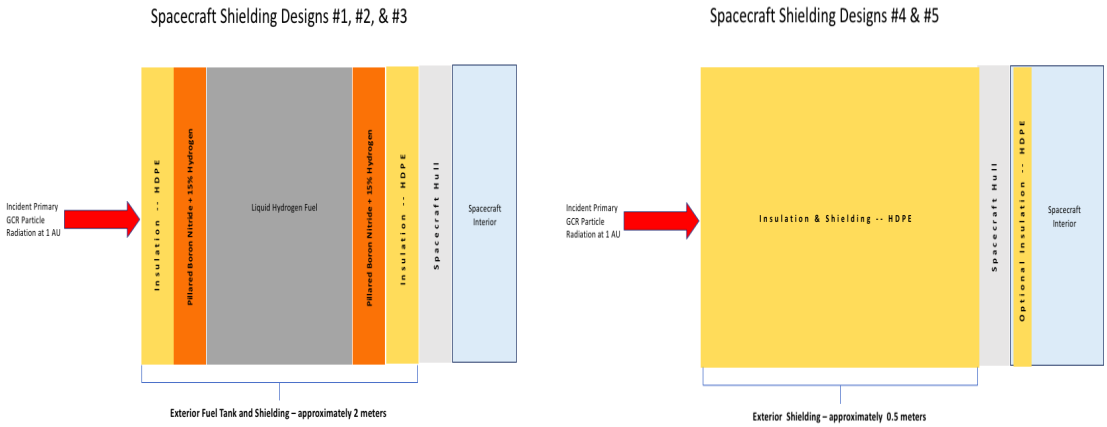

(a) Exterior Fuel Tank Designs. (b) Exterior Polyethylene Designs.

Figure 6.25 : Basic Configurations for Alternative Spacecraft Shielding Designs.

The parameters for the five design configurations are shown in Table 6.6.
As can be seen, each shielding design configuration is 50 gm/cm^2 in areal density, but of course would have different actual physical thicknesses, depending on the material used in each layer. In general, the first three designs (Figure 6.25a) have an approximate physical thickness of 2.0 - 3.0 meters, while the last two designs (Figure 6.25b) have an approximate thickness of 0.5 meters (50 cm).

The dose equivalent analysis of the five shielding designs is shown in Figure 6.26. The ultimate answer on how well each shielding design performs is the dose equivalent

Material	Design 1	Design 2	Design 3	Design 4	Design 5
HDPE	10	10	10	40	45
PBN+H15%	7	7	5	0	0
LH2	12.5	12.5	20	0	0
PBN+H15%	7	7	5	0	0
HDPE	8.5	8.5	5	0	0
Aluminum Hull	5	0	0	5	5
PBN+H15% Hull	0	5	5	0	0
HDPE Interior	0	0	0	5	0

Table 6.6 : Shielding Design Materials and Areal Density Thickness (gm/cm^2).

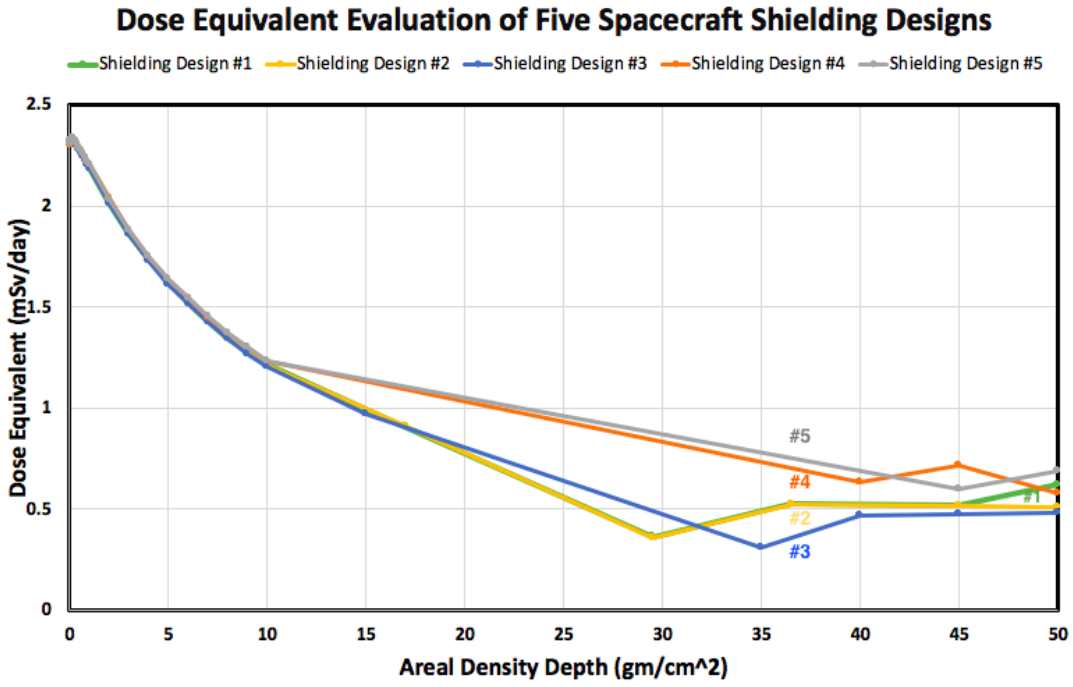

Figure 6.26 : Comparative Analysis of Five Spacecraft Shielding Designs.

exposure rate behind 50 gm/cm^2 of shielding material, because that represents the position of the interior of the spacecraft. However, the interim data is useful in illustrating how each layer of the shield performs, and is instructive for optimizing

the result by changing materials and thicknesses of the various layers in the design.

It is clear from the data that Design #3 provides the lowest dose equivalent exposure rate at an areal density depth of 50 gm/cm^2, but it is also the largest structure physically, having an actual thickness of 3.12 meters. While this may seem somewhat impractical to construct, the fuel tank configuration of Figure 6.25a could perhaps be wrapped around a spacecraft in the construction phase in low Earth orbit, and then fueled in LEO as well, before proceeding on its three-year mission. Moreover, it is no more impractical to build than other shielding designs that have been proposed in recent years, including, e.g., the huge 100-ton, or more, magnetic shielding systems discussed in Chapter 5, which have been proffered by Nobel laureates and others.

Selecting the best performing design of each type – Design #3 (exterior fuel tank) and Design #4 (exterior insulation) – allows further comparative analysis, as shown in Figure 6.27.

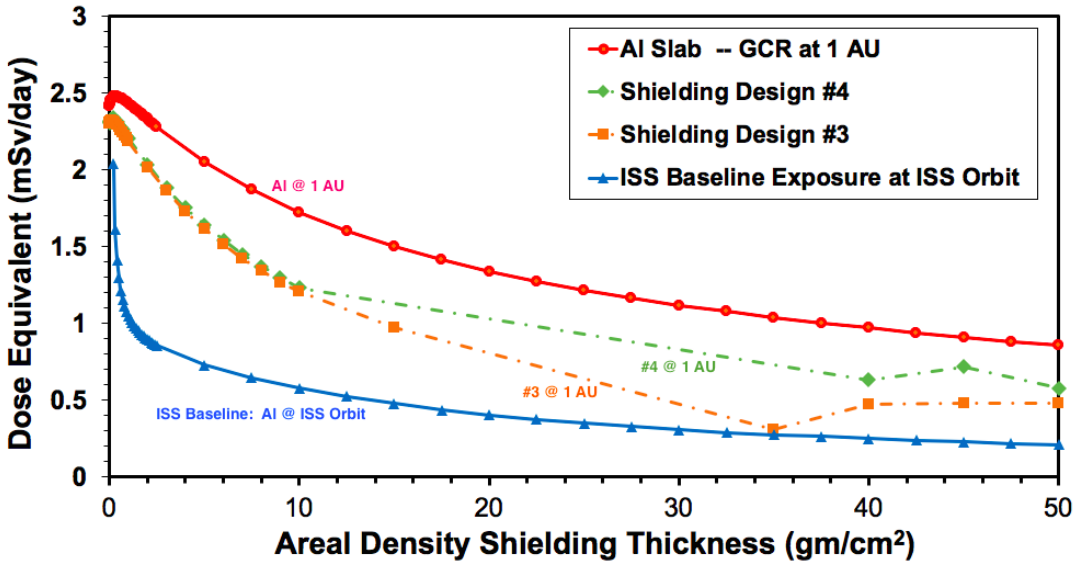

Figure 6.27 : Comparative Analysis of Two Spacecraft Shielding Designs Operating in 1 AU Radiation Environment, and Standard Aluminum Operating in 1 AU and ISS Orbit Radiation Environments.

The standard aluminum shielding in the radiation environments at 1 AU and at the ISS Orbit, respectively, defines the range in which a shielding design must perform; e.g., it should be better than the standard aluminum hull, with the objective of replicating the radiation environment achieved in the ISS. Here, both designs provide an ultimate dose equivalent exposure rate at 50 gm/cm^2 that are very close, with Design #4 having about a 0.1 mSv/day higher rate than Design #3 – which is about a 0.12 Sv increased exposure on a three-year mission, and possibly a significant difference in the evaluation process in that it is about 25% of the lowest range of NASA's stated career level exposure.

The NISS number analysis, shown in Figure 6.28, adds some further useful information to aid in evaluating the various shielding designs, and perhaps provides some insight into being able to rely on the ISS astronaut medical data to assess long-term space voyage radiation exposure risks.

These data show that both shielding designs are much closer to the ISS Baseline dose equivalent exposure rate level at the interior of the spacecraft – at an areal density of 50 gm/cm^2 – than can be achieved with aluminum, and that Design #3 is the best with a NISS = 1.19, versus a NISS = 1.43 for Design #4.

All things being equal – and they are *not* – one would select Design #3, and perhaps even try to improve on it a bit by making the liquid hydrogen fuel tank somewhat thicker. But Design #3 is already 3.12 meters thick, and already presents a tricky on-orbit construction challenge. While Design #4 is only some 50 cm thick, it would also have to be constructed in LEO; i.e., the exterior polyethylene insulation used in Design #4 is probably too fragile to launch unprotected, and would likely have to be attached in construction efforts on orbit. However, it is clear that the standard aluminum shielding option at 50 gm/cm^2 is also not workable, as it would require

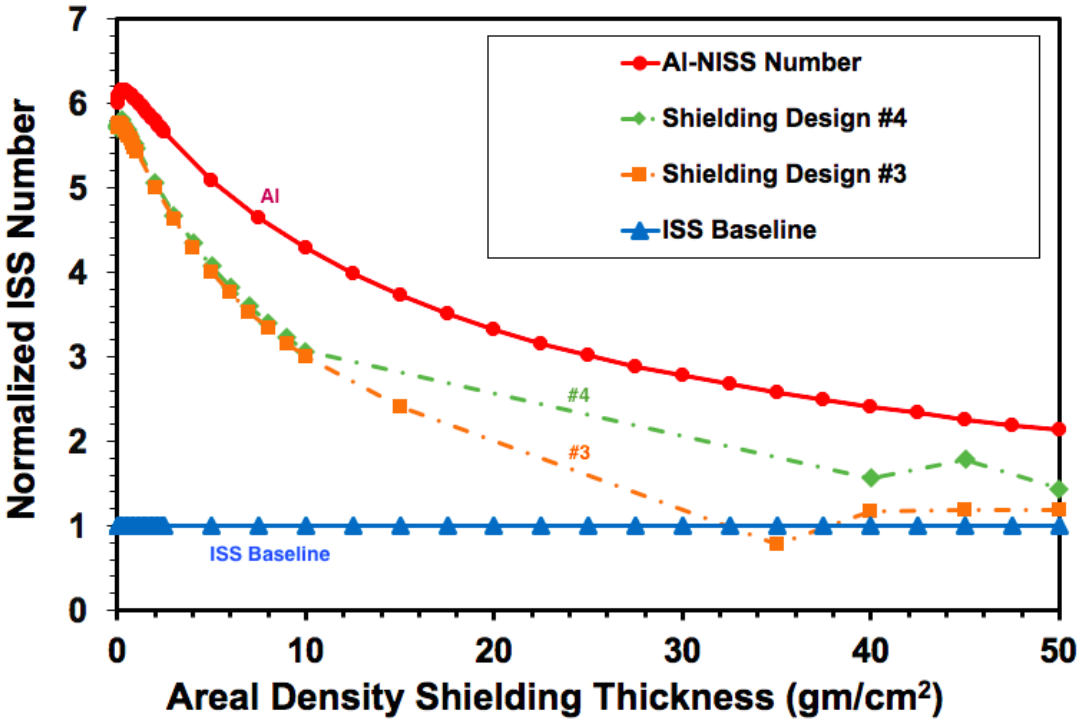

Figure 6.28 : Comparative NISS Number Analysis of Two Spacecraft Shielding Designs and Standard Aluminum.

a very heavy spacecraft with walls of aluminum some 18.5 *cm* thick, and even then would not provide near the same level of protection as either Design #3 or Design#4.

In the final analysis, Design #4 offers some promise as a simple workable design approach with currently available materials. The boron nitride with infused hydrogen hybrid nano-structure material could improve any design, but that new material is not yet available to add to the structural arsenal for spacecraft fabrication, nor is it fully tested for use in the cis-lunar radiation environment. In addition, using a liquid hydrogen fuel tank adds considerable radiation protection attributes, but the fuel tank design options are cumbersome, and operational handling of liquid hydrogen in space would likely be both difficult and dangerous. Finally, perhaps Design #4 could

be improved by making the exterior HDPE somewhat thicker, and thereby reduce the NISS number from the current 1.43 to one closer to the ISS Baseline exposure level; though from a positive perspective this design is already much better than standard 5 gm/cm^2 aluminum hulls, which have a NISS number of 5.1; i.e., a dose equivalent exposure rate at 1 AU that is over five-times that in the interior of the International Space Station.

But the dose equivalent exposure rate accomplished at 1 AU with Design #4 (HDPE-Al) is still some 0.18 mSv/day higher than the ISS Baseline exposure rate, which would result in an increased exposure of about 0.2 Sv on a three-year mission over the ISS exposure level. That may be a significant addition to career exposure limits set by NASA for some astronauts (particularly the young ones), thus continued work on new materials and designs may be justified. Additionally, it must be left to the medical doctors to decide whether a NISS number in the range of 1.43 is close enough to the ISS Baseline to make the ISS astronaut medical data useful in assessing radiation exposure risks on long-term missions in the cis-lunar space region.

Habitat Radiation Shielding Designs on the Moon and Mars

Another often-stated objective – but after almost 50-years not yet accomplished – is to return humans to the Moon to establish a so-called "moon base" for exploration, scientific, and even commercial purposes. Thus, it may be instructive to assess the radiation protection situation for habitats on the Moon.

The design constraints are somewhat different than those considered for spacecraft in that the physical size limitations are not so critical, but transporting construction materials to the Moon would be time consuming and expensive. Thus, the studies that have been done have focused on using *in situ* structures, such as lava tubes,

and utilizing lunar regolith as a building and shielding material. [163] [89] The other major design difference is that the primary incident GCR radiation is cut in half on the surface of the Moon, because the celestial body itself blocks half of the isotropic GCR radiation; but, of course, the shielding material causes secondary emissions, as does the Moon's surface itself, and that must be considered as part of a dose equivalent exposure rate. In addition, unlike the Earth, the Moon has no atmosphere or magnetic field to aid in radiation attenuation.

A rough first approximation of the effectiveness of lunar regolith as a radiation shielding material is to evaluate its Mass Stopping Power number – MSP. This is relatively easy to do knowing the weight fraction composition of lunar regolith (with a density of 2.0 gm/cm^3): oxygen (0.456); silicon (0.207); aluminum (0.176); calcium (0.136); iron (0.015); magnesium (0.005); sodium (0.004); and titanium (0.001). [89] Doing the calculation results in an MSP = 0.498, just slightly higher than aluminum; thus from an "absorbed dose" standpoint one would expect lunar regolith to be just very slightly better in absorbing GCR ions than aluminum. Of course, this is not the whole story, in that it may behave differently in terms of generating secondary emissions, particularly given that it does contain more small quantities of heavier elements than pure aluminum.

Radiation protection evaluation on Mars has similar nuances, and has been the subject of several studies. [205] The primary GCR flux will be slightly higher than that at 1 AU in the vicinity of Earth, since Mars is about 1.524 AU from the sun – perhaps an insignificant difference as compared to the solar wind shock boundary that defines the heliosphere at approximately 100 AU, where the GCR enters the vicinity of the solar system. And while Mars has no significant magnetic field to attenuate the GCR radiation, it does have a slight atmosphere that attenuates the

radiation in a vertical direction by about 16 gm/cm^2 of Martian atmosphere (95.9% CO_2; 2.0% Ar; 1.9% N_2; 0.14% O_2; 0.05% CO), and to a slightly greater extent for GCR ions approaching at lower angles toward the horizon through thicker slices of the atmosphere; and, of course, the Martian celestial body blocks half of the primary incident GCR.

Just as on the Moon, the building and shielding material will likely be the *in situ* Martian soil. It is estimated to have a density of 1.7 gm/cm^3, with the following composition by weight fraction: 45.41% SiO_2; 16.73% Fe_2O_3; 16.73% FeO; 8.35% MgO; 6.73% CaO; and 7.4% H_2O. [206] This results in a calculated MSP = 0.503, which would indicate only slightly better "absorbed dose" shielding characteristics than lunar regolith. But the relatively higher amounts of iron and heavier elements would also indicate the likelihood of more dangerous secondary emissions, like neutrons, than might occur with lunar regolith, and certainly more than would occur with pure aluminum or HDPE.

One study claims to have compared various materials in the 1 AU, Lunar, and Martian radiation environments, as shown in Figure 6.29. [9]

As previously discussed, this chart contains information that is suspect; e.g., it admits being "Modified from Wilson et al. (1997), courtesy of NASA," but doesn't indicate how. Further, the analysis omits entirely any consideration of secondary emitted albedo neutron exposure, and the earlier NASA work referred to contains nothing about a material called "H Nanofibers," noted in the charts.

Nevertheless, the data in Figure 6.29 allows for several useful conclusions. First, the GCR induced radiation environment on the Moon is about half of that at 1 AU in cis-lunar space – an expected result given that half of the incident GCR is blocked. Second, the radiation environment on Mars is even less than that on the Moon –

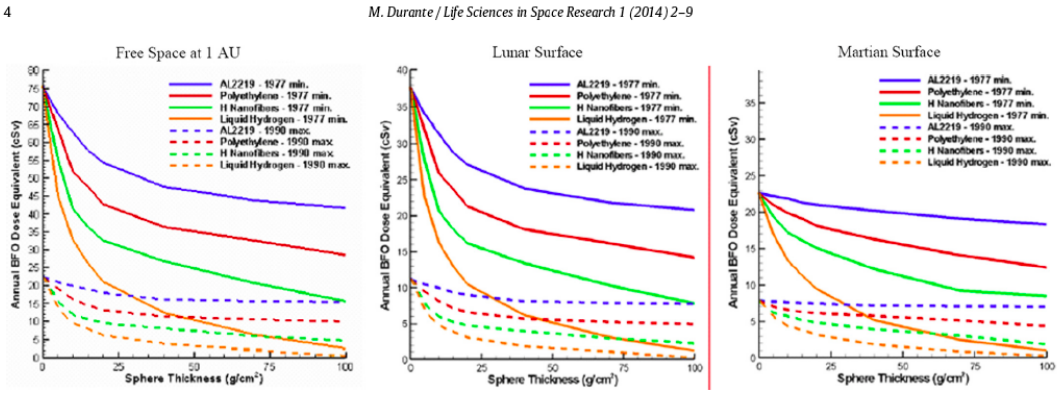

Fig. 1. Estimated impact of the shielding using different materials (aluminum, polyethylene, hydrogen nanofibers or liquid hydrogen) on the annual dose equivalent. The dose is calculated in the blood forming organs (BFO) using the radiation environment data relative to the 1977 solar minimum (solid lines) or 1990 solar maximum (dashed lines). Simulations using HZETRN are for deep space, moon or Mars surface (without albedo neutrons and pion-electromagnetic cascade). Modified from Wilson et al. (1997), courtesy of NASA.

Figure 6.29 : Comparative GCR Induced Radiation Exposure Levels Behind Various Shielding Materials in the 1 AU, Lunar and Martian Radiation Environments. From Durante, 2014.

another expected result given that half the incident primary GCR is blocked by the planet itself, and there exists a thin atmosphere that further attenuates the radiation.

But there is an additional, perhaps important, conclusion that presents itself in light of the previous research presented here. As shown in Figure 6.23, liquid hydrogen as a shielding material in the 1 AU radiation environment will create the same dose equivalent exposure rate behind a depth of 12.5 gm/cm^2 LH_2 as exists in the interior of the ISS; i.e., such shielding has a NISS number of 1.0, for which there is much astronaut medical data on radiation exposure risks. Thus, using that metric as a comparative tool, it appears that in the first chart in Figure 6.29 (1 AU radiation environment) that the 12.5 gm/cm^2 areal density depth for liquid hydrogen provides an exposure level of 27 $cSv/year$. If it is assumed that this also would be the exposure level for what this author calculated – "BFO Dose Equivalent" – inside the ISS, and it is further assumed that the same modeling parameters were used by that author

to generate the other charts in this Figure 6.29, then some useful information can be obtained for exposure levels and relative health risks on the Moon and on Mars.

For example, looking at the middle graph in Figure 6.29, the 27 $cSv/year$ exposure rate is achieved with about 25 gm/cm^2 of aluminum shielding on the Moon, or about 12.5 gm/cm^2 of polyethylene – about 10 cm and 12.5 cm of material, respectively. One can easily envision a habitat shielded with that thickness of HDPE, and if lunar regolith has shielding characteristic not too much different from aluminum, it would require a "lunar brick" thicknesses in the range of only 12-15 cm to create on the Moon the same radiation exposure rate that exists on the ISS.

In similar fashion, looking at the right-side graph in Figure 6.29, the 27 $cSv/year$ exposure rate is achieved without any shielding at all on Mars, so that habitat shielding of any kind can improve the radiation exposure levels to less than that found on the ISS. Note, however, that with "Martian brick" shielding, one would want to have sufficient thickness to absorb the initial secondary emissions, and simulations of lunar regolith appear to indicate that this could be achieved easily beyond a thickness of some 10 cm, though thicker bricks may be required to absorb all the secondary neutron emissions – perhaps on the order of 50 - 100 cm. [89]

Though more detailed work would appear to be warranted for the Lunar and Martian radiation environments – which is beyond the scope of this research – it seems upon cursory examination that it will be a fairly easy job to establish habitats on the Moon and Mars with radiation environments as good or better than that currently experienced on the International Space Station, and maybe one approaching levels encountered on Earth. That makes the ISS astronaut medical data relevant to assessing radiation exposure risks on the Moon and Mars, and clearly reveals that the greater challenge is finding adequate radiation shielding materials for the 1 AU

cis-lunar radiation environment; i.e., for that time period during the voyage to the Moon, Mars or the asteroids.

Chapter 7

Sensitivity and Uncertainty Analysis

"Education is the kindling of a flame, not the filling of a vessel."
——Socrates, classical Greek (Athenian) philosopher credited as one of the founders of Western philosophy, and as being the first moral philosopher of the Western ethical tradition (470 - 399 BC)

"Shall I refuse my dinner because I do not fully understand the process of digestion?"
——Oliver Heaviside FRS, an English self-taught electrical engineer, mathematician, and physicist, when criticized for lack of rigor in developing new methods for solving differential equations, but later named a Fellow of the Royal Society and awarded an honorary doctorate (1850 - 1925)

"Life is made up of a series of judgments on insufficient data, and if we waited to run down all our doubts, it would flow past us."
——Billings Learned Hand, an American judge and judicial philosopher, served on the United States Court of Appeals for the Second Circuit, was the first to expressly inject economics into legal decision-making, and is the most quoted judge who never sat on the Supreme Court (1872 - 1961)

If practical use is to be made of any mathematically-based models for spacecraft radiation shielding design, it is essential to discuss the sources and magnitude of potential error and uncertainty embedded in those models, including model formulation errors (including simplifying assumptions, input sprectra, and impact assessment metrics), data uncertainty, and the error associated with numerical methods. We examine each model module involved in evaluating spacecraft radiation shielding materials and protocols for potential sources of error and uncertainty, as well as an assessment of how those uncertainties propagate to the determination of the commonly used evaluation metric, dose equivalent radiation exposure rate. Thus, the GCR input, radiation transport, and biological assessment modules are examined in turn as to their contribution to the uncertainty in determining shielding design parameters. In addition, the potential error embedded in our new shielding evaluation metric proposed in this

research thesis is examined in the context of its intended purpose to mitigate the uncertainties involved in setting appropriate shielding design parameters.

The results of our work have revealed: (1) that use of the ISS Baseline calibrated method for radiation shielding evaluation (introduced in Chapter 6) reduces the uncertainty in estimating the mass of required shielding from 60% down to about 15%, for operations in the 1 *AU* cis-lunar region, thus better assuring astronaut safety and better controlling mass tolerances and costs; (2) that thicker shielding materials can increase radiation levels in interior shielding locations, due to back-scatter neutron emissions, that can adversely impact equipment and sensor readings; and (3) that users of the 1D MULASSIS Monte Carlo code should be aware that the wide difference in dose equivalent results obtained as compared to HZETRN is explained primarily by the MULASSIS GCR physics module under valuing the contribution of the heavier GCR ions as compared to the lighter ions, by the number of different ions considered in the respective models, and by the method by which the GCR spectra is input into the MULASSIS code. As previously discussed, evaluating space radiation shielding must be done on a strictly comparative basis only, and even then there remains uncertainty as to whether future astronauts will be adequately protected from radiation exposure until long-term medical assessments are made.

7.1 The Galactic Cosmic Ray Models

The development of the two GCR input modules used in this research was reviewed in Section 4.3 – the 2010 Badhwar-O'Neill (BON) model for HZETRN, and the CREME96 model for MULASSIS. As discussed previously, these models are semi-empirical in that they modulate the GCR spectrum over time to emulate changes in flux caused by the 11-year solar cycle by numerically solving an equation that de-

scribes the change in flux throughout the solar system, and then calibrate those calculations with a history of actual measurements from the cis-lunar region. [136] In our research, however, we are concerned only with the GCR radiation flux generated by these models at 1 *AU* and at a single point in time; i.e., a "snapshot" in time and space during periods of minimum solar activity (maximum GCR flux) or maximum solar activity (minimum GCR flux), because the spectra at these times at 1 *AU* encompass the radiation environment intensity boundaries most useful for shielding design considerations. Consequently, in our work we are concerned only with the data uncertainty arising from the steady-state determination of the GCR flux at a single point in the solar system (1 *AU*) by the various GCR models in common use, and how well they tie to actual measurement data; thus, any error in the numerical methods used to calculate the modulated GCR flux over the 11-year solar cycle is of little concern here, particularly as the calibration data for both extremes of solar activity is in the 1 *AU* region of primary interest. As the HZETRN code transports all 59 ions primarily present in the GCR, the BON2010 model was verified as to ion flux distribution in Section 6.1, and noted favorable comparison to published data. Here we examine the variability in ion flux predicted in the 1 *AU* cis-lunar region of space between the various GCR models in common use, as well as efforts to verify these model predictions with data from measurements on space probes. In addition, the impact on the calculated radiation exposure metric – dose equivalent – is determined as a function of the variability in GCR flux prediction by the various GCR models.

First, we determined the sensitivity of the change in ion flux and dose equivalent for the primary GCR model used in this research between a "solar minimum" and "solar maximum" condition; the two points of primary design interest caused by the 11-year solar cycle modulation of the GCR intensity (e.g., *see* Section 2.1). Our

Figure 7.1 shows the GCR ion flux for the BON2010 model for both "solar min" and "solar max" conditions, for primary GCR ions of hydrogen, helium, and iron at 1 AU. In each case the flux is diminished during the "solar max" condition, as would be expected due to the increased intensity of the interplanetary magnetic field carried by the solar wind from the Sun. The spread in the calculated flux for the hydrogen ions reach a maximum of 135 $particles/(cm^2 - day - MeV/n)$ at a kinetic energy of about 350 MeV/n; a flux decrease of 78% in solar maximum periods versus solar minimum periods. The difference in flux between "solar min" and "solar max" decreases as the ion atomic weight increases, and that difference also decreases as the ion kinetic energy increases (easier to visualize on Figure 7.1b). All GCR ions have similar distributions, with modulation effect negligible above 10 GeV/n.

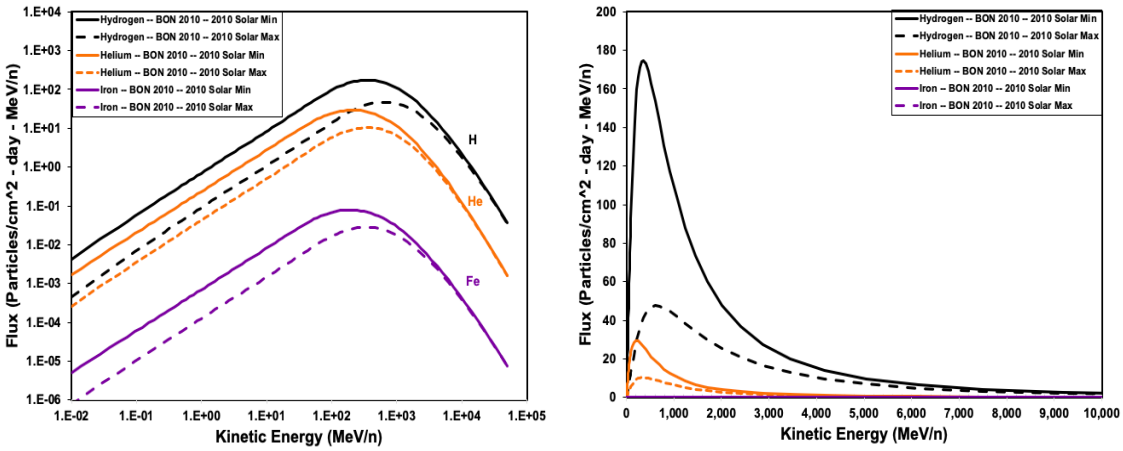

(a) GCR Flux on Log-Log Scale.

(b) GCR Flux on Linear Scale.

Figure 7.1 : GCR Flux for Hydrogen, Helium, and Iron Ions generated by the 2010 Badhwar-O'Neill model for input to HZETRN (Solid lines for 2010 Solar Minimum; Dashed lines for 2001 Solar Maximum.)

Thus, since the total kinetic energy imparted by the primary GCR flux can be estimated by calculating the total energy of the hydrogen ions, plus that of the helium ions, plus that of the iron ions times a factor of 56 to account for all the other heavier

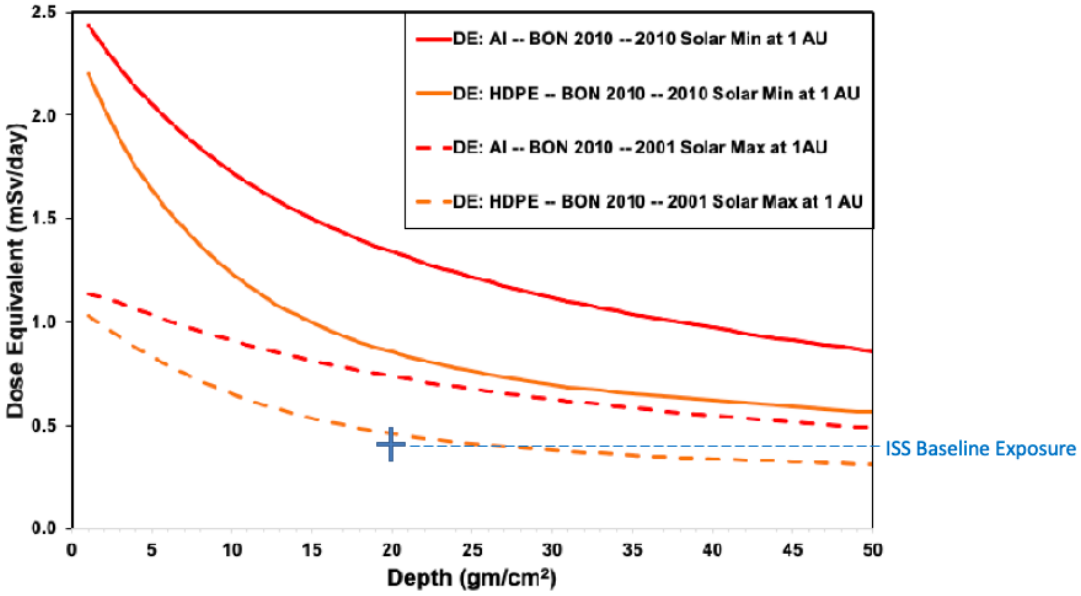

Figure 7.2 : Dose Equivalent Comparison behind Aluminum and Polyethylene Shielding Material, as between 2010 Solar Minimum (solid lines) and 2001 Solar Maximum (dashed lines) – BON2010 GCR Model, with ICRP-60 Biological Weighting Factors.

ions in the GCR (*see* Section 6.1 for our previous discussion), then the total kinetic energy imparted by the GCR spectrum at solar minimum is about $4.99\times10^{6} MeV/day$ and about $2.39\times10^{6} MeV/day$ at solar maximum, or about a 53% reduction in total kinetic energy imparted per day during solar maximum periods.

While the change in GCR flux between solar minimum and maximum conditions for each primary ion in the GCR is of interest, it is the relative biological harm caused behind various shielding materials that is of ultimate concern. Figure 7.2 shows our determination of the calculated dose equivalent behind various thicknesses of aluminum and polyethylene (HDPE) exposed to the 1 *AU* GCR in the cis-lunar region, comparing the radiation exposure rate for both solar minimum and maximum conditions. In essence this illustrates the difference in absorbed energy behind various thicknesses of shielding material, scaled for biological harm as per ICRP-60.

The range in exposure rate, between "solar min" and "solar max" conditions, behind typical aluminum shielding for spacecraft is 1.02 mSv/day for 5 gm/cm^2, and 0.6 mSv/day at 20 gm/cm^2; or a decrease in exposure rate during solar maximum conditions of some 50% and 45%, respectively. The data for HDPE is similar in trend, indicating a range of 0.81 mSv/day for 5 gm/cm^2, and 0.39 mSv/day at 20 gm/cm^2; or a decrease in exposure rate during solar maximum conditions of some 49% and 46%, respectively – for all practical purposes, the same decrease as for aluminum. Thus, the reduction in total energy imparted per unit time by the full GCR spectrum bears an almost direct one-to-one correlation to the change in calculated dose equivalent exposure rate.

These are not unexpected results given the large flux decrease in the GCR during solar maximum conditions, and underscores the sensitivity (and thus the importance of the accuracy) of the GCR input parameters on the dose equivalent calculation. Put in more practical terms, the difference in exposure rate between "solar min" and "solar max" conditions with 20 gm/cm^2 of aluminum shielding would indicate a cumulative difference in exposure of 0.66 Sv over a three-year space voyage, a significant portion of most astronauts' career limitation. Moreover, the data for HDPE material under "solar max" conditions illustrates that an exposure rate at 1 AU of 0.41 mSv/day could be achieved with 25 gm/cm^2 HDPE (about 25 cm actual thickness), thereby meeting the ISS Baseline exposure rate discussed earlier in Section 6.1. Our analysis then begs the question: Why not execute the contemplated three-year long space voyages during periods of solar maximum? But while there may be some merit to that idea, one must also consider the fact that during periods of solar maximum the dangerous SPE threat is much greater (e.g., *see* Section 2.1).

To begin to understand the potential error in estimating the true GCR flux, we

first examine the flux parameters of the various GCR models in common use, given that the GCR input flux can cause significant changes in the dose equivalent exposure rate calculation. Figures 7.3 and 7.4 show our determination of flux data for GCR hydrogen, helium, and iron ions at the 1 AU radiation environment for four difference GCR models: the 2010 Badhwar-O'Neill, 2013 Matthia, 2016 SINP, and 2014 Badhwar-O'Neill (all at 2010 Solar Minimum) used by the HZETRN radiation transport code. As a general observation, these models tend to good agreement in GCR flux above 1 GeV/n in kinetic energy, but show an increasing difference as the particle energy decreases below 1 GeV/n. Another commonly used GCR model is the CREME96 (at 1977 solar minimum) used by the MULASSIS Monte Carlo code, as shown in Figure 7.7, where the disagreement between the BON2010 model and the CREME96 model in the lower energy ranges is quite large (a factor we discuss later in our comparison of HZETRN and MULASSIS results).

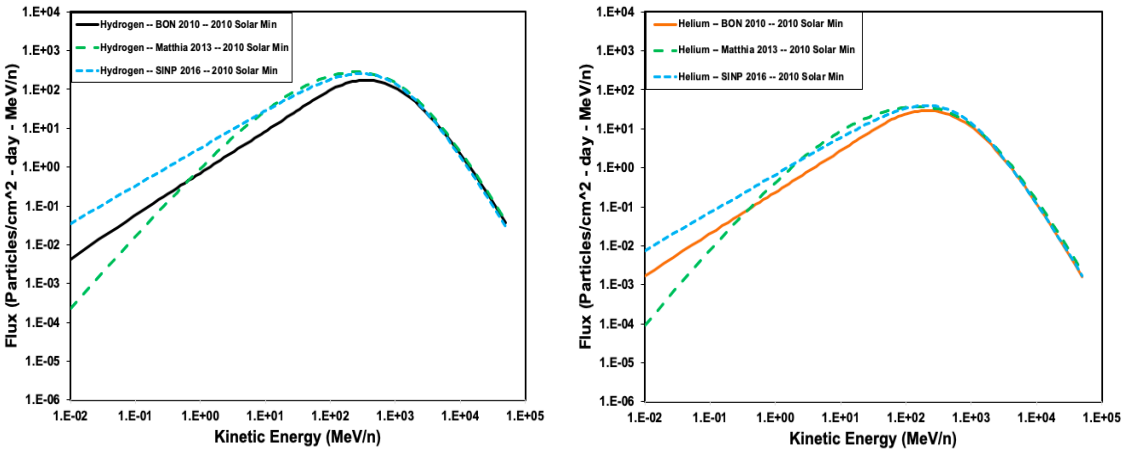

(a) GCR Hydrogen Flux.

(b) GCR Helium Flux.

Figure 7.3 : GCR Flux for Hydrogen and Helium ions generated by Three Models: 2010 Badhwar-O'Neill, 2013 Matthia, and 2016 SINP (all at 2010 Solar Minimum).

To better understand the magnitude of the differences in these GCR models and

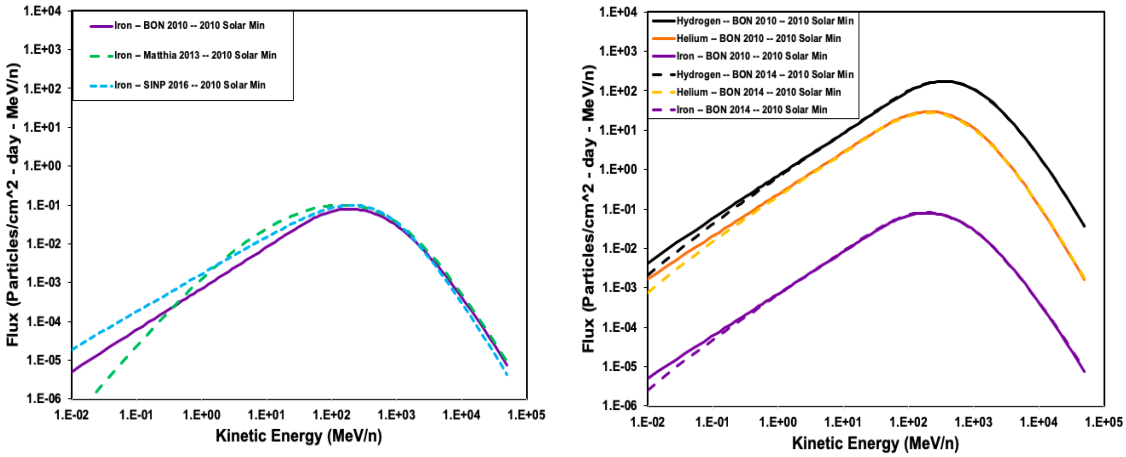

(a) GCR Iron Flux. (b) BON2010 to BON2014 Comparison.

Figure 7.4 : (a) GCR Flux for Iron ion generated by Three Different Models: 2010 Badhwar-O'Neill, 2013 Matthia, and 2016 SINP (all at 2010 Solar Minimum); and (b) Comparison between Badhwar-O'Neill (BON) 2014 and Badhwar-O'Neill (BON) 2010 GCR Models (both at 2010 Solar Minimum), for H, He, and Fe Ions.

the propagated sensitivity in the dose equivalent calculation, we calculated the integrated total kinetic energy imparted by the full GCR spectrum in accordance with the procedure developed in Section 6.1, between the energy range of 1 MeV/n to 50 GeV/n (which puts all models on a comparable energy range basis and comprises 99.86% of the total energy represented in the models). In addition, we used the HZETRN radiation transport code to determine the dose equivalent exposure rate obtained by using the four GCR models compatible with that code (2010 Badhwar-O'Neill, 2013 Matthia, 2016 SINP, and 2014 Badhwar-O'Neill), all at the same 2010 solar minimum, as shown in our Figure 7.5.

The primary differences in these GCR models involve variations in the parameters used to modulated the GCR spectra through the 11-year sunspot cycle (attempting to replicate past cycles) and the source of empirical data used to calibrate them to the 1 AU radiation environment. [207] [137] Our Figure 7.5 shows that two recently

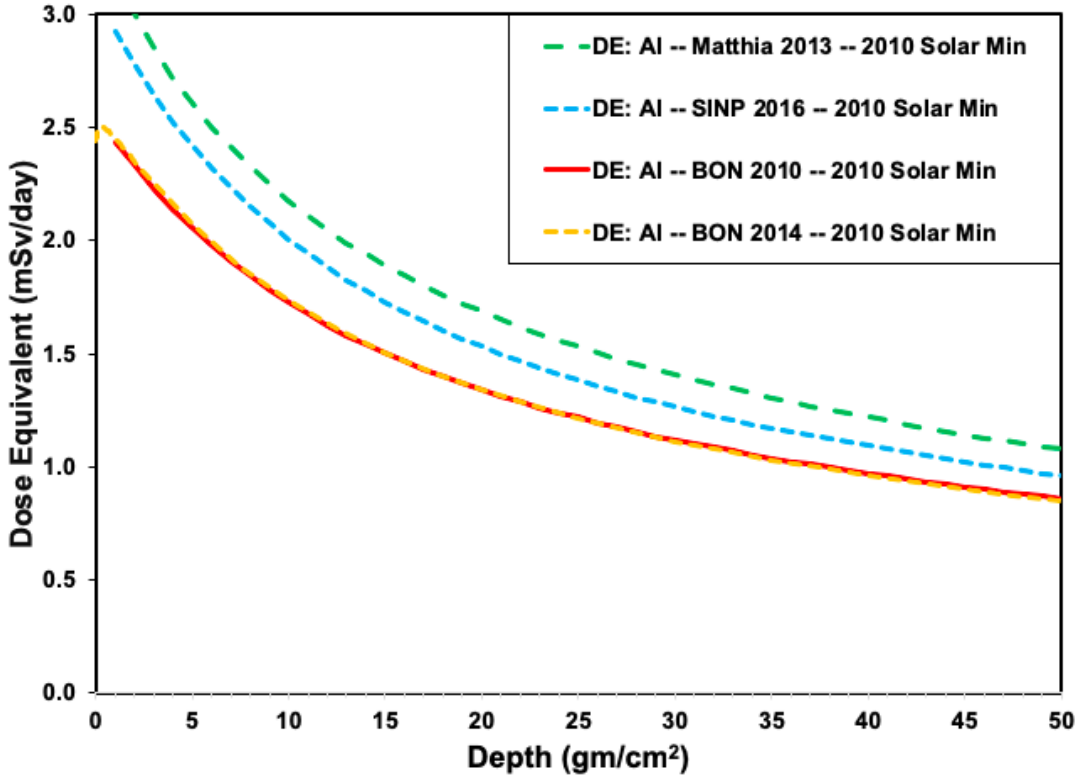

Figure 7.5 : Dose Equivalent Comparison behind Aluminum Shielding Material, as between 2010 Badhwar-O'Neill, 2013 Matthia, 2016 SINP GCR, and 2014 Badhwar-O'Neill Models (all at 2010 Solar Minimum), with ICRP-60 Weighting Factors.

developed GCR models set up to provide input to the NASA HZETRN code produce higher dose equivalent calculations than the BON2010 and BON2014 models (which are almost equal). We discuss below the reasons for primarily using the BON2010 in our research. For comparative purposes, at 5 gm/cm^2 of aluminum the dose equivalent is 18% higher for the SINP 2016 Model, and 26% higher for the Matthia 2013 Model, representing a range of 0.55 mSv/day, with a mean dose equivalent exposure rate of 2.36 mSv/day and a standard deviation of 0.23 mSv/day. At 20 gm/cm^2 of aluminum the dose equivalent is 14% higher for the SINP 2016 Model, and 26% higher for the Matthia 2013 Model, representing a range of 0.35 mSv/day, with a mean dose equivalent exposure rate of 1.52 mSv/day and a standard deviation of 0.14 mSv/day. Considering the range of the data, the calculated dose equivalent exposure rates from the four different models appear to vary to within $\pm 18 - 19\%$ of the mean (i.e., within two standard deviations, for a 95% confidence level, assuming the data is normally distributed), which is in general agreement with the $\pm 20\%$ uncertainty reported in the literature. [140] Thus, the total calculated exposure uncertainty over a three-year mission is on the order of 0.6 Sv for 5 gm/cm^2 of aluminum shielding, and 0.38 Sv for 20 gm/cm^2 of aluminum shielding. Thus, this uncertainty range over a three-year mission is a significant portion of many astronaut's career exposure limits set by NASA, and must be considered in the previous shielding evaluation procedures.

Table 7.1 shows our calculated total integrated kinetic energy for a particular GCR model and the resulting calculated dose equivalent exposure rate we determined behind aluminum. The results for the four GCR model inputs to HZETRN indicate generally a linear correlation between total kinetic energy and resulting dose equivalent in the noted kinetic energy interval, with a linear least-squares regression for dose equivalent at 5 gm/cm^2 of $DE_{Al-5} = 0.3525(KE)+0.2853$, and a similarly constrained

linear regression for dose equivalent at 20 gm/cm^2 of $DE_{Al-20} = 0.2155(KE)+0.2534$.

GCR Model Comparisons

Model	Total Kinetic Energy ($MeV \times 10^6/day$)	DE - Al (5 gm/cm^2)	DE - Al (20 gm/cm^2)
BON 2010	4.99	2.05	1.34
BON 2014	4.94	2.07	1.34
SINP 2016	6.12	2.42	1.53
Matthia 2013	6.52	2.60	1.69
CREME96	7.63	[0.57]	[0.51]

Table 7.1 : Total Calculated GCR Kinetic Energy and Resulting Calculated Dose Equivalent using HZETRN for BON2010, BON2014, Matthia 2013, and SINP 2016 GCR Models; and using MULASSIS for the CREME96 Model (at solar mins).

But we get a very different dose equivalent result from the CREME96 GCR model using MULASSIS, about which more will be said when we discuss the comparison between the HZETRN deterministic code and the MULASSIS Monte Carlo method in the next section. For now, as shown in Figure 7.7, it is sufficient to say that the CREME96 GCR model compares favorably with the BON2010 model (both at respective solar minimums – but different ones), except below 100 MeV/n, where the ion distributions begin to diverge, and especially below 10 MeV/n, where the CREME96 model predicts wildly higher flux for all ions considered. This difference has the effect of increasing the total integrated kinetic energy over the entire GCR energy spectrum predicted by CREME96 far above that of the other models, and assuming the rough linear relationship between dose equivalent and total kinetic energy, derived above from the data, held true when extrapolated beyond the data, then one would expect HZETRN to produce comparable dose equivalent values using the CREME96 GCR model on the order of $DE_{Al-5} = 2.97\ mSv/day$, and $DE_{Al-20} =$

1.89 mSv/day. However, the MULASSIS code using CREME96 produces much lower dose equivalent values, as shown in Table 7.1, a matter that is inconsistent with the higher GCR integrated total energy produced by the CREME96 model, and one that will be discussed more fully in Section 7.2.2, where a comparison between MULASSIS and HZETRN is examined.

Finally, NASA has recently completed an analysis of several GCR model flux predictions as compared to recently published data for hydrogen and helium ions, and some heavier ions, from the Alpha Magnetic Spectrometer (AMS) mounted outside the International Space Station. [207] Specifically, this study compared the measured flux of those ions to the flux predicted by the Badhwar-O'Neill (BON) 2014, Matthia 2013, and SINP 2016 GCR Models. After converting the AMS data, reported as a function of Rigidity (e.g., *see* Section 6.1), to Kinetic Energy, the NASA study simply examined the absolute relative difference of the flux predicted by the GCR model as compared to the AMS flux data, as follows:

$$|Rd| = \frac{1}{N} \sum_{i=1}^{N} \frac{|F_{model,i} - F_{data,i}|}{F_{data,i}}$$

where N is the total number of kinetic energy bins, the predicted GCR model flux in bin i is $F_{model,i}$, and the AMS data flux in bin i is $F_{data,i}$. [207] The sum $|Rd| \times 100$ is the average percent difference between model prediction and AMS data across the energy range.

The results of this NASA work are shown in Figure 7.6, and over-all indicate that the BON2014 GCR model matches the AMS data for hydrogen over the entire energy range better than the other models considered, being only slightly worse than the SINP and Matthia GCR models in the energy range of 1.5 - 4 GeV/n. For the

$\|Rd\|$ in % for selected energy ranges (GeV/n)					
Model	< 1.5	1.5–4	> 4	4–20	Full Spectrum
Hydrogen					
SINP	19	8.2	**14**	23	15
DLR	14	**5.3**	22	**2.7**	20
ISO*	61	27	16	8.7	23
BON2014	**1.8**	9.1	16	9.7	**14**
Helium					
SINP	**0.95**	7.5	18	18	15
DLR	2.7	**2.4**	**2.8**	**1.2**	**2.7**
ISO*	19	13	4.1	4.7	7.6
BON2014	12	12	17	14	16
Boron-to-carbon ratio					
SINP	21	11	110	22	86
DLR	5.0	3.1	29	5.3	23
ISO*	4.6	**1.3**	23	8.2	17
BON2014	**2.1**	2.3	**12**	**3.8**	**9.3**

Figure 7.6 : Absolute relative flux as a percentage between AMS data and various GCR models, including Badhwar-O'Neill (BON) 2014, Matthia 2013 (denoted as "DLR"), and SINP 2016. From Norbury (2018).

helium ion, the BON2014 model is only slightly worse than the other models, with the Matthia model the best over most of the energy range, and the SINP model the best in the lowest energy range. For the heavier ions represented by the boron-to-carbon ratio data, the BON2014 model was clearly the best. NASA's conclusion to this study was that the Badhwar-O'Neill 2014 (BON2014) GCR model best replicated the AMS data, of the models considered (but see our conclusion below regarding the BON2010 model).

The "ISO" GCR model considered and noted in Figure 7.6 is similar to the CREME96 model, and was very poor in matching the AMS data, particularly in the lower energy ranges. That NASA analysis, plus the Figure 7.7 illustrating the large deviation from the BON2010 model for ion flux in the lower energy levels, is

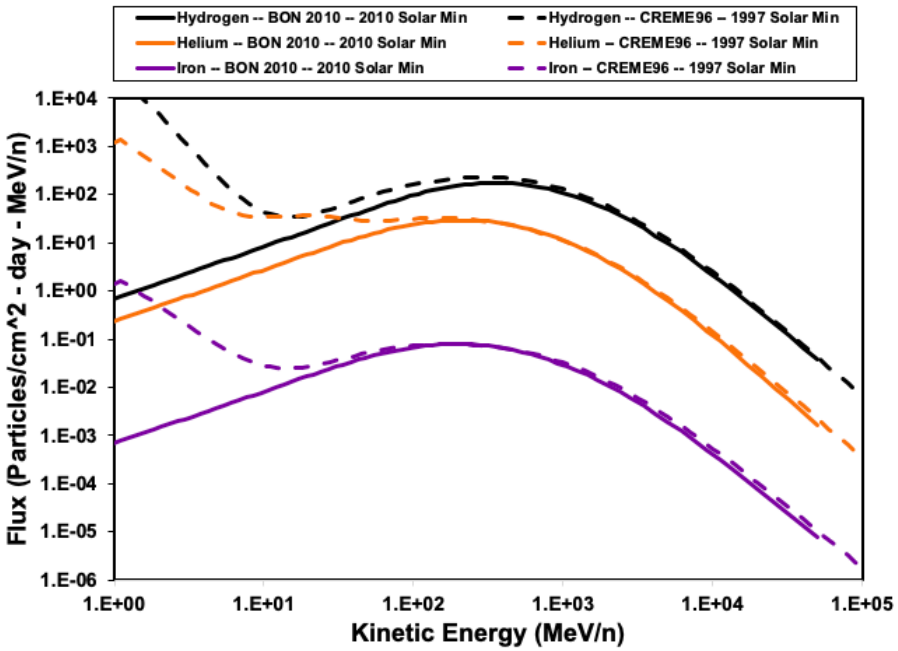

Figure 7.7 : GCR Flux Comparison between 2010 Badhwar-O'Neill and CREME96 Models, at 2010 and 1997 solar minimum, respectively.

strong evidence that the CREME96 GCR model is inaccurate below 50 MeV/n, and should not be relied upon for dose equivalent calculations. However, as noted below, the CREME96 GCR model is not responsible for the large differences in dose equivalent calculations between HZETRN and MULASSIS; but helped to mask those differences.

In addition, we have compared the GCR ion spectra of the BON2010 and BON2014 models, and conclude that they compare very favorably, differing only slightly in the low energy ranges, as shown in our Figure 7.4b. The total integrated kinetic energy generated by the BON2014 model at the 2010 solar minimum is about 4.94 $\times 10^6 MeV/day$, which is about 1% less than that from the BON2010 model used in this research for the fundamental HZETRN calculations. This translates into a negligible difference in dose equivalent calculations: (1) at 5 gm/cm^2 of aluminum

shielding, $DE_{Al-5} = 2.05 mSv/day$ for BON2010 versus $DE_{Al-5} = 2.07 mSv/day$ for BON2014 (slightly less than 1% difference); and (2) at 20 gm/cm^2 of aluminum shielding, the dose equivalent calculations are identical to two decimal places. More importantly, since the BON2010 model has a slightly higher flux in the low energy ranges, it approaches the flux generated by the Matthia 2013 model in that energy range, which in the NASA study is actually better than the BON2014 model for much of the hydrogen energy range and most of the helium energy range, insofar as matching the AMS data. The BON2010 model is more fully described in Section 4.3.1, and was chosen for use in this research primarily because it was the only GCR model that utilized all of the actual GCR measurements from 1955 to 2010 for calibration purposes [136]; and many other published research studies have used it, and for that additional reason, it was important that our research results presented here be reported on a comparable basis. Though development of the BON2014 GCR model introduced some improvements, particularly in the way solar modulation is handled [21]; nevertheless, in view of the recent AMS data a good argument can be made that the BON2010 model is at least as good, and maybe better, in matching the AMS data than the BON2014 model. Moreover, the improved solar modulation results for the BON2014 are largely irrelevant to our analyses, which depend primarily on a maximum GCR intensity snapshot at "solar min" conditions.

In conclusion in regard to the commonly used GCR models, the propagated uncertainty to the dose equivalent calculation between these models (BON2010, Matthia 2013, and SINP 2016) is on the order of ±20%. However, calculations comparing the BON2010 and BON2014 GCR models with respect to the dose equivalent metric show very small deviations (less than 1%). Importantly, the recent analysis of new AMS GCR ion data leans favorably toward the BON2010 GCR model as to over-

all accuracy in depicting the 1 *AU* GCR spectrum. Thus, our decision to use the BON2010 GCR model as a reliable base-case GCR input is justified.

7.2 The Radiation Transport Models

The uncertainty in the radiation transport models reveals itself in GCR and biological harm modelling errors and algorithm errors associated with numerical approximations, with the former by far the greater concern. As discussed previously in Sections 4.1, 4.2, and 4.3.2, NASA began working on a deterministic radiation transport code in the 1970s in order to evaluate the radiation hazards involved in spaceflight, which came to be called HZETRN, while other research organizations employed Monte Carlo approaches, one of which is MULASSIS, primarily a research product of ESA. We have primarily used the HZETRN transport code in our research because it is more widely used in the field and in reported studies, but we did use MULASSIS for an important comparative analysis regarding biological assessment model variations that could not be done with the HZETRN code (*see* Figure 2.11 and associated text), and for an initial fluence analysis. MULASSIS was intended as an easy-to-use quick 1D MOnte Carlo tool by ESA, and thus we have also examined the reasons for the large difference in absolute values of the calculated dose equivalent metric between HZETRN and MULASSIS (*see* Figures 6.10 and 6.12, and accompanying text). In addition, NASA has done extensive studies to minimize the relative error in its numerical approximations to within 0.2% [208], has verified the HZETRN code results against simplified one-particle analytical calculations to within 2% [96], and against simplified one-particle ion beam experiments to within 5% [97], as well as one study comparing HZETRN and three-dimensional Geant4 Monte Carlo simulations on very simplified geometries, for which "the dose equivalent results from

HZETRN and Geant4 are not far from each other, but the HZETRN dose equivalent values behind shielding are often lower than those from Geant4" (due to using an earlier version of HZETRN without neutron back-scatter, and without quantifying the differences, but which from Figures 4 & 11 are within 10%). [142] Nevertheless, NASA has stated the modelling uncertainties could still impose "an uncertainty factor of 2 or more in exposure predictions" for the reported dose equivalent metric. [96]

7.2.1 The HZETRN Radiation Transport Code

The HZETRN radiation transport code is based on a one-dimensional marching algorithm, which propagates the incident GCR radiation spectrum into a target shielding material and follows the attenuation of primary incident ions and generation of secondary emissions with respect to depth. Particle fluence depth profiles are obtained and dose-depth relationships calculated from them, from which other commonly used metrics are calculated, such as dose equivalent exposure rates. [209]

The Particle Radiation Transport Equations

The fundamental approach in the development of the radiation transport equations used as the basis for HZETRN was using conservation principles to express a time-independent one-dimensional steady-state flux density of the incident GCR ions and secondary emissions as follows:

$$\frac{\partial}{\partial x}\phi_j(x,E) = \frac{\partial}{\partial E}\left[\phi_j(x,E)\frac{1}{A_j}S_j(E)\right] - \sigma_j(E)\phi_j(x,E) + \sum_k \int_E^\infty \sigma_{jk}(E,E')\phi_k(x,E')dE' \quad (7.1)$$

where the rate of change of flux of type j particles with kinetic energy E as a function of depth x in the target material equals (1) the rate of decrease in flux of type j particles at a depth of x in the target material with kinetic energy E due to loss of energy and subsequent particle absorption as a result of the Coulombic stopping

force of the target electron field (recalling that $S_j(E)$ is negative and is equal to the change in E per unit distance), minus (2) the type j particles with kinetic energy E absorbed by nuclear collisions in accordance with the cross sections $\sigma_j(E)$, plus (3) the type j particles produced with kinetic energy E as a result of all interaction processes with all particles k with kinetic energy E', as dictated by the production cross sections $\sigma_{jk}(E, E')$ (each absorption or production term expressed in units of number of particles per unit mass per kinetic energy level E, where depth in the target material is expressed in terms of areal density (gm/cm^2)).

Re-arranging terms allows for a more convenient form, where on the left hand side of the equation are the terms associated with atomic and nuclear reactions that slow down and absorb the incident ion particle, and on the right hand side of the equation are the terms that account for the creation of secondary emissions (including neutrons) as the radiation particle projectiles impact the target medium:

$$\Big[\frac{\partial}{\partial x} - \frac{\partial}{\partial E}\frac{1}{A_j}S_j(E) + \sigma_j(E)\Big]\phi_j(x, E) \quad = \quad \sum_k \int_E^\infty \sigma_{jk}(E, E')\phi_k(x, E')dE' \quad (7.2)$$

with the boundary condition $\phi_j(0, E) = f_j(E)$. Thus, this formulation allows determination of the ion flux density, $\phi_j(x, E)$, of an ion particle type j with an atomic mass number, A_j, with an atomic charge, Z_j, and energy E (MeV) (these and other terms required to compute $S_j(E)$, *see* Eq. 3.5), at a depth of x (g/cm^2) in a shielding medium, where the boundary condition spectrum, $f_j(E)$, is considered to be a known function over a broad energy spectrum (i.e., the GCR model input spectra previously discussed). Equation 7.2 describes the transport of light particles, including neutrons and ions with $Z \leq 2$. [106] *See* Appendix A.5 for related details.

In contrast to the light particle transport, for heavier ions it has been shown that the projectile fragments in a collision continue to travel straight ahead at approximately the same energy, while target fragments from such collisions are produced isotropically and are immediately absorbed, and thus can be ignored insofar as transport is concerned [209], which greatly simplifies the equation (a correction to dose is made after the transport is completed and the flux profiles are computed). [108] [106] The absence of target fragments in the heavy ion transport procedure allows taking the summation over all projectiles with mass greater than that of the produced secondary ion type j, and thus the transport equation for heavy ions is simplified from that in Equation 7.2 as follows (with the upper summation limited to 59 ions):

$$\Big[\frac{\partial}{\partial x} - \frac{1}{A_j}\frac{\partial}{\partial E}S_j(E) + \sigma_j(E)\Big]\phi(x,E) \quad = \quad \sum_{k>j}\sigma_{jk}(E)\phi_k(x,E) \qquad (7.3)$$

where the equal velocity assumption allows the variation in production cross sections between the projectile energy, E', and projectile fragment energy, E, to be ignored, and thus $\sigma_{jk}(E)$ is the production cross section in which a k-type particle with kinetic energy E produces a j-type particle with the same energy. [108] [106]

NASA's Numerical Approximation for the Transport Equations

NASA's approach to solving Equations 7.2 and 7.3 has evolved over the years, and involves a combination of analytical and numerical methods that first involves transforming the transport equation from spatial and energy variables to spatial and proton range variables, then transforming this integro-differential equation into integral form that is then expressed in an explicit marching procedure. The numerical procedures include developing (1) an energy grid to cover the relevant range of the subject radiation environment, and a stopping power and ion range grid to provide

these values for all 59 ions transported when called for in a calculation, (2) a cubic Langrange interpolating polynomial scheme to call data from the energy and range grids, and (3) a modified trapezoidal method to approximate the integrals. NASA has developed an interactive database comprised of 14,365 cross-section estimates to account for the electronic and nuclear interactions for the 59 ion species included, plus ion fragments, which are correlated to experimental data where available [97], and a table of the cross sections at each energy grid point is generated for use in each calculation step. [210] The fundamental assumptions include transport of the incident GCR ions through a specified shielding material based on the straight-ahead, one-dimensional conservation approximation equations stated above. [209]

The transformation from spatial and energy variables to spatial and ion ranges is done to simplify numerical procedures by introducing a single residual proton range coordinate, r, for all ions [108], and is accomplished by employing Hans Bethe's theory (*see* Equation 3.5), whereby the stopping power and range of other particles can be expressed as a function of those quantities for protons, as follows:

$$S_j(E) = \frac{A_p Z_j^2}{A_j Z_p^2} S_p(E) \qquad\qquad \frac{Z_j^2}{A_j} r_j(E) = \frac{Z_p^2}{A_p} r_p(E)$$

where A and Z are the atomic weight and charge, respectively, of protons (p) and the other (heavier) ions (j). [96] It follows then that a scaling parameter ν_j can be defined as:

$$\nu_j r_j(E) \approx \nu_k r_k(E) \qquad where \qquad \nu_j = \frac{Z_j^2}{A_j}$$

and recalling that the range of a type j ion is a function of its stopping power, such that:

$$r_j(E) \equiv A_j \int_0^E \frac{dE'}{S_j(E')} dE'$$

and thus the proton stopping power, $S_p(E)$, can be approximated as:

$$\nu_j S_p(E) \approx \frac{1}{A_j} S_j(E)$$

Then to complete the transformation to spatial and range variables, the scaled fluence, $\psi(x,r)$, and scaled production cross section, $s_{jk}(r,r')$, in terms of proton stopping power and the common residual proton range, r, are defined as follows:

$$r = \int_0^E \frac{dE'}{S_p(E')} dE'$$

$$\psi(x,r) \equiv \bar{\nu_j} S_p(E) \phi(x,E)$$

$$s_{jk}(r,r') \equiv S_p(E) \sigma_{jk}(E,E')$$

noting that a modified scaling factor, $\bar{\nu_j}$, is defined as equal to 1.0 if $j = n$ and equal to ν_j if $j \neq n$, in order to avoid a trivial solution for neutrons. Thus, after completing the spatial and range transformation, and further transforming the light particle transfer equation into integral form, Equation 7.2 simplifies the transport equation expressed in terms of spatial and range variables into one with only integrals to evaluate as follows:

$$\begin{aligned} \psi_j(x,r) &= e^{-\beta_j(r,x)} \psi_j(0, r+\nu_j x) \\ &\quad + \sum_k \frac{\bar{\nu_j}}{\bar{\nu_k}} \int_0^x \int_{r+\nu_j x'}^{\infty} e^{-\beta_j(r,x')} s_{jk}(r+\nu_j x', r') \psi_k(x-x', r') dr' dx' \end{aligned} \tag{7.4}$$

where the exponential integrating factor is $\beta_j(r,x) = \int_0^x \sigma_j(r+\nu_j l) dl$. [106] This

equation is then rewritten in the form of an explicit marching procedure for light particles in terms of step-size h as follows:

$$\begin{aligned}\psi_j(x+h,r) &= e^{-\beta_j(r,h)}\psi_j(x,r+\nu_j h) \\ &+ \sum_k \frac{\bar{\nu_j}}{\bar{\nu_k}} \int_0^x \int_{r+\nu_j x'}^{\infty} e^{-\beta_j(r,x')-\beta_k(r',h-x')} \\ &\times s_{jk}(r+\nu_j x', r')\psi_k(x, r'+\nu_k(h-x'))dr'dx'\end{aligned} \tag{7.5}$$

where the new scaled fluence on the left hand side represents particles of type j at position $x+h$ with range r. This new scaled fluence is calculated from the terms on the right hand side of the equation: (1) the exponential term represents attenuation due to nuclear absorption within a step-size h; (2) the current scaled fluence on the right hand side represents type j particles at position x with residual range $r+\nu_j h$, with the difference in range values representing the energy down shift caused by atomic interactions within the step-size h; and (3) the summation and integral terms represent production of light particles, along with nuclear absorption and atomic slowing down over the step-size h. To facilitate convergence, the step-size should be sufficiently small such that $h << 1/\sigma_j(r)$ (i.e., much less than the nuclear mean free path); thus, since the nuclear mean free path lengths are on the order of many gm/cm^2, then a step-size of $h \leq 1.0 gm/cm^2$ is sufficient to assure that the particles will not have travelled far enough to suffer a nuclear collision. [209] [208] *See* Appendix A.5 for more detailed analysis of the mathematical evolution of the transport equation, as well as the subsequent development of a numerical approximation.

The numerical approximation to Equation 7.5 begins with establishing the energy and range grids in order to facilitate subsequent calculations: the energy grid is

designed to represent the input radiation environment, and the range grid is a discrete set of proton range values designed to facilitate calculations in scaled spatial and range variables, and both grids thus facilitate conversion of an energy grid value to a range grid value, and vice-versa, using the equation for r given above. In terms of residual range, a table of ranges and stopping powers are computed for ions from Z=1 to Z=92 over a broad energy grid, and at any point in the code where stopping powers or ranges are needed, an interpolation is performed over the pre-generated database to get the needed result. [96]

To evaluate the source particle integrals in Equation 7.5, NASA first employs a modified single midpoint method to simplify the integral over x' from 0 to h, which NASA has described in private conversations as "basically a composite trapezoidal rule." However, using a range-based calculation procedure reveals a further convergence consideration regarding the maximum step-size, requiring that $h << r/\nu_j \approx r_j$. This constraint arises because of the very short proton ranges at the low end of the energy spectrum; e.g., the range of a 100 MeV proton in aluminum is $\approx 10 gm/cm^2$ (thus a step-size of 0.5 - 1.0 gm/cm^2 will suffice), but a 10 MeV proton has a range in aluminum of only $\approx 0.17 gm/cm^2$, and a 1 MeV proton has a range in aluminum of only $\approx 0.004 gm/cm^2$ before coming to rest (*see* Figure A.6). Thus, NASA has determined that a maximum step-size of 0.5 gm/cm^2 should be implemented at this time, consistent with the error tolerance mention at the beginning of this section. [106]

Next, the secondary particle production cross sections for charged particles is defined as $F_{jk}^{\nabla}(r, r'; h)$, and estimated by the scaled difference of the production cross sections at the two different energy levels, E and E', based on the change in residual range incurred in the step-size h, and the remaining exponential attenuation terms are simplified by using a first order series expansions, which for a step-size of 0.5 gm/cm^2

has been shown to produce negligible errors [106]. And lastly, the final integral is approximated with a "one-point quasi-midpoint rule" that is extended over several sub-intervals to a "quasi-composite trapezoidal rule" (as described by NASA) which is evaluated over several sub-intervals, x_i, with a corresponding sub-range, r_i, within a given step-size region (where $\bar{r_m} \equiv (r_{m+1} + r_m)/2$), which results in the final form of the light particle transport equation approximation as:

$$\begin{aligned}\psi_j(x+h, r_i) &= e^{-\sigma_j(r_i)h}\psi_j(x, r_i + \nu_j h) \\ &+ \sum_k \frac{\bar{\nu_j}}{\bar{\nu_k}} \sum_{m=1}^{N-1} e^{-\sigma_j(r_i)h/2 - \sigma_k(r_m)h/2)} F_{jk}^{\nabla}(r_i, \bar{r_m} + \nu_j h/2); h) \\ &\times [\Psi_j(x, r_m + (\nu_j + \nu_k)h/2) - \Psi_j(x, r_{m+1} + (\nu_j + \nu_k)h/2)]\end{aligned} \tag{7.6}$$

where the integral fluence is defined as:

$$\Psi_j(x, r) \equiv \int_r^{\infty} \psi_j(x, r'')dr'' = \bar{\nu_j} \int_E^{\infty} \phi_j(x, E)$$

by making a change of variables ($r'' = r' - \nu_j h/2$), and is evaluated using a "composite Simpson's rule" approximation method (private conversation with NASA). It should also be noted that the marching light particle transport Equation 7.6 requires that the integral fluence be computed and interpolated at each sub-interval step, and thus the integral is evaluated by continuously updating the fluence of each j-type particle, over the entire spectrum of particles, after each sub-interval, having started with the total fluence of j-type particles over the entire spectrum of particles in the radiation environment as a given input initial condition at the shielding boundary.

To evaluate the heavy ion transport set out in Equation 7.3, first complete the spatial and energy (x, E) transformation to spatial and range (x, r), as was done for

the light particles, by defining the scaled heavy ion fluence as:

$$\psi_j(x,r) \equiv \nu_j S_p(E)\phi_j(x,E)$$

and $\sigma_{jk}(E)$ is replaced with $\sigma_{jk}(r)$, as range and energy are convertible as previously shown, which results in a scaled transport equation for heavy ions which can be expressed in integral form as follows:

$$\begin{aligned}\psi_j(x,r) &= e^{-\beta_j(r,x)}\psi_j(0,r+\nu_j x) \\ &\quad + \sum_{k>j}\frac{\nu_j}{\nu_k}\int_0^x e^{-\beta_j(r,x')}\sigma_{jk}(r+\nu_j x')\psi_k(x-x',r-\nu_j x')dx'\end{aligned} \tag{7.7}$$

where the exponential integrating factor is $\beta_j(r,x) = \int_0^x \sigma_j(r+\nu_j t)dt$, and which employs ν_j instead of $\bar{\nu_j}$ as was done with the light particle equation, because here only heavy ions with $Z > 2$ are being transported, thus there is no need to account for the trivial scaling solution as all $\nu_j > 0$. [106] This equation is then rewritten in the form of a marching procedure for heavy ions in terms of step-size h as follows:

$$\begin{aligned}\psi_j(x+h,r) &= e^{-\beta_j(r,h)}\psi_j(x,r+\nu_j h) \\ &\quad + \sum_{k>j}\frac{\nu_j}{\nu_k}\int_0^h e^{-\beta_j(r,x')-\beta_k(r+\nu_j x',h-x')}\sigma_{jk}(r+\nu_j x') \\ &\quad \times \psi_k(x,r+\nu_j x'+\nu_k(h-x'))dx'\end{aligned} \tag{7.8}$$

where the new scaled fluence on the left hand side represents particles of type j at position $x+h$ with range r. This new scaled fluence is calculated from the terms on the right hand side of the equation: (1) the exponential term represents attenuation

due to nuclear absorption within a step-size h; (2) the current scaled fluence on the right hand side represents type j particles at position x with residual range $r + \nu_j h$, with the difference in range values representing the energy down shift caused by atomic interactions within the step-size h; and (3) the summation and integral terms represent production of the lighter j-type heavy ions from heavier k-type ions, along with nuclear absorption and atomic slowing down over the step-size h.

The numerical approximation of Equation 7.8 proceeds by (1) approximating the integral over x' from 0 to h by expanding the production cross section and scaled fluence in a Taylor series, neglecting all second order terms, and (2) approximating the integrals in the argument of the exponential functions in similar fashion by expanding in a Taylor series, and neglecting all second order terms. [211] This results in the final heavy ion transport marching procedure, as follows:

$$\begin{aligned}\psi_j(x+h,r) &= e^{-\beta_j(r,h)}\psi_j(x,r+\nu_j h) \\ &\quad + \sum_{k>j}\frac{\nu_j}{\nu_k}\sigma_{jk}(r+\nu_j h/2) \\ &\quad \times \psi_k(x,r+(\nu_j+\nu_k)h/2)\frac{e^{-\sigma_j(r+\nu_j h/2)h} - e^{-\sigma_k(r+(\nu_j+\nu_k)h/2)h}}{\sigma_k(r+(\nu_j+\nu_k)h/2) - \sigma_j(r+\nu_j h/2)}\end{aligned} \tag{7.9}$$

These approximations allow the integrals to be evaluated exactly, and thus the only numerical technique required to evaluate this Equation 7.9 is interpolation, using the same cubic Langrange interpolating polynomial that is used for the light particle calculations. [106] *See* Appendix A.5 for further details.

The Full Numerical Solution and Error Estimates

The GCR radiation environment is composed of protons, alpha particles and heavier ions with $Z > 2$, thus to simultaneously transport all of these particles through a

target medium, the light particle and heavy ion marching algorithms must be coupled. The complete coupled marching algorithm in HZETRN for the full GCR radiation environment is written as:

$$\begin{aligned}\psi_j(x+h,r_i) &= e^{-\sigma_j(r_i)h}\psi_j(x,r_i+\nu_j h) \\ &+ H(J-j)\sum_k \frac{\bar{\nu_j}}{\bar{\nu_k}} \sum_{m=1}^{N-1} e^{-\sigma_j(r_i)h/2-\sigma_k(r_m)h/2)} F_{jk}^{\nabla}(r_i,\bar{r_m}+\nu_j h/2);h) \\ &\times [\Psi_j(x,r_m+(\nu_j+\nu_k)h/2)-\Psi_j(x,r_{m+1}+(\nu_j+\nu_k)h/2)] \\ &+ \sum_{k>J^*} \frac{\nu_j}{\nu_k}\sigma_{jk}(r+\nu_j h/2) \\ &\times \psi_k(x,r+(\nu_j+\nu_k)h/2)\frac{e^{-\sigma_j(r+\nu_j h/2)h}-e^{-\sigma_k(r+(\nu_j+\nu_k)h/2)h}}{\sigma_k(r+(\nu_j+\nu_k)h/2)-\sigma_j(r+\nu_j h/2)}\end{aligned} \tag{7.10}$$

where the index J^* refers to the heaviest light ion (^{4}He), and the Heaviside function is defined as $H(J-j) \equiv 0$ if $j > J$, or 1 if $j \leq J$; and the lower limit of the last summation term is defined as $J^* \equiv j$ if $j > J$, or J if $j \leq J$. Thus, the physical interpretation is straightforward whereby the new scaled fluence at position $x+h$ with residual range (energy) r_i is calculated from the terms on the right hand side of the equation: (1) the exponential term represents attenuation due to nuclear absorption within a step-size h; (2) the current scaled fluence on the right hand side represents type j particles at position x with residual range $r_i+\nu_j h$, with the difference in range values representing the energy down shift caused by atomic interactions within the step-size h; (3) the double summation term is the source of light particles produced from light projectiles, and is only evaluated if the particle subscript j refers to a light particle; and (4) the single summation term is the source for both light and heavy particles produced from heavy ion projectiles (which is the coupling mechanism

between the light particle and heavy ion transport equations).

The total charged-particle field $\phi(x, E)$ is calculated at each step by sampling the interactive database of cross sections, and converting from the total flux $\psi(x, r)$ for all ions in succession to a flux as a function of depth into the target and kinetic energy, by calculating the appropriate stopping power ($S(E)$) for each ion, thus facilitating relating the total ion spectrum at some point x to that spectrum at a point $x + h$; and thereby enabling propagation of the ion spectrum from the boundary of the shielding material (at $x = 0$) to any interior point. [209] [208] The stopping power $S(E)$ is calculated using the Bethe-Bloch formula set out in Equation 3.5 (without the empirical correction factors) [209], except for low energies, where NASA uses empirical data called through a look-up table for better accuracy. [209] Once the ion spectrum is known at a particular point in the target medium, and recalling the definition of an ion's range as a function of energy noted above ($r(E)$), then the absorbed dose per unit mass (D) and dose equivalent (H) behind the shielding, can be calculated:

$$D(x, > E) = \int_E^\infty \psi(x, r(E))dE \qquad H(x, > E) = \int_E^\infty Q(E)\psi(x, r(E))dE$$

which are the metrics commonly used in shielding design studies for protection against GCRs. [96] [208]

NASA has reported on efforts to minimize the numerical error in its marching algorithm by testing various interpolation procedures related to the many iterative calculations requiring use of the internal energy and range grids, including calling the interactive database and look-up tables as a function of energy, and by varying the step size. The net result of this work was to initially settle on a step size up to $h = 1gm/cm^2$ for targets up to $150gm/cm^2$ total areal density, thereby optimizing

code efficiency, while obtaining an acceptable relative error to within 0.2%. [208] This criterion was later changed to $h_{max} \leq 0.5 gm/cm^2$ to minimize the error induced by the very short range of very low energy particles that would be missed with larger step sizes, with what NASA reports, but does not quantify, as an acceptable decrease in run efficiency. [211] NASA also took initial steps to attempt to validate the resulting deterministic HZETRN code against other transport codes, with what NASA reported as "mixed results" [96]; even recently acknowledging the wide disparity between HZETRN and MULASSIS results reported by Bernabeu [42], but without analysis as to possible reasons for the large differences.[1] [108] NASA then undertook to benchmark its numerical procedure for a single ion against a simplified analytical solution and against single-ion laboratory experiments, all at a single incident energy into an aluminum target, which confirmed the numerical procedure to within 2% at a step-size $h = 1 gm/cm^2$ with respect to the simplified analytical benchmark [96], and to within $\pm 5\%$ with respect to the laboratory single-beam experiments. [97] Nevertheless, NASA acknowledges that major uncertainties are introduced through the estimates of the thousands of cross sections used in the HZETRN interactive database, not to mention the underlying simplifying assumptions, including the one-dimensional approach and "straight-ahead" propagation of secondary emissions. As NASA concluded: "Taken together, they [these assumptions and biological impact models] could easily impose an uncertainty factor of 2 or more in exposure predictions." [96]

[1] In connection with the initial development of the marching algorithm in 1975, NASA conducted initial verification by using it to transport a single 1 GeV proton in water and found reasonable agreement in the calculated dose as compared to a Monte Carlo simulation of a proton. [212]. Some 40-years later, another study found encouragingly good agreement between HZETRN results and three-dimensional Monte Carlo simulations with the Geant4 code for a variety of GCR ions, but concluded: "This study demonstrates both the consistency and inconsistency among these transport models in their typical space radiation predictions; further studies will be required to pinpoint the exact physics modules in these models that cause the differences and thus may be improved." [142]

The Back-scatter Enhancement Effect in HZETRN

A recent enhancement to HZETRN to include the effect of back-scattered neutrons, which slightly modifies the "straight ahead assumption" fundamental to the code development, has important ramifications for shielding design. In particular, the consideration of these neutrons can have important consequences for dose equivalent calculations and related strutures and sensors, depending upon the type and amount of shielding material used. To investigate this back-scatter effect, we ran a series of simulations to explore how the effect on target geometric definition would induce different dose equivalent results, including by varying the data collection intervals within the target and by varying the thickness (i.e., areal density) of shielding designs under consideration.

Our results shown in Figure 7.8 indicate a wide disparity in calculated dose equivalent in aluminum at, for example, a depth of 20 gm/cm^2 of 0.17 mSv/day, or a 13% increase at that depth when the shield design is 100 gm/cm^2 as opposed to 50 gm/cm^2. We also ran simulations for other materials, as shown in Figure 7.8, where the difference in interior exposure rate is much less for when, for example, polyethylene is added to the interior of a shield design. These are important observations which have not been reported in terms of shielding evaluation, where equipment or sensors sensitive to radiation exposure are concerned, and in comparing or trying to replicate data in the literature.

For example, the calculations indicate that if additional shielding (or equipment racks or supplies, all of which will have areal densities) are mounted or placed on the interior wall of the ISS, then the radiation exposure rate at the wall and at the hull interior locations will increase, thus impacting any sensors or equipment sandwiched into interior locations. Thus, an additional 50 gm/cm^2 of effective aluminum shielding

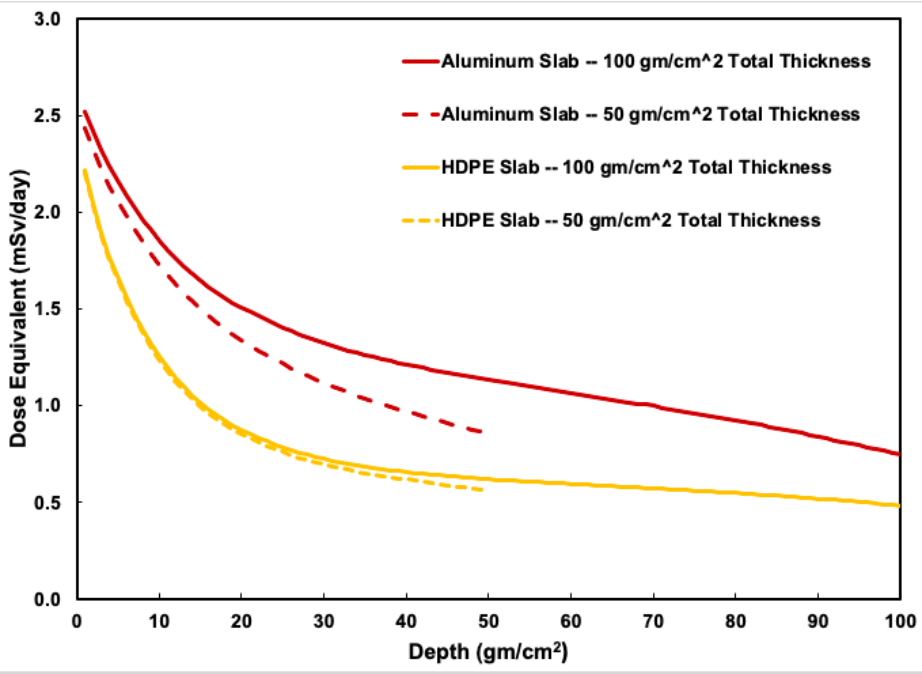

Figure 7.8 : Comparison of Dose Equivalent Results at interior points as Target Material Depth (Thickness) is varied, using HZETRN, Badhwar-O'Neill (BON) 2010 GCR Model (at 2010 Solar Minimum), and ICRP-60.

by additional material or other equipment causing the same areal density impact, will increase the dose equivalent rate at the 20 gm/cm^2 location by 13%, and even more if the initial wall location was at 50 gm/cm^2.

After discussions with NASA Langley representatives, it appears that these variations in interior results are due to back-scatter in one-dimension (along the x-axis) of secondary neutrons, a physics module feature that had been recently incorporated in HZETRN. This would make practical real-world sense in that a thicker shielding material will generate more back-scattered emissions (particularly neutrons with a very large range), and is also consistent with the fact that aluminum produces a larger secondary emission spectrum than polyethylene. Our results indicate that when comparing shielding designs of different areal densities that due consideration

be given to the back-scatter effect induced by shielding geometry input, particularly if intermediate dose metrics are important to the design.[2]

This natural phenomenon where incident radiation produces secondary emissions, some of which will back-scatter, which is now embedded in HZETRN as an exception to the "straight ahead" assumption, is important to consider during the shielding evaluation process. There are many practical implications to knowing how the dose equivalent exposure rate changes within the outer and inner boundaries of a shielding design as the design is modified, because sensitive equipment or materials are often placed in interior locations; e.g., computer chips or dosimeter measuring devices that would be negatively impacted by an increased radiation dose or in the case of sensors may alter their data output results. *See* Kodaira 2014 and Wilson 2005 regarding placement of dosimeters in Mir, the ISS, and the Shuttle spacecraft. [10] [97] This is particularly true in multilayer shielding designs, where an effort is made to "tune" the shielding to absorb various particles in particular layers of the shield. [171] Thus, we conducted additional simulation studies with the HZETRN code to analyze this phenomenon. First, the increase in dose equivalent over a range of depths within a shielding material as a function of adding more material to the inner boundary of the shield was examined, as shown in our Figure 7.9.

Figure 7.9a shows the dose equivalent metric we calculated in the 1 AU radiation environment, and Figure 7.9b is the same calculated metric in the LEO radiation environment at the ISS orbit (both shown with the same scale for comparative pur-

[2] Note that this consideration does not impact the analysis of our HZETRN results in previous sections of this thesis because care was taken to compare various shielding designs only with the same areal density; for example, when calibrating a shielding design evaluation model in the LEO radiation environment to obtain an ISS Baseline design number to be used for evaluating shielding in the 1 *AU* cis-lunar environment (as explained in Chapter 6), the same areal density shielding model should be used, a point we have made repeatedly in order to obtain comparable results.

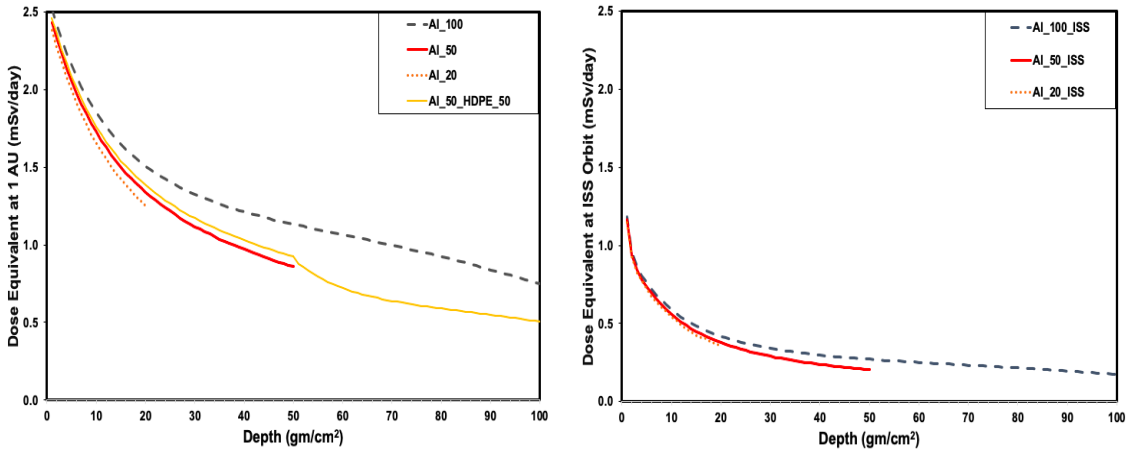

(a) Dose Equivalent at 1 AU. (b) Dose Equivalent at ISS Orbit.

Figure 7.9 : Calculated Dose Equivalent exposure rate changes at interior points as a function of total shielding thickness (using HZETRN with aluminum slab geometry and 2010 Badhwar-O'Neill GCR Model at 2010 Solar Minimum).

poses). The solid red curve in each figure is the dose equivalent for an aluminum slab geometry with a maximum thickness of 50 gm/cm^2, which is the standard model used in our research (note that the solid red curve in Figure 7.9b is the familiar "ISS Baseline" exposure rate calculated in Chapter 6). In both figures it is clear that the dose equivalent at interior points within the shielding increases as a function of total thickness of the shield model employed. The data indicate that the relative increase due to this back-scatter effect in the HZETRN transport code is essentially the same for both radiation environments over our shielding thickness range of interest. For example, our calculations show that the dose equivalent exposure rate at the 20 gm/cm^2 depth increases by 20.8% as the modelled shielding total thickness increases from 50 to 100 gm/cm^2 due to the back-scatter effect in the 1 AU environment, while the comparative percentage increase in the LEO ISS orbit radiation environment is 20.0%. Some difference is to be expected because the two radiation environments are composed of a different spectra of particles and kinetic energies, mostly in the

proton and neutron species. Even this small difference between the 1 *AU* and LEO environment can be eliminated in the shielding evaluation analysis of a single material if care is taken to use identical areal density geometries for the various shielding designs examined (i.e., *see* following discussion of the "scaling-up" error in Section 7.3). However, the fundamental point to be made here from a practical design standpoint is that by adding additional thickness to a given thickness of shielding – here aluminum – will increase the radiation exposure rate at the original interior point of the shielding barrier, and if this has negative impact on equipment and sensors located at that point, it may outweigh the perceived benefit of additional shielding.[3]

We found no effect in interior exposure rate results by changing data collection intervals, as might be done when evaluating thin layers of target material or in multilayer shielding designs, though it is noted that too large an interval between data collection points may cause missing some rapidly-changing nonlinear features in the results.

There are a few additional conclusions from our work shown in Figures 7.8 and 7.9 that have not been reported in the literature and are worth noting.

First, the back-scatter effect manifests itself slightly differently in multilayer shielding design configurations. The yellow solid curve in Figure 7.9a shows the back-scatter impact on dose equivalent by adding up to 50 gm/cm^2 of polyethelene (HDPE) to a 50 gm/cm^2 slab of aluminum (as compared to adding an additional 50 gm/cm^2 of

[3] As we mentioned previously in Chapter 6, as aluminum shielding gets thicker its effectiveness actually *decreases*, due to secondary neutron production, as demonstrated in a NASA study by Singleterry, et al. (2013). [196] This study found that aluminum dose equivalent rate starts to increase with thicknesses above 100 gm/cm^2, thus worsening the shielding effectiveness, until the exposure rate starts to decrease again slightly beyond 300 gm/cm^2. But this study was done with HZETRN employing a model shield thickness of 500 gm/cm^2, and the break-over point for a pure aluminum shield would change as a function of total modelled shielding thickness; i.e., as shown in Figure 7.8 no local minimum in dose equivalent for aluminum is detected with a 100 gm/cm^2 model.

aluminum), as shown by the grey dashed line. Here, our calculations show that the increase in dose equivalent at the 20 gm/cm^2 depth, due to the back-scatter effect in the 1 AU environment, increases by only 8.6% in two shielding models of identical total thickness of 100 gm/cm^2, because the additional thickness beyond 50 gm/cm^2 is HDPE rather than aluminum. This is consistent with the physics that HDPE has many fewer secondary emission particles than aluminum. It also highlights the need to include, in any shielding analysis, the material behind the shield; i.e., is it a human body, water supply, various equipment composed of heavier metallic components? Each will have a different back-scatter impact, and should be accounted for to ensure correct operation of equipment or sensors located in an interior point.[4]

Finally, we examined the change in the neutron flux and the dose equivalent exposure rate at various particular points within a shielding design (e.g., where sensitive equipment might be located) due to the back-scatter effect as a function of total shielding thickness. First we determined the neutron flux profiles at various points in a target medium of aluminum, as shown in our Figure 7.10. Figure 7.10a shows our calculations for the flux of neutrons at a depth of 20 gm/cm^2 in aluminum targets (or shields) ranging in thickness from 20 - 100 gm/cm^2; thus, 20 gm/cm^2 target flux is a baseline flux without back-scatter from the aluminum shield, while the thicker targets illustrate the increase in flux of neutrons due to back-scatter in the aluminum

[4] To account for the back-scatter effect, all materials should be included in the modelled analysis. Thus, if examining an aluminum shield, for example, but a thick metallic equipment rack is installed on the interior side, then that equipment rack should be included in the shielding analysis, as it may add protection to the interior space, but may also add radiation exposure levels to interior points in the shielding or to equipment mounted on the interior wall of the shield. This would also be true for other materials placed on the interior side of any shield, but materials like HDPE and water will obviously have lower secondary back-scatter emissions than heavier materials. In addition, if modelling the shielding for a habitat on the surface of the Moon or Mars, it will be important to include the Lunar or Martian soil at the floor of the model, as back-scatter particles will be emitted and impact the radiation environment on the interior of the habitat.

target at that depth as the shield material is increased. The results show a marked increase in the flux of back-scatter neutrons in the lower energy ranges below 100 MeV, which as discussed in Chapter 2 carry the highest radiation weighting factor. The same trend is shown in Figure 7.10b, where the two lower curves are flux calculations without neutron back-scatter from the target material, because the depth is at the extreme interior point of the shield, while the upper curve shows significant neutron back-scatter flux at the 50 gm/cm^2 depth with a 100 gm/cm^2 thick shield. Obviously, from a practical standpoint in shielding design, it will be important to try to minimize this back-scatter effect if the interior radiation exposure rates are of concern due to sensitive equipment or sensor locations.

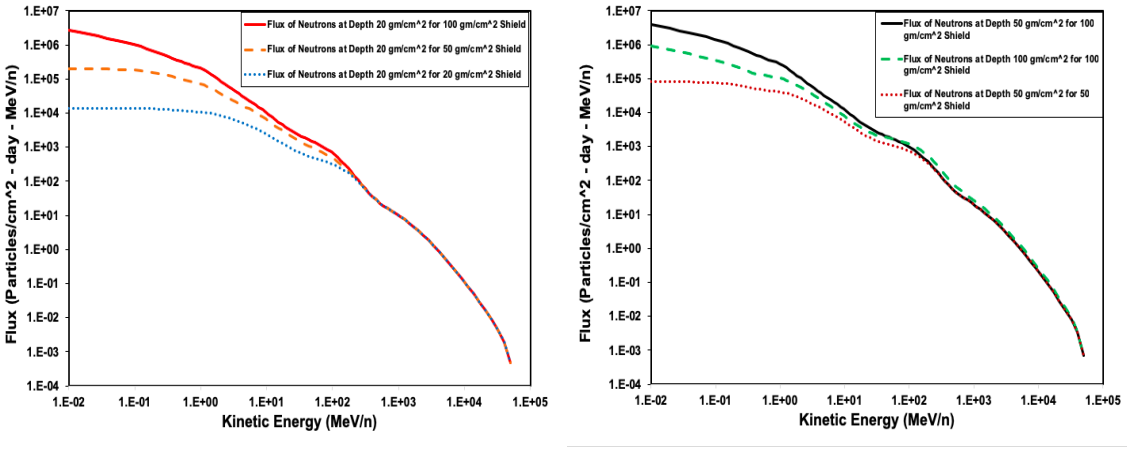

(a) Neutron Flux at 20 gm/cm^2. (b) Neutron Flux at 50 & 100 gm/cm^2.

Figure 7.10 : Neutron flux at particular interior points as a function of total shielding thickness (using HZETRN with aluminum slab geometry and 2010 Badhwar-O'Neill GCR Model at 2010 Solar Minimum in 1 AU environment).

In order to delineate the back-scatter effect we calculated the change in dose equivalent at a series of depths for total target thicknesses ranging from 10 - 100 gm/cm^2, as shown in our Figure 7.11. Our calculations shown in Figure 7.11a indicate that within our range of interest for aluminum shielding thickness (10 - 100 gm/cm^2) that the

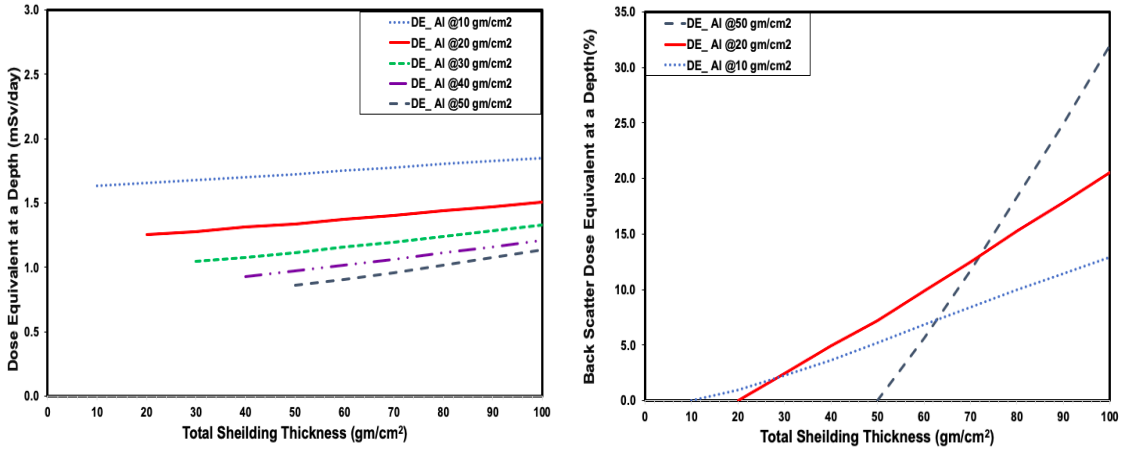

(a) Back-scatter effect at 1 AU. (b) Percentage of back-scatter.

Figure 7.11 : Calculated Dose Equivalent exposure rate changes at particular interior points as a function of total shielding thickness (using HZETRN with aluminum slab geometry and 2010 Badhwar-O'Neill GCR Model at 2010 Solar Minimum in 1 AU environment).

back-scatter effect at a particular interior point in the shield increases almost linearly within this narrow range of increasing total shielding thickness of a uniform material (here aluminum) in a constant (1 AU) radiation environment. This indicates that for each incremental increase in shield thickness beyond the point of measurement, that an equal increment of dose equivalent exposure rate is imparted by the back-scatter neutron spectra for the relatively thin target of interest here, which comports with the physical reality that neutron radiation has a very long range, as it is not slowed by the electron field as are ions. Figure 7.11b shows our calculation of the percentage of the dose equivalent exposure rate at a particular interior point attributable to back-scatter as a function of total shielding thickness. Thus, for example, if one were installing a sensitive probe of some kind at the 20 gm/cm^2 point within a shield design (the solid red curve), the radiation dose markedly increases at that point as more shielding material is added: with a total aluminum shield thickness of 20 gm/cm^2 in

the 1 AU environment the dose equivalent exposure rate at that interior point is 1.25 mSv/day, but the exposure rate at that point increases markedly if the total shield thickness is increased to 100 gm/cm^2 to 1.51 mSv/day, which is a 19.2% increase due to the back-scatter effect. Note also that the back-scatter effect as a percentage of total exposure rate decreases for shallower locations of probes or equipment; such that, for example, a probe placed at a 10 gm/cm^2 location will only experience a 12.8% increase in exposure rate due to the back-scatter effect by thickening the shield from 10 to 100 gm/cm^2, but of course it will have a higher overall exposure rate due to the primary incident radiation at its shallower location (i.e., for a 100 gm/cm^2 shield the overall exposure rate at the 10 gm/cm^2 interior location is 1.85 mSv/day, and 1.64 mSv/day at the 10 gm/cm^2 interior location). Depending on the thickness of the shielding and other equipment, one may consider finding an interior minimum radiation exposure location to place sensors or equipment, recognizing, of course, that it will change if the overall material thickness and composition of the hull and shielding changes at some future time.

Though the additional shielding material in these hypothetical examples is added to ostensibly further protect the interior of the spacecraft, the resulting increase in radiation dose in the interior portions of the shield may adversely impact the operation of equipment or sensors located at interior points, or at least alter sensor responses. Thus, the changes in dose rate caused by back-scatter need to be considered from many practical standpoints, in addition to ensuring that comparative geometries are used for over-all shielding design evaluation to achieve consistent and truly comparable results.

7.2.2 The MULASSIS Monte Carlo Code

The MULASSIS radiation transport code is based on a Monte Carlo approach, which solves the stochastic nature of radiation-matter interactions by tracking the evolution of a large number of particle histories from the incident GCR radiation spectrum as those particles undergo different possible interactions, and then calculates the statistical average behavior of the system. [128] While it is fairly common practice to employ a Monte Carlo approach to verify a deterministic numerical calculation, only one study has been reported in the literature (the "Bernabeu study"), which found good agreement between HZETRN and MULASSIS when using an SPE radiation source input, but poor agreement when using an isotropic GCR radiation source input (with MULASSIS under-predicting the dose equivalent metric by about half with respect to HZETRN). [42] We have examined the Bernabeu study published results and procedures, and have also run an additional set of comparative simulations with MULASSIS and HZETRN, and find a larger difference, which we conclude is due to MULASSIS running only three ions, instead of the GCR 59 ions run with HZETRN (plus back-scatter neutrons), a difference in the way the two codes calculate the dose and dose equivalent of the heavy ions in the GCR, and a difference resulting from the choice made in the way an isotropic GCR radiation spectrum is input to MULASSIS. Although we found the absolute value of the calculated dose equivalent metric very different between MULASSIS and HZETRN, we also confirmed that MULASSIS provides the same trends and comparative results regarding the efficacy of various shielding materials, and thus it is useful for shielding analysis on a comparative basis (as we discussed previously in Chapter 6). *See* our computed data using MULASSIS as compared to that in the Bernabeu study shown in Figure 6.12, and discussion in the accompanying text as to comparison with our HZETRN results.

The MULASSIS code is the result of work sponsored by the European Space Agency (ESA), and is an attempt to take portions of the three-dimensional Geant4 Monte Carlo code developed at CERN and create a one-dimensional version that runs more quickly on a simple slab geometry (i.e., simulation time reduced from days to minutes). [128] The research community has not been able to adequately verify the absolute value of the dose equivalent exposure rates for isotropic GCR radiation environments between MULASSIS and HZETRN, nor provide hard quantifiable conclusions as to the noted differences. Bernabeu, et al. (2007) commented on the wide difference in the GCR result as follows: "Discrepancies in dose equivalent values are probably due to the LET calculation procedure and to the fact that only protons, α particles and Fe ions have been simulated in MULASSIS, whereas HZETRN uses all HZE ions up to U." [42] NASA also commented on the wide disparity in dose equivalent calculations between MULASSIS and HZETRN in the Bernabeu study: "We note that differences between deterministic and Monte Carlo approaches tend to grow near the exit of the water column that may be caused by neutron (and lesser proton) leakage on the back surface that is not present in the current form of 2005 HZERN." [108] Neither response attempts to quantify the differences with any particular aspect of the two approaches to calculating dose equivalent.

Finally, there has been a reported study comparing a previous version of the HZETRN code (without neutron back-scatter implemented) and a three-dimensional Monte Carlo simulation of a slab geometry using the Geant4 code, which returned results that were within 10% for dose equivalent (as mentioned above), though the authors concluded that "further studies will be required to pinpoint the exact physics in these models that cause the differences and thus may be improved, verified and validated." [142] We concede (as does the developer of MULASSIS) that differences

in the physics modules in HZETRN and other codes will likely cause differences – perhaps 10% as found in the referenced study here, but that is a relatively small variation compared to the difference found in the Bernabeu study.[5]

We used MULASSIS in this research for limited purposes: (1) to see if we could replicate the Bernabeu results with respect to the relative GCR radiation shielding capability of various materials (which we did as discussed in Chapter 6, and further discuss below); (2) to conduct a comparative fluence analysis of secondary neutron emissions from various GCR ions behind various shielding materials; and (3) to evaluate the comparative impact of using different biological assessment models in calculating a dose equivalent rate behind various shielding materials, which could not be done with the HZETRN code. As our research efforts using MULASSIS were on a comparative basis only, and we had verified that MULASSIS correctly replicated shielding evaluation trend results as compared to our HZETRN analyses (as discussed in Chapter 6), we are confident in our conclusions drawn from that work.

As discussed previously in Section 4.3.3, a convergence study was completed with the MULASSIS code to determine an efficient number of particle histories to collect per simulation run and an adequate accuracy, in order to make comparisons with the HZETRN code without introducing significant additional error (*see* Figure 4.10). Each MULASSIS simulation can run only one ion type through a specific shield geometry to a particular depth at a time, with run times of over 15 minutes for one million particles, about 3 minutes for 100,000 particles, and about 30 - 60 seconds for 10,000 particles. Thus, to obtain data on even a simple shielding design at a

[5] In a private conversation with Dr. Pete Truscott, one of the developers of MULASSIS, he admitted to not having seen the Bernabeu study, but warned that MULASSIS (and Geant4) Monte Carlo codes use different physics modelling approaches than HZETRN, and while each code "has its advantages and disadvantages, they are very different."

specified GCR exposure, for a single material, at ten thickness variations, for only 3 ion types (e.g., hydrogen, helium, and iron), requires 30 separate simulation runs. For the purposes of the convergence study, a full series of million particle runs were made, and results compared to the same simulation runs for 100,000 particles and 10,000 particles. The absolute relative difference percentage in the calculated dose equivalent metric at 10,000 particles was 1.3%, as compared to that for 100,000 particles of 0.1%. The data for all three runs has a mean dose equivalent value of 0.182 Sv/yr (at a depth of 20 gm/cm^2 in an aluminum target exposed to a GCR radiation environment), with a standard deviation of 0.0015 Sv/yr, indicating a relatively small spread in the data. As a result, for test runs on a particular geometry and data collection intervals we used simulations of 10,000 particles, and for final data simulations running 100,000 particles was employed, which gave our final results an acceptable relative error of around 0.1%, deemed satisfactory for these comparative analyses between HZETRN and MULASSIS, where the differences are orders of magnitude greater.

We have analyzed the difference in dose equivalent results between MULASSIS and HZETRN from three perspectives: (1) unpacking the published data in the Bernabeu study, (2) running our own simulations with each code using the different GCR input spectra that are integrated with those codes, and (3) running our own simulations with each code, but modifying the input GCR spectra for MULASSIS to accept the same GCR model we used for HZETRN (the BON2010).

In the Bernabeu study, they purported to make simulation runs with HZETRN and MULASSIS, comparing calculated dose equivalent exposure rates behind aluminum using "a similar geometry setup and the same input fluences," including "SPE protons from the February 1956 event and GCR for 1 year fluence in solar minimum conditions (Wilson et al., 2006)." [42] The Bernabeu study found excellent agree-

ment between HZETRN and MULASSIS for the Solar Particle Event (SPE), but wide divergence with the GCR radiation input. Bernabeu's HZETRN GCR result was reported as a ratio of MULASSIS dose equivalent to HZETRN dose equivalent; thus we have separated out the HZETRN result from the reported ratio, and plotted the resulting data in our Figure 7.12 as the middle dotted line. In Figure 7.12 we have also plotted Bernabeu's MULASSIS result as the lower dashed line (which we replicated, *see* Figure 6.12), and our HZETRN result is plotted in the upper solid line (*see* Figure 6.10). Note, for example, at the 20 gm/cm^2 aluminum target thickness, that Bernabeu study results report a dose equivalent value of 0.51 mSv/day from MULASSIS, and 0.98 mSv/day from their HZETRN result; whereas our HZETRN calculations result in a dose equivalent at the same depth of 1.34 mSv/day. Thus, our result here is 2.6 times Bernabeu's MULASSIS result, and about 1.4 times Bernabeu's HZETRN result. However, we also point out that in the Bernabeu study GCR comparison results they are vague on precisely how they handled the GCR input: "In order to reproduce the scheme used by HZETRN, source particles were fired along the normal to the slab with no angular spread." [42] It is uncertain what this means; however, we note from our own testing that forcing the GCR spectra to a "parallel beam" configuration, rather than a randomly selected angular distribution befitting an isotropic radiation source, increases the deposited dose some four-fold, and thus results in a much higher dose equivalent value than obtained with HZETRN.

The top and bottom curves in Figure 7.12 were verified by our simulations to determine the dose equivalent exposure rate behind various thicknesses of aluminum with the ICRP-60 biological assessment model, using the MULASSIS code with the CREME96 GCR model at the 1977 solar minimum, as compared to the HZETRN code with the Badhwar-O'Neil 2010 GCR model at the 2010 solar minimum. As

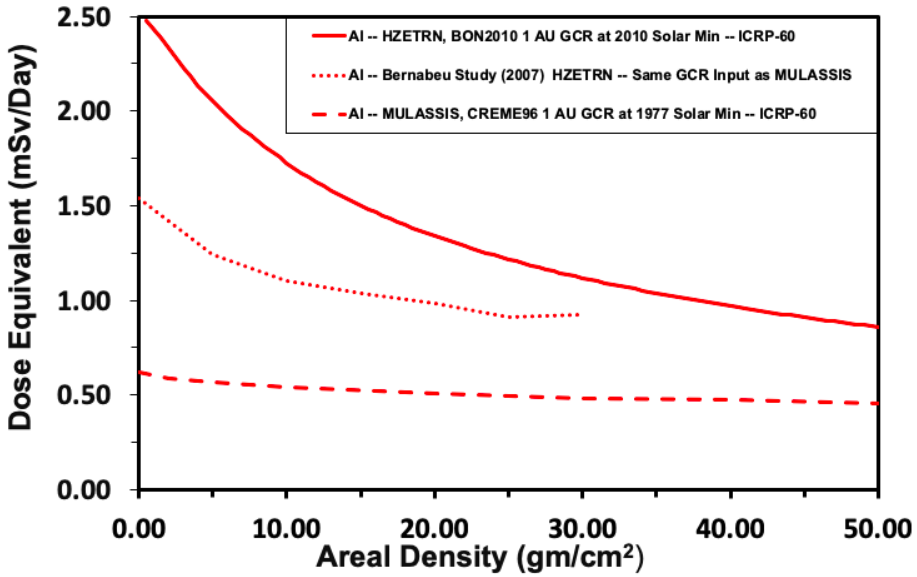

Figure 7.12 : Comparison of Dose Equivalent Results as between MULASSIS with the CREME96 GCR model (at 1977 solar minimum) and HZETRN with the Badhwar-O'Neill 2010 GCR Model (at 2010 Solar Minimum), and both using ICRP-60.

discussed previously, our MULASSIS results in this research were able to replicate those reported in the Bernabeu (2007) study [42], with the MULASSIS result some 0.83 mSv/day less than the HZETRN result at a depth of 20 gm/cm^2 of aluminum, or some 62% lower. The only external difference between the MULASSIS Monte Carlo dose equivalent calculation and the deterministic HZETRN numerical approach is that two different GCR models were employed (the two that are integrated with the respective codes). However, as we point out below, the different GCR model inputs do not cause the widely different results, because comparison of the two GCR models, which we illustrated in Figure 7.7, and the total integrated flux energy calculation we determined, as shown in Table 7.1, clearly indicates that the MULASSIS result should be higher due to the higher total flux energy in the CREME96 GCR model.

Finally, we ran additional test simulations with the MULASSIS code on a simple

aluminum slab geometry and compared to HZETRN results with the same geometry, utilizing for both the same GCR model – the Badwhar-O'Neill (BON2010) GCR model at the 2010 solar minimum. This was accomplished by manually inputting the GCR flux versus energy data for the hydrogen, helium, and iron ions from the BON2010 model, one at a time, into the MULASSIS radiation environment module, and then running each particle though sufficient simulations to determine the calculated dose equivalent exposure rate behind varying thicknesses of the aluminum shielding material.

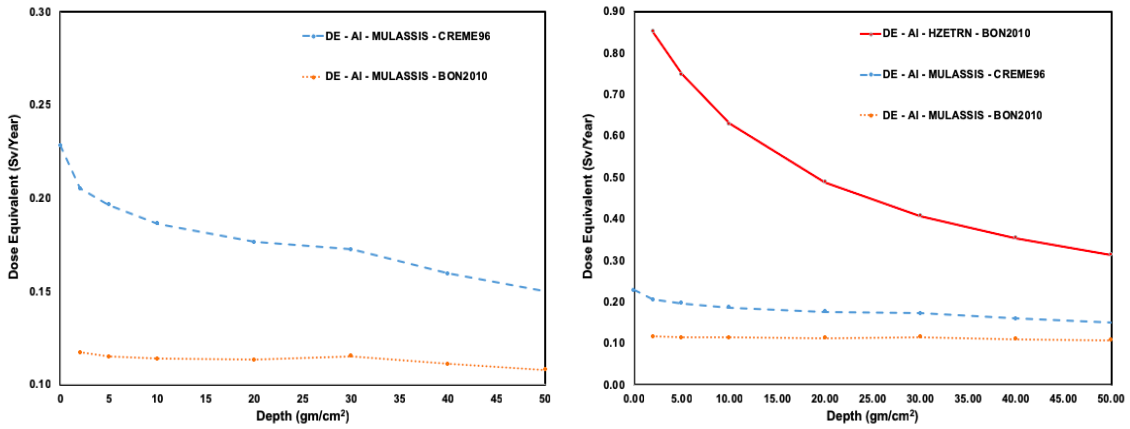

(a) MULASSIS GCR Comparison. (b) MULASSIS v. HZETRN Comparison.

Figure 7.13 : Calculated Dose Equivalent exposure rates comparing MULASSIS with HZETRN using the same aluminum slab geometry and same GCR Model: 2010 Badhwar-O'Neill (at 2010 Solar Minimum).

As we show in Figure 7.13a, the top line shows our calculated dose equivalent using the MULASSIS code with the original CREME96 GCR model at the 1977 solar minimum, which replicated the Bernabeu study results (same data and scale as shown in Figure 6.12b); and as anticipated from the earlier discussion in this section, the BON2010 GCR model gives a lower calculated dose equivalent. This is in part due to the higher flux of ions in the energy range below 50 MeV/n in the

CREME96 GCR model, as shown in our Figure 7.7. Figure 7.13b shows the large discrepancy between the calculated dose equivalent using HZETRN as compared to MULASSIS, as previously discussed, and illustrates that the discrepancy is even larger when both transport codes use the same GCR model, the BON2010 – with a difference at 20 gm/cm^2 of aluminum of about 0.376 $Sv/year$, or about four times higher using HZETRN on an absolute value basis.

One obvious explanation for the large difference using the BON2010 GCR model is that with MULASSIS we are transporting only three ions, whereas HZETRN transports 59 ions. But this is not the full explanation, because MULASSIS and HZETRN also differ in the way the deposited dose in the target material (LET) is calculated for the various ions, which of course propagates directly to the dose equivalent calculation after scaling with the biological assessment model. For example, our calculations using the BON2010 GCR model in both MULASSIS and HZETRN indicate that MULASSIS under-estimates the contribution of the heavier iron ion, when compared to the HZETRN result, as shown in Table 7.2.

Contribution to Dose Equivalent

Ion Type	MULASSIS (%)	HZETRN (%)
Hydrogen - H	72.8	49.0
Helium - He	27.0	35.0
Iron - Fe	0.02	15.0

Table 7.2 : Comparison of percentage contribution to calculated dose equivalent as between three primary GCR ions for MULASSIS and HZETRN, at 20 gm/cm^2 depth in an aluminum target (using Badhwar-O'Neill BON2010 GCR Models at 2010 Solar Minimum and ICRP-60).

The MULASSIS results do not conform to what is expected from the physics: at

relatively shallow depths in the target one expects the heavier ions to have a relatively more significant contribution to dose (LET) and dose equivalent due to their relatively shorter range than the lighter ions, particularly hydrogen. But our calculations show that at 20 gm/cm^2 into an aluminum target that MULASSIS predicts hydrogen ions as dominating the dose equivalent calculation, while HZETRN is much less.

Our data indicates that both models predict larger contributions by the iron ion at shallower depths in the aluminum target, as expected considering the physics and the shorter range of the iron ions; e.g., at 2 gm/cm^2 into an aluminum target with the same simulations as done for Table 7.2, MULASSIS indicates the Fe ion contributes 0.1% to the dose equivalent calculation, whereas HZETRN indicates the Fe ion contributes 50.5% at that depth (as between those three ions: H, He, and Fe). While the trend is the same with both transport models, HZETRN is more in line with what is expected from the physics, as shown in Figure 2.12 (large relative contribution of heavier GCR ions to dose equivalent metric), and the discussion on this issue by Durante, et al.[6] [38] This is further illustrated in Figure 7.14.

In our Figure 7.14a we show the calculated percentage contribution to the total dose equivalent exposure rate in aluminum from GCR hydrogen, helium, and all heavier ions grouped together, for both HZETRN (solid lines) and MULASSIS (dashed lines). Clearly the MULASSIS results show a dramatically lower percent contribution from all heavier ions, which would dramatically reduce the total dose equivalent value (particularly since the heavier ions all carry the high weighting factor under ICRP-60). Moreover, it is clear from Figure 7.14b that the range of primary GCR iron ions

[6] NASA studies agree: "Of particular importance are the HZE particles with their large LET and associated quality factors providing large contributions to dose equivalent. For example, the Fe ions of the galactic cosmic rays are known to contribute about one third of the total dose equivalent inside [certain] space structures." [97]

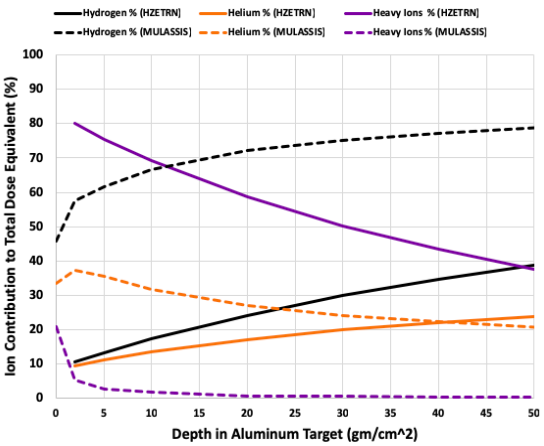

(a) HZETRN & MULASSIS Comparison.

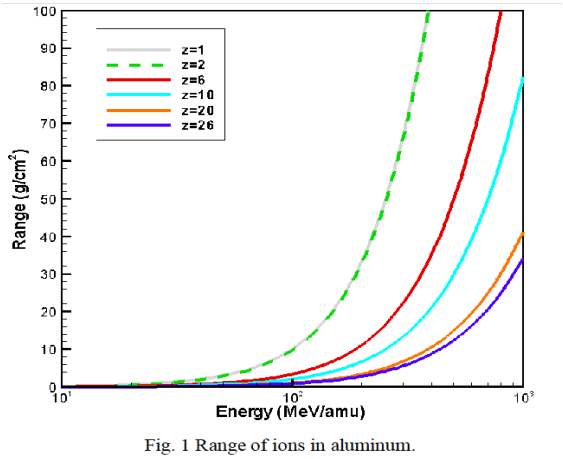

Fig. 1 Range of ions in aluminum.

(b) Range of Ions in Aluminum.

Figure 7.14 : (a) GCR Ion Contribution to Total Dose Equivalent exposure rates comparing MULASSIS with HZETRN with an aluminum slab geometry (2010 Badhwar-O'Neill (at 2010 Solar Minimum), and ICRP-60); (b) Range of Ions in Aluminum as a Function of Kinetic Energy, from Wilson, et al. (2005).

of mid-level energy (1 GeV/n)) would have a range in aluminum of some 30 gm/cm^2, where they would deposit their maximum energy. [97] This fact is not consistent with the calculated MULASSIS contribution of all heavier ions to dose equivalent in the low single-digit percentage points as shallow as 10 gm/cm^2, and thus raises doubt as to the proper functioning of the physics packages for the GCR section of the code.

Though Bernabeu, et al. did not expressly comment on this issue, or publish any data, it is likely this is what they were alluding to when commenting on the large discrepancy between MULASSIS and HZETRN for GCR dose equivalent calculations when they said: "Although protons and alphas account for 98% of the total fluence, the high LET of the heavy ions not included in MULASSIS runs can represent an important contribution to the dose equivalent." The problem is not only that one transports only the three main GCR ions when running MULASSIS simulations, but

the LET calculation for the heavier ions in MULASSIS is also a contributing factor.[7]

One way to approximate a corrected dose equivalent calculation for MULASSIS (external to the code itself) is to simply ratio-up the calculated dose equivalent to account for the 56 ions not run in a typical MULASSIS simulation, using the relative contribution of iron ions as calculated by HZETRN as a proxy for all heavy ions (an approximation that is based on the relative fluence of heavy ions in the GCR, as we showed in Section 6.1). While the three ions considered with MULASSIS (H, He, and Fe) account for the bulk of the flux in the GCR, the high LET of the heavy ions ($Z > 2$) not included in MULASSIS simulation runs undoubtedly represent an important contribution to the dose equivalent. To test this, we ran a series of HZETRN calculations with the BON2010 model impinging an aluminum target, which indicated that these three ions (H, He, and Fe) account for only 40% to 64% of the total calculated dose equivalent, depending on depth into the aluminum target medium (the three ions account for 40.3% of the total dose equivalent at a depth of 2 gm/cm^2, and 63.9% at a depth of 50 gm/cm^2, with protons dominating at the deeper depth due to their longer range); e.g., at 20 gm/cm^2 of an aluminum target, those three ions account for 49% of the total dose equivalent. Thus, if one were to double the MULASSIS dose equivalent result at that depth using the BON2010 GCR model to account for the contribution of the 56 missing heavy ions, the result would be 0.226 Sv/yr, still only about 46% of the HZETRN result, but in the right

[7] One contributing factor may be the way in which the physics packages (from the 3D Geant4) are implemented in the 1D MULASSIS for these simulations; and they are different for the SPE and GCR radiation environment inputs. The Low Energy electromagnetic (LEEM) processes are used for SPE cases and Standard Electromagnetics (EM) for GCR calculations. [42] This is an issue to investigate possibly involving the internal MULASSIS code that may partially explain the calculated low ratio impact for the iron ions on the calculated dose equivalent metric, particularly at the shallower depths in the target medium, shown in Table 7.2, which also causes the flatter curves for our MULASSIS calculations shown in Figure 6.12 at the shallower depths, as compared to our HZETRN calculations in Figure 6.10.

direction. An alternate approach is to use the BON2010 value from MULASSIS (from Figure 7.13b), remove the iron ion contribution, and then weight the respective light and heavier ions in accordance with the HZETRN calculated percentages, as shown in Figure 7.14a, which would give an adjusted approximation of 0.234 Sv/yr.[8] Either method gives approximately the same result and would be a justified adjustment for the limited purpose of demonstrating the impact of the number of ions and heavy ion weighting issues, since the LET bears a direct relationship to calculated dose equivalent, and under both biological assessment models the heavy ions are treated equally in terms of weighting or quality factor (*see* Chapter 2).

Another modelling choice that could account for the remaining large discrepancy between MULASSIS and HZETRN results for GCR inputs, is in the way MULASSIS allows a choice of particle flux beam orientation from a "cosine law" angular distribution or a parallel beam, and how that input flux is chosen to be adjusted from the GCR model output to conform to units necessary as an input to the MULASSIS transport code. We replicated the main features of the Bernabeu study by using the "cosine law" beam orientation method at the broadest angular distribution, and we also ran test simulations with the parallel beam incident flux, which resulted in a 4-fold higher dose calculation, which would provide even much higher dose equivalent results than we obtained with HZETRN.[9] Thus, we conclude that the "cosine law"

[8] The calculated dose equivalent at 20 gm/cm^2 in aluminum for MULASSIS using the BON2010 GCR model is 0.113 Sv/yr, as shown in Figure 7.13b, running only H, He, and Fe ions. Assuming the iron is 15% of this value under our HZETRN ion contribution calculations, as shoen in Table 7.2, then the hydrogen and helium contribution is 0.09605 Sv/yr, which we calculate should be 41% of the total dose equivalent value at the 20 $gm.cm^2$ depth, as shown in Figure 7.14a. Thus, all heavy ions should account for 59%, or 0.1382 Sv/yr, and the total is 0.234 Sv/yr – still short of our HZETRN calculation of 0.489 Sv/yr, shown in Figure 7.13b.

[9] The Bernabeu study noted that comparing "cosine law" incident beams with "normal" incident beams resulted in a four to five fold lesser dose deposition in the target using the "cosine law" beam option [42], which is similar to our results comparing the "cosine law" and "parallel" beam options.

beam orientation option is the correct input method, and it also is consistent with the physics of inputting the isotropic GCR spectra to the one-dimensional slab geometry (i.e., in the random selection procedure employed by the Monte Carlo method, it makes physical sense to allow GCR ions to arrive at the face of the slab geometry at the full multitude of angles facing the radiation environment, rather than having all ion beams perpendicular to the face of the slab).

However, the GCR input data was converted from an isotropic fluence to a one-dimensional approximation by dividing the GCR model fluence by 4π steradians, and by doing so we were able to replicate the GCR results in the Bernabeu study with respect to both the shielding effectiveness of various materials and the calculated dose equivalent metric.[10] But recalling that the Bernabeu study found that the two approaches (MULASSIS and HZETRN) were in close agreement when dealing with an SPE radiation input, but not with a GCR flux input, indicates that this conversion factor from the GCR model output to the MULASSIS one-dimensional GCR fluence input should be 2π steradians, as an alternative boundary condition, so that the full radiation field facing the slab geometry is preserved. An SPE is not an isotropic source, but rather is emitted by the Sun and travels as an impulse particle field radially outward along magnetic field lines, as discussed in Section 2.1. We note that the MULASSIS code radiation field inputs, which are separate for SPEs and GCRs, handle the SPE input differently than the GCR input, calling

[10] We followed the Bernabeu, et al. procedures as to both use of the "cosine law" beam option and the recommended conversion factor to the GCR model output, before inputting it into MULASSIS, and by doing so replicated their results with respect to the sheilding effectiveness of various materials in a GCR environment and as to calculated values of the dose equivalent metric. [42] This method of converting the GCR isotropic spectra relied upon a 1986 approximation for a simple procedure to transform depth-dose results for slab targets into spatial distributions of absorbed dose within spherical targets [213], done well before MULASSIS was conceived, and therefore, may not be compatible with the internal MULASSIS code, which was transforming the Geant4 three-dimensional structure into a one-dimensional model.

for a "point source" fluence input, rather than a particle beam option. If this 2π correction option is made to the GCR fluence input to MULASSIS (rather than 4π), it essentially doubles the fluence, but maintains the same GCR spectra with respect to energy distribution; therefore the total integrated kinetic energy of the input radiation environment will double. The impact on the dose equivalent metric as a function of total kinetic energy in the GCR field (maintaining a constant ion species distribution) was previously calculated and shown in our Figure 7.2 in comparing dose equivalent calculations at "solar min" versus "solar max" conditions with GCR spectra of similar species distribution, but diminished total integrated energy. In those calculations, we determined that a 53% reduction in the total integrated kinetic energy of a GCR spectrum would result in a dose equivalent metric reduction of 50% and 45% at 5 and 20 gm/cm^2, respectively, in an aluminum target. Thus, in round numbers, adjusting the GCR input fluence by a factor of 2 to MULASSIS, as we suggest, would double the total integrated kinetic energy (since the species spectra distribution is kept constant with respect to energy), and would result in approximately doubling the dose equivalent metric. In that case, the previously adjusted (for number and weight of heavy ions) MULASSIS result would double to return a 0.452 Sv/yr calculated dose equivalent, which is within 8% of our HZETRN result with the same BON2010 GCR model.

Undoubtedly, as both Bernabeu, et al. and NASA surmise, and the developer of MULASSIS confirms, the two transport codes (MULASSIS and HZETRN) utilize different internal physics models that contribute to the different dose equivalent calculations. But our analysis indicates that most of the difference in absolute value of the calculated dose equivalent metric results from (1) not running all 59 ions in both codes, (2) the under-valuing of the dose equivalent contribution of heavier ions

by MULASSIS, and (3) the GCR fluence input conversion factor. The LET calculation for heavier ions, which are much lower in MULASSIS, may be a "physics model" difference, and is subsumed within the first correction approximation as we demonstrated above. However, we note that there is some evidence that the physics models have been shown to be relatively close (within 10%) in the 3D Geant4 Monte Carlo comparison study to HZETRN previously discussed [142], though they may not function in the same manner when applied to the 1D MULASSIS GCR set up. Thus, with respect to the isotropic GCR environment, we recommend using MULASSIS only for evaluation of the types of comparative analyses with other MULASSIS simulations we performed in our research, which adequately confirmed, in trend, the GCR fluence and relative shielding effectiveness studies done with HZETRN; but, MULASSIS results concerning how it calculates LET values for heavier ions is a serious point of concern and deserves further study. On balance, HZETRN is much faster and easier to use for initial comparative shielding evaluations, and when calibrated to actual ISS exposure data, as we suggest in Chapter 6, can improve assessment of shielding designs in the 1 *AU* radiation environment. Thus, as mentioned previously, these results simply underscore the need to evaluate shielding designs on a strictly comparable modelling basis.

7.3 The Biological Assessment Models

In Sections 2.3 and 4.3.1, and the discussion associated with Figure 2.11, the wide difference in calculated dose equivalent was demonstrated with an identical shielding evaluation model set up, but changing only the ICRP-60 and ICRP-103 biological assessment models. The dose equivalent difference determined with the MULASSIS code simulations was on the order of a 45% increase in the dose equivalent calculation

using ICRP-60, over the newer ICRP-103 model. The comparison could not be done with the HZETRN code, as it has embedded in its calculations the older ICRP-60 model. These widely disparate results obviously inject an uncertainty on the order of a factor of 2 into the dose equivalent calculated result, which would likely impact the HZETRN code on a similar basis and magnitude as the MULASSIS code, as both ICRP models are merely scaling factors applied to the calculated absorbed dose for each ion or neutron in order to estimate ultimate biological harm.

This large uncertainty injected into the shielding evaluation modelling scheme, without any human medical data to verify it, obviously casts doubt on the calculated dose equivalent metric as a "true value." This state of affairs is admitted by NASA in noting that while "great progress has been made in developing codes for space shielding ... [i]t is likewise clear that major uncertainties remain in the environmental model, the nuclear cross sections, and the methods for estimating biological risk." [96] It was precisely this biological assessment uncertainty that guided our research effort to calibrate the HZETRN model results to the radiation environment experienced on the International Space Station, where long-term radiation exposure medical data has been, and continues to be, collected and assessed on a large number of astronauts, as previously discussed in Section 6.1.

The work in calibrating the HZETRN calculated results in the ISS LEO radiation environment involved adjusting the effective shielding thickness for the ISS in order that the calculated dose equivalent equaled the dose equivalent as measured from radiation exposure data from "crew passive dosimeters" inside the ISS travelling in the same radiation environment as utilized in the modelling set up. Then that calibrated "ISS Baseline" exposure rate model is used to evaluate shielding with a 1 *AU* GCR radiation environment input; i.e., every model element stays the same except for

the radiation environment. The NISS number metric introduced in Chapter 6 is the ratio between the dose equivalent calculation in the calibrated LEO environment as compared to that in the 1 *AU* GCR radiation environment. Thus, the NISS number approaches 1.0 as the shielding design in the 1 *AU* environment comes closer to replicating the internal ISS radiation environment, where there is medical data that will better aid in assessing ultimate long-term radiation hazard risks.

The ISS Baseline and NISS number approach has at least two sources of uncertainty in calibrating the shielding evaluation model to the true radiation exposure data: (1) dosimeter errors and uncertainties due to instrument measurement errors, uncertainty involved in conversion of dosimeter data to an equivalent dose equivalent rate, and variations in the internal ISS radiation environment induced by the ISS altitude variation, the modulation of the GCR by solar activity, and any stochastic events, such as SPEs or relative location of the astronaut within the ISS with corresponding effective shielding changes; and (2) uncertainty in the HZETRN dose equivalent calculation at a relatively low radiation input level in the LEO environment as compared to the 1 *AU* radiation environment.

The errors and uncertainties regarding the dosimeter measurements, and the related things noted above in item (1), were discussed, but not quantified, in connection with reporting the NASA data used in this research to illustrate how the ISS Baseline metric works [194]. The critical aspect to those items measuring the radiation exposure experienced inside the ISS is in ensuring that the measurements are consistently done in a standardized way so that meaningful correlations to health outcomes can be assessed, which is the ultimate objective. Of course, as additional dosimeter data is collected in order to better tie the dosimeter measurements to a consistent measurement of the radiation exposure, such can be used to better calibrate the shielding

evaluation models.

As to the second source of uncertainty, a comparison of how the HZETRN model calculates the dose equivalent behind a standard aluminum target material with varying GCR inputs is instructive, part of which we discussed previously in Section 7.1, and specifically in the text relating to Figure 7.2, Figure 7.5, and Table 7.1.

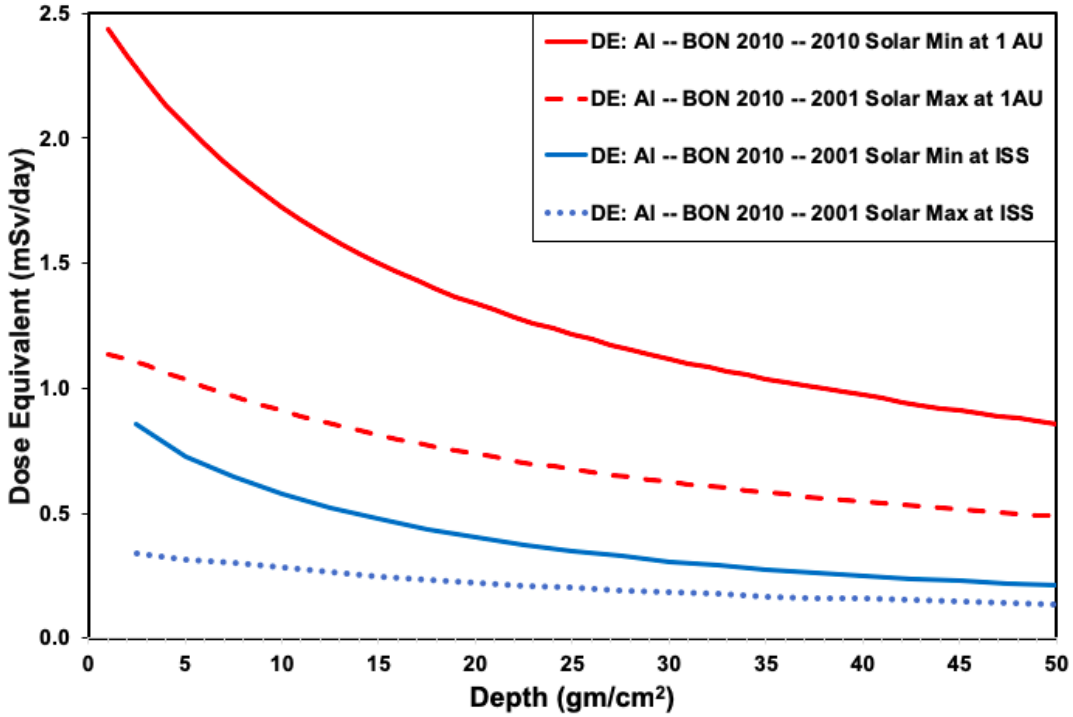

Figure 7.15 : Dose Equivalent Comparison behind Aluminum Shielding Material for 1 *AU* and ISS Orbit Radiation Environments, using 2010 Badhwar-O'Neill GCR Model (at both "solar min and max") with ICRP-60 Biological Weighting Factors.

To extend our previous analysis, our Figure 7.15 shows the calculated dose equivalent behind various thicknesses of aluminum for four radiation environments generated with the same GCR model (BON 2010): the 1 *AU* cis-lunar GCR environment at both solar minimum and maximum, and the LEO ISS orbit radiation environment at both solar minimum and maximum. As can be seen, the calculated dose equivalent is

generally in the same proportion beyond a shielding target thickness of 20 gm/cm^2, which is the minimum depth (or thickness) of spacecraft shielding anticipated with current materials for operations in the cis-lunar region. The question we now examine is: What error is injected into the shielding evaluation model as the radiation environment input spectrum is "scaled up" from LEO to 1 AU?

Spectrum Energy Contrast

Radiation Environment	Total Kinetic Energy ($MeV \times 10^6/day$)	DE - Al-5 (mSv/day)	DE - Al-20 (mSv/day)
BON 2010 (Solar Min)	4.99	2.05	1.34
BON 2010 (Solar Max)	2.39	1.03	0.74
LEO ISS Orbit (Solar Min)	1.42	0.73	0.41
LEO ISS Orbit (Solar Max)	0.81	0.32	0.22

Table 7.3 : Total Calculated Kinetic Energy and Resulting Calculated Dose Equivalent for Various Radiation Environments at 1 AU and ISS Orbit, behind Aluminum shielding of 5 gm/cm^2 and 20 gm/cm^2 areal densities (Al-5 and Al-20), using HZETRN with Badhwar-O'Neill BON 2010, and ICRP-60.

To illustrate how the HZETRN model "scales up," we calculated the total integrated kinetic energy for each radiation environment and compared that to our calculated dose equivalent behind shielding at specified depths, as shown in our Table 7.3, with the results plotted on our Figure 7.16. In Figure 7.16 we have plotted the data set out in Table 7.3 as the solid round and triangular markers (the top set of round points denote the dose equivalent in an aluminum target at 5 gm/cm^2, and the triangular points are for the same target at a depth of 20 gm/cm^2), connected by solid lines; whereas the dotted lines are a simple linear regression of those respective data points. The data indicates that the HZETRN code dose equivalent calculation scales-up generally in a linear fashion with respect to total spectrum energy behind a

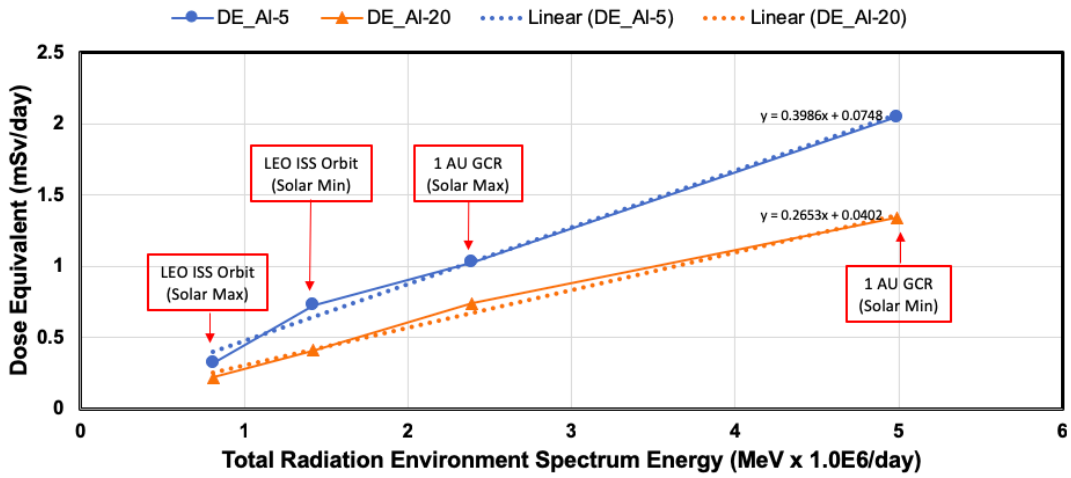

Figure 7.16 : Calculated Dose Equivalent Variation as a Function of Radiation Environment Total Spectrum Energy, for 1 *AU* and ISS Orbit, using 2010 Badhwar-O'Neill GCR Model with ICRP-60 Biological Weighting Factors.

shielding of a specific areal density. This is to be expected as long as the ion species and ion flux energy distribution and spectral shape all remain the same, and only the total spectrum energy is changed. Of course, that is not precisely the situation, especially as between the 1 *AU* radiation environment and that in LEO in the ISS orbit. As shown in Figure 6.4, the lower energy GCR ions are cut off by the magnetosphere, and, in addition, the LEO environment has a population of albedo neutrons, and there is also a high flux of relatively low energy protons that impact the ISS when it traverses the South Atlantic Anomaly (SAA) of the lower Van Allen belt.[11] Thus, the LEO radiation environment has a slightly different species and energy distribu-

[11] For the calculation of the total energy spectrum in LEO, only protons with energies greater than 200 MeV are included, as protons below that energy level are stopped by the ISS effective 20 gm/cm^2 aluminum shielding (e.g., *see* Figure 3.6). In addition, ISS astronauts do not pass through the SAA very often because the precession of the ISS orbit from east to west is at a rate of about 4 degrees per day (depending on its altitude and orbital eccentricity). Thus, the ISS travels through the SAA only once every 3 months, and precesses through it in about 2-3 orbits, during which the ISS is in the SAA for only a few minutes on each of those orbits. Reference: MECH 592 orbital mechanics notes and private conversation with Dr. Leroy Chiao.

tion than the GCR spectrum in cis-lunar space. As a result of the different radiation weighting factors involved in converting an absorbed dose into a dose equivalent metric, the HZETRN model will not scale-up precisely linearly from the LEO to 1 AU radiation environments. However, the error appears small, as shown in Figure 7.16. One would expect the true value of calculated dose equivalent to be zero in a zero-energy environment, yet the least-squares approximation misses the zero-intercept by 0.04 - 0.07 mSv/day (approximately 5% for estimates projected to the 1 AU solar minimum environment). In addition, the linear fit to the dose equivalent data calculated from the total spectrum energy has a standard deviation of the errors for DE_{Al-5} of 0.07 mSv/day, and for DE_{Al-20} of 0.05 mSv/day; again, in the range of 5% from the value calculated by HZETRN.

Finally, the scaled-up calculated dose equivalent in the 1 AU environment incurs a relative error from 0.3% to 7.3% from that determined by HZETRN, depending on shielding thickness and the specific 1 AU condition, with scaling up to solar minimum conditions exhibiting less than a 2% error, regardless of the shielding thickness. Thus, for design purposes, scaling the HZETRN dose equivalent calculations from the LEO environment (which are calibrated to actual ISS exposure data) to the 1 AU radiation environment introduces only a relatively small uncertainty in the dose equivalent determination, in the range of 5%, particularly since design considerations should logically be based on solar minimum conditions (i.e., maximum GCR flux).[12]

[12]It is important to bear in mind that the ISS Baseline procedure and "scaling-up" error have been demonstrated here using a simple slab geometry, and at a specified internal radiation exposure objective of 0.41 mSv/day. These criteria can be changed, of course; e.q., one may want to decrease the radiation exposure "safety factor" as discussed previously, or one may want to change the geometry, and, for example, use a spherical geometry to better replicate a spacecraft. These changes could be made, but it woud be important in that event to re-calibrate the shielding evaluation model and also to re-calibrate the error determination procedure using the same geometry.

7.4 Summary of the Total Uncertainty Analysis

In determining the total error in a model or a system, one would normally calculate the "root-sum-square" of all of the contributing errors; i.e., the square root of the sum of the uncertainties introduced in each stage of the model or system. [214] However, that is not so easily done here because the ultimate uncertainty is the health impact from various radiation environments. Thus, NASA and others have suggested that the uncertainty in GCR models is ±10% [38], and that such propagates to an uncertainty in dose equivalent calculations of ±20%. [140] But the biological assessment models are unverified, and even NASA admits the shielding evaluation tools could easily be off by a factor of 2 or more in terms of providing an accurate dose equivalent result that correlates with human radiation risk, and perhaps propagate "an order of magnitude uncertainty in shield mass requirements." [96]

Our research adds a new metric to consider in shielding design that is calibrated to actual long-term human radiation exposure data on the ISS, from which human medical histories will eventually correlate the radiation exposure to verifiable radiation risk assessment, and has only a relatively small inherent uncertainty in scaling-up to the 1 AU radiation environment, in the range of 5% of the calculated dose equivalent in the 1 AU radiation environment. It is of practical importance to reduce the error in the calculated dose equivalent behind shielding, particularly as the sensitivity in shielding thickness increases markedly with respect to dose equivalent as the thickness increases, as is shown in Figure 7.15. Thus, for example, at 1 AU during solar minimum conditions, for aluminum in the range of 20 gm/cm^2, a 10% error in dose equivalent will propagate to an error of 5 gm/cm^2 in required thickness (or 25%), while a 20% error in dose equivalent will induce an error of 12 gm/cm^2 in required

thickness (or 60%); and it gets worse as the shielding material increases in thickness.[13] Thus, for this example for aluminum, the difference in actual thickness required in order to accommodate the error band at the higher error in dose equivalent (20%) versus an assessment method with lower error (10%) would be some 7 gm/cm^2 or about 2.6 *inches* (which translates to a 35% improvement in thickness accuracy, and thus mass accuracy). Similarly, if the error in dose equivalent assessment could be reduced to 5% by the use of the proposed new metric presented in our research, then in the 20 gm/cm^2 thickness range for aluminum, the induced error in thickness (and mass) required would be reduced to 3 gm/cm^2, or about 15%.

The proposed new radiation shielding evaluation metric maintains the ICRP-60 scaling differentiation of biological damage for different radiation species, but neutralizes the uncertainty in using those weighting factors directly to predict biological damage by calibrating the LEO/ISS HZETRN calculation to actual exposure data, and then scaling it up to a calculated 1 *AU* environment by using precisely the same model, except for the GCR input to HZETRN; thereby making the calibrated ISS Baseline dose equivalent exposure rate a verifiable design objective for the 1 *AU* radiation environment in terms of more accurately predicting the health risk for the future contemplated space voyages. If the ISS Baseline is the design objective for

[13] These calculations over short perturbations in assumed error in the range of 20 gm/cm^2 for the calculated dose equivalent are close to linear with respect to depth (i.e., thickness). For more accuracy over the full range of depths in the aluminum target, one may also conveniently estimate the error induced in thickness accuracy by errors in dose equivalent by using a close approximation to the aluminum dose equivalent versus depth curve at solar minimum in Figure 7.15 as follows:

$$DE_{Al-SolMin} = (-2 \times 10^{-5})x^3 + 0.0022x^2 - 0.0934x + 2.4821$$

which is a third-order polynomial curve fitting with the coefficient of determination $r^2 = 0.99879$ (the relative difference of the sum of the squares around the mean of the data as compared to that of the regression line), obtained from available regression software packages in VBA code. This polynomial fits the dose equivalent versus areal depth data for aluminum in this example with a correlation coefficient $r = 0.99927$, which represents a good fit to the actual data ($r = 1.0$ signifies that a line explains 100% of the variability of the data).

future operations in the 1 AU radiation environment, use of the new design metric and procedure allows estimating the mass of shielding required in such spacecraft with an error on the order of 15% – a marked improvement over the estimates NASA currently suggests of some 60% or even higher, as discussed above.

Chapter 8

Future Study: Ion Particle Wave Diffraction

"The actual state of our knowledge is always provisional, and there must be, beyond what is actually known, immense new regions to discover."
—Louis-Victor-Pierre-Raymond, 7e duc de Broglie, French physicist, Nobel Laureate, Foreword to D. Bohm, *Causality and Chance in Modern Physics*, 1984 at p. x (1892-1987)

"L'avenir, tu n'as point à le prévoir mais à le permettre."
—Antoine Marie Jean-Baptiste Roger, comte de Saint-Exupéry, French writer, poet, aristocrat, journalist, and pioneering aviator, from the posthumously published *Citadelle*, éd. Gallimard, 1948, chap. LVI, p. 167 ("Your task is not to foresee the future, but to enable it.") (1900-1944)

"If you're not the lead dog, the view never changes."
—Robert Charles Benchley, American humorist, newspaper columnist and film actor (1889-1945)

In 1924 a not-so-young student (age 32) at the Sorbonne in Paris, Louis de Broglie, submitted his doctoral thesis in physics – having been delayed somewhat by first matriculating in the humanities before taking up the study of physics, and then by military service during World War I. In his thesis de Broglie proposed a simple hypothesis: that any moving particle or object had an associated wave. He had no proof; rather his research was pure intuition and focused on the proposition that electrons under certain conditions might exhibit wave-like phenomena, such as diffraction, just as Albert Einstein had recently postulated that light exhibits both wave and particle characteristics. It was enough to earn his PhD, and a few years later in 1927 was proved experimentally by others, which serendipitously elevated the importance of the initial academic inspiration to a level where de Broglie was credited with creating a new field of physics – *mécanique ondulatoire*, or wave mechanics. For this he won the Nobel Prize in Physics in 1929, and thus secured his place in history. [215]

This present research into GCR radiation shielding materials includes, as a supplement intended for future work, a far more modest hypothesis: that the GCR particle radiation and its secondary emissions may also exhibit wave-like behavior that can be appropriately harnessed by passive shielding materials in order to reduce their harmful impact. Thus, it is shown that it is theoretically possible to alter the path of these GCR particles, that cannot be stopped completely by any reasonable shielding regime, by channelling them through new nano-scaled materials in order that diffraction "safe zones" are created behind the shielding material, or in some situations achieve controlled reflection. This is a purely aspirational proposal, and the naysayers may be numerous. But certainly part of an engineer's job is to push the theory toward practical solutions, even if not fully developed or wholly envisioned, because though the new idea may at first seem to lead nowhere, such thinking can ignite a spark in others that will take them on a journey of enlightenment that sets the world ablaze with new discoveries – *Ite, inflammate omnia!* Thus, the underlying principle for this aspirational hypothesis is presented, but the experimental proof and practical applications, if any, are left for later study.

8.1 Wave Behavior of Particle Radiation

Intrigued by Albert Einstein's conclusion in 1905 that light must have both wave-like and particle-like characteristics in order to explain the photoelectric effect, Louis de Broglie later hypothesized in a 1923 technical note published in *Nature*, that particles must also exhibit wave-like behavior: "The path of a luminous atom is no longer straight when this atom crosses a narrow opening; that is diffraction. It is then *necessary* to give up the inertia principle, and we must suppose that any moving body follows always the ray of its phase wave; its path will then bend by passing

through a sufficiently small aperture." [216]

It was not a popular view. In fact, de Broglie's academic supervisor, renowned French physicist Paul Langevin, reportedly confided in some of his colleagues during the Fourth Solvay Conference in 1924, about his student de Broglie: "his ideas, of course, are nonsensical, but he develops them with such elegance and brilliance that I have accepted his thesis." [217] But de Broglie was proven correct just a few years later in an experiment reported in 1927 by Davisson and Germer, where they successfully demonstrated a diffraction pattern by a beam of electrons directed against a single crystal of nickel. [218]. A few months later, Professor G. P. Thomson, son of the famous Cambridge physicist Sir J. J. Thomson, reported a similar diffraction result from particles emitted from cathode rays, not knowing whether they were atoms or molecules. [219] And these experiments were confirmed in rapid succession by several others using various forms of electron beams. [215] Later, Davisson and Thompson shared the 1937 Nobel Prize in Physics for this work.

De Broglie recounted his thought process by first considering Max Planck's hypothesis about black body radiation, at the dawn of the development of quantum mechanics in 1900, that the energy exchange between a resonator material and radiation takes place only in integer multiples of $h\nu$, where ν is the frequency of the radiation and $h = 6.62607 \times 10^{-34} joule - sec$ was a new empirically determined constant (later dubbed Planck's constant, and for which work Planck won the 1918 Nobel Prize in Physics): "Les échanges d'énergie entre les résonateurs (ou la matière) et le rayonnement n'ont lieu que par quantités finies égales à h fois la fréquence, h étant une nouvelle constante universelle de la physique." [220]

By 1905, de Broglie recounted that in studying the photoelectric effect, experiments had shown that the energy of the ejected electrons was proportional to the

frequency of the incoming radiation, and not its energy, as had been presumed. Albert Einstein explained this result by considering that the incoming light behaved like particles of energy in units of $h\nu$, and thus when an electron in the target material absorbed an energy $h\nu$, and the ejection required w, then the ejected electron had an energy of $h\nu - w$, which was shown experimentally. De Broglie credits Einstein's instinct for this insight (for which Einstein won the 1921 Nobel Prize in Physics): "Cette loi s'est trouvée bien vérifiée. Avec sa profonde intuition, M. Einstein sentit qu'il y avait lieu de revenir en quelque manière à la conception corpusculaire de la lumière et émit l'hypothèse que toute radiation de fréquence ν est divisée en atomes d'énergie de valeur $h\nu$." [220]

Einstein's 1905 paper on special relativity, introducing the equivalence of mass and energy, also caught de Broglie's eye. De Broglie introduced the topic as follows:"Une des plus importantes conceptions nouvelles introduites par la Relativité est celle de l'inertie de l'énergie. D'après Einstein, l'énergie doit être considérée comme ayant de la masse et toute masse représente de l'énergie. La masse et l'énergie sont toujours reliées l'une à l'autre par la relation générale:

$$énergie = masse \times c^2$$

c étant la constante dite "vitesse de la lumière," mais que nous préférons nommer "vitesse limite de l'énergie" pour des raisons exposées plus loin." [220]

The essence of de Broglie's idea was to calculate the wavelength of a particle by equating Einstein's relationship between energy and mass with Planck's theory that every quantum of a wave has a discrete amount of energy, as shown in what became

known as the Planck-Einstein formula; the energy, he reasoned, must be the same:

$$E = mc^2 \quad and \quad E = h\nu$$

And then taking a short-cut around the relativistic derivation, one knows that particles will not travel at the speed of light, but rather at some velocity v.[1] Thus:

$$E = mv^2 = h\nu$$

[1] The formula $E = mc^2$ really refers to an object that is moving with a "relativistic mass;" whereas, for an object at rest, the precise formulation refers to the "rest mass," as follows: $E = m_0c^2$. Although it will ultimately get to the same answer, de Broglie's initial derivation took the more rigorous starting point for calculating the kinetic energy in terms of the total energy (expressed in terms of the rest mass) minus the rest energy, as follows:

$$E_k = \frac{m_0c^2}{\sqrt{1-\beta^2}} - m_0c^2 = m_0c^2\left[\frac{1}{\sqrt{1-\beta^2}} - 1\right] = m_0c^2\left[1 + \frac{1}{2}(\frac{v}{c})^2 + \frac{3}{8}(\frac{v}{c})^4 + ... - 1\right] \Rightarrow v << c \Rightarrow \frac{1}{2}m_0v^2$$

Which, if resolved by the first two terms of a Taylor series expansion, then the kinetic energy tends to the classical formulation when the velocity is much smaller than the speed of light. This relativistic approach caused de Broglie to equate the "mass" energy and the "wave" energy in the rest frame of reference, resulting in $h\nu_0 = m_0c^2$; but that in turn led to calculating a lower frequency in a moving frame based upon relativistic time dilation ($\nu = \nu_0\sqrt{1-\beta^2}$), but a higher frequency in the moving frame when calculated on the relativistic transformation based on wave phenomenon ($\nu = \nu_0\frac{1}{\sqrt{1-\beta^2}}$). [216] [217]

De Broglie resolved this apparent mathematical conundrum by postulating a fictitious wave associated with the particle that had a frequency of ν, and a "phase velocity" higher than that of the speed of light ($v_p = c/\beta > c$); but which was allowed because it transferred no energy itself, but rather was deemed an inner vibration in phase with the particle's wave, later dubbed the "pilot wave." [216] Equating the energy of a wave and the relativistic energy of a particle provides the relationship $E = h\nu = m_0c^2/\sqrt{1-\beta^2}$, then the relativistic momentum may be written as follows:

$$p = \frac{m_0v}{\sqrt{1-\beta^2}} = \frac{h\nu}{c^2}v = \frac{h}{\lambda}$$

after multiplying times one, in the form of wave energy ($(h\nu)/(m_0c^2/\sqrt{1-\beta^2})$, and returning to the fictitious wave with velocity, $v = c^2/v_p$, and recalling that wavelength, $\lambda = v_p/\nu$. [217]

When de Broglie presented this mathematical approach at the Fifth Solvay Conference in 1927 (devoted to electrons and photons), it was heavily criticized by no lesser physicists than Heisenberg, Pauli, Dirac, Bohr, and others [221] [222] [223]; but by this time experiments had proven the point and de Broglie won the 1929 Nobel Prize in Physics anyway. Twenty-five years later the "pilot wave" theory was revived by Bohm and others [221] [224] [225], and more recently it has been shown that an elegant alternative deduction of the de Broglie relationship can be obtained directly from Lorentz transformations and the Planck-Einstein equation ($E = h\nu$). [217]

Then, substituting in the relationship between wavelength and frequency, $\lambda = v/\nu$:

$$E = mv^2 = h\nu = hv/\lambda$$

And then finally solving for the wavelength in terms of the mass and velocity of the particle (i.e., its momentum) provides:

$$\lambda = \frac{hv}{mv^2} = \frac{h}{mv} = \frac{h}{p} \tag{8.1}$$

This last expression being the one that made de Broglie famous, as shown in Figure 8.1, though interestingly in his PhD thesis de Broglie does not present his conclusions in this form in Chapter 1, where the derivation is made, but rather at the end in Chapter 7. [220] [217]

(a) Fondation et Institut Louis de Broglie, 23, rue Marsoulan, 75012 PARIS: $\lambda = \frac{h}{mv}$.

(b) Fifth Solvay Conference on Physics (M. de Broglie, 2d row, 3rd from the right).

Figure 8.1 : Fondation et Institut Louis de Broglie, and Participants at Fifth Solvay Conference on Physics in 1927, at Brussels, Belgium.

De Broglie knew that the next step was finding a way to mathematically describe a physical system in space and time, where the wave-particle duality effects were

evident in the emerging quantum world; and he tried, but it was a European colleague that first proposed a linear partial differential equation for this purpose in 1926, Erwin Schrödinger. The so-called "Schrödinger equation" became the foundation of quantum mechanics, the solutions of which support the dual nature of waves and matter, and can result in discrete quantized energy levels. [226] The Schrödinger equation was developed principally from Planck's discovery of the quantized energy of photons and de Broglie's initial hypothesis, and resulted in a wave equation to describe the probability of finding a particle within a certain differential volume at a particular time,[2] based on classical energy conservation and consistent with the de Broglie relations. For this contribution, Schrödinger won the 1933 Nobel Prize in Physics (which he shared with Paul Dirac).

But as renowned physicist Richard Feynman remarked, the Schrödinger equation was not *derived*; rather it was *deduced* – some even say "guessed at" – to describe the equations of motion of a wave function in quantum physics: "Where did we get that equation from? Nowhere. It is not possible to derive it from anything you know. It came out of the mind of Schrödinger." [228] Even so, the validity of the Schrödinger equation rests on the fact that "it satisfactorily explains non-relativistic

[2] For example, to describe the diffraction pattern experimentally observed that proved de Broglie's hypothesis about the wave-particle duality, one needs to describe the probability distribution of the emitted particles passing through an opening, which can be done (borrowing from electromagnetic theory) with a wave function, $\Psi(x,t)$, for which the absolute square value will be equal to the probability that the particle will be found in the interval dx at time t:

$$\Psi^*(x,t)\Psi(x,t) = |\Psi(x,t)|^2 \quad \textit{provided} \quad \int_{-\infty}^{\infty} \Psi^*(x,t)\Psi(x,t) = 1$$

where $\Psi^*(x,t)$ is the complex conjugate of the wave function, and $\Psi(x,t)$ is normalized as shown so that the probability solution does not exceed unity. Thus, the quantity $|\Psi(x,t)|^2$ is the probability density in one-dimension, with units of probability per unit length. [227] The wave function, $\Psi(x,t)$, by itself, does not provide any physical information, but requires first that a form of the wave function be assumed, and then solved in terms of the physical parameters that describe the system of interest.

quantal phenomenon." [227][3] Later, relativistic wave equations were developed by

[3] Richard Feynman has also provided this perspective on the "derivation" of the Schrödinger equation: "When Schrödinger first wrote it down, he gave a kind of derivation based on some heuristic arguments and some brilliant intuitive guesses. Some of the arguments he used were even false, but that does not matter; the only important thing is that the ultimate equation gives a correct description of nature." [229] With that introduction, one can describe the total mechanical energy of a particle as the sum of its kinetic and potential ($U(x)$) energy:

$$E = \frac{1}{2}mv^2 + U(x) = \frac{p^2}{2m} + U(x)$$

Then recalling the Planck-Einstein relationship ($E = h\nu$) and the de Broglie wavelength ($p = h/\lambda$) that formalized the wave-particle duality concept, the total mechanical energy of the particle can be rewritten including both important quantal relations as follows:

$$E = h\nu = 2\pi\hbar\nu = \hbar\omega = \frac{p^2}{2m} + U(x) = \frac{(\hbar k)^2}{2m} + U(x)$$

where the angular frequency is $\omega = 2\pi\nu$, the reduced Planck's constant is $\hbar = \frac{h}{2\pi}$, and the wave number is $k = \frac{2\pi}{\lambda}$. One can then begin with the general expression for a solution to a wave function for a particle moving in the $+x$ direction, and insert the terms of the physical system of interest:

$$\Psi(x,t) = Ae^{-i\omega(t-\frac{x}{v})} \quad Then, \quad \Psi(x,t) = Ae^{-i2\pi(\nu t-\frac{x}{\lambda})} = Ae^{-i2\pi(\frac{Et}{2\pi\hbar}-\frac{xp}{2\pi\hbar})} = Ae^{-\frac{i}{\hbar}(Et-xp)}$$

including $\omega = 2\pi\nu$, $v = \nu\lambda$, $\nu = \frac{E}{2\pi\hbar}$, and the de Broglie wavelength, $\lambda = \frac{h}{p} = \frac{2\pi\hbar}{p}$. Thus the wave function form of the total mechanical energy for the system of interest is:

$$E\Psi(x,t) = \frac{p^2}{2m}\Psi(x,t) + U(x)\Psi(x,t)$$

Then, the first and second partial derivatives of the wave function solution with respect to x are:

$$\frac{\partial\Psi(x,t)}{\partial x} = Ae^{-\frac{i}{\hbar}(Et-xp)}(\frac{ip}{\hbar}) \quad and \quad \frac{\partial^2\Psi(x,t)}{\partial x^2} = Ae^{-\frac{i}{\hbar}(Et-xp)}(-\frac{p^2}{\hbar^2}) = -\frac{p^2}{\hbar^2}\Psi(x,t)$$

And then differentiating the same wave function solution with respect to t provides:

$$\frac{\partial\Psi(x,t)}{\partial t} = Ae^{-\frac{i}{\hbar}(Et-xp)}(-\frac{iE}{\hbar}) = -\frac{iE}{\hbar}\Psi(x,t)$$

Then, rearranging terms:

$$p^2\Psi(x,t) = -\hbar^2\frac{\partial^2\Psi(x,t)}{\partial x^2} \quad and \quad E\Psi(x,t) = -\frac{\hbar}{i}\frac{\partial\Psi(x,t)}{\partial t}$$

And by substituting these expressions back into the total mechanical energy equation:

$$\frac{\hbar}{i}\frac{\partial\Psi(x,t)}{\partial t} = \frac{\hbar^2}{2m}\frac{\partial^2\Psi(x,t)}{\partial x^2} - U(x)\Psi(x,t)$$

which is the one-dimensional time dependent Schrödinger equation – a homogeneous linear differential equation for the total energy of the particle with the two fundamental relations of quantum physics included, the de Broglie wavelength and the Planck relation. [230] [227]

Dirac and others to describe systems where quantum mechanics and special relativity simultaneously apply. [231] [232]

Though there is still debate about the details of the mathematical proof of de Broglie's original hypothesis that under certain circumstances particles will exhibit wave-like behavior, there is no doubt that it has been proved again and again experimentally, and with much larger particles than the electrons initially considered.

For example, atoms of helium (^{4}He) have been shown to exhibit wave behavior, in that they have been employed in focusing microscopy in a similar fashion to photons and electrons. In fact, helium would be a preferred particle for microscopy because it is non-penetrating, chemically inert and causes no physical damage to the specimen being imaged. Thus, in work toward developing what is called a "De Broglie Microscope," the focusing is accomplished by running the beam of helium atoms through free-standing so-called "Fresnel plates," which deflect and focus via diffraction through a concentric grating of open and opaque annular rings: "Focusing nonetheless takes place, a purely quantum mechanical effect and a direct manifestation of the wave nature of the atom." [233] The authors also report that: "Atom diffraction from a linear grating of period a can be described semi-classically as the transfer to the atom of one or more quanta $2\pi/a$ of transverse momentum." [233] It is obvious from this work that what can be focused by the action of diffraction of a particle the size of an atom, can also de-focus or diffuse the incident beam. [234]

In another experiment, de Broglie wave interference was observed by diffraction of C_{60} fullerenes through a free-standing nano-fabricated silicon grating with 50-nanometer wide slits placed at a period of 100-nanometers. [235] The "Buckminsterfullerene" – sometimes also called a "buckyball" – was discovered in 1985 at Rice University by Dr. Richard Smalley and others, and has a diameter of about 1.1 nano-

meter, an atomic weight of 720 atomic mass units (amu), and molecular weight of 720.99 gm/mol. Other experiments have shown diffraction for electrons, atoms, and neutrons, but by 1999 the observed diffraction of C_{60} molecules was among the largest particles where the de Broglie diffraction has been clearly detected. [235]

Recently, it has been reported that a diffraction lens focusing device has been demonstrated in the laboratory for de Broglie matter waves of a neutral atomic beam using a simple system of two axially positioned pin holes, with a focal length in the range of 0.13 - 6 cm. [234] This may find additional practical applications as it is a simpler and more effective way to passively manipulate a beam of atoms or neutrons, than the diffraction achieved by using a perpendicular laser beam to manipulate an electron beam [236], or the previously discussed Fresnel zone plates, which deflect and focus atomic beams via diffraction through a concentric grating of interspaced open and opaque concentric rings, but are difficult to fabricate. [234]

Additional improvements have recently been reported in diffraction-based so-called "de Broglie microscope" techniques [237], and grating diffraction improvements that may soon allow these techniques to be applied to larger particles on the order of $10^4 - 10^6$ amu. [238] In fact, recent experiments (2011-13) have reported observable matter-wave diffraction phenomenon for a complex organic molecule of 430 atoms, with a nominal size of 60Å, a mass of 6,910 amu, and a de Broglie wavelngth on the order of $\lambda = h/mv \approx 1pm$ (1 picometer = 10^{-2}Å= 10^{-12} meter). [239] Another has detected matter-wave diffraction patterns for an even larger particle comprised of 810 atoms, with a mass of 10,123 amu ($C_{284}H_{190}F_{320}N_4S_{12}$), under conditions where the de Broglie wavelength was about 500 fm (1 femtometer = 10^{-15} meter). [240]

The work on matter-wave phenomenon to cause passive manipulation of particle beams has come a long way since de Broglie's initial hypothesis and Davisson's sub-

sequent experimental proof in the mid-1920s. The relevance of all this research on the diffraction of atom-sized particles is its potential application to passively manipulating GCR particle radiation in a way that would improve shielding effectiveness, perhaps by employing new nano-materials that have a structure spacing small enough to induce diffraction (or reflection) over some portion of the GCR energy spectrum. Some differences to keep in mind are that the primary incident GCR ion particles are much smaller, and higher kinetic energy, than the large particles for which such diffraction phenomenon has been observed; but perhaps these characteristics are not so for many secondary emissions. The relevance of this investigation is not diminished, even if it may be applicable to only part of the GCR radiation spectrum.

8.2 Matter-Wave Diffraction of GCR Ions

Diffraction of a propagated wave occurs when it passes an obstacle or opening; first observed with light in the mid-1600s, and in 1803 was experimentally shown that it resulted from the interference of light waves as a result of passing the obstacle. [241] Diffraction also occurs when waves pass through a medium that has a varying refractive index, such imposing the same effect as the edge of an obstacle. As shown earlier in this Chapter 8, de Broglie and others have shown that the diffraction phenomenon also occurs as a result of the wave-like characteristics of particles.

Diffraction of a wave is generally believed to be most pronounced when the wave encounters an opening that is comparable in size to its wavelength (perhaps dictating use of materials with varying opening sizes), but this assumption may not apply at the quantum level. Thus, it is of interest to know the wavelength of the particles making up the GCR radiation spectrum, and its secondary emissions, and the general size parameters of shielding materials that might induce diffraction.

Calculating the de Broglie wavelength is a relatively simple matter mathematically. Thus, the non-relativistic de Broglie wavelength for an electron moving at a speed of $2.2 \times 10^6 m/s$ is as follows:

$$\lambda = \frac{h}{p} = \frac{h}{mv} = \frac{6.63 \times 10^{-34} J - s}{(9.1 \times 10^{-31} kg)(2.2 \times 10^6 m/s)} = 3.31 \times 10^{-10} meters = 331 pm$$

noting that the electron in a hydrogen atom travels at about $2.2 \times 10^6 m/s$, and recalling that in SI units $1J = 1kg - m^2/s^2$. And similarly, for a sodium atom travelling at 30,000 m/s, the de Broglie wavelength is:

$$\lambda = \frac{h}{mv} = \frac{6.63 \times 10^{-34} J - s}{(3.817 \times 10^{-26} kg)(3.0 \times 10^4 m/s)} = 0.579 \times 10^{-12} meters = 0.579 pm$$

Of course, in these examples the particles are travelling at less than 1% of the speed of light, and even if it was assumed that the sodium atom traveled as fast as the electron in this example, it would have a much shorter de Broglie wavelength than the electron due to its greater mass (e.g., in that case $\lambda_{Na} = 0.00789 pm$). To be precise and include the relativistic effect on the mass of the particle (i.e., the relativistic mass increases with increasing speed: $m = \gamma m_0$ [242]), the calculation for the de Broglie wavelength would be modified as follows:

$$p = \gamma m_0 v = \frac{m_0 v}{\sqrt{1 - \frac{v^2}{c^2}}} \quad thus \quad \lambda = \frac{h}{p} = \frac{h}{\gamma m_0 v} = \frac{h}{m_0 v}\sqrt{1 - \frac{v^2}{c^2}}$$

where m_0 is the particle's rest mass (*see*, e.g., Equation 3.9). For the examples given above, the impact is negligible, but that is not true for much of the primary incident GCR particle radiation.

Therefore, to properly calculate the de Broglie wavelength of many GCR ions, it

is necessary to consider relativistic effects. The first step is to determine the speed of the GCR ions, which can be calculated from their kinetic energy, as follows:

$$E_t = mc^2 = E_{rest} + E_k = m_0c^2 + E_k = \gamma m_0 c^2$$

Thus, the kinetic energy is:

$$E_k = \gamma m_0 c^2 - m_0 c^2 = m_0 c^2(\gamma - 1)$$

Thus, solving for γ, since it contains the velocity term sought (e.g., $\beta = v/c$), results in the following:

$$\gamma = 1 + \frac{E_k}{m_0 c^2}$$

$$\gamma \equiv \frac{1}{\sqrt{1-\beta^2}} = \frac{1}{\sqrt{1-\frac{v^2}{c^2}}} = 1 + \frac{E_k}{m_0 c^2}$$

Then, inverting and squaring both sides, allows solving for the velocity in a straight forward manner:

$$1 - \frac{v^2}{c^2} = \frac{1}{(1+\frac{E_k}{m_0c^2})^2} \qquad \Rightarrow \qquad v = c \times \sqrt{1 - \frac{1}{(1+\frac{E_k}{m_0c^2})^2}}$$

And from this velocity, the de Broglie wavelength can be calculated using the equation above (same as Equation 3.9).[4]

[4] Often, the kinetic energy of GCR ions is given in units of energy per nucleon, MeV/n, where $E_k = AE_{k/n}$, A is the atomic weight of the ion, and the rest energy of a nucleon (i.e., a proton or a neutron, which have almost the same mass) is about $m_n = 938 MeV/c^2$. Thus, for any ion, the velocity would be calculated as follows:

$$\gamma = \frac{E_k}{m_0c^2} + 1 = \frac{AE_{k/n}}{Am_nc^2} + 1 = \frac{E_{k/n}}{m_nc^2} + 1 \quad and \quad v = c \times \sqrt{1 - \frac{1}{(1+\frac{E_{k/n}}{m_nc^2})^2}}$$

Thus, an initial step in determining whether a passive diffraction shielding scheme might be employed against GCR radiation or its secondary emissions, is to determine the de Broglie wavelength of the particles in question. Using the equations developed above and the GCR ion flux versus energy spectrum shown previously in Figure 6.1, as calculated with the baseline Badhwar-O'Neill 2010 GCR model at the 2010 solar minimum, provides the calculated de Broglie wavelength data for the GCR ions of hydrogen, helium and iron, as well as the trapped protons and albedo neutrons in the ISS orbit, shown in Figure 8.2.

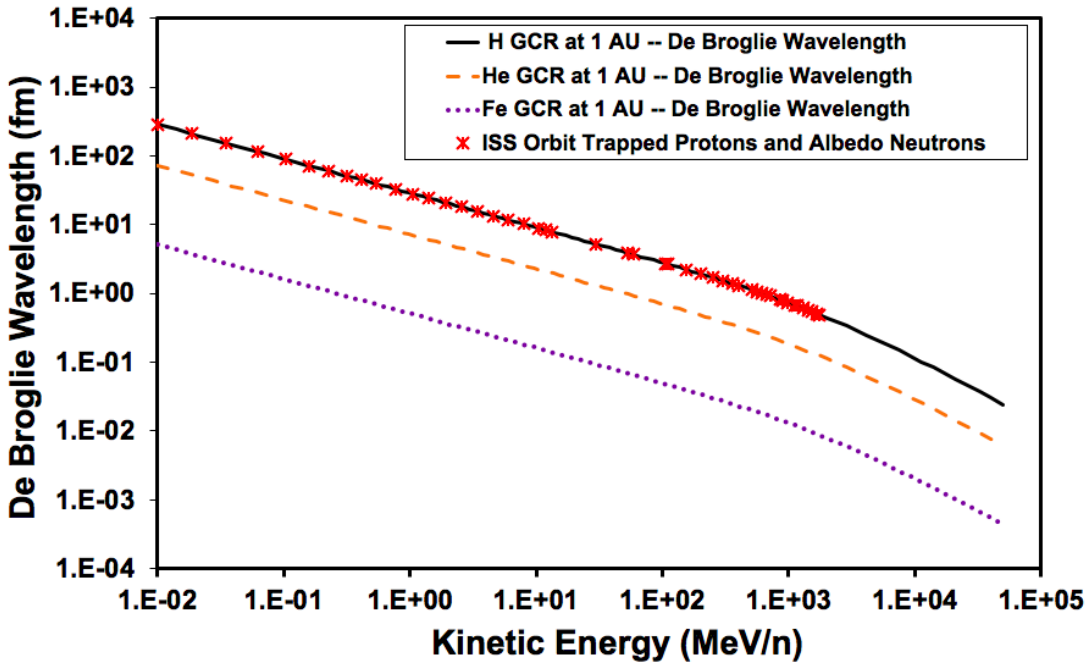

Figure 8.2 : Calculated de Broglie Wavelengths of Various GCR Particles at 1 *AU* Environment, and for Trapped Protons and Albedo Neutrons in ISS Orbit (2010 Badhwar-O'Neill Model at 2010 Solar Minimum).

Obviously, these calculated de Broglie particle wavelengths are relatively small, due in large part to the high velocity of the GCR particles over most of each particle's energy spectrum; i.e., travelling at relativistic speeds for energies greater than 150 MeV/n,

which equates to about $0.5c$. But as mentioned previously, diffraction patterns have been observed for particles with de Broglie wavelengths in the femtometer size range, albeit a bit larger than most shown in Figure 8.2, and for much larger particles. Recalling that the maximum flux of all GCR ions in the 1 AU radiation environment is about 200 to 500 MeV/n (*see* Figure 6.1), it is perhaps of interest to note that the de Broglie wavelengths vary by about two orders of magnitude from the lightest GCR particle to the heaviest in that flux range; and, indeed, that ratio appears to be relatively constant over the entire GCR energy spectrum.

Another radiation environment of interest includes that in low Earth orbit in the specific orbit of the International Space Station, where the GCR flux and energy levels are greatly reduced by the magnetosphere, and where significant secondary neutrons are produced, as shown in Figure 6.4. And another would be the radiation environment inside the ISS, behind a nominal shielding thickness of 20 gm/cm^2 of aluminum. In both of these radiation environments there will be particles of all energy levels represented in the primary GCR spectrum, but the flux nodes of average energy per nucleon will be lower in the ISS orbit, and lower still inside the ISS, as expected. This is illustrated in Figure 8.3, where it is clear that the flux of neutrons outside the ISS is actually lower than inside. This result obtains because of the albedo neutron flux created as a result of GCR ions reacting with upper atmosphere constituents (recalling that the neutron flux in the primary GCR at 1 AU is essentially nil), and clearly shows that the aluminum shielding is actually making the situation worse with respect to free neutrons. Of course, the situation is different with positively charged GCR ions, like iron, as would be expected; the primary GCR ion flux is first reduced by the magnetosphere, then further reduced and slowed by the aluminum shielding by the "stopping power" and "nuclear collision" mechanisms discussed in Chapter 3.

It should be noted that the danger to humans posed by free neutrons will still exist in the cis-lunar radiation environment, even though absent from the primary GCR flux, because they are created as secondary emissions by the spacecraft's shielding material.

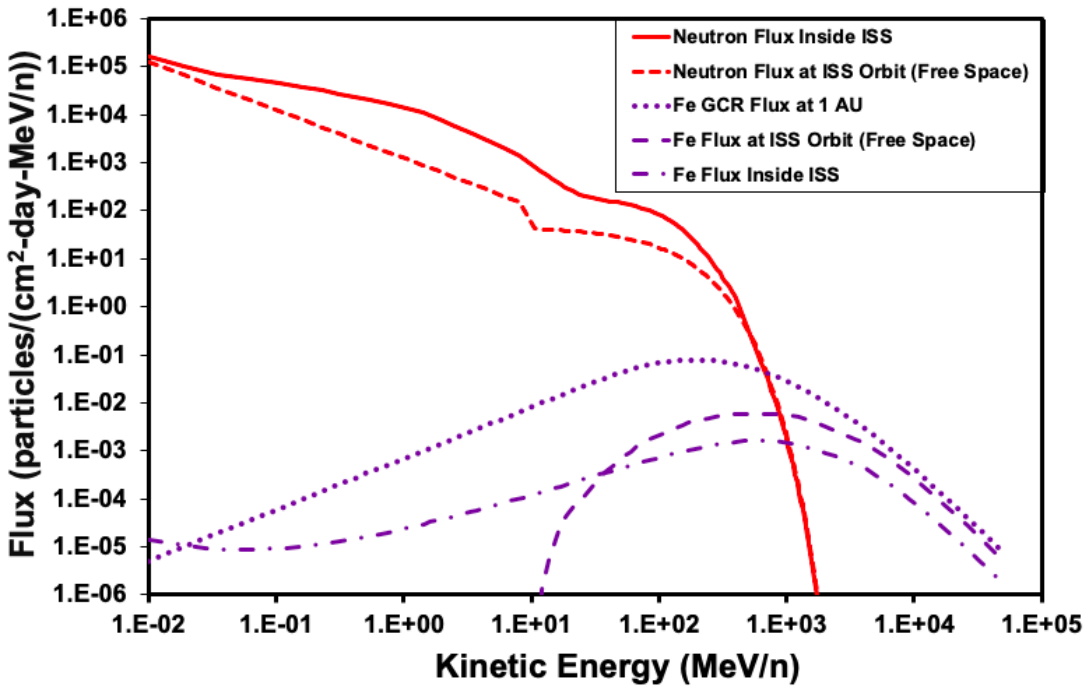

Figure 8.3 : Particle Flux of Neutrons and Iron resulting from GCR Radiation at the Orbit of the International Space Station, assuming 20 gm/cm^2 Equivalent of Aluminum Shielding (2010 Badhwar-O'Neill GCR Model, at 2010 Solar Minimum).

In terms of possibly providing a shielding material layer – or multiple interlaced layers – that might take advantage of particle wave diffraction physics, it is of interest to note the de Broglie wavelength ranges for the GCR-induced radiation in each of these environments. For example, as shown in Figure 8.4, the calculated de Broglie wavelengths are shown for protons and neutrons for both the primary GCR at 1 *AU* (protons only) and both particles in the ISS orbit. The calculated de Broglie

wavelengths for protons and neutrons will fall along the hydrogen ion curve, because they are all a single nucleon and thus have essentially the same mass, making the wavelength a function of the particle's kinetic energy. Thus, the de Broglie wavelength for protons and neutrons in any of the radiation environments of interest (including at 1 AU, inside a spacecraft at 1 AU, the ISS orbit, and inside the ISS) can simply be picked off this single curve by knowing the particle's velocity (a function of its kinetic energy), or by utilizing Equation 3.9. Of course, for the other ions in the GCR and secondary emissions one must also take into consideration the variations in mass.

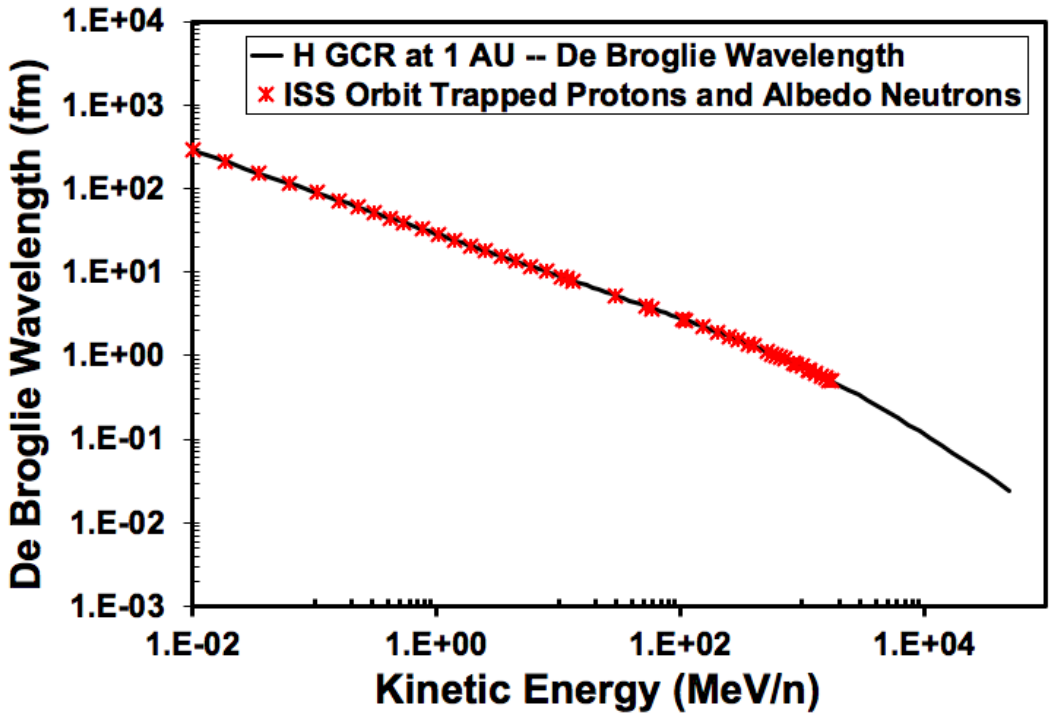

Figure 8.4 : Calculated de Broglie Wavelengths of Neutrons and Protons at ISS Orbit, overlaid on the Calculated de Broglie Wavelength of GCR Protons at 1 AU (2010 Badhwar-O'Neill GCR Model, at 2010 Solar Minimum).

Perhaps of greater utility is the de Broglie wavelengths for representative energy levels of trapped protons and albedo neutrons in specific locations in the LEO envi-

ronment, as well as that for ions at 1 AU and for representative energy levels behind the ISS standard shielding of 20 gm/cm^2 of aluminum, which are shown in Table 8.1.

GCR Ion Particle Wavelengths
At 1 AU, LEO, and Inside ISS

Particle & Location	Kinetic Energy (MeV/n)	De Broglie Wavelength (femtometers)
GCR Proton at 1 AU	1,000	0.732
Proton at ISS Orbit	200	1.93
Neutron at ISS Orbit	0.2	64.1
Proton Inside ISS	42	4.37
Neutron Inside ISS	1.83	21.2

Table 8.1 : Typical de Broglie Wavelengths for Various Primary and Secondary GCR Particles at Representative Kinetic Energy Levels.

As can be seen in Table 8.1, these values can be easily picked off the Hydrogen ion line of Figure 8.4, as protons and neutrons have very close to the same rest mass, and the typical average kinetic energy of each particle will be lower as the primary GCR radiation encounters the magnetosphere and ISS shielding; the exception being that the secondary neutron flux and energy actually increases over the albedo flux found in the ISS orbit, as a result of GCR particles impacting the ISS aluminum shielding. Consequently, the average kinetic energies of neutrons are actually a bit higher inside the ISS than outside in the ISS orbit. Given that a significant portion of the secondary neutron flux inside the ISS is at energy levels that are in the range of 10^{-2} - 10^{3} MeV, where the harm to humans has been judged the highest [38], any additional shielding layer that can be placed inside the ISS behind the aluminum that could diminish the neutron particle flux or intensity could be very beneficial in reducing human health risks. As mentioned previously, these particles are of relatively low energy, but they

carry a very high quality factor in terms of harm to humans. *See* Figure 6.4, and accompanying text.

Though beyond the scope of my present research effort, from a design standpoint a shielding material may need a relatively small opening in order to induce useful passive diffraction of the radiation particle, given the relatively small calculated de Broglie wavelengths of GCR ions and secondary emissions. Whether diffraction can be induced by the particle passing through an opening size on the order of one wavelength, or some larger multiple, will have to be modeled and solved numerically by some formulation of "standard Kirchhoff diffraction theory" to mathematically describe the diffraction field, and then such analysis should be tested experimentally. [235] [234] [237] However, recent experiments have observed diffraction patterns where the opening is much larger than the de Broglie wavelength of the subject particle; e.g., one thousand times the de Broglie wavelength of the particle [238], to as high as five million times the de Broglie wavelength [240]. Focusing on neutrons as an example, one notes that the diameter of a neutron is approximately 1.6 fm, which may be the lower limit for passing through a physical slit, but may not limit materials that effect diffraction by other means, such as a change in refractive index or simply passing an edge. However, an additional challenge may be the ability to achieve a small enough opening, given that fabricating spacings and openings in materials becomes difficult in the nano-meter range, and even naturally occurring atomic spacing in nano-materials such as graphene are on the order of 1.4Å(140,000 fm), which of course could possibly be interlaced to create smaller apertures. [233] In addition, there exist additional effects at the quantum level that can reduce the apparent size of an aperture. [238] Thus, most neutrons with the de Broglie wavelengths shown in Figure 8.4 may be candidates for diffraction through an appropriately sized opening,

and perhaps neutrons and ions with even smaller de Broglie wavelengths may exhibit diffraction by other means.

8.3 Matter-Wave Considerations for GCR Shielding

The work on matter-wave phenomenon to cause passive manipulation of particle beams has come a long way since de Broglie's initial hypothesis and Davisson's subsequent experimental proof in the mid-1920s. It has become clear that particles the size of an atom and larger can be focused and de-focused by the diffraction process. [234] Thus, it would seem an open question whether the physical reality of a particle's wave-like characteristics could allow the passive manipulation of GCR particle radiation in a way that would improve shielding effectiveness, perhaps by employing new nano-materials that have a structural spacing small enough to induce diffraction – and thereby passively move or channel the radiation particles – over some portion of the GCR energy spectrum, or that of the secondary emissions. Certainly, diffraction patterns have been detected for particles with de Broglie wavelengths in the 500 fm range [240], but admittedly the primary GCR ions are smaller in size and have shorter wavelengths over much of their energy spectrum. However, at some point in traversing shielding materials the GCR ions are slowed, and there may be a point in that process where the de Broglie wavelength gets large enough that a thin diffraction layer may be beneficially added to a shielding design to diffuse or reflect some of the primary or secondary radiation particles into the lateral mass of the shield. For low energy primary ions, such a design may not be worth the effort, as those ions can already be effectively shielded; but the dangerous lower energy neutron emissions – immune to the "stopping power" mechanism – may present an opportunity for a practical beneficial application of diffraction. Moreover, these secondary neu-

trons are ubiquitous wherever primary GCR ions interact with spacecraft shielding, the Earth's atmosphere, or *in situ* or surface materials, such as might be used on the Moon or Mars for habitat construction. Thus, experimental work and further tailored simulations may be warranted to answer the question.

There has been some theoretical work in the emerging field of atomic optics and interferometry regarding the diffraction of atomic de Broglie waves by material or optical structures in order to manipulate the atomic particle beam. [243] This, and other similar work, may be of interest in shielding designs in that the diffraction and reflection of particles with de Broglie wave characteristics is found possible, all depending on the energy of the incident atomic beam and the angle it impacts the diffraction grating; i.e., at some incident angle the diffraction grating begins to behave as a so-called "atomic mirror." More recent work in this area has demonstrated the ability to reflect atoms by physical grating surfaces when the de Broglie wavelengths corresponding to the atomic motion perpendicular to the interface is larger than the characteristic length associated with the surface, thus producing a solid-state atomic mirror; albeit for atoms with larger de Broglie wavelengths in the nanometer range than calculated above for primary GCR particles. [244] [245] One can envision possibly using a diffraction grating scheme as part of an outer layer of shielding to take advantage of any particle reflection opportunities before GCR particles begin to traverse the shield in question, but such would likely be less effective as an inner layer of a shielding design, since the reflected particles would re-enter the main shielding material and produce back-scattered secondary emissions.

There has been no discussion in the literature about using a diffraction scheme as a way to de-focus or otherwise diffuse an incident GCR primary or secondary radiation particle. This may be because the de facto general assumption has been that the

diffraction phenomenon is best observed when the diffraction grating or opening is around the same size as the wavelength in question – and certainly, as demonstrated above, the de Broglie wavelength in the GCR ion particle radiation is very small, even by nano-scale material standards. But, neither has it been reported as a useless endeavor; and, moreover, there have been some efforts at using both the matter-wave characteristics along with active application of a small current to channel incident radiation in ways to improve shielding effectiveness.

For example, NASA scientists in 2011 patented a shielding method aimed at protons and neutrons in the space environment that used an array of carbon nanostructures coated with an electrically active polymer that is connected to a battery, and activated by the incident radiation, which allows some channelling or dissipation of the incident radiation (US Patent No. 7,923,709). [246] In another effort that took into account the use of diffraction grating techniques to create an atomic mirror (along the lines described above), a patent was issued to Los Alamos scientists in 2011, for an invention that utilized nanostructures with an applied electric current to create within a very thin shielding material a way to channel radiation. Though developed with shielding nuclear reactors in mind, the patent describes potential applications for such a material to be used as spacecraft shielding, though no estimates as to effectiveness for that purpose are given (US Patent No. 8,067,758). [247] Finally, a patent was recently issued in 2017 that purports to claim a more effective shielding material comprised of polarized dielectric materials in layers such that a passive internal electric field is established that will create an electric force to retard incoming GCR radiation in the space environment (US Patent No. 9,728,289). This invention is only vaguely described as to method of manufacture and shielding effectiveness, and appears to be similar to the US Patent No. 8,067,758, except that its purportedly new

inventive idea is to generate an internal electric field passively through juxtaposition of certain specified materials.[5] [248]

The above-described patented inventions provide a general feel for the direction of the "state-of-the-art" in shielding material design, and certainly leaves the door open to investigate matter-wave diffraction possibilities. Even if diffraction-based design considerations were found to be practical only for relatively low energy neutrons, they would still add a significant weapon to shielding protocols for spacecraft and space habitats on the Moon or Mars.

Late in his life Louis de Broglie offered this thought in the Foreword to David Bohm's book, *Causality and Chance in Modern Physics*: "The actual state of our knowledge is always provisional, and there must be, beyond what is actually known, immense new regions to discover." [249] NASA's Langley Research Center recently echoed this sentiment in their August 10, 2018 announcement for a call for research ideas regarding the problem of space radiation shielding: "NASA Langley Research Center is now seeking abstracts for concepts, including revolutionary ones, to address the problem of shielding astronauts from galactic cosmic rays ... [t]he Space Radiation Group here at NASA Langley (the team that developed and maintains OLTARIS) will be hosting a 'Blue Sky' workshop to discuss novel ideas to address the problems of shielding astronauts from galactic cosmic rays. All ideas and concepts, including far-out ones that we may not have considered before, are welcome." [250] Perhaps the

[5] This patent seems weak on its face. First, neither named inventor appears to be associated with any research institution, and neither has authored any peer-reviewed publications of any kind. In addition, the discussion of the background of the invention and purported applications reveals only a superficial understanding of the GCR radiation shielding problem and underlying science, not to mention that the required disclosed "preferred embodiment" of the invention only vaguely describes how to make the material in question, and its effectiveness at a calculated 17.5 MeV energy reduction is minuscule as compared to the peak GCR flux with ion energies in the range of 1 GeV/n. Finally, if the only inventive element is layering known polarized dielectric materials, it may very well be obvious in view of the prior art, and therefore invalid pursuant to 35 U.S.C. §103.

research presented here is prescient, in that it is clear that innovative solutions to the radiation protection problem are still being sought by the American agency charged with executing the contemplated long-term exploratory space voyages.

This Chapter 8 is intended only as an introduction to a possible future fruitful research path for better GCR shielding designs, and is not intended as an in-depth dissertation on the subject. In summary, the present research merely presents a modest hypothesis: that the GCR particle radiation and its secondary emissions may exhibit wave-like behavior that can be appropriately harnessed by passive shielding materials in order to reduce their harmful impact. Thus, it is shown that it is theoretically possible to passively alter the path of these GCR particles by diffraction, thereby presenting the possibility that diffraction "safe zones" could be created behind the shielding material. This preliminary research is intended only as an introduction to a possible future fruitful research path for better GCR shielding designs; a teaser for a problem that will require an interdisciplinary team effort to properly investigate. However, it is beyond doubt that one potential avenue for advances in GCR shielding effectiveness will be through the invention of new materials that enhance or compliment the traditional and well understood "stopping power" physics involved in slowing and stopping GCR ions discussed in Chapter 3. Indeed, as one NASA study of spacecraft and space habitat shielding options concluded: "Clearly, a materials development program to develop shielding technology is highly desirable." [41] Thus, the underlying principle for this hypothesis is presented, but the experimental proof and practical applications, if any, are left for later study.

Chapter 9

Conclusion

"It is not the critic who counts; not the man who points out how the strong man stumbles, or where the doer of deeds could have done them better. The credit belongs to the man who is actually in the arena, whose face is marred by dust and sweat and blood; who strives valiantly; who errs, who comes short again and again, because there is no effort without error and shortcoming; but who does actually strive to do the deeds; who knows great enthusiasms, the great devotions; who spends himself in a worthy cause; who at the best knows in the end the triumph of high achievement, and who at the worst, if he fails, at least fails while daring greatly, so that his place shall never be with those cold and timid souls who neither know victory nor defeat."
—Theodore Roosevelt, 26th President of the United States, author, explorer, and soldier, delivered *The Man in the Arena* excerpt in his speech *Citizenship in a Republic* at the Sorbonne, Paris, France on April 23, 1910 (1858-1919)

"We shall not cease from exploration, and the end of all our exploring will be to arrive where we started and know the place for the first time."
—T. S. Eliot, British poet, playwright, and Nobel Laureate, in *The Four Quartets*, 1943 (1888-1965)

"I never knew a man who had better motives for all the trouble he caused."
—Graham Greene, English novelist, in *The Quiet American*, 1955, Penguin ed. p. 60 (1904-1991)

Galactic Cosmic Ray radiation is a critical hazard that humans and equipment will encounter in the longer spaceflight missions currently contemplated to the Moon and Mars, in the region of cis-lunar space outside the protective zone afforded by the Earth's magnetosphere in low Earth orbit. Current radiation shielding materials and designs will cause many astronauts on these contemplated nominally three-year voyages to exceed the annual and/or career limits of radiation exposure set by NASA. Thus, any improvements in radiation shielding materials and designs appropriate for spacecraft are of paramount interest.

The research results presented here include improved methods for evaluating

spacecraft shielding against GCR for spacecraft operating in the 1 *AU* cis-lunar region of space, and also provide an empirical metric for comparing the relative exposure rates to that encountered on the inside of the International Space Station – a way of analyzing the data that allows comparison with comparable data tied to actual medical histories of ISS astronauts, in order to improve radiation risk assessment. The new evaluation metrics and procedures are used to evaluate several potential practical shielding designs for spacecraft operating in the cis-lunar region, and a cursory analysis is made of habitat radiation shielding on the Moon and Mars.

The results of our research effort are referenced in Section 1.4 and the Chapters referred to therein, and a more detailed summary of our key research results follows:

1. ISS Baseline Spacecraft Shielding Evaluation Method

A) Developed a novel method for evaluating shielding materials and designs for spacecraft intended to operate in the cis-lunar GCR radiation environment on long-term voyages that results in better assurance for protecting astronaut health risks from radiation exposure and decreases the uncertainty in determining the required mass of shielding material. These results will be very valuable to NASA and to those engineering companies planning operations in space.

• Calibrated a shielding evaluation model (comprised of the BON2010 GCR module (modified for the LEO radiation environment), slab geometry with water phantom to represent a human, HZETRN radiation transport code, and ICRP-60 radiation weighting factors) to actual radiation exposure measurements on astronauts on the ISS by adjusting the notional ISS shielding until the model calculated value for dose equivalent exposure rates was equal to the measured rates; dose equivalent is the metric used to evaluate human health risks. This produced a model that calculated true exposure rates in the LEO environment, which had not been done before.

• Took the calibrated model and changed the radiation environment to the GCR environment at 1 AU, and used that model to evaluate various shielding materials to determine how close one could get to replicating the ISS exposure rate in the 1 AU radiation environment.

• Determined that this method of evaluating shielding for 1 AU operations had an uncertainty of about 5% in the dose equivalent calculation due to scaling-up from the LEO radiation environment to 1 AU; and that such would propagate to a 15% uncertainty in determination of required radiation shielding mass (much better than NASA's approach >60%).

• Determined that the BON2010 GCR model best replicated recently published radiation data from the Alpha Magnetic Spectrometer, and thus used it in all calculations.

• Quantified the uncertainty propagated to the dose equivalent exposure rate by the two commonly used biological assessment models and found that to be in the range of 45%; an uncertainty avoided by using the ISS Baseline method.

• Determined that the method currently employed by NASA to evaluate shielding propagated a minimum uncertainty to the dose equivalent calculation in the range of 20% (due to GCR input models), and accepted NASA's evaluation that their biological assessment model could cause the dose equivalent calculation to be off by a factor of 2.

B) Why this wasn't done before is unknown to me, but may be that most of the research in this area is done by NASA and ESA under specific internal grants for specifically identified projects.

C) This new shielding evaluation method for the first time ties actual human health data from the astronauts on the ISS (through actual radiation exposure mea-

surements) to shielding evaluation analysis, and will greatly decrease costs in being able to determine shielding material mass requirements to better tolerances. Thus, it contributes to astronaut health and safety, and to decreased costs of conducting space exploration. The main features of this new method were recently published. [13]

2. Using the ISS Baseline Method to Evaluate Operations at 1 AU

A) Determined that with current materials it will be difficult to replicate the ISS radiation environment for spacecraft operating in the 1 AU radiation environment, but certain designs allow getting close.

• Evaluated five different shielding designs, including multilayer designs, and narrowed them down to two that were the best and/or most practical, to demonstrate how close one could get to replicating the ISS environment, and thus tie to astronaut health data.

• Determined that current shielding materials could be employed in reasonable quantities to replicate the ISS environment for operations at 1 AU if the space voyages were timed to coincide with solar maximum activity conditions (i.e., minimum GCR flux).

B) These determinations have not been done to our knowledge, though others have used uncalibrated dose equivalent results published in the literature to evaluate spacecraft shielding on the Moon or for a Mars voyage, but such determinations are not calibrated to actual radiation exposure measurements, and thus suffer from the uncertainties noted above for the NASA approach (with inherent propagated uncertainty as to mass requirements of over 60%).

C) These results demonstrate the utility of the ISS Baseline method in determining shielding requirements that are calibrated to human health histories and to

actual radiation measurements, and the recent publication of these examples will help demonstrate the method.

3. Developed a Fluence Analysis Shielding Evaluation Technique

A) To avoid the large uncertainties introduced by the biological assessment models, developed a way to evaluate certain aspects of radiation shielding by analysis of the radiation fluence spectrum behind various shielding materials.

B) It is likely that this had not been done before because it is a very time-consuming process. Even though it allows evaluating shielding without the uncertainty of biological assessment models, it is primarily useful for "tuning" multilayer designs to select materials to block particularly identified radiation particles.

C) This fluence analysis method has the best utility in examining the type of particles behind multilayer shielding designs in order to select the best materials to block particular types of particles; e.g., for blocking dangerous neutron secondary emissions. To the best of our knowledge, this had not been proposed for GCR shielding evaluation until we published it. [14]

4. Evaluate a New Material as a Space Radiation Shield

A) Evaluated a newly developed material called pillared boron nitride nanostructures as a potential radiation shield; a material initially developed for hydrogen fuel storage for automobiles. It was found that the material was superior to aluminum because it was twice as effective in shielding GCR radiation, and also provided structural capability with less mass.

B) Not done before because nobody involved in making this material had thought about using it in a space application.

C) New materials are needed to better shield GCR radiation, and this result demonstrates the utility of looking outside one's narrow field for potential candidates. This demonstration of the utility of nanostructures infused with hydrogen will hopefully encourage others to look for even better candidates.

5. Neutron Back-scatter Impact on Sensors and Equipment in Spacecraft

A) Quantified the effect of neutron back-scatter on the dose equivalent rate on interior structures in a spacecraft due to the addition of interior shielding or other materials, such as equipment racks, and determined that the interior radiation intensity would increase significantly, depending on the material, and would therefore alter sensor readings or damage interior mounted equipment.

B) Not done before with respect to spacecraft design issues, but one paper demonstrated the concept on the interior radiation field of a lunar habitat due to neutron back-scatter from the lunar soil.

C) Important to consider in evaluating shielding because adding shielding material may worsen the interior radiation environment. Also demonstrated that the back-scatter effect can be greatly diminished by selection of materials with, for example, low neutron production cross sections (e.g., an example where fluence analysis proves to be a useful evaluation method).

6. Comparison of HZETRN and MULASSIS Results

A) Determined that the one-dimensional MULASSIS Monte Carlo code does not replicate the values for dose equivalent obtained from the one-dimensional HZETRN deterministic code because (1) MULASSIS typically does not run all 59 primary GCR ions; (2) MULASSIS under-values the heavy ion ($Z > 2$) dose equivalent calculation

by an order of magnitude; and (3) the GCR input spectrum to convert from isotropic to one-dimensional geometry may be off by a factor of two.

B) One published study noticed the wide differences in calculated dose equivalent from MULASSIS and HZETRN, and NASA has commented on it, but both without quantifying the differences and tying those differences to specific reasons.

C) The utility of this result is to those wishing to use a simple, fast Monte Carlo procedure like MULASSIS for one-dimensional analysis in the GCR environment. The comparative trends will give the same results as HZETRN, but the values for the dose equivalent metric with MULASSIS will be widely different, and should not be relied upon.

The results of our research effort are summarized in Figure 9.1.

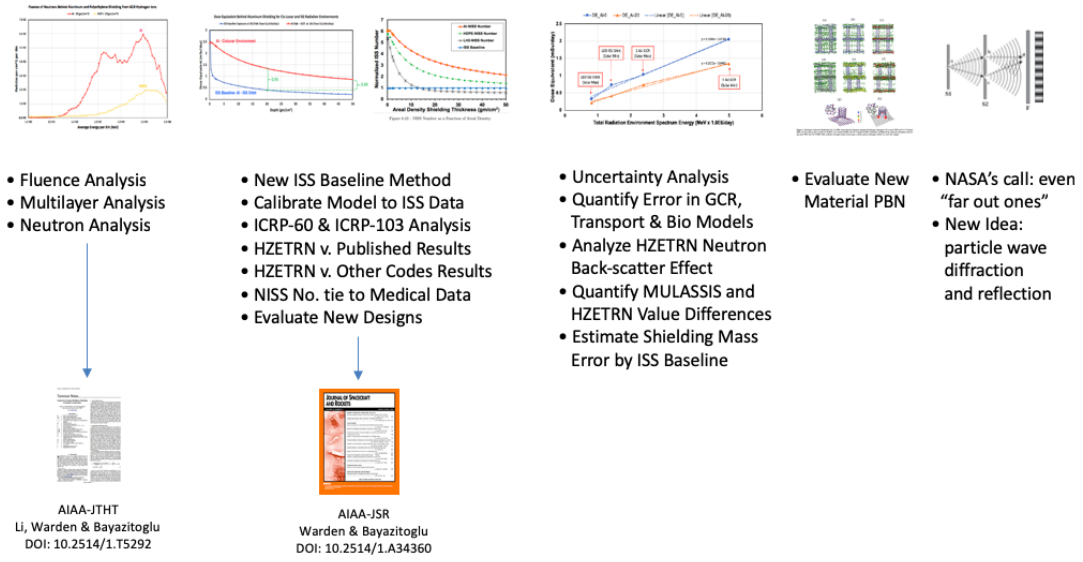

Figure 9.1 : Results Summary for Improved Radiation Shielding Evaluation.

Finally, several areas for further research have been identified, including: (1) an interdisciplinary comprehensive analysis of various hybrid nanomaterials and nanos-

tructures specifically focused on using them as combination structural elements and spacecraft shielding, including actual experimentation; (2) further investigation of potential new materials that could improve hydrogen infusion content, and thereby improve radiation shielding characteristics; (3) further investigation of using lunar regolith and Martian soil on the Moon and Mars, respectively, as shielding materials to determine the extent to which Earth-like radiation exposure rates can be created inside habitats on those celestial bodies; (4) further investigation by those in the medical field to assess the relative increase health risks expected as a function of radiation exposures that exceed the ISS Baseline exposure rate, an effort that has also been tangentially suggested by others in a different context [49]; and (5) further investigation of the potential for passively deflecting high energy GCR ions by wave-like diffraction through appropriate materials, possibly including actual experimentation.

Appendices

Appendix A

Key Equations

"It is not the mountain we conquer, but ourselves."
—Sir Edmund Percival Hillary, New Zealand mountaineer and explorer (1919-2008)

"Sometimes it is the people no one can imagine anything of who do the things no one can imagine."
—Alan Turing, English computer scientist, mathematician, logician, cryptanalyst, philosopher, and theoretical biologist; credited with breaking the German Enigma code in WWII (1912-1954)

A.1 Lorentz Factor Derivation

The Lorentz factor is the term that arises in the derivations of Lorentz transformations that accurately specify the coordinates of a given event in different inertial reference systems that are moving relative to each other. The Lorentz factor, commonly denoted by γ, becomes a significant factor when one reference frame is moving at so-called "relativistic speeds" with respect to the other; for example, when observing the impact of high energy ions from Galactic Cosmic Rays in a shielding material. If the calculation of such quantities as momentum or kinetic energy are desired within an accuracy of a few percentage points, then relativistic speed may be in the realm of 10-percent of the speed of light, c.

The key distinction between standard Galilean transformation and Lorentz transformation is the physical assumption that the speed of light is the same in both inertial reference frames, regardless of the motion of the source, thus both the space and time coordinates transform partly into each other, leading to the concepts of time

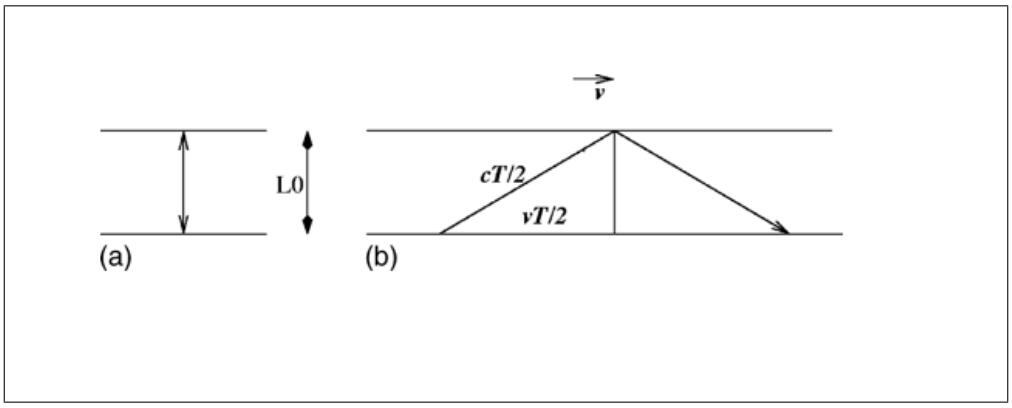

Figure A.1 : Light clock at rest (a) and moving (b). From J.-M. Lévy; American Journal of Physics 2007, 75, 615-618.

dilation and dimensional contraction in the direction of movement.

There are many approaches to the derivation of the Lorentz factor, but a simple one employs determining the time required for light to travel a given distance as viewed from a reference frame in which the light source is placed, and then from another reference frame moving with respect to the first.

Consider a light source in the rest frame of Figure A.1 at the bottom which reflects a beam of light from a mirror at the top, where the interval of time required to travel from the source to the top and back again – the period between two ticks of the light clock – is $T_0 = 2L_0/c$. But a stationary observer of the moving frame traveling at velocity v sees the light travel a distance $cT/2$ from the source to the top, during which period of time the moving frame has traveled a distance $vT/2$.

Thus, employing the Pythagorean Theorem, from the standpoint of the stationary observer:

$$(cT/2)^2 = L_0^2 + (vT/2)^2 = (cT_0/2)^2 + (vT/2)^2$$

$$c^2T^2 = c^2T_0^2 + v^2T^2$$

$$T=\frac{1}{\sqrt{1-(v^2/c^2)}}T_0=\gamma T_0$$

Therefore, the Lorentz Factor is:

$$\gamma=\frac{1}{\sqrt{1-(v^2/c^2)}} \tag{A.1}$$

As the time period in the moving frame, from the standpoint of the stationary observer, is longer by a factor of γ, it appears to the stationary observer that time itself has slowed in the moving inertial frame. [251]

A slightly more complicated derivation of the Lorentz Factor examines the transformation of coordinates from a rest inertial frame S to a moving inertial frame S′ as shown in Figure A.2.

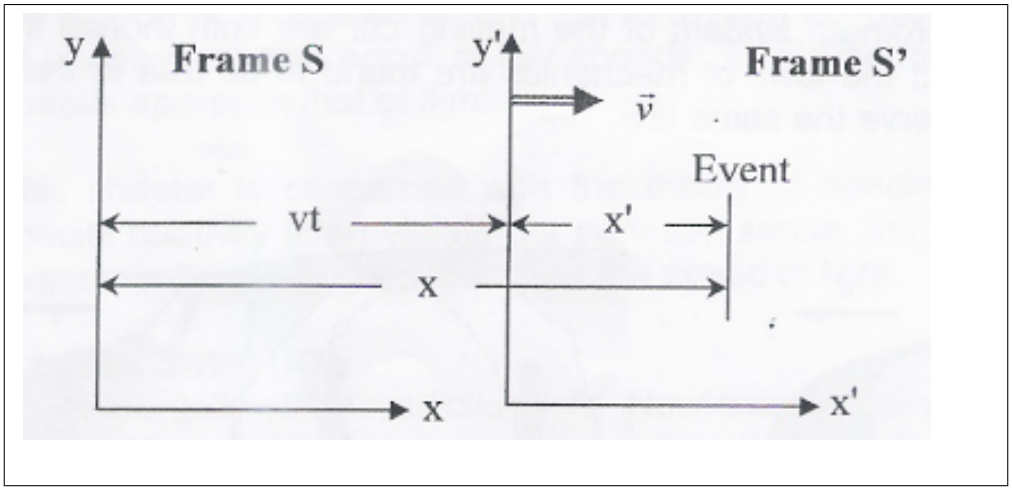

Figure A.2 : Rest inertial frame S and moving inertial frame S′ with a relative velocity v, with the respective coordinates of a single Event being (t, x, y, z) and (t', x', y', z'). Adapted from W. Rindler, Introduction to Special Relativity, 2d Ed. 1991.

Assuming relative movement only in the x-direction to simplify the example, the

observer from the S frame sees the event at (t, x) while the observer in the S′ frame places the same event at (t', x'). The classical relation between these two sets of coordinates – the so-called Galilean transformation – is:

$$t'=t, \quad x'=x-vt, \quad y'=y, \quad z'=z$$

But differentiating with respect to $t'=t$ immediately reveals the problem by noting that $\frac{dx'}{dt'}=\frac{dx}{dt}-v$, or $u'_1=u_1-v$. Thus, if a particle has a velocity $u'_1=c$ along the x′-axis in the S′ frame, by the classical law of velocity addition, $u_1=c+v$ in the S frame. But of course this violates Einstein's law that the speed of light is the same for all inertial observers, regardless of the motion of the source.

In addition, it is assumed that space itself is both homogeneous and isotropic: that is, the laws of physics do not change from one place to another in space. The condition that space is isotropic means that physical values do not change with orientation of the reference frame; e.g., observers in the two different reference frames would agree on the value of their relative velocity with respect to each other, v, as a 180 degree coordinate rotation simply reverses their roles. Moreover, the condition of homogeneity imposes the requirement that any transform from one inertial frame to the other be linear, of the form $x'=Ax+B$, because any additional nonlinear terms – like Cx^2, for example – would cause the transform itself to vary under coordinate translations. Thus, the transformation from the S to the S′ inertial reference frame must be linear, regardless of the reference frame one starts from, and we may denote that factor as γ, and re-write the spatial relationship in the x-direction between the

two inertial reference frames as follows:

$$x'=\gamma(x-vt)$$

$$x=\gamma(x'+vt')$$

And since the speed of light is the same in both reference frames, requiring that $x=ct$ and $x'=ct'$, it then follows that:

$$xx'=\gamma^2(xx'+xvt'-x'vt-v^2tt')$$

And substituting in $x=ct$ and $x'=ct'$, and solving for γ reveals:

$$c^2tt'=\gamma^2(c^2tt'+vctt'-vct't-v^2tt')$$

$$\gamma^2=\frac{1}{1-(v^2/c^2)} \qquad \Rightarrow \qquad \gamma=\frac{1}{\sqrt{1-(v^2/c^2)}}$$

Thus, the Lorentz factor is γ, and the Lorentz transformations between the S frame and the S$'$ frame for this example become:

$$t'=\gamma(t-vx/c^2), \quad x'=\gamma(x-vt), \quad y'=y, \quad z'=z$$

As expected, these resolve to the old Galilean transformations when $v<<c$. [252]

To complete the analysis, one finds that the mass of an object in motion is dependent on γ and the rest mass, m_0: $m=\gamma m_0$. Further, relativistic momentum is $p=mv=\gamma m_0 v$; and relativistic kinetic energy is $E_k=E-E_0=(\gamma-1)m_0c^2$. [253]

A.2 Elastic Collision Energy Loss Derivation

For GCR ions traversing a shielding material, the energy loss by elastic collisions with electrons through Coulomb interactions is the major energy loss channel, while there is an additional minor component attributed to collisions with the nuclei in the material. However, for the secondary neutron emissions elastic collisions with the target nuclei is the primary stopping mechanism. [27] Elastic collisions are defined by a scenario where the particles interacting are the same before and after the collision and kinetic energy and momentum are conserved – sometimes referred to as the classic "pool ball" collision.[1] In the case of HZE ions interacting with electrons, the "collision" usually does not result in actual physical contact, but takes place within a range, often called the "impact parameter" b.

The physical scenario in two-dimensions is illustrated in Figure A.3 – obviously, real-world scattering takes place in three-dimensions, but that adds unnecessary complexity at this juncture. Despite the illustration scale, initially envision that the projectile m_1 is the incident HZE ion impacting the target medium at velocity v_1, and that the target m_2 is a stationary electron in the target medium (thus, v_2=0). The collision then occurs somewhere within impact parameter b, and after the collision, the HZE ion alters its path by angle θ, with a new velocity of u_1, and the electron alters its path by angle ϕ, with a new velocity of u_2.

In order to determine the energy transferred to the electron, one must calculate KE_e=$\frac{1}{2}m_2u_2^2$. Since this is an elastic collision, kinetic energy and momentum are conserved. Considering the kinetic energy and treating the total momentum of the

[1] By contrast, in inelastic collisions, which occur less frequently, the kinetic energy is not conserved, rather some of the energy is absorbed by the target atom, resulting in excitation or ionization. The other possible scenario is a nuclear reaction, involving creation of secondary emissions of new atomic products or individual atomic constituents (such as neutrons), fragmentation products that quickly decay, and electromagnetic radiation. [38]

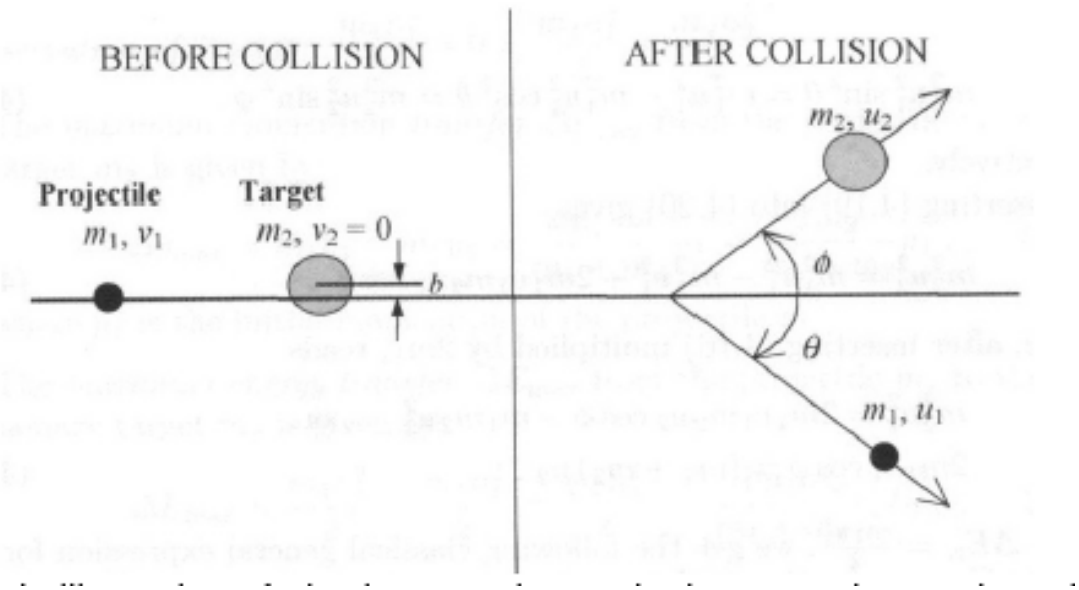

Figure A.3 : Two-Dimensional Elastic Collision Scenario. Adapted from Class Notes, MECH 592 & PHYS 541, Rice University.

system as a vector quantity in the $x - y$ plane, results in the following relationships:

$$\frac{1}{2}m_1v_1^2 + \frac{1}{2}m_2v_2^2 \quad = \quad \frac{1}{2}m_1v_1^2 + 0 \quad = \quad \frac{1}{2}m_1u_1^2 + \frac{1}{2}m_2u_2^2$$

$$m_1v_{1x} + m_2v_{2x} \quad = \quad m_1v_{1x} + 0 \quad = \quad m_1u_1cos\theta + m_2u_2cos\phi$$

$$m_1v_{1y} + m_2v_{2y} \quad = \quad 0 + 0 \quad = \quad m_1u_1sin\theta + m_2u_2sin\phi$$

Given the initial conditions of m_1, m_2, v_1, and v_2=0, it is obvious that there are still four unknowns and only three equations, thus there is no unique solution unless at least one of the unknowns is specified. Note that the same situation obtains if the relationships are written for three-dimensions, which requires designating additional angels to specify the velocity vector in the $x - y - z$ coordinate system, or to transform the problem specification to polar coordinates. But without specifying further

conditions beyond the masses and initial pre-impact velocities of the two particles, no unique solution can be obtained.

Simplification of the problem to a perfect head-on collision allows viewing the collision scenario in one-dimension, where a unique solution can be found. Doing so also provides the useful metric of the maximum energy transferable from the incident HZE ion to the target electron, which devolves from simply calculating the change in kinetic energy of the incident HZE ion, and by the conservation principle that differential must reside in the target particle (given that it was initially stationary); and moreover, this differential kinetic energy is the maximum energy that can be transferred because the velocity vector operates in a single direction (i.e., the impact parameter b=0, ϕ=0, and θ=0 to specify forward scattering (i.e., $m_1 > m_2$) or $\theta=\pi$ to specify back-scattering (i.e., $m_1 < m_2$)).

Thus, the principle of conservation of energy provides that:

$$E = \frac{1}{2}m_1 v_1^2 + \frac{1}{2}m_2 v_2^2 = \frac{1}{2}m_1 u_1^2 + \frac{1}{2}m_2 u_2^2$$

And, the principle of conservation of momentum provides that:

$$P = m_1 v_1 + m_2 v_2 = m_1 u_1 + m_2 u_2$$

Thereby, providing two equations with only two unknowns when the masses and initial velocities of the two particles are specified. Combining these two equations and solving for the final velocities of the two particles yields:

$$u_1 = \frac{(m_1 - m_2)v_1}{m_1 + m_2} + \frac{2m_2 v_2}{m_1 + m_2} \qquad u_2 = \frac{2m_1 v_1}{m_1 + m_2} - \frac{(m_1 - m_2)v_2}{m_1 + m_2}$$

Next, simplifying the problem further by setting the initial velocity of the target electron at zero (v_2=0) to replicate the scenario of the HZE ion hitting the target shielding material, and then solving for the maximum energy transfer as the difference between the initial and final kinetic energy of the incident HZE ion, yields the following after substituting in the above expression for u_1:

$$Q_{max} = \frac{1}{2}m_1v_1^2 - \frac{1}{2}m_1u_1^2 = \frac{4m_1m_2(\frac{1}{2}m_1v_1^2)}{(m_1+m_2)^2} = \frac{4m_1m_2(KE_{i-m_1})}{(m_1+m_2)^2} \quad \text{(A.2)}$$

Thus, this expression can be conveniently used to calculated the maximum transfer of energy to a target particle by simply knowing the mass of both the incident and target particles, and the incident particle's initial kinetic energy; e.g., a 50 MeV proton colliding with a target electron, or, alternatively, a 10 MeV secondary neutron colliding with an aluminum atom nucleus in a shielding material. Note also in this scenario that when m_1=m_2, then u_1=0, indicating that the incident particle is completely stopped, and all kinetic energy is transferred to the target particle.

Another useful simplification is to consider the scenario where m_1>>m_2, as is the case for an HZE ion from the GCR impacting shielding and colliding with a target electron. In that case:

$$Q_{max}=\frac{4m_1m_2(KE_{i-m_1})}{(m_1+m_2)^2}\rightarrow m_1>>m_2\rightarrow\frac{4m_1m_2(KE_{i-m_1})}{m_1^2}=\frac{4m_2(KE_{i-m_1})}{m_1}=2m_2v_1^2 \quad \text{(A.3)}$$

This formulation allows quick calculation of the maximum energy transfer per collision between a heavy particle, like an HZE ion projectile, and an electron target particle, by knowing either the incident particle's initial kinetic energy or its initial velocity before impact; e.g., Q_{max}=$2m_ev_{HZE-ion}^2$.

A.3 Ion Stopping Power Derivation

The GCR radiation is comprised of mostly positively charged ions stripped of their electrons, and thus as they traverse a material they are slowed by the action of the force between the outer-shell electrons and the ion given by Coulomb's inverse-square law:

$$F{=}k_0\frac{q_1q_2}{r^2}{=}k_0\frac{(Ze)(e)}{r^2} \tag{A.4}$$

where the Coulomb constant $k_0{=}8.99\times10^9Nm^2C^{-2}$, Z is the atomic charge of the ion, e is the charge of an electron, and r is the distance between the incident ion and the target electron. This situation is depicted in Figure A.4.

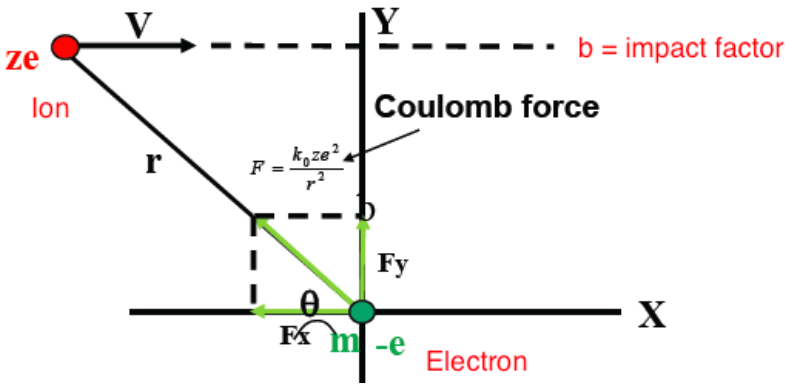

Figure A.4 : Stopping Power of Ion-Electron Interaction in Target Medium. From Lecture Notes, MECH 592 & PHYS 541, Rice University.

The Stopping Power may be derived from a classical mechanics standpoint (á la Niels Bohr) by making the following assumptions: (1) a heavy charged particle (+Ze) travels swiftly past an electron (e^-) at a distance b (the impact factor); (2) the collision happens so quickly that the electron does not move, and thus as a result, the x-component of the force, F_x, transfers no net momentum (because the electron

remains stationary); and (3) the incident HZE ion is fully stripped of its electrons and is much heavier than the target electron.

The transfer of momentum is only through the y-component of the Coulomb force, and is calculated, (noting that force is defined as the rate of change of momentum $F{=}\frac{dp}{dt}{=}m\frac{dv}{dt}{=}ma$), as follows:

$$p{=}\int_{-\infty}^{\infty}F_y dt{=}\int_{-\infty}^{\infty}F cos\theta dt{=}\int_{-\infty}^{\infty}k_0\frac{(Ze)(e)}{r^2}cos\theta dt{=}k_0Ze^2\int_{-\infty}^{\infty}\frac{cos\theta}{r^2}dt \tag{A.5}$$

At $t{=}0$ the HZE incident ion crosses the y-axis, thus $cos\theta{=}b/r$, allowing a symmetrical integral:

$$p{=}k_0Ze^2\int_{-\infty}^{\infty}\frac{1}{r^2}\frac{b}{r}dt{=}2k_0Ze^2\int_{0}^{\infty}\frac{b}{r^3}dt \tag{A.6}$$

Then, noting by the Pythagorean theorem that $r^2{=}a^2+b^2$, where along the x-axis, $a^2{=}v^2t^2$, then $r^2{=}v^2t^2+b^2$, or $r{=}\sqrt{v^2t^2+b^2}$, then it follows that:

$$p{=}2k_0Ze^2\int_{0}^{\infty}\frac{b}{(v^2t^2+b^2)^{3/2}}{=}2bk_0Ze^2\int_{0}^{\infty}\frac{dt}{(v^2t^2+b^2)^{3/2}} \tag{A.7}$$

And evaluating the integral $t{\to}\infty$ yields:

$$\lim_{t\to\infty}\Big[\frac{t}{b^2(b^2+v^2t^2)^{1/2}}\Big]{=}\lim_{t\to\infty}\Big[\frac{1}{b^2(\frac{b^2}{t^2}+v^2)^{1/2}}\Big]{=}\frac{1}{b^2v}$$

And evaluating the integral as $t{\to}0$ yields:

$$\lim_{t\to 0}\Big[\frac{t}{b^2(b^2+v^2t^2)^{1/2}}\Big]{=}0$$

Thus:

$$p{=}2bk_0Ze^2(\frac{1}{b^2v}){=}\frac{2k_0Ze^2}{bv} \tag{A.8}$$

To determine the energy transferred by one ion-electron collision at impact distance b, and recalling that $p{=}m_ev$, then the energy transferred is:

$$Q{=}\frac{1}{2}m_ev^2{=}\frac{p^2}{2m_e}{=}\frac{1}{2m_e}\Big[\frac{2k_0Ze^2}{bv}\Big]^2{=}\frac{2k_0^2Z^2e^4}{m_ev^2b^2} \tag{A.9}$$

In traversing a distance dx in the target medium with a uniform density of n electrons per unit volume, the incident HZE ion with charge Ze will encounter $2\pi nbdbdx$ electrons. Thus, the differential energy loss of the incident HZE ion would simply be the number of electrons encountered times the energy loss per encounter, Q:

$$dE{=}Q2\pi nbdbdx$$

And it follows that the differential rate of energy loss – often referred to as the Linear Energy Transfer (LET) – is shown as a negative quantity by convention to indicate that energy is *lost* by the incident HZE ion, and is expressed as follows:

$$-\frac{dE}{dx}{=}2\pi nQbdb$$

The differential energy loss is evaluated by integrating over all possible energy losses as a function of the impact parameter b, as follows:

$$-\frac{dE}{dx}{=}2\pi n\int_{Q_min}^{Q_max}Qbdb{=}2\pi n\int_{b_min}^{b_max}Qbdb{=}2\pi n\int_{b_min}^{b_max}\Big[\frac{2k_0^2Z^2e^4}{m_ev^2b^2}\Big]bdb$$

And completing the integration, the the differential rate of energy loss by the incident HZE ion due to Coulomb interactions with electrons in the target medium is:

$$-\frac{dE}{dx}=\frac{4\pi nk_0^2Z^2e^4}{m_ev^2}\int_{b_{min}}^{b_{max}}\frac{1}{b}db=\frac{4\pi nk_0^2Z^2e^4}{m_ev^2}\ln\frac{b_{max}}{b_{min}} \tag{A.10}$$

The final step involves determining the range of the impact parameter b from a classical mechanics perspective. The logarithm term – sometimes called the "collision factor" or "stopping number" – simply scales the energy loss due to each ion-electron collision based upon the size of the impact parameter, and has been the subject of various approaches over the years to fine tune the differential energy loss calculation.

One method evaluates the range of impact parameter b at its extremes based upon the physical assumptions as to the nature of the ion-electron impact.

Thus, as to b_{max}: As b becomes larger, the encounter between the HZE ion and the target electron becomes softer and longer in time (corresponding to Q_{min}). To satisfy the initial assumption that the passage of the HZE ion is very sudden, one may impose the restriction that the passage must take place in less time than the period of the electron in its orbit, or $T=\frac{1}{\omega}$, where ω is the orbital frequency (obviously, $\omega=\frac{2\pi r_{orbit}}{v_e}$). If the time elapsed of the collision is on the order of the frequency of motion of the electron, then its orbit will be minimally perturbed. The time require for the ion to travel the length of the impact parameter b is simply $t=b/v$. Thus, for the interaction to close the gap of the impact parameter b in less time than the electron period, requires that $\frac{b}{v}\leq\frac{1}{\omega}$; and it follows that $b_{max}=\frac{v}{\omega}$.

And, as to b_{min}: The minimum distance for the impact parameter size can be determined because b must be at least as large as the wave associated with HZE ion where an effective head-on collision occurs (thus Q_{max}), i.e., the de Broglie wavelength,

which is $\lambda = \frac{h}{mv}$. Thus, $b_{min} \approx \frac{h}{mv}$.

Thus, in its classical formulation the differential energy loss becomes:

$$-\frac{dE}{dx} = \frac{4\pi n k_0^2 Z^2 e^4}{m_e v^2} \ln \frac{v/\omega}{h/mv} = \frac{4\pi n k_0^2 Z^2 e^4}{m_e v^2} \ln \frac{mv^2}{h\omega}$$

Another, perhaps more useful method, evaluates the impact parameters based on the differential energy imparted at each extreme of the range using the previously derived relationship: $Q(b) = \frac{1}{2} m_e v^2 = \frac{2k_0^2 Z^2 e^4}{m_e v^2 b^2}$.

The minimum energy transferred will be at b_{max}, and that energy can be reasonably estimated as the minimum ionization potential of the target material. Thus, setting $Q_{min} = I$, results in $b_{max} = \sqrt{\frac{2k_0 Z^2 e^4}{m_e v^2 I}}$.

Likewise, the maximum energy transfer occurs at b_{min} with a head-on collision, where, from a previous derivation for maximum energy transfer between a heavy ion and an electron, it follows that $Q_{max} = 2m_e v^2$. Thus, $b_{min} = \sqrt{\frac{2k_0 Z^2 e^4}{2m_e^2 v^4}}$.

Then by substituting into the previously derived general expression, one gets the classical derivation of the differential rate of energy loss, attributed to Niels Bohr [71], as follows:

$$-\frac{dE}{dx} = \frac{4\pi n k_0^2 Z^2 e^4}{m_e v^2} \ln \frac{b_{max}}{b_{min}} = \frac{4\pi n k_0^2 Z^2 e^4}{m_e v^2} \ln \sqrt{\frac{2m_e v^2}{I}} = \frac{4\pi n k_0^2 Z^2 e^4}{m_e v^2} \frac{1}{2} \ln \frac{2m_e v^2}{I} \quad \text{(A.11)}$$

where I is the mean ionization potential of the target material, which has been estimated in a number of ways, including $I = \omega h$, or as $I = \omega h/2$, or as $I = h\omega/Z_T$, or with empirical expressions like $I = 11.2 + 11.7 eV Z_T$, for $2 \leq Z_T \leq 13$, and etc. [72] [73].

But by 1932 Hans Bethe proposed a modification to the "collision factor" to take into account the quantum effects, which primarily impacted the formulation of b_{min},

as the energy transfer at b_{max} is considerably smaller. In addition, the relativistic nature of ions was also taken into account around the same time by incorporating the Lorentz factor transformations (previously derived). The result was what has become the most popular and most used equation – the so-called relativistic formulation of the differential rate of energy loss, as follows:

$$-\frac{dE}{dx}=\frac{4\pi nk_0^2Z^2e^4}{m_ev^2}\ln\frac{2m_ev^2}{I}=_{v\rightarrow c}=\frac{4\pi nk_0^2Z^2e^4}{m_ec^2\beta^2}\left[\ln\frac{2m_ec^2\beta^2}{I(1-\beta^2)}-\beta^2\right] \tag{A.12}$$

where $\beta=v/c$. [254] Obviously, when $v<<c$, then the collision factor reverts to the classical mode, as shown ($\ln\frac{2m_ev^2}{I}$). It is additionally noted in connection with this formulation that at lower projectile velocities for the HZE ions, the impact parameter for Coulomb scattering ($b\approx\frac{2Ze^2}{mv^2}$) is greater than the de Broglie wavelength, meaning that the projectile will act more classically, or particle-like (E.g., *see* Everhart, 1955 [78]). Of course this is not true at higher velocities.

In more recent years, various correction factors have been appended to the Bethe formulation, most of which impact the calculation slightly, but only at relatively low energy levels for the projectile ion (e.g., $ke<20MeV/n$). [255] [72] These correction factors include: (1) the shell correction term $C(\beta)/Z_T$, to account for ionization variations when the projectile velocity is comparable to the velocities of the electrons in the target atoms; (2) the Barkas correction term $Z_pL_1(\beta)$, to account for polarization within the target medium due to low-energy collisions between the projectile and distant electrons, which accounts for the observed effect of different ranges for various particles and their antiparticles (e.g., positive and negative pions); (3) the Bloch correction term $Z_p^2L_2(\beta)$, to account for differences between classical and quantum

mechanical range-energy calculations for the projectile ion; and (4) the Mott and density correction term $L_3(\beta)$, to account for electron scattering of highly charged nuclei, and for dense target mediums, to account for the reduction in the rate of energy loss of the projectile due to the dielectric polarization of atoms caused by the passage of the incident charged particle. [72] [9] These various correction factors have been appended to the basic relativistic formulation of the differential rate of energy loss of an ion traversing a medium, and by convention noted with a negative sign to indicate *energy loss* of the incident ion $(-\frac{dE}{dx})$, all of which is approximately equal to the Stopping Power of the target medium when considering Galactic Cosmic Ray ions incident on shielding materials[2], as follows:

$$S=\frac{4\pi Z_p^2 \rho Z_T N_A e^4}{A_T m_e \beta^2 c^2}\left[ln\Big(\frac{2m_e c^2\beta^2\gamma^2}{I}\Big) - \beta^2 - \frac{C\big(\beta\big)}{Z_T} + Z_p L_1\big(\beta\big) + Z_p^2 L_2\big(\beta\big) + L_3\big(\beta\big)\right] \quad \text{(A.13)}$$

[72] [68] [75] Here the density of the target medium is (ρ), its charge (Z_T), its atomic weight (A_T), and the Avogadro number is (N_A).[3]

---

[2] Recall that the Linear Energy Transfer (LET) is defined as the average energy *locally deposited* by an ion passing through a material: $LET{=}-\frac{dE}{dx}$. Recall also that Stopping Power (S) is defined as the average energy lost by a charged particle passing through a material, which is equal to the LET plus secondary radiation energy losses (bremsstrahlung + Cherenkov + nuclear collisions). But for HZE ions in the GCR, $S{\approx}LET{=}-\frac{dE}{dx}$.

[3] As can be seen, the front part of this formulation is essentially the same as the Bethe relativistic formulation, when one considers that the Coulomb constant in SI units is $k_0{=}\frac{1}{4\pi\epsilon_0}{=}c^2 \times 10^{-7} H/m$ (where ϵ_0 is the magnetic field free space permittivity in a vacuum, and H (henry), is in units of $kg{-}m^2{-}C^{-2}) = 8.987{\times}10^9 N{-}m^2{-}C^{-2}$, and that target material electron density is $n{=}N_A Z_T \rho / A_T$.

A.4 Boltzmann Equation Application to GCR Ion Transport

The starting point for deriving an equation to describe the GCR particle transport through a target medium is by balancing the change in particle flux as it crosses a small volume of material with the gains and losses caused by nuclear collisions; i.e., the flux density of the radiation $\phi_j(\mathbf{x},\mathbf{\Omega},E)$ at a particular location, assuming a steady-state flow. The problem is depicted in Figure A.5, a closed, convex, homogeneous differential volume of target material, e.g., a sphere in three dimensions.

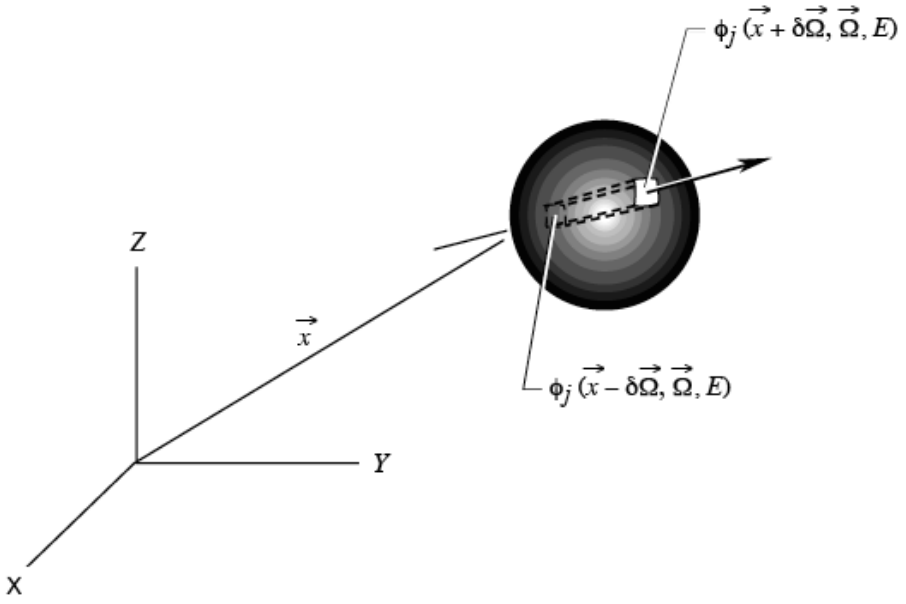

Figure A.5 : Transport of Particles through a Spherical Region. From Wilson, 1991.

The relevant transport equations are derived on the basis of conservation principles by considering a region of space filled with matter described by appropriate atomic and nuclear cross sections. Because the volume of any material is mostly electrons, the interaction of energetic ions passing through any material is primarily with these electrons. The long range of the nuclear Coulomb field – the elastic collision of

the ion with target nuclei – also presents a sizable cross section to the passing ion. While ion collisions are dominated by these two processes, the individual collisions themselves, which do not require actual physical contact but occur within a zone defined by the impact parameter, result in the exchange of only small amounts of energy and have little effect on the passing ions (i.e., the ions continue to traverse the medium generally along their incident path). Although most collisions in the target medium are the Coulomb collisions with orbital electrons and nuclei, the rare nuclear reactions are important to consider because of the larger amount of energy transferred in the reaction, and because of the generation of new energetic particles – secondary emissions of different ions and neutrons. [68]

The numbers tell the story:

$$\sigma_j(E) \quad = \quad \sigma_j^{at}(E) + \sigma_j^{el}(E) + \sigma_j^{nr}(E) \tag{A.14}$$

where the total cross section is the sum of microscopic atomic, elastic collision, and nuclear reaction cross sections, which are approximately as follows for typical GCR ions impacting standard materials (and also noting the approximate energy transfer per interaction):

$$\sigma_j^{at}(E) \approx 10^{-16} cm^2 \qquad \Delta E_{at} \approx 10^2 eV$$

$$\sigma_j^{el}(E) \approx 10^{-19} cm^2 \qquad \Delta E_{el} \approx 10^6 eV$$

$$\sigma_j^{nr}(E) \approx 10^{-24} cm^2 \qquad \Delta E_{nr} \approx 10^8 eV$$

[68] [38] Another way to envision the relative magnitudes of each kind of interaction is to note that the number of atomic collisions that occur in a centimeter of ordinary matter is $\approx 10^6/cm$, and the number of Coulombic elastic collisions is only $\approx 10^3/cm$;

whereas at the other extreme there may be only a few nuclear reactions per centimeter, and for neutrons, of course, $\sigma_n^{at}(E) \approx 0$ (where neutron interactions are dominated by elastic scattering, for which mean free paths will vary with energy).[4] [38]

With that preliminary information, and referring to Figure A.5, a small differential volume enclosed by a sphere of radius δ is shown. The surface element is given by $\delta^2 d\mathbf{\Omega}$, and when projected through the center of the sphere forms a flux tube through which particles may pass and be accounted for. Since the flux density is defined as $\phi_j(\mathbf{x},\mathbf{\Omega},E)$, the number of j type particles leaving the surface element is given by $\phi_j(\mathbf{x}+\delta\mathbf{\Omega},\mathbf{\Omega},E)(\delta^2 d\mathbf{\Omega})$, and the number entering at the opposite end of the flux tube would be $\phi_j(\mathbf{x}-\delta\mathbf{\Omega},\mathbf{\Omega},E)(\delta^2 d\mathbf{\Omega})$, where $\mathbf{x}$ is a position vector to the center of the sphere, $\mathbf{\Omega}$ is the direction vector perpendicular to the surface element $\delta^2 d\mathbf{\Omega}$, and E is the particle energy. The number of particles entering and leaving the flux tube would be equal if the interior was a vacuum, but if considering a target medium the number of particles leaving would differ from the number entering by the gains and losses associated with atomic and nuclear collisions, as follows:

$$\begin{aligned}
\phi_j(\mathbf{x}+\delta\mathbf{\Omega},\mathbf{\Omega},E)(\delta^2 d\mathbf{\Omega}) &= \phi_j(\mathbf{x}-\delta\mathbf{\Omega},\mathbf{\Omega},E)(\delta^2 d\mathbf{\Omega}) \\
+ \quad \delta^2 d\mathbf{\Omega}\int_{-\delta}^{\delta}\Big[\sum_k \iint \sigma_{jk}(E,E',\mathbf{\Omega},\mathbf{\Omega}')\phi_k(\mathbf{x}+l\mathbf{\Omega},\mathbf{\Omega}',E')d\mathbf{\Omega}'dE'\Big]dl \\
- \quad \delta^2 d\mathbf{\Omega}\int_{-\delta}^{\delta}\sigma_j(E)\phi_j(\mathbf{x}+l\mathbf{\Omega},\mathbf{\Omega},E)dl
\end{aligned}$$

[4] As to the matter of transfer of the kinetic energy of the incident GCR ion into new secondary radiations – for which unique cross sections must be calculated – one must consider several processes, including direct knockout of nuclear constituents, resonant excitation followed by particle emission, pair production, and possible coherent effects within the nucleus. Through these processes, a single particle incident on a shield may attenuate through energy transfer to electrons of the target medium, or generate a cascade of secondaries which could cause an increase in exposure to humans or equipment behind the shielding medium. Furthermore, the process that dominates depends on energy, particle type, and composition of the target medium. [68]

On the left side of this equation is the expression for the number of j type particles leaving the flux tube at the surface element of the sphere. And on the right side of this equation are three terms, which account for (1) the number of j type particles entering the flux tube through the opposite surface element, *plus* (2) the j type particles generated within the flux tube, integrated over its total volume, $2\delta(\delta^2 d\mathbf{\Omega})$, where the cross section $\sigma_{jk}(E,E',\mathbf{\Omega},\mathbf{\Omega}')$ represents all processes by which type k particles moving in direction $\mathbf{\Omega}'$ with energy E' create a type j particle that moves in direction $\mathbf{\Omega}$ with energy E, *minus* (3) the loss of j type particles by all processes within the flux tube, integrated over its same total volume, where the total cross section for such interactions is $\sigma_j(E)$, as shown in Eq. A.14. [96]

By expansion of terms on both sides of the equation and retaining only those terms to the order of δ^3 (recognizing that the terms $O(\delta^4)\rightarrow 0$ as $\delta\rightarrow 0$), yields:

$$\begin{aligned}(\delta^2 d\mathbf{\Omega})\Big[\phi_j(\mathbf{x},\mathbf{\Omega},E)+\delta\mathbf{\Omega}\cdot\nabla\phi_j(\mathbf{x},\mathbf{\Omega},E)\Big] &= (\delta^2 d\mathbf{\Omega})\Big[\phi_j(\mathbf{x},\mathbf{\Omega},E)-\delta\mathbf{\Omega}\cdot\nabla\phi_j(\mathbf{x},\mathbf{\Omega},E)\Big] \\ &+ 2\delta\sum_k\iint\sigma_{jk}(E,E',\mathbf{\Omega},\mathbf{\Omega}')\phi_k(\mathbf{x},\mathbf{\Omega}',E')d\mathbf{\Omega}'dE' \\ &- 2\delta\sigma_j(E)\phi_j(\mathbf{x},\mathbf{\Omega},E)\end{aligned}$$

and by dividing through by the flux tube cylindrical volume, $2\delta(\delta^2 d\mathbf{\Omega})$, yields:

$$\mathbf{\Omega}\cdot\nabla\phi_j(\mathbf{x},\mathbf{\Omega},E)=\sum_k\iint\sigma_{jk}(E,E',\mathbf{\Omega},\mathbf{\Omega}')\phi_k(\mathbf{x},\mathbf{\Omega}',E')d\mathbf{\Omega}'dE'-\sigma_j(E)\phi_j(\mathbf{x},\mathbf{\Omega},E) \quad \text{(A.15)}$$

which is the same as Eq. 4.2, the time-independent form of the Boltzmann equation, but requires further simplification to be useful in practical applications. [96] [68]

NASA and academic collaborators have been working for the past 40 years to simplify this formulation of the GCR radiation transport problem sufficiently to make a useful tool for evaluating shielding, and then in some respects to enhance that effort as faster computers and new numerical methods have been developed. The result was the development of the HZETRN (High-Charge-Energy Transport) code [68] [97] [106] [103], with modifications and improvements continuing to this day, and HZETRN has recently been made more widely available to researchers through an internet-accessed version called OLTARIS (On-Line Tool for the Assessment of Radiation In Space). [107] The key simplification measures are summarized below.

First, handling the millions of atomic collisions per centimeter of ordinary matter that an impinging ion has with the target medium electrons has been transformed from a discrete examination of each interaction into the so-called continuous slowing down approximation (CSDA), on the assumptions that the exchange of energy happens so quickly and with so many interactions, that it can be viewed as a continuous process, by factoring out and evaluating the atomic microscopic cross section contributions in terms of Stopping Power. Recognizing that the total atomic cross section for delivering energy to the orbital electrons from the GCR ion traversing the target medium can be expressed as follows:

$$\sigma_j^{at}(E) \quad = \quad \sum_n \sigma_{jn}^{at}(E)$$

where n labels the target medium atom excitation levels; and because for positively charged ions the Coulombic atomic and molecular interactions contribute most to the

Stopping Power, so that it can be formulated as follows:

$$S_j(E) \quad = \quad \sum_n \epsilon_n \sigma_{jn}^{at}(E)$$

where ϵ_n represents the corresponding electronic excitation energy; then these relationships provide a convenient direct relationship between the atomic cross section and energy deposition by the ion particle. [96] [103] Accordingly, the atomic cross section terms in Eq. A.15 can be rewritten as follows:

$$\sum_k \iint \sigma_{jk}^{at}(E,E',\mathbf{\Omega},\mathbf{\Omega'})\phi_k(\mathbf{x},\mathbf{\Omega'},E')d\mathbf{\Omega'}dE' - \sigma_j^{at}(E)\phi_j(\mathbf{x},\mathbf{\Omega},E)$$

$$= \quad \sum_n \sigma_{jn}^{at}(E+\epsilon_n)\phi_j(\mathbf{x},\mathbf{\Omega},E+\epsilon_n) - \sigma_j^{at}\phi_j(\mathbf{x},\mathbf{\Omega},E)$$

$$\approx \quad \sum_n \sigma_{jn}^{at}(E)\phi_j(\mathbf{x},\mathbf{\Omega},E) + \sum_n \epsilon_n \frac{\partial}{\partial E}\Big[\sigma_{jn}^{at}(E)\phi_j(\mathbf{x},\mathbf{\Omega},E)\Big] - \sigma_j^{at}\phi_j(\mathbf{x},\mathbf{\Omega},E)$$

$$= \quad \frac{\partial}{\partial E}\Big[S_j(E)\phi_j(\mathbf{x},\mathbf{\Omega},E)\Big]$$

where $S_j(E)$ is the Stopping Power associated with ion particle type j, and can be evaluated independently by calculating the LET in accordance with Eq. 3.5, and the various cross sections calculated by some form of Eq. 3.6, or experimentally determined input data. [96] With these relationships for the continuous slowing down approximation, the three-dimensional Boltzmann formulation for GCR transport through a medium set forth in Eq. A.15 can be rewritten as follows:

$$\mathbf{\Omega}\cdot\nabla\phi_j(\mathbf{x},\mathbf{\Omega},E) - \frac{\partial}{\partial E}\Big[S_j(E)\phi_j(\mathbf{x},\mathbf{\Omega},E)\Big] + \sigma_j(E)\phi_j(\mathbf{x},\mathbf{\Omega},E)$$
$$= \quad \sum_k \iint \sigma_{jk}(E,E',\mathbf{\Omega},\mathbf{\Omega'})\phi_k(\mathbf{x},\mathbf{\Omega'},E')d\mathbf{\Omega'}dE' \quad \text{(A.16)}$$

where the cross sections in Eq. A.16 now include only the nuclear contributions. [96] Thus, the right hand side of Eq. A.16 excludes all atomic and molecular collision processes, which now appear on the left hand side of the equation in terms of an energy shifting operator, in addition to terms describing spatial drift and nuclear absorption terms. [103]

Second, to further simply the Boltzmann formulation, it may be reduced to a one dimensional analysis. This enables a measure of computational simplicity by numerical means, and such a simplifying assumption is justified by the fact that the GCR ions impacting a target medium are slowed down in large part by the Coulombic collisions with target electrons and nuclei, interactions which in most respects do not involve a physical collision, but rather a passing within the zone of the impact parameter b (*see* Eq. A.11). Thus, the path of the principle incident ion is not altered to any great degree, as demonstrated by the representative GCR ion tracks in a silicon target, shown in Figure 3.2. As a result, Eq. A.16, after rearranging terms, can be rewritten in one dimension, as follows (which is precisely Eq. 4.3):

$$\Big[\frac{\partial}{\partial x} - \frac{\partial}{\partial E}S_j(E) + \sigma_j(E)\Big]\phi_j(x,E) \quad = \quad \sum_k \int \sigma_{k\rightarrow j}(E,E')\phi_k(x,E')dE' \qquad \text{(A.17)}$$

where x is now the scalar location along the x-axis. This is the formulation of the Boltzmann transport equation for GCR traversing a target medium that is incorporated in the NASA HZETRN code and OLTARIS. [96] [105] [68] [97] [108] [104] [103] Thus, this formulation allows determination by numerical means of the heavy ion flux density, $\phi_j(x,E)$, of an ion particle type j with an atomic mass number, A_j, with an atomic charge, Z_j, and energy E (MeV/n) (*see* Eq. 3.5), at a depth of x (g/cm^2)

in a shielding medium. Since the original implementation, some enhancements have been included, particularly in better describing the cross sections, and consideration has recently been given to adding limited three dimensional aspects. [103] [110] [111]

It is also helpful to examine each term of the one dimensional Boltzmann equation for transport of GCR ions through a target medium, Eq. A.17, in order to understand the focus of each term, as follows:

The so-called drift operator is the rate of change of the flux of type j particles with kinetic energy E at a depth of x in the target material:

$$\frac{\partial}{\partial x}\phi_j(x,E) \quad \Rightarrow\left[\frac{cm^2}{gm}\right]\left[\frac{\#}{cm^2-E}\right]=\left[\frac{\#}{gm-E}\right]$$

The continuous slowing down approximation term (CSDA) is calculated from the Stopping Power associated with each ion type, by calculating the linear energy transfer of the ion (LET):

$$\left[\frac{\partial}{\partial E}S_j(E)\right]\phi_j(x,E) \quad = \quad \left[\frac{\partial}{\partial E}\frac{dE}{dx}\right]\phi_j(x,E) \quad \Rightarrow\left[\frac{cm^2}{gm}\right]\left[\frac{\#}{cm^2-E}\right]=\left[\frac{\#}{gm-E}\right]$$

The nuclear attenuation term accounts for type j particles that are absorbed in the target medium (recalling that in this formulation the cross section has only nuclear elastic collision and reaction components):

$$\sigma_j(E)\phi_j(x,E) \quad \Rightarrow\left[\frac{cm^2}{gm}\right]\left[\frac{\#}{cm^2-E}\right]=\left[\frac{\#}{gm-E}\right]$$

The nuclear production term accounts for all processes by which a type k particle of energy E' may produce a type j particle of energy E, again recalling that in this formulation the cross section has only nuclear elastic collision and reaction components,

and noting that by definition : $\sigma_{k\to j}(E,E') \equiv \frac{d}{dE}\sigma_{k\to j}(E') \Rightarrow \left[\frac{1}{E}\frac{cm^2}{gm}\right] = \left[\frac{cm^2}{gm-E}\right]$:

$$\sum_k \int \sigma_{k\to j}(E,E')\phi_k(x,E')dE' \quad \Rightarrow \left[\frac{cm^2}{gm-E}\right]\left[\frac{\#}{cm^2-E'}\right]\left[\frac{E'}{1}\right] = \left[\frac{\#}{gm-E}\right]$$

Note also that (1) depth into the target medium, x, is measured in terms of "areal thickness" expressed in units of $\left[\frac{gm}{cm^2}\right]$, (2) cross sections, e.g., $\sigma_j(E)$, are related to the probability of a particular interaction occurring in the interaction volume in units of $\left[\frac{cm^2}{gm}\right]$ (the inverse of areal thickness), (3) the Stopping Power, $S_j(E) \approx -\frac{dE}{dx}$, is measured in units of $\left[\frac{E}{g/cm^2}\right]$ where depth is measured as areal thickness, and (4) the differential flux, $\phi_j(x,E)$, is in units of $\left[\frac{\#}{cm^2-E}\right]$. [256] [257]

With this information, the one dimensional Boltzmann equation for GCR radiation transport in a target medium can be constructed from the simplest construct (which can be solved analytically), to the more complicated form that requires the numerical methods embedded in the HZETRN code, as follows:

As a first order approximation, consider neglecting nuclear reactions completely, so that the rate of change of flux of type j particles, with energy E at a particular depth in the target medium, is equal to CSDA term, i.e., the energy loss due solely to interactions with target electrons – a formulation that can be solved analytically:

$$\frac{\partial}{\partial x}\phi_j(x,E) - \left[\frac{\partial}{\partial E}S_j(E)\right]\phi_j(x,E) \quad = \quad 0$$

where $S_j(E)$ is calculated as the LET of type j particles as a function of kinetic energy, E.

Then, adding complexity (and accuracy), the nuclear attenuation term may be added, which accounts for losses of type j particles associated with nuclear interactions and

are considered "absorbed" by the medium (another formulation that can be solved analytically):

$$\frac{\partial}{\partial x}\phi_j(x,E) - \Big[\frac{\partial}{\partial E}S_j(E)\Big]\phi_j(x,E) + \sigma_j(E)\phi_j(x,E) \quad = \quad 0$$

Finally, the nuclear production term may be added to account for all processes by which type k particles might produce a type j particle at a given energy (a formulation that requires numerical computation to solve):

$$\frac{\partial}{\partial x}\phi_j(x,E) - \Big[\frac{\partial}{\partial E}S_j(E)\Big]\phi_j(x,E) + \sigma_j(E)\phi_j(x,E) \quad = \quad \sum_k \int \sigma_{k\to j}(E,E')\phi_k(x,E')dE'$$

And after rearranging terms, yields:

$$\Big[\frac{\partial}{\partial x} - \frac{\partial}{\partial E}S_j(E) + \sigma_j(E)\Big]\phi_j(x,E) \quad = \quad \sum_k \int \sigma_{k\to j}(E,E')\phi_k(x,E')dE'$$

which is precisely Eq. A.17 that is implemented in the HZETRN and OLTARIS. [256]

A.5 NASA HZETRN Ion Transport Numerical Algorithm

The HZETRN radiation transport code is based on a one-dimensional marching algorithm, which propagates the incident GCR radiation spectrum into a target shielding material and follows the attenuation of primary incident ions and generation of secondary emissions with respect to depth. Particle fluence depth profiles are obtained and dose-depth relationships calculated from them, from which other commonly used metrics are calculated, such as dose equivalent exposure rates.

NASA has done extensive studies to minimize the relative error in its numerical approximations to within 0.2% [208], has verified the HZETRN code results against simplified one-particle analytical calculations to within 2% [96], and against simplified one-particle ion beam experiments to within 5% [97], as well as one study comparing HZETRN and three-dimensional Monte Carlo simulations on very simplified slab geometries to within 10%. [142] Nevertheless, because of the simplifying assumptions made in formulating the ion transport equations and the biological assessment models, NASA admits that the dose equivalent metrics reported in the literature could have "an uncertainty factor of 2 or more in exposure predictions." [96]

As discussed in detail in Section 4.1, the fundamental approach in the development of HZETRN was using conservation principles to express a time-independent one-dimensional steady-state flux density of the incident GCR ions and secondary emissions as follows:

$$\frac{\partial}{\partial x}\phi_j(x,E)=\frac{\partial}{\partial E}\left[\phi_j(x,E)\frac{1}{A_j}S_j(E)\right]-\sigma_j(E)\phi_j(x,E)+\sum_k\int_E^\infty\sigma_{jk}(E,E')\phi_k(x,E')dE' \qquad \text{(A.18)}$$

where the rate of change of flux of type j particles with kinetic energy E as a function of depth x in the target material equals (1) the rate of decrease in flux of type j particles at a depth of x in the target material with kinetic energy E due to loss

of energy and subsequent particle absorption as a result of the Coulombic stopping force of the target electron field (recalling that $S_j(E)$ is negative and is equal to the change in E per unit distance), minus (2) the type j particles with kinetic energy E absorbed by nuclear collisions in accordance with the cross sections $\sigma_j(E)$, plus (3) the type j particles produced with kinetic energy E as a result of all interaction processes with all particles k with kinetic energy E', as dictated by the production cross sections $\sigma_{jk}(E,E')$ (each absorption or production term expressed in units of number of particles per unit mass per kinetic energy level E, where depth in the target material is expressed in terms of areal density (gm/cm^2)).

Re-arranging terms allows for a more convenient form, where on the left hand side of the equation are the terms associated with atomic and nuclear reactions that slow down and absorb the incident ion particle, and on the right hand side of the equation are the terms that account for the creation of secondary emissions from the radiation particles:

$$\Big[\frac{\partial}{\partial x} - \frac{\partial}{\partial E}\frac{1}{A_j}S_j(E) + \sigma_j(E)\Big]\phi_j(x,E) \quad = \quad \sum_k \int_E^{\infty} \sigma_{jk}(E,E')\phi_k(x,E')dE' \qquad \text{(A.19)}$$

with the boundary condition $\phi(0,E)=f_j(E)$. Thus, this formulation allows determination of the ion flux density, $\phi_j(x,E)$, of an ion particle type j with an atomic mass number, A_j, with an atomic charge, Z_j, and energy E (MeV) (these and other terms required to compute $S_j(E)$, *see* Eq. 3.5), at a depth of x (g/cm^2) in a shielding medium, where the boundary condition spectrum, $f_j(E)$, is considered to be a known function over a broad energy spectrum.

NASA's approach to solving Equation A.19 has evolved over the years, as ex-

plained in recent conversations with Dr. Tony Slaba at the Langley Research Center, and involves a combination of analytical and numerical methods that first involves transforming the transport equation from spatial and energy variables to spatial and proton range variables, then transforming this integro-differential equation into integral form that is then expressed in an explicit marching procedure. The numerical procedures include developing (1) an energy grid to cover the relevant range of the subject radiation environment, and a stopping power and ion range grid to provide these values for all 59 ions transported when called for in a calculation, (2) a cubic Langrange interpolating polynomial scheme to call data from the energy and range grids, and (3) a modified trapezoidal method to approximate the integrals. NASA has developed an interactive database comprised of 14,365 cross-section estimates to account for the most likely electronic and nuclear interactions for the 59 ion species included, plus ion fragments, which are correlated to experimental data where available. [97] The fundamental assumptions include transport of the incident GCR ions through a specified shielding material based on the straight-ahead, one-dimensional conservation approximation equation stated above. [209] However, the numerical process for evaluating the subject equation is separated into two parts: the fully energy dependent transport equation for the light particles (protons, helium, and neutrons), and a slightly simplified form for all heavier ions that treats the interaction cross sections as constant with respect to energy, based on the simplifying assumption that for the heavier ions the secondary emissions have an energy and direction very nearly the same as the projectile, whereas that is not true for the lighter particles. [106]

The transformation from spatial and energy variables to spatial and ion ranges is accomplished by employing Hans Bethe's theory (*see* Equation 3.5), whereby the stopping power and range of other particles can be expressed as a function of those

quantities for protons, as follows:

$$S_j(E)=\frac{A_p Z_j^2}{A_j Z_p^2} S_p(E) \qquad\qquad \frac{Z_j^2}{A_j} r_j(E)=\frac{Z_p^2}{A_p} r_p(E)$$

where A and Z are the atomic weight and charge, respectively, of protons (p) and the other (heavier) ions (j). [96] It follows then that a scaling parameter ν_j can be defined as:

$$\nu_j r_j(E) \approx \nu_k r_k(E) \qquad where \qquad \nu_j=\frac{Z_j^2}{A_j}$$

and recalling that the range of a type j ion is a function of its stopping power, such that:

$$r_j(E) \equiv A_j \int_0^E \frac{dE'}{S_j(E')} dE'$$

and thus the proton stopping power, $S_p(E)$, can be approximated as:

$$\nu_j S_p(E) \approx \frac{1}{A_j} S_j(E)$$

which allows the transport equation to be written in terms of proton stopping power:

$$\Big[\frac{\partial}{\partial x} - \frac{\partial}{\partial E} S_p(E) + \sigma_j(E)\Big] \phi(x,E) \quad = \quad \sum_k \int_E^\infty \sigma_{jk}(E,E') \phi_k(x,E') dE' \qquad \text{(A.20)}$$

which is the transport equation for light particles, where the assumption that particle secondaries will travel in the same direction with approximately the same energy does not hold, thus both projectile and target fragments are included in the transport procedure requiring summation over all particles k with energy E' producing a light

ion or neutron, and the variation in production cross sections as a function of energy must be taken into account.

Then to complete the transformation to spatial and range variables, the scaled fluence, $\psi(x,r)$, and scaled production cross section, $s_{jk}(r,r')$, in terms of proton stopping power and the common residual proton range, r, are defined as follows:

$$r=\int_0^E \frac{dE'}{S_p(E')}dE'$$

$$\psi(x,r)\equiv\bar{\nu_j}S_p(E)\phi(x,E)$$

$$s_{jk}(r,r')\equiv S_p(E)\sigma_{jk}(E,E')$$

noting that a modified scaling factor, $\bar{\nu_j}$, is defined as equal to 1.0 if $j=n$ and equal to ν_j if $j\neq n$, in order to avoid a trivial solution for neutrons. Thus, Equation A.20 for light particle transport simplifies in form to:

$$\Big[\frac{\partial}{\partial x}-\nu_j\frac{\partial}{\partial r}+\sigma_j(r)\Big]\psi_j(x,r) \quad = \quad \sum_k \frac{\bar{\nu_j}}{\bar{\nu_k}}\int_r^\infty s_{jk}(r,r')\psi_k(x,r')dr'$$

which allows Equation A.20 to be rewritten as a function of only the depth into the target medium (x) and the residual range of the protons (r) and all other particles with a higher energy, expressed in terms of proton range (r'), creating light particles. Using the proton stopping power and range as a scaling factor ($r\approx\nu_j r_j$) greatly simplifies subsequent calculations, and as can be seen from Figure A.6 induces only minor error in range calculations, and only at the very lowest ion energy levels.

A final mathematical step is taken to transform this equation into one with only

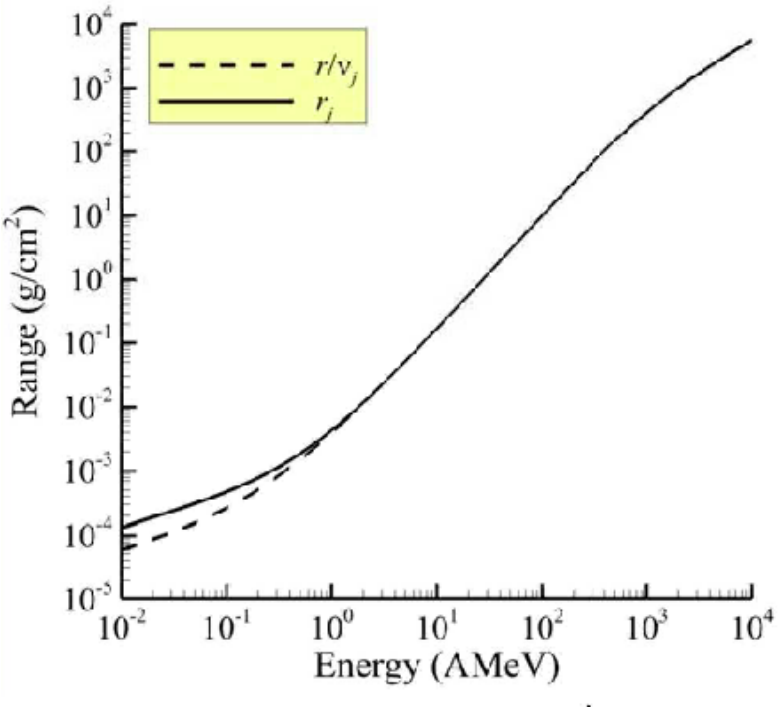

Figure A.6 : Comparison of Scaled Proton Range, r/ν_j, and actual ^{4}He range, r_j as a function of ion energy (MeV/n), as provided by Dr. Tony Slaba of NASA's Langley Research Center (TP-216213).

integrals to evaluate[5], as follows:

$$\begin{aligned}\psi_j(x,r) = & e^{-\beta_j(r,x)}\psi_j(0,r+\nu_j x) \\ & + \sum_k \frac{\bar{\nu_j}}{\bar{\nu_k}} \int_0^x \int_{r+\nu_j x'}^{\infty} e^{-\beta_j(r,x')} s_{jk}(r+\nu_j x', r')\psi_k(x-x', r')dr'dx'\end{aligned} \tag{A.21}$$

where the exponential integrating factor is $\beta_j(r,x) = \int_0^x \sigma_j(r+\nu_j l)dl$. [106] This equation

[5] NASA determined that converting the transport equation to spatial and range coordinates, scaled to the residual range, r, of a proton, would simplify subsequent numerical procedures, and that converting the transport equation to integral form avoided the introduction of unstable roots that occurred with a straightforward finite differencing of the transport equation which included coupled partial differential and integral equations. [108] The mathematical procedure to transform the integro-differential equation into integral form is detailed in the Appendicies to NASA Technical Report 2010-216213. [211]

is then rewritten in the form of an explicit marching procedure in terms of step-size h as follows, by first noting that a simplified marching formulation as:

$$\psi_j(x+h,r)=e^{-\beta_j(r,h)}\psi_j(x,r+\nu_j h)$$

is the exact solution to the homogeneous transport equation:

$$\Big[\frac{\partial}{\partial x}-\nu_j\frac{\partial}{\partial r}+\sigma_j(r)\Big]\psi_j(x,r) \quad =0$$

where secondary particle production through nuclear interactions is neglected, and accounts for only the loss of particles due to atomic interactions and nuclear absorption. [211] Extending the marching procedure to the secondary particle production term results in the full explicit marching procedure for light particles:

$$\begin{aligned}\psi_j(x+h,r)=&e^{-\beta_j(r,h)}\psi_j(x,r+\nu_j h)\\ &+\sum_k\frac{\bar{\nu_j}}{\bar{\nu_k}}\int_0^x\int_{r+\nu_j x'}^{\infty}e^{-\beta_j(r,x')-\beta_k(r',h-x')}\\ &\times s_{jk}(r+\nu_j x',r')\psi_k(x,r'+\nu_k(h-x'))dr'dx'+O(h^2)\end{aligned} \tag{A.22}$$

where the new scaled fluence on the left hand side represents particles of type j at position $x+h$ with range r. This new scaled fluence is calculated from the terms on the right hand side of the equation: (1) the exponential term represents attenuation due to nuclear absorption within a step-size h; (2) the current scaled fluence on the right hand side represents type j particles at position x with residual range $r+\nu_j h$, with the difference in range values representing the energy down shift caused by atomic interactions within the step-size h; and (3) the summation and integral terms

represent production of light particles, along with nuclear absorption and atomic slowing down over the step-size h. To facilitate convergence, the step-size should be sufficiently small such that $h<<1/\sigma_j(r)$ (i.e., much less than the nuclear mean free path); thus, since the nuclear mean free path lengths are on the order of many gm/cm^2, then a step-size of $h\leq 1.0 gm/cm^2$ is sufficient to assure that the particles will not have travelled far enough to suffer a nuclear collision. [209] [208]

The numerical approximation to Equation A.22 begins with establishing the energy and range grids in order to facilitate subsequent calculations: the energy grid is a discrete set of energy values distributed from a minimum energy, E_{min}, to a maximum energy, E_{max}, to represent the input radiation environment, where E_i is the ith component; and the range grid is a discrete set of proton range values distributed from a minimum proton range, r_{min}, to a maximum proton range, r_{max}, where r_i is the ith component. For each, the total grid size is indexed from i=1 to i=N, with equal log_{10} spacing, and as both are related as a function of stopping power, $S_j(E)$, this facilitates conversion of an energy grid value to a range grid value, and vice-versa using the equation for r given above. In terms of residual range, a table of ranges and stopping powers are computed for ions from Z=1 to Z=92 over a broad energy grid, and at any point in the code where stopping powers or ranges are needed, an interpolation is performed over the pre-generated database to get the needed result. For example, the quantity in the marching algorithm, $\psi_j(x,r+\nu_j h)$ for j-type ions must be evaluated for range values not on the prescribed r-grid, and thus a cubic Lagrange interpolating polynomial is employed to facilitate those calculations. [96]

To evaluate the source particle integrals in Equation A.22, NASA first employs a modified single midpoint method to simplify the integral over x' from 0 to h, yielding

the following:[6]

$$\begin{aligned}\psi_j(x+h,r) = & e^{-\beta_j(r,h)}\psi_j(x,r+\nu_j h) \\ & + \sum_k \frac{\bar{\nu_j}}{\bar{\nu_k}} \int_{r+\nu_j h/2}^{\infty} e^{-\beta_j(r,h/2)-\beta_k(r',h/2)} \\ & \times \left[\int_0^h s_{jk}(r+\nu_j x',r')dx'\right]\psi_k(x,r'+\nu_k h/2)dr'\end{aligned} \tag{A.23}$$

where the approximation method has decoupled the source particle integrals, but injects a further convergence consideration regarding the maximum step-size, requiring that $h<<r/\nu_j \approx r_j$. This constraint arises because of the very short proton ranges at the low end of the energy spectrum; e.g., the range of a 100 MeV proton in aluminum is $\approx 10 gm/cm^2$ (thus a step-size of 0.5 - 1.0 gm/cm^2 will suffice), but a 10 MeV proton has a range in aluminum of only $\approx 0.17 gm/cm^2$, and a 1 MeV proton has a range in aluminum of only $\approx 0.004 gm/cm^2$ before coming to rest (*see* Figure A.6). Thus, at a step-size of 0.5 gm/cm^2 this approximation will inject some error by systematically under-predicting the source integral for secondary particle production from projectiles with very low ranges; however, on a dose equivalent metric basis the error is minor as it pertains only to particles with very low energies. [106]

To calculate the secondary particle production cross sections for charged particles, the following term is defined:

---

[6] NASA's Dr. Tony Slaba has described this in private conversations as "basically a composite trapezoidal rule" where for integrable functions a(x), b(x), and c(x):

$$\int_0^h a(x)b(x)c(x)dx \approx a(h/2)\left[\int_0^h b(x)dx\right]c(h/2)$$

which is sufficiently accurate if a(x) and c(x) are nearly constant over the interval [0,h] [108].

$$F_{jk}^{\nabla}(r,r';h) \equiv \int_0^h s_{jk}(r+\nu_j x', r')dx' = \frac{1}{\nu_j}\left[\int_0^{\epsilon(r+\nu_j h)} \sigma_{jk}(E,E')dE - \int_0^{\epsilon(r)} \sigma_{jk}(E,E')dE\right]$$

where the term $\epsilon(r)$ is the energy associated with the proton range r.[7]

The remaining exponential attenuation terms are simplified by using a first order series expansions, which for a step-size of 0.5 gm/cm^2 have been shown to produce negligible errors [106]:

$$e^{-\beta_j(r,h)} = e^{-\int_0^h \sigma_j(r,-\nu_j t)dt} \approx e^{-\sigma_j(r)h}$$

$$e^{-\beta_j(r,h/2)} = e^{-\int_0^{h/2} \sigma_j(r,-\nu_j t)dt} \approx e^{-\sigma_j(r)h/2}$$

$$e^{-\beta_k(r',h/2)} = e^{-\int_0^{h/2} \sigma_k(r',-\nu_k t)dt} \approx e^{-\sigma_k(r')h/2}$$

Thus, the light particle transport equation is now reduced to:

$$\begin{aligned}\psi_j(x+h,r) = e^{-\sigma_j(r)h}\psi_j(x, r+\nu_j h) \\ + \sum_k \frac{\bar{\nu_j}}{\bar{\nu_k}} \int_{r+\nu_j h/2}^{\infty} e^{-\sigma_j(r)h/2 - \sigma_k(r')h/2)} \\ \times F_{jk}^{\nabla}(r,r';h)\psi_k(x, r'+\nu_k h/2)dr'\end{aligned} \tag{A.24}$$

The final integral is approximated with a "composite quasi-midpoint method" which is evaluated over several sub-intervals, x_i, with a corresponding sub-range, r_i, within a given step-size region (where $\bar{r_m} \equiv (r_{m+1} + r_m)/2$), which results in the final form of the light particle transport equation approximation as:[8]

[7] For neutron fragments, denoted by $j{=}n$: $F_{nk}^{\nabla}(r,r';h) \equiv \int_0^h s_{nk}(r+\nu_n x', r')dx' = h s_{nk}(r,r')$.

[8] NASA's Dr. Tony Slaba has described this in private conversations as a "one-point quasi-

$$\psi_j(x+h,r_i)=e^{-\sigma_j(r_i)h}\psi_j(x,r_i+\nu_j h) + \sum_k \frac{\bar{\nu_j}}{\bar{\nu_k}} \sum_{m=1}^{N-1} e^{-\sigma_j(r_i)h/2-\sigma_k(r_m)h/2} F_{jk}^{\nabla}(r_i,\bar{r_m}+\nu_j h/2);h) \times [\Psi_j(x,r_m+(\nu_j+\nu_k)h/2) - \Psi_j(x,r_{m+1}+(\nu_j+\nu_k)h/2)] \quad \text{(A.25)}$$

where the integral fluence is defined as:

$$\Psi_j(x,r) \equiv \int_r^{\infty} \psi_j(x,r'')dr'' = \bar{\nu_j} \int_E^{\infty} \phi_j(x,E)$$

by making a change of variables ($r''=r'-\nu_j h/2$), and is evaluated using a "composite Simpson's rule" approximation method (private conversation with NASA's Dr. Tony Slaba). It should also be noted that the marching light particle transport Equation A.25 requires that the integral fluence be computed and interpolated at each sub-interval step, and thus the integral is evaluated by continuously updating the fluence of each j-type particle, over the entire spectrum of particles, after each sub-interval, having started with the total fluence of j-type particles over the entire spectrum of particles in the radiation environment as a given input initial condition at the shielding boundary.

Figure A.7 provides a general description of the light particle marching algorithm

---

midpoint rule" that is extended over several sub-intervals to a "quasi-composite trapezoidal rule" where the approximation of the integral for functions f(x)and g(x) is as follows:

$$\int_a^b f(x)g(x)dx \approx f(\bar{x}) \int_a^b g(x)dx \approx \sum_{i=1}^{N-1} f(\bar{x_i}) \int_{x_i}^{x_{i+1}} g(x)dx$$

where $\bar{x}=(a+b)/2$, and is accurate if $f(x)$ is nearly constant over the interval $[a,b]$; or if not, then the composite quasi-midpoint rule is used, where $x_1=a$, $x_N=b$, and $\bar{x_i}=(x_i+x_{i+1})/2$, and which requires that the sub-intervals $[x_i,x_{i+1}]$ to be sufficiently small such that $f(x)$ is nearly constant over the sub-intervals.

transport process as implemented in HZETRN. Thus, the required input boundary condition parameters are the initial and final positions as well as the boundary flux/fluence at the initial position. The next step is to determine the maximum step-size (where h_{max}<$0.5gm/cm^2$), and integer P such that P iterations of the light particle marching equation will propagate the fluences of all particles in the radiation spectrum from the initial position to the final position in the target material. Once the constant step-size has been determined, the exponential attenuation term and production cross sections are computed for all values of proton range, r, on the r-grid, drawing on the interactive database of cross sections and look-up tables, as appropriate, through various sub-routines based on semi-empirical and parametric models (*see* NASA Technical Paper 2887). [209]. These values are then used repeatedly within the main loop. Once the main loop is entered, the integral fluence must be computed by updating from the boundary condition for absorbed and secondary emission particles during the interval, and the differential and integral fluences must be interpolated for each particle type and each range value. [211] NASA continues to work on improvements to this analytical/numerical procedure to improve computational efficiency and precision, as well as to better account for the small errors induced by step-size efficiency compromises, particularly at the very low particle energy end of the radiation spectrum. [106]

In contrast, for heavier ions it has been shown that the projectile fragments in a collision continue to travel straight ahead at approximately the same energy, while target fragments from such collisions are produced isotropically and are immediately absorbed, and thus can be ignored insofar as transport is concerned, which greatly simplifies the equation (with a correction made by empirical data to dose after the flux profiles are computed). The absence of target fragments in the heavy ion transport

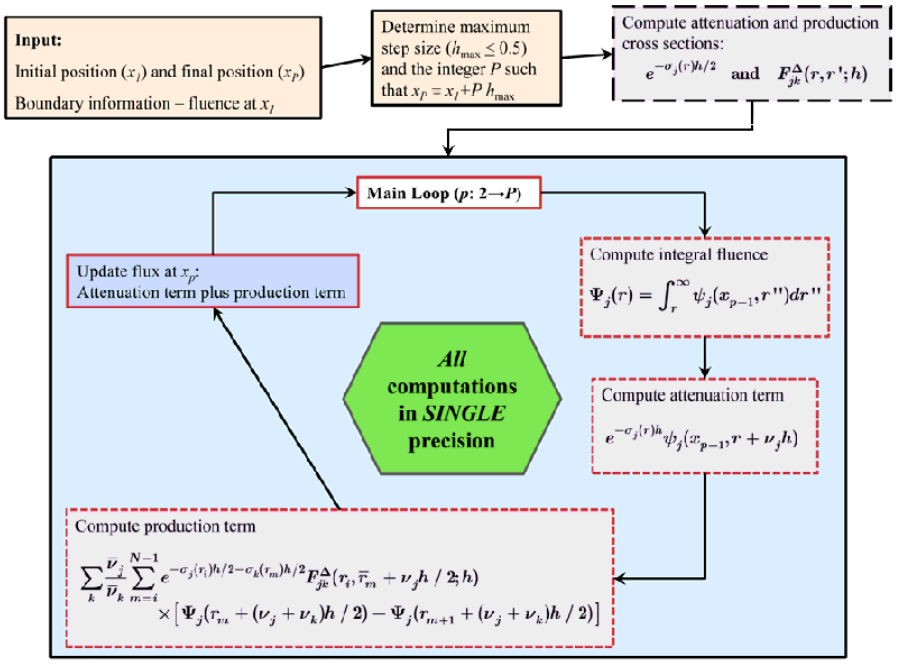

Figure A.7 : HZETRN Light Particle Transport Procedure implemented in OLTARIS, as provided by Dr. Tony Slaba of NASA's Langley Research Center (TP-216213).

procedure allows taking the summation over all projectiles with mass greater than that of the produced secondary ion type j, and thus the transport equation for heavy ions in terms of proton stopping power is simplified from that in Equation A.19 as follows:

$$\left[\frac{\partial}{\partial x} - \nu_j \frac{\partial}{\partial E} S_p(E) + \sigma_j(E)\right]\phi(x,E) \quad = \quad \sum_{k>j} \sigma_{jk}(E)\phi_k(x,E) \tag{A.26}$$

where the equal velocity assumption allows the variation in production cross sections with energy to be ignored, and the heavy ion fluences are scaled with $\nu_j S_p(E)$. [108]

To complete the spatial and energy (x,E) transformation to spatial and range (x,r), as was done for the light particles, the scaled heavy ion fluence is defined as:

$$\psi_j(x,r) \equiv \nu_j S_p(E) \phi_j(x,E)$$

and $\sigma_{jk}(E)$ is replaced with $\sigma_{jk}(r)$, as range and energy are convertible as previously shown, which results in a scaled transport equation for heavy ions as follows:

$$\Big[\frac{\partial}{\partial x} - \nu_j \frac{\partial}{\partial r} + \sigma_j(r)\Big]\psi_j(x,r) \quad = \quad \sum_{k>j} \frac{\nu_j}{\nu_k} \sigma_{jk}(r) \psi_k(x,r)$$

which employs ν_j instead of $\bar{\nu_j}$ as was done with the light particle equation, because here only heavy ions with $Z>2$ are being transported, thus there is no need to account for the trivial scaling solution as all $\nu_j>0$.

As before, a final mathematical step is taken to transform this equation into one with only integrals to evaluate:

$$\begin{aligned} \psi_j(x,r) = & e^{-\beta_j(r,x)} \psi_j(0, r + \nu_j x) \\ & + \sum_{k>j} \frac{\nu_j}{\nu_k} \int_0^x e^{-\beta_j(r,x')} \sigma_{jk}(r + \nu_j x') \psi_k(x - x', r - \nu_j x') dx' \end{aligned} \tag{A.27}$$

where the exponential integrating factor is $\beta_j(r,x) = \int_0^x \sigma_j(r + \nu_j t) dt$. [106] This equation is then rewritten in the form of a marching procedure in terms of step-size h as follows:

$$\begin{aligned} \psi_j(x+h,r) = & e^{-\beta_j(r,h)} \psi_j(x, r + \nu_j h) \\ & + \sum_{k>j} \frac{\nu_j}{\nu_k} \int_0^h e^{-\beta_j(r,x')} \sigma_{jk}(r + \nu_j x') \psi_k(x + h - x', r + \nu_j x') dx' \end{aligned} \tag{A.28}$$

Then, as before, the first order homogeneous solution is used to note that:

$$\psi_k(x+h-x',r-\nu_j x')=e^{-\beta_k(r+\nu_j x',h-x')}\psi_k(x,r+\nu_j x'+\nu_k(h-x'))+O(h)$$

in accordance with Wilson, et al. 2006 [108], and after substituting back into the previous equation, results in the heavy ion marching procedure as follows:

$$\begin{aligned}\psi_j(x+h,r)=&e^{-\beta_j(r,h)}\psi_j(x,r+\nu_j h)\\&+\sum_{k>j}\frac{\nu_j}{\nu_k}\int_0^h e^{-\beta_j(r,x')-\beta_k(r+\nu_j x',h-x')}\sigma_{jk}(r+\nu_j x')\\&\times\psi_k(x,r+\nu_j x'+\nu_k(h-x'))dx'+O(h^2)\end{aligned}\tag{A.29}$$

where the new scaled fluence on the left hand side represents particles of type j at position $x+h$ with range r. This new scaled fluence is calculated from the terms on the right hand side of the equation: (1) the exponential term represents attenuation due to nuclear absorption within a step-size h; (2) the current scaled fluence on the right hand side represents type j particles at position x with residual range $r+\nu_j h$, with the difference in range values representing the energy down shift caused by atomic interactions within the step-size h; and (3) the summation and integral terms represent production of the lighter j-type heavy ions from heavier k-type ions, along with nuclear absorption and atomic slowing down over the step-size h.

The numerical approximation of Equation A.29 proceeds by (1) approximating the integral over x' from 0 to h by expanding the production cross section and scaled fluence in a Taylor series, neglecting all second order terms, and (2) approximating the integrals in the argument of the exponential functions in similar fashion by expanding

in a Taylor series, and neglecting all second order terms. [211][9] This results in the final heavy ion transport marching procedure, as follows:

$$\begin{aligned}\psi_j(x+h,r) = & e^{-\beta_j(r,h)}\psi_j(x,r+\nu_j h) \\ & + \sum_{k>j}\frac{\nu_j}{\nu_k}\sigma_{jk}(r+\nu_j h/2) \\ & \times \psi_k(x,r+(\nu_j+\nu_k)h/2)\frac{e^{-\sigma_j(r+\nu_j h/2)h} - e^{-\sigma_k(r+(\nu_j+\nu_k)h/2)h}}{\sigma_k(r+(\nu_j+\nu_k)h/2) - \sigma_j(r+\nu_j h/2)}\end{aligned} \tag{A.30}$$

These approximations allow the integrals to be evaluated exactly, and thus the only numerical technique required to evaluate this Equation A.30 is interpolation, using the same cubic Langrange interpolating polynomial that is used for the light particle calculations. [106]

The GCR radiation environment is composed of protons, alpha particles and heavier ions with $Z>2$, thus to simultaneously transport all of these particles through a

---

[9] Expanding the production cross section and particle fluence terms in a Taylor series results in:

$$\sigma_{jk}(r+\nu_j x') = \sigma_{jk}(r+\nu_j h/2) + O(x')$$

$$\psi_k(x,r+\nu_j x'\nu_k(h-x')) = \psi_k(x,r+(\nu_j+\nu_k)h/2) + O(x')$$

Similarly, the Taylor series expansion for the exponential terms are given as:

$$\beta_j(r,x') = \int_0^{x'}\sigma_j(r+\nu_j t)dt \approx \int_0^{x'}\sigma_j(r+\nu_j h/2)dt = \sigma_j(r+\nu_j h/2)x' + O((x')^2)$$

$$\begin{aligned}\beta_k(r+\nu_j x', h-x') &= \int_0^{h-x'}\sigma_k(r+\nu_j x'+\nu_k t)dt \approx \int_0^{h-x'}\sigma_k(r+\nu_j x'+\nu_k h/2)dt \\ &= \sigma_k(r+\nu_j x'+\nu_k h/2)(h-x') \approx \sigma_k(r+(\nu_j+\nu_k)h/2) + O((x')^2)\end{aligned}$$

Thus, the integral is evaluates as:

$$\begin{aligned}\int_0^h e^{-\beta_j(r,x')-\beta_k(r+\nu_j x', h-x')}dx' &\approx \int_0^h e^{-\sigma_j(r+\nu_j h/2)x') - \sigma_k(r-(\nu_j-\nu_k)h/2)(h-x')}dx' \\ &= \frac{e^{-\sigma_j(r+\nu_j h/2)h} - e^{-\sigma_k(r+(\nu_j+\nu_k)h/2)h}}{\sigma_k(r+(\nu_j+\nu_k)h/2) - \sigma_j(r+\nu_j h/2)} + O((x')^2)\end{aligned}$$

target medium, the light particle and heavy ion marching algorithms must be coupled. The complete HZETRN marching algorithm for the GCR environment is written as:

$$\begin{aligned}\psi_j(x+h,r_i) = & e^{-\sigma_j(r_i)h}\psi_j(x,r_i+\nu_j h) \\ & + H(J-j)\sum_k \frac{\bar{\nu_j}}{\bar{\nu_k}} \sum_{m=1}^{N-1} e^{-\sigma_j(r_i)h/2-\sigma_k(r_m)h/2)} F_{jk}^{\nabla}(r_i,\bar{r_m}+\nu_j h/2);h) \\ & \times [\Psi_j(x,r_m+(\nu_j+\nu_k)h/2) - \Psi_j(x,r_{m+1}+(\nu_j+\nu_k)h/2)] \\ & + \sum_{k>J^*} \frac{\nu_j}{\nu_k}\sigma_{jk}(r+\nu_j h/2) \\ & \times \psi_k(x,r+(\nu_j+\nu_k)h/2) \frac{e^{-\sigma_j(r+\nu_j h/2)h} - e^{-\sigma_k(r+(\nu_j+\nu_k)h/2)h}}{\sigma_k(r+(\nu_j+\nu_k)h/2) - \sigma_j(r+\nu_j h/2)}\end{aligned} \tag{A.31}$$

where the index J^* refers to the heaviest light ion (^{4}He), and the Heaviside function is defined as $H(J-j)\equiv 0$ if $j>J$, or 1 if $j\leq J$; and the lower limit of the last summation term is defined as $J^*\equiv j$ if $j>J$, or J if $j\leq J$. Thus, the physical interpretation is straightforward whereby the new scaled fluence at position $x+h$ with residual range (energy) r_i is calculated from the terms on the right hand side of the equation: (1) the exponential term represents attenuation due to nuclear absorption within a step-size h; (2) the current scaled fluence on the right hand side represents type j particles at position x with residual range $r_i+\nu_j h$, with the difference in range values representing the energy down shift caused by atomic interactions within the step-size h; (3) the double summation term is the source of light particles produced from light projectiles, and is only evaluated if the particle subscript j refers to a light particle; and (4) the single summation term is the source for both light and heavy particles produced from heavy ion projectiles (which is the coupling mechanism between the light particle and heavy ion transport equations).

The total charged-particle field $\phi(x,E)$ is calculated at each step by sampling the interactive database of cross sections, and converting from the total flux $\psi(x,r)$ for all ions in succession to a flux as a function depth into the target and kinetic energy, by calculating the appropriate stopping power ($S(E)$) for each ion, thus facilitating relating the total ion spectrum at some point x to that spectrum at a point $x + h$; and thereby enabling propagation of the ion spectrum from the boundary of the shielding material (at x=0) to any interior point. [209] [208] The stopping power $S(E)$ is calculated using the Bethe-Bloch formula set out in Equation 3.5, except for low energies, when empirical data is employed through a look-up table. [209] Once the ion spectrum is known at a particular point in the target medium, and recalling the definition of an ion's range as a function of energy noted above ($r(E)$), then the absorbed dose per unit mass (D) and dose equivalent (H) behind the shielding, can be calculated:

$$D(x,>E)=\int_E^\infty \psi(x,r(E))dE \qquad\qquad H(x,>E)=\int_E^\infty Q(E)\psi(x,r(E))dE$$

which are the metrics commonly used in shielding design studies for protection against GCRs. [96] [208]

Appendix B

Simulation and Calculation Data

"To confine our attention to terrestrial matters would be to limit the human spirit."
—Stephen William Hawking, English theoretical physicist (1942-2018)

"Beginnings are apt to be shadowy, and so it is with that great mother of life, the sea. ... It is a curious situation that the sea, from which life first arose should now be threatened by the activities of one form of that life. But the sea, though changed in a sinister way, will continue to exist; the threat is rather to life itself."
—Rachel Carson, an American marine biologist, author, and conservationist whose writings are credited with advancing the environmental movement and led to the creation of the U.S. Environmental Protection Agency, from her best-selling book *The Sea Around Us (1951)* (1907-1964)

This Appendix provides representative radiation transport input boundary conditions and calculations, along with representative raw data, so that the research conclusions in this thesis can be better understood and replicated.

B.1 OLTARIS Data for GCR Radiation in Cis-Lunar Space

The foundation calculations for all comparisons in this research, and indeed in any independently done analysis, is to start with a GCR radiation environment in the cis-lunar space region that can then be used in all subsequent evaluations.

The first step is to input the free-space GCR radiation environment that will be the boundary condition for transport through the various materials to be evaluated. For the base-case analyses, the Badhwar-O'Niell 2010 model has been selected, with the heliosphere diffusion and deceleration parameters set to calibrate to balloon and satellite data corresponding to the solar minimum of year 2010. [107] [138] This GCR model provides the flux of 59 different particle species (neutrons plus 58 ion species) in

units of particles/$(cm^2-day-MeV/n)$ as input to the radiation transport calculations used to trace the various ions as they travel through shielding materials. Thus, the raw data includes 100 energy steps (from 0.1 MeV/n to 50 GeV/n) for each of the 59 particle species, each of which is explained in Figure B.1.

Isotope	A	Z	Isotope	A	Z	Isotope	A	Z
Neutron	1	0	^{1}H	1	1	^{2}H	2	1
^{3}H	3	1	^{3}He	3	2	^{4}He	4	2
^{6}Li	6	3	^{7}Li	7	3	^{8}Be	8	4
^{9}Be	9	4	^{10}B	10	5	^{11}B	11	5
^{12}C	12	6	^{13}C	13	6	^{14}N	14	7
^{15}N	15	7	^{16}O	16	8	^{17}O	17	8
^{18}F	18	9	^{19}F	19	9	^{20}Ne	20	10
^{21}Ne	21	10	^{22}Ne	22	10	^{23}Na	23	11
^{24}Mg	24	12	^{25}Mg	25	12	^{26}Mg	26	12
^{27}Al	27	13	^{28}Si	28	14	^{29}P	29	15
^{30}S	30	16	^{31}S	31	16	^{32}S	32	16
^{33}Cl	33	17	^{34}Ar	34	18	^{35}Cl	35	17
^{36}Ar	36	18	^{37}K	37	19	^{38}Ar	38	18
^{39}K	39	19	^{40}Ca	40	20	^{41}Ca	41	20
^{42}Ca	42	20	^{43}Sc	43	21	^{44}Ti	44	22
^{45}Ti	45	22	^{46}Ti	46	22	^{47}Ti	47	22
^{48}V	48	23	^{49}V	49	23	^{50}Cr	50	24
^{51}Cr	51	24	^{52}Cr	52	24	^{53}Mn	53	25
^{54}Mn	54	25	^{55}Fe	55	26	^{56}Fe	56	26
^{57}Co	57	27	^{58}Ni	58	28			

Figure B.1 : Isotopes Available in OLTARIS. *See* Singleterry, 2011.

A sample of the raw flux data is shown in Figure B.2, for hydrogen and iron ions in the GCR flux at 1 AU. The complete data for all 59 particle species comprises several pages of data, and was used to create Figures 6.1 and 6.2.

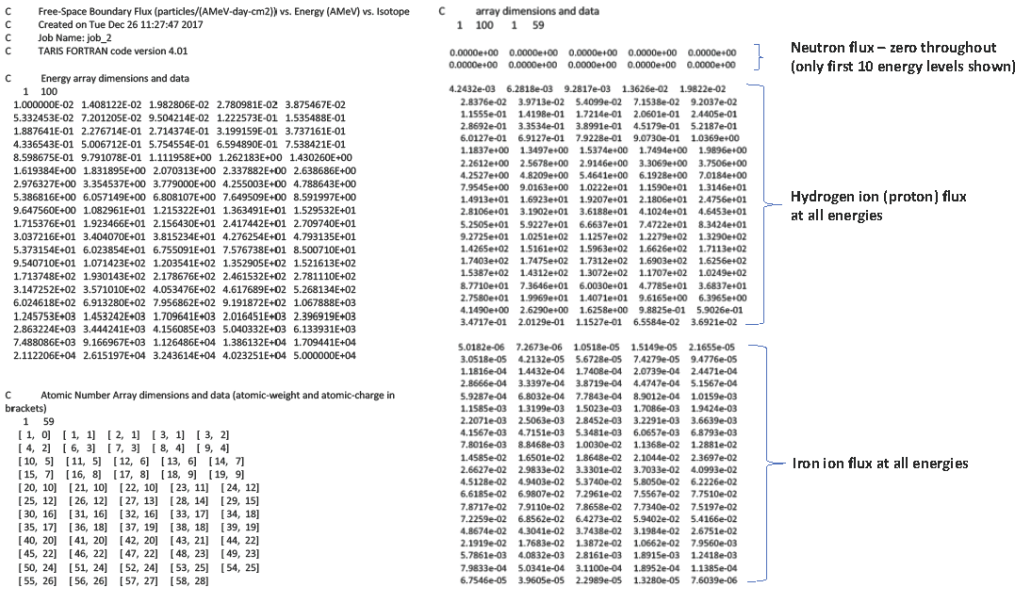

Figure B.2 : Sample GCR Flux Data at 1 *AU* for Hydrogen and Iron Ions.

B.2 OLTARIS Data for Radiation at ISS Orbit

The calculation of the radiation environment at the orbit of the International Space Station is a bit more involved, but starts with the same GCR model – Badhwar-O'Neill 2010 model, with parameters set for the 2010 solar minimum activity level.

The orbit of the ISS for this research is taken at 400 kms altitude, with an inclination of 51.6° to the equatorial plane. The altitude causes about 39% of the isotropic GCR flux to be blocked by the Earth, and the magnetosphere attenuates the remaining primary GCR flux even more. The orbit inclination causes the ISS to spend a small amount of time traversing a part of the proton-rich lower Van Allen belt, and both the inclination and altitude give rise to exposure to albedo neutron flux as a result of secondary emissions as some GCR particles interact with constituents in the upper atmosphere.

The resulting particle radiation flux field is used as an input to the radiation transport models when evaluating shielding materials and protocols in LEO at the ISS orbit. In particular, it is used to establish the baseline radiation exposure in the ISS, for which there already exists a wealth of medical data that allows determining radiation health risk assessments.

A sample of the raw flux data at the ISS orbit is shown in Figure B.3, for hydrogen and iron ions, and in Figure B.4, for hydrogen ions in the lower Van Allen belt and for albedo neutrons. The complete data for all 59 particle species comprises several pages of data, and was used to create Figures 6.4 and 6.5.

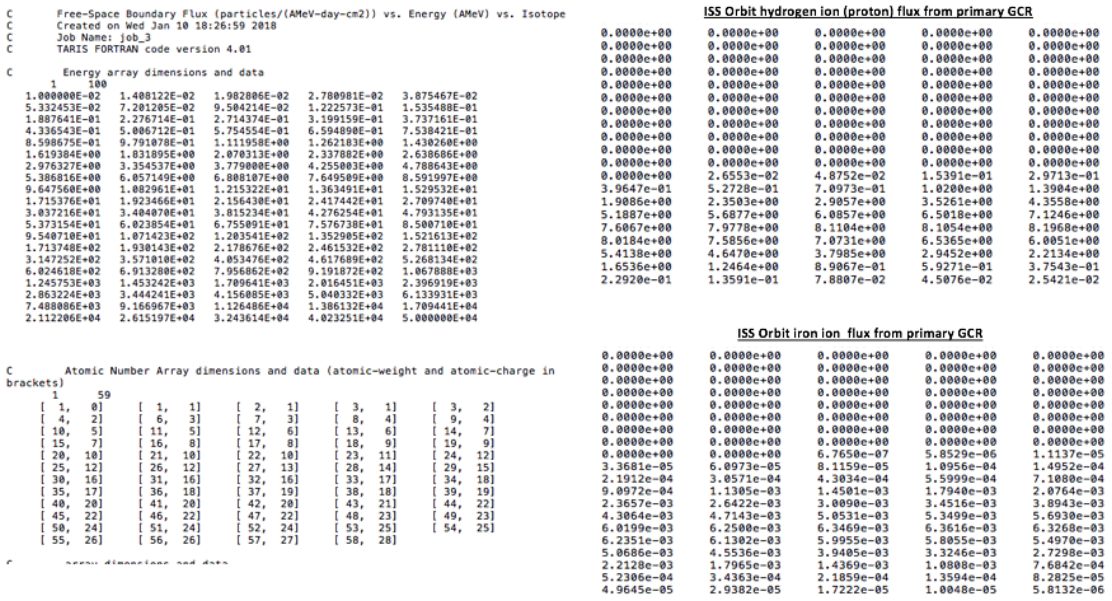

```
C       Free-Space Boundary Flux (particles/(AMeV-day-cm2)) vs. Energy (AMeV) vs. Isotope
C       Created on Wed Jan 10 18:26:59 2018
C       Job Name: job_3
C       TARIS FORTRAN code version 4.01

C        Energy array dimensions and data
      1     100
  1.000000E-02   1.408122E-02   1.982806E-02   2.780981E-02   3.875467E-02
  5.332453E-02   7.201205E-02   9.504214E-02   1.222573E-01   1.535488E-01
  1.887641E-01   2.276714E-01   2.714374E-01   3.199159E-01   3.737161E-01
  4.336543E-01   5.006712E-01   5.754554E-01   6.594890E-01   7.538421E-01
  8.598675E-01   9.791078E-01   1.111958E+00   1.262183E+00   1.430260E+00
  1.619384E+00   1.831895E+00   2.070313E+00   2.337882E+00   2.638686E+00
  2.976327E+00   3.354537E+00   3.779000E+00   4.255003E+00   4.788643E+00
  5.386816E+00   6.057149E+00   6.808107E+00   7.649509E+00   8.591997E+00
  9.647560E+00   1.082961E+01   1.215322E+01   1.363491E+01   1.529532E+01
  1.715376E+01   1.923466E+01   2.156430E+01   2.417442E+01   2.709740E+01
  3.037216E+01   3.404070E+01   3.815234E+01   4.276254E+01   4.793135E+01
  5.373154E+01   6.023854E+01   6.755091E+01   7.576738E+01   8.500710E+01
  9.540710E+01   1.071423E+02   1.203541E+02   1.352905E+02   1.521613E+02
  1.713748E+02   1.930143E+02   2.178676E+02   2.461532E+02   2.781110E+02
  3.147252E+02   3.571010E+02   4.053476E+02   4.617689E+02   5.268134E+02
  6.024618E+02   6.913280E+02   7.956862E+02   9.191872E+02   1.067888E+03
  1.245753E+03   1.453242E+03   1.709641E+03   2.016451E+03   2.396919E+03
  2.863224E+03   3.444241E+03   4.156085E+03   5.040332E+03   6.133931E+03
  7.488086E+03   9.166967E+03   1.126486E+04   1.386132E+04   1.709441E+04
  2.112206E+04   2.615197E+04   3.243614E+04   4.023251E+04   5.000000E+04

C        Atomic Number Array dimensions and data (atomic-weight and atomic-charge in
brackets)
      1     59
     [  1,   0]     [  1,   1]     [  2,   1]     [  3,   1]     [  3,   2]
     [  4,   2]     [  6,   3]     [  7,   3]     [  8,   4]     [  9,   4]
     [ 10,   5]     [ 11,   5]     [ 12,   6]     [ 13,   6]     [ 14,   7]
     [ 15,   7]     [ 16,   8]     [ 17,   8]     [ 18,   9]     [ 19,   9]
     [ 20,  10]     [ 21,  10]     [ 22,  10]     [ 23,  11]     [ 24,  12]
     [ 25,  12]     [ 26,  12]     [ 27,  13]     [ 28,  14]     [ 29,  15]
     [ 30,  16]     [ 31,  16]     [ 32,  16]     [ 33,  17]     [ 34,  18]
     [ 35,  17]     [ 36,  18]     [ 37,  19]     [ 38,  18]     [ 39,  19]
     [ 40,  20]     [ 41,  20]     [ 42,  20]     [ 43,  21]     [ 44,  22]
     [ 45,  22]     [ 46,  22]     [ 47,  22]     [ 48,  23]     [ 49,  23]
     [ 50,  24]     [ 51,  24]     [ 52,  24]     [ 53,  25]     [ 54,  25]
     [ 55,  26]     [ 56,  26]     [ 57,  27]     [ 58,  28]
```

ISS Orbit hydrogen ion (proton) flux from primary GCR

```
0.0000e+00   0.0000e+00   0.0000e+00   0.0000e+00   0.0000e+00
0.0000e+00   0.0000e+00   0.0000e+00   0.0000e+00   0.0000e+00
0.0000e+00   0.0000e+00   0.0000e+00   0.0000e+00   0.0000e+00
0.0000e+00   0.0000e+00   0.0000e+00   0.0000e+00   0.0000e+00
0.0000e+00   0.0000e+00   0.0000e+00   0.0000e+00   0.0000e+00
0.0000e+00   0.0000e+00   0.0000e+00   0.0000e+00   0.0000e+00
0.0000e+00   0.0000e+00   0.0000e+00   0.0000e+00   0.0000e+00
0.0000e+00   0.0000e+00   0.0000e+00   0.0000e+00   0.0000e+00
0.0000e+00   0.0000e+00   0.0000e+00   0.0000e+00   0.0000e+00
0.0000e+00   0.0000e+00   0.0000e+00   0.0000e+00   0.0000e+00
0.0000e+00   2.6553e-02   4.8752e-02   1.5391e-01   2.9713e-01
3.9647e-01   5.2728e-01   7.0973e-01   1.0200e+00   1.3904e+00
1.9086e+00   2.3503e+00   2.9857e+00   3.5261e+00   4.3558e+00
5.1887e+00   5.6877e+00   6.0857e+00   6.5018e+00   7.1246e+00
7.6067e+00   7.9778e+00   8.1104e+00   8.1054e+00   8.1968e+00
8.0184e+00   7.5856e+00   7.0731e+00   6.5365e+00   6.0051e+00
5.4138e+00   4.6470e+00   3.7985e+00   2.9452e+00   2.2134e+00
1.6536e+00   1.2464e+00   8.9067e-01   5.9271e-01   3.7543e-01
2.2920e-01   1.3591e-01   7.8807e-02   4.5076e-02   2.5421e-02
```

ISS Orbit iron ion flux from primary GCR

```
0.0000e+00   0.0000e+00   0.0000e+00   0.0000e+00   0.0000e+00
0.0000e+00   0.0000e+00   0.0000e+00   0.0000e+00   0.0000e+00
0.0000e+00   0.0000e+00   0.0000e+00   0.0000e+00   0.0000e+00
0.0000e+00   0.0000e+00   0.0000e+00   0.0000e+00   0.0000e+00
0.0000e+00   0.0000e+00   0.0000e+00   0.0000e+00   0.0000e+00
0.0000e+00   0.0000e+00   0.0000e+00   0.0000e+00   0.0000e+00
0.0000e+00   0.0000e+00   0.0000e+00   0.0000e+00   0.0000e+00
0.0000e+00   0.0000e+00   0.0000e+00   0.0000e+00   0.0000e+00
0.0000e+00   0.0000e+00   6.7650e-07   5.8529e-06   1.1137e-05
3.3681e-05   6.0973e-05   8.1159e-05   1.0956e-04   1.4952e-04
2.1912e-04   3.0571e-04   4.3034e-04   5.5999e-04   7.1080e-04
9.0972e-04   1.1305e-03   1.4501e-03   1.7940e-03   2.0764e-03
2.3657e-03   2.6422e-03   3.0090e-03   3.4516e-03   3.8943e-03
4.3064e-03   4.7143e-03   5.0531e-03   5.3499e-03   5.6930e-03
6.0199e-03   6.2500e-03   6.3469e-03   6.3616e-03   6.3268e-03
6.2351e-03   6.1302e-03   5.9955e-03   5.8055e-03   5.4970e-03
5.0686e-03   4.5536e-03   3.9405e-03   3.3246e-03   2.7298e-03
2.2128e-03   1.7965e-03   1.4369e-03   1.0808e-03   7.6842e-04
5.2306e-04   3.4363e-04   2.1859e-04   1.3594e-04   8.2825e-05
4.9645e-05   2.9382e-05   1.7222e-05   1.0048e-05   5.8132e-06
```

Figure B.3 : Sample GCR Flux Data at ISS Orbit for Hydrogen and Iron Ions.

Note that the data demonstrates what one would expect at the ISS orbit for GCR flux: the neutron flux is zero (thus not shown), and both the proton and iron ion flux numbers are very low (zero) for low kinetic energy ions, because their energy per nucleon is below that which can penetrate the magnetosphere.

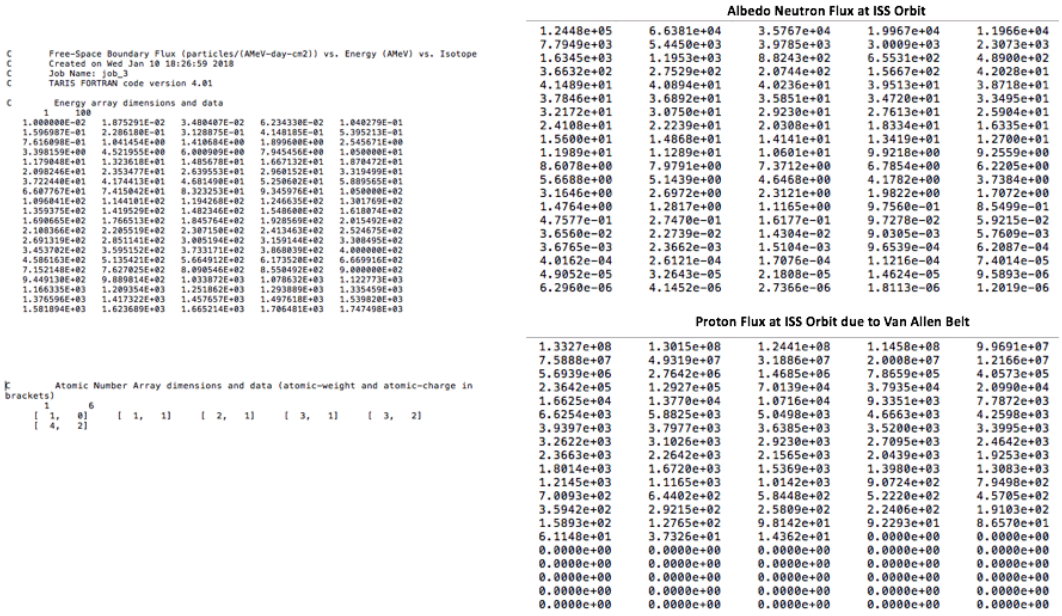

```
C       Free-Space Boundary Flux (particles/(AMeV-day-cm2)) vs. Energy (AMeV) vs. Isotope
C       Created on Wed Jan 10 18:26:59 2018
C       Job Name: job_3
C       TARIS FORTRAN code version 4.01

C         Energy array dimensions and data
        1     100
  1.000000E-02   1.875291E-02   3.480407E-02   6.234330E-02   1.040279E-01
  1.596987E-01   2.286180E-01   3.128875E-01   4.148185E-01   5.395213E-01
  7.616898E-01   1.041454E+00   1.410684E+00   1.899600E+00   2.545671E+00
  3.398159E+00   4.521955E+00   6.000909E+00   7.945456E+00   1.050000E+01
  1.379048E+01   1.323618E+01   1.485678E+01   1.667132E+01   1.870472E+01
  2.098246E+01   2.353477E+01   2.639553E+01   2.960152E+01   3.319499E+01
  3.722440E+01   4.174413E+01   4.681490E+01   5.250602E+01   5.889565E+01
  6.607767E+01   7.415042E+01   8.323253E+01   9.345976E+01   1.050000E+02
  1.096041E+02   1.144101E+02   1.194268E+02   1.246635E+02   1.301769E+02
  1.359375E+02   1.419529E+02   1.482346E+02   1.548000E+02   1.618074E+02
  1.690665E+02   1.766513E+02   1.845764E+02   1.928569E+02   2.015492E+02
  2.108366E+02   2.205519E+02   2.307150E+02   2.413463E+02   2.524675E+02
  2.691319E+02   2.851141E+02   3.005194E+02   3.159144E+02   3.304495E+02
  3.453702E+02   3.595152E+02   3.733171E+02   3.868039E+02   4.000000E+02
  4.586163E+02   5.135421E+02   5.664912E+02   6.173520E+02   6.669916E+02
  7.152148E+02   7.627025E+02   8.090546E+02   8.550492E+02   9.000000E+02
  9.449130E+02   9.889814E+02   1.033072E+03   1.078632E+03   1.122773E+03
  1.166335E+03   1.209354E+03   1.251862E+03   1.293889E+03   1.335459E+03
  1.376596E+03   1.417322E+03   1.457657E+03   1.497618E+03   1.539820E+03
  1.581894E+03   1.623689E+03   1.665214E+03   1.706481E+03   1.747498E+03


C         Atomic Number Array dimensions and data (atomic-weight and atomic-charge in
brackets)
        1     6
     [ 1,   0]     [ 1,   1]     [ 2,   1]     [ 3,   1]     [ 3,   2]
     [ 4,   2]
```

Albedo Neutron Flux at ISS Orbit

1.2448e+05	6.6381e+04	3.5767e+04	1.9967e+04	1.1966e+04
7.7949e+03	5.4450e+03	3.9785e+03	3.0009e+03	2.3073e+03
1.6345e+03	1.1953e+03	8.8243e+02	6.5531e+02	4.8900e+02
3.6632e+02	2.7529e+02	2.0744e+02	1.5667e+02	4.2028e+01
4.1489e+01	4.0894e+01	4.0236e+01	3.9513e+01	3.8718e+01
3.7846e+01	3.6892e+01	3.5851e+01	3.4720e+01	3.3495e+01
3.2172e+01	3.0750e+01	2.9230e+01	2.7613e+01	2.5904e+01
2.4108e+01	2.2239e+01	2.0308e+01	1.8334e+01	1.6335e+01
1.5600e+01	1.4868e+01	1.4141e+01	1.3419e+01	1.2700e+01
1.1989e+01	1.1289e+01	1.0601e+01	9.9218e+00	9.2559e+00
8.6078e+00	7.9791e+00	7.3712e+00	6.7854e+00	6.2205e+00
5.6688e+00	5.1439e+00	4.6468e+00	4.1782e+00	3.7384e+00
3.1646e+00	2.6972e+00	2.3121e+00	1.9822e+00	1.7072e+00
1.4764e+00	1.2817e+00	1.1165e+00	9.7560e-01	8.5499e-01
4.7577e-01	2.7470e-01	1.6177e-01	9.7278e-02	5.9215e-02
3.6560e-02	2.2739e-02	1.4304e-02	9.0305e-03	5.7609e-03
3.6765e-03	2.3662e-03	1.5104e-03	9.6539e-04	6.2087e-04
4.0162e-04	2.6121e-04	1.7076e-04	1.1216e-04	7.4014e-05
4.9052e-05	3.2643e-05	2.1808e-05	1.4624e-05	9.5893e-06
6.2960e-06	4.1452e-06	2.7366e-06	1.8113e-06	1.2019e-06

Proton Flux at ISS Orbit due to Van Allen Belt

1.3327e+08	1.3015e+08	1.2441e+08	1.1458e+08	9.9691e+07
7.5888e+07	4.9319e+07	3.1886e+07	2.0008e+07	1.2166e+07
5.6939e+06	2.7642e+06	1.4685e+06	7.8659e+05	4.0573e+05
2.3642e+05	1.2927e+05	7.0139e+04	3.7935e+04	2.0990e+04
1.6625e+04	1.3770e+04	1.0716e+04	9.3351e+03	7.7872e+03
6.6254e+03	5.8825e+03	5.0498e+03	4.6663e+03	4.2598e+03
3.9397e+03	3.7977e+03	3.6385e+03	3.5200e+03	3.3995e+03
3.2622e+03	3.1026e+03	2.9230e+03	2.7095e+03	2.4642e+03
2.3663e+03	2.2642e+03	2.1565e+03	2.0439e+03	1.9253e+03
1.8014e+03	1.6720e+03	1.5369e+03	1.3980e+03	1.3083e+03
1.2145e+03	1.1165e+03	1.0142e+03	9.0724e+02	7.9498e+02
7.0093e+02	6.4402e+02	5.8448e+02	5.2220e+02	4.5705e+02
3.5942e+02	2.9215e+02	2.5809e+02	2.2406e+02	1.9103e+02
1.5893e+02	1.2765e+02	9.8142e+01	9.2293e+01	8.6570e+01
6.1148e+01	3.7326e+01	1.4362e+01	0.0000e+00	0.0000e+00
0.0000e+00	0.0000e+00	0.0000e+00	0.0000e+00	0.0000e+00
0.0000e+00	0.0000e+00	0.0000e+00	0.0000e+00	0.0000e+00
0.0000e+00	0.0000e+00	0.0000e+00	0.0000e+00	0.0000e+00
0.0000e+00	0.0000e+00	0.0000e+00	0.0000e+00	0.0000e+00
0.0000e+00	0.0000e+00	0.0000e+00	0.0000e+00	0.0000e+00

Figure B.4 : Sample Flux Data at ISS Orbit for Van Allen Belt Trapped Protons and Secondary Albedo Neutrons.

Similarly, the data for the trapped protons and albedo neutrons makes sense at a glance. First, now there are neutrons showing up in the incident flux – these are not in the primary GCR, but are a result of secondary emissions in the upper atmosphere. Second, contrary to the proton flux in the GCR, the trapped protons in the lower Van Allen belt have a very high flux at very low kinetic energy levels, and then the flux drops off rather rapidly as the energy increase – going to zero in the 100 MeV/n range, as expected.

B.3 OLTARIS Data: Dose and Dose Equivalent Calculations

For all the dose and dose equivalent calculations used to evaluate various shielding materials and designs, the GCR input flux is from the Badhwar-O'Neill 2010 model, with the 2010 solar minimum parameters, and for dose equivalent the ICRP-60 radiation weighting factors are used; i.e., all the same model metrics unless otherwise noted. The only variable will be the type of material evaluated, and layered configuration; and unless otherwise noted the configuration will be a slab.

Sample data for an aluminum slab is presented here as an illustration, with data gathered within the aluminum slab at 1 gm/mm^2 intervals for the first 1 gm/cm^2, then at 1 gm/cm^2 intervals up until 5 gm/cm^2, and then at 5 gm/cm^2 intervals thereafter – all thickness intervals expressed in terms of areal density. This ensures capturing the initial flux of secondary emissions generated in the aluminum in detail. A slab 50 gm/cm^2 is used, even though the radiation is further diminished by a thicker slab, because that thickness equates to about 18.5 cm, which is beyond the practical limit for the thickness of a spacecraft hull.

The raw data for dose and dose equivalent is shown in Figure B.5.

Al Slab Absorbed Dose						Al Slab Dose Equivalent				
	GCR - ISS	P&N - ISS	TOTAL - ISS	GCR - 1 AU			GCR - ISS	P&N - ISS	TOTAL - ISS	GCR - 1AU
Depth (gm/cm^2)	Dose (mGy/day)	Dose (mGy/day)	Dose (mGy/day)	Dose (mGy/day)		Depth (gm/cm^2)	Dose Eq (mSv/day)	Dose Eq (mSv/day)	Dose Eq (mSv/day)	Dose Eq (mSv/day)
0.01	0.041427	4.5393	4.580727	0.37003		0.01	0.28124	21.505	21.78624	2.4159
0.02	0.041614	2.8049	2.846514	0.37089		0.02	0.28293	11.646	11.92893	2.4249
0.03	0.041788	2.148	2.189788	0.3715		0.03	0.28451	8.1497	8.43421	2.431
0.04	0.041954	1.7927	1.834654	0.37201		0.04	0.28603	6.3419	6.62793	2.436
0.05	0.042116	1.567	1.609116	0.37245		0.05	0.28751	5.2326	5.52011	2.4403
0.06	0.042274	1.4094	1.451674	0.37285		0.06	0.28895	4.4807	4.76965	2.4441
0.07	0.042428	1.2925	1.334928	0.37323		0.07	0.29037	3.9365	4.22687	2.4476
0.08	0.042581	1.2018	1.244381	0.37358		0.08	0.29176	3.524	3.81576	2.4509
0.09	0.042731	1.1292	1.171931	0.37391		0.09	0.29313	3.2002	3.49333	2.4539
0.1	0.042879	1.0695	1.112379	0.37423		0.1	0.29448	2.9392	3.23368	2.4568
0.2	0.044275	0.77597	0.820245	0.37702		0.2	0.30717	1.7349	2.04207	2.4808
0.3	0.044882	0.66226	0.707142	0.38005		0.3	0.30888	1.3047	1.61358	2.4798
0.4	0.045431	0.59999	0.645421	0.38266		0.4	0.3104	1.1026	1.413	2.4805
0.5	0.045875	0.55884	0.604715	0.38455		0.5	0.31127	0.98361	1.29488	2.4752
0.6	0.046259	0.52882	0.575079	0.38608		0.6	0.31182	0.9038	1.21562	2.4679
0.7	0.046626	0.50551	0.552136	0.38753		0.7	0.3124	0.84571	1.15811	2.4623
0.8	0.046933	0.48662	0.533553	0.38855		0.8	0.31261	0.80111	1.11372	2.4523
0.9	0.047219	0.47074	0.517959	0.38947		0.9	0.31276	0.76563	1.07839	2.4425
1	0.047497	0.45732	0.504817	0.39038		1	0.31296	0.73635	1.04931	2.4341
1.1	0.047755	0.4456	0.493355	0.39116		1.1	0.31305	0.71159	1.02464	2.4248
1.2	0.047982	0.43521	0.483192	0.39173		1.2	0.31298	0.69032	1.0033	2.4135
1.3	0.048207	0.42597	0.474177	0.39232		1.3	0.31294	0.67174	0.98468	2.4034
1.4	0.048428	0.41764	0.466068	0.39293		1.4	0.31295	0.65531	0.96826	2.3943
1.5	0.048636	0.41007	0.458706	0.39345		1.5	0.31289	0.64061	0.9535	2.3849
1.6	0.048817	0.40317	0.451987	0.39378		1.6	0.31266	0.62739	0.94005	2.3732
1.7	0.048996	0.39695	0.445946	0.39413		1.7	0.31246	0.61519	0.92765	2.3625
1.8	0.049174	0.39098	0.440154	0.3945		1.8	0.3123	0.60416	0.91646	2.3527
1.9	0.049351	0.38535	0.434701	0.39489		1.9	0.31216	0.59402	0.90618	2.3435
2	0.049512	0.38004	0.429552	0.39517		2	0.31192	0.58466	0.89658	2.3334
2.1	0.049648	0.37503	0.424678	0.39528		2.1	0.3115	0.576	0.8875	2.3213
2.2	0.049785	0.37041	0.420195	0.39542		2.2	0.31111	0.56846	0.87957	2.31
2.3	0.049922	0.36584	0.415762	0.39558		2.3	0.31075	0.56085	0.8716	2.2994
2.4	0.050058	0.36145	0.411508	0.39576		2.4	0.31043	0.5536	0.86403	2.2894
2.5	0.050194	0.35724	0.407434	0.39596		2.5	0.31013	0.54667	0.8568	2.28
5	0.052525	0.28255	0.335075	0.3964		5	0.29905	0.42907	0.72812	2.0525
7.5	0.05304	0.23507	0.28901	0.3945		7.5	0.28701	0.35876	0.64577	1.8745
10	0.05482	0.1985	0.25332	0.39112		10	0.27449	0.30541	0.5799	1.7252
12.5	0.055444	0.16829	0.223734	0.38746		12.5	0.26277	0.26172	0.52449	1.6023
15	0.055919	0.14304	0.198959	0.38383		15	0.25213	0.22494	0.47707	1.5003
17.5	0.056301	0.1223	0.178601	0.38032		17.5	0.24259	0.19449	0.43708	1.4151
20	0.056565	0.10533	0.161895	0.37659		20	0.23364	0.16934	0.40298	1.3403
22.5	0.05672	0.091674	0.148394	0.37259		22.5	0.22508	0.14927	0.37435	1.2733
25	0.056911	0.079983	0.136894	0.36923		25	0.21793	0.132	0.34993	1.2184
27.5	0.056894	0.069805	0.126699	0.36479		27.5	0.21008	0.11687	0.32695	1.163
30	0.056946	0.06128	0.118226	0.36109		30	0.20361	0.10408	0.30769	1.1175
32.5	0.056989	0.054165	0.111154	0.35756		32.5	0.19774	0.093291	0.291031	1.0773
35	0.056909	0.048378	0.105287	0.35343		35	0.19168	0.084335	0.276015	1.0375
37.5	0.056865	0.043188	0.100053	0.34972		37.5	0.18639	0.076267	0.262657	1.0029
40	0.056835	0.038577	0.095412	0.34626		40	0.18161	0.069032	0.250642	0.97183
42.5	0.05667	0.034506	0.091176	0.34206		42.5	0.17643	0.062555	0.238985	0.93959
45	0.056522	0.030915	0.087437	0.3381		45	0.1717	0.056743	0.228443	0.91017
47.5	0.056418	0.027748	0.084166	0.33455		47.5	0.16749	0.051512	0.219002	0.88368
50	0.056348	0.024955	0.081303	0.33133		50	0.16366	0.046786	0.210446	0.8594

Figure B.5 : Sample Dose and Dose Equivalent Calculations in Aluminum Slab at ISS Orbit and Cis-lunar Space.

These calculations include the contribution by all of the 59 particles, including neutrons and all ions in atomic weight up to nickel. These calculations were used, for example, to generate Figure 6.6. The underlying data includes the dose equivalent calculation for each particle, as shown in Figure B.6.

Dose Equivalent by Particle Type -- GCR at 1 AU (mSv/day)

Particle Atomic Wt	Depth = 0 gm/cm^2	Depth = 5 gm/cm^2	Depth = 20 gm/cm^2	Depth = 50 gm/cm^2
0	0.051566	0.064222	0.08822	0.068153
1	0.16409	0.27166	0.3232	0.33228
2	2.72E-19	0.022992	0.030603	0.034449
3	2.84E-19	0.007873	0.011559	0.01316
4	9.54E-19	0.040999	0.053021	0.055644
5	0.081073	0.23058	0.22979	0.20424
6	2.16E-18	0.00011041	0.00022911	0.00018936
7	0.00076014	0.00080354	0.00055494	0.00025407
8	3.90E-18	0.00009781	0.0001968	0.00018034
9	0.00084548	0.00099728	0.00088075	0.00051071
10	6.21E-18	0.00071357	0.0013729	0.0010694
11	0.0076433	0.0077177	0.0049868	0.0021222
12	0.066484	0.05639	0.027669	0.008845
13	9.15E-18	0.00080046	0.0014347	0.0010207
14	0.030687	0.026637	0.014355	0.0049451
15	1.92E-17	0.0011944	0.0020303	0.0013227
16	0.21926	0.16271	0.069617	0.01797
17	3.93E-17	0.00087015	0.0015127	0.0010072
18	7.00E-17	0.00092199	0.001586	0.0010352
19	0.0049374	0.0052854	0.0040806	0.0018429
20	0.074538	0.053895	0.022887	0.0056568
21	1.14E-16	0.0012196	0.0019988	0.0011973
22	1.14E-16	0.00081534	0.001337	0.0007959
23	0.019699	0.018116	0.011919	0.0047027
24	0.19195	0.13008	0.050736	0.01094
25	2.57E-16	0.0013671	0.0021714	0.0012073
26	2.57E-16	0.0012757	0.002022	0.0011153
27	0.03851	0.030196	0.015696	0.0048593
28	0.23513	0.15867	0.062517	0.013609
29	0.0090707	0.0092895	0.0068592	0.0027363
30	8.73E-16	5.8284E-06	0.000016145	0.000015595
31	8.73E-16	0.00037538	0.0006091	0.0003278
32	0.062973	0.045977	0.020626	0.0051923
33	1.12E-15	0.000036013	0.000056753	0.000029894
34	1.42E-15	2.7703E-06	4.2202E-06	2.1003E-06
35	0.013724	0.013741	0.0096427	0.003516
36	1.42E-15	0.00021397	0.00032764	0.00016172
37	1.78E-15	0.000029722	0.00004455	0.000021423
38	0.033932	0.027424	0.014418	0.0041455
39	0.029948	0.024629	0.01356	0.0040878
40	0.091345	0.059468	0.020744	0.0033966
41	2.13E-15	0.00050861	0.00081075	0.00042594
42	2.13E-15	0.0037913	0.0053992	0.0023581
43	0.01896	0.01792	0.011974	0.0039692
44	2.42E-15	0.000093535	0.00013845	0.000065612
45	2.42E-15	0.00035636	0.00051982	0.00023726
46	2.42E-15	0.001633	0.0022803	0.00095799
47	0.073507	0.04894	0.019257	0.0039944
48	2.53E-15	0.0015092	0.0020885	0.00086375
49	0.035701	0.026951	0.01319	0.0032793
50	2.64E-15	0.0012095	0.0016272	0.00064431
51	2.64E-15	0.0023515	0.0030548	0.0011263
52	0.077637	0.051092	0.019111	0.0035016
53	2.75E-15	0.0032665	0.0041277	0.0014665
54	0.050542	0.036489	0.015942	0.0032268
55	2.86E-15	0.0044535	0.0055272	0.0018371
56	0.59296	0.35179	0.10399	0.012762
57	0.0029851	0.0019739	0.00075603	0.00013805
58	0.029299	0.017819	0.0054492	0.00069979

Dose Equivalent by Particle Type -- GCR and Protons & Neutrons at ISS Orbit (mSv/day)

Dose Equivalent due to GCR at ISS

Particle Atomic Wt	Depth = 0 gm/cm^2	Depth = 5 gm/cm^2	Depth = 20 gm/cm^2	Depth = 50 gm/cm^2
0	0.0091115	0.011321	0.01571	0.0128
1	0.0165	0.034675	0.04728	0.056132
2	2.72E-19	0.0039071	0.0053735	0.0066133
3	2.84E-19	0.0012167	0.0018838	0.0024023
4	9.54E-19	0.0060738	0.0085613	0.010189
5	0.0092151	0.032537	0.036333	0.03726
6	2.16E-18	9.9609E-06	0.000027186	0.000029332
7	0.000081885	0.000081268	0.000065868	0.000037783
8	3.90E-18	7.0854E-06	0.000021211	0.000026372
9	0.00009537	0.00010278	0.0001003	0.00007477
10	6.21E-18	0.000043017	0.00012456	0.00013953
11	0.00047944	0.00053348	0.00046049	0.00026789
12	0.0027881	0.0030753	0.0022944	0.0010723
13	9.15E-18	0.000043743	0.00012326	0.00013038
14	0.0015108	0.0016479	0.0012962	0.0006485
15	1.92E-17	0.000071923	0.00019046	0.00018459
16	0.011975	0.0117	0.0074608	0.0027769
17	3.93E-17	0.000066846	0.00017514	0.00017067
18	7.00E-17	0.000079052	0.00020197	0.00019138
19	0.00041765	0.00050191	0.00052439	0.00033792
20	0.0054057	0.0049717	0.0030252	0.0010647
21	1.14E-16	0.00011508	0.00027841	0.00024185
22	1.14E-16	0.000075026	0.00018565	0.00015989
23	0.0017775	0.0019459	0.0017703	0.0009988
24	0.01602	0.013975	0.0077995	0.0023888
25	2.57E-16	0.00015439	0.00035411	0.00028292
26	2.57E-16	0.00014512	0.00033103	0.00026171
27	0.0039841	0.0037864	0.0027041	0.0011843
28	0.023516	0.020076	0.011121	0.0034204
29	0.0011925	0.0013695	0.0013539	0.00076564
30	8.73E-16	8.74E-07	3.3032E-06	4.4129E-06
31	8.73E-16	0.000055451	0.0001222	0.000091556
32	0.006017	0.0069787	0.0042087	0.0014775
33	1.12E-15	5.7378E-06	0.000012524	9.1631E-06
34	1.42E-15	4.64E-07	9.77E-07	6.71E-07
35	0.0020883	0.0022835	0.0020792	0.0010517
36	1.42E-15	0.000036506	0.000076133	0.000051426
37	1.78E-15	5.1865E-06	0.000010666	7.0241E-06
38	0.0051619	0.0047546	0.0032591	0.0012863
39	0.0044008	0.0042422	0.0031486	0.0013164
40	0.01308	0.010327	0.0048255	0.0010695
41	2.13E-15	0.000095789	0.00020809	0.00014768
42	2.13E-15	0.00071088	0.0013778	0.00081248
43	0.0029331	0.0033508	0.0030574	0.0013783
44	2.42E-15	0.000018381	0.000037034	0.000023574
45	2.42E-15	0.000069767	0.00013833	0.000084759
46	2.42E-15	0.00032382	0.00061055	0.00034285
47	0.010755	0.0089524	0.0048507	0.0013789
48	2.53E-15	0.00029915	0.00056165	0.00031081
49	0.0054913	0.0051275	0.003439	0.0011611
50	2.64E-15	0.00024244	0.00044841	0.00023609
51	2.64E-15	0.00047693	0.00084021	0.00041308
52	0.01218	0.0099482	0.0050676	0.0012538
53	2.75E-15	0.00066381	0.0011481	0.00054389
54	0.0085003	0.0074916	0.0043748	0.0011772
55	2.86E-15	0.00099932	0.001651	0.00071692
56	0.097822	0.072983	0.029152	0.0047368
57	0.00048205	0.00040867	0.00021394	0.000052344
58	0.0051682	0.0038887	0.0015919	0.00026946

Dose Equivalent due to P&N at ISS

Particle Atomic Wt	Depth = 0 gm/cm^2	Depth = 5 gm/cm^2	Depth = 20 gm/cm^2	Depth = 50 gm/cm^2
0	0.0084724	0.0098062	0.011103	0.0068785
1	61487	0.36991	0.13418	0.031086
2	2.88E-20	0.0045815	0.0025096	0.00093833
3	2.91E-20	0.0017455	0.00097602	0.00036414
4	1.71E-19	0.0079112	0.0039027	0.0014003
5	1.72E-19	0.035115	0.016678	0.0061389

Figure B.6 : Sample Dose and Dose Equivalent Calculations at Various Thickness Points in Aluminum Slab, at ISS Orbit and Cis-lunar Space, done Particle-by-Particle.

To generate Figures 6.7 and 6.8, the dose equivalent generated by each of the 59 particles was accumulated particle-by-particle for all data collection points thickness points designated in the aluminum slab.

B.4 OLTARIS Dose Equivalent Calibration Calculations

The calibration calculations to allow comparisons to published results, as well as to set standard parameters for this research for comparative purposes, included examination of aluminum, liquid hydrogen, polyethylene, and hydrogenated boron nitride nanotubes. The GCR boundary condition is the 2010 BON model with the 2010 solar minimum, and quality factor model is ICRP-60. The standard densities were used for aluminum and liquid hydrogen, while the density of HDPE was assumed to be 1.0 gm/cm^3) and that of the NASA hydrogenated boron nanotubes was assumed to be 1.4 gm/cm^3, although there was conflicting data on that point in the literature, as mentioned in the text. The raw data is shown in Figure B.7.

Al Slab Dose Eq (mSv/day)						L_H2 Slab GCR - 1AU Dose Eq (mSv/day)			HDPE_Slab GCR - 1AU Dose Eq (mSv/day)			H2_BNNT Slab GCR - 1AU Dose Eq (mSv/day)		
		GCR - ISS	P&N - ISS	TOTAL - IS	Al_Slab GCR - 1AU									
Al Thickness (cm)	Depth (gm/cm^2)	Dose Eq (mS	Dose Eq (mS	Dose Eq (mS	Dose Eq (mSv/day)	H2 Thickness (cm)	Depth (gm/c	Dose Eq (mSv/day)	HDPE Thickness (cm	Depth (gm/c	Dose Eq (mSv/day)	H2_BNNT Thickness (cm	Depth (gm/c	Dose Eq (mSv/day)
0.003703704	0.01	0.28124	21.505	21.78624	2.4159	0.141242938	0.01	2.1546	0.01	0.01	2.3038	0.007142857	0.01	2.3253
0.007407407	0.02	0.28293	11.646	11.92893	2.4249	0.282485876	0.02	2.1553	0.02	0.02	2.3083	0.014285714	0.02	2.3307
0.011111111	0.03	0.28451	8.1497	8.43421	2.431	0.423728814	0.03	2.1563	0.03	0.03	2.3116	0.021428571	0.03	2.3345
0.014814815	0.04	0.28603	6.3419	6.62793	2.436	0.564971751	0.04	2.1574	0.04	0.04	2.3142	0.028571429	0.04	2.3376
0.018518519	0.05	0.28751	5.2126	5.52011	2.4403	0.706214689	0.05	2.1586	0.05	0.05	2.3166	0.035714286	0.05	2.3403
0.022222222	0.06	0.28895	4.4807	4.76965	2.4441	0.847457627	0.06	2.1597	0.06	0.06	2.3187	0.042857143	0.06	2.3427
0.025925926	0.07	0.29037	3.9365	4.22687	2.4476	0.988700565	0.07	2.1608	0.07	0.07	2.3206	0.05	0.07	2.3449
0.02962963	0.08	0.29176	3.524	3.81576	2.4509	1.129943503	0.08	2.1619	0.08	0.08	2.3224	0.057142857	0.08	2.3469
0.033333333	0.09	0.29313	3.2002	3.49333	2.4539	1.271186441	0.09	2.1629	0.09	0.09	2.3241	0.064285714	0.09	2.3488
0.037037037	0.1	0.29448	2.9392	3.23368	2.4568	1.412429379	0.1	2.164	0.1	0.1	2.3258	0.071428571	0.1	2.3507
0.074074074	0.2	0.30717	1.7349	2.04207	2.4808	2.824858757	0.2	2.1724	0.2	0.2	2.3391	0.142857143	0.2	2.3656
0.111111111	0.3	0.30888	1.3047	1.61358	2.4798	4.237288136	0.3	2.1108	0.3	0.3	2.3194	0.214285714	0.3	2.3499
0.148148148	0.4	0.3104	1.1026	1.413	2.4805	5.649717514	0.4	2.0729	0.4	0.4	2.3076	0.285714286	0.4	2.3407
0.185185185	0.5	0.31127	0.98361	1.29488	2.4752	7.062146893	0.5	2.0268	0.5	0.5	2.2902	0.357142857	0.5	2.3259
0.222222222	0.6	0.31182	0.9038	1.21562	2.4679	8.474576271	0.6	1.9825	0.6	0.6	2.2721	0.428571429	0.6	2.3103
0.259259259	0.7	0.3124	0.84571	1.15811	2.4623	9.88700565	0.7	1.948	0.7	0.7	2.258	0.5	0.7	2.2981
0.296296296	0.8	0.31261	0.80111	1.11372	2.4523	11.29943503	0.8	1.9036	0.8	0.8	2.2382	0.571428571	0.8	2.2806
0.333333333	0.9	0.31276	0.76563	1.07839	2.4425	12.71186441	0.9	1.863	0.9	0.9	2.2195	0.642857143	0.9	2.264
0.37037037	1	0.31296	0.73635	1.04931	2.4341	14.12429379	1	1.8289	1	1	2.2036	0.714285714	1	2.2498
0.407407407	1.1	0.31305	0.71159	1.02464	2.4248	15.53672316	1.1	1.794	1.1	1.1	2.1869	0.785714286	1.1	2.2348
0.444444444	1.2	0.31298	0.69032	1.0033	2.4135	16.94915254	1.2	1.7547	1.2	1.2	2.1674	0.857142857	1.2	2.2172
0.481481481	1.3	0.31294	0.67174	0.98468	2.4034	18.36158192	1.3	1.7205	1.3	1.3	2.1502	0.928571429	1.3	2.2016
0.518518519	1.4	0.31295	0.65531	0.96826	2.3943	19.7740113	1.4	1.6903	1.4	1.4	2.1348	1	1.4	2.1877
0.555555556	1.5	0.31289	0.64061	0.9535	2.3849	21.18644068	1.5	1.6602	1.5	1.5	2.1191	1.071428571	1.5	2.1734
0.592592593	1.6	0.31266	0.62739	0.94005	2.3732	22.59887006	1.6	1.6251	1.6	1.6	2.1004	1.142857143	1.6	2.1564
0.62962963	1.7	0.31246	0.61519	0.92765	2.3625	24.01129944	1.7	1.5937	1.7	1.7	2.0834	1.214285714	1.7	2.1408
0.666666667	1.8	0.3123	0.60416	0.91646	2.3527	25.42372881	1.8	1.5653	1.8	1.8	2.0678	1.285714286	1.8	2.1266
0.703703704	1.9	0.31216	0.59402	0.90618	2.3435	26.83615819	1.9	1.5396	1.9	1.9	2.0535	1.357142857	1.9	2.1135
0.740740741	2	0.31192	0.58466	0.89658	2.3334	28.24858757	2	1.5119	2	2	2.0378	1.428571429	2	2.0991
0.777777778	2.1	0.3115	0.576	0.8875	2.3213	29.66101695	2.1	1.4798	2.1	2.1	2.0194	1.5	2.1	2.0821
0.814814815	2.2	0.31111	0.56846	0.87957	2.31	31.07344633	2.2	1.4505	2.2	2.2	2.0023	1.571428571	2.2	2.0663
0.851851852	2.3	0.31075	0.56085	0.8716	2.2994	32.48587571	2.3	1.4235	2.3	2.3	1.9863	1.642857143	2.3	2.0516
0.888888889	2.4	0.31043	0.5536	0.86403	2.2894	33.89830508	2.4	1.3987	2.4	2.4	1.9714	1.714285714	2.4	2.0378
0.925925926	2.5	0.31013	0.54667	0.8568	2.28	35.31073446	2.5	1.3757	2.5	2.5	1.9575	1.785714286	2.5	2.0249
1.851851852	5	0.29905	0.42907	0.72812	2.0525	70.62146893	5	0.91407	5	5	1.6384	3.571428571	5	1.7259
2.777777778	7.5	0.28701	0.35876	0.64577	1.8745	105.9322034	7.5	0.65934	7.5	7.5	1.4106	5.357142857	7.5	1.5083
3.703703704	10	0.27449	0.30541	0.5799	1.7252	141.2429379	10	0.50532	10	10	1.2337	7.142857143	10	1.3365
4.62962963	12.5	0.26277	0.26172	0.52449	1.6023	176.5536723	12.5	0.41445	12.5	12.5	1.0992	8.928571429	12.5	1.2037
5.555555556	15	0.25213	0.22494	0.47707	1.5003	211.8644068	15	0.36009	15	15	0.99646	10.71428571	15	1.1005
6.481481481	17.5	0.24259	0.19449	0.43708	1.4151	247.1751412	17.5	0.32676	17.5	17.5	0.91748	12.5	17.5	1.0199
7.407407407	20	0.23364	0.16934	0.40298	1.3403	282.4858757	20	0.30473	20	20	0.85367	14.28571429	20	0.95357
8.333333333	22.5	0.22508	0.14927	0.37435	1.2733	317.7966102	22.5	0.28924	22.5	22.5	0.80083	16.07142857	22.5	0.89767
9.259259259	25	0.21793	0.132	0.34993	1.2184	353.1073446	25	0.27921	25	25	0.76135	17.85714286	25	0.85516
10.18518519	27.5	0.21008	0.11687	0.32695	1.163	388.4180791	27.5	0.27015	27.5	27.5	0.72385	19.64285714	27.5	0.81405
11.11111111	30	0.20361	0.10408	0.30769	1.1175	423.7288136	30	0.26388	30	30	0.69595	21.42857143	30	0.78287
12.03703704	32.5	0.19774	0.093291	0.291031	1.0773	459.039548	32.5	0.25885	32.5	32.5	0.67304	23.21428571	32.5	0.7568
12.96296296	35	0.19168	0.084335	0.276015	1.0375	494.3502825	35	0.25389	35	35	0.65146	25	35	0.73188
13.88888889	37.5	0.18639	0.076267	0.262657	1.0029	529.6610169	37.5	0.24986	37.5	37.5	0.63389	26.78571429	37.5	0.71122
14.81481481	40	0.18161	0.069032	0.250642	0.97183	564.9717514	40	0.24635	40	40	0.61876	28.57142857	40	0.69317
15.74074074	42.5	0.17643	0.062555	0.238985	0.93959	600.2824859	42.5	0.24228	42.5	42.5	0.60294	30.35714286	42.5	0.67423
16.66666667	45	0.1717	0.056743	0.228443	0.91017	635.5932203	45	0.23862	45	45	0.58856	32.14285714	45	0.65689
17.59259259	47.5	0.16749	0.051512	0.219002	0.88368	670.9039548	47.5	0.23545	47.5	47.5	0.57532	33.92857143	47.5	0.64087
18.51851852	50	0.16366	0.046786	0.210446	0.8594	706.2146893	50	0.23267	50	50	0.56236	35.71428571	50	0.62535

Figure B.7 : Sample Dose Equivalent Calculations for Various Materials at Physical Thickness Points for 1 *AU* GCR Cis-lunar Space Radiation Environment.

B.5 MULASSIS Representative Data

The analysis with the MULASSIS simulation codes is straightforward. The three incident particles considered from GCR spectrum, H, He, and Fe, are run independently at the areal densities noted (corresponding to thickness), and then the captured dose equivalent is calculated by summing the results along with the appropriate weighting factor. In similar fashion, the fluence analysis is run for each particle type and shielding thickness, with the number of neutrons emitted at the back end of the shielding model captured and counted by differential energy bin.

Prior to beginning these analyses, test simulation runs were made to determine the optimal number of input particles required for each simulation run to have convergence of the Monte Carlo results, given the input spectrum and geometry employed. It was determined that utilizing 100,000 input particles per simulation run took only modest computer time per run, and produced essentially the same results as running ten-times that number of particles, but with much longer computer time required per run.

	Dose Equivalent (Sv/year)	ICRP 60				
Thickness	Al	PE	Al+PE	LH2	Al+PE+Al	BN+H	Al BN H
g/cm2							
0	2.272E-01	2.272E-01	2.279E-01	2.278E-01	2.279E-01	2.278E-01	2.27E-01
2	2.154E-01	2.140E-01	2.164E-01	2.068E-01	2.164E-01	2.146E-01	2.15E-01
5	2.074E-01	2.030E-01	2.078E-01	1.927E-01	2.082E-01	2.057E-01	2.06E-01
10	1.964E-01	1.928E-01	1.939E-01	1.787E-01	1.977E-01	1.912E-01	1.93E-01
20	1.865E-01	1.820E-01	1.799E-01	1.654E-01	1.832E-01	1.769E-01	1.80E-01
30	1.765E-01	1.726E-01	1.724E-01	1.565E-01	1.740E-01	1.657E-01	1.66E-01
40	1.725E-01	1.610E-01	1.629E-01	1.434E-01	1.647E-01	1.597E-01	1.54E-01
60	1.597E-01	1.480E-01	1.500E-01	1.201E-01	1.483E-01	1.377E-01	1.40E-01
80	1.417E-01	1.322E-01	1.323E-01	1.063E-01	1.384E-01	1.293E-01	1.30E-01
100	1.331E-01	1.158E-01	1.185E-01	9.125E-02	1.245E-01	1.109E-01	1.17E-01

Figure B.8 : Sample Dose Equivalent Calculations using MULASSIS Monte Carlo Simulation for Various Materials for 1 *AU* GCR Cis-lunar Space Radiation Environment.

The fluence analysis calculations with MULASSIS involve accumulation of massive amounts of data from multiple runs of the Monte Carlo radiation transport code, where each ion must be run separately to collect data for each particle that one wants to evaluate behind shielding of a specified material at a specified depth in that material. To attach all the data would require many pages of computer output, but for simplicity in verifying the procedure I have appended the neutron fluence data for secondary neutrons produced by hydrogen ions in the GCR in aluminum shielding of 10 gm/cm^2 and of 20 gm/cm^2, as shown in Figures B.9 and B.10.

THICKNESS	10			Al - 10 gm/cm^2
Elow	Eup	Emean	Value	Error
keV	keV	keV	particles/cm2/bin	particles/cm2/bin
1.00E+00	1.26E+00	1.21E+00	2.35E-05	1.67E-05
1.26E+00	1.58E+00	0.00E+00	0.00E+00	0.00E+00
1.58E+00	2.00E+00	1.66E+00	6.74E-05	5.56E-05
2.00E+00	2.51E+00	2.37E+00	4.44E-06	4.44E-06
2.51E+00	3.16E+00	0.00E+00	0.00E+00	0.00E+00
3.16E+00	3.98E+00	3.58E+00	2.69E-05	1.79E-05
3.98E+00	5.01E+00	4.46E+00	2.19E-05	1.78E-05
5.01E+00	6.31E+00	5.61E+00	3.21E-05	1.70E-05
6.31E+00	7.94E+00	6.91E+00	7.74E-05	3.59E-05
7.94E+00	1.00E+01	8.98E+00	1.04E-04	3.26E-05
1.00E+01	1.26E+01	1.14E+01	7.15E-05	2.52E-05
1.26E+01	1.58E+01	1.46E+01	2.26E-04	6.29E-05
1.58E+01	2.00E+01	1.79E+01	2.62E-04	7.35E-05
2.00E+01	2.51E+01	2.29E+01	3.19E-04	1.12E-04
2.51E+01	3.16E+01	2.82E+01	3.00E-04	5.90E-05
3.16E+01	3.98E+01	3.49E+01	6.01E-04	8.39E-05
3.98E+01	5.01E+01	4.54E+01	6.81E-04	1.18E-04
5.01E+01	6.31E+01	5.71E+01	1.06E-03	1.66E-04
6.31E+01	7.94E+01	7.30E+01	1.50E-03	2.02E-04
7.94E+01	1.00E+02	8.98E+01	1.90E-03	1.62E-04
1.00E+02	1.26E+02	1.13E+02	2.08E-03	1.94E-04
1.26E+02	1.58E+02	1.42E+02	2.42E-03	1.82E-04
1.58E+02	2.00E+02	1.80E+02	3.83E-03	2.54E-04
2.00E+02	2.51E+02	2.24E+02	4.66E-03	3.19E-04
2.51E+02	3.16E+02	2.82E+02	5.99E-03	3.10E-04
3.16E+02	3.98E+02	3.58E+02	7.47E-03	6.76E-04
3.98E+02	5.01E+02	4.51E+02	8.54E-03	3.58E-04
5.01E+02	6.31E+02	5.65E+02	1.03E-02	4.20E-04
6.31E+02	7.94E+02	7.10E+02	1.26E-02	6.57E-04
7.94E+02	1.00E+03	8.95E+02	1.39E-02	5.24E-04
1.00E+03	1.26E+03	1.12E+03	1.57E-02	5.22E-04
1.26E+03	1.58E+03	1.42E+03	1.88E-02	7.29E-04
1.58E+03	2.00E+03	1.78E+03	2.02E-02	6.52E-04
2.00E+03	2.51E+03	2.24E+03	2.11E-02	6.40E-04
2.51E+03	3.16E+03	2.82E+03	2.08E-02	6.40E-04
3.16E+03	3.98E+03	3.55E+03	2.30E-02	7.04E-04
3.98E+03	5.01E+03	4.48E+03	2.27E-02	7.95E-04
5.01E+03	6.31E+03	5.64E+03	2.32E-02	8.43E-04
6.31E+03	7.94E+03	7.09E+03	2.37E-02	7.91E-04
7.94E+03	1.00E+04	8.92E+03	2.30E-02	9.02E-04
1.00E+04	1.26E+04	1.12E+04	2.53E-02	1.35E-03
1.26E+04	1.58E+04	1.42E+04	2.43E-02	1.06E-03
1.58E+04	2.00E+04	1.80E+04	2.58E-02	2.36E-03
2.00E+04	2.51E+04	2.24E+04	2.58E-02	9.30E-04
2.51E+04	3.16E+04	2.85E+04	2.70E-02	9.51E-04
3.16E+04	3.98E+04	3.57E+04	3.09E-02	2.47E-03
3.98E+04	5.01E+04	4.48E+04	2.92E-02	1.07E-03
5.01E+04	6.31E+04	5.63E+04	3.09E-02	1.03E-03
6.31E+04	7.94E+04	7.11E+04	3.24E-02	1.16E-03
7.94E+04	1.00E+05	8.95E+04	3.17E-02	1.14E-03
1.00E+05	1.26E+05	1.12E+05	3.32E-02	1.13E-03
1.26E+05	1.58E+05	1.41E+05	3.27E-02	1.21E-03
1.58E+05	2.00E+05	1.78E+05	3.23E-02	1.34E-03
2.00E+05	2.51E+05	2.24E+05	2.83E-02	1.49E-03
2.51E+05	3.16E+05	2.83E+05	2.57E-02	1.23E-03
3.16E+05	3.98E+05	3.59E+05	2.65E-02	3.13E-03
3.98E+05	5.01E+05	4.48E+05	2.02E-02	8.22E-04
5.01E+05	6.31E+05	5.61E+05	1.96E-02	2.04E-03
6.31E+05	7.94E+05	7.05E+05	1.62E-02	8.04E-04
7.94E+05	1.00E+06	8.91E+05	1.20E-02	5.75E-04

Figure B.9 : Fluence Data for Neutrons behind Aluminum – $10 gm/cm^2$.

THICKNESS	20			Al - 20 gm/cm^2
Elow	Eup	Emean	Value	Error
keV	keV	keV	particles/cm2/bin	particles/cm2/bin
1.00E+00	1.26E+00	1.04E+00	1.37E-05	1.37E-05
1.26E+00	1.58E+00	1.44E+00	5.39E-05	3.12E-05
1.58E+00	2.00E+00	0.00E+00	0.00E+00	0.00E+00
2.00E+00	2.51E+00	2.31E+00	3.93E-05	2.33E-05
2.51E+00	3.16E+00	2.95E+00	2.10E-04	1.29E-04
3.16E+00	3.98E+00	3.58E+00	7.86E-05	3.65E-05
3.98E+00	5.01E+00	4.32E+00	1.55E-04	6.21E-05
5.01E+00	6.31E+00	5.48E+00	1.79E-04	1.16E-04
6.31E+00	7.94E+00	7.17E+00	4.81E-04	1.54E-04
7.94E+00	1.00E+01	8.66E+00	3.13E-04	8.32E-05
1.00E+01	1.26E+01	1.13E+01	4.45E-04	1.15E-04
1.26E+01	1.58E+01	1.43E+01	5.38E-04	1.01E-04
1.58E+01	2.00E+01	1.80E+01	1.01E-03	1.65E-04
2.00E+01	2.51E+01	2.29E+01	1.26E-03	2.14E-04
2.51E+01	3.16E+01	2.85E+01	1.36E-03	1.76E-04
3.16E+01	3.98E+01	3.58E+01	2.40E-03	2.38E-04
3.98E+01	5.01E+01	4.48E+01	3.12E-03	2.80E-04
5.01E+01	6.31E+01	5.66E+01	5.25E-03	6.30E-04
6.31E+01	7.94E+01	7.14E+01	6.11E-03	4.70E-04
7.94E+01	1.00E+02	8.80E+01	6.72E-03	4.86E-04
1.00E+02	1.26E+02	1.12E+02	7.24E-03	6.42E-04
1.26E+02	1.58E+02	1.43E+02	8.63E-03	6.06E-04
1.58E+02	2.00E+02	1.79E+02	1.08E-02	1.00E-03
2.00E+02	2.51E+02	2.29E+02	1.41E-02	1.80E-03
2.51E+02	3.16E+02	2.83E+02	1.67E-02	7.57E-04
3.16E+02	3.98E+02	3.58E+02	2.02E-02	8.04E-04
3.98E+02	5.01E+02	4.48E+02	2.40E-02	9.99E-04
5.01E+02	6.31E+02	5.66E+02	2.92E-02	1.19E-03
6.31E+02	7.94E+02	7.14E+02	3.16E-02	1.12E-03
7.94E+02	1.00E+03	8.97E+02	3.28E-02	1.16E-03
1.00E+03	1.26E+03	1.12E+03	3.87E-02	1.38E-03
1.26E+03	1.58E+03	1.42E+03	4.51E-02	2.21E-03
1.58E+03	2.00E+03	1.78E+03	4.65E-02	1.40E-03
2.00E+03	2.51E+03	2.24E+03	4.62E-02	1.40E-03
2.51E+03	3.16E+03	2.82E+03	4.39E-02	1.42E-03
3.16E+03	3.98E+03	3.56E+03	4.26E-02	1.37E-03
3.98E+03	5.01E+03	4.46E+03	4.28E-02	1.38E-03
5.01E+03	6.31E+03	5.59E+03	4.51E-02	2.05E-03
6.31E+03	7.94E+03	7.10E+03	3.94E-02	1.23E-03
7.94E+03	1.00E+04	8.91E+03	4.12E-02	1.67E-03
1.00E+04	1.26E+04	1.13E+04	3.91E-02	1.35E-03
1.26E+04	1.58E+04	1.41E+04	4.09E-02	1.44E-03
1.58E+04	2.00E+04	1.79E+04	3.96E-02	1.27E-03
2.00E+04	2.51E+04	2.24E+04	4.27E-02	1.56E-03
2.51E+04	3.16E+04	2.82E+04	4.50E-02	1.40E-03
3.16E+04	3.98E+04	3.55E+04	5.01E-02	1.84E-03
3.98E+04	5.01E+04	4.47E+04	5.41E-02	2.07E-03
5.01E+04	6.31E+04	5.66E+04	5.42E-02	1.84E-03
6.31E+04	7.94E+04	7.10E+04	5.60E-02	1.92E-03
7.94E+04	1.00E+05	8.92E+04	5.96E-02	2.08E-03
1.00E+05	1.26E+05	1.12E+05	5.66E-02	1.73E-03
1.26E+05	1.58E+05	1.42E+05	5.47E-02	1.87E-03
1.58E+05	2.00E+05	1.78E+05	5.08E-02	1.78E-03
2.00E+05	2.51E+05	2.24E+05	4.41E-02	1.62E-03
2.51E+05	3.16E+05	2.83E+05	4.24E-02	2.73E-03
3.16E+05	3.98E+05	3.55E+05	3.47E-02	1.33E-03
3.98E+05	5.01E+05	4.48E+05	3.73E-02	3.33E-03
5.01E+05	6.31E+05	5.61E+05	2.76E-02	1.25E-03
6.31E+05	7.94E+05	7.06E+05	2.42E-02	1.20E-03
7.94E+05	1.00E+06	8.94E+05	1.76E-02	9.17E-04

Figure B.10 : Fluence Data for Neutrons behind Aluminum – $20 gm/cm^2$.

Bibliography

[1] D. Lario, "Advances in modeling gradual solar energetic particle events," *Advances in Space Research*, vol. 36, no. 12, pp. 2279–2288, 2005.

[2] C. Scott-Conner, D. Masys, and C. Liverman, eds., *Review of NASA's Evidence Reports on Human Health Risks: 2016 Letter Report*. National Academies Press, 2017.

[3] V. K. Parihar, B. Allen, K. K. Tran, T. G. Macaraeg, E. M. Chu, S. F. Kwok, N. N. Chmielewski, B. M. Craver, J. E. Baulch, M. M. Acharya, *et al.*, "What happens to your brain on the way to mars," *Science advances*, vol. 1, no. 4, p. e1400256, 2015.

[4] F. A. Cucinotta and E. Cacao, "Non-targeted effects models predict significantly higher mars mission cancer risk than targeted effects models," *Scientific Reports*, vol. 7, 2017.

[5] M. D. Delp, J. M. Charvat, C. L. Limoli, R. K. Globus, and P. Ghosh, "Apollo lunar astronauts show higher cardiovascular disease mortality: Possible deep space radiation effects on the vascular endothelium," *Scientific reports*, vol. 6, p. 29901, 2016.

[6] R. Tripathi, J. Wilson, and R. Youngquist, "Exploring the feasibility of electrostatic shielding for spacecrafts," in *Space 2005*, p. 6604, 2005.

[7] J. C. Chancellor, R. S. Blue, K. A. Cengel, S. M. Auñón-Chancellor, K. H. Rubins, H. G. Katzgraber, and A. R. Kennedy, "Limitations in predicting the space radiation health risk for exploration astronauts," *npj Microgravity*, vol. 4, no. 1, p. 8, 2018.

[8] J. C. Chancellor, G. B. Scott, and J. P. Sutton, "Space radiation: the number one risk to astronaut health beyond low earth orbit," *Life*, vol. 4, no. 3, pp. 491–510, 2014.

[9] M. Durante, "Space radiation protection: destination mars," *Life sciences in space research*, vol. 1, pp. 2–9, 2014.

[10] S. Kodaira, R. Tolochek, I. Ambrozova, H. Kawashima, N. Yasuda, M. Kurano, H. Kitamura, Y. Uchihori, I. Kobayashi, H. Hakamada, *et al.*, "Verification of shielding effect by the water-filled materials for space radiation in the international space station using passive dosimeters," *Advances in Space Research*, vol. 53, no. 1, pp. 1–7, 2014.

[11] C. Francis A, S. Lisa C, S. Judy L, T. Shelia A, K. MY, *et al.*, "Galactic and solar cosmic ray shielding in deep space," tech. rep., NASA Technical Paper 3682, 1997.

[12] A. Borggräfe, M. Quatmann, and D. Nölke, "Radiation protective structures on the base of a case study for a manned mars mission," *Acta Astronautica*, vol. 65, no. 9, pp. 1292–1305, 2009.

[13] D. Warden and Y. Bayazitoglu, "New comparative metric for evaluating spacecraft radiation shielding," *Journal of Spacecraft and Rockets*, pp. 1–15, 2018.

[14] X. Li, D. Warden, and Y. Bayazitoglu, "Analysis to evaluate multilayer shielding of galactic cosmic rays," *Journal of Thermophysics and Heat Transfer*, vol. 32, no. 2, pp. 525–531, 2017.

[15] P. M. O'Neill, "Badhwar–o'neill galactic cosmic ray model update based on advanced composition explorer (ace) energy spectra from 1997 to present," *Advances in Space Research*, vol. 37, no. 9, pp. 1727–1733, 2006.

[16] L.-L. Zhao and G. Qin, "An observation-based gcr model of heavy nuclei: Measurements from cris onboard ace spacecraft," *Journal of Geophysical Research: Space Physics*, vol. 118, no. 5, pp. 1837–1848, 2013.

[17] E. C. Stone, C. Cohen, W. Cook, A. Cummings, B. Gauld, B. Kecman, R. Leske, R. Mewaldt, M. Thayer, B. Dougherty, *et al.*, "The cosmic-ray isotope spectrometer for the advanced composition explorer," *Space Science Reviews*, vol. 86, no. 1, pp. 285–356, 1998.

[18] H. E. Spence, A. Case, M. Golightly, T. Heine, B. Larsen, J. Blake, P. Caranza, W. Crain, J. George, M. Lalic, *et al.*, "Crater: The cosmic ray telescope for the effects of radiation experiment on the lunar reconnaissance orbiter mission," *Space Science Reviews*, vol. 150, no. 1, pp. 243–284, 2010.

[19] B. Ehresmann, D. M. Hassler, C. Zeitlin, J. Guo, J. Köhler, R. F. Wimmer-Schweingruber, J. K. Appel, D. E. Brinza, S. C. Rafkin, S. I. Böttcher, *et al.*, "Charged particle spectra measured during the transit to mars with the mars science laboratory radiation assessment detector (msl/rad)," *Life sciences in space research*, vol. 10, pp. 29–37, 2016.

[20] J. A. Van Allen, "Radiation belts around the earth," *Scientific American*, vol. 200, no. 3, pp. 39–47, 1959.

[21] P. O'Neill, S. Golge, and T. Slaba, "Badhwar-o'neill 2014 galactic cosmic ray flux model description," tech. rep., NASA/TP 2015-218569, 2015.

[22] J. Adams, A. F. Barghouty, M. Mendenhall, R. Reed, B. Sierawski, K. Warren, J. Watts, and R. Weller, "Crème: The 2011 revision of the cosmic ray effects on micro-electronics code," *IEEE Transactions on Nuclear Science*, vol. 59, no. 6, pp. 3141–3147, 2012.

[23] N. A. Schwadron, J. Blake, A. Case, C. J. Joyce, J. Kasper, J. Mazur, N. Petro, M. Quinn, J. A. Porter, C. Smith, *et al.*, "Does the worsening galactic cosmic radiation environment observed by crater preclude future manned deep space exploration?," *Space Weather*, vol. 12, no. 11, pp. 622–632, 2014.

[24] E. Benton and E. Benton, "Space radiation dosimetry in low-earth orbit and beyond," *Nuclear Instruments and Methods in Physics Research Section B: Beam Interactions with Materials and Atoms*, vol. 184, no. 1, pp. 255–294, 2001.

[25] Y. Bayazitoglu and M. N. Özısık, *A textbook for heat transfer fundamentals*. Begell, 2013.

[26] S. Koontz, "Space flight ionizing radiation environments," tech. rep., NASA JSC Technical Presentation, 2017.

[27] T. C. Slaba, "Radiation transport methods for space applications," tech. rep., NASA Space Radiation Summer School Presentation-Brookhaven National Laboratory, 2015.

[28] J. Adams Jr, D. Hathaway, R. Grugel, J. Watts, T. Parnell, J. Gregory, and R. Winglee, "Revolutionary concepts of radiation shielding for human exploration of space," tech. rep., NASA/TM—2005–213688, 2005.

[29] M. Spurio, "The cosmic rays and our galaxy," in *Particles and Astrophysics*, pp. 23–54, Springer, 2015.

[30] A. I. Mrigakshi, D. Matthiä, T. Berger, G. Reitz, and R. F. Wimmer-Schweingruber, "Estimation of galactic cosmic ray exposure inside and outside the earth's magnetosphere during the recent solar minimum between solar cycles 23 and 24," *Advances in Space Research*, vol. 52, no. 5, pp. 979–987, 2013.

[31] B. Klamm, "Passive space radiation shielding: Mass and volume optimization of tungsten-doped polyphenolic and polyethylene resins," tech. rep., NASA Ames Research Center Technical Report, 2015.

[32] M. Xapsos, C. Stauffer, T. Jordan, C. Poivey, D. Haskins, G. Lum, A. Pergosky, D. Smith, and K. LaBel, "How long can the hubble space telescope operate reliably?–a total dose perspective," *IEEE Transactions on Nuclear Science*, vol. 61, no. 6, pp. 3356–3362, 2014.

[33] A. Emmanuel, J. Raghavan, R. Harris, and P. Ferguson, "A comparison of radiation shielding effectiveness of materials for highly elliptical orbits," *Advances in Space Research*, vol. 53, no. 7, pp. 1143–1152, 2014.

[34] S. R. F. L. Pete Truscott, Karen Ford and D. Heynderickx, "Assessment of shielding strategies, dose enhancement effects and shielding tools for meo and jovian missions," tech. rep., RADECS 2010 Proceedings, 2010.

[35] S. S. Board, N. R. Council, *et al.*, *Space radiation hazards and the vision for space exploration: report of a workshop*, pp. 7–24. National Academies Press, 2006.

[36] J. Simpson, "Elemental and isotopic composition of the galactic cosmic rays," *Annual Review of Nuclear and Particle Science*, vol. 33, no. 1, pp. 323–382, 1983.

[37] J. Norbury, "Space radiation," tech. rep., NASA Langley Research Center-Space Radiation Summer School Presentation-Brookhaven National Laboratory, 2015.

[38] M. Durante and F. A. Cucinotta, "Physical basis of radiation protection in space travel," *Reviews of Modern Physics*, vol. 83, no. 4, p. 1245, 2011.

[39] J. F. Ziegler, "Terrestrial cosmic ray intensities," *IBM Journal of Research and Development*, vol. 42, no. 1, pp. 117–140, 1998.

[40] N. Schwadron, A. Boyd, K. Kozarev, M. Golightly, H. Spence, L. Townsend, and M. Owens, "Galactic cosmic ray radiation hazard in the unusual extended solar minimum between solar cycles 23 and 24," *Space Weather*, vol. 8, no. 5, 2010.

[41] J. Wilson, J. Miller, A. Konradi, and F. Cucinotta, "Shielding strategies for human space exploration," *NASA Conference Publication 3360*, vol. 1, no. 1, pp. 1–493, 1997.

[42] J. Bernabeu and I. Casanova, "Geant4-based radiation hazard assessment for human exploration missions," *Advances in Space Research*, vol. 40, no. 9, pp. 1368–1380, 2010.

[43] M. Moreno-Villanueva, M. Wong, T. Lu, Y. Zhang, and H. Wu, "Interplay of space radiation and microgravity in dna damage and dna damage response," *Npj Microgravity*, vol. 3, no. 1, p. 14, 2017.

[44] A. Singh, D. Siingh, and R. Singh, "Impact of galactic cosmic rays on earth's atmosphere and human health," *Atmospheric environment*, vol. 45, no. 23, pp. 3806–3818, 2011.

[45] F. A. Cucinotta, M.-H. Y. Kim, L. J. Chappell, and J. L. Huff, "How safe is safe enough? radiation risk for a human mission to mars," *PLoS One*, vol. 8, no. 10, p. e74988, 2013.

[46] UNSCEAR, "Sources and effects of ionizing radiation," tech. rep., United Nations 2008 Report to the General Assembly, 2008.

[47] I. Morison, *Introduction to astronomy and cosmology*. John Wiley & Sons, 2008.

[48] T. C. Slaba, A. A. Bahadori, B. D. Reddell, R. C. Singleterry, M. S. Clowdsley, and S. R. Blattnig, "Optimal shielding thickness for galactic cosmic ray environments," *Life Sciences in Space Research*, vol. 12, pp. 1–15, 2017.

[49] J. C. Chancellor, R. S. Blue, K. A. Cengel, S. M. Auñón-Chancellor, K. H. Rubins, H. G. Katzgraber, and A. R. Kennedy, "Limitations in predicting the space radiation health risk for exploration astronauts," *arXiv preprint arXiv:1710.07311*, vol. 1, no. 1, pp. 1–15, 2017.

[50] ICRP, "Icrp publication 103 extract," tech. rep., The International Commission on Radiological Protection, 2007.

[51] ICRP, *ICRP Publication 60: 1990 Recommendations of the International Commission on Radiological Protection*. No. 60, Elsevier Health Sciences, 1991.

[52] J. Valentin *et al.*, *The 2007 Recommendations of the International Commission on Radiological Protection*. Elsevier Oxford, UK, 2007.

[53] A. D. Wrixon, "New icrp recommendations," *Journal of radiological protection*, vol. 28, no. 2, p. 161, 2008.

[54] M. S. Clowdsley, J. W. Wilson, M.-H. Kim, B. M. Anderson, and J. E. Nealy, "Radiation protection quantities for near earth environments – aiaa technical report," tech. rep., AIAA, 2004.

[55] E. Rask, "The radiation challenge," tech. rep., NASA EP200808116MSFC, 2008.

[56] A. M. Sieffert, "Astronaut health & safety regulations: Ionizing radiation," *Scitech Lawyer*, vol. 10, no. 4, p. 20, 2014.

[57] F. A. Cucinotta, S. Hu, N. A. Schwadron, K. Kozarev, L. W. Townsend, and M.-H. Y. Kim, "Space radiation risk limits and earth-moon-mars environmental models," *Space Weather*, vol. 8, no. 12, 2010.

[58] R. A. English, R. E. Benson, J. Bailey, and C. Barnes, "Apollo experience report: Protection against radiation," tech. rep., NASA Technical Note D-7080, 1973.

[59] F. A. Cucinotta, N. Hamada, and M. P. Little, "No evidence for an increase in circulatory disease mortality in astronauts following space radiation exposures," *Life sciences in space research*, vol. 10, pp. 53–56, 2016.

[60] R. L. Hughson, A. Helm, and M. Durante, "Heart in space: effect of the extraterrestrial environment on the cardiovascular system," *Nature Reviews Cardiology*, vol. 15, no. 3, p. 167, 2018.

[61] J. Mazur, "Space environment effects on space systems," tech. rep., The Aerospace Corporation-Workshop on Science Associated With the Lunar Exploration Architecture, 2007.

[62] M. D. Griffin, *Space vehicle design*. AIAA, 2004.

[63] A. Thomson and B. Taylor, "Guide for the use of the international system of units (nist special publication 811 2008 edition)," tech. rep., National Institute of Standards and Technology, US Government Printing Office, 2008.

[64] F. A. Cucinotta, M.-H. Y. Kim, and L. J. Chappell, "Space radiation cancer risk projections and uncertainties," tech. rep., NASA/TP-2013-217375, 2013.

[65] F. A. Cucinotta and M. Durante, "Cancer risk from exposure to galactic cosmic rays: implications for space exploration by human beings," *The lancet oncology*, vol. 7, no. 5, pp. 431–435, 2006.

[66] G. Santina, P. Nieminen, H. Evansa, E. Daly, F. Lei, P. Truscott, C. Dyer, B. Quaghebeur, and D. Heynderickx, "New geant4 based simulation tools for space radiation shielding and effects analysis," *Nuclear Physics B-Proceedings Supplements*, vol. 125, pp. 69–74, 2003.

[67] J. Wilson, F. Cucinotta, J. Miller, J. Shinn, S. Thibeault, R. Singleterry, L. Simonsen, and M. Kim, "Approach and issues relating to shield material design to protect astronauts from space radiation," *Materials & design*, vol. 22, no. 7, pp. 541–554, 2001.

[68] J. W. Wilson, F. F. Badavi, F. A. Cucinotta, J. L. Shinn, G. D. Badhwar, R. Silberberg, C. Tsao, L. W. Townsend, and R. K. Tripathi, "Hzetrn: Description of a free-space ion and nucleon transport and shielding computer program," tech. rep., NASA Technical Paper 3495, 1995.

[69] V. Yadav, S. Sirisha, and S. Bhatnagar, "Study for stopping power of proton in different materials–a geant4 simulation," in *Proceedings of the DAE Symp. on Nucl. Phys*, vol. 57, p. 734, 2012.

[70] S. Tavernier, *Experimental techniques in nuclear and particle physics*. Springer Science & Business Media, 2010.

[71] N. Bohr, "Lx. on the decrease of velocity of swiftly moving electrified particles in passing through matter," *The London, Edinburgh, and Dublin Philosophical Magazine and Journal of Science*, vol. 30, no. 178, pp. 581–612, 1915.

[72] H. Bichsel, "Stopping power and ranges of fast ions in heavy elements," *Physical Review A*, vol. 46, no. 9, p. 5761, 1992.

[73] J. F. Ziegler, M. D. Ziegler, and J. P. Biersack, "Srim–the stopping and range of ions in matter (2010)," *Nuclear Instruments and Methods in Physics Research Section B: Beam Interactions with Materials and Atoms*, vol. 268, no. 11, pp. 1818–1823, 2010.

[74] H. Bethe, "Bremsformel für elektronen relativistischer geschwindigkeit," *Zeitschrift für Physik*, vol. 76, no. 5-6, pp. 293–299, 1932.

[75] H. Paul and D. Sánchez-Parcerisa, "A critical overview of recent stopping power programs for positive ions in solid elements," *Nuclear Instruments and Methods*

in Physics Research Section B: Beam Interactions with Materials and Atoms, vol. 312, pp. 110–117, 2013.

[76] S. John, L. W. Townsend, J. W. Wilson, and R. K. Tripathi, "Geometric model from microscopic theory for nuclear absorption," tech. rep., NASA Technical Paper 3324, 1993.

[77] H. Bradt and B. Peters, "The heavy nuclei of the primary cosmic radiation," *Physical Review*, vol. 77, no. 1, p. 54, 1950.

[78] E. Everhart, G. Stone, and R. Carbone, "Classical calculation of differential cross section for scattering from a coulomb potential with exponential screening," *Physical Review*, vol. 99, no. 4, p. 1287, 1955.

[79] L. Sihver, C. Tsao, R. Silberberg, T. Kanai, and A. Barghouty, "Total reaction and partial cross section calculations in proton-nucleus (z t 26) and nucleus-nucleus reactions (z p and z t 26)," *Physical Review C*, vol. 47, no. 3, p. 1225, 1993.

[80] D. A. Bromley, "Treatise on heavy-ion science. vol. 6: astrophysics, chemistry, and condensed matter," 1984.

[81] M. Berger, "Pstar: Stopping-power and range tables for protons," 2002.

[82] A. Das and T. Ferbel, "Introduction to nuclear and particle physics. introduction, problems, exercises," 1995.

[83] J. F. Ziegler, M. D. Ziegler, and J. P. Biersack, *SRIM: the stopping and range of ions in matter*. Cadence Design Systems, 2008.

[84] S. Guetersloh, C. Zeitlin, L. Heilbronn, J. Miller, T. Komiyama, A. Fukumura, Y. Iwata, T. Murakami, and M. Bhattacharya, "Polyethylene as a radiation shielding standard in simulated cosmic-ray environments," *Nuclear Instruments and Methods in Physics Research Section B: Beam Interactions with Materials and Atoms*, vol. 252, no. 2, pp. 319–332, 2006.

[85] C. Zeitlin, S. B. Guetersloh, L. H. Heilbronn, and J. Miller, "Measurements of materials shielding properties with 1gev/nuc 56 fe," *Nuclear Instruments and Methods in Physics Research Section B: Beam Interactions with Materials and Atoms*, vol. 252, no. 2, pp. 308–318, 2006.

[86] T. C. Slaba, S. R. Blattnig, J. W. Norbury, A. Rusek, C. La Tessa, and S. A. Walker, "Gcr simulator reference field and a spectral approach for laboratory simulation," tech. rep., NASA/TP-2015-218698, 2015.

[87] C. La Tessa, M. Sivertz, I.-H. Chiang, D. Lowenstein, and A. Rusek, "Overview of the nasa space radiation laboratory," *Life sciences in space research*, vol. 11, pp. 18–23, 2016.

[88] J. C. Chancellor, S. Guetersloh, K. Cengel, J. Ford, and H. G. Katzgraber, "Emulation of the space radiation environment for materials testing and radiobiological experiments," *arXiv preprint arXiv:1706.02727*, 2017.

[89] Y. Jia and Z. Lin, "The radiation environment on the moon from galactic cosmic rays in a lunar habitat," *Radiation research*, vol. 173, no. 2, pp. 238–244, 2010.

[90] J. Bernabeu and I. Casanova, "Moon surface radiation environment analysis for february 1956 solar event conditions," *Advances in Space Research*, vol. 42, no. 12, pp. 1906–1912, 2008.

[91] T. W. Bonner, "Collisions of neutrons with atomic nuclei," *Physical Review*, vol. 45, no. 9, p. 601, 1934.

[92] G. S. Bauer, "Physics and technology of spallation neutron sources," *Nuclear Instruments and Methods in Physics Research Section A: Accelerators, Spectrometers, Detectors and Associated Equipment*, vol. 463, no. 3, pp. 505–543, 2001.

[93] M. Coeck, F. Vermeersch, and F. Vanhavere, "Neutron shielding evaluation for a small fuel transport case," *Nuclear Instruments and Methods in Physics Research Section A: Accelerators, Spectrometers, Detectors and Associated Equipment*, vol. 476, no. 1, pp. 273–276, 2002.

[94] D. Chichester and B. Blackburn, "Radiation fields from neutron generators shielded with different materials," *Nuclear Instruments and Methods in Physics Research Section B: Beam Interactions with Materials and Atoms*, vol. 261, no. 1, pp. 845–849, 2007.

[95] S. A. Thibeault, J. H. Kang, G. Sauti, C. Park, C. C. Fay, and G. C. King, "Nanomaterials for radiation shielding," *MRS Bulletin*, vol. 40, no. 10, pp. 836–841, 2015.

[96] J. W. Wilson, S. Y. Chun, F. F. Badavi, L. W. Townsend, and S. L. Lamkin, "Hzetrn: a heavy ion/nucleon transport code for space radiations," tech. rep., NASA Technical Paper 3146-December 1991, 1991.

[97] J. W. Wilson, R. K. Tripathi, C. J. Mertens, S. R. Blattnig, M. S. Clowdsley, F. A. Cucinotta, J. Tweed, J. H. Heinbockel, S. A. Walker, and J. E. Nealy,

"Verification and validation: High charge and energy (hze) transport codes and future development," tech. rep., NASA/TP-2005-213784, 2005.

[98] S. P. Parker, *McGraw-Hill dictionary of scientific and technical terms*. McGraw-Hill Book Co., 1984.

[99] G. M. Kremer, *An introduction to the Boltzmann equation and transport processes in gases*. Springer Science & Business Media, 2010.

[100] S. Höfner, "The equations of fluid dynamics and their connection with the boltzmann equation," tech. rep., Department of Physics and Astronomy Uppsala University, 2008.

[101] S. Harris, *An introduction to the theory of the Boltzmann equation*. Courier Corporation, 2004.

[102] F. Rohrlich, "A poem by ludwig boltzmann," *American Journal of Physics*, vol. 60, no. 11, pp. 972–973, 1992.

[103] J. W. Wilson, T. C. Slaba, F. F. Badavi, B. D. Reddell, and A. A. Bahadori, "Advances in nasa radiation transport research: 3dhzetrn," *Life Sciences in Space Research*, vol. 2, pp. 6–22, 2014.

[104] J. E. Nealy, F. A. Cucinotta, J. W. Wilson, F. F. Badavi, T. P. Dachev, B. Tomov, S. A. Walker, G. De Angelis, S. R. Blattnig, and W. Atwell, "Pre-engineering spaceflight validation of environmental models and the 2005 hzetrn simulation code," *Advances in space research*, vol. 40, no. 11, pp. 1593–1610, 2007.

[105] J. Wilson, L. Townsend, J. Shinn, F. Cucinotta, R. Costen, F. Badavi, and S. Lamkin, "Galactic cosmic ray transport methods: past, present, and future," *Advances in Space Research*, vol. 14, no. 10, pp. 841–852, 1994.

[106] T. C. Slaba, S. R. Blattnig, and F. F. Badavi, "Faster and more accurate transport procedures for hzetrn," *Journal of Computational Physics*, vol. 229, no. 24, pp. 9397–9417, 2010.

[107] R. C. Singleterry, S. R. Blattnig, M. S. Clowdsley, G. D. Qualls, C. A. Sandridge, L. C. Simonsen, T. C. Slaba, S. A. Walker, F. F. Badavi, J. L. Spangler, *et al.*, "Oltaris: On-line tool for the assessment of radiation in space," *Acta Astronautica*, vol. 68, no. 7, pp. 1086–1097, 2011.

[108] J. W. Wilson, R. K. Tripathi, F. F. Badavi, and F. A. Cucinotta, "Standardized radiation shield design method: 2005 hzetrn," tech. rep., SAE Technical Paper, 2006.

[109] R. C. Singleterry Jr, S. R. Blattnig, M. S. Clowdsley, G. D. Qualls, C. A. Sandridge, L. C. Simonsen, J. W. Norbury, T. C. Slaba, S. A. Walker, F. F. Badavi, *et al.*, "Oltaris: On-line tool for the assessment of radiation in space," tech. rep., NASA/TP-2010-216722, 2010.

[110] J. W. Wilson, T. C. Slaba, F. F. Badavi, B. D. Reddell, and A. A. Bahadori, "3dhzetrn: Shielded icru spherical phantom," *Life sciences in space research*, vol. 4, pp. 46–61, 2015.

[111] J. W. Wilson, T. C. Slaba, F. F. Badavi, B. D. Reddell, and A. A. Bahadori, "3dhzetrn: Neutron leakage in finite objects," *Life sciences in space research*, vol. 7, pp. 27–38, 2015.

[112] N. Metropolis, "The beginnings of monte carlo method," *Los Alamos Science*, vol. 15, no. 125-130, p. 30, 1987.

[113] T. A. Brunner, "Forms of approximate radiation transport," tech. rep., Sandia National Laboratories, 2002.

[114] H. A. Metropolis, "Monte carlo and the maniac," *Los alamos Science*, vol. 14, 1986.

[115] R. Eckhardt, "Stan ulam, john von neumann, and the monte carlo method," *Los Alamos Science*, vol. 15, no. 131-136, p. 30, 1987.

[116] N. Metropolis and S. Ulam, "The monte carlo method," *Journal of the American statistical association*, vol. 44, no. 247, pp. 335–341, 1949.

[117] I. M. Sobol, *A primer for the Monte Carlo method*. CRC press, 1994.

[118] T. Pinsky, "Monte carlo transport codes for use in the space radiation environment," tech. rep., Physics Department, University of Houston, 2015.

[119] G. Santin, *Chapter II Radiation Interaction Physics and Simulation*. ESA-Radiation and its Effects on Components and Systems (RADECS), 2013.

[120] S. Agostinelli, J. Allison, K. a. Amako, J. Apostolakis, H. Araujo, P. Arce, M. Asai, D. Axen, S. Banerjee, G. Barrand, *et al.*, "Geant4—a simulation toolkit," *Nuclear instruments and methods in physics research section A: Accelerators, Spectrometers, Detectors and Associated Equipment*, vol. 506, no. 3, pp. 250–303, 2003.

[121] D. Wright, "Geant4: Monte carlo transport codes for use in the space radiation environment," tech. rep., CERN, 2015.

[122] F. Ballarini, G. Battistoni, M. Brugger, M. Campanella, M. Carboni, F. Cerutti, A. Empl, A. Fasso, A. Ferrari, E. Gadioli, *et al.*, "The physics of the fluka code: Recent developments," *Advances in Space Research*, vol. 40, no. 9, pp. 1339–1349, 2007.

[123] T. Sato, K. Niita, N. Matsuda, S. Hashimoto, Y. Iwamoto, T. Furuta, S. Noda, T. Ogawa, H. Iwase, H. Nakashima, *et al.*, "Overview of particle and heavy ion transport code system phits," *Annals of Nuclear Energy*, vol. 82, pp. 110–115, 2015.

[124] L. Sihver, "Monte carlo transport codes for use in the space radiation environment," tech. rep., NASA JSC, 2015.

[125] T. Goorley, "Monte carlo transport codes for use in the space radiation environment," tech. rep., NASA JSC, 2012.

[126] Geant4-Collaboration, "Geant4 user's guide for toolkit developers," tech. rep., GEANT4 Collaboration, 2014.

[127] J. Allison, K. Amako, J. Apostolakis, P. Arce, M. Asai, T. Aso, E. Bagli, A. Bagulya, S. Banerjee, G. Barrand, *et al.*, "Recent developments in geant4," *Nuclear Instruments and Methods in Physics Research Section A: Accelerators, Spectrometers, Detectors and Associated Equipment*, vol. 835, pp. 186–225, 2016.

[128] P. Truscott, F. Lei, C. Dyer, B. Quaghebeur, D. Heyndericks, P. Nieminen, H. Evans, E. Daly, A. Mohammadzadeh, and G. Hopkinson, "Mulassis-monte carlo radiation shielding simulation tool for space applications made easy," in *ESA Special Publication*, vol. 536, p. 191, 2004.

[129] F. Lei, R. Truscott, C. Dyer, B. Quaghebeur, D. Heynderickx, R. Nieminen, H. Evans, and E. Daly, "Mulassis: A geant4-based multilayered shielding simulation tool," *IEEE Transactions on Nuclear Science*, vol. 49, no. 6, pp. 2788–2793, 2002.

[130] J. H. Adams Jr, "Cosmic ray effects on microelectronics. part 4," tech. rep., NAVAL RESEARCH LAB WASHINGTON DC, 1986.

[131] R. Nymmik, M. Panasyuk, T. Pervaja, and A. Suslov, "A model of galactic cosmic ray fluxes," *International Journal of Radiation Applications and Instrumentation. Part D. Nuclear Tracks and Radiation Measurements*, vol. 20, no. 3, pp. 427–429, 1992.

[132] G. Badhwar and P. O'Neill, "An improved model of galactic cosmic radiation for space exploration missions," *International Journal of Radiation Applications and Instrumentation. Part D. Nuclear Tracks and Radiation Measurements*, vol. 20, no. 3, pp. 403–410, 1992.

[133] G. D. Badhwar and P. O'Neill, "Galactic cosmic radiation model and its applications," *Advances in Space Research*, vol. 17, no. 2, pp. 7–17, 1996.

[134] A. J. Tylka, J. H. Adams, P. R. Boberg, B. Brownstein, W. F. Dietrich, E. O. Flueckiger, E. L. Petersen, M. A. Shea, D. F. Smart, and E. C. Smith, "Creme96: A revision of the cosmic ray effects on micro-electronics code," *IEEE Transactions on Nuclear Science*, vol. 44, no. 6, pp. 2150–2160, 1997.

[135] R. Nymmik, "Improved environment radiation models," *Advances in Space Research*, vol. 40, no. 3, pp. 313–320, 2007.

[136] P. M. O'Neill, "Badhwar–o'neill 2010 galactic cosmic ray flux model—revised," *IEEE Transactions on Nuclear Science*, vol. 57, no. 6, pp. 3148–3153, 2010.

[137] S. Golge, P. O'Neill, and T. Slaba, "Nasa galactic cosmic radiation environment model: Badhwar-o'neill (2014)," tech. rep., The 34th International Cosmic Ray Conference, 2015.

[138] A. I. Mrigakshi, D. Matthiä, T. Berger, G. Reitz, and R. F. Wimmer-Schweingruber, "How galactic cosmic ray models affect the estimation of radiation exposure in space," *Advances in Space Research*, vol. 51, no. 5, pp. 825–834, 2013.

[139] T. Slaba, "Comparison and validation of gcr models," tech. rep., NASA NAC HEO/SMD Joint Committee Technical Briefing, 2015.

[140] T. C. Slaba, X. Xu, S. R. Blattnig, and R. B. Norman, "Gcr environmental models iii: Gcr model validation and propagated uncertainties in effective dose," *Space Weather*, vol. 12, no. 4, pp. 233–245, 2014.

[141] D. Matthiä, T. Berger, A. I. Mrigakshi, and G. Reitz, "A ready-to-use galactic cosmic ray model," *Advances in Space Research*, vol. 51, no. 3, pp. 329–338, 2013.

[142] Z. Lin, J. Adams, A. Barghouty, S. Randeniya, R. Tripathi, J. Watts, and P. Yepes, "Comparisons of several transport models in their predictions in typical space radiation environments," *Advances in Space Research*, vol. 49, no. 4, pp. 797–806, 2012.

[143] S. Aghara, S. Sriprisan, R. Singleterry, and T. Sato, "Shielding evaluation for

solar particle events using mcnpx, phits and oltaris codes," *Life sciences in space research*, vol. 4, pp. 79–91, 2015.

[144] J. H. Heinbockel, T. C. Slaba, R. K. Tripathi, S. R. Blattnig, J. W. Norbury, F. F. Badavi, L. W. Townsend, T. Handler, T. A. Gabriel, L. S. Pinsky, *et al.*, "Comparison of transport codes, hzetrn, hetc and fluka, using 1977 gcr solar minimum spectra," tech. rep., NASA/TP-2009-215956, 2009.

[145] J. H. Heinbockel, T. C. Slaba, R. K. Tripathi, S. R. Blattnig, J. W. Norbury, F. F. Badavi, L. W. Townsend, T. Handler, T. A. Gabriel, L. S. Pinsky, *et al.*, "Comparison of the transport codes hzetrn, hetc and fluka for galactic cosmic rays," *Advances in Space Research*, vol. 47, no. 6, pp. 1089–1105, 2011.

[146] T. C. Slaba, B. B. Reddell, A. A. Bahadori, and M. S. Clowdsley, "Benchmark analysis for space radiation transport codes in thick shielding for gcr environments," tech. rep., NASA-HRP Investigators' Workshop, 2016.

[147] A. Borggräfe, M. Quatmann, and D. Nölke, "Radiation protective structures on the base of a case study for a manned mars mission," *Acta Astronautica*, vol. 65, no. 9, pp. 1292–1305, 2009.

[148] D. Stephens, L. Townsend, J. Miller, C. Zeitlin, and L. Heilbronn, "Monte carlo transport model comparison with 1a gev accelerated iron experiment: heavy-ion shielding evaluation of nasa space flight-crew foodstuff," *Advances in Space Research*, vol. 30, no. 4, pp. 901–905, 2002.

[149] A. Emmanuel and J. Raghavan, "Experimental validation of simulations of radiation shielding effectiveness of materials by mulassis," *Advances in Space Research*, vol. 58, no. 11, pp. 2376–2384, 2016.

[150] N. Chirskaya, L. Novikov, and E. Voronina, "Computer modelling of ionized radiation impact on micro-structured materials," tech. rep., WDS'15 Proceedings of Contributed Papers — Physics-ISBN 978-80-7378-311-2, 2015.

[151] A. I. Mrigakshi, D. Matthiä, T. Berger, G. Reitz, and R. F. Wimmer-Schweingruber, "Assessment of galactic cosmic ray models," *Journal of Geophysical Research: Space Physics*, vol. 117, no. A8, 2012.

[152] N. Barghouty, "Radiation transport and space-radiation related efforts at nasa's marshall space center," tech. rep., 11th Geant4 Space Users Workshop, Hiroshima, Japan, 2015.

[153] P. Spillantini, M. Casolino, M. Durante, R. Mueller-Mellin, G. Reitz, L. Rossi, V. Shurshakov, and M. Sorbi, "Shielding from cosmic radiation for interplanetary missions: active and passive methods," *Radiation measurements*, vol. 42, no. 1, pp. 14–23, 2007.

[154] W. Burger, R. Battiston, V. Calvelli, R. Musenich, V. Datskov, A. Della Torre, F. Venditti, S. Hovland, R. Meinke, S. Van Sciver, *et al.*, "Active magnetic shielding for long duration manned space missions," in *Proceedings of the 6th IAASS Conference, Montreal*, 2013.

[155] W. Von Braun, "Will mighty magnets protect voyagers to planets," *Popular Science*, vol. 198, p. 98100, 1969.

[156] V. Choutko, P. McIntyre, R. Romero, A. Sattarov, and S. Ting, "Design options for a superconducting toroid shield for manned spacecraft," tech. rep., Texas AM, MIT, CERN, 2007.

[157] S. Westover, R. Battiston, R. Meinke, S. Van Sciver, and R. Singleterry, "Active radiation shielding utilizing high temperature superconductors," tech. rep., NIAC Symposium, 2012.

[158] S. Westover, R. Meinke, W. Burger, A. Ilin, S. Nerolich, and S. Washburn, "Magnet architectures and active radiation shielding study-sr2s workshop," tech. rep., NIAC MAARSS, 2014.

[159] J. Barthel and N. Sarigul-Klijn, "Adaptive, readily morphing, optimized radiation shielding for transit habitats: Flyby mars mission," *Journal of Spacecraft and Rockets*, vol. 54, no. 6, pp. 1–6, 2017.

[160] M. Vuolo, M. Giraudo, R. Musenich, V. Calvelli, F. Ambroglini, W. Burger, and R. Battiston, "Monte carlo simulations for the space radiation superconducting shield project (sr2s)," *Life sciences in space research*, vol. 8, pp. 22–29, 2016.

[161] S. Washburn, S. Blattnig, R. Singleterry, and S. Westover, "Analytical-hzetrn model for rapid assessment of active magnetic radiation shielding," *Advances in Space Research*, vol. 53, no. 1, pp. 8–17, 2014.

[162] T. Malik, "Lunar shields: Radiation protection for moon-based astronauts," http://www.space.com/658-lunar-shields-radiation-protection-moon-based-astronauts.html, 2005.

[163] D. G. Angelis, J. Wilson, M. Clowdsley, J. Nealy, D. Humes, and J. Clem, "Lunar lava tube radiation safety analysis," *Journal of radiation research*, vol. 43, no. Suppl, pp. S41–S45, 2002.

[164] I. Schneider, A. Daga, P. de Leon, and G. Harris, "Interim report for the human exploration of the moon and mars: Space radiation protection and mitigation

strategies for a long term duration lunar base," in *40th International Conference on Environmental Systems*, p. 6220.

[165] A. R. Kennedy, "Biological effects of space radiation and development of effective countermeasures," *Life sciences in space research*, vol. 1, pp. 10–43, 2014.

[166] M. Cerri, W. Tinganelli, M. Negrini, A. Helm, E. Scifoni, F. Tommasino, M. Sioli, A. Zoccoli, and M. Durante, "Hibernation for space travel: impact on radioprotection," *Life sciences in space research*, vol. 11, pp. 1–9, 2016.

[167] S. Nambiar and J. T. Yeow, "Polymer-composite materials for radiation protection," *ACS applied materials & interfaces*, vol. 4, no. 11, pp. 5717–5726, 2012.

[168] S. A. Thibeault, C. C. Fay, S. E. Lowther, K. D. Earle, G. Sauti, J. H. Kang, C. Park, and A. M. McMullen, "Radiation shielding materials containing hydrogen, boron, and nitrogen: Systematic computational and experimental study. phase i – nasa niac final report," tech. rep., NASA NIAC Final Report, 2012.

[169] S. A. Thibeault, C. C. Fay, G. Sauti, J. H. Kang, and C. Park, "Us patent app: Radiation shielding materials containing hydrogen, boron and nitrogen," Nov. 19 2012. US Patent App. 13/694,325.

[170] L. Pohl and D. T. Britt, "The radiation shielding potential of ci and cm chondrites," *Advances in Space Research*, vol. 59, no. 6, pp. 1473–1485, 2017.

[171] J. Yang, G. Ma, X. Li, C. Liu, D. Yang, and S. He, "Effects of multilayer and multimaterial structures on space proton radiation protection," *Nuclear Instruments and Methods in Physics Research Section B: Beam Interactions with Materials and Atoms*, vol. 365, pp. 352–356, 2015.

[172] A. Emmanuel and J. Raghavan, "Influence of structure on radiation shielding effectiveness of graphite fiber reinforced polyethylene composite," *Advances in Space Research*, vol. 56, no. 7, pp. 1288–1296, 2015.

[173] Z. Shayer, "Radiation-shielding material using hydrogen-filled glass microspheres," June 21 2011. US Patent 7,964,859.

[174] N. Kuznetsov, R. Nymmik, M. Panasyuk, A. Denisov, and N. Sobolevsky, "Estimation of radiation risk for astronauts on the moon," *Cosmic Research*, vol. 50, no. 3, pp. 216–220, 2012.

[175] J. Sohn, S. Oh, and Y. Yi, "Lunar cosmic ray radiation environments during luna and lunar reconnaissance orbiter missions," *Advances in Space Research*, vol. 54, no. 6, pp. 1113–1118, 2014.

[176] G. Reitz, D. Matthiä, D. M. Hassler, R. Wimmer-Schweingruber, B. Ehresmann, C. Zeitlin, J. Guo, and J. Koehler, "Radiation measurements of the mars science lab radiation assessment detector (msl-rad) on the surface of mars," in *46th International Conference on Environmental Systems ICES2016 Vienna, Austria Conference Proceedings*, no. 437, pp. 3504–3512, 2016.

[177] C. La Tessa, S. Guetersloh, L. Heilbronn, J. Miller, L. Sihver, and C. Zeitlin, "Fragmentation of 1gev/nucleon iron ions in thick targets relevant for space exploration," *Advances in Space Research*, vol. 35, no. 2, pp. 223–229, 2005.

[178] W. Zhong, G. Sui, S. Jana, and J. Miller, "Cosmic radiation shielding tests for uhmwpe fiber/nano-epoxy composites," *Composites Science and Technology*, vol. 69, no. 13, pp. 2093–2097, 2009.

[179] J. W. Norbury, W. Schimmerling, T. C. Slaba, E. I. Azzam, F. F. Badavi, G. Baiocco, E. Benton, V. Bindi, E. A. Blakely, S. R. Blattnig, *et al.*, "Galactic cosmic ray simulation at the nasa space radiation laboratory," *Life sciences in space research*, vol. 8, pp. 38–51, 2016.

[180] M. Vallarta, "On the energy of cosmic radiation allowed by the earth's magnetic field," *Physical Review*, vol. 74, no. 12, p. 1837, 1948.

[181] D. Cooke, J. Humble, M. Shea, D. Smart, N. Lund, I. Rasmussen, B. Byrnak, P. Goret, and N. Petrou, "On cosmic-ray cut-off terminology," *Il Nuovo Cimento C*, vol. 14, no. 3, pp. 213–234, 1991.

[182] D. Matthiä, *The radiation environment in the lower atmosphere: A numerical approach*. PhD thesis, Kiel, Christian-Albrechts-Universität, Diss., 2009, 2009.

[183] M. Aguilar, J. Alcaraz, J. Allaby, B. Alpat, G. Ambrosi, H. Anderhub, L. Ao, A. Arefiev, P. Azzarello, E. Babucci, *et al.*, "The alpha magnetic spectrometer (ams) on the international space station: Part i–results from the test flight on the space shuttle," *Physics Reports*, vol. 366, no. 6, pp. 331–405, 2002.

[184] G. D. Badhwar, F. A. Cucinotta, and A. Konradi, "Shuttle measurements of galactic cosmic radiation let spectra," *Advances in Space Research*, vol. 18, no. 12, pp. 159–165, 1996.

[185] J. I. Vette, "The nasa/national space science data center trapped radiation environment model program, 1964-1991," tech. rep., National Space Science Data Center (NSSDC) World Data Center A for Rockets and Satellites (WDC-A-RS) National Aeronautics and Space Administration, 1991.

[186] C. Laird, "Studies of neutron and proton nuclear activation in low-earth orbit," tech. rep., NASA Marshall Spaceflight Center, 1982.

[187] M. Clowdsley, J. Wilson, J. Shinn, F. Badavi, J. Heinbockel, and W. Atwell, "Neutron environment calculations for low earth orbit," tech. rep., SAE Technical Paper, 2001.

[188] J. Wilson, F. Cucinotta, M. Golightly, J. Nealy, G. Qualls, F. Badavi, G. De Angelis, B. Anderson, M. Clowdsley, N. Luetke, *et al.*, "International space station: A testbed for experimental and computational dosimetry," *Advances in space research*, vol. 37, no. 9, pp. 1656–1663, 2006.

[189] J. W. Wilson, F. F. Badavi, M.-H. Y. Kim, M. S. Clowdsley, J. H. Heinbockel, F. A. Cucinotta, G. D. Badhwar, W. Atwell, and S. L. Huston, "Natural and induced environment in low earth orbit," tech. rep., NASA TM 2002 211668, 2002.

[190] J. C. McDowell, "The edge of space: Revisiting the karman line," *Acta Astronautica*, vol. 151, pp. 668–677, 2018.

[191] G. De Angelis, J. Clem, P. Goldhagen, and J. Wilson, "A new dynamical atmospheric ionizing radiation (air) model for epidemiological studies," *Advances in space research*, vol. 32, no. 1, pp. 17–26, 2003.

[192] W. Suparta and S. Zulkeple, "Spatial analysis of galactic cosmic ray particles in low earth orbit/near equator orbit using spenvis," in *Journal of Physics: Conference Series*, vol. 495, p. 012040, IOP Publishing, 2014.

[193] I. G. Usoskin, G. A. Bazilevskaya, and G. A. Kovaltsov, "Solar modulation parameter for cosmic rays since 1936 reconstructed from ground-based neutron

monitors and ionization chambers," *Journal of Geophysical Research: Space Physics*, vol. 116, no. A2, 2011.

[194] H. Wu, W. Atwell, F. A. Cucinotta, and C.-h. Yang, "Estimate of space radiation-induced cancer risks for international space station orbits - nasa tm 104818," tech. rep., NASA TM 104818, 1996.

[195] J. Barthel and N. Sarigul-Klijn, "Radiation production and absorption in human spacecraft shielding systems under high charge and energy galactic cosmic rays: Material medium, shielding depth, and byproduct aspects," *Acta Astronautica*, vol. 144, no. 1, pp. 254–262, 2018.

[196] R. Singleterry, "Radiation engineering analysis of shielding materials to assess their ability to protect astronauts in deep space from energetic particle radiation," *Acta Astronautica*, vol. 91, pp. 49–54, 2013.

[197] C. Sandridge, *Email:Model Calibration: OLTARIS User Feedback, dated January 14, 2018.* NASA Langley Research Center, 2018.

[198] J. E. Estevez, M. Ghazizadeh, J. G. Ryan, and A. D. Kelkar, "Simulation of hydrogenated boron nitride nanotube's mechanical properties for radiation shielding applications," *Int. J. Chem. Sci. Eng*, vol. 8, pp. 63–67, 2014.

[199] F. Xu, X. Jia, W. Lu, C. Zhou, Y. Guo, J. Fei, and C. Yang, "Utilization of trash for radiation protection during manned space missions," *Acta Astronautica*, vol. 151, pp. 585–594, 2018.

[200] F. Shayeganfar and R. Shahsavari, "Oxygen-and lithium-doped hybrid boron-nitride/carbon networks for hydrogen storage," *Langmuir*, vol. 32, no. 50, pp. 13313–13321, 2016.

[201] N. Sakhavand and R. Shahsavari, "Synergistic behavior of tubes, junctions, and sheets imparts mechano-mutable functionality in 3d porous boron nitride nanostructures," *The Journal of Physical Chemistry C*, vol. 118, no. 39, pp. 22730–22738, 2014.

[202] N. Sakhavand and R. Shahsavari, "Dimensional crossover of thermal transport in hybrid boron nitride nanostructures," *ACS applied materials & interfaces*, vol. 7, no. 33, pp. 18312–18319, 2015.

[203] Y. Zhang and X. Cheng, "Hydrogen storage on li coated bc3 honeycomb sheet," *Chinese Journal of Chemistry*, vol. 35, no. 8, pp. 1329–1332, 2017.

[204] S. R. Naqvi, G. S. Rao, W. Luo, R. Ahuja, and T. Hussain, "Hexagonal boron nitride (h-bn) sheets decorated with oli, ona, and li2f molecules for enhanced energy storage," *ChemPhysChem*, vol. 18, no. 5, pp. 513–518, 2017.

[205] D. Matthiä, B. Ehresmann, H. Lohf, J. Köhler, C. Zeitlin, J. Appel, T. Sato, T. Slaba, C. Martin, T. Berger, *et al.*, "The martian surface radiation environment–a comparison of models and msl/rad measurements," *Journal of Space Weather and Space Climate*, vol. 6, p. A13, 2016.

[206] B. J. Chow, T. Chen, Y. Zhong, and Y. Qiao, "Direct formation of structural components using a martian soil simulant," *Scientific reports*, vol. 7, no. 1, p. 1151, 2017.

[207] J. W. Norbury, K. Whitman, K. Lee, T. C. Slaba, and F. F. Badavi, "Comparison of space radiation gcr models to recent ams data," *Life sciences in space research*, vol. 18, pp. 64–71, 2018.

[208] J. L. Shinn and J. W. Wilson, "An efficient hzetrn (a galactic cosmic ray transport code)," tech. rep., NASA Technical Paper 3147, 1992.

[209] J. W. Wilson, L. W. Townsend, J. E. Nealy, S. Y. Chun, B. Hong, W. W. Buck, S. Lamkin, B. D. Ganapol, F. Khan, and F. A. Cucinotta, "Bryntrn: A baryon transport model," tech. rep., NASA Technical Paper 2887, 1989.

[210] J. L. Shinn, S. John, R. K. Tripathi, J. W. Norbury, J. W. Wilson, and L. W. Townsend, "Fully energy-dependent hzetrn (a galactic cosmic-ray transport code)," tech. rep., NASA Technical Paper TP-3243, 1992.

[211] T. C. Slaba, S. R. Blattnig, and F. F. Badavi, "Faster and more accurate transport procedures for hzetrn," tech. rep., NASA Technical Paper 2010-216213, 2010.

[212]

[213] S. M. Seltzer, "Conversion of depth-dose distributions from slab to spherical geometries for space-shielding applications," *IEEE Transactions on Nuclear Science*, vol. 33, no. 6, pp. 1292–1297, 1986.

[214] R. J. Moffat, "Describing the uncertainties in experimental results," *Experimental thermal and fluid science*, vol. 1, no. 1, pp. 3–17, 1988.

[215] L. De Broglie, "The wave nature of the electron," *Nobel lecture*, vol. 12, pp. 244–256, 1929.

[216] L. De Broglie, "Waves and quanta," *Nature*, vol. 112, no. 2815, p. 540, 1923.

[217] F. Logiurato, "Relativistic derivations of de broglie and planck-einstein equations," *Journal of Modern Physics*, vol. arXiv preprint, no. arXiv:1208.0119,

pp. 1–8, DOI: 10.4236/jmp.2014.51001, 2012.

[218] C. Davisson and L. H. Germer, "The scattering of electrons by a single crystal of nickel," *Nature*, vol. 119, no. 2998, p. 558, 1927.

[219] G. P. Thomson and A. Reid, "Diffraction of cathode rays by a thin film," *Nature*, vol. 119, no. 3007, p. 890, 1927.

[220] L. De Broglie, *Recherches sur la théorie des quanta*. PhD thesis, Migration-université en cours d'affectation, 1924.

[221] G. Lochak, "The evolution of the ideas of louis de broglie on the interpretation of wave mechanics," *Foundations of Physics*, vol. 12, no. 10, pp. 931–953, 1982.

[222] M.-C. Combourieu and H. Rauch, "The wave-particle dualism in 1992: A summary," *Foundations of physics*, vol. 22, no. 12, pp. 1403–1434, 1992.

[223] G. Lochak, "Louis de broglie's conception of physics," *Foundations of Physics*, vol. 23, no. 1, pp. 123–131, 1993.

[224] D. Bohm and B. Hiley, "The de broglie pilot wave theory and the further development of new insights arising out of it," *Foundations of Physics*, vol. 12, no. 10, pp. 1001–1016, 1982.

[225] J. S. Bell, "On the impossible pilot wave," *Foundations of Physics*, vol. 12, no. 10, pp. 989–999, 1982.

[226] Z. M. Zhang, *Nano/Microscale Heat Transfer*. McGraw-Hill Companies, 2007.

[227] C. E. Burkhardt and J. J. Leventhal, *Foundations of Quantum Physics*. Springer Science & Business Media, 2008.

[228] A. J. Hey and P. Walters, *The New Quantum Universe*. Cambridge University Press, 2003.

[229] R. P. Feynman, R. B. Leighton, and M. Sands, *Lectures on Physics, Vol. III*. Addison-Wesley Reading (Mass), 1965.

[230] N. P. BARDE, S. D. PATIL, M. K. Pravin, and P. B. Pranav, "Deriving time dependent schrödinger equation from wave-mechanics, schrödinger time independent equation, classical and hamilton-jacobi equations," *Leonardo Electronic Journal of Practices and Technologies*, vol. 14, no. 26, pp. 31–48, 2015.

[231] H. Ioannidou, "Explicit derivation of the relativistic schrödinger equation," *Il Nuovo Cimento B (1971-1996)*, vol. 79, no. 1, pp. 67–75, 1984.

[232] B. Baeumer, M. M. Meerschaert, and M. Naber, "Stochastic models for relativistic diffusion," *Physical Review E*, vol. 82, no. 1, p. 011132, 2010.

[233] R. Doak, R. Grisenti, S. Rehbein, G. Schmahl, J. Toennies, and C. Wöll, "Towards realization of an atomic de broglie microscope: helium atom focusing using fresnel zone plates," *Physical Review Letters*, vol. 83, no. 21, p. 4229, 1999.

[234] R. R. Letfullin and T. F. George, "Diffractive lens for matter-wave beams," in *Optical Components and Materials IV*, vol. 6469, pp. 64690N–1–12, International Society for Optics and Photonics, 2007.

[235] M. Arndt, O. Nairz, J. Vos-Andreae, C. Keller, G. Van der Zouw, and A. Zeilinger, "Wave–particle duality of c 60 molecules," *nature*, vol. 401, no. 6754, p. 680, 1999.

[236] D. L. Freimund, K. Aflatooni, and H. Batelaan, "Observation of the kapitza–dirac effect," *Nature*, vol. 413, no. 6852, p. 142, 2001.

[237] V. Balykin, "Atomic diffraction microscope of the de broglie waves," *Laser Physics*, vol. 20, no. 1, pp. 47–51, 2010.

[238] T. Juffmann, S. Nimmrichter, M. Arndt, H. Gleiter, and K. Hornberger, "New prospects for de broglie interferometry," *Foundations of Physics*, vol. 42, no. 1, pp. 98–110, 2012.

[239] S. Gerlich, S. Eibenberger, M. Tomandl, S. Nimmrichter, K. Hornberger, P. J. Fagan, J. Tüxen, M. Mayor, and M. Arndt, "Quantum interference of large organic molecules," *Nature communications*, vol. 2, p. 263, 2011.

[240] S. Eibenberger, S. Gerlich, M. Arndt, M. Mayor, and J. Tüxen, "Matter–wave interference of particles selected from a molecular library with masses exceeding 10000 amu," *Physical Chemistry Chemical Physics*, vol. 15, no. 35, pp. 14696–14700, 2013.

[241] T. Young, "I. the bakerian lecture. experiments and calculations relative to physical optics," *Philosophical transactions of the Royal Society of London*, vol. 94, pp. 1–16, 1804.

[242] T. Sandin, "In defense of relativistic mass," *American Journal of Physics*, vol. 59, no. 11, pp. 1032–1036, 1991.

[243] R. Deutschmann, W. Ertmer, and H. Wallis, "Reflection and diffraction of atomic de broglie waves by an evanescent laser wave," *Physical Review A*, vol. 47, no. 3, p. 2169, 1993.

[244] D. Kouznetsov and H. Oberst, "Scattering of atomic matter waves from ridged surfaces," *Physical Review A*, vol. 72, no. 1, p. 013617, 2005.

[245] H. Oberst, D. Kouznetsov, K. Shimizu, J.-i. Fujita, and F. Shimizu, "Fresnel diffraction mirror for an atomic wave," *Physical review letters*, vol. 94, no. 1, p. 013203, 2005.

[246] B. Chen and C. P. McKay, "Radiation shielding systems using nanotechnology," Apr. 12 2011. US Patent 7,923,709.

[247] L. Popa-Simil and C. I. Muntele, "Nano-structured nuclear radiation shielding," Nov. 29 2011. US Patent 8,067,758.

[248] O. S. Poggi and M. P. Vecchio, "Passive radiation shield," Aug. 8 2017. US Patent 9,728,289.

[249] D. Bohm, *Causality and chance in modern physics*. Routledge, 2004.

[250] C. Sandridge, *Email:Space Radiation Shielding Blue Sky Workshop, dated August 10, 2018*. NASA Langley Research Center, 2018.

[251] J.-M. Lévy, "A simple derivation of the lorentz transformation and of the accompanying velocity and acceleration changes," *American Journal of Physics*, vol. 75, no. 7, pp. 615–618, 2007.

[252] W. Rindler, *Introduction to special relativity*. International Atomic Energy Agency (IAEA), 1991.

[253] D. J. Griffiths, *Introduction to electrodynamics*. Prentice Hall, 2013.

[254] H. Paul, "The stopping power of matter for positive ions," in *Modern practices in radiation therapy*, InTech, 2012.

[255] B. Weaver and A. Westphal, "Energy loss of relativistic heavy ions in matter," *Nuclear Instruments and Methods in Physics Research Section B: Beam Interactions with Materials and Atoms*, vol. 187, no. 3, pp. 285–301, 2002.

[256] T. Slaba, "Radiation transport methods for space applications," tech. rep., NASA Space Radiation Summer School Brookhaven National Laboratory June 19, 2015, 2015.

[257] J. Norbury, "Space radiation transport results," tech. rep., NASA Space Radiation Summer School June 3 - 26, 2015 Brookhaven National Laboratory, 2015.